# Modélisation multiphysique de flammes turbulentes suitées avec la prise en compte des transferts radiatifs et des transferts de chaleur pariétaux.

Pedro Rodrigues

université PARIS-SACLAY

NNT : 2018SACLC041

CentraleSupélec

# Modélisation multiphysique de flammes turbulentes suitées avec la prise en compte des transferts radiatifs et des transferts de chaleur pariétaux

Thèse de doctorat de l'Université Paris-Saclay
préparée à CentraleSupélec

École doctorale n°579 : Sciences mécaniques et énergétiques, matériaux et géosciences (SMEMAG)
Spécialité de doctorat : Combustion

Thèse présentée et soutenue à Gif-sur-Yvette, le 08/06/2018, par

**Pedro Rodrigues**

Composition du Jury :

| | |
|---|---|
| Bénédicte Cuenot<br>CFD/Combustion Project Leader, CERFACS | Rapporteur |
| Abderrahman El Bakali<br>Professeur, Université de Lille 1 (PC2A – UMR 8522) | Rapporteur |
| Jean Caudal<br>Ingénieur, Air Liquide | Examinateur |
| Klaus Peter Geigle<br>Researcher, DLR | Examinateur |
| Vincent Giovangigli<br>Directeur de recherche, Ecole Polytechnique (CMAP - UMR 7641) | Président du jury |
| Nasser Darabiha<br>Professeur, CentraleSupélec (EM2C - UPR 288) | Directeur de thèse |
| Benedetta Franzelli<br>Chargée de recherche, CentraleSupélec (EM2C - UPR 288) | Co-Encadrante |
| Olivier Gicquel<br>Professeur, CentraleSupélec (EM2C - UPR 288) | Co-Encadrant |
| Ronan Vicquelin<br>Maître de conférences, CentraleSupélec (EM2C - UPR 288) | Co-Encadrant |

Thèse de doctorat

Laboratoire d'Energétique Moléculaire
& Macroscopique, Combustion
EM2C – UPR288

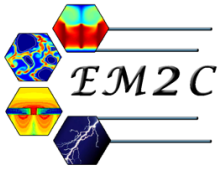



**Université Paris-Saclay**
Espace Technologique / Immeuble Discovery
Route de l'Orme aux Merisiers RD 128 / 91190 Saint-Aubin, France

# Remerciements

Je souhaite remercier tout d'abord les différents membres de mon jury. Merci à Abderrahman El Bakali et à Bénédicte Cuenot pour avoir accepter d'être les rapporteurs de mon manuscript. Merci également à Vincent Giovangigli qui a accepté d'être le président de ce jury, ainsi qu'à Klaus Peter Geigle et Jean Caudal pour avoir accepter leurs rôles d'examinateurs. Je vous remercie à tous pour vos différentes remarques que ce soit à la lecture du manuscript ou à la séance de questions pendant la soutenance qui ont permis d'enrichir nettement le travail en identifiant et discutant des futurs travaux nécessaires sur le sujet de cette thèse.

Je tiens également à remercier chaleureusement toutes les personnes qui ont encadré et largement contribué à ce travail : Nasser Darabiha, mon directeur de thèse ainsi que mes co-encadrants, Benedetta Franzelli, Olivier Gicquel et Ronan Vicquelin. Chacun d'entre vous a apporté sa pierre à l'édifice : Nasser à travers la mise à disposition du code Regath et toute ton expérience et tes conseils, Benedetta à travers ton encadrement quotidien et ton expertise grandissante sur le domaine des suies, Olivier à travers ton expertise sur le rayonnement, la mise à disposition du code Rainier et ta capacité à me donner les bons conseils pour pouvoir arriver au but final de cette thèse et enfin Ronan, pour ta capacité d'analyse multi-disciplinaire, la mise à disposition des codes Commcomb et Agath, la rigueur que tu m'as transmis et les nombreux échanges forts intéressants sur tous les aspects de cette thèse. J'ai énormément appris auprès de vous tous, merci.

Je remercie également Bernard Labégorre, Youssef Joumani, Jean Caudal et Thierry Schuller pour m'avoir fait confiance et avoir participé également à ce travail à travers le suivi de la chaire Oxytec entre le CNRS, CentraleSupélec et Air Liquide dans laquelle cette thèse s'est inscrite.

Je pense enfin à tous les doctorants et post-doctorants que j'ai pu rencontré au cours de ces trois années. Tout d'abord et bien sûr tous mes collègues de bureau : Wenjie Tao, Antoine Renaud, Benjamin Robbes, Milan Pelletier, Robin Nez, Pierre Mariotto, Augustin Tibere-Inglesse, Ciprian Dumitrache, Nancy Kings, Meng Xia, Mathieu Blanchard, Mathieu Roussillo, Hernando Maldon-

ado et Arnaud Gallant. Je remercie aussi mes collègues de "point doctorants" avec qui on a très souvent partagé et résolu nos problèmes : Théa Lancien, Lorella Palluotto, Arthur Degenève, Nicolas Dumont, Chaï Koren et Maxime Philip. Et puis les autres, anciens ou nouveaux, avec qui j'ai également beaucoup échangé : Amanda Pieyre, Leo Cunha, Pedro Volpiani, Mélody Cailler, Erwan Pannier, Agnes Bodor, Kevin Torres, Kevin Prieur, Cédric Mehl, Giampaolo Maio, Abigail De La Rosa, Laurent Tranchant, Gizem Okyay, Macole Sabat, Davy Nayigizente, Lantao Yu, Guillaume Vignat, Livia Tardelli, Nicolas Minesi, David Mercier, Aurélien Genot, Mohammed Essadki, Yacine Bechane, Quentin Binauld, Yi Ding, Valentin Dupif, Thomas Epalle, Renaud Gaudron, Paul Jourdaine, Wafa Bandhaou, Manuel Gonzalez, Jan Mateu Armengol, Marco Gatti, Giunio De Luca, Adrien Chatelier, Claire Beauchesne, et bien d'autres que j'ai sûrement oublié de citer et je m'en excuse par avance ! En tout cas, plein de nouveaux amis avec qui je resterai proche pendant longtemps j'espère !

Un grand merci aussi à l'ensemble du personnel administratif et technique du laboratoire pour toutes les aides et services qu'ils ont pu m'apporter et qu'ils apportent tous les jours : Nathalie Rodrigues, Brigitte Llobel, Noï Lavaud, Sébastien Turgis, Jean-Michel Dupays, Clément Mirat, mais aussi Erika Jean Bart, Yannick Le Teno pour les différentes aides pendant les cours d'activités expérimentales et Philippe pour les différents échanges que nous avons pu avoir.

Merci aussi à Franck Richecoeur et à Thierry Schuller pour m'avoir permis de réaliser des missions d'enseignement en parallèle de ma thèse. Ce fût une expérience très enrichissante et j'espère avoir encore l'occasion d'enseigner ces prochaines années à CentraleSupélec !

Je remercie également tous mes amis (centraliens des promos 2013-2014, thalésiens et ex-thalésiens, grenoblois, ...) qui ont pu ou pas venir à ma soutenance mais qui l'ont vécu à travers de multiples soirées où j'essayais de vous expliquer le sujet et les avancées de ma thèse !

Enfin, je remercie toute ma famille, qui sait toujours être là dans les étapes importantes de ma vie et également me soutenir et m'encourager. Merci d'avoir été présent pour la soutenance et d'avoir grandement contribuer à l'organisation du pot de thèse. Sans vous, ça n'aurait pas été pareil, c'est sûr !

À bientôt à tous !

# Abstract

Numerical simulations are used by engineers to design robust and clean industrial combustors. Among pollutants, soot control is an urgent societal issue and a political-industrial priority, due to its harmful impact on health and environment. Soot particles size plays an important role in its negative effect. It is therefore important to predict not only the total mass or number of emitted particles, but also their population distribution as a function of their size. In addition, soot particles can play an important role in thermal radiation. In confined configurations, controlling heat transfer related to combustion is a key issue to increase the robustness and the life cycle of combustors by avoiding wall damages. In order to correctly determine these heat losses, radiative and wall convective heat fluxes must be accounted for. They depend on the wall temperature, which is controlled by the conjugate heat transfer between the fluid and solid domains. Heat transfer impacts the flame stabilization, pollutants formation and soot production itself. Therefore, a complex coupling exists between these phenomena and the simulation of such a multi-physics problem is today recognized as an extreme challenge in combustion, especially in a turbulent flow, which is the case of most industrial combustors. Thus, the objective of this thesis is to develop a multi-physics modeling enabling the simulation of turbulent sooting flames including thermal radiation and wall heat transfer. The retained methods based on Large-Eddy Simulation (LES), a soot sectional model, conjugate heat transfer, a Monte Carlo radiation solver are combined to achieve a state-of-the-art framework. The available computational resources make nowadays affordable such simulations that will yield present-day reference results. The manuscript is organized in three parts. The first part focuses on the definition of a detailed model for the description of soot production in laminar flames. For this, the sectional method is retained here since it allows the description of the particle size distribution (PSD). The method is validated on laminar premixed and diffusion ethylene/air flames before analyzing the dynamics of pulsed diffusion flames. In the second part, an LES formalism for the sectional method is developed and used to investigate two different turbulent flames: a non-premixed jet flame and a confined pressurized swirled flame. Predicted temperature and soot volume fraction levels and topologies are compared to experimental data. Good predictions are obtained and the different soot processes in such flames are analyzed through the

study of the PSD evolution. In these first simulations, wall heat losses rely on experimental measurements of walls temperature, and a coarse optically-thin radiation model. In the third part, to increase the accuracy of thermal radiation description, a Monte Carlo approach enabling to solve the Radiative Transfer Equation with detailed radiative properties of gaseous and soot phases is used and coupled to the LES solver. This coupled approach is applied for the simulation of the turbulent jet flame. Quality of radiative fluxes prediction in this flame is quantified and the nature of radiative transfers is studied. Then, a whole coupled modeling of turbulent combustion accounting for soot, conjugate heat transfer and thermal radiation is proposed by coupling three dedicated codes. This strategy is applied for a high-fidelity simulation of the confined pressurized burner. By comparing numerical results with experimental data, the proposed approach enables to predict both the wall temperature and the flame stabilization. The different simulations show that soot formation processes are impacted by the heat transfer description: a decrease of the soot volume fraction is observed with increasing heat losses. This highlights the requirement of accurate description of heat transfer for future developments of soot models and their validation.

# Résumé

Les simulations sont utilisées pour concevoir des chambres de combustion industrielles robustes et peu polluantes. Parmi les polluants, l'émission de particules de suies constitue une question sociétale et une priorité politico- industrielle, en raison de leurs impacts néfastes sur la santé et l'environnement. La taille des particules de suies joue un rôle important sur ces effets. Il est donc important de prévoir non seulement la masse totale ou le nombre de particules générées, mais également leur distribution en taille (PSD). De plus, les suies peuvent jouer un rôle important dans le rayonnement thermique. Dans des configurations confinées, la prédiction des transferts de chaleur est une question clé pour augmenter la robustesse des chambres de combustion. Afin de déterminer correctement ces transferts, les flux radiatifs et de conducto-convectifs aux parois doivent être pris en compte. Enfin, la température pariétale est aussi contrôlée par les transferts conjugués de chaleur entre les domaines fluides et solides. L'ensemble de ces transferts thermiques impactent la stabilisation de la flamme, la formation de polluants et la production de suies elle-même. Il existe donc un couplage complexe entre ces phénomènes et la simulation d'un tel problème multiphysique est aujourd'hui reconnu comme un important défi. Ainsi, l'objectif de cette thèse est de développer une modélisation multiphysique permettant la simulation de flammes suitées turbulentes avec le rayonnement thermique et les transferts conjugués de chaleur associés aux parois. Les méthodes retenues sont basées sur la Simulation aux Grandes Échelles (LES), une description en taille des suies, des transferts conjugués et un code Monte Carlo pour le rayonnement. La combinaison de telles approches est réalisable grâce aux ressources de calcul aujourd'hui disponibles afin d'obtenir des résultats de référence. Le manuscrit est organisé en trois parties. La première partie se concentre sur le développement d'un modèle détaillé pour la description de la production de suies dans les flammes laminaires. Pour cela, la méthode sectionnelle est retenue ici car elle permet la description de la PSD. La méthode est validée sur des flammes laminaires éthylène/air. Dans la deuxième partie, un formalisme LES spécifique à la méthode sectionnelle est développé et utilisé pour étudier deux flammes turbulentes : une flamme jet non-prémélangée et une flamme swirlée pressurisée confinée. Les champs de température et de fraction volumique de suies sont comparés aux données expérimentales. De bonnes prédictions sont obtenues et l'évolution des particules de suies dans de telles

flammes est analysée à travers l'étude de l'évolution de leur PSD. Dans ces premières simulations, les pertes de chaleur aux parois reposent sur des mesures expérimentales de la température aux parois, et un modèle de rayonnement simple. Dans la troisième partie, une approche Monte Carlo permettant de résoudre l'équation de transfert radiatif avec des propriétés radiatives détaillées des phases gazeuse et solide est utilisée et couplée au solveur LES. Cette approche est appliquée à l'étude de la flamme jet turbulente. La prédiction des flux thermiques est comparée aux données expérimentales et la nature des transferts radiatifs est étudiée. Ensuite, une modélisation couplée de la combustion turbulente prenant en compte la production de suies, les transferts conjugués de chaleur et le rayonnement thermique est proposée en couplant les trois codes dédiés. Cette stratégie est appliquée pour la simulation du brûleur pressurisé confiné. L'approche proposée permet à la fois de prédire la température des parois et la bonne stabilisation de la flamme. Les processus de formation de suies se révèlent être affectés par la modélisation des transferts thermiques. Ceci souligne l'importance d'une description précise de ces transferts thermiques dans les développements futurs de modèles de production de suies et leur validation.

# Contents

# Introduction

## Global context

Today, 81,1 % of the world's total energy supply is based on fossil resources (Fig. 1(a)). While, use of other resources for primary energy supplies grow (as observed between 1973 and 2014 in Fig. 1(b)), fossils and therefore combustion processes represent the major resource for world's energy supply. It can also be observed in Fig. 1(a), that the total demand on energy is still increasing. This implies strong issues on both ability of producers to respond to this demand and their capacity to provide such energy while preserving environment. It is then necessary to face the uncertain availability of hydrocarbon resources, and to avoid the harmful emissions of their combustion processes.

It is well known that $CO_2$, one of the main combustion products, has a strong impact on global warning. However, it is not the only one: incomplete combustion products, such as carbon monoxide, nitrogen oxides, unburned hydrocarbons and soot particles have also an important impact on global warning, but also in a more general way, on environment and health diseases. That is why mastering the different processes leading to the formation of such pollutants is an important issue.

In this thesis, we focus on the study of soot particles formation. These particles are generally issued from incomplete fuel rich combustion. They can be responsible of high radiation fluxes in combustors, which can be desired or not depending on the industrial applications. Then, radiative heat transfer is also studied in details in this thesis.

Next paragraphs detail first the different issues linked to negative impacts of soot particles emission as a pollutant, but also their applications in some industries where their high radiative contributions are used in order to enhance industrial processes.

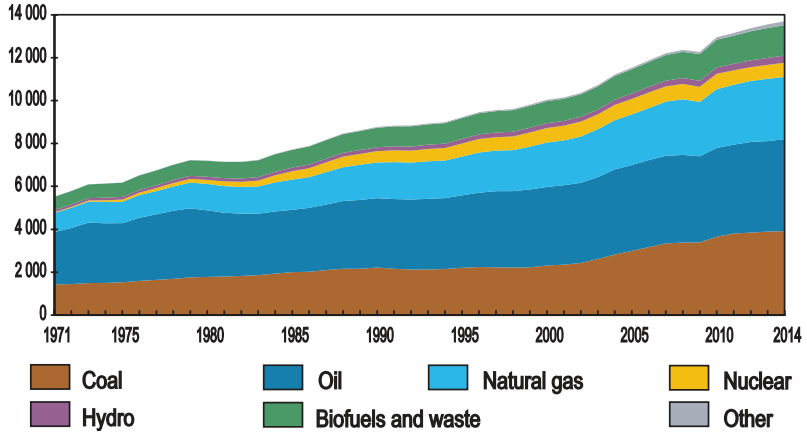


(a) World total primary energy supply from 1971 to 2014 by fuel (Mtoe) including international aviation and international marine bunkers.

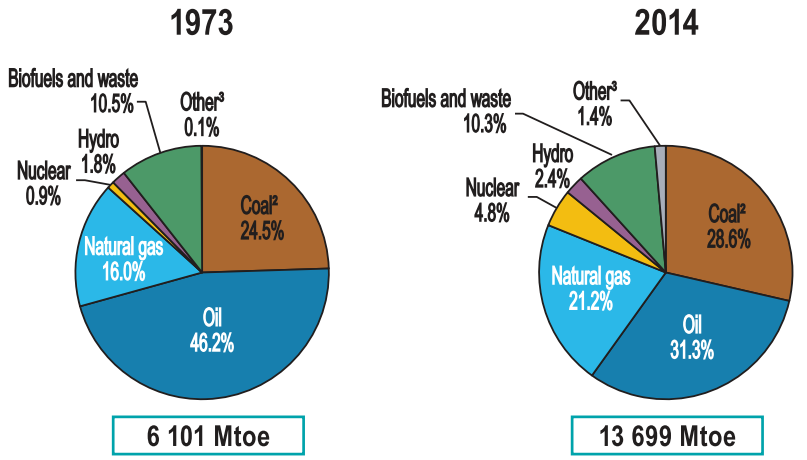


(b) 1973 and 2014 fuel shares of total primary energy supply.

**Figure 1:** *Total primary energy supply by fuel. The "Other" category includes geothermal, solar, wind, and heat primary supply (from IEA (2016)).*

# Negative impacts of soot particles emission

## Impact on health

One of the main issues of soot particles emission is human health. Figure 2 illustrates the different risks associated to the size of deposited particles. Exposition to soot particles can lead to multiple health effects (EPA 1999):

- Changes in lung function and increased respiratory symptoms,
- Changes in lung tissues and structure,
- Altered respiratory defense mechanisms,
- Aggravation of respiratory and cardiovascular diseases,
- Premature mortality.

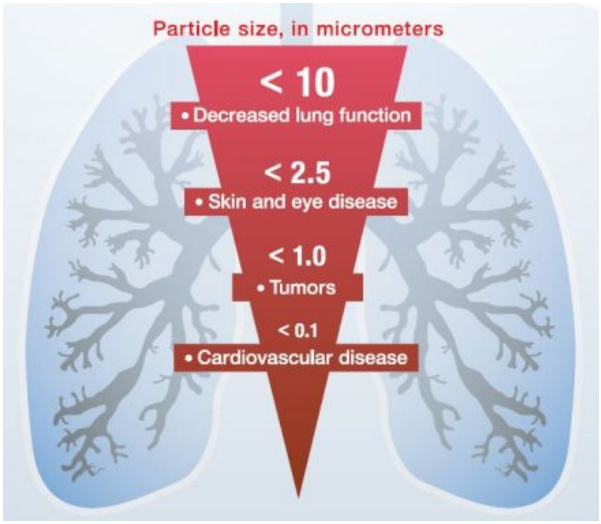


**Figure 2:** *Health risks according to particle size (extracted from Brüning (2006)).*

The thinest particles, named PM 0.1, corresponding to particles with a diameter lower than 100 nm, and which can infiltrate deep into the lungs (Donaldson et al. 2005), can lead to cardiovascular diseases. Tumors can be enhanced from PM 1 (particles with diameter lower than 1 $\mu$m) exposition, skin and eye diseases from PM 2.5 (particles with diameter lower than 2.5 $\mu$m) exposition and decreased lung function from PM 10 (particles with diameter lower than 10 $\mu$m) exposition. A recent study from O'Connor et al. (2008) has also shown that risks of asthma and other pulmonary diseases are enhanced when exposing children to PM 2.5.

## Impact on atmospheric pollution and global warming

Soot particles also largely contribute on atmospheric pollution, soiling, visibility degradation, but also safety effects for aircraft from reduced visibility (EPA 1999). Numerous worldwide agencies track such soot particles emissions, such as Air Parif which tracks particles emissions of different sizes in the Ile-de-France region arround Paris, France. Figure 3 illustrates the evolution of the mean PM 10 concentrations over one year, for 2007, 2010, 2013 and 2016.

While recent regulations (detailed hereafter) have enabled a large reduction of such particles emission along years, pics of PM 10 concentration are still observed (Fig. 4). Indeed, such particles are small enough to be transported in the atmosphere through the different meteorological events, instead of being deposed on the ground due to their weight. Then, when meteorological conditions do not transport and disperse such particles, they stay in suspension near their emission point. They are also responsible for part of the stratospheric ozone damage (Kamm et al. 1999; Shiraiwa et al. 2011).

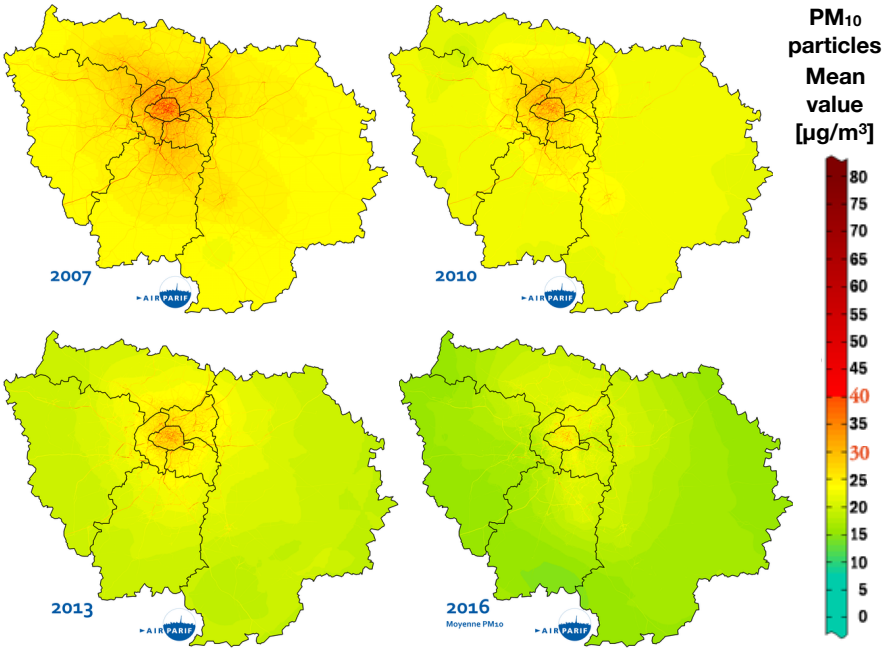


**Figure 3:** *Evolution of mean PM 10 concentrations over one year in the Ile-de-France region (data from AirParif (2017))*

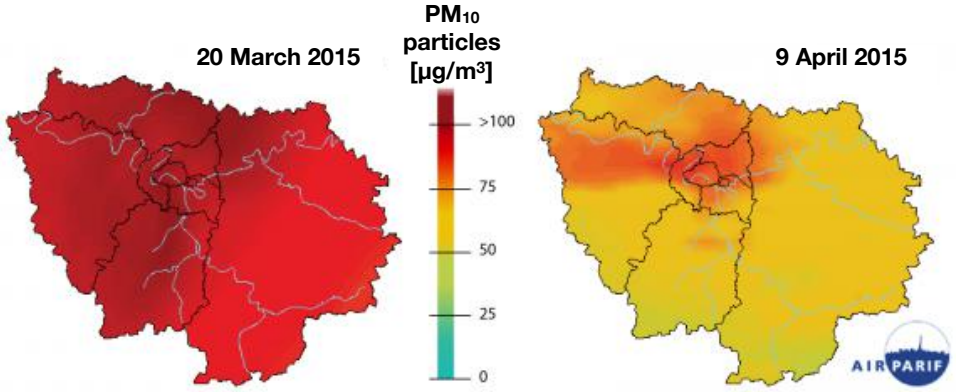


**Figure 4:** *Recent pics of PM 10 concentrations in Ile-de-France region (data from AirParif (2017))*

Soot particles also contribute in a more general manner to global warming (Jacobson 2002). To illustrate this, the radiative forcing caused by aviation operations can be analyzed. Radiative forcing corresponds to the difference between energy absorbed by the Earth and energy radiated back to space. When Earth receives more incoming energy that it radiates to space, a positive radiative forcing is observed and increases Earth warming. Figure 5 quantifies

such effects on total radiative forcing based on 2005 emissions and forecasts for 2020 and 2050 with contribution of sulfate, $CH_4$, $CO_2$, $O_3$, contrails, $H_2O$ and black carbon (soot). Soot plays then also a role on general global warming. Indeed, black carbon aerosols absorb sunlight and then warm the atmosphere. They contribute also to clouds dissolution due to global warming. The global atmosphere temperature increase due to black carbon emissions is estimated to 0.14 K between 1957 and 2006 (Quaas 2011).

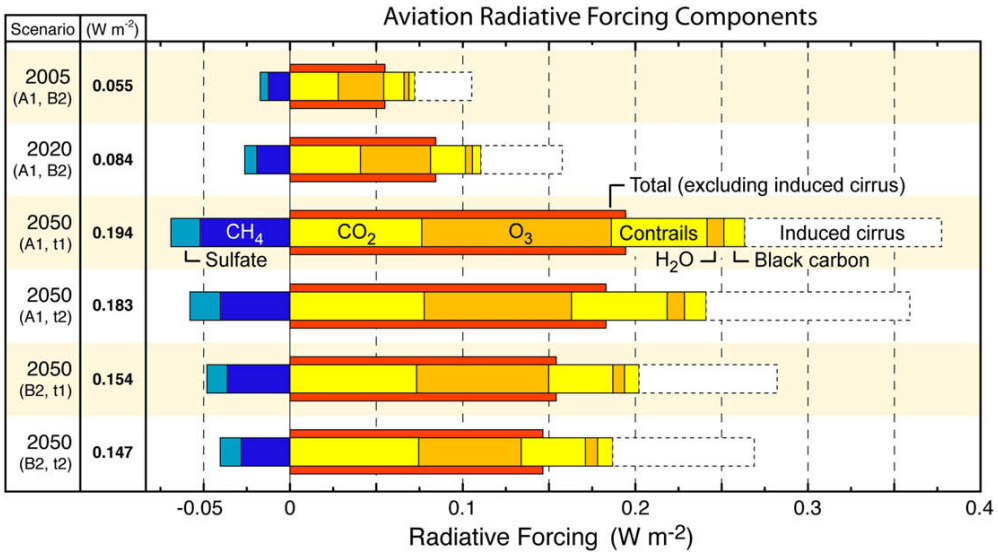


**Figure 5:** *Aviation Radiative Forcing components for 2005, 2020 and 2050 forecast for four different scenarios A1(t1), A1(t2), B1(t1), and B1(t2) (not detailed here) (extracted from Lee et al. (2009)).*

# Soot particles and industry

## Automotive and aeronautical industries

In automotive industry, internal combustion engines reactions between fuel and air provide the power supply, but also generate pollutants. The way this combustion is realized classifies the cars in three different categories: Diesel, Gasoline Direct Injection (DI) and Gasoline spark engines. For a spark engine, ignition is generally triggered by a spark plug, and the propagation of a premixed fuel/air flame is obtained. For a Diesel or a DI engine, auto-ignition is realized at high temperature and pressure and a diffusion flame between a very fuel rich region near fuel spray and air is obtained. The efficiency of spark engines is limited by the possible auto-ignition of the mixture: low compression ratio has to be considered. In diesel or DI engines however, as auto-ignition is used to control the combustion process, high pressure can be used. Then, in general, Diesel and DI engines are more efficient than classical spark engines.

Diesel has also a higher heating value compared to gasoline. All these reasons made Diesel engines widely used in European Union during the last decades. Figure 6 illustrates these trends in several countries of the Western Europe with the proportion of Diesel powered cars among the new cars sales. An important increase of Diesel powered cars can be noticed from 1990 to 2012 in Western Europe, from 14 % until 56%, with even some countries as France, Portugal, Spain and Ireland, where pic values of respectively 77%, 69%, 71%, and 73% have been attained.

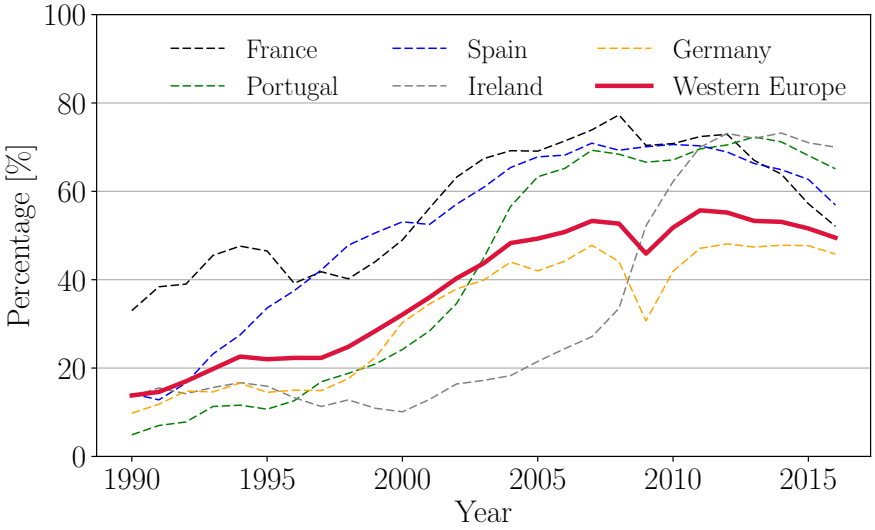


**Figure 6:** *Percentage of Diesel powered cars among the new cars sales in Western Europe, France, Portugal, Spain, Ireland and Germany from 1985 to 2016 (Source: ACEA (2017)).*

Non-premixed combustion process implies regions with very poor and very rich equivalence ratios. Pollutants formation is indeed very sensitive to equivalence ratio and temperature. Figure 7 illustrates the evolution of CO, $NO_x$ and soot emissions according to the mixture equivalence ratio and local temperature. Locally rich mixtures lead to soot formation whereas near-stoechiometric and lean mixtures at high temperatures lead to $NO_x$ formation. At the same time, low temperatures lead to CO formation. Then, appropriate burning conditions need to be set up in order to minimize such pollutants emissions.

As mentioned previously, the European union and other controlling agencies increase the control of such emissions with more and more drastic norms. Figure 8 presents the evolution of EURO norms (European emission standards) for diesel and gasoline engines that manufacturers must comply. HC corresponds to hydrocarbons (such as soot aromatic precursors), PM corresponds to particulate matter, PN corresponds to particles with a diameter larger than 23 nm, THC corresponds to total hydrocarbons emission and NMHC correspond to

non-methane hydrocarbons. In particular, norms on particulate matter (soot) have been divided by respectively 28 and 19 between 1992 and 2014 for diesel and spark ignition engines. From Euro 5 norms (respectively Euro 6), norms on particle number have also been introduced for Diesel (respectively Gasoline) engines. Therefore, understanding of soot formation processes and soot particles size distributions mechanisms are crucial in order to correctly comply with these new regulations.

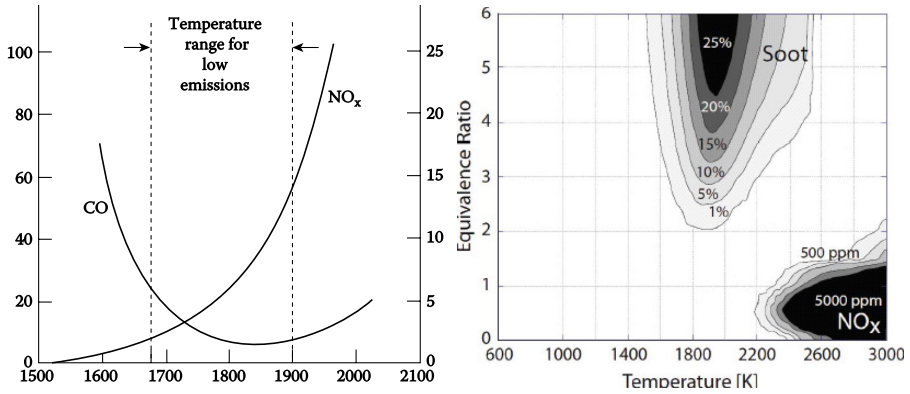


**Figure 7:** *Evolution of pollutants formation according to local burning conditions. Left: Influence of primary-zone temperature on* CO *and* $NO_x$ *emissions (extracted from Lefebvre (1998)). Right: Equivalence ratio and temperature effects on soot and* $NO_x$ *formation (extracted from Kamimoto and Bae (1988)).*

These increasingly restrictive norms, especially for diesel engines, lead recently some manufacturers to not respect law. This has been the case with the *Diesel-gate* in 2015, where the Volkswagen group was convicted of having intentionally programmed more than eleven million diesel engines to emit less $NO_x$ during their emissions testing than during their real-world driving (EPA2015 ). In a political context, several cities, such as Rome or Paris, plan to ban diesel engines from city centre by 2025. That is why, since 2015, as it can be clearly observed in Fig. 6, the percentage of Diesel powered cars among the new cars sales is decreasing.

In USA, similar regulations have been instaured by the United States Environmental Protection Agency (EPA). In 2011, McCubbin (2011) estimated that such standards have avoided per year, 35 700 premature deaths, 2 350 heart attacks, 23 290 hospital and emergency room visits, 29 800 cases of acute bronchitis and 1.4 million of aggravated asthma cases, proving then the efficiency of such regulations.

The same issues appear in the aeronautical industry. As the RPK (revenue passenger-kilometers calculated as the sum of the number of passengers times

the number of kilometers traveled for each flight) grows faster and faster, the fuel consumption in aeronautical industry increases too, as well as aviation $CO_2$ emissions (see Fig. 9). Indeed, impact of aviation in total $CO_2$ emissions is not negligible and it continues growing: it constituted 2.5% of total $CO_2$ emissions in 2007.

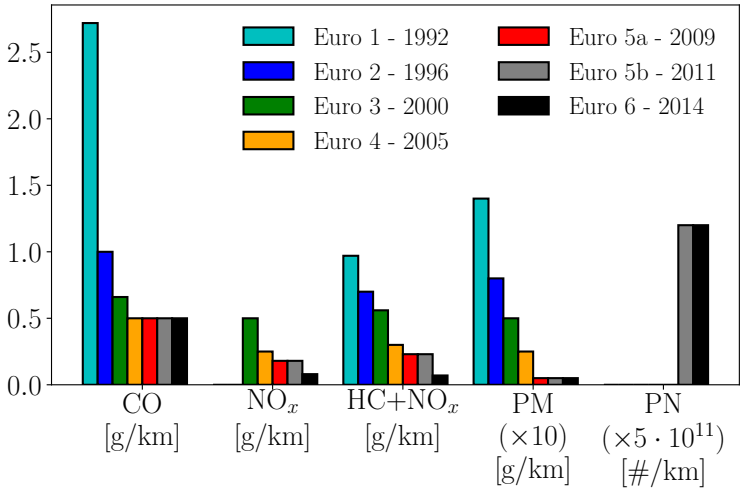


(a) Diesel engines

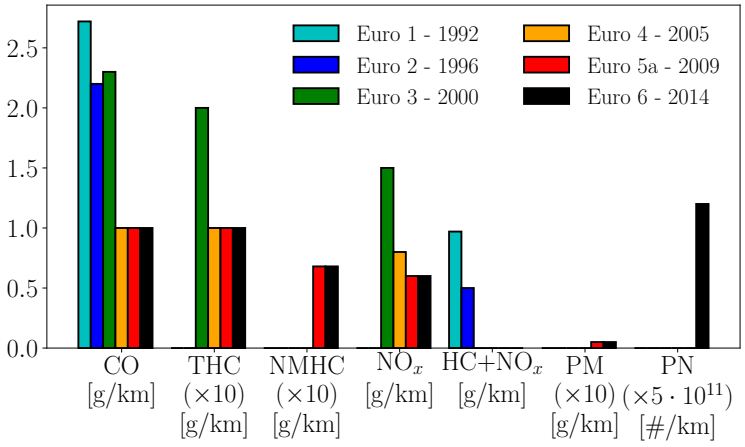


(b) Gasoline engines

**Figure 8:** *Euro standards for each pollutant type and colored by standard for diesel and gasoline engines*

This more and more frequent use of airplanes implies also changes in atmosphere composition for several species: $CO_2$, $NO_x$, $H_2O$, $SO_x$, HC and soot, participating to pollution but also climate change. Figure 10 represents schematically such changes on atmospheric pollutant concentrations.

Then, in order to face these increases in pollutants emissions from aviation operations, and in the context of the COP21, the 21$^{th}$ Conference Of Parties of the United Nations Framework Convention on Climate Change (UNFCCC) organized in Paris in 2015, ICAO has adopted in 2017 new $CO_2$ emissions standard for aircraft. $NO_x$ emissions standards have also been adopted in 2012 by ICAO. Emissions standards for particulate matter emissions are also planned. Development of methodologies for predicting soot emissions have been recently enhanced by the aeronautical industry: as an example, the SOPRANO European project, that gathers several European laboratories and industrials, aims at boost investigation efforts about understanding of soot formation processes.

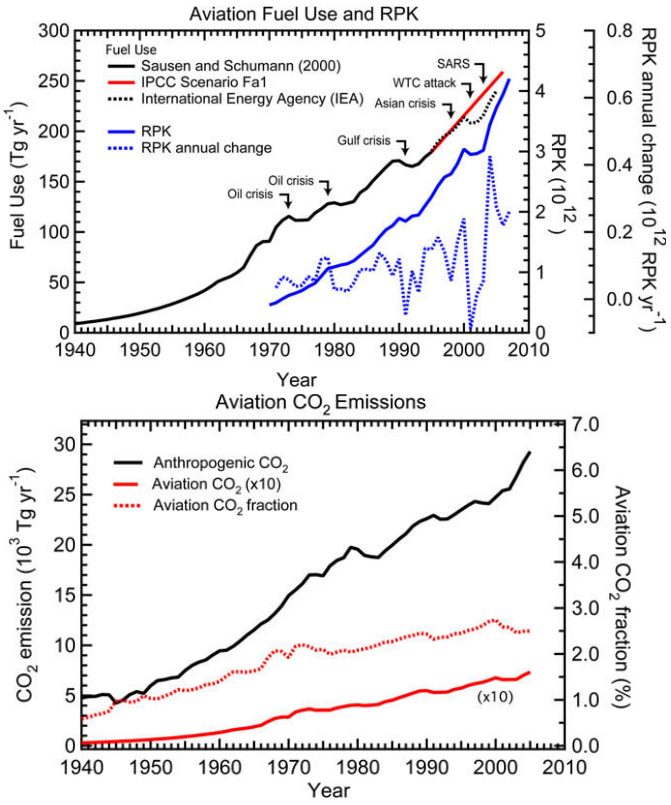


**Figure 9:** ***(Top)*** *Aviation fuel usage beginning in 1940 from Sausen and Schumann (2000) and extended with data from IEA (2007) and the IPCC Fa1 scenario of Baughcum et al. (1999). The arrows indicate world events that potentially threatened global aviation use. Also shown is the growth in air passenger traffic from 1970 to 2007 in billions (1012) of revenue passenger kilometers (RPK) (near right hand axis) (source: ICAO, 19 Sept. 2007) and the annual change in RPK.* ***(Bottom)*** *Growth in* $CO_2$ *emissions in Tg* $CO_2 \cdot yr^{-1}$ *for all anthropogenic activities and from aviation fuel burn (left hand axis), and the fraction of total anthropogenic CO2 emissions represented by aviation CO2 emissions (%) (right hand axis).*
*(extracted from Lee et al. (2009)).*

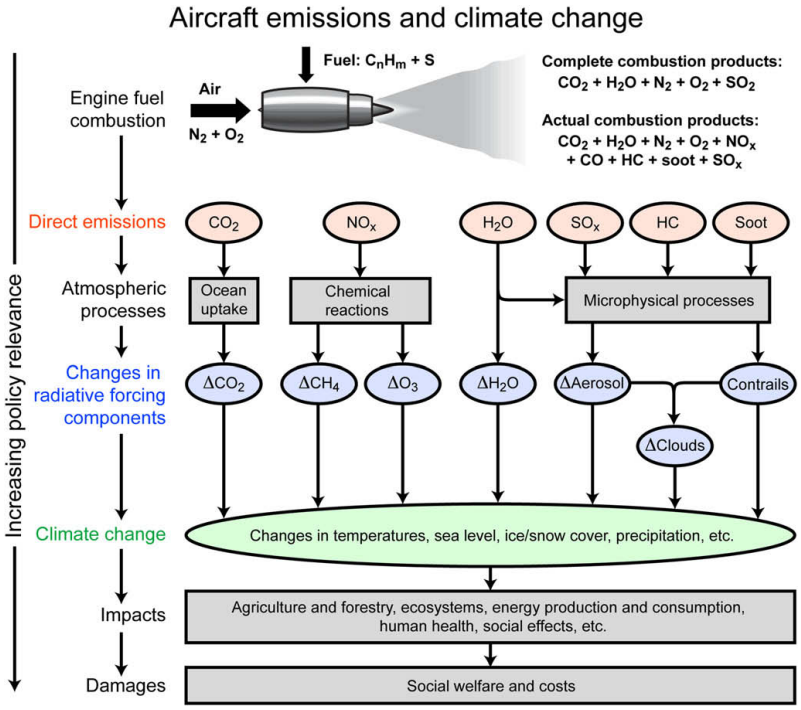


**Figure 10:** *Principal emissions from aviation operations and the atmospheric processes that lead to changes in radiative forcing components (extracted from Lee et al. (2009)).*

## Syngas production via methane auto-thermal reforming

The industrial Chair and ANR OxyTec between Air Liquide, CNRS and CentraleSupelec deal with the better understanding of the different phenomena and their interactions inside oxygen-enriched combustion configurations, and more precisely for the numerical part of the Chair, the development of numerical tools to simulate such interactions.

Indeed, in Air Liquide applications, oxy-ombustion processes are especially involved in methane auto-thermal reforming (ATR) for production of syngas from natural gas. This process can be described through two global chemical reactions (Pena et al. 1996):

$$CH_4 + H_2O \rightarrow CO + 3H_2 \tag{1}$$

$$CH_4 + \frac{3}{2}O_2 \rightarrow CO + 2H_2O \tag{2}$$

The basic idea of auto-thermal methane reforming (ATR) is to use the energy released by the exothermic oxidation reaction of methane (chemical reaction (2)) to favor reforming reaction (chemical reaction (1)), which is highly endothermic.

Figure 11 illustrates the principle of an ATR reactor. Natural gas and oxygen are preheated and mixed with water vapor. The two resulting gas flows ($CH_4$ + $H_2O$ and $O_2$ + $H_2O$) are injected separately from the top of the reactor where the methane reacts mainly with $O_2$ via partial oxidation (chemical reaction (2)). When all the oxygen has been consumed the reforming reactions of methane in the presence of water (chemical reaction (1)) takes place and is predominant (Caudal 2013).

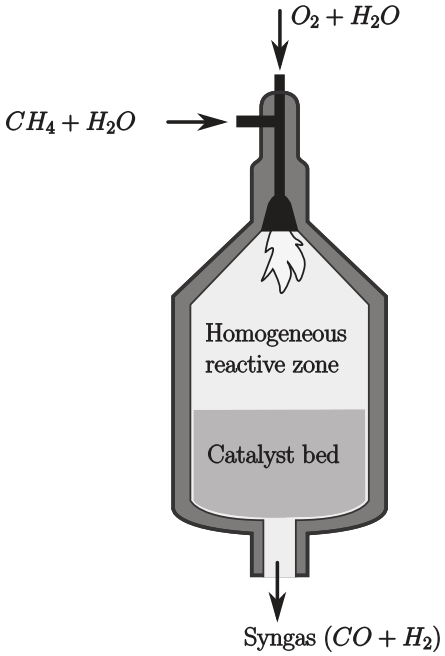


**Figure 11:** *ATR reactor principle (extracted from Caudal (2013)).*

The $O_2/CH_4$ volume ratio of the input gases is generally between 0.55 and 0.60, which corresponds to an equivalence ratio $\Phi = 2X_{CH_4}/X_{O_2}$ of the chemical reaction (2) of the order of 3.5, where $X_{CH_4}$ and $X_{O_2}$ are the methane and oxygen molar fractions, respectively. Adjusting this ratio, and the $H_2O/CH_4$ ratio at the reactor inlet, it is possible to modify the composition of the syngas at the outlet of the reactor, in particular the $H_2/CO$ ratio, depending on the type of desired application.

It is then important to notice that the high equivalence ratio $\Phi$ leads to large production of soot (see Fig. 7). This production of soot particles leads generally to a decrease of the catalyst bed efficiency. By adding $O_2$, and therefore decreasing the equivalence ratio, soot particles are oxidized and total soot volume fraction is reduced. However, this leads to a higher production of CO, and therefore a decrease of $H_2/CO$ ratio, which can be incompatible with the desired final syngas application. That is why soot formation and oxidation processes must be well known in such industrial application processes.

## Furnaces industry

By contrast with automotive and aeronautical applications where soot production is undesired, soot particles are widely used in industrial furnaces such as in glass melting industry. Indeed, these industrial furnaces involve radiative heat transfer in order to improve the melting of the glass bath. High thermal efficiency and high uniform incident heat flux are required in order to obtain good glass bath quality. Soot plays an important role on such applications, largely increasing the radiative heat transfer. Indeed, Fig. 12 compares the spectrographs of radiation from clear (non-sooty flame) and luminous (sooty flame), illustrating $CO_2$, $H_2O$ and soot contributions to the total spectral intensity. In such industrial applications, temperature can range from 1400 to 1900 K, then, the wavelengths participating to radiative exchanges are comprised between 0.75 $\mu$m and 15 $\mu$m. For low wavelengths of interest, soot particles present an intense wide-band spectrum (not overlapping with $CO_2$ and $H_2O$ gaseous bands), largely increasing the total radiative flux of luminous flames compared to non-luminous ones.

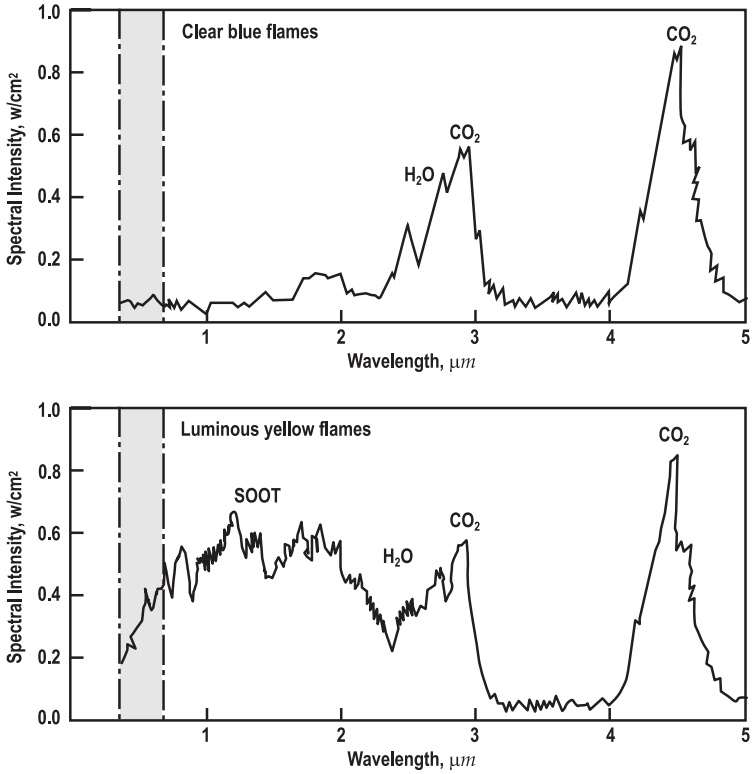


**Figure 12:** *Spectrographs of radiation from clear and luminous flames. Nonluminous flame (top graph) are blue; luminous flames (lower graph) are yellow and emit soot particle radiation (extracted from Trinks et al. (2004)).*

Soot particles production has therefore to be well understood in order to be able

to predict such participation of soot particles in radiative transfers. Moreover, the incident radiative fluxes on the refractories used in such furnaces have to be well mastered in order to prevent material damages. In order to meet these two competing objectives, a good understanding of combustion, soot formation and radiative processes is then necessary to accurately predict combustion and radiative transfers.

In oxy-combustion applications, in which oxygen is used instead of air for combustion, higher temperatures are attained increasing then the low-spectral range of interest and then soot contribution in total radiative exchanges. Such interrogations match also the goal of the ANR OxyTec, in which the present thesis is involved.

## Objectives of the thesis

Considering all the different aspects presented in the previous sections, the main objectives of this thesis are defined as:

1. *Developing a detailed model based on a sectional method for soot particles size distributions predictions in laminar canonical flames*,
2. *Proposing a formalism to transpose this detailed modeling for the simulation of turbulent sooting flames*,
3. *Evaluating the capacity of a detailed multi-physics framework in predicting radiative thermal fluxes from sooting flames and wall temperatures of confined pressurized sooting burners and their reciprocal effects on soot formation.*

## Organization of the manuscript

The manuscript contains three parts:

- **Part I** is dedicated to laminar sooting flames modeling.
  In Chapter 1, the different physical and chemical mechanisms of soot particles evolution in flames are presented. The complexity and uncertainties of such processes are discussed. Then, the different numerical methodologies proposed in literature in order to predict soot formation are presented: from simplified empirical and semi-empirical models based generally on fitted coefficients, towards more detailed and sophisticated models enabling to describe more precisely the different evolution processes. These different numerical methodologies are compared regarding their cost, quality of description, and capacity to describe soot particles morphology but also the particles size distribution (PSD) evolution. Then, the choice of the selected method is justified.
  In Chapter 2, the selected models in this work and their correspond-

ing equations are presented for the different phenomena involved in soot production. The different equations of the selected numerical methodology, the *sectional method*, enabling to solve the particles size distribution are introduced and detailed. Then, the models and numerical methodology are validated by comparing numerically predicted evolution of soot volume fraction and particles size distributions with experimental measurements in 1-D laminar premixed flames. Quality of soot volume fraction predictions with the proposed model is also assessed in other configurations, such as counterflow laminar diffusion flames and pressurized laminar premixed flames. Finally, this detailed sectional method is applied to the study of transient dynamics of soot production in 1-D flames submitted to unsteady harmonic strain rate oscillations. This canonical academic study is representative of fluctuations encountered in turbulent configurations, enabling then to identify and model soot production response in such complex applications. Parameters governing this production response are identified and a global model for soot production response in such canonical cases is proposed.

- In **Part II**, the development and implementation of an Large Eddy Simulation (LES) formalism for describing soot production in turbulent configurations in the solver AVBP is presented in Chapter 3. The LES formalism is based on a classical tabulation technique coupled with a $\beta$-PDF model for the gaseous phase description.
  An "intermittency" subgrid model for soot from the literature is extended to the sectional method, allowing the investigation of the soot particles size distribution in turbulent flames.
  The LES formalism is then applied to two different turbulent sooting flames: an atmospheric ethylene-air sooting jet diffusion flame in Chapter 4 and a confined pressurized sooting ethylene-air swirled flame in Chapter 5. For both cases, soot production mechanisms and particles size distributions dynamics are analyzed in details.

- **Part III** deals with multi-physics coupled simulations. First, state-of-the-art of gaseous and soot radiative properties models as well as methodologies for the resolution of radiative transfer equation (RTE) are detailed in Chapter 6. The proposed methodology is based on ck modeling of gaseous radiative properties, RDG theory without scattering for particles radiative properties and Monte Carlo resolution of the RTE. The code RAINIER gathering this methodology is presented. Improvements done in this methodology during this thesis in order to increase the efficiency of such approach are also presented.
  Then in Chapter 7, this approach is coupled with the LES solver with the formalism detailed in Chapter 3 for the simulation of the turbulent jet diffusion flame presented in Chapter 4. Capacity of the proposed

coupled methodology to predict radiative fluxes from luminous radiation is investigated.
However, in confined pressurized flames, temperature at walls must also be predicted in order to account correctly for heat losses. The wall temperature field is the result of the coupling between heat transfer from the flow in the combustion chamber and heat conduction within the solid parts of the combustor. This so-called conjugate heat transfer must be taken into account to predict the wall temperature. Then, in Chapter 8, the conjugate heat transfer modeling strategy with the coupling of AVBP and AVTP codes is presented. It is further applied for the coupled simulation of the pressurized confined burner of Chapter 5 and its capacity to predict wall temperatures accounting while neglecting radiation is investigated.
Finally in Chapter 9, in order to account for both radiative and wall heat losses, a whole AVBP/AVTP/RAINIER coupled approach is presented and applied to the simulation of the pressurized burner accounting for detailed radiation modeling, conjugate heat transfer and soot production. Soot production prediction, wall heat fluxes, radiative transfers inside the combustion chambers and wall temperatures are analyzed in details and compared with experiments. Impact of heat losses on soot production are also assessed by looking at impact of radiative energy transfer and wall heat losses.

## Acknowledgement

*This thesis has been carried out in the context of the ANR (ANR grant ANR-12-CHIN-0001) and Chair OxyTec ("Oxy-combustion and Heat Transfer for new energy technologies"), where CentraleSupelec, the CNRS and the industrial company Air Liquide worked together in order to improve knowledge and mastery of oxy-combustion technologies for gaseous, liquid and solid fuels for systems operating under high pressure.*

# List of publications

## Peer-reviewed journals

- P. Rodrigues, B. Franzelli, R. Vicquelin, O. Gicquel, N. Darabiha, *Unsteady dynamics of PAH and soot particles in laminar counterflow diffusion flames*, Proceedings of the Combustion Institute 36, Issue 1, 2017, Pages 927–924.
- P. Rodrigues, B. Franzelli, R. Vicquelin, O. Gicquel, N. Darabiha, *Coupling an LES approach and a soot sectional model for the study of sooting turbulent non-premixed flames*, Combustion and Flame 190, 2018, Pages 477–499.
- P. Rodrigues, R. Vicquelin, B. Franzelli, N. Darabiha, O. Gicquel, *Analysis of heat transfer mechanisms in a confined pressurized sooting ethylene/air flame by coupling large-eddy simulation, conjugate heat transfer and thermal radiation*, Proceedings of the Combustion Institute, under review.

## Peer-reviewed conference publications

- L. Palluotto, N. Dumont, P. Rodrigues, C. Koren, R. Vicquelin, O. Gicquel, *Comparison of Monte Carlo Methods Efficiency to Solve Radiative Energy Transfer in High Fidelity Unsteady 3D Simulations*, Proceedings of the ASME Turbo Expo: Power for Land, Sea and Air, Volume 5A: Heat Transfer, Number 50879, June 26-30, 2017, Charlotte, North Carolina USA.
- P. Rodrigues, O. Gicquel, B. Franzelli, N. Darabiha, R. Vicquelin, *Coupled Monte-Carlo simulation of a Turbulent Sooting Diffusion Jet Flame*, Eurotherm Seminar 110 - Computational Thermal Radiation in Participating Media - VI, April 11-13, 2018, Cascais, Portugal.
- P. Rodrigues, O. Gicquel, N. Darabiha, K.P. Geigle, R. Vicquelin, *Assessment of external heat transfer modeling of a laboratory-scale combustor inside a pressure-casing environment*, Proceedings of the ASME Turbo Expo: Turbomachinery Technical Conference & Exposition, June 11-15, 2018, Oslo, Norway.

# Part I

# Laminar Sooting flames modeling

# Introduction

Soot particles production process can be decomposed in very complex phenomena. Study of sooting flames requires adequate detailed models of these phenomena in order to correctly assess soot particles formation and consumption. The main formation steps, their impact on soot particles geometrical characteristics and their different models in literature are presented in Chapter 1. A focus is also given on all the uncertainties that remain today in the understanding of the different physical and chemical processes.

Description of particles size distributions is also a key point for prediction of soot particles in such turbulent flames. Simplest models generally assume a mean particle volume size at each control volume. Advanced models, such as method of moments, solve moments of particles volume (and potentially surface) space distribution for each control volume. Sectional approaches aim at discretizing the volume space distribution in order to provide full particles size distributions. Finally, Monte Carlo methods do not assume any shape of the particles size distribution and solves stochastically the volume and surface distributions for each control volume.
Morphology of a soot aggregate is also a key point to be described in order to correctly evaluate the different physical phenomena underlying soot particles evolution. Some of the previous numerical methods enable to describe such morphological aspects of soot particles. All these methods are described in Chapter 1. Finally, the pros and cons of the different methods are discussed and the choice of the sectional method in this manuscript is justified.

The physical and chemical processes and the state-of-the-art sectional method describing the particles size distribution retained in this thesis are detailed in Chapter 2. The proposed strategy is then validated through the simulation of laminar premixed flames at atmospheric and elevated pressure. The quality of soot prediction in counterflow diffusion flames is evaluated. Then, this model is applied to the study of unsteady behavior of soot production when submitted to strain rate oscillations. Such effects give some indications of soot production behavior in turbulent flames where high fluctuations of strain rate over a wide range of frequencies can be encountered. Response of the different mechanisms involved in soot production are analyzed in details and compared to

the response of classical burnt gases but also with the flame response behavior. Finally, quality of soot production predictions are discussed regarding the variability of sectional models and uncertainties that remain in soot modeling.

# Chapter 1

# Generalities on soot and its modeling

*In this chapter, generalities about soot production and its modeling are discussed.*

*First, the terminology used to describe a soot particle is introduced. Then, the soot particles formation mechanisms and their corresponding impact on soot particles geometrical characteristics are detailed.*

*Second, the different numerical methods from the literature for soot particles evolution predictions are described. Then, the selected one, the sectional method is briefly introduced and the pros and cons of this method compared to other methods are presented and discussed.*

## Contents



## 1.1 Soot particles geometrical description

Figure 1.1 presents two examples of soot particles extracted from atmospheric jet flames. The first one corresponds to a soot aggregate extracted at the bottom of an atmospheric ethylene/air flame. It is composed of few spherical particles, called primary particles. The second one corresponds to a soot aggregate extracted more downstream of a propane/air jet flame. Compared with the first one which as a characteristic dimension length of several hundreds of nanometers and is composed of several hundreds of primary particles, this soot aggregate is composed of several thousands of primary particles and as a characteristic dimension length of several micrometers.

In fact, a soot particle can be generally considered as either a spherical particle or an aggregate composed of primary particles.
In this manuscript, a soot particle will be described through its volume $v$ and its surface $s$, and they will be classified in two classes:

- spherical particles with a diameter $d = (6v/\pi)^{1/3} = (s/\pi)^{1/2}$.
- aggregates composed of $n_p$ non-interpenetrating primary particles with the same primary particle $d_p$. These quantities are schematically represented in Fig. 1.2, and can be expressed as a function of the volume $v$

and surface $s$ of the soot particle as:

$$\begin{cases} d_p = \dfrac{6v}{s} \\ n_p = \dfrac{s^3}{36\pi v^2} \end{cases} \tag{1.1}$$

Then a spherical particle can also be described as an aggregate with $n_p = 1$ and $d_p = d$.

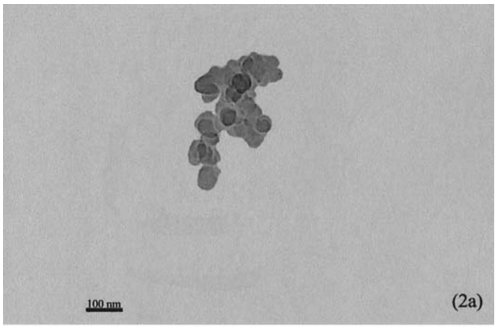


(a) Soot aggregate extracted at the bottom of an atmospheric ethylene/air flame, where the first soot aggregates are formed (extracted from Xu et al. (2003))

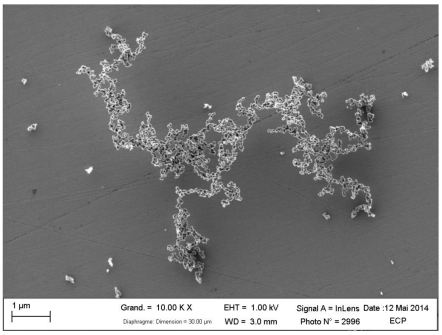


(b) Scanning Electron Microscopy (SEM) observation of a soot aggregate sample collected from an atmospheric propane/air flame (extracted from Okyay (2016))

**Figure 1.1:** *Examples of soot particles extracted from flames.*

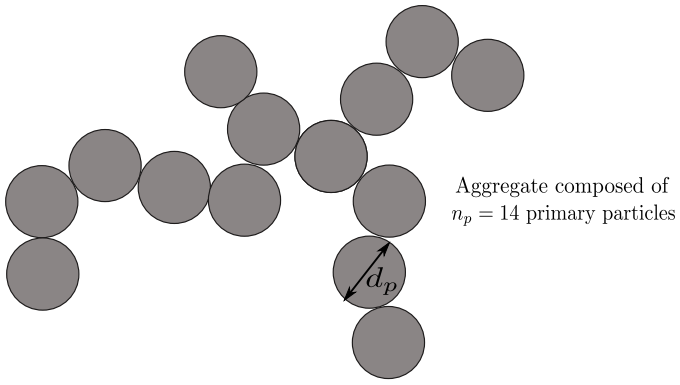


**Figure 1.2:** *Schematic of a soot aggregate composed of $n_p = 14$ primary particles with the same diameter $d_p$.*

In their work, Jullien and Botet (1987) and Samson et al. (1987) have introduced the notion of fractality of soot particles by demonstrating that for a soot aggregate, $n_p$ and $d_p$ are generally linked through the following relationship:

$$n_p \propto d_p^{-D_f} \tag{1.2}$$

where $D_f$ is the fractal dimension of the soot particle.

Table 1.1 presents a literature review of the values of the fractal dimension computed or measured in literature. A good consistency between the different experimental values can be observed with a global variation between 1.6 and 2.0. In numerical modeling of combustion, the most common value used for the fractal dimension is $D_f = 1.8$ and this value will be retained in this manuscript.

| Publication | Type | Combustible and comburant | $D_f$ [-] |
|---|---|---|---|
| Meakin (1983) | Simulation | - | 1.82 |
| Samson et al. (1987) | 3-D TEM | Acetylene and air | 1.4 |
| Samson et al. (1987) | 2-D TEM | Acetylene and air | 1.47 |
| Jullien and Botet (1987) | Simulation | - | 1.78 ± 0.04 |
| Mountain and Mulholland (1988) | Simulation | - | 1.7 to 1.9 |
| Zhang et al. (1988) | TEM | Methane and oxygen | 1.72 ± 0.10 |
| Mulholland et al. (1988) | Simulation | - | 1.89 to 2.07 |
| Megaridis and Dobbins (1989) | 2-D TEM | Ethylene and air | 1.62 ± 0.04 |
| Megaridis and Dobbins (1989) | 2-D TEM | Ethylene and air | 1.74 ± 0.06 |
| Cai et al. (1993) | ALS | Methane and air | 1.74 |
| Puri et al. (1993) | ALS | - | 1.4 |
| Wu and Friedlander (1993) | Simulation | - | 1.84 |
| Köylü and Faeth (1994) | ALS | Acetylene and air | 1.86 |
| Köylü and Faeth (1994) | 2-D TEM | Acetylene and air | 1.67 |
| Köylü and Faeth (1994) | ALS | Ethylene and air | 1.75 |
| Köylü and Faeth (1994) | 2-D TEM | Ethylene and air | 1.66 |
| Cai et al. (1995) | 2-D TEM | Methane and air | 1.74 |
| Cai et al. (1995) | 3-D TEM | Methane and air | 1.74 |
| Sorensen and Feke (1996) | 2-D TEM | Acetylene and air | 1.8 |
| Colbeck et al. (1997) | TEM | Diesel and air | 2.04 |
| Colbeck et al. (1997) | TEM | Butane and air | 1.97 |
| Brasil et al. (2000) | Simulation | - | 1.82 |
| di Stasio (2001) | 2-D TEM | Acetylene and air | 1.8 |
| Onischuk et al. (2003) | Simulation | Propane and air | 1.7 ± 0.1 |
| Hu et al. (2003) | TEM | Ethylene and air | 1.74± 0.11 |
| Hu et al. (2003) | TEM | Acetylene and air | 1.77 to 1.88 |
| Wentzel et al. (2003) | 3-D TEM | Diesel and air | 1.70 |
| Chandler et al. (2007) | 3-D TEM | Diesel and air | 1.80 |
| Okyay (2016) | Tomography | Propane and air | 1.79 |
| Okyay (2016) | Tomography | Propane and air | 1.93 |

**Table 1.1:** *Summary of measured and computed values of the fractal dimension $D_f$ in literature (extracted and completed from Maugendre (2009)). ALS corresponds to Angular Light Scattering and TEM corresponds to Transmission Electron Microscopy.*

In order to describe soot collisional phenomena of such aggregates (described in details in Section 1.3.3), the collisional diameter $d_c$ must be introduced. This collisional diameter is expressed as a function of the number of primary particles $n_p$, the primary particles diameter $d_p$ and the fractal dimension $D_f$ of the soot aggregate:

$$d_c = d_p n_p^{1/D_f}. \tag{1.3}$$

## 1.2 Formation of soot precursors

The first step of soot particles formation is the formation of gaseous soot precursors. Due to numerous uncertainties that remain in this process, numerous models exist in literature. The most common one is linked to the H-Abstraction-$C_2H_2$-Addition (HACA) mechanism proposed by Frenklach and Wang (1994) and is described below.

It starts from the degradation of hydrocarbons by pyrolysis which leads to the formation of smaller carbon species, such as acetylene ($C_2H_2$) and benzene ($C_6H_6 \equiv A_1$), which is the first aromatic ring. The repetitive assembly of this elementary ring leads to the formation of a large diversity of large flat molecules called Polycyclic Aromatic Hydrocarbon (PAH), as pyrene corresponding to four aromatic rings ($C_{16}H_{10} \equiv A_4$) or coronene corresponding to seven aromatic rings ($C_{24}H_{12} \equiv A_7$). These PAHs grow via the addition of acetylene which is described by the HACA mechanism (Frenklach and Wang 1994). The successive steps of this mechanism are illustrated in Fig. 1.3 in the case where the addition is done on benzene.

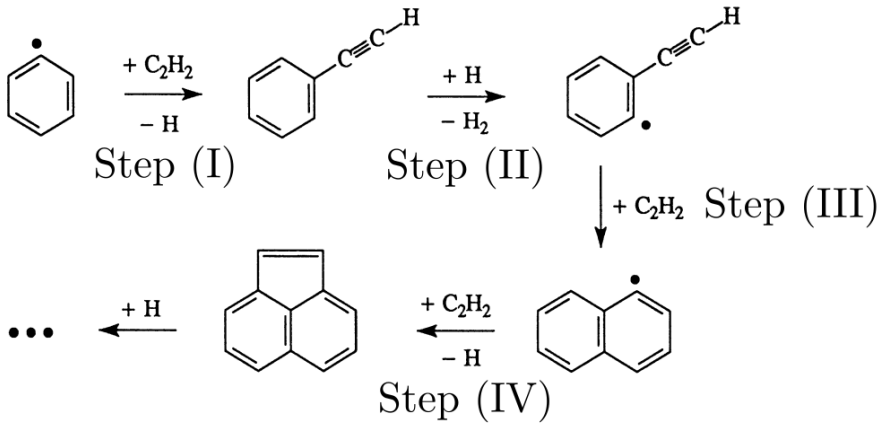


**Figure 1.3:** H-*Abstraction*-$C_2H_2$-*Addition pathway of PAH growth (from Frenklach and Wang (1994)).*

The HACA mechanism consists of a first step (I) where the acetylene molecule

reacts with the benzene radical by radical addition process. Step (II) creates a new radical by extracting a hydrogen atom out of the carbon molecule. This extraction is produced by the attack of another hydrogen atom present in the medium. It is this same reaction that provided the initial free radical benzene. In step (III), another molecule of $C_2H_2$ reacts with the new radical to form a new ring. In this case, the cyclization induces the delocalization of the radical site of step (II). Finally, step (IV) consists of a new cyclization, and the loss of the radical site. These steps are then repeated to form PAH of larger and larger size.

PAHs grow through this mechanism until they reach a characteristic size where nucleation occurs. The nature of these particles is still poorly known and the boundary between the gas-phase macro-molecule and the "solid particle" is difficult to establish. It is generally considered that between these two steps (gas-phase macro-molecule and a solid particle), a dimerization process (collision of two PAHs) occurs (Schuetz and Frenklach 2002). Then, the collision of two dimers is supposed to imply the inception of a solid soot particle (Blanquart and Pitsch 2007; Mueller et al. 2009b). The expressions governing this collision process will be described in Section 1.3.3.

## 1.3 Soot particles dynamics & reactivity

### 1.3.1 Global quantities & population balance equation

At the macroscopic level, the two quantities of interest for soot particles are their total number $N_{\text{soot}}^{\text{tot}}$ and their total mass $M_{\text{soot}}^{\text{tot}}$.

In the following, and as generally assumed, we will consider that the soot particles density is constant and equal to $\rho_s = 1.86 \cdot 10^3$ kg/m$^3$. Then, the total mass of soot particles $M_{\text{soot}}^{\text{tot}}$ and the total volume of these particles $V_{\text{soot}}^{\text{tot}}$ are linked through the following relationship:

$$M_{\text{soot}}^{\text{tot}} = \rho_s V_{\text{soot}}^{\text{tot}} \tag{1.4}$$

We will focus here in obtaining the total number of particles $N_{\text{soot}}^{\text{tot}}$ and their total volume $V_{\text{soot}}^{\text{tot}}$.
Theses quantities are obtained through their corresponding quantities per unit volume: the particles number density $N_{\text{part}}$ and the soot volume fraction $f_V$. For a given volume $V$ of the considered system, the following relations are obtained:

$$\begin{cases} V_{\text{soot}}^{\text{tot}} = \displaystyle\int_V f_V dV \\ N_{\text{soot}}^{\text{tot}} = \displaystyle\int_V N_{\text{part}} dV \end{cases} \tag{1.5}$$

In this thesis, one of the objective is to be able to describe the evolution of the particles size distribution (PSD) in all the computational domain. Moreover, as soot particles surface growth, oxidation, condensation and coagulation phenomena are strongly linked with their own size, describing the PSD enables to increase the description fidelity of these phenomena. To do so, two quantities are introduced:

- the soot volume fraction distribution $q(v)$ over the volume space $v$ described by soot particles,
- the particles number density function (NDF) $n(v)$ over the volume space $v$ described by soot particles[1].

$f_V$ and $N_{\text{part}}$ can then be calculated as:

$$\begin{cases} f_V = \displaystyle\int_0^{+\infty} q(v)dv \\ N_{\text{part}} = \displaystyle\int_0^{+\infty} n(v)dv \end{cases} \tag{1.6}$$

A relationship between $n(v)$ et $q(v)$ can be obtained. Indeed, considering an elementary volume $dv$ of the soot particles volume space, the infinitesimal part of soot particles volume fraction $q(v)dv$ having a volume belonging to the interval $[v, v+dv]$ is equal to the product of the number density of soot particles $n(v)dv$ belonging to the interval $[v, v+dv]$ by the volume of these soot particles $v$:

$$n(v)vdv = q(v)dv \quad \Leftrightarrow \quad n(v) = q(v)/v \tag{1.7}$$

Table 1.2 summarizes the nomenclature of the different quantities and their unity.

| Quantity | Unity | Description |
|---|---|---|
| $V$ | [$m^3$] | Volume of the system |
| $N_{\text{soot}}^{\text{tot}}$ | [-] | Total number of soot particles in the volume $V$ |
| $V_{\text{soot}}^{\text{tot}}$ | [$m^3$] | Total volume of soot particles in the volume $V$ |
| $f_V$ | [-] | Soot volume fraction |
| $N_{\text{part}}$ | [$m^{-3}$] | Particles number density |
| $v$ | [$m^3$] | Volume of a soot particle |
| $q(v)$ | [$m^{-3}$] | Volume distribution (over the volume space described by soot particles) of $f_V$ |
| $n(v)$ | [$m^{-6}$] | Volume distribution (over the volume space described by soot particles) of $N_{\text{part}}$ |

**Table 1.2:** *Nomenclature of the different quantities used for the soot particles description*

[1] In this thesis, the NDF will be considered as mono-variate, *i.e.* only function of the of the soot particles volume $v$.

The volume distribution $n(v)$ of the particles number density follows the population balance equation (PBE) governing its temporal and spatial evolution:

$$\begin{aligned} &\frac{\partial n}{\partial t} + \nabla \cdot (\mathbf{u}n) - \nabla \cdot \left( C_{\text{th}} \nu \frac{\nabla T}{T} n \right) = \nabla \cdot (D_s \nabla n) + \dot{n}_s \\ \Leftrightarrow \quad &\frac{\partial n}{\partial t} + \nabla \cdot \left( (\mathbf{u} + \mathbf{v_T}) \, n \right) = \nabla \cdot (D_s \nabla n) + \dot{n}_s \end{aligned} \tag{1.8}$$

where:

- $\mathbf{v_T} = -C_{\text{th}} \nu \frac{\nabla T}{T}$ is the thermophoretic velocity,
- $\nu$ is gas kinematic viscosity,
- $D_s$ is the particles soot diffusion coefficient,
- $\dot{n}_s$ is the source term of the volume distribution $n(v)$. It accounts for particles dynamics (nucleation, condensation and coagulation) and particles reactivity with the gaseous phase (surface growth and oxidation).

### 1.3.2 Transport phenomena for soot particles

**Molecular Diffusion**

Soot particles diffusion coefficient $D_s$ has been studied by Epstein (1924) where the diffusion force $\mathcal{F}_R$ applied over a spherical particle of diameter $d$ is expressed by considering the particle as a perfect thermal conductor:

$$\mathcal{F}_R = \left( 1 + \frac{\alpha_T \pi}{8} \right) \frac{\pi}{3} N m \bar{c} d^2 v_{\text{part,gas}} = \mu_f v_{\text{part,gas}} \tag{1.9}$$

with:

- $m$ the mass of gas particle,
- $N$ the gas particles number density,
- $\bar{c} = \sqrt{\frac{8 k_b T}{m \pi}}$, the brownian velocity of the gas particles where $k_b$ is the Boltzmann constant,
- $v_{\text{part,gas}}$ the velocity of the particle is the gas referential,
- $\mu_f$ the equivalent friction coefficient,
- $\alpha_T$ the thermal accomodation factor expressing the fraction of heat flux exchanged between the particle surface and the surrounding gas molecules. This constant is usually taken equal to $\alpha_T = 0.9$ (Waldmann and Schmitt 1966; Blanquart and Pitsch 2009; Yapp et al. 2015).

Using the Einstein relation linking the equivalent friction coefficient $\mu_f$ to the diffusion coefficient $D_s$ of the soot particle, one obtains:

$$\mu_f = \frac{k_b T}{D_s} \tag{1.10}$$

Then, for a soot particle with a diameter $d$, the soot diffusion coefficient $D_s$ of

this particle writes:

$$\begin{aligned} D_s &= \frac{k_b T}{\left(1+\frac{\alpha_T \pi}{8}\right)\frac{\pi}{3} N m \bar{c} d^2} \\ &= 3\left(1+\frac{\alpha_T \pi}{8}\right)^{-1} \frac{1}{d^2} \frac{k_b T}{N m \sqrt{\frac{8 k_b T}{m\pi}}\pi} \\ &= \frac{3}{2}\left(1+\frac{\alpha_T \pi}{8}\right)^{-1} \frac{1}{d^2}\sqrt{\frac{k_b T}{2m\pi}}\frac{1}{N} \end{aligned} \tag{1.11}$$

With the relations $\rho = Nm$ and $m = W_{\text{gas}}/N_A$ where $W_{\text{gas}}$ is the gas molar weight and $N_A$ is the Avogadro number, $D_s$ can finally be expressed as:

$$D_s = \frac{3}{2\rho}\left(1+\frac{\alpha_T \pi}{8}\right)^{-1} \frac{1}{d^2}\sqrt{\frac{W_{\text{gas}} k_b T}{2\pi N_A}} \tag{1.12}$$

**Thermophoresis**

For soot particles, the thermophoretic velocity $\mathbf{v}_{\text{T}}$ is opposed to the temperature gradient and consequently particles are transported from hot regions towards low temperature regions. The thermophoresis phenomenon is then not negligible in the presence of important temperature gradient.

The expression of the thermophoresis velocity for soot particles comes from the works of Waldmann and Schmitt (1966) and Derjaguin et al. (1966). The thermophoretic velocity is formulated in the case of a *free molecular* regime of particles (small particles verifying Knudsen number $\text{Kn} = 2\lambda_{\text{gas}}/(d) \gg 1$, with $\lambda_{\text{gas}}$ the gas mean free path):

$$\mathbf{v_T} = -C_{\text{th}} \nu \frac{\nabla T}{T} \tag{1.13}$$

with:

$$C_{\text{th}} = \frac{3}{4}\left(1+\frac{\pi \alpha_T}{8}\right)^{-1} \approx 0.554. \tag{1.14}$$

### 1.3.3 Soot particles collision dynamics

Three collision phenomena are involved in soot particles evolution:

- The nucleation of the soot particle described here through the collision of two dimers. It implies a gain in the soot volume fraction $f_V$ and the particles number density $N_{\text{part}}$. For the corresponding nascent particles, the number of primary particles $n_p$ is equal to 1 and the primary particles diameter $d_p$ depend on the soot precursor involved in the nucleation process.
- The condensation phenomenon which corresponds to the collision of a soot particle with a gaseous dimer. The number of primary particles

$n_p$ per aggregates and the particles number density $N_{\text{part}}$ are unchanged through this mechanism and it implies an increase of the primary particles diameter $d_p$ and the soot volume fraction $f_V$.

- Coagulation and agglomeration which are two analogous phenomena. Coagulation corresponds to the formation a bigger soot spherical particle from the collision of two smaller soot spherical particles. Agglomeration corresponds to the formation of a soot aggregate by collision of two smaller aggregates (no sphericity of the particles is assumed). Since two soot particles are necessary for the formation of a larger soot particle, these phenomena imply a decrease of the total particles number density $N_{\text{part}}$ but the soot volume fraction $f_V$ remains unchanged. Coagulation and agglomeration differ on their impact on the primary particle diameter $d_p$ and number $n_p$. For the coagulation process, the particle is considered spherical after collision. Then, $d_p$ increases and $n_p$ remains unchanged. For the agglomeration process however, a point-to-point contact is considered between the two smaller aggregates. Then, $d_p$ remains unchanged and $n_p$ increases. However, no distinction is generally considered between these phenomena in literature. That is why in the following, agglomeration and coagulation will be always considered as equivalent.

All these phenomena are described by the **Smoluchowski equation**, presented in the following paragraph.

**Smoluchowski equation**

The Smoluchowski equation (Smoluchowski 1916) expresses the gain $\dot{n}^c(v)$ of distribution of particles number density due to particle collisions. For a particle of size $v$, this source term is expressed through the collision frequencies $\beta_{u,v}$ of the particles of size $v$ with all other particles of any size $u$ (resulting in a loss of particles with size $v$), and the collision frequencies $\beta_{v-u,u}$ of all particles of size $u$ with any other particle of size $v-u$ (resulting in a gain of particles with size $v$). $\dot{n}^c(v)$ can then be expressed as:

$$\dot{n}^c(v) = \frac{1}{2}\int_0^v \beta_{v-u,u} n(u) n(v-u) du - \int_0^\infty \beta_{u,v} n(u) n(v) du. \tag{1.15}$$

The Smoluchowski equation is only function of the size of the different particles and not their nature. Then, in order to express the source terms for a soot particle of size $v$ for each phenomena (nucleation, condensation and coagulation), several types of particles with size $u$ and $v-u$ have to be considered:

- both in the gaseous state (dimers) for nucleation,
- one in the gaseous state (dimer) and the other one in the solid state for condensation,
- both in the solid state for coagulation.

**Expression of the collision frequency of collision between two particles**

The collision frequency $\beta_{u,v}$ between a particle of size $u$ and a particle of size $v$ depends on the value of the Knudsen number of the considered particles. The Knudsen number ($\mathrm{Kn_u}$) is defined for a particle of size $u$ as follows:

$$\mathrm{Kn_u} = \frac{2\lambda_{\mathrm{gas}}}{d_{c,u}} \tag{1.16}$$

where $d_{c,u}$ corresponds to the collisional diameter of the considered particle of size $u$: $d_{c,u} = d_{p,u} n_{p,u}^{1/D_f}$. If the soot particle is considered spherical, then $n_{p,u} = 1$ and $d_{c,u} = d_{p,u} = d_u$ where $d_u$ is the spherical particle diameter.

$\lambda_{\mathrm{gas}}$ is the gas mean free path expressed as:

$$\lambda_{gas} = \frac{RT}{\pi\sqrt{2} d_{gas}^2 N_A P} \tag{1.17}$$

where $R$ is the perfect gas constant, $T$ the temperature, $N_A$ the Avogadro number, $P$ the pressure and $d_{\mathrm{gas}}$ the diameter of a gas particle, considered constant and equal to 0.2 nm.

**Collision regimes**

Three different physical regimes can be identified according to the value of the Knudsen number (Kazakov and Frenklach 1998):

- If the pressure is sufficiently low or if thermal agitation is low or if the particles are small enough (corresponding to $\mathrm{Kn_u}$>10), the regime is considered as "**molecular**". The collision frequency $\beta_{u,v}$ between particles of size $u$ and particles of size $v$ is expressed as:

$$\beta_{u,v} = \beta_{u,v}^{fm} = \epsilon_{u,v} \left(\frac{3}{4\pi}\right)^{1/6} \sqrt{\frac{6k_bT}{\rho_s}} \sqrt{\frac{1}{u} + \frac{1}{v}} \left(\left(\frac{\pi}{6}\right)^{1/3} (d_{c,u} + d_{c,v})\right)^2 \tag{1.18}$$

  with $\epsilon_{u,v}$ a sticking coefficient taking into account the interactions between particles (**Van der Waals** interactions). Its value depends on the considered soot particles collision phenomena and will be discussed in the next paragraph.

- If the pressure is sufficiently high or if the particles are large enough or if thermal agitation is important ($\mathrm{Kn_u}$<0.1), the collision regime is

"**continuous**". The collision frequency $\beta_{u,v}$ between particles of size $u$ and particles of size $v$ is expressed as:

$$\beta_{u,v} = \beta^c_{u,v} = \frac{2k_bT}{3\mu}(d_{c,u} + d_{c,v})\left(\frac{Cu_u}{d_{c,u}} + \frac{Cu_v}{d_{c,v}}\right) \tag{1.19}$$

with:

$$\mu = \frac{C_1 T^{3/2}}{T + C_2} \quad \text{the dynamic gas viscosity,}$$
$$\mathrm{Cu_u} = 1 + 1.257\mathrm{Kn_u} \quad \text{the corrective Cunningham coefficient for a particle of size } u \tag{1.20}$$

- For $0.1<\mathrm{Kn_u}<10$, the collisional regime is called "**intermediate**". The collision frequency $\beta_{u,v}$ is expressed as a harmonic mean of the molecular collision frequency $\beta^{fm}_{u,v}$ and the continuous collision frequency $\beta^c_{u,v}$:

$$\beta_{u,v} = \beta^{tr}_{u,v} = \frac{\beta^{fm}_{u,v}\beta^c_{u,v}}{\beta^{fm}_{u,v} + \beta^c_{u,v}} \tag{1.21}$$

**Van der Waals $\epsilon_{u,v}$ amplification factors for a free molecular regime**
In the case of a free molecular regime, Van der Waals interactions involve an amplification factor $\epsilon_{u,v}$ in the expression of the collision frequency (equation (1.18)).
The amplification factor is calculated for spherical particles with a radius $a = \left(\frac{3u}{4\pi}\right)^{1/3}$ and a radius $b = \left(\frac{3v}{4\pi}\right)^{1/3}$ through the following equation (Alam 1987):

$$\epsilon_{u,v} = \frac{1}{2(a+b)^2 k_b T}\int_0^{1+\frac{a}{b}}\left[\left(\frac{dE}{dr} + r\frac{d^2E}{dr^2}\right) exp\left\{-\frac{1}{k_bT}\left(\frac{r}{2}\frac{dE}{dr} + R\right)\right\} r^4\right]\frac{dr}{b} \tag{1.22}$$

with $E(r)$ the Van der Waals potential, expressed as (Alam 1987; Pailthorpe and Russel 1982):

$$E(r) = -\frac{A}{6}\left[\frac{2ab}{r^2-(a+b)^2} - \frac{2ab}{r^2-(a-b)^2} + \ln\left(\frac{r^2-(a+b)^2}{r^2-(a-b)^2}\right)\right] \tag{1.23}$$

where $A$ is the *Hamaker* constant.

Therefore, these amplification factors are dependent on the volumes of the colliding particles and no universal values of these amplification factors can be determined for each phenomenon.
Marchal (2008) proposed to determine these values through an asymptotical analysis. The corresponding values are:

- $\epsilon_{u,v} = 2.5$ for nucleation,
- $\epsilon_{u,v} = 1.3$ for condensation,
- $\epsilon_{u,v} = 2.2$ for coagulation.

Although they are not universal, these values will be considered through this manuscript.

**Limitations and uncertainties of soot particles collision dynamics descriptions**

Many uncertainties remain in the description of collision dynamics descriptions related to soot particles formation:

- Nucleation phenomenon is the process with the major uncertainties nowadays. Even if dimerization process is today recognized as the major process involved in soot particles nucleation, numerous other hypotheses exist in literature, as the polymerization by acetylene process which has been considered in the work of Aubagnac-Karkar et al. (2015). Moreover, some studies have shown that nucleation process can be reversible and this reversibility should be taken into account in our models (Eaves et al. 2015). Finally, sticking coefficients of this process are also unknown and a lot of different models have been proposed in the literature (Yapp et al. 2015; Wang et al. 2015).
- Condensation and coagulation processes have also their part of uncertainties through their collision regime modeling and the corresponding collision efficiencies for which numerous different values can be found in literature (Marchal 2008; Mueller et al. 2009b; Saggese et al. 2015).
- Even if coagulation and agglomeration do not have the same impact of the primary particles diameter $d_p$ and number $n_p$, no distinction of these phenomena in their description is generally considered.

### 1.3.4 Soot particles surface reactions

Soot particles interact at their surface with the surrounding species in the gas phase through two main mechanisms:

- The surface growth phenomenon is responsible for an increase of the total mass. It acts through carbon addition at the surface of soot particles. Acetylene ($C_2H_2$) is considered as the main species involved in this carbon addition phenomenon. The number of primary particles $n_p$ per aggregates and the particles number density $N_{\text{part}}$ are unchanged through this mechanism and it implies an increase of the primary particles diameter $d_p$ and the soot volume fraction $f_V$.
- The oxidation phenomenon is responsible for the decrease of the total soot mass. It acts by extracting carbon atoms on the surface of the primary particles. The two main known oxidants are dioxygen $O_2$ and the OH radical. Atomic oxygen O and the $CO_2$ and $H_2O$ species have also been

identified as potential oxidants, but with a much less important effect (Xu et al. 2003). The number of primary particles $n_p$ per aggregates and the particles number density $N_{\text{part}}$ are unchanged through this mechanism and it implies a decrease of the primary particles diameter $d_p$ and the soot volume fraction $f_V$.

Different mechanisms have been proposed to describe this reactivity and are described below.

### The HACA mechanism

In their study, Frenklach and Wang (1994) proposed an analogy between chemical reactions taking place on the PAHs surface and those occurring on the soot particles surface. The chemical mechanism involved in surface growth mechanism is then supposed to be similar as the Hydrogen-Abstraction/Carbon-Addition (HACA) mechanism used generally for the PAHs evolution modeling and described in Fig. 1.3. It corresponds to reactions (a) to (d) presented in Table 1.3, where $C_{n_C}H$ represents a soot particle with $n_C$ carbon atoms, and $C^*_{n_C}$ the associated radical. $C^*_{n_C}$ is first created by the abstraction of a hydrogen atom at the surface of the soot particle by another hydrogen atom (reaction (a)). Reaction (b) is the associated deactivation reaction. As for PAHs, the key species responsible for growth is acetylene ($C_2H_2$). It reacts at the surface of a soot particle radical $C^*_{n_C}$ via reactions (c) or (d). Reaction (c) leads to the deactivation of an active site particle, which is assumed to occur at high temperature (Frenklach and Wang 1994), whereas reaction (d) conserves the active site at the surface of the soot particle, which is assumed to occur preferentially at low temperatures (Wang et al. 1996). Finally the reactions (e) and (f) represent the oxidation of soot particles due to the presence of respectively $O_2$ and OH molecules.

| | Num. | Reaction | Ref. |
|---|---|---|---|
| Surface growth | (a) | $C_{n_C}H + H \rightleftharpoons C^*_{n_C} + H_2$ | Frenklach and Wang (1994) |
| | (b) | $C^*_{n_C} + H \rightarrow C_{n_C}H$ | Frenklach and Wang (1994) |
| | (c) | $C^*_{n_C} + C_2H_2 \rightarrow C_{n_C+2}H + H$ | Frenklach and Wang (1994) |
| | (d) | $C^*_{n_C} + C_2H_2 \rightarrow C^*_{n_C+2} + H_2$ | Wang et al. (1996) |
| Oxidation | (e) | $C^*_{n_C} + O_2 \rightarrow$ products | Frenklach and Wang (1994) |
| | (f) | $C^*_{n_C} + OH \rightarrow$ products | Frenklach and Wang (1994) |

**Table 1.3:** ***HACA mechanism:*** *Reactions and references in literature.*

## The HACA-RC mechanism

### Reactions and Arrhenius law parameters

In their study, Mauss et al. (1994) proposed a modified version of the HACA mechanism: the Hydrogen-Abstraction/Carbon-Addition Ring-Closure (HACA-RC) mechanism. Table 1.4 presents the reactions and Arrhenius law parameters of the HACA-RC mechanism proposed by Mauss et al. (1994). Two main changes can be noticed:

- Reaction 2 which accounts for the radical consuming influence of $H_2O$,
- Reaction 3 is here reversible (which was considered irreversible before) to account for the limitation of surface growth at high temperatures.

This mechanism will be used in the present manuscript.

| Num. | Reaction | k | A | $\beta$ | $E_a$ [kJ/mol] |
|---|---|---|---|---|---|
| **1** | $C_{n_C}H + H \underset{k_{1b}}{\overset{k_{1f}}{\rightleftharpoons}} C^*_{n_C} + H_2$ | $k_{1f}$ | $1.000 \cdot 10^{14}$ | 0.0 | 0.0 |
| | | $k_{1b}$ | $1.439 \cdot 10^{13}$ | 0.0 | -37.63 |
| **2** | $C_{n_C}H + OH \underset{k_{2b}}{\overset{k_{2f}}{\rightleftharpoons}} C^*_{n_C} + H_2O$ | $k_{2f}$ | $1.630 \cdot 10^{8}$ | 1.4 | 6.10 |
| | | $k_{2b}$ | $1.101 \cdot 10^{8}$ | 1.4 | 31.14 |
| **3** | $C^*_{n_C} + H \underset{k_{3b}}{\overset{k_{3f}}{\rightleftharpoons}} C_{n_C}H$ | $k_{3f}$ | $1.000 \cdot 10^{13}$ | 0.0 | 0.0 |
| | | $k_{3b}$ | 0.000 | 0.0 | 0.0 |
| **4** | $C^*_{n_C} + C_2H_2 \underset{k_{4b}}{\overset{k_{4f}}{\rightleftharpoons}} C^*_{n_C}C_2H_2$ | $k_{4f}$ | $3.500 \cdot 10^{13}$ | 0.0 | 0.0 |
| | | $k_{4b}$ | $3.225 \cdot 10^{14}$ | 0.0 | 181.69 |
| **5** | $C^*_{n_C}C_2H_2 \underset{k_{5b}}{\overset{k_{5f}}{\rightleftharpoons}} C_{n_C+2}H + H$ | $k_{5f}$ | $1.000 \cdot 10^{10}$ | 0.0 | 20.0 |
| | | $k_{5b}$ | $8.770 \cdot 10^{11}$ | 0.0 | 74.44 |
| **6** | $C^*_{n_C} + O_2 \overset{k_{6f}}{\rightarrow} C^*_{n_C-2} + 2CO$ | $k_{6f}$ | $1.000 \cdot 10^{12}$ | 0.0 | 8.4 |
| **6'** | $C^*_{n_C}C_2H_2 + O_2 \overset{k_{6'f}}{\rightarrow} C^*_{n_C} + 2HCO$ | $k_{6'f}$ | $1.000 \cdot 10^{12}$ | 0.0 | 8.4 |
| **7** | $C_{n_C}H + OH \overset{k_{7f}}{\rightarrow} C^*_{n_C-2} + CH + HCO$ | $k_{7f}$ | Efficiency : $\gamma_{OH} = 0.13$ | | |

**Table 1.4:** ***HACA-RC mechanism:*** *Reactions and Arrhenius law parameters*

The values of the Arrenhius laws parameters are taken from Mauss et al. (2006) and the reaction rate of oxidation by OH molecules (reaction 7) has been updated based on the works of Siegla et al. (1981); El-Leathy et al. (2002); Xu et al. (2003). Details on the expression of the source terms for this mechanism are presented below.

### Expression of surface growth and oxidation source terms

Surface growth results in an increase of mass at the soot particles surface: as described by the HACA-RC mechanism, a $C_2H_2$ molecule is added to the surface of a soot particle by surface kinetic reactions. Oxidation, on the contrary, results in a loss of soot particles mass. The oxidation reactions presented in the *HACA-RC* mechanism describe the withdrawal of two carbon atoms and one or two H atoms at the soot particles surface. We consider here only a reduction

of the soot particle by $v_{C_2}$, the volume of two carbons.

The reaction rates corresponding to surface growth ($\dot{q}_{\text{sg}}$) and oxidation ($\dot{q}_{\text{ox}}$) phenomena can be expressed as a function of the reaction rates of the HACA-RC mechanism. The following expressions are obtained:

$$\begin{aligned}
\dot{q}_{\text{sg}} &= q_4 = k_{4f}[C^*_{n_C}][C_2H_2] - k_{4b}[C^*_{n_C}C_2H_2] \\
\dot{q}_{O_2} &= q_6 + q_{6'} = k_{6f}[O_2]([C^*_{n_C}] + [C^*_{n_C}C_2H_2]) \\
\dot{q}_{OH} &= q_7 = k_{7f}[C_{n_C}H][OH] \\
\dot{q}_{\text{ox}} &= \dot{q}_{O_2} + \dot{q}_{OH}
\end{aligned} \tag{1.24}$$

In order to evaluate these source terms, it is necessary to evaluate not only the species concentrations (OH, $C_2H_2$, $O_2$, ...) obtained from gas phase kinetics, but also, the radical sites concentrations of $C^*_{n_C}$, $C^*_{n_C}C_2H_2$ and $C_{n_C}H$. The two first quantities correspond to the radical active sites concentration at the surface of soot particles. The number of these radical active sites is considered at equilibrium during the reactions characteristic time scales. These species are therefore considered in a quasi-stationary state and the detailed derivations necessary to obtain the expressions of these concentrations are given in Appendix A.1.1.2.

$[C_{n_C}H]$ corresponds to the active sites concentration at the surface of a soot particle. This quantity can be evaluated knowing i) the number of active sites per unit surface of soot particle ($\lambda_{\text{soot}}$), ii) the proportion $\alpha$ of these sites which are actives, iii) the surface distribution of the soot particles $s$ and iv) the volume distribution of the particles number density $n(v)$:

$$[C_{n_C}H] = \int_0^{+\infty} \frac{\alpha \lambda_{\text{soot}} s n(v)}{N_A} dv \tag{1.25}$$

The number of active sites is obtained assuming that each active site occupies a surface corresponding to the surface of $C_2H_2$ molecule (Netzell 2006): $s_{C_2} = s(v_{C_2})$. Then the number of sites per unit surface verifies:

$$\lambda_{\text{soot}} s_{C_2} = 1 \tag{1.26}$$

If the particles are spherical, one may consider the following relation between the volume of a particle $v$ and its corresponding surface $s$:

$$\frac{s}{s_{C_2}} = \left(\frac{v}{v_{C_2}}\right)^{2/3} \tag{1.27}$$

Now, using Eq. (1.26), one can write:

$$\lambda_{\text{soot}} s = \lambda_{soot} s_{C_2} \left(\frac{v}{v_{C_2}}\right)^{\frac{2}{3}} = \left(\frac{v}{v_{C_2}}\right)^{\frac{2}{3}} \tag{1.28}$$

As it will be discussed later, the proposed model takes into account the impact of the soot particles fractal properties, and therefore the increase of their surface for a same volume. To do so, the function $\theta(v)$ is introduced and defined in order to verify:

$$\frac{s}{s_{C_2}} = \left(\frac{v}{v_{C_2}}\right)^{\frac{\theta(v)}{3}} \tag{1.29}$$

Then, this hypothesis implies that one given soot particle volume corresponds to one given soot particle surface.
$[C_{n_C}H]$ can finally be evaluated as:

$$[C_{n_C}H] = \alpha \int_{v=0}^{+\infty} \frac{n(v)}{N_A} \left(\frac{v}{v_{C_2}}\right)^{\frac{\theta(v)}{3}} dv \tag{1.30}$$

**Limitations and uncertainties in the HACA mechanisms**

Even if the HACA mechanism is today considered as the reference mechanism for soot surface process, many uncertainties remain:

- In some studies, it has been shown that particles aging has an influence on surface mechanism. A decrease of the number of active sites at the surface of soot particles has been noticed, decreasing then the reactivity of the particles surface. Liu et al. (2006) and Frenklach and Wang (1991) explained this reactivity decrease by the graphitization of soot particles, corresponding to carbon atoms rearrangement in order to form a more ordered structure. Then, the number of active sites on which the addition of acetylene is carried out preferentially decreases. Several studies have proposed a way to model this effect adding a correction factor $\alpha$ (constant (Dworkin et al. 2011; Chernov et al. 2012; Veshkini et al. 2014) or function of local gas temperature (Appel et al. 2000)) to the surface growth rate corresponding to the proportion of site which are actives (see Eq. (1.25)). Exhaustive analysis of the impact of this parameter has been also realized by Keita (2017) but no universal formulation has been determined today and it is still an open topic.
- Other studies (Hwang and Chung 2001; Wang et al. 2015), based on initial studies of Frenklach and Warnatz (1987); Pitsch (1996) for PAHs have proposed that H abstraction from soot particles can also occur via reactions with methyl ($CH_3$), ethynyl ($C_2H$), and propadienyl ($C_3H_3$) radicals. They have modified the HACA mechanism by adding the following reactions:

$$\begin{aligned} C_{n_C}H + C_2H &\rightarrow C^*_{n_C} + C_2H_2 \\ C_{n_C}H + CH_3 &\rightarrow C^*_{n_C} + CH_4 \\ C_{n_C}H + C_3H_3 &\rightarrow C^*_{n_C} + C_3H_4 \end{aligned} \tag{1.31}$$

These modifications lead to better results for the prediction of soot particles evolution in counterflow diffusion flames compared to the classical HACA mechanism, which tends to underpredict soot production.

- Finally, the constant of reactions involved in the HACA mechanism are uncertain and many differences can be observed in literature, even in the constants of the HACA mechanism of the kinetic scheme used for the PAHs growth.

### 1.3.5 Summary of the main steps of soot particles evolution

The main evolution steps considered in this manuscript for describing soot particles during their growth, oxidation and collisional processes are schematically summarized in Fig. 1.4.

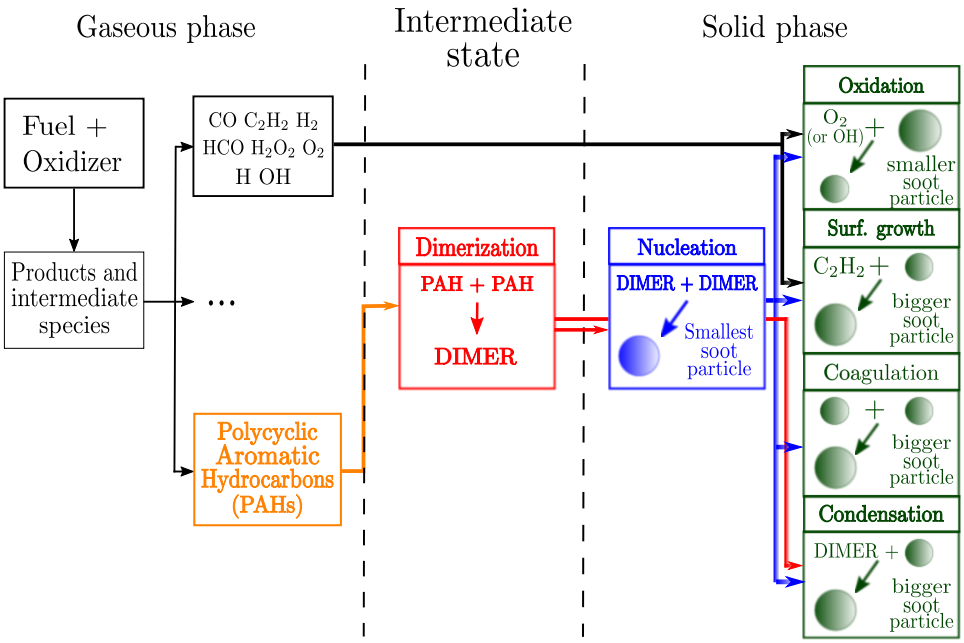


**Figure 1.4:** *Schematic representation of soot formation processes*

From a description of the gaseous phase, six main phenomena are then considered and have to be modeled:

- ***Dimer formation***,
- ***Nucleation***,
- ***Condensation***,
- ***Coagulation and agglomeration***,
- ***Surface growth***,
- and ***Oxidation***.

## 1.4 Methods for the numerical modeling of soot particles evolution

In the previous sections, the different phenomena governing soot particles evolution were described. In order to describe soot particles evolution, different numerical methodologies have been developed in literature: empirical/semi-empirical models, kinetic models, sectional methods, methods of moments or stochastic methods.
The general principle of each methodology is described in the present section. Then, the different pros and cons of these methodologies are discussed and the choice of the sectional method in the present manuscript is justified.

Finally, details of different existing models for each one of these methodologies can be found in Appendix A, Section A.2.

### 1.4.1 Empirical/semi-empirical models

These methods are generally based on empirical and ad-hoc formulation of soot formation processes and simple transport equations (Tesner et al. 1971; Moss et al. 1989; Kennedy et al. 1990; Said et al. 1997; Zhubrin 2009; Leung et al. 1991; Brookes and Moss 1999). Generally, a maximum of two transport equations are considered in order to describe soot particles evolution in terms of mass and/or number density.

The main advantage of such methods is their very low cost. However, they present many drawbacks:

- Transport equations source terms are generally based on unphysical-based expressions,
- They are not universal: case-dependent fitted parameters are used in the transport equations source terms,
- They do not provide access to the soot particles size distribution (PSD) or number density function (NDF) evolution,
- They do not enable to describe the morphology of soot particles in terms of surface/volume ratio evolution.

### 1.4.2 Kinetic models

Kinetic models are based on detailed kinetic schemes of soot formation processes. According to their size, particles are gathered in classes, generally called **"BINs"**, which are part of the global kinetic schemes (Richter et al. 2005; Saggese et al. 2015). Then, soot particles classes are considered as chemical species and their evolution are solved together with the other chemical species of the kinetic scheme.

The main advantages of this method are:

- They provide access to the PSD particles evolution,
- They are based on detailed description of the chemical and physical processes and interactions with the gaseous phase can be easily handled.

Its main drawbacks are:

- The method is expensive as it requires the combined resolution of the global kinetic scheme which generally involves, accounting for the soot particles classes, more than 200 species and 1 000 reactions,
- The NDF is generally mono-variate and is considered only function of the soot particles volume. However, morphology can be accounted for by imposing a surface-volume relationship depending on the soot particles size, as proposed by Saggese et al. (2015).

### 1.4.3 Methods of moments

The methods of moments are based on the description of the particles size distribution (PSD) or number density function (NDF) through their statistical moments (Frenklach and Harris 1987; Marchisio and Fox 2005; Blanquart and Pitsch 2009; Mueller et al. 2009a; Yuan et al. 2012; Madadi-Kandjani and Passalacqua 2015; Salenbauch et al. 2015; Nguyen et al. 2016; Selvaraj et al. 2016). Moments can be univariate (in the particles volume or surface space) or multi-variate.

For a uni-variate description of the particles size distribution (in the particles volume space), the moment $M_x$ of order $x$ is generally formulated as:

$$M_x = \int_{v=0}^{+\infty} n(v) v^x dv. \tag{1.32}$$

For a bi-variate volume-surface description of the PSD, the moment of order $x$ in the volume space and $y$ in the surface space can be formulated as:

$$M_{x,y} = \int_{v=0}^{+\infty} \int_{s=0}^{+\infty} v^x s^y dv ds. \tag{1.33}$$

It can then be observed that the first moments $M_{0,0}$, $M_{1,0}$ and $M_{0,1}$ characterize respectively the particles number density, the total soot volume (and therefore the soot volume fraction) and the total soot surface. Determining all the moments for $(x, y) \in [0, +\infty[\times[0, +\infty[$ is equivalent to define all the particles size distribution without any assumption. In practice, only the first moments are considered and the description of the PSD is considered as precise enough. Transport equations are solved for each one of the selected moments. The source terms depend on the different moment weights, gas phase parameters, the transported moments but also unknown moments which need to be closed.

The main advantages of this method are:

- They are based on detailed description of the different physical and chemical phenomena,
- Mono-variate (in the particles volume or surface space) or bi-variate volume-surface description of the PSD can be considered enabling to describe the soot particles morphology.

Its main drawbacks are:

- They present a high mathematical complexity. Indeed, the different moment source terms are generally function of non-transported moments, and closure problems need to be solved,
- Most of the methods of moments do not provide access to the PSD (or NDF). The PSD can be reconstructed based on the values of the transported moments but the reconstruction is generally expensive.

### 1.4.4 Sectional methods

The sectional approach consists in dividing the PSD into different classes of particles with neighboring size (Gelbard and Seinfeld 1980). These classes are generally called **"sections"**. To delimit the volume space occupied by these sections, different solutions are possible. The one proposed by Netzell et al. (2007) describes a power law for the volume space occupied by each section $i$. For a discretization with $N_{\text{sect}}$ sections, the maximum volume $v_i^{\max}$ of a particle size of the section $i$ verifies the following relation:

$$v_i^{\max} = v^{\text{MIN}} \left( \frac{v^{\text{MAX}}}{v^{\text{MIN}}} \right)^{i/N_{\text{sect}}} \tag{1.34}$$

where $v^{\text{MIN}}$ and $v^{\text{MAX}}$ correspond respectively to the smallest and biggest soot particle.
Then, in a mono-variate description of the soot particles size distribution the PSD is solved by solving one or several moments of the soot particles size distribution inside each section $i$, depending on the description of the soot volume fraction density inside each section.

The main advantages of this method are:

- They are based on detailed description of the different physical and chemical phenomena,
- Mono-variate (in the particles volume or surface space) or bi-variate volume-surface description of the PSD can be considered enabling to describe the soot particles morphology. For mono-variate description of the PSD, the morphology can be accounted for by imposing a surface-volume relationship depending on the soot particles size.

Its main drawbacks are:

- The method is expensive and is generally considered as unaffordable when bi-variate surface-volume description of the PSD or NDF is considered.

- The numerical accuracy depends on the number of sections used for the PSD or NDF discretization. More than 20 sections are generally required in order to have a correct numerical accuracy for a mono-variate description.

### 1.4.5 Stochastic methods

In order to avoid any assumption on the PSD shape, Monte Carlo techniques have been applied to the solution of soot population balances (Mitchell and Frenklach 1998; Balthasar and Kraft 2003; Celnik et al. 2007). The soot particles are represented through a discrete list of particles and their evolution is solved using an explicit Monte Carlo technique.
However, due to its extremely high cost and the large number of shots needed for the convergence, this methodology is not affordable in practical complex configurations. Nevertheless, the Monte Carlo approach is generally employed in order to validate the development of other models for PSD prediction, such as the sectional methods or methods of moments in academic configurations.

The main advantages of this method are:

- No assumption is realized on the PSD or NDF shape,
- Detailed description of physical and chemical soot processes can be taken into account,
- Bi-variate volume-surface description of PSD or NDF can be considered,
- The corresponding solutions can be considered as reference solutions of the soot population balance equation.

Its main drawbacks are:

- Its coupling with gas phase chemical kinetics description requires specific numerical methods (Celnik et al. 2007),
- Its expensive cost due to the large number of shots required for numerical convergence.

### 1.4.6 Comparison between the different categories of numerical methods

Table 1.5 compares the different categories of numerical methods in terms of quality of soot evolution process description, PSD/NDF description, soot particles morphology description, universality and cost.

Empirical and semi-empirical methods present the lowest cost but are generally based on coarse description of the different soot particles evolution processes, without morphology description and description of the PSD. Moreover, their tuned parameters are highly case dependent. Methods of moments present also a low cost but depending on their formulation, they often do not provide access to the PSD and they can present high complexity in terms of mathematical

closure.

In this thesis, the main goal is to describe the PSD evolution in 3-D turbulent simulations. Kinetic, sectional and stochastic methods are the methods enabling to describe it without expensive reconstruction methods. Kinetic models require the transport of the corresponding kinetic scheme together with the BINs, which is unaffordable in 3-D simulations. Stochastic methods are intrinsically expensive methods and can not be selected in 3-D simulations. The sectional method can be easily coupled with tabulation techniques for the gaseous phase description. That is why this method can be considered as the method providing access to this PSD at the lowest cost, and will be considered in this manuscript. Details on the corresponding sectional model will be presented in Chapter 2, Section 2.2.

| **Method** | **Soot evolution processes description** | **PSD/NDF description** | **Morphology description** | **Mathematical complexity** | **Cost** |
|---|---|---|---|---|---|
| (Semi-) empirical | - - | - | - | ++ | ++ |
| Kinetic | + | + | + | + | - - |
| Methods of moments | + | - | ++ | - - | + |
| Sectional | + | + | + | + | - |
| Stochastic | + | ++ | ++ | - | - - - |

**Table 1.5:** *Comparison between the different categories of numerical methods. Green crosses correspond to advantages and red dashes corresponds to drawbacks.*

## 1.5 Conclusion

In this chapter, geometrical characteristics of soot particles have been introduced.

Then, soot particles dynamics and reactivity processes and their impact on soot particles geometrical characteristics have been presented. Six main processes are involved in soot particles formation: PAHs dimerization, nucleation, condensation, surface growth, oxidation and coagulation. The numerous uncertainties on the state-of-the-art description of these processes have been discussed.

Then, the different methods for predicting soot particles evolution have been presented and the sectional method has been chosen for its capacity to predict the particles size distribution at a reasonable cost: next chapter will present the different equations governing the developed sectional model in this thesis.

# Chapter 2

# The Sectional Method

*The sectional method developed and employed in this thesis is presented in details. Then, its validation for premixed flames at atmospheric and elevated pressures is presented. Its accuracy in counterflow diffusion flames configurations is also investigated.*

*Then, the unsteady behavior of soot production is analyzed in laminar configurations by studying the response of soot production to strain rate fluctuations. Unsteady laminar counterflow diffusion flames with an imposed oscillating strain rate are investigated both analytically and numerically. An analytical linearized model is developed in order to predict the identified unsteady response of soot production.*

*Finally, variability and uncertainties that remain in numerical modeling of sooting flames are discussed.*

## Contents

## 2.1 Gas phase and soot precursors description

Although the sectional model only describes the solid phase, its performance is strictly related to the selected gas phase description and it is therefore necessary to present the sectional model as a package combining both a gas phase description and the equations related to the solid phase. Indeed, any modification of the gas phase leads to modifications in the description of the solid phase. Thus, the models selected for the gaseous and solid phases are described in this Chapter and no modification of the models and their parameters will be considered for all the following chapters of the manuscript.

For the prediction of soot particles evolution in flames, in addition to the global gas properties (temperature, flame speed, ...), soot precursors and gaseous species participating to the soot surface reactivity ($C_2H_2$, OH, $O_2$, ...) must be predicted as a first step.

### 2.1.1 Flame general properties description

Several kinetic schemes have been considered here to select the most optimized for the objectives of our study. We want at least to verify the correct prediction of ethylene-air flame general properties (laminar flame speed $S_L$, temperature, etc..). Details of the mechanisms considered are listed in Table 2.1.

| Name | Nb. of species | Nb. of reactions | Largest hydrocarbon | Reference |
|---|---|---|---|---|
| ABF | 101 | 544 | $C_{16}H_{10}$ | Appel et al. (2000) |
| MARCHAL | 154 | 850 | $C_{16}H_{10}$ | Marchal (2008) |
| MAUSS | 82 | 457 | $C_{16}H_{10}$ | Mauss (1998) |
| CHERNOV | 102 | 831 | $C_{20}H_{12}$ | Chernov et al. (2014) |
| SLAVINSKAYA | 94 | 719 | $C_{20}H_{12}$ | Slavinskaya et al. (2012) |
| POLIMI | 170 | 5465 | $C_{16}H_{10}$ | Richter et al. (2005) |
| USC-II | 111 | 784 | $C_8H_6$ | Wang et al. (2007) |
| KM2 | 202 | 1351 | $C_{24}H_{12}$ | Wang et al. (2013) |

**Table 2.1:** *Studied kinetic schemes*

First, prediction of laminar flame speeds of ethylene-air premixed flames at 1 atm, cold gas temperature of 298 K and for different equivalence ratios are presented in Fig. 2.1. Results are compared to experimental data of Egolfopoulos et al. (1991); Hassan et al. (1998); Jomaas et al. (2005).

It can be observed that five mechanisms predict well the laminar flame speed: USC-II, KM2, POLIMI, CHERNOV and SLAVINSKAYA. In order to determine the reference mechanism that will be used for all soot simulations in this thesis, next section compares their predictions for polycyclic aromatic hydrocarbons (PAH) with experiments in literature.

### 2.1.2 Prediction of PAHs

Figure 2.2 presents a comparison of the prediction of several species for the flame experimentally studied by Castaldi et al. (1996). It corresponds to a burner stabilized $C_2H_4$(21.3%)/ $O_2$(20.9%)/ Ar(57.8%) premixed flame ($\phi = 3.06$, 7.56 L/min gas flow rate, cold gas temperature of 298 K, pressure of 1 atm). USC-II scheme is not considered here as it only contains the smallest polycyclic aromatic hydrocarbon: the benzene ($C_6H_6$). Soot production is not considered in these calculations. Then, it is important to remind that as PAHs are consumed for soot production, it is expected that PAHs are slightly overestimated by the different mechanisms.

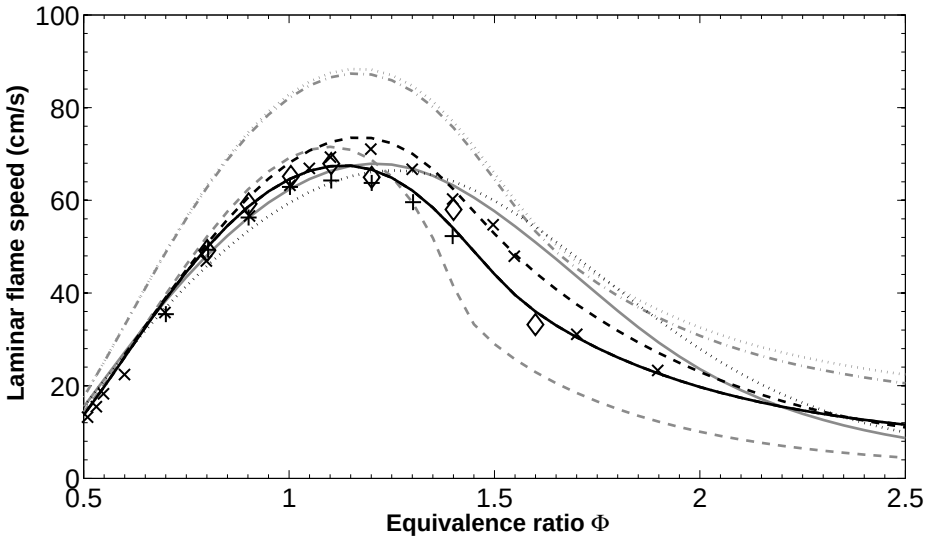


**Figure 2.1:** *Comparison of ethylene flame speeds for different schemes (ABF (Appel et al. 2000) : (···), Marchal et al. (Marchal et al. 2009) (–·–), Mauss et al. (Mauss 1998) (– –), Chernov et al. (Chernov et al. 2014) (–), Slavinskaya et al. (Slavinskaya et al. 2012) (···), USC-II (Wang et al. 2007) (–·–), Richter et al. (Richter et al. 2005) (– –), KM2 (Wang et al. 2013) (–) ). Comparison with experiments (Egolfopoulos et al. (Egolfopoulos et al. 1991) (×), Hassan et al. (Hassan et al. 1998) (◊), Jomaas et al. (Jomaas et al. 2005) (+)). Results for the schemes USC-II and KM2 are superposed.*

Concerning major species, a good agreement is obtained for the different mechanisms. For PAHs, better predictions are obtained by the KM2, SLAVINSKAYA and CHERNOV mechanisms. It should be noted that only the KM2 scheme predicts the concentrations of PAHs larger than pyrene ($A_4$). Then, for the $A_4R_5$ concentration, only the result with this kinetic scheme is presented and good predictions are overall obtained.

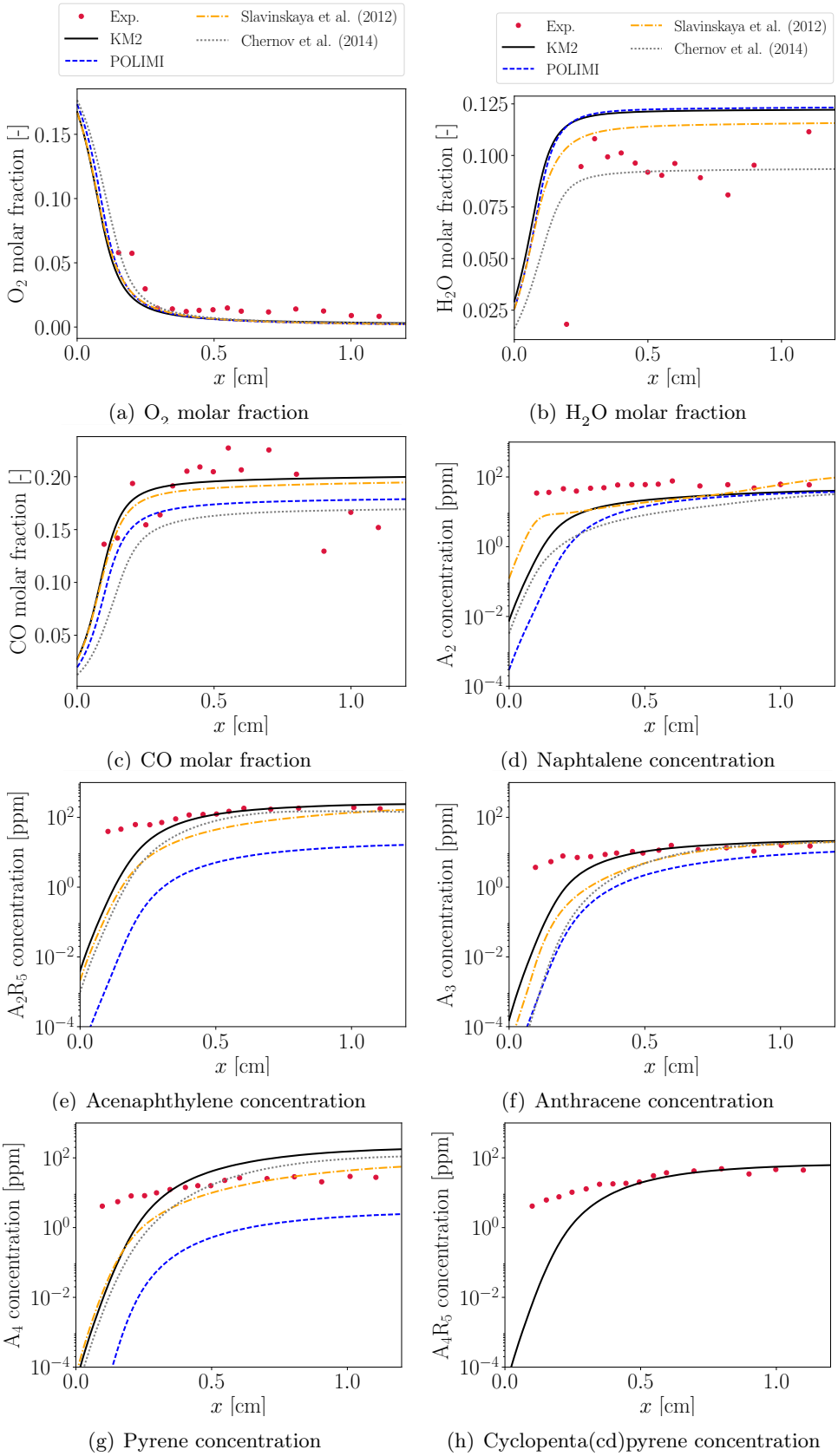


(a) $O_2$ molar fraction

(b) $H_2O$ molar fraction

(c) CO molar fraction

(d) Naphtalene concentration

(e) Acenaphthylene concentration

(f) Anthracene concentration

(g) Pyrene concentration

(h) Cyclopenta(cd)pyrene concentration

**Figure 2.2:** *Species profiles in a* $C_2H_4/O_2/Ar$ *premixed flame. Numerical predictions with the KM2, POLIMI, CHERNOV and SLAVINSKAYA mechanisms are compared with experiments from Castaldi et al. (1996).*

Figure 2.3 presents a comparison of the prediction of several soot precursors for the flame experimentally studied by Ciajolo et al. (1996); Ciajolo et al. (2001). It corresponds to a burner-stabilized premixed flame $C_2H_4(44.4\%)/\ O_2(55.6\%)$ ($\phi = 2.40$, cold gas velocity $u_0 = 2$ cm/s, cold gas temperature of 298 K, pressure of 1 atm), retained for the International Sooting Flame (ISF) workshop (ISF3 2017). For this flame, it can be observed that a better agreement is obtained for the KM2 kinetic scheme compared to the other mechanisms.

Moreover, in their study, Wang et al. (2013) have shown that a good agreement in PAHs evolution prediction is obtained in ethylene-air counterflow diffusion flames. For all these reasons, we choose the KM2 mechanism for all simulations presented in the present work.

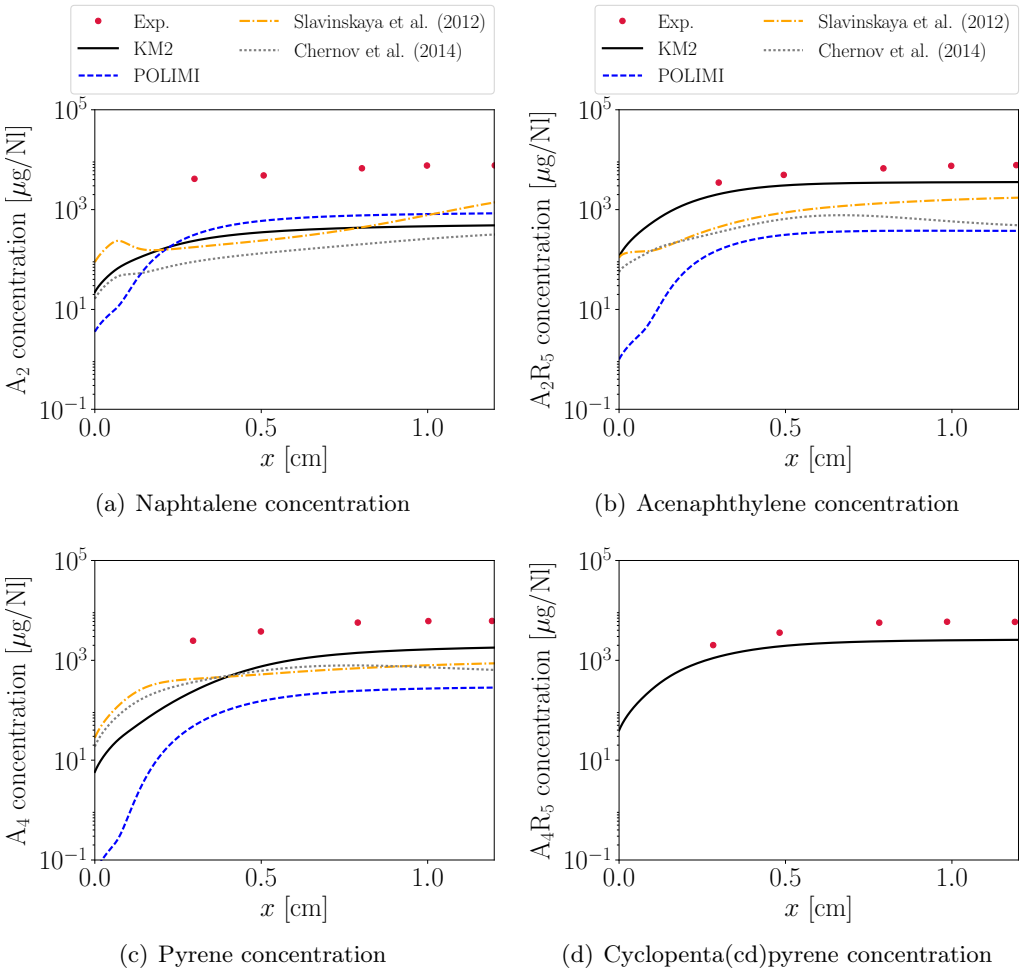


(a) Naphtalene concentration

(b) Acenaphthylene concentration

(c) Pyrene concentration

(d) Cyclopenta(cd)pyrene concentration

**Figure 2.3:** *Gaseous soot precursors numerical predictions obtained by KM2, POLIMI, CHERNOV and SLAVINSKAYA mechanism compared with experiments data of Ciajolo et al. (1996); Ciajolo et al. (2001).*

### 2.1.3 Supplementary validations of the kinetic scheme

#### 2.1.3.1 Methane-air and propane-air mixtures

Prediction of laminar flame speeds for the chosen scheme has also been studied in the case of ethylene-air, methane-air and propane-air mixtures (see Fig. 2.4). Results are compared to experimental data of the literature and a good prediction of the flame speeds for the three studied fuels is obtained with the selected scheme.

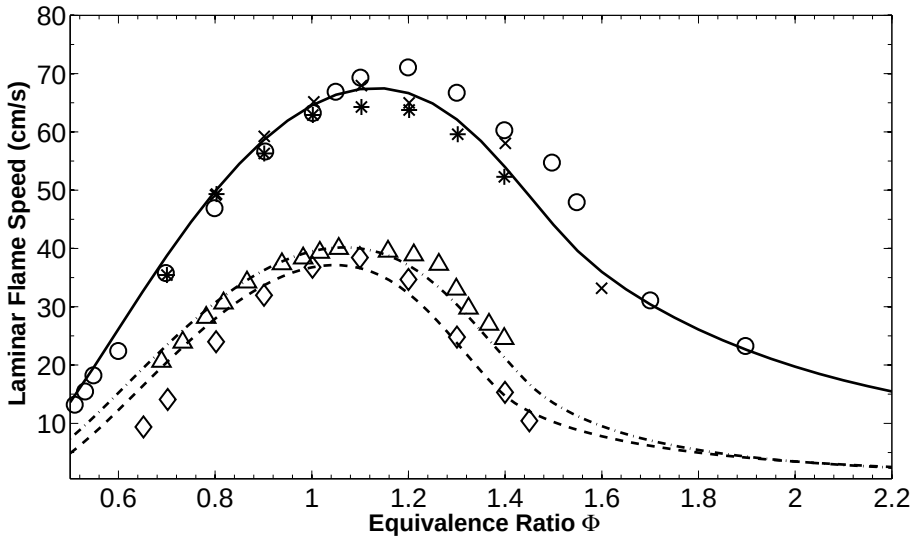


**Figure 2.4:** *Laminar flame speeds for methane (– –), propane (– · –) and ethylene (–) flames for the scheme KM2. Comparison with experiments for methane (Van Maaren et al. (Van Maaren and De Goey 1994) (◇)), propane (Vagelopoulos et al. (Vagelopoulos and Egolfopoulos 1998) (△)) and ethylene (Egolfopoulos et al. (Egolfopoulos et al. 1991) (○), Hassan et al. (Hassan et al. 1998) (×), Jomaas et al. (Jomaas et al. 2005) (∗)) .*

#### 2.1.3.2 Laminar flame speed for ethylene-air mixtures at higher pressures

Figure 2.5 compares the prediction of the ethylene-air mixture flame speed at different pressures (1 bar, 2 bar and 5 bar) and for an inlet temperature of 298 K with experiments. A good prediction for all these pressures is obtained for the selected mechanism. The predicted laminar flame speed at 3 bar is also added to the plot, as it is the pressure considered in Chapters 5, 8 and 9.

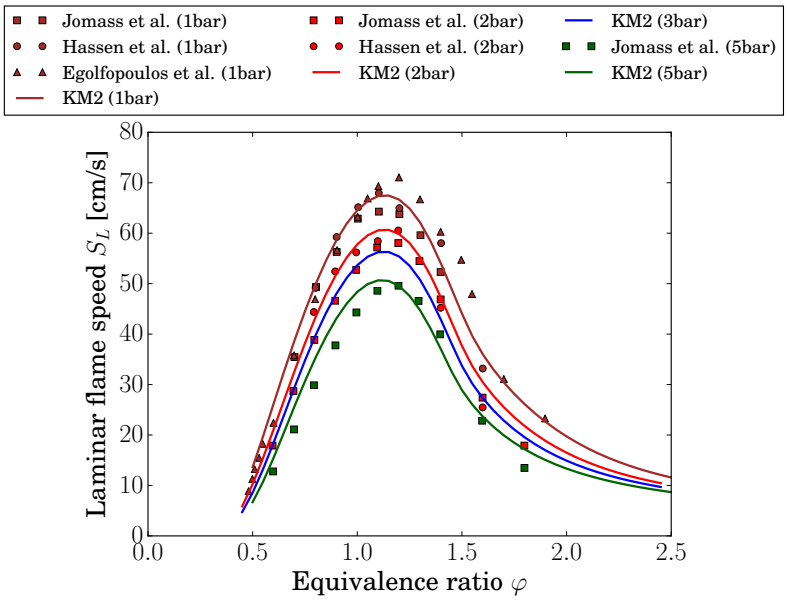


**Figure 2.5:** *Ethylene-air flame speeds at 1, 2, 3 and 5 bars obtained with the KM2 scheme. The experimental data are from Egolfopoulos et al. (1991); Hassan et al. (1998); Jomaas et al. (2005)*

## 2.2 Equations of the sectional model

### 2.2.1 Particles size distribution discretization

As previously explained in Chapter 1, the sectional approach consists in dividing the PSD into $N_{\text{sect}}$ different classes of particles with neighboring size (Gelbard and Seinfeld 1980), called **"sections"**. Each section $i$ represents particles with a volume between $v_i^{\min}$ and $v_i^{\max}$.

Here, the PSD is assumed constant in each section. Then, only one moment inside each section is solved, i.e. the total soot volume fraction $Q_{s,i}$ of the section $i$, defined as:

$$Q_{s,i} = \int_{v_i^{\min}}^{v_i^{\max}} q_i(v). \tag{2.1}$$

Inside each section $i$, the soot volume fraction density $q(v)$ is considered constant and equal to $q_i = q(v_i^{\text{mean}})$ with $v_i^{\text{mean}} = (v_i^{\min} + v_i^{\max})/2$. Figure 2.6 illustrates the corresponding discretization of the particles size distribution (PSD).

The volume particle number density $n(v)$ for each section is then evaluated for $v \in [v_i^{\min}, v_i^{\max}]$ as:

$$n(v) = q_i/v \tag{2.2}$$

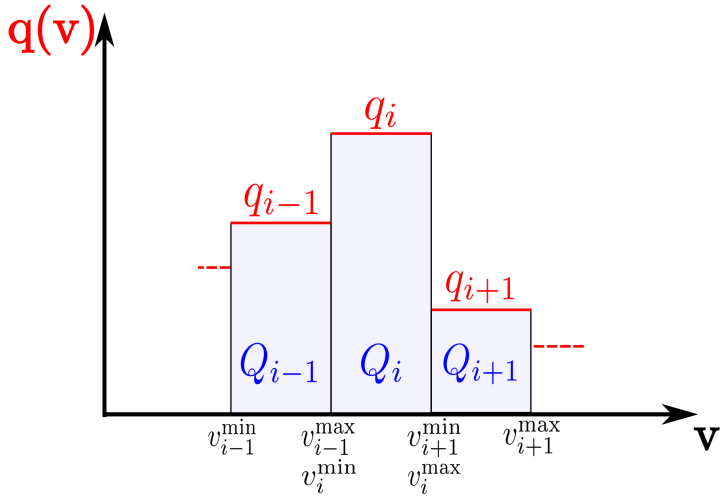


**Figure 2.6:** *Discretization of the soot volume fraction density $q(v)$.*

Then the soot volume fraction $Q_{s,i}$ and the particles number density $N_i$ relative to the section $i$ writes:

$$\begin{aligned} Q_{s,i} &= \int_{v_i^{\min}}^{v_i^{\max}} q(v)dv = q_i \left(v_i^{\max} - v_i^{\min}\right) \\ N_i &= \int_{v_i^{\min}}^{v_i^{\max}} n(v)dv = q_i \int_{v_i^{\min}}^{v_i^{\max}} \frac{dv}{v} = q_i \ln\left(\frac{v_i^{\max}}{v_i^{\min}}\right) \end{aligned} \tag{2.3}$$

The total soot volume fraction $f_V$ and particle number density $N_{\text{part}}$ are evaluated as:

$$\begin{aligned} f_V &= \int_0^{\infty} q(v)dv = \sum_{i=1}^{N_{\text{sect}}} Q_{s,i} = \sum_{i=1}^{N_{\text{sect}}} q_i \left(v_i^{\max} - v_i^{\min}\right) \\ N_{\text{part}} &= \int_0^{\infty} n(v)dv = \sum_{i=1}^{N_{\text{sect}}} N_i = \sum_{i=1}^{N} q_i \ln\left(\frac{v_i^{\max}}{v_i^{\min}}\right) \end{aligned} \tag{2.4}$$

The particles size distribution discretization is done as follows:

- The first section is defined so that it contains all the nascent particles generated from the collisions of two dimers of different sizes, depending on the number of PAHs considered,
- For $i \in [\![2, N_{\text{sect}} - 1]\!]$, the volume intervals of the sections follow a geometrical progression, as proposed by Netzell et al. (2007):

$$\begin{aligned} v_i^{\max} &= v_1^{\max} \left(\frac{v^{\text{MAX}}}{v_1^{\max}}\right)^{\frac{i-1}{N_{\text{sect}}-2}} \\ v_i^{\min} &= v_{i-1}^{\max} \end{aligned} \tag{2.5}$$

- The last section can be considered as a "trash" section which contains very big unexpected soot particles from $v^{\mathrm{MAX}}$ to $v^{\mathrm{BIG}}$ and guarantees soot mass conservation. The value of $v^{\mathrm{BIG}}$ is chosen as an unattainable soot particle volume. The value of $v^{\mathrm{MAX}}$ corresponds to a characteristic volume of the expected biggest soot particles and is chosen as the maximum soot particle volume resolved accurately.

This constructed discretization ensures that the volume interval $[v_i^{\min}, v_i^{\max}]$ described by each section $i$ is bigger than the sum of all the volume intervals of the smaller sections, enabling an easier handling of coagulation source terms for each section.

### 2.2.2 Discretized equations

Discretizing Eq. (1.8) for each class of particle $i$, the PBE for each section writes:

$$\frac{\partial n_i}{\partial t} + \nabla \cdot ((\mathbf{u} + \mathbf{v_T})\, n_i) = \nabla \cdot (D_{s,i} \nabla n_i) + \dot{n}_{s,i} \tag{2.6}$$

where $\mathbf{u}$ is the gas velocity, $\mathbf{v_T}$ is the thermophoretic velocity and $\dot{n}_{s,i}$ is the source term for the section $i$.

Then, multiplying this equation by $v$, the volume of each particle, and integrating this equation for $v \in \left[v_i^{\min}, v_i^{\max}\right]$, one obtains:

$$\begin{aligned} &\frac{\partial}{\partial t}\left(\int_{v_i^{\min}}^{v_i^{\max}} n_i(v) v dv\right) + \nabla \cdot \left((\mathbf{u} + \mathbf{v_T}) \int_{v_i^{\min}}^{v_i^{\max}} n_i(v) v dv\right) \\ &= \nabla \cdot \left(D_{s,i} \nabla \left(\int_{v_i^{\min}}^{v_i^{\max}} n_i(v) v dv\right)\right) + \int_{v_i^{\min}}^{v_i^{\max}} \dot{n}_{s,i} v dv \\ \Leftrightarrow\ &\frac{\partial Q_{s,i}}{\partial t} + \nabla \cdot ((\mathbf{u} + \mathbf{v_T})\, Q_{s,i}) = \nabla \cdot (D_{s,i} \nabla Q_{s,i}) + \dot{Q}_{s,i} \end{aligned} \tag{2.7}$$

Moreover, noting $V_{\mathrm{soot},i}$ ($M_{\mathrm{soot},i}$) the total volume (the total mass) of soot particles belonging to the section $i$, and $V$ ($M$) the total volume (the total mass) of the considered system, one can write $M_{\mathrm{soot},i} = \rho_s V_{\mathrm{soot},i}$ and $M = \rho V$. Now we use the relations $Y_{s,i} = M_{\mathrm{soot},i}/M$ and $Q_{s,i} = V_{\mathrm{soot},i}/V$ respectively for soot mass fraction and soot volume fraction relative to the $i^{\mathrm{th}}$ section. Then, $Q_{s,i}$ can be expressed as a function of a mass fraction relative to the section $i$, $Y_{s,i}$, the gas density $\rho$, and the density of soot particles $\rho_s$:

$$Q_{s,i} = \frac{M_{\mathrm{soot},i}}{\rho_s V} = \frac{Y_{s,i} M}{\rho_s V} = \frac{\rho}{\rho_s} Y_{s,i}. \tag{2.8}$$

Eq. (2.7) can be rewritten as:

$$\frac{\partial \rho Y_{s,i}}{\partial t} + \nabla \cdot (\rho(\mathbf{u} + \mathbf{v_T}) Y_{s,i}) = \nabla \cdot (D_{s,i} \nabla (\rho Y_{s,i})) + \rho_s \dot{Q}_{s,i} \tag{2.9}$$

In a similar way to the Fick's law for the gaseous species, the following assumption is done:

$$\nabla \cdot (D_{s,i} \nabla(\rho Y_{s,i})) \approx \nabla \cdot (\rho D_{s,i} \nabla(Y_{s,i})) \tag{2.10}$$

It is however important to notice that this assumption has a negligible impact, as molecular diffusion transport is generally negligible for soot particles.

Finally, the soot mass fraction $Y_{s,i}$ of the section $i$ follows the transport equation:

$$\frac{\partial \rho Y_{s,i}}{\partial t} + \nabla \cdot (\rho(\mathbf{u} + \mathbf{v_T}) Y_{s,i}) = \nabla \cdot (\rho D_{s,i} \nabla(Y_{s,i})) + \rho_s \dot{Q}_{s,i} \tag{2.11}$$

$\dot{Q}_{s,i} = \rho \dot{q}_{s,i}$ is the production rate (in $\mathrm{s}^{-1}$) of the soot volume fraction for the $i^{\text{th}}$ section. The production rate $\dot{q}_{s,i}$ of the soot volume fraction for the $i^{\text{th}}$ section accounts for:

- nucleation (subscript $_{\text{nu}}$), considered as the coalescence of two dimers,
- condensation (subscript $_{\text{cond}}$), considered as the coalescence of a dimer at a soot particle surface,
- surface growth (subscript $_{\text{sg}}$) and oxidation (subscript $_{\text{ox}}$), describing the surface reactivity of soot particles,
- coagulation (subscript $_{\text{coag}}$), corresponding to the collision of two solid particles resulting in a bigger soot particle.

$\dot{q}_{s,i}$ (in $\mathrm{m}^3.\mathrm{kg}^{-1}.\mathrm{s}^{-1}$) can then be expressed as:

$$\dot{q}_{s,i} = \dot{q}_{\text{nu},i} + \dot{q}_{\text{cond},i} + \dot{q}_{\text{sg},i} + \dot{q}_{\text{ox},i} + \dot{q}_{\text{coag},i} \tag{2.12}$$

With the final goal of the use of this method in an LES simulation (Parts II and III of this manuscript), it is convenient to rewrite all the source terms as a product of two contributions, in order to highlight their dependence on the gaseous and solid characteristics:

$$\begin{aligned}
\dot{q}_{\text{nu},i} &= \dot{q}^{\text{gas}}_{\text{nu},i} \dot{q}^{\text{solid}}_{\text{nu},i} \\
\dot{q}_{\text{cond},i} &= \dot{q}^{\text{gas}}_{\text{cond},i} \dot{q}^{\text{solid}}_{\text{cond},i} \\
\dot{q}_{\text{sg},i} &= \dot{q}^{\text{gas}}_{\text{sg},i} \dot{q}^{\text{solid}}_{\text{sg},i} \\
\dot{q}_{\text{ox},i} &= \dot{q}^{\text{gas}}_{\text{ox},i} \dot{q}^{\text{solid}}_{\text{ox},i} \\
\dot{q}_{\text{coag},i} &= \dot{q}^{\text{fm,gas}}_{\text{coag},i} \dot{q}^{\text{fm,solid}}_{\text{coag},i} + \dot{q}^{\text{c1,gas}}_{\text{coag},i} \dot{q}^{\text{c1,solid}}_{\text{coag},i} + \dot{q}^{\text{c2,gas}}_{\text{coag},i} \dot{q}^{\text{c2,solid}}_{\text{coag},i}
\end{aligned} \tag{2.13}$$

where the superscripts $^{\text{gas}}$ and $^{\text{solid}}$ respectively correspond to the gaseous and soot dependence parts of each soot source term, which will be detailed in Section 2.2.5. It should be noted that the gaseous contribution parts depend only on $T$, $\rho$, the dynamic viscosity $\mu$, the pressure $P$, and the HACA-RC mechanism-involved species concentrations.

### 2.2.3 Morphological description

Compared to the classical sectional models, in the present approach a soot particle is not always considered as spherical but its morphology depends on its size. For this, a soot particle of a given volume $v$ and surface $s$ is here considered as an aggregate composed of $n_p = s^3/(36\pi v^2)$ primary spherical particles with a diameter $d_p = 6v/s$. The evolution of the particle surface $s$ is provided as a function of its volume $v$ as:

$$\left(s/s_{C_2}\right) = \begin{cases} \left(v/v_{C_2}\right)^{2/3} & \text{for } v < v_1, \\ \left(v/v_{C_2}\right)^{\theta(v)/3} & \text{for } v > v_1 \end{cases} \tag{2.14}$$

with:

$$\theta(v) = 3.0 \cdot \frac{(\log(v/v_1)) + 2/3 \cdot \left(\log(v_1/v_{C_2})\right)}{\log(v/v_{C_2})} \tag{2.15}$$

where $v_1 = 10^{2.6}$ nm$^3$ denotes the volume beyond which a soot particle is no longer considered as spherical. $s_{C_2}$ and $v_{C_2}$ are respectively the surface and volume of a spherical molecule composed of two carbon atoms. Quantities $\theta(v)$, $d_p(v)$ and $n_p(v)$ are supposed constant for each section $i$ and their values $\theta_i$, $d_{p,i}$ and $n_{p,i}$ are evaluated at $v_i^{\text{mean}} = (v_i^{\min} + v_i^{\max})/2$. This relation has been derived in Rodrigues et al. (2017) by fitting numerical results available in literature (Mueller et al. 2009a; Salenbauch et al. 2015) and it impacts not only surface reactions descriptions but also collisional phenomena via the value of the collisional diameter $d_c$, function of the primary particles diameter $d_p$ and the number of primary particles $n_p$. Figure 2.7 illustrates this correlation and its comparison with literature data.
It should be noticed that for $v < v_1$, particles are spherical, so that $n_p = 1$ and $d_p = (6v/\pi)^{1/3}$.

Finally, it is important to notice that this empirical law is not universal and is case dependent. However, it enables to not discretize both volume and surface space of soot particles, and therefore, it is a good compromise between CPU cost and accuracy for a sectional method.

### 2.2.4 PAHs, dimers and soot precursors

Dimer, an intermediate state for the polycyclic aromatic hydrocarbons (PAH) between the gaseous and the solid phases, is here obtained from the collision of two PAHs (Blanquart and Pitsch 2007; Mueller et al. 2009b). As suggested by (Blanquart and Pitsch 2007), these dimers are considered as the soot precursors. In the presented model, the dimerization of seven PAHs ($N_{\text{PAH}} = 7$) having four or more aromatic rings are considered, from the pyrene ($A4$) up to

coronen ($A7$).

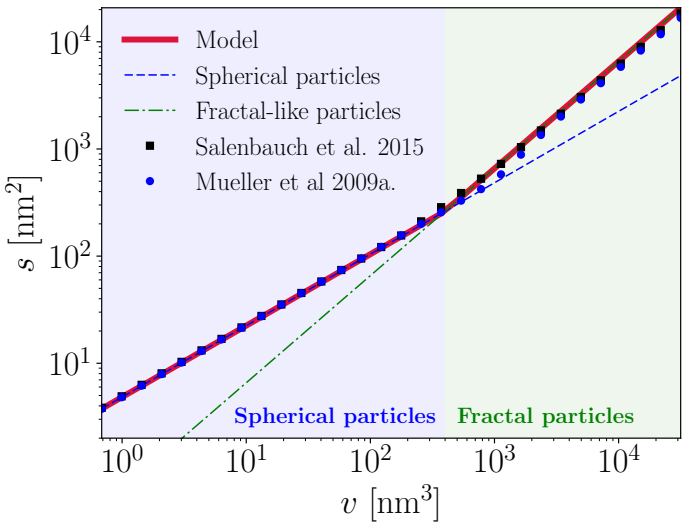


**Figure 2.7:** *Presumed relationship between soot particle surface and soot particle volume. Data from the literature (Mueller et al. 2009a; Salenbauch et al. 2015) obtained with bi-variate moments resolution on one laminar premixed ethylene/air flame are also presented.*

The dimerization production rate $\dot{Q}^{\mathrm{d}}_{\mathrm{PAH}_k}$ for a PAH$_i$ is given by:

$$\dot{Q}^{\mathrm{d}}_{\mathrm{PAH}_k} = 2 v_{\mathrm{PAH}_k} \gamma_k \left( \frac{4\pi k_b T}{m_k} \right)^{1/2} d^2_{\mathrm{PAH}_k} [\mathrm{PAH}_k]^2 N_A^2 \tag{2.16}$$

where $d_{\mathrm{PAH}_k}$ is the diameter of a PAH$_k$ particle (supposed spherical), $N_A$ the Avogadro number, $k_b$ the Boltzmann constant, $T$ the gas temperature, and $m_k$ the mass of the particle PAH$_k$. $v_{\mathrm{PAH}_k}$ is the volume of a PAH$_k$ evaluated as $v_{\mathrm{PAH}_k} = n_{C_{\mathrm{PAH}_k}} v_{C_2}/2$ where $n_{C_{\mathrm{PAH}_k}}$ is the number of C atoms of the PAH$_k$. $\gamma_k = C_N m_k^4$ is the sticking coefficient factor for PAH$_k$ with $C_N$ a constant equal to $1.5 \cdot 10^{-11} g^{-4}$ (Blanquart and Pitsch 2007).

The seven PAHs involved in the dimerization process, their chemical formula, their name in the KM2 kinetic scheme (Wang et al. 2013), their molar mass and their corresponding dimerization sticking coefficient are listed in Table 2.2.

| PAH name | PAH name in the KM2 scheme | Chemical formula | Molar mass [g/mol] | $\gamma_k$ | Molecular organization |
|---|---|---|---|---|---|
| Pyrene (A4) | A4 | $C_{16}H_{10}$ | 202 | 0.0250 | 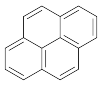 |
| Chrysene (A5) | CHRYSEN | $C_{18}H_{12}$ | 228 | 0.0406 | 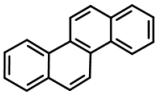 |
| Benzo(a)pyrene (A5) | BAPYR | $C_{20}H_{12}$ | 252 | 0.0606 | 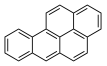 |
| Benzo(e)pyrene (A5) | BEPYREN | $C_{20}H_{12}$ | 252 | 0.0606 | 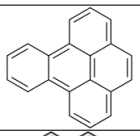 |
| Perylene (A5) | PERYLEN | $C_{20}H_{12}$ | 252 | 0.0606 | 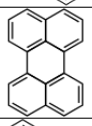 |
| Benzoperylene (A6) | BGHIPER | $C_{22}H_{12}$ | 276 | 0.0871 | 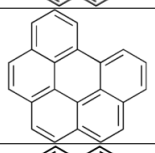 |
| Coronene (A7) | CORONEN | $C_{24}H_{12}$ | 300 | 0.1216 | 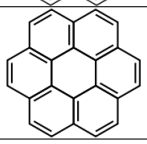 |

**Table 2.2:** *Involved PAHs considered for the dimerization process modeling.*

To account for these multiple PAHs involved in dimerization process, an equivalent lumped PAH with mass fraction of $Y_{\mathrm{PAH}}$ is considered. Its mass fraction and total dimerization source term are evaluated as:

$$\begin{aligned} Y_{\mathrm{PAH}} &= \sum_{k=1}^{N_{\mathrm{PAH}}} Y_{\mathrm{PAH}_k} \\ \dot{Q}_{\mathrm{DIM}} &= \sum_{k=1}^{N_{\mathrm{PAH}}} \dot{Q}^{\mathrm{d}}_{\mathrm{PAH}_k} \end{aligned} \tag{2.17}$$

This lumped equivalent PAH leads to an equivalent dimer with a volume $v_{\mathrm{d}}$ evaluated as:

$$v_d = 2 \cdot \frac{\sum_{k=1}^{N_{\mathrm{PAH}}} \dot{Q}^{\mathrm{d}}_{\mathrm{PAH}_k}}{\sum_{k=1}^{N_{\mathrm{PAH}}} \dot{Q}^{\mathrm{d}}_{\mathrm{PAH}_k} / (2 v_{\mathrm{PAH}_k})}. \tag{2.18}$$

It will vary in the calculation depending on the local PAHs concentration.
For the calculation of the dimers number density $N_d$, a quasi-steady-state assumption is considered between their production from the gaseous phase and their consumption by nucleation and condensation (Blanquart and Pitsch 2007; Mueller et al. 2009b):

$$\dot{Q}_{\mathrm{DIM}} = \rho \sum_{i=1}^{N_{\mathrm{sect}}} \left( \dot{q}_{\mathrm{nu},i} + \dot{q}_{\mathrm{cond},i} \right). \tag{2.19}$$

### 2.2.5 Soot source terms

#### 2.2.5.1 Nucleation

Coalescence of two dimers is considered for the formation of the smallest soot nuclei (Blanquart and Pitsch 2007; Mueller et al. 2009b) through the Smoluchowski equation (Smoluchowski 1916). The source term for nucleation is:

$$\dot{q}_{\mathrm{nu},i} = v_{\mathrm{d}} \beta_{\mathrm{d}} N_{\mathrm{d}}^2 \delta_{i1} / \rho \tag{2.20}$$

where $\beta_{\mathrm{d}}$ corresponds to the collision frequency of dimers occuring in a free molecular regime:

$$\beta_{\mathrm{d}} = \epsilon_{\mathrm{nu}} \left( \frac{3}{4\pi} \right)^{1/6} \sqrt{\frac{6 k_b T}{\rho_s}} 4\sqrt{2} v_{\mathrm{d}}^{1/6} \tag{2.21}$$

where $\epsilon_{\mathrm{nu}} = 2.5$ is the amplification factor due to Van der Waals interactions (Marchal 2008). The Kronecker delta factor $\delta_{i1}$ in Eq. (2.20) enables the nucleation source term to be considered only in the first section of the particles size distribution.

#### 2.2.5.2 Condensation

It is considered as the coalescence of a dimer at a soot particle surface. The condensation source term of a section $i$ is expressed as:

$$\dot{q}_{\mathrm{cond},i} = \dot{q}_{\mathrm{cond},i}^{\mathrm{gas}\to i} + \dot{q}_{\mathrm{cond},i}^{i-1\to i} - \dot{q}_{\mathrm{cond},i}^{i\to i+1} \tag{2.22}$$

where $\dot{q}_{\mathrm{cond},i}^{\mathrm{gas}\to i}$, $\dot{q}_{\mathrm{cond},+}^{i-1\to i}$ and $\dot{q}_{\mathrm{cond},-}^{i\to i+1}$ respectively correspond to the rate of mass of dimer particles that will condensate on particles of section $i$, to the rate of particle mass that will enter into section $i$ due to condensation with particles of section $i-1$, and to the rate of particle mass that will move from section $i$

to section $i+1$ due to condensation. They are respectively evaluated as:

$$\begin{aligned}
\dot{q}_{\text{cond},i}^{\text{gas}\to i} &= \frac{N_\text{d}}{\rho} v_\text{d} \int_{v_i^{\min}}^{v_i^{\max}-v_\text{d}} \beta_{\text{d},i} n(w) dw \\
\dot{q}_{\text{cond},i}^{i-1\to i} &= \frac{N_\text{d}}{\rho} \int_{v_{i-1}^{\max}-v_\text{d}}^{v_{i-1}^{\max}} \beta_{\text{d},i-1} n(w)(w+v_\text{d}) dw \\
\dot{q}_{\text{cond},i}^{i\to i+1} &= \frac{N_\text{d}}{\rho} \int_{v_i^{\max}-v_\text{d}}^{v_i^{\max}} \beta_{\text{d},i} n(w)\ w\ dw
\end{aligned} \tag{2.23}$$

where the collisional frequency of a dimer with a soot particle has been considered constant by section and evaluated at $v_i^{\text{mean}}$:

$$\begin{aligned}
\beta_{\text{d},i} =& \epsilon_\text{cond} \left(\frac{3}{4\pi}\right)^{1/6} \sqrt{\frac{6k_bT}{\rho_s}} \\
& \sqrt{\frac{1}{v_\text{d}} + \frac{1}{v_i^{\text{mean}}}} \left(v_\text{d}^{1/3} + \left(\frac{\pi}{6}\right)^{1/3} d_{c,i}\right)^2
\end{aligned} \tag{2.24}$$

where $\epsilon_\text{cond} = 1.3$ is the amplification factor due to Van der Waals interactions (Marchal 2008). For each section $i$, the collisional diameter $d_{c,i}$ is considered constant and evaluated as a function of $n_{p,i}$, $d_{p,i}$ and the fractal dimension $D_f$ of particles (considered equal to 1.8):

$$d_{c,i} = d_{p,i} n_{p,i}^{1/D_f}. \tag{2.25}$$

#### 2.2.5.3 Surface growth and oxidation

Soot particle surface growth and oxidation occur at its surface.
As for condensation and keeping the same notations of Eq. (2.22), the corresponding source terms for a section $i$ write as:

$$\begin{aligned}
\dot{q}_{\text{sg},i} &= \dot{q}_{\text{sg},i}^{\text{gas}\to i} + \dot{q}_{\text{sg},i}^{i-1\to i} - \dot{q}_{\text{sg},i}^{i\to i+1} \\
\dot{q}_{\text{ox},i} &= -\dot{q}_{\text{ox},i}^{i\to\text{gas}} + \dot{q}_{\text{ox},i}^{i+1\to i} - \dot{q}_{\text{ox},i}^{i\to i-1}
\end{aligned} \tag{2.26}$$

Based on Eq. (A.11) of Appendix A, Section A.1.1.3 and Eq. (1.30) of Chapter 1, $\dot{q}_{\text{sg},i}^{\text{gas}\to i}$, $\dot{q}_{\text{sg},i}^{i-1\to i}$ and $\dot{q}_{\text{sg},i}^{i\to i+1}$ can be expressed as:

$$
\begin{aligned}
\dot{q}_{\mathrm{sg},i}^{\mathrm{gas}\to i} &= \alpha\frac{K_{\mathrm{sg}}}{\rho}v_{C_2}\int_{v_i^{\min}}^{v_i^{\max}-v_{C_2}}\left(\frac{w}{v_{C_2}}\right)^{\frac{\theta_i}{3}} n(w)dw \\
\dot{q}_{\mathrm{sg},i}^{i-1\to i} &= \alpha\frac{K_{\mathrm{sg}}}{\rho}\int_{v_{i-1}^{\max}-v_{C_2}}^{v_{i-1}^{\max}}\left(\frac{w}{v_{C_2}}\right)^{\frac{\theta_{i-1}}{3}} n(w)(w+v_{C_2})dw \\
\dot{q}_{\mathrm{sg},i}^{i\to i+1} &= \alpha\frac{K_{\mathrm{sg}}}{\rho}\int_{v_i^{\max}-v_{C_2}}^{v_i^{\max}}\left(\frac{w}{v_{C_2}}\right)^{\frac{\theta_i}{3}} n(w)\ w\ dw
\end{aligned}
\tag{2.27}
$$

and $\dot{q}_{\mathrm{ox},i}^{i\to\mathrm{gas}}$, $\dot{q}_{\mathrm{ox},i}^{i+1\to i}$ and $\dot{q}_{\mathrm{ox},i}^{i\to i-1}$ can be expressed as:

$$
\begin{aligned}
\dot{q}_{\mathrm{ox},i}^{i\to\mathrm{gas}} &= \alpha v_{C_2}\frac{K_{\mathrm{ox}}}{\rho}\int_{v_i^{\min}+v_{C_2}}^{v_i^{\max}}\left(\frac{w}{v_{C_2}}\right)^{\frac{\theta_i}{3}} n(w)dw \\
\dot{q}_{\mathrm{ox},i}^{i+1\to i} &= \alpha\frac{K_{\mathrm{ox}}}{\rho}\int_{v_{i+1}^{\min}}^{v_{i+1}^{\min}+v_{C_2}}\left(\frac{w}{v_{C_2}}\right)^{\frac{\theta_{i-1}}{3}} n(w)(w-v_{C_2})dw \\
\dot{q}_{\mathrm{ox},i}^{i\to i-1} &= \alpha\frac{K_{\mathrm{ox}}}{\rho}\int_{v_i^{\min}}^{v_i^{\min}+v_{C_2}}\left(\frac{w}{v_{C_2}}\right)^{\frac{\theta_i}{3}} n(w)\ w\ dw
\end{aligned}
\tag{2.28}
$$

where $K_{\mathrm{sg}}$ and $K_{\mathrm{ox}}$ are reaction constants obtained with the HACA-RC mechanism.
From now and for all next chapters, the proportion of sites which are active at the surface of a particle $\alpha$ will be considered as equal to 1.

#### 2.2.5.4 Coagulation

The coagulation corresponds to the collision of two solid particles resulting in a bigger soot particle. When particles from a section $j$ and a section $k$ collide, the resultant particle has a volume comprised in the interval $[v_{\min,j}+v_{\min,k}; v_{\max,j}+v_{\max,k}]$. Let us note by $\dot{N}_{\mathrm{coag}}^{j,k\to i}$ the particle number rate of particles received by the section $i$ from the collision of particles from sections $j$ and $k$, and by $\dot{N}_{ij}^{\mathrm{out}}$ the particle number rate of particles from section $i$ which collide with particles of another section $j$:

$$
\begin{aligned}
\dot{N}_{\mathrm{coag}}^{j,k\to i} &= \iint_{v+w\in[v_i^{\min},v_i^{\max}]} \beta_{j,k}n_j(v)n_k(w)dvdw \\
\dot{N}_{ij}^{\mathrm{out}} &= \int_{v_i^{\min}}^{v_i^{\max}}\int_{v_j^{\min}}^{v_j^{\max}} \beta_{i,j}n_i(v)n_j(w)dvdw
\end{aligned}
\tag{2.29}
$$

It is important to note that $\dot{N}_{\text{coag}}^{j,k\to i}$ is non-zero only if it exists a particle of volume $v \in [v_j^{\min}, v_j^{\max}]$ and a particle of volume $w \in [v_k^{\min}, v_k^{\max}]$ respecting $v + w \in [v_i^{\min}, v_i^{\max}]$.
The global coagulation source term then writes:

$$\dot{q}_{\text{coag},i} = \frac{1}{\rho} \int_{v_{\min,i}}^{v_{\max,i}} \left( \sum_{j,k=1}^{i} \dot{N}_{coag}^{j,k\to i} - \sum_{j=1}^{N_{\text{sect}}} \dot{N}_{ij}^{\text{out}} \right) v dv \tag{2.30}$$

In these equations, the collision frequency $\beta_{i,j}$ between a particle of section $i$ and a particle of section $j$ is evaluated at $v_i^{\text{mean}}$ and $v_j^{\text{mean}}$. Here, a transition regime between the free molecular regime (superscript $^{\text{fm}}$) and the continuum regime (superscript $^{\text{c}}$) has been chosen for the description of collisions. For the collisions between a particle of section $i$ and a particle of section $j$, $\beta_{i,j}$ is then expressed as:

$$\beta_{i,j} = \frac{\beta_{i,j}^{\text{fm}} \beta_{i,j}^{\text{c}}}{\beta_{i,j}^{\text{fm}} + \beta_{i,j}^{\text{c}}} \approx \min(\beta_{i,j}^{\text{fm}}, \beta_{i,j}^{\text{c}}) \tag{2.31}$$

with:

$$\begin{aligned} \beta_{i,j}^{\text{fm}} &= \epsilon_{\text{coag}} \left( \frac{3}{4\pi} \right)^{1/6} \sqrt{\frac{6k_bT}{\rho_s}} \sqrt{\frac{1}{v_i^{\text{mean}}} + \frac{1}{v_j^{\text{mean}}}} (d_{c,i} + d_{c,j})^2 \\ \beta_{i,j}^{\text{c}} &= \frac{2k_bT}{3\mu} (d_{c,i} + d_{c,j}) \left( \frac{\text{Cu}_i}{d_{c,i}} + \frac{\text{Cu}_j}{d_{c,j}} \right) \end{aligned} \tag{2.32}$$

where $\epsilon_{\text{coag}} = 2.2$ is an amplification factor due to Van der Waals interactions (Marchal 2008), $\mu$ is the gas dynamic viscosity, and $\text{Cu}_j$ is the Cunningham corrective coefficient for a particle of section $j$ (Cunningham 1910):

$$\text{Cu}_j = 1 + 1.257\text{Kn}_j = 1 + 1.257\frac{2\lambda_{\text{gas}}}{d_{c,j}} \tag{2.33}$$

where $\text{Kn}_j$ and $d_{c,j}$ are the Knudsen number and collisional diameter of a particle of size $j$.

## 2.3 Validation on laminar steady flames

### 2.3.1 Soot prediction in premixed atmospheric configurations

For the model validation in premixed configurations, the 1-D premixed laminar flame of Abid et al. (2009) is retained since it presents the most complete measurements of the particles size distribution function among the flames selected by the International Sooting Flame (ISF) workshop (ISF3 2017). Other premixed atmospheric configurations have also been studied and the corresponding results are gathered in Appendix A, Section A.1.2.

The retained configuration consists of a burner stabilized premixed ethylene/oxygen/argon flame with an equivalence ratio $\Phi = 2.07$. The corresponding composition in terms of mass and molar fractions is shown in Table 2.3. The fresh gas velocity at 298 K and 1 atm is 8.0 cm/s.

| | $C_2H_4$ | $O_2$ | Ar |
|---|---|---|---|
| Mass fraction | 0.1268 | 0.2097 | 0.6635 |
| Molar fraction | 0.1630 | 0.2370 | 0.6000 |

**Table 2.3:** *Premixed composition of the studied premixed flames.*

It is important to notice that several techniques exist in order to measure the particles size distribution of soot particles. The *tubular-probe sampling technique* used by Zhao et al. (2003), Zhao et al. (2005) and Abid et al. (2008) was one of the first to provide detailed particles size distributions at any point above laminar flames. Its principle is presented in Fig. 2.8.

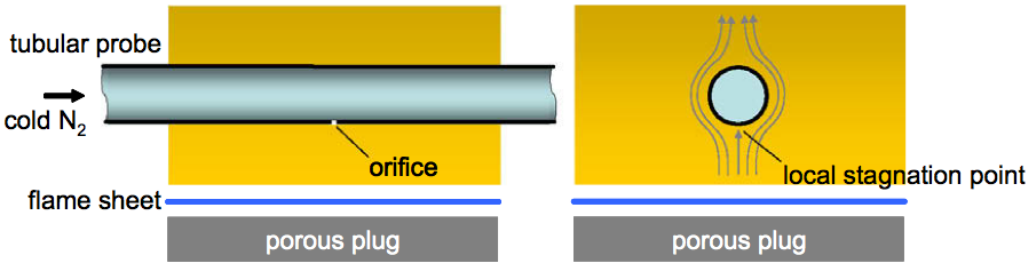


**Figure 2.8:** *Tubular-probe sampling technique : Measurement principle (extracted from Abid et al. (2009)).*

However, it was demonstrated that the presence of the tube clearly perturbs the flow around it and therefore the lifetime of soot particles (Abid et al. 2009; Saggese et al. 2016; Xuan and Blanquart 2016). In addition, due to multi-dimensionality of the flow, boundary conditions were not very well defined and rigorous comparisons with detailed 1-D resolutions were therefore not possible.

The other approach initially developed by Abid et al. (2008) enables to obtain a configuration that can as a first approach be modeled by an quasi 1-D set of equations based on a burner-stabilized stagnation (**BSS**) approach. In order to have the most rigorously-defined boundary conditions for numerical simulations, the soot particles removal is integrated into the stagnation plate positioned at a well defined height above the burner. A schematic diagram of this technique is presented in Fig. 2.9.

The burner used in Abid et al. (2009) has a diameter equal to 5 cm and the

flames are isolated from the ambient air by a concentric nitrogen flow with a speed of 25 cm/s (298 K & 1 atm). The temperature profiles are measured using a thermocouple.

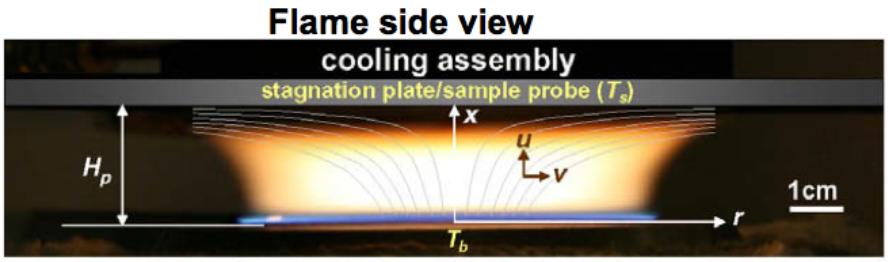


(a) *Frontal view*

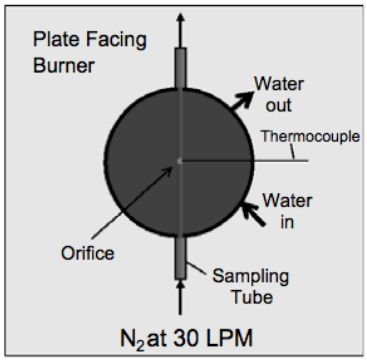


(b) *Bottom view*

**Figure 2.9:** *BSS flame approach : Measurement principle (extracted from Abid et al. (2009)).*

For the removal of soot particles, a 8 cm diameter disk per 1.3 cm thick is used and acts as a stagnation plan. The position of the plate above the burner, $H$, is measured with an accuracy of $\pm 0.025$ cm. The temperature of the stagnation plate $T_s$ is also measured using a thermocouple of type K. The orifice through which the soot particles are taken has a diameter of 127 $\mu$m. When the soot particles are removed, they are immediately diluted in a cold nitrogen flow with a volume flow rate of 30 L/min (at 298 K & 1 atm). The dilution ratio (DR) is quantified by measuring the pressure drop $\Delta P$ through the orifice. PSD of soot particles are finally obtained through a scanning mobility particle sizing. Based on this PSD and Eq. (2.4) , soot volume fractions $f_V$ and particles number density $N_{\text{part}}$ are experimentally determined.

It should be noted that from a numerical point of view, for each height of the stagnation plate, $H$, a different flame is calculated with well-defined boundary conditions at the outlet of the burner and at the level of the stagnation plane.

The Table 2.4 summarizes the studied configurations (data from Camacho et al. (2015)).

| $H$ [cm] | $T_b$ [K] | $T_s$ [K] | DR |
|---|---|---|---|
| 0.40 | 473 | 500 | 712 |
| 0.45 | 473 | 499 | 712 |
| 0.55 | 473 | 497 | 712 |
| 0.60 | 473 | 495 | 615 |
| 0.70 | 473 | 492 | 615 |
| 0.80 | 473 | 490 | 615 |
| 1.00 | 473 | 488.7 | 615 |
| 1.20 | 473 | 486 | 615 |

**Table 2.4:** *Premixed flame case: details on the different studied configurations. $H$: plate height above the burner, $T_b$: temperature of the burner, $T_s$: stagnation plate temperature, DR: dilution ratio.*

#### 2.3.1.1 Experimental dataset

Several experimental results are available:

- the Particles Size Distribution (PSD) of soot particles at each height above the burner,
- the total soot volume fraction $f_V$ and the particles number density $N_{\text{part}}$ at each height,
- the temperature profiles for each one of the different flames (*i.e.* for each plate height above the burner).

These data will be compared with numerical predictions in Section 2.3.1.4.

#### 2.3.1.2 Numerical modeling: axisymmetric stagnant flow

##### 2.3.1.2.1 Hypothesis and notations

Since the flow is axisymmetric, the cylindrical coordinates ($r$, $\theta$, $x$) are used in the following. Thus, the velocity field $\mathbf{u}$ is expressed as:

$$\mathbf{u}(r,x) = u(r,x)\vec{e}_r + v(r,x)\vec{e}_x. \tag{2.34}$$

On the other hand, invariance according to the $\theta$ coordinate of the problem implies that the different physical quantities ($T$, $p$, $\mathbf{u}$, $Y_k$ and $Y_{s,i}$) depend only on the radial coordinate $r$ and on the axial coordinate $x$.

The problem is thus an axisymmetric 2-D problem. Nevertheless, Robert J.Kee (2003) proposed a formulation of the problem that enables the resolution of this problem in a 1-D formulation, over the axi-symmetry axis. The code REGATH-1D-CF (Darabiha 1992) which is used here is based on this formulation.

The only hypothesis in this formulation is to consider that at the vicinity of the jet axis the fields of temperature, species (and consequently the mass fractions of the different sections of soot) are functions only of the axial coordinate $x$. Then, the corresponding transport equations are:

*Energy conservation:*

$$\rho v c_p \frac{\partial T}{dx} = \frac{\partial}{\partial x}\left(\lambda \frac{\partial T}{\partial x}\right) - \sum_{k=1}^{K} \rho Y_k V_k c_{pk} \frac{\partial T}{\partial x} - \sum_{k=1}^{K} h_k W_k \dot{\omega}_k + P^{\mathrm{R}} \tag{2.35}$$

*Species mass fractions conservation:*

$$\rho v \frac{\partial Y_k}{\partial x} = -\frac{\partial}{\partial x}(\rho Y_k V_k) + W_k \dot{\omega}_k \tag{2.36}$$

*Soot section mass fractions $Y_{s,i}$ conservation:*

$$\rho v \frac{\partial Y_{s,i}}{\partial x} - \frac{\partial}{\partial x}\left(0.554 \mu \frac{1}{T} \frac{\partial T}{\partial x} Y_{s,i}\right) = \frac{\partial}{\partial x}(\rho D_{s,i} \nabla Y_{s,i}) + \rho_s \dot{Q}_{s,i} \tag{2.37}$$

The momentum must also be function of only the axial coordinate $x$ :

$$\rho v = (\rho v)(x) \tag{2.38}$$

so that the mass conservation in cylindrical coordinates writes:

$$\frac{\partial \rho v}{\partial x} + \frac{1}{r}\frac{\partial r \rho u}{\partial r} = 0 \quad \Leftrightarrow \quad \frac{\partial r \rho v}{\partial x} + \frac{\partial r \rho u}{\partial r} = 0 \tag{2.39}$$

We define then a stream function $\psi(r, x)$, satisfying the mass conservation:

$$\begin{cases} \dfrac{\partial \psi}{\partial r} = r \rho v \\ -\dfrac{\partial \psi}{\partial x} = r \rho u \end{cases} \tag{2.40}$$

On the other hand, based on Eq. (2.38), the stream function $\psi(r, x)$ can be expressed as:

$$\begin{aligned} \rho v = (\rho v)(x) \quad &\Leftrightarrow \quad \frac{1}{r}\frac{\partial \psi}{\partial r} = U(x) \\ &\Leftrightarrow \quad \frac{\partial \psi}{\partial r} = r U(x) \\ &\Rightarrow \quad \psi(r, x) = r^2 U(x) \end{aligned} \tag{2.41}$$

with $U$ a function depending only on the axial coordinate $x$.

The velocity fields $u$ and $v$ can then be expressed as a function of the quantity $U$:

$$(2.40), (2.41) \Rightarrow \begin{cases} v = \dfrac{2U}{\rho} \\ u = -\dfrac{r}{\rho}\dfrac{dU}{dx} \end{cases} \tag{2.42}$$

#### 2.3.1.3 Final resolved system of equations

It can then be demonstrated (Robert J.Kee 2003) that the set of equations can be rewritten as a function of the variables $(v, \widehat{U})$, with $\widehat{U}$ a function of the coordinate $x$ defined by:

$$\widehat{U} = -\frac{1}{\rho}\frac{dU}{dx} \tag{2.43}$$

The corresponding set of equations writes:

- *Mass conservation:*

$$\frac{d(\rho v)}{dx} + 2\rho\widehat{U} = 0 \tag{2.44}$$

- *Radial moment equation:*

$$\rho v\frac{d\widehat{U}}{dx} + \rho\widehat{U}^2 = -J + \frac{d}{dx}\left(\mu\frac{d\widehat{U}}{dx}\right) \tag{2.45}$$

- *Axial moment equation:*

$$\rho v\frac{dv}{dx} = -\frac{dp}{dx} + \frac{4}{3}\frac{d}{dx}\left(\mu\frac{dv}{dx} - \mu\widehat{U}\right) + 2\mu\frac{d\widehat{U}}{dx} \tag{2.46}$$

- *Energy conservation:*

$$\rho v c_p\frac{dT}{dx} = \frac{d}{dx}\left(\lambda\frac{dT}{dx}\right) - \sum_{k=1}^{K}\rho Y_k V_k c_{pk}\frac{dT}{dx} - \sum_{k=1}^{K} h_k W_k\dot{\omega}_k + P^{\mathrm{R}} \tag{2.47}$$

- *Species conservation:*

$$\rho v\frac{dY_k}{dx} = -\frac{d}{dx}(\rho Y_k V_k) + W_k\dot{\omega}_k \tag{2.48}$$

- *Soot section mass fractions $Y_{s,i}$:*

$$\rho v\frac{dY_{s,i}}{dx} - \frac{d}{dx}\left(0.554\mu\frac{\nabla T}{T}Y_{s,i}\right) = \frac{d}{dx}(\rho D_{s,i}\nabla Y_{s,i}) + \rho_s\dot{Q}_{s,i} \tag{2.49}$$

- *Equation of state (perfect gas):*

$$p = \rho RT\sum_{k=1}^{K}\frac{Y_k}{W_k} \tag{2.50}$$

where $J$ is an unknown of the problem and corresponds to the radial pressure gradient $\frac{1}{r}\frac{\partial p}{\partial r}$, which is constant throughout all the domain:

$$J = \frac{1}{r}\frac{\partial p}{\partial r} = \text{constant} \quad \Rightarrow \quad \frac{\partial J}{\partial x} = 0 \tag{2.51}$$

It is important to note here that the equation of the axial moment is decoupled from the other equations. Generally, this equation is not solved since it is not necessary in order to obtain the variables of interest. Solving this equation allows to obtain the axial pressure gradient.

In Eq. (2.47), $P^{\mathrm{R}}$ corresponds to the radiative source term. Here, radiation from CO, $CO_2$ and $H_2O$ gaseous species is taken into account through the Statistical Narrow-Band (SNB) model (see Chapter 6, Section 6.2.1.4). For the soot particles, they are considered as aggregates of non-overlapped spherical primary particles and the RDG/RDG-FA theory is applied to these primary particles without considering scattering (see Chapter 6, Section 6.2.2.7).

### Boundary conditions

The burner is considered here at $x = 0$, and the stagnation plane at $x = H$.

- Boundary conditions at $x = 0$:

$$\begin{cases} \rho v = \rho_b u_b \\ u = 0 \Rightarrow \widehat{U} = 0 \\ T = T_b \\ \rho Y_k V_k = \rho_b u_b (Y_{k,b} - Y_k) \\ Y_{s,i} = 0 \end{cases} \tag{2.52}$$

  where:
  - $\rho_b u_b$ corresponds to the mass flow rate per unit surface at the burner exit,
  - $T_b$ corresponds to the gas temperature at the burner exit,
  - $V_k$ is the diffusion velocity of species $k$, calculated at the first grid point,
  - $Y_{k,b}$ is the mass fraction of species $k$ at the burner inlet.

- Boundary conditions at $x = H$:

$$\begin{cases} \rho v = 0 \\ u = 0 \Rightarrow \widehat{U} = 0 \\ T = T_s \\ \rho Y_k V_k = 0 \\ \dfrac{dY_{s,i}}{dx} = 0 \end{cases} \tag{2.53}$$

It is then important to notice here that a zero-velocity condition is applied at the stagnation plane, increasing the residence time of soot particles. This is not representative of the experiments as the particles are extracted through a hole so that they do not see this zero-velocity region before aspiration. The impact of this boundary condition will be discussed in the following section.

#### 2.3.1.4 Numerical results

In order to compare our numerical model for each of the heights where the stagnation plate has been positioned experimentally for sampling, it is therefore necessary from a numerical point of view to carry out a simulation for each burner height. The obtained results are presented in the following paragraph and compared with experimental measurements from Camacho et al. (2015) and numerical results from Saggese et al. (2015) obtained with a kinetic scheme method for soot prediction through BINs (see Section A.2.3 of Appendix A).

##### 2.3.1.4.1 Temperature profiles

The temperature profiles obtained for each of the heights analyzed are presented in Fig. 2.10 and compared with the experimental values (symbols). For all these flames, a very good agreement is obtained between experimental measurements and numerically-predicted temperatures, validating therefore the gaseous phase description.

##### 2.3.1.4.2 Comparison of soot predictions with literature and experiments

In this section, results obtained using the 1-D classical formulation presented in Section 2.3.1.3 are initially discussed. However, as shown in literature (Camacho et al. 2015; Saggese et al. 2015; Xuan and Blanquart 2016), aspiration of particles at the stagnation plane impacts the flow and, consequently, the soot particles residence time at the measured position. Different techniques enabling to take into account these effects are here proposed and the corresponding results are also presented.

**Global quantities: soot volume fraction and particles number density**

Figure 2.11 presents the global quantities (soot volume fraction, left, and particles number density, right) obtained with the 1-D classical formulation, compared with experimental measurements (orange circles) and numerical results (black dashed lines) of Saggese et al. (2015). It can be observed that soot

volume fraction tends to be over-predicted and particles number density are under-predicted (red dashed lines) compared to experiments.

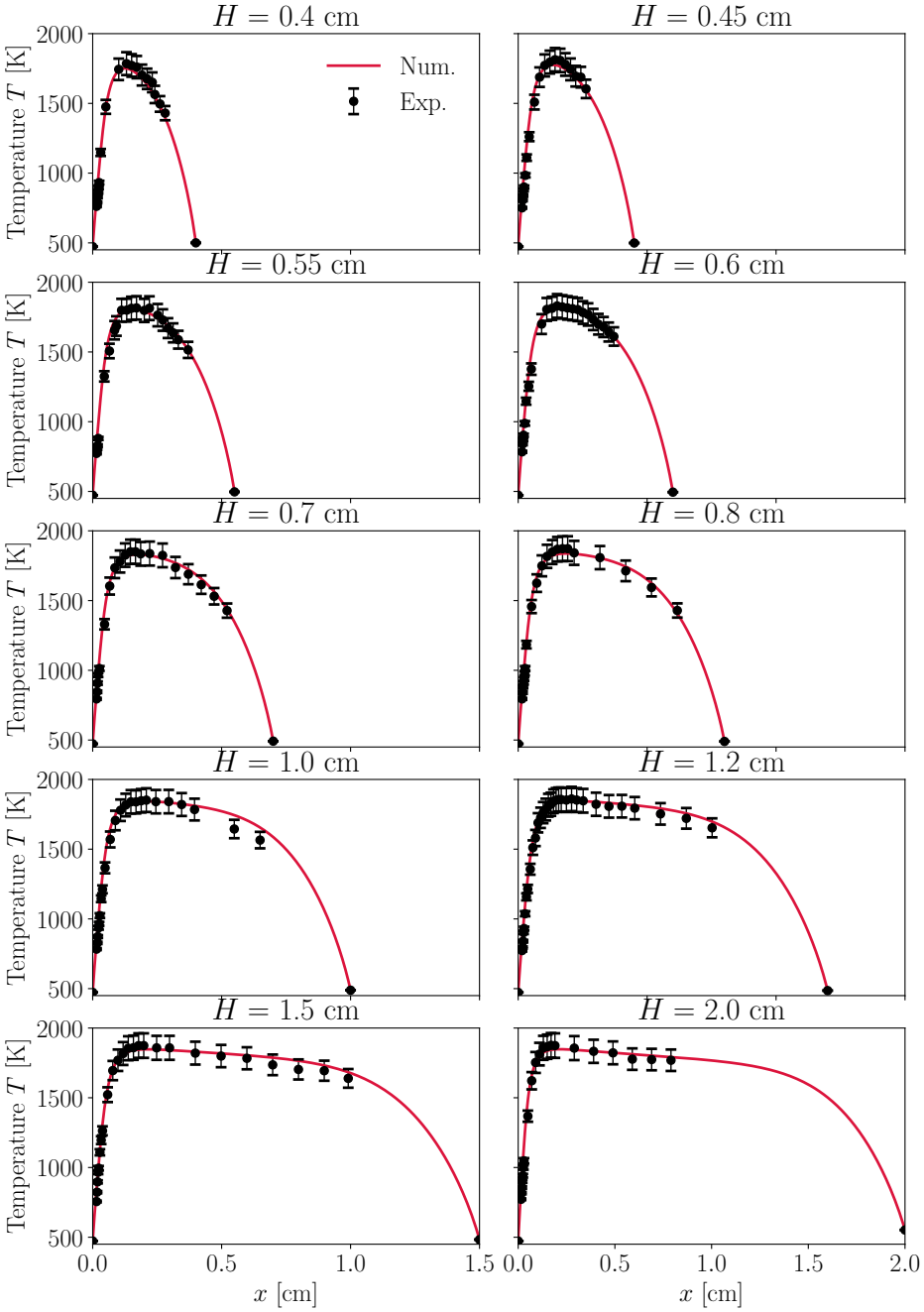


**Figure 2.10:** *Comparison between numerical and experimental temperature profiles (Camacho et al. 2015) for the different positions of the plate above the burner.*

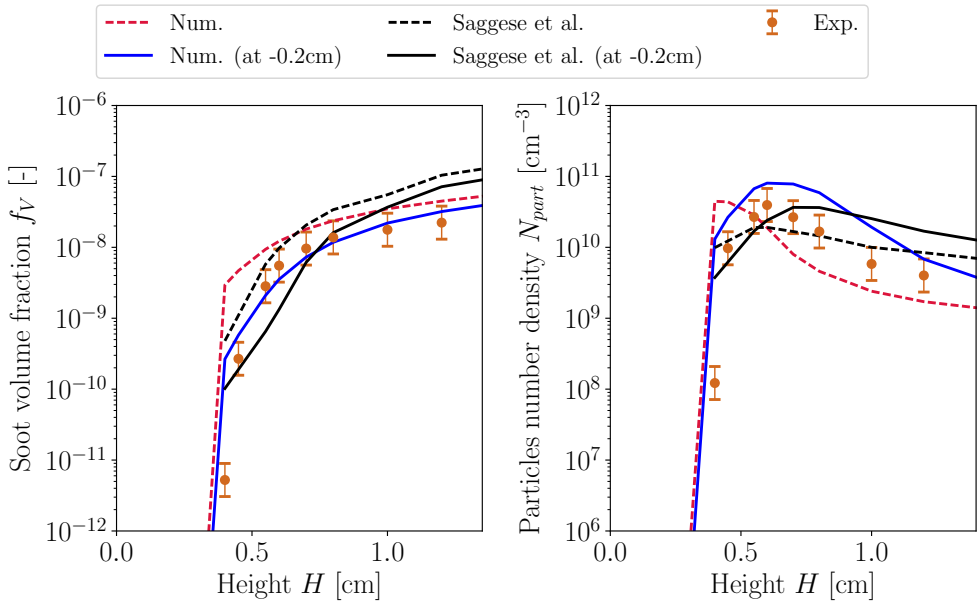


**Figure 2.11:** *Comparisons between numerical soot volume fraction and particles number density evolution (with and without a shift of 0.2 cm in numerical results) with the experimental measurements from Camacho et al. (2015) and the numerical results obtained in literature by Saggese et al. (2015) (with and without a shift of 0.2 cm in numerical results).*

This may be due to the zero-velocity boundary condition at the stagnation plane, which increases the residence time of soot particles in the simulation artificially modifying their history (Camacho et al. 2015; Saggese et al. 2015; Xuan and Blanquart 2016). In order to take into account this effect, it has been proposed by Camacho et al. (2015) and Saggese et al. (2015) to shift the results by 0.2 cm and to compare the soot volume fraction, particles number density and particles size distributions at this distance of the stagnation plane. The corresponding results (-0.2 cm) are presented in solid lines, and a better agreement is obtained compared with experimental measurements.

### Particles Size Distributions

Figure 2.12 presents the numerical predictions for the particles size distribution (PSD) at each height above the burner (at the stagnation plane in dashed lines and shifted by 0.2 cm in solid lines). A comparison with the three sets of measurements presented in Camacho et al. (2015) and numerical results obtained in literature are also presented. Three set of measurements (named "Stanford 1", "Stanford 2" and "Stanford 3" in the figures) have been realized in order to demonstrate the reproducibility of these measurements.

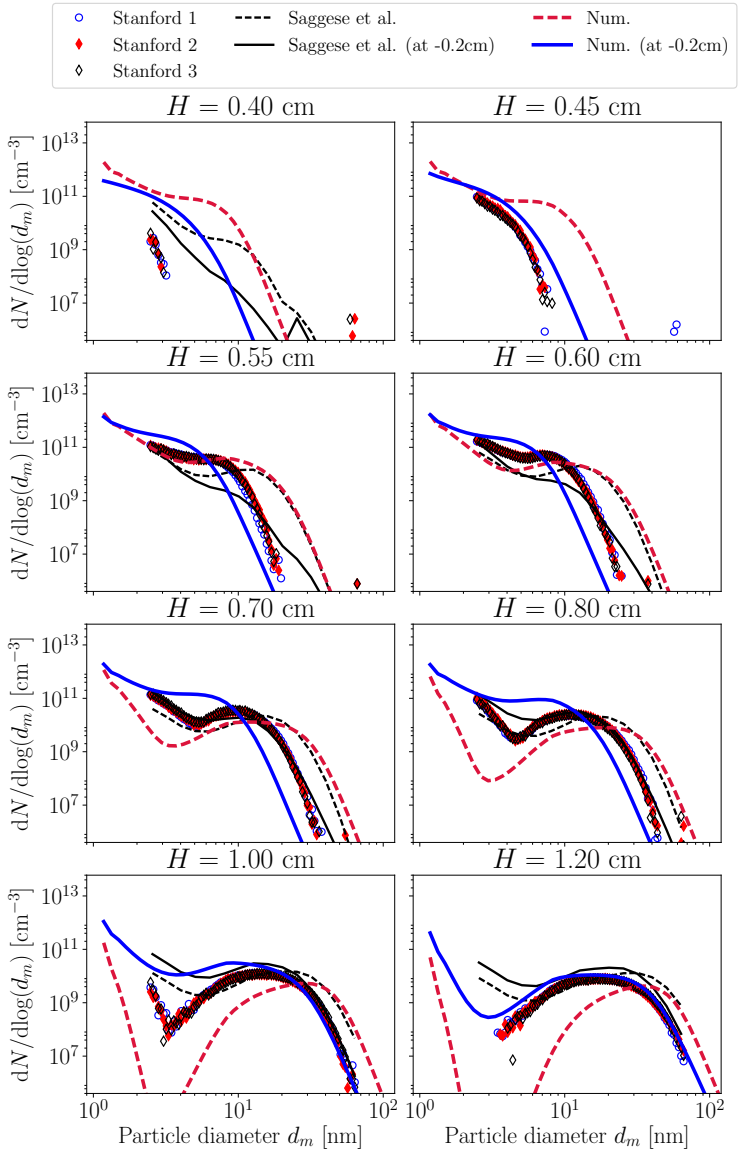


**Figure 2.12:** *Comparison between numerical predicted soot particles size distributions at $x = H$ and $x = H - 0.2$ cm with the experimental measurements from Camacho et al. (2015) and the numerical results obtained in literature by Saggese et al. (2015) (at $x = H$ and $x = H - 0.2$ cm).*

It can be observed that for the two last heights above the burner ($H = 1.00$ cm and $H = 1.20$ cm) good results are obtained compared with experiments by shifting the results by 0.2 cm. Good quality of results was also obtained in literature by Saggese et al. (2015). However, for smaller distances between the burner and the stagnation plane, the experimental PSD seems to correspond to intermediate states between the PSD at the stagnation plane and the PSD

shifted by 0.2 cm from the stagnation plane. This can be due to some modeling errors but it may also indicate that a simple shift is not sufficient to correctly treat the aspiration effects for all distances. Alternative methods to correct the aspiration effect will be proposed in Section 2.3.1.6.

#### 2.3.1.5 Analysis of soot production in premixed flames

Figure 2.13 presents a typical view of the BSS flame for a burner to stagnation plane distance $H = 1.0$ cm. As observed in the profiles of Fig. 2.11, soot volume fraction increases up to the stagnation plane, whereas particles number density is maximum at the beginning of the sooting zone due to nucleation process, and then decreases with the coagulation process (the oxidation process of small particles may contribute to the decrease of $N_{\text{part}}$, but it is negligible for this configuration).

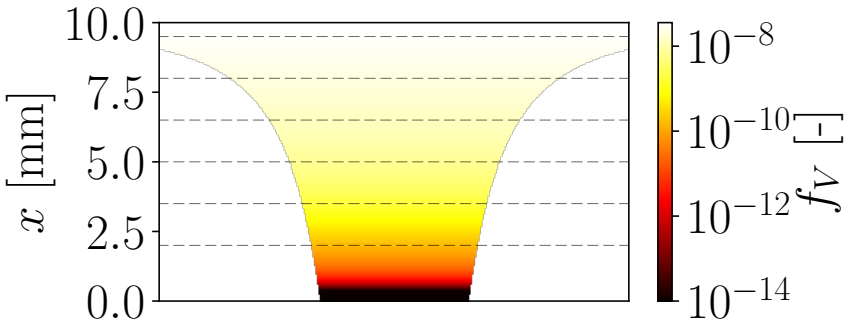


(a) Soot volume fraction $f_V$

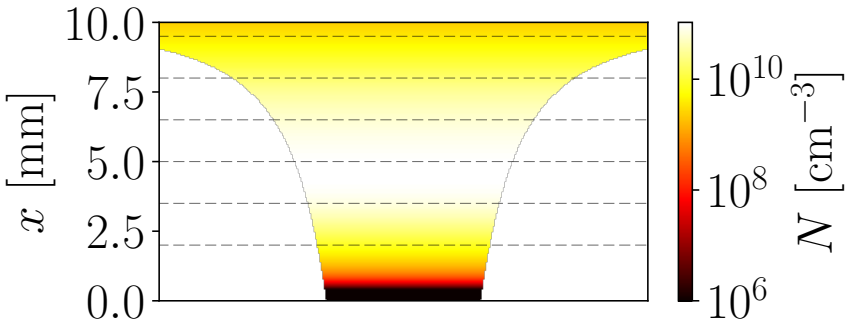


(b) Particles number density $N_{\text{part}}$

**Figure 2.13:** *Representative view of the BSS flame for a burner to stagnation plane distance $H = 1.0$ cm.*

Figure 2.14 presents the evolution of the particles size distribution and the different volume source terms for each sections at the six heights represented in dashed lines in Fig. 2.13.

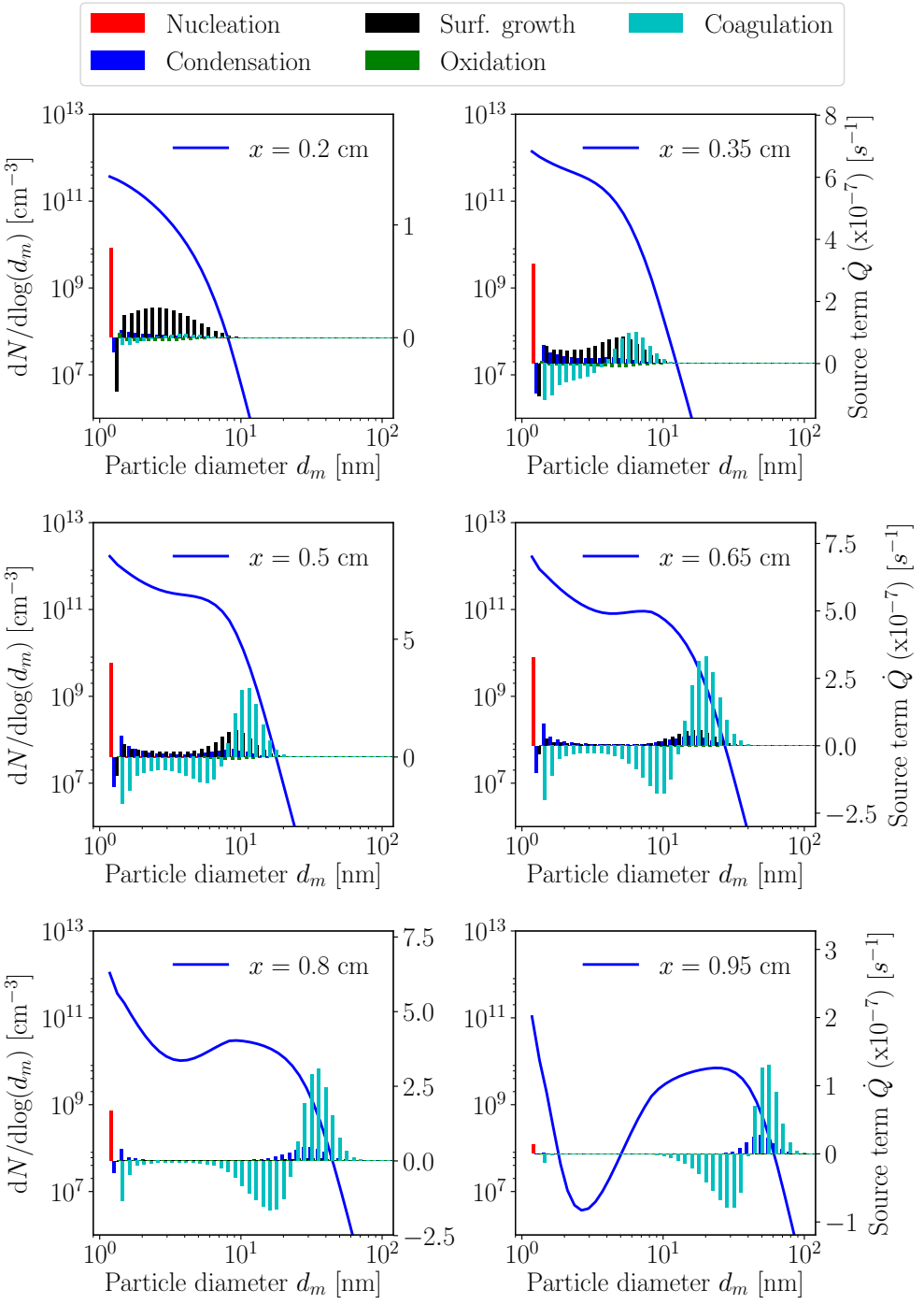


**Figure 2.14:** *Evolution of the particles size distribution (PSD) and nucleation, condensation, surface growth, oxidation and coagulation volume source terms at different positions above the burner for the flame with a burner to stagnation plane distance of* $H = 1.0$ *cm.*

Looking at these evolutions, one can observe that nucleation process is initially predominant so that a first peak of the PSD is observed for small diameters at $x = 0.2$ cm. Then, these first nucleated particles grow through surface growth process until $x = 0.35$ cm. From $x = 0.5$ cm to $x = 0.8$ cm, coagulation and nucleation become the major phenomena in soot particles evolution. The permanent nucleation combined with the coagulation process of bigger particles change the shape of the PSD, from a one-peak PSD shape to a two-peaks PSD shape. The contribution of surface growth decreases in this region due to a decrease of temperature. Near the stagnation wall, at $x = 0.95$ cm, coagulation and condensation are the two major processes involved in soot particles evolution.

#### 2.3.1.6 Methods for treating the aspiration effects

In order to take into account the aspiration effects, the best approach would be to consider 2-D detailed calculations, as the one proposed by Xuan and Blanquart (2016). However, due to prohibitive computational costs when using a detailed description for both the gas and solid phases, two alternative approaches are here proposed:

1. The first one, called **"Iso-conv1"**, consists of calculating the real convective time of soot particles and looking at the PSD at this convective time.

   Indeed, the aspiration dilution ratio DR can be expressed as:

   $$DR = \left(\frac{L_0}{L_{\text{sample}}}\right)\left(\frac{T_0}{T_{\text{sample}}}\right)\left(\frac{\mu_0}{\mu_{\text{m,sample}}}\right) \tag{2.54}$$

   where:
   - $L_0$ (at 298 K & 1atm), is the nitrogen volume flow rate used for the immediate dilution of aspired soot particles,
   - $L_{\text{sample}}$ (298 K & 1 atm), is the volume flow rate sampled through the orifice,
   - $T_0$ the diluent temperature,
   - $T_{\text{sample}}$ the gas temperature of the flow sampled through the orifice,
   - $\mu_{\text{m,sample}}$ (respectively $\mu_0$) the dynamic viscosity of the sampled flow (respectively of the diluent)

   Based on data from Camacho et al. (2015), the following data are retained:
   - $L_0 = 30$ L/min
   - $T_0 = 298$ K
   - $T_{\text{sample}} = 555$ K

- $\frac{\mu_{\text{m,sample}}}{\mu_0} = 1.6$

Moreover, the sampling volume flow rate $\dot{q}_{\text{sample}}$ at the sampled gas temperature (555K) can be expressed as a function of $L_{\text{sample}}$ through the following relationship:

$$\begin{aligned}
\dot{q}_{\text{sample}} &= \left(\frac{\rho_{298\text{ K}}}{\rho_{555\text{K}}}\right) L_{\text{sample}} \\
&= \left(\frac{T_{\text{sample}}}{T_0}\right) L_{\text{sample}} \\
&= \left(\frac{T_{\text{sample}}}{T_0}\right)\left(\frac{L_0}{DR}\right)\left(\frac{T_0}{T_{\text{sample}}}\right)\left(\frac{\mu_0}{\mu_{\text{m,sample}}}\right) \\
&= \left(\frac{L_0}{DR}\right)\left(\frac{\mu_0}{\mu_{\text{m,sample}}}\right)
\end{aligned} \tag{2.55}$$

In addition, the orifice diameter is equal to $d_{\text{orifice}} = 127\ \mu$m. Then, aspiration velocity $v_{\text{aspi,max}}$ at the orifice position is equal to:

$$v_{\text{aspi,max}} = \frac{4\dot{q}_{\text{sample}}}{\pi d_{\text{orifice}}^2} \tag{2.56}$$

Assuming that the aspiration velocity near the wall $v_{\text{aspi}_{\text{nw}}}(\tilde{r})$ is only function of the distance $\tilde{r}$ separating the particles and the orifice, mass conservation implies:

$$\begin{aligned}
& \rho_{\text{sample}}\dot{q}_{\text{sample}} && = \rho(\tilde{r})(2\pi\tilde{r}^2 v_{\text{aspi}_{\text{nw}}}(\tilde{r})) \\
\Leftrightarrow \quad & v_{\text{aspi}_{\text{nw}}}(\tilde{r}) && = \frac{\rho_{\text{sample}}\dot{q}_{\text{sample}}}{\rho(\tilde{r})(2\pi\tilde{r}^2)} \\
& && \simeq \frac{\dot{q}_{\text{sample}}}{2\pi\tilde{r}^2}
\end{aligned} \tag{2.57}$$

Considering the results obtained in Eq. (2.56) (velocity at the orifice position) and (2.57) (aspiration flow near the stagnation plane), the aspiration velocity $v_{\text{aspi}}(\tilde{r})$ can be approximated as:

$$\begin{aligned}
v_{\text{aspi}}(\tilde{r}) &= \min(v_{\text{aspi}_{\text{nw}}}(\tilde{r}), v_{\text{aspi,max}}) \\
&= \min\left(\frac{4\dot{q}_{\text{sample}}}{\pi d_{\text{orifice}}^2}, \frac{\dot{q}_{\text{sample}}}{2\pi\tilde{r}^2}\right)
\end{aligned} \tag{2.58}$$

Then, one may consider that an effective velocity $v_{\text{effect}}(z)$ of the particles can be defined over all the flame:

$$\begin{aligned}
v_{\text{effect}}(z) &= v_{\text{solved}}(z) + v_{\text{aspi}}(z) \\
&= v_{\text{solved}}(z) + \min\left(\frac{4\dot{q}_{\text{sample}}}{\pi d_{\text{orifice}}^2}, \frac{\dot{q}_{\text{sample}}}{2\pi(H-z)^2}\right).
\end{aligned} \tag{2.59}$$

The effective convective residence time ($\tau_{\text{conv}_{\text{eff}}}(z)$) and the resolved one ($\tau_{\text{conv}_{\text{solved}}}(z)$) can then be expressed as:

$$\begin{cases} \tau_{\text{conv}_{\text{eff}}}(z) = \displaystyle\int_0^z \frac{dz'}{v_{\text{effect}}(z')} \\ \tau_{\text{conv}_{\text{solved}}}(z) = \displaystyle\int_0^z \frac{dz'}{v_{\text{solved}}(z')} \end{cases} \tag{2.60}$$

Then, taking the value $z_{\text{iso-conv}}$ for which $\tau_{\text{conv}_{\text{eff}}}(H) = \tau_{\text{conv}_{\text{solved}}}(z_{\text{iso-conv}})$ enables to retrieve the particles state at the same residence time as the one obtained in experiments. Soot volume fraction, particles number density and soot particles size distributions are then plotted for $z = z_{\text{iso-conv}}$.

2. The second one, called **"Iso-conv2"**, consists of modifying the resolved equations by adding the velocity $v_{\text{aspi}}(z)$ in the convective terms of the equations presented in 2.3.1.3, then solving these equations and plotting the results at the point corresponding to the stagnation plane.

Next paragraphs present the obtained results for both methods.

Figure 2.15 presents the obtained global quantities (soot volume fraction and particles number density) for the two correction techniques, compared with experimental measurements and numerical results of Saggese et al. (2015). A good agreement is now obtained with the **"Iso-conv"** correction method when comparing with experiments, and the impact of soot particles aspiration on the quality of soot predictions can clearly be seen.

Figure 2.16 presents the obtained results for the particles size distribution (PSD) using the two proposed correction techniques, compared with experiments and results in literature. Again, it can be observed that the results obtained with the **"Iso-conv"** correction technique are very well predicted for burner-to-stagnation plane distances between 0.55 cm and 1.20 cm. For smaller distances ($H = 0.40$ cm and $H = 0.45$ cm), the PSD is still shifted towards bigger soot particles. At these distances, the impact of aspiration is even more important, and one can suggest that even the proposed correction is not sufficient to model this impact.

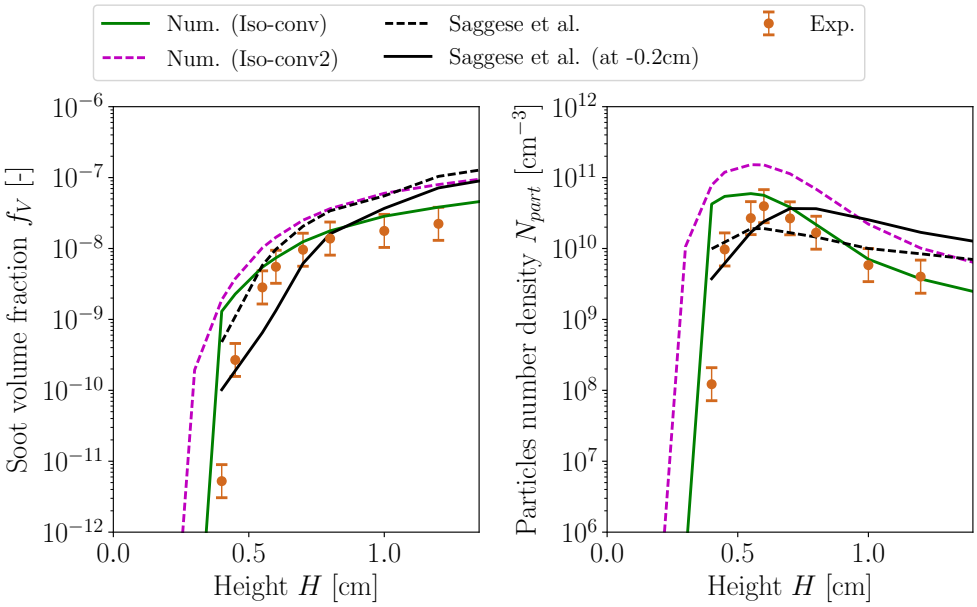


**Figure 2.15:** *Comparison between numerical soot volume fraction and particles number density with the two corrections techniques obtained the experimental measurements from Camacho et al. (2015) and the numerical results obtained in literature by Saggese et al. (2015).*

#### 2.3.1.7 Impact of the number of sections on results

The sensitivity of the model to the number of sections in laminar flames is studied here. Fig. 2.17 presents the impact of this number of sections on the calculated soot volume fraction $f_V$, particles number density $N_{\text{part}}$ and particles size distribution (PSD) at the stagnation plane for the flame with a height above burner $H = 1$ cm.

The previous calculations have been performed with 50 sections. It can be observed in Fig. 2.17 that this number of sections is good enough to obtain a precise estimation of the three considered quantities. However, for 3-D simulations purpose (Parts II & III), 25 is considered as the minimum number of sections needed to correctly reproduce the soot volume fraction. For this quantity, negligible errors on global quantities are observed when comparing the results with calculations based on more sections, whereas some discrepancies are observed on the PSD.

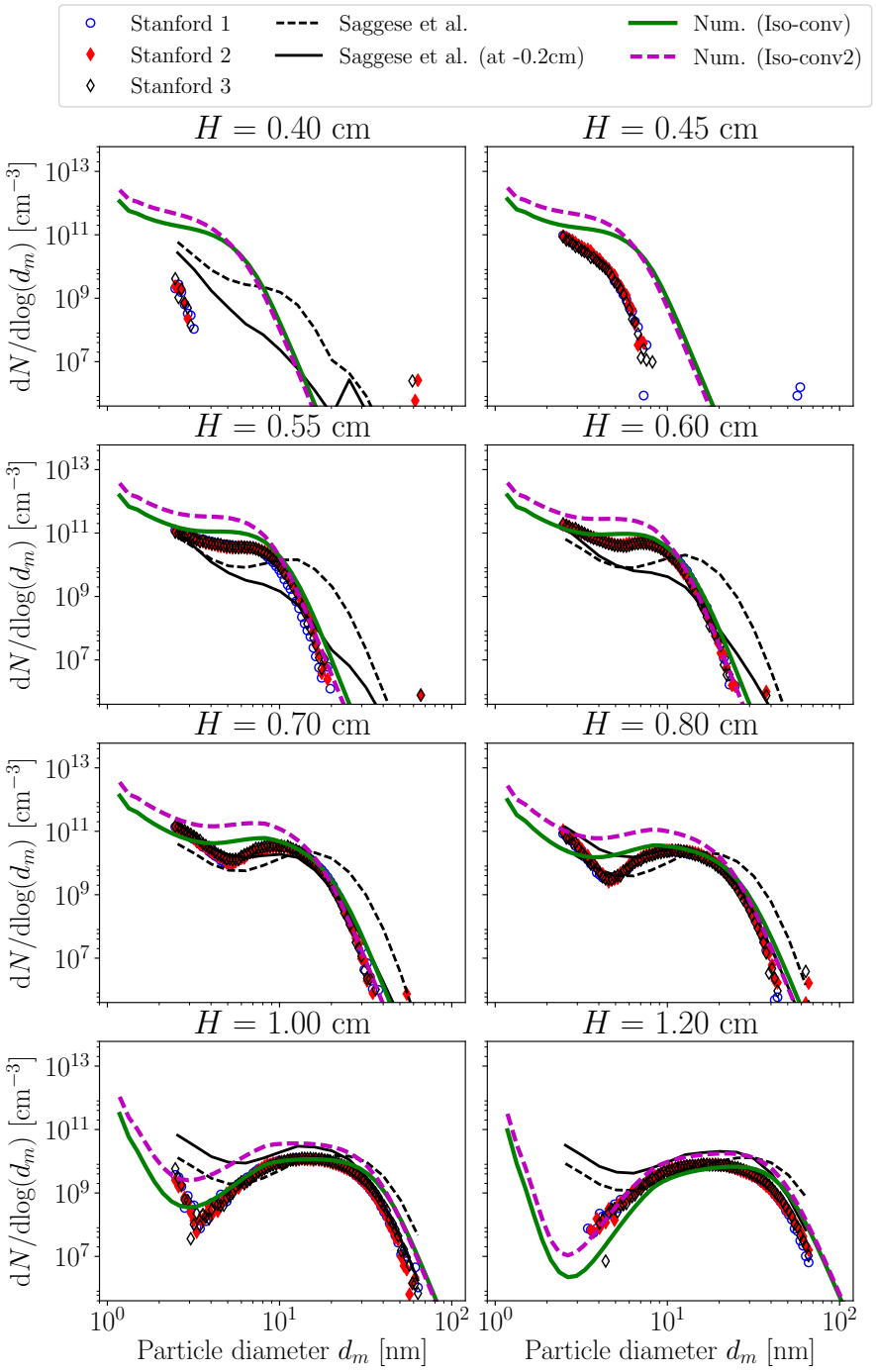


**Figure 2.16:** *Comparisons between numerical predicted soot particles size distributions obtained using the two corrections techniques with the experimental measurements from Camacho et al. (2015) and the numerical results obtained in literature by Saggese et al. (2015)*

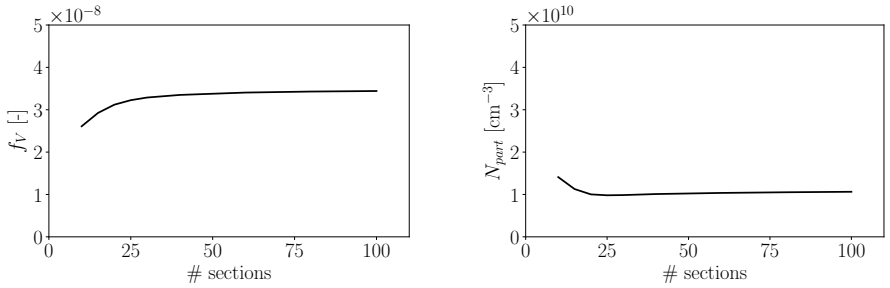


(a) Soot volume fraction $f_V$ (b) Particles number density ($N_{\text{part}}$)

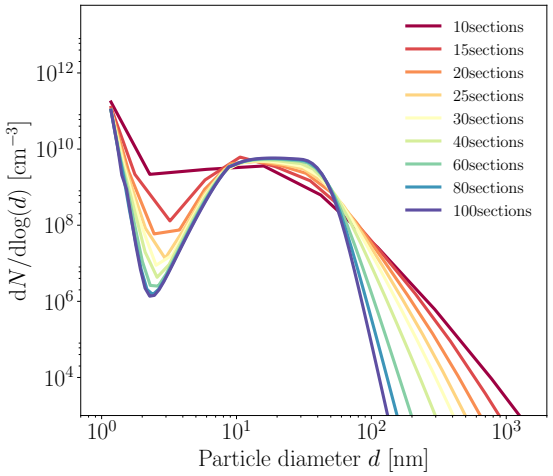


(c) Particles size distribution (PSD)

**Figure 2.17:** *Impact of the number of sections used in the sectional method for the prediction of soot volume fraction $f_V$, particles number density $N_{part}$ and the particles size distribution (PSD). The considered case corresponds to the flame with a height above burner $H = 1$ cm.*

### 2.3.2 Soot prediction in pressurized premixed configurations

#### 2.3.2.1 Experimental data

The experimental configuration investigated in Tsurikov et al. (2005) consists of laminar ethylene/air premixed sooting flames at 3 bar and 5 bar. Figure 2.18 presents the corresponding burner. In order to stabilize the sooting flame of interest, the flame is surrounded by a nonsooting "shielding flame". Both flames are stabilized with water-cooled matrix. This outer flame enables also to reduce oxidation and heat losses at the flame edges, and to shield the inner flame from the cold surroundings. The flames are surrounded by an air coflow and the burner/coflow assembly is installed in a water-cooled steel pressure

housing with optical access. Evolution of the soot volume fraction as a function of the height above burner (HAB) are measured through Laser-Induced Incandescence (LII) technique.

Table 2.5 summarizes the different studied configurations. The pressure varies from 3 bar to 5 bar and the equivalence ratio $\phi$ from 2.05 to 2.50. The volume flow rates are expressed in standard liters per minute, and the corresponding mass flow rate per unit surface $\rho u$ is calculated based on the values of these volume flow rates.

| Flame # | $P$ [bar] | $\phi$ | $\dot{Q}_{C_2H_4}$ [slpm] | $\dot{Q}_{air}$ [slpm] | $\rho u$ [g/cm$^2$/s] |
|---|---|---|---|---|---|
| 3 | 3 | 2.30 | 1.71 | 10.67 | 0.01983 |
| 4 | 3 | 2.50 | 1.86 | 10.67 | 0.02006 |
| 5 | 5 | 2.05 | 1.91 | 13.31 | 0.02439 |
| 6 | 5 | 2.40 | 2.19 | 13.07 | 0.02444 |

**Table 2.5:** *Tsurikov et al. (2005) experimental database of soot volume fraction measurements in pressurized laminar ethylene-air flames.*

#### 2.3.2.2 Numerical modeling and results

These flames are computed with the 1-D-freely-propagating formulation of the REGATH code, with burner-stabilized type boundary conditions. The selected kinetic scheme (KM2) which has been validated for the prediction of laminar flame speed of ethylene-air mixtures at elevated pressure (see Section 2.1.3.2) is used for the prediction of the gaseous phase and the presented sectional model is used for the prediction of the solid phase. As for the previous calculations, radiation from soot particles, $CO_2$, $H_2O$ and CO species are taken into account in the energy equation.

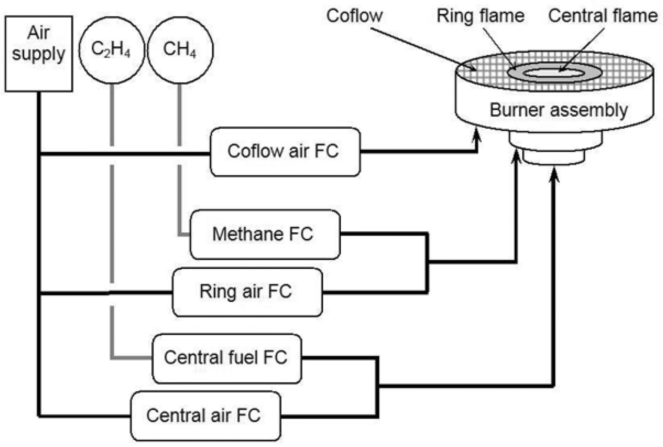


**Figure 2.18:** *Burner used in Tsurikov et al. (2005) experiments.*

Figure 2.19 presents the comparison between the experimental measurements (and their corresponding uncertainties) and the obtained numerical results for the four studied cases. A good agreement with experimental measurements is obtained, except for the flame # 5 ($P = 5$ bar, $\phi = 2.05$) where soot volume fraction is over-predicted by a factor two.

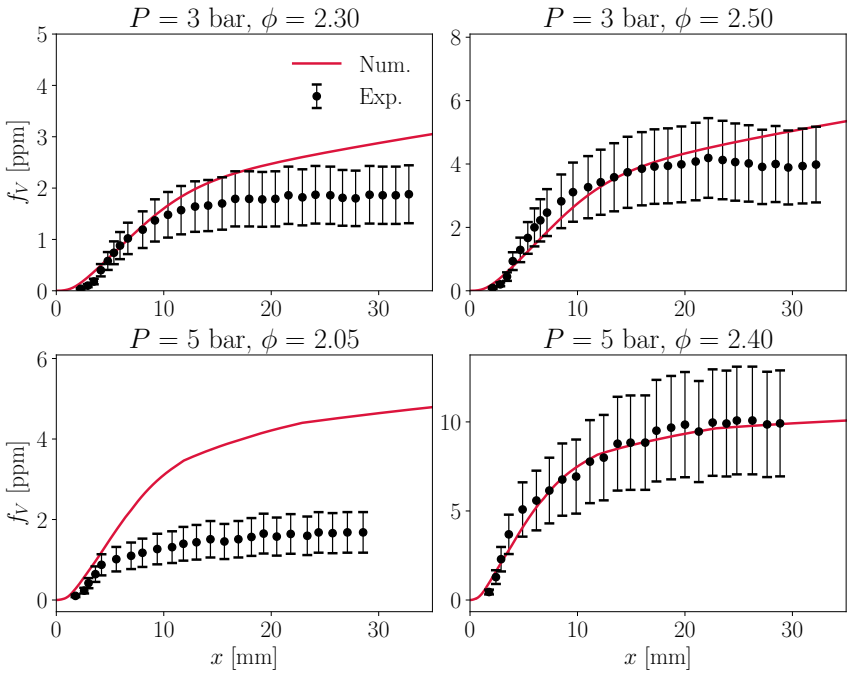


**Figure 2.19:** *Comparison between LII experimental data (Tsurikov et al. 2005) and numerical predictions of $f_V$ for the four studied cases at 3 and 5 bar. The corresponding flame # are presented in Table 2.5.*

### 2.3.3 Diffusion configurations

#### 2.3.3.1 Experimental configuration

The flames studied here have been experimentally investigated by Decroix and Roberts (1999); Decroix and Roberts (2000); Welle et al. (2003); Xiao et al. (2005), and correspond to counterflow diffusion flames pure fuel/air. Stationary soot production behavior has been studied as function of the global strain rate for three different fuels: methane, propane and ethylene. Four global strain rates (GSR) haven been investigated: 15 $s^{-1}$, 30 $s^{-1}$, 60 $s^{-1}$ and 90 $s^{-1}$. This global strain rate GSR ($K$) is defined as:

$$K = \text{GSR} = \frac{2u_0}{L} \tag{2.61}$$

where $u_0$ is the air velocity at the nozzle and $L = 12.7$ mm corresponds to the distance separating the two nozzles.

The cold temperature for both fuel and air is $T_f = 294$ K. Table 2.6 summarizes the characteristics of the different studied configurations.

| Global strain rate [$s^{-1}$] | 15 | 20 | 30 | 40 | 50 | 60 |
|---|---|---|---|---|---|---|
| Air inlet velocity [cm/s] | 9.525 | 12.7 | 19.05 | 25.4 | 31.75 | 38.1 |
| Methane inlet velocity [cm/s] | 21.175 | | 42.35 | | | |
| Propane inlet velocity [cm/s] | 7.7 | 10.267 | 15.4 | 20.253 | 25.667 | 30.8 |
| Ethylene inlet velocity [cm/s] | 12.1 | | 24.2 | | | |

**Table 2.6:** *Laminar counterflow diffusion flames studied by Decroix and Roberts (2000)*

### 2.3.3.2 Numerical results

Figure 2.20 presents the comparison between the predicted evolution of the maximum soot volume fraction as a function of the applied global strain rate for the three different fuels studied by Decroix and Roberts (2000).

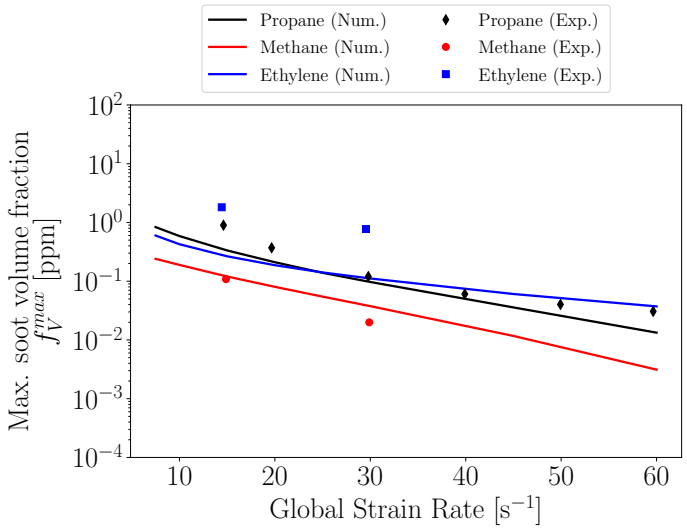


**Figure 2.20:** *Comparison of the predicted maximum soot volume fraction as a function of the applied global strain rate with experiments of Decroix and Roberts (2000) for the three studied fuels: methane, propane and ethylene.*

Good predictions are obtained for methane and propane fuels with discrepancies lower than a factor of two. However, ethylene predictions are lower by a factor of five compared with experiments.

#### 2.3.3.3 Analysis of soot production in diffusion flames

Figure 2.21 presents the normalized profiles of gaseous and soot quantities for the ethylene counterflow diffusion flame at a global strain rate of 30 $s^{-1}$.

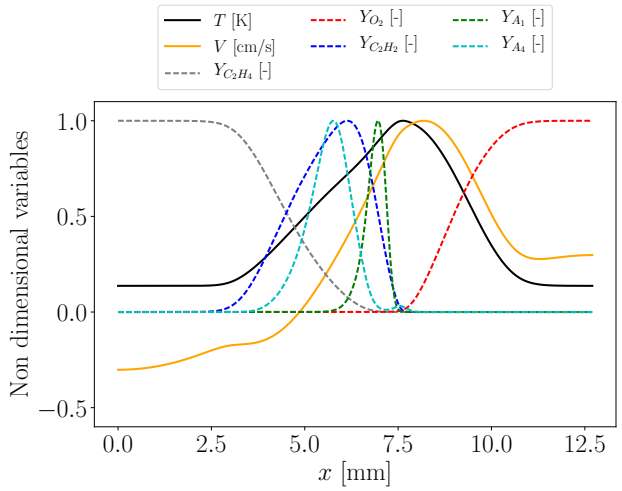


(a) Normalized profiles of temperature, gas velocity, $C_2H_4$, $O_2$, $C_2H_2$, $A_1$ and $A_4$ mass fractions

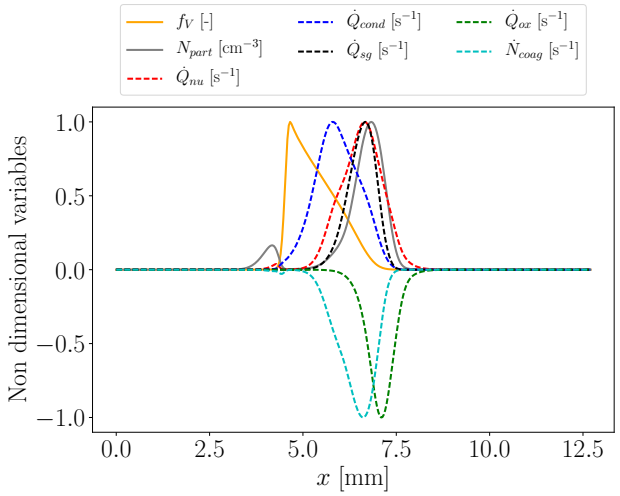


(b) Normalized profiles of soot volume fraction, particles number density and the different volume source terms involved in soot production.

**Figure 2.21:** *Normalized profiles of gaseous and soot quantities for an ethylene counterflow diffusion flame at a global strain rate of 30 $s^{-1}$.*

Soot volume fraction maximum is placed near the stagnation point (null velocity at $x = 4.85$ cm). It is slightly shifted to the left due to thermophoretic effect that transports the particles to cold regions leading to a null velocity for soot particles at $x = 4.65$ cm. Particles nucleate in rich regions on the oxidizer

side (right side) where aromatics start to be present ($A_1$, $A_2$, $A_3$, $A_4$ ...). Then, particles are transported towards richer zones and grow through surface growth and condensation phenomena until the stagnation plane. In this regions of high residence time, even if $Y_{C_2H_2}$ is still present and one can expect an important role of surface growth process, the two main phenomena involved in soot production are coagulation and condensation phenomena, in analogy with what has been observed closed to the stagnation plane of the premixed configuration.

Figure 2.22 presents the evolution of soot volume fraction profile and the nucleation, condensation, surface growth and oxidation source terms. It can be observed that the most important source term is surface growth, followed by condensation and nucleation process. Finally, oxidation is the lower volume source term in this flame.

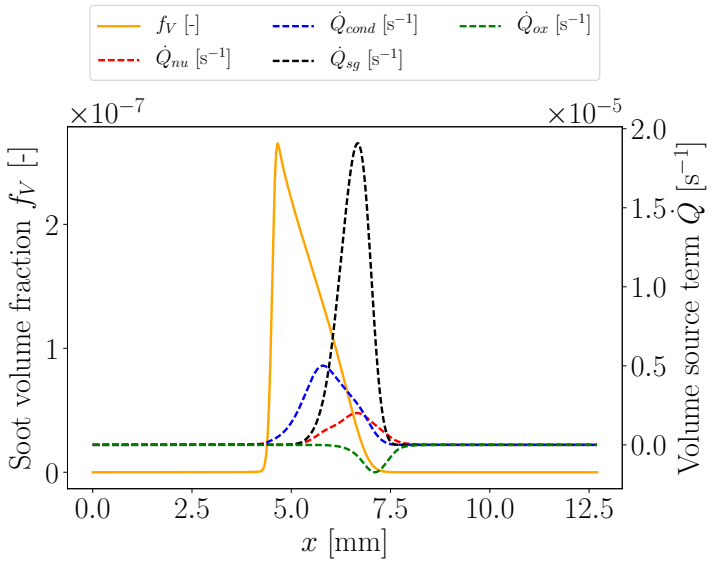


**Figure 2.22:** *Profiles of soot volume fraction, nucleation, condensation, surface growth and oxidation volume source terms for an ethylene counterflow diffusion flame at a global strain rate of 30 $s^{-1}$.*

Figure 2.23 presents the soot particles size distributions and volume source terms at different positions of this flame. The corresponding positions are plotted in dashed lines in Fig. 2.24 with a representation of the soot volume fraction and particle number density fields.

At $x = 0.75$ cm, the particles nucleate and a one-peak PSD shape is observed. Then, from $x = 0.70$ cm to $x = 0.65$ cm, particles growth through surface growth phenomenon and the one-peak PSD shape is conserved. With surface growth, particles diameter increases and therefore their collision probability increases. At the same time, particles are near the stagnation plane and their residence time increases. Then, coagulation and condensation processes are

predominant from $x = 0.6$ cm and until the stagnation plane. The coagulation process combined with the persistent nucleation process lead to a two-peak PSD shape as it can be observed for $x = 0.55$ cm and $x = 0.5$ cm.

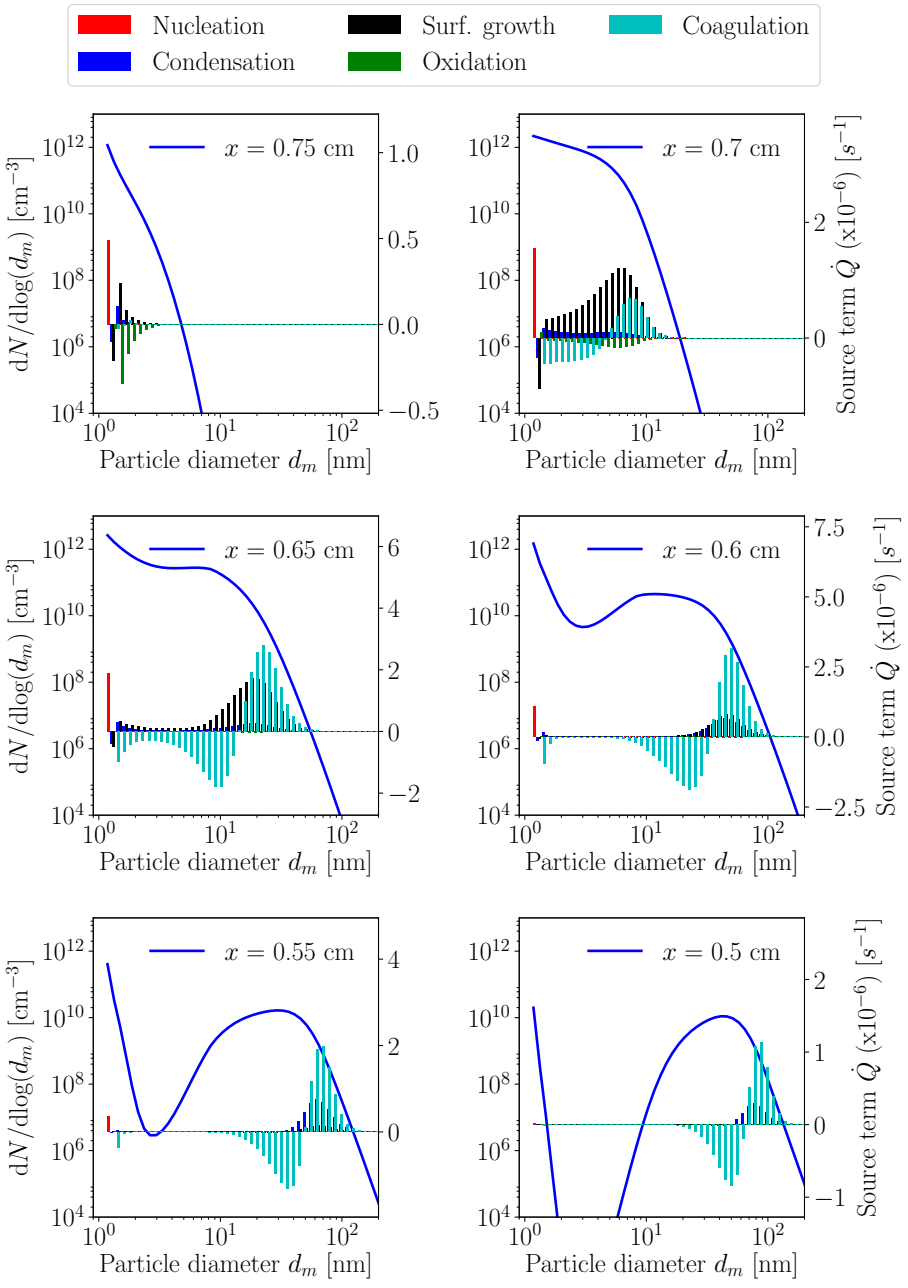


**Figure 2.23:** *Evolution of the particles size distribution (PSD) and nucleation, condensation, surface growth, oxidation and coagulation volume source terms at different positions of the ethylene-air counterflow diffusion flame with a GSR=30 $s^{-1}$.*

Is is important to observe that condensation and coagulation processes are two phenomena that are involved in regions where residence time scales are high. This observation will be retrieved in next section by the analysis of characteristic time scales. These long time scales are responsible for the unsteady response of production dynamics in the pulsed flames that will be detailed in the next section.

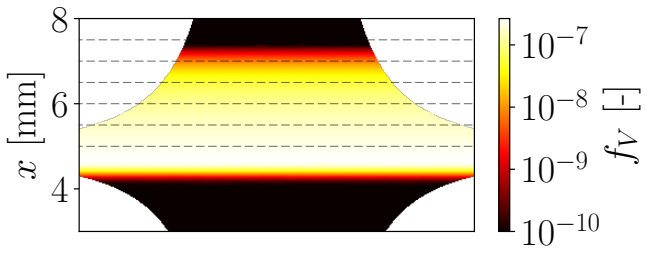


(a) Soot volume fraction $f_V$

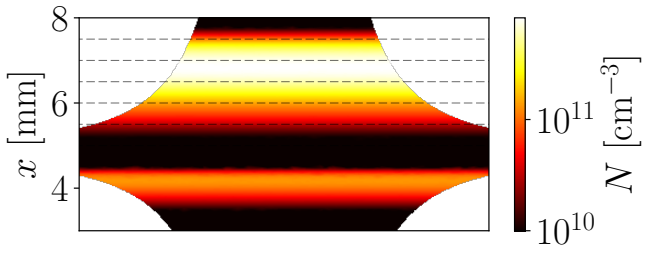


(b) Particles number density $N_{\text{part}}$

**Figure 2.24:** *Representation of the soot volume fraction and particles number density fields in an ethylene-air counterflow diffusion flame for a global strain rate of 30 $s^{-1}$.*

## 2.4 Application to the study of pulsed laminar flames

*This section presents results presented in a publication in the journal Proceedings of the Combustion Institute (Rodrigues et al. 2017).*

Most of the combustion facilities are characterized by high Reynolds number flames where turbulent eddies are expected. The local strain rate usually fluctuates in a wide amplitude range and with random fluctuation frequencies (Attili et al. 2014). These turbulent eddies are also responsible for variable length scale recirculation zones, introducing a wide range of residence times for soot particles, strong intermittency and dynamics features in soot production (Xin and Gore 2005; Franzelli et al. 2015).

One of the most popular approaches used to simulate turbulent non-premixed flames is the flamelet approach, based on a quasi-steady response of the flame

characteristics to the local strain rate fluctuations (Peters 1984; Veynante and Vervisch 2002).

The development of such models being motivated by the application to numerical simulations of turbulent flames, the response of soot to strain rate fluctuations is here investigated by looking at unsteady laminar counterflow diffusion flames (Cuenot et al. 2000; Haworth et al. 1989; Candel 2002).
Specifically to soot context, previous experimental works have been performed in a diffusion laminar flame by introducing sinusoidal velocity variations at both opposed nozzles (Decroix and Roberts 2000; Santoianni et al. 2001) . They showed that soot production response to these fluctuations was phase-lagged and damped when increasing the oscillation frequency. A particular hierarchical behavior was observed: soot volume fraction response is more phase-lagged and damped compared to soot precursors response, which are also more phase-lagged and damped than the temperature response (Xiao et al. 2005). Cuoci et al. (Cuoci et al. 2009) numerically investigated these flames with good prediction of unsteadiness soot dynamics, confirming the experimental observations. Nevertheless, a lack of knowledge remained on the origin of soot response to unsteady strain fluctuations. Moreover, when computing counterflow diffusion flames with unsteady velocities at the nozzle exits, a phase lag exists between the global strain rate and the local strain rate (Cuoci et al. 2009), increasing the complexity of the phenomena. In the other hand, other studies (Xuan and Blanquart 2014) also studied the transient behavior of PAHs production by studying their response to one-step variation of the strain rate. The objective was to derive tabulation methods relative to PAHs in a turbulent combustion modeling context, but no specific study of the soot particles hierarchical response to unsteady fluctuations completed these works.

The objective of this section is the characterization of soot response to strain rate oscillations and to identify the physical phenomena underlying the phase lag and damping observed in soot production. In order to avoid the phase lag between the global and the local strain rate, a strain-imposed formulation is considered in this work and unsteadiness is introduced by varying the imposed flame strain rate $a(t)$ with time for a given pulsation $\omega$, an initial strain rate $A_0$ and fluctuation amplitude $\alpha A_0$:

$$a(t) = A_0 + \alpha A_0 sin(\omega t) = A_0 \left[1 + \alpha sin(2\pi f t)\right]. \tag{2.62}$$

Both analytical and numerical approaches are considered here to study the evolution of the soot precursors and of the particles size distribution (PSD) with the strain rate $a(t)$.

This section is organized as follows. First, an analytical model is proposed in Section 2.4.1 in the limit of a linear behavior, i.e. small oscillation amplitudes. This model predicts the unsteady response on the basis of steady flame results.

Then, soot production in unsteady laminar flames is numerically studied using the detailed sectional model discussed in the present Chapter. The flame response is then investigated for the configuration described in Section 2.4.2.1. The unsteady behavior is analyzed in Section 2.4.2.2 for different frequencies at small amplitude in terms of global quantities and PSD. Analytical results will be compared to the numerical ones in Section 2.4.3.1 to prove their validity. The causes of phase lag and damping in soot production will then be identified by combining information from numerical and analytical results. Finally, numerical simulations at high amplitudes are analyzed in Section 2.4.3.2 to completely characterize the soot response to unsteady strain rate oscillations and to discuss the limits of the analytical model.

### 2.4.1 Analytical model for pulsed sooted flames

In order to investigate the response of soot production to strain rate fluctuations, a linearized analytical model is developed in the following to predict the response of the maximum of a flame variable $\theta$ to strain rate oscillations at a given pulsation $\omega$. The complex form of the fluctuating strain rate $a_1(t) = a(t) - A_0$ is denoted by $\hat{a}_1(\omega) = \alpha A_0 e^{i(\omega t+\pi/2)}$. The corresponding response of the maximum value of $\theta$, namely $\theta^{\max}(t) = \theta_0^{\max} + \theta_1^{\max}(t)$ with $\theta_1^{\max}(t) = \theta_1^{\max}(\omega) sin(\omega t - \varphi_{\theta^{\max}}(\omega))$, is represented by the complex number $\hat{\theta}_1^{\max}(\omega) = \theta_1^{\max}(\omega) e^{i(\omega t+\pi/2-\varphi_{\theta^{\max}}(\omega))}$. This response is fully characterized by the transfer function $T_{\theta^{\max}}(\omega) = \hat{\theta}_1^{\max}(\omega)/\hat{a}_1(\omega)$.

Starting from the previous works (Cuenot et al. 2000; Haworth et al. 1989; Candel 2002), the transfer function is split into two terms: the transfer function $T_{\text{unst}}^{\text{finite},\theta}(\omega)$, introducing an equivalent steady strain rate $A_\theta$ seen by the quantity $\theta$, and the transfer function $T_{\text{steady}}^{\theta^{\max}|A_\theta}(\omega)$, describing the response of $\theta^{\max}$ to the equivalent steady strain rate $A_\theta$.

#### 2.4.1.1 Equivalent steady strain rate

The 1-D steady strained flames can generally be parametrized as a function of a mixture fraction $z$. In the $z$-space, the steady strained flames are described by the following equations (Poinsot and Veynante 2012):

$$\rho u \frac{\partial z}{\partial x} - \frac{\partial}{\partial x}\left(\frac{\lambda}{c_p}\frac{\partial z}{\partial x}\right) = 0 \tag{2.63}$$

$$-\chi_f \frac{\partial^2 \theta}{\partial z^2} = \dot{\omega}_\theta \tag{2.64}$$

where $\theta = Y_k$ or $T$, $\dot{\omega}_\theta$ its source term, $\chi_f$ is the scalar dissipation rate at the position $x_f$ of the flame, $u$ the axial velocity, $x$ the axial coordinate, $c_p$ the mixture heat capacity and $\lambda$ the mixture thermal conductivity.

The velocity field is parametrized by the strain rate $a$ and verifies then:

$$\rho u(x) = -\rho_f a \xi(x) \tag{2.65}$$

with $\xi(x)$ representing the variation of density along the flame axis:

$$\xi(x) = \int_{x_f}^{x} (\rho/\rho_f)\, dx + x_f \tag{2.66}$$

The general solution of Eqs. (2.63) and (2.64) are of the form:

$$z(x) = \mathrm{erf}(\eta(x)) \tag{2.67}$$

with:

$$\eta(x) = \frac{\xi(x)}{2\kappa \left(\lambda/\rho c_p\right)_f^{1/2}} \tag{2.68}$$

$$\kappa = \sqrt{1/2a} \tag{2.69}$$

Now, we consider a flame characterized by an infinitely fast chemistry where we apply a varying strain rate $a(t)$. Then, the unsteady evolution of this flame is characterized by the following equations:

$$\text{Unsteady diffusion zone:} \qquad \rho \frac{\partial z}{\partial t} + \rho u a(t) \frac{\partial z}{\partial x} = \frac{\partial}{\partial x}\left(\frac{\lambda}{c_p}\frac{\partial z}{\partial x}\right) \tag{2.70}$$

$$\text{Quasi-steady reaction zone:} \qquad -\chi_f \frac{\partial^2 \theta}{\partial z^2} = \dot{\omega}_\theta \tag{2.71}$$

To solve these equations, as for the steady strained flame case, we find a solution of the form $z = \mathrm{erf}(\eta)$ with $\eta(x,t) = \xi(x,t)/K(t)$. Then, noting that:

$$\begin{aligned} \frac{\partial \xi}{\partial t} &= \frac{\rho}{\rho_f} u' & \frac{\partial \xi}{\partial x} &= \frac{\rho}{\rho_f} \\ \frac{\partial \eta}{\partial t} &= \frac{\rho u'}{\rho_f K} - \frac{\eta}{K}\frac{\partial K}{\partial t} & \frac{\partial \eta}{\partial x} &= \frac{\rho}{\rho_f K} \end{aligned} \tag{2.72}$$

the following equation for $z$ can be obtained:

$$\frac{\partial^2 z}{\partial \eta^2} + \frac{\eta}{\left(\lambda/\rho c_p\right)_f}\left(K\frac{\partial K}{\partial t} + a(t)K^2\right)\frac{\partial z}{\partial \eta} = 0 \tag{2.73}$$

As $z = \mathrm{erf}(\eta)$, $K(t)$ satisfies the following differential equation:

$$\frac{\partial K^2(t)}{\partial t} + 2a(t)K^2(t) = 4\left(\frac{\lambda}{\rho c_p}\right)_f \tag{2.74}$$

The solution of this equation is (Haworth et al. 1989; Cuenot et al. 2000):

$$K^2(t) = 4\left(\frac{\lambda}{\rho c_p}\right)_f \frac{\int_0^t e^{2a_{\text{int}}(t')}dt'}{e^{2a_{\text{int}}(t)}} \tag{2.75}$$

where $a_{\text{int}}(t) = \int_0^t a(t')dt'$.

Finally, solving Eq. (2.73), one finally obtains $z(x,t) = \text{erf}(\eta(x,t))$ with $\eta(x,t) = \frac{\xi(x)}{2\kappa(t)\left(\lambda/\rho c_p\right)_f^{1/2}}$. $\kappa(t)$ verifes:

$$\kappa(t) = \left(\frac{\int_0^t e^{2a_{\text{int}}(t')dt'}}{e^{2a_{\text{int}}(t)}}\right)^{1/2} \tag{2.76}$$

Then, comparing Eqs. (2.69) and (2.76), under the assumption of infinitely fast chemistry, the unsteady flame acts at each time $t$ as an equivalent steady counterflow flame at constant strain rate equal to the instantaneous strain rate $A(t)$ verifying (Haworth et al. 1989; Cuenot et al. 2000; Candel 2002):

$$A(t) = \frac{e^{2a_{\text{int}}(t)}}{2\int_0^t e^{2a_{\text{int}}(t')}dt'} \tag{2.77}$$

Differentiating this equation, $A(t)$ verifies:

$$\frac{dA}{dt} = -2A^2(t) + 2A(t)a(t). \tag{2.78}$$

Assuming a linear response of $A(t) = A_0 + A_1(t)$ with $a(t) = A_0 + a_1(t)$, i.e. small fluctuations of $a(t)$ around $A_0$, the transfer function $T^{\text{inf}}_{\text{unst}}(\omega)$ between $\hat{A}_1(\omega)$ and $\hat{a}_1(\omega)$ in the case of infinitely fast chemistry is given by:

$$T^{\text{inf}}_{\text{unst}}(\omega) = \frac{\widehat{A}_1(\omega)}{\widehat{a}_1(\omega)} = \frac{1}{1 + j\omega/(2A_0)}. \tag{2.79}$$

When finite-rate chemistry is considered, the following equation must be solved for the species and temperature ($\theta = Y_k$ or $T$):

$$\rho\frac{\partial\theta}{\partial t} - \chi_f\frac{\partial^2\theta}{\partial z^2} = \dot{\omega}_\theta \tag{2.80}$$

As $z$ verifies the same equation as before, $\chi_f$ is here a linear function of $A(t)$ previously determined. The idea is here to find for each quantity $\theta$, an equivalent steady strain rate $A_\theta(t)$ such that $\theta$ verifies the following steady equivalent equation:

$$-\chi_{f,\theta}\frac{\partial^2\theta}{\partial z^2} = \dot{\omega}_\theta \tag{2.81}$$

with $\chi_{f,\theta}$ a linear function of $A_\theta(t)$.

This analysis can already be found in literature (Cuenot et al. 2000), and the equivalent strain rate $A_\theta(t)$ verifies the following equation as a function of $A(t)$:

$$\frac{\partial A_\theta}{\partial t} = \frac{A_\theta(t) - A(t)}{A_\theta(t)} \frac{\dot{\Omega}_\theta(t)}{(d\theta/dA)_\Omega} = \frac{A(t) - A_\theta(t)}{\gamma_\theta(t)}, \tag{2.82}$$

where $\dot{\Omega}_\theta = \dot{\omega}_T^{\max}/(\rho c_p)$ for $\theta = T$ and $\dot{\Omega}_\theta = W_k \dot{\omega}_k^{\max}/\rho$ for $\theta = Y_k$. $\rho$ and $c_p$ are evaluated at the position where $\dot{\omega}_\theta$ is maximum. $(d\theta/dA)_\Omega$ represents the variation of $\theta$ where $\dot{\omega}_\theta$ is maximum with a steady strain rate. $\gamma_\theta(t)$ is defined as $\gamma_\theta(t) = -(d\theta/dA)_\Omega A_\theta(t)/\dot{\Omega}_\theta(t)$.

To find the linearized response of $A_\theta(t)$, $A_\theta(t)$ and $\gamma_\theta(t)$ are written as: $A_\theta(t) = A_0 + A_{\theta_1}(t)$ and $\gamma_\theta(t) = \gamma_{\theta_0} + \gamma_{\theta_1}(t)$, where $A_0$, $\gamma_{\theta_0}$, are the values of respectively $A_\theta(t)$, and $\gamma_\theta(t)$ for the initial steady flame. By linearizing Eq. (2.82), one obtains:

$$\frac{\partial A_{\theta_1}}{\partial t} = \left(A_1(t) - A_{\theta_1}(t)\right) \gamma_{\theta_0}^{-1}. \tag{2.83}$$

Combining the Fourier transform of Eq. (2.83) and Eq. (2.79), the following transfer function $T_{\text{unst}}^{\text{finite},\theta}(\omega)$ between $\hat{A}_{\theta_1}(\omega)$ and $\hat{a}_1(\omega)$ is obtained:

$$T_{\text{unst}}^{\text{finite},\theta}(\omega) = \frac{\hat{A}_{\theta_1}(\omega)}{\hat{a}_1(\omega)} = \frac{1}{1 + j\omega\gamma_{\theta_0}} \frac{1}{1 + j\omega/(2A_0)}. \tag{2.84}$$

#### 2.4.1.2 Steady response of the maximum value

The objective is here to obtain an analytical model for the response of the maximum value $\theta^{\max}$ of a quantity $\theta \in \{Y_k, T\}$. No general procedure exists in literature. Here as the response of the equivalent steady strain rate $A_\theta(t)$ has been determined in the previous section for each quantity, the flame response is analyzed by looking at steady conditions.

For $\theta \in \{T, Y_k\}$, it has been observed that in the neighborhood of a given strain rate $A_0$, the dependency of $\theta^{\max}$ for a steady flame with strain rate $A$ is given by (Huijnen et al. 2010):

$$(\theta^{\max}(A)/\theta^{\max}(A_0)) = (A/A_0)^{p_\theta} \tag{2.85}$$

with $p_\theta$ a characteristic constant. Linearizing Eq. (2.85) with $\theta^{\max}(t) = \theta_0^{\max} + \theta_1^{\max}(t)$ gives $\theta_1^{\max}(t) = \frac{p_\theta \theta_0^{\max}}{A_0} A_\theta(t)$.
However, the forthcoming comparison with the detailed computation demonstrates the requirement to introduce an additional delay in the response to

the unsteady strain rate oscillations. Linking this delay to the chemical time seems particularly relevant for soot precursors and particles, whose chemistry is mainly sequential so that all the reactions necessary for the formation have to respond before getting the response of $\theta^{\max}$. This delay is then assumed to be equal to the characteristic chemical time scale $\tau_\theta$ of the quantity of interest $\theta$ defined hereafter: $\theta^{\max}(t)$ reacts then at the equivalent strain rate $A_\theta(t-\tau_\theta)$. The validity of this hypothesis will be verified in Section 2.4.3.1. The response of $\theta_1^{\max}(t)$ is therefore expressed as:

$$\begin{aligned} &\theta_1^{\max}(t) = p_\theta \theta_0^{\max} A_\theta(t-\tau_\theta)/A_0 \\ \Rightarrow\ &T_{\text{steady}}^{\theta^{\max}|A_\theta}(\omega) = p_\theta \theta_0^{\max} e^{-j\omega\tau_\theta}/A_0 \end{aligned} \tag{2.86}$$

where $T_{\text{steady}}^{\theta^{\max}|A_\theta}(\omega) = \hat{\theta}_1^{\max}(\omega)/\hat{A}_{\theta_1}(\omega)$ represents the transfer function between $\hat{\theta}_1^{\max}(\omega)$ and $\hat{A}_{\theta_1}(\omega)$.

The characteristic time scale $\tau_k$ for the $k^{\text{th}}$ species is defined as (IM et al. 1999):

$$\tau_k = [X_k]^{\max}/\dot{\omega}_k^{\max} = (\rho Y_k)^{\max} / (W_k \dot{\omega}_k^{\max}) \tag{2.87}$$

where $[X_k]$, $Y_k$, $W_k$ and $\dot{\omega}_k$ are the molar concentration, the mass fraction, the molecular weight and the molar production rate of the $k^{\text{th}}$ species.
This definition is appropriate when considering stable species, which is the case for the considered PAHs. When considering radicals or very fast species, the definitions proposed in Xuan and Blanquart (2014) based on consumption or production chemical rates should be preferred.

In the same way, the characteristic time scale $\tau_T$ of the flame can be defined as $\tau_T = (\rho c_p T)^{\max}/\dot{\omega}_T^{\max}$, with $c_p$ the mixture mass specific heat capacity and $\dot{\omega}_T$ the heat release rate.
As for the species, a time scale $\tau_{s,i}$ for the soot particles in the $i^{\text{th}}$ section can be defined as:

$$\tau_{s,i} = (\rho Y_{s,i})^{\max} / \left(\rho_s (\dot{Q}_{s,i})^{\max}\right) \tag{2.88}$$

#### 2.4.1.3 Transfer function $T_{\theta^{\max}}(\omega)$

From the definitions of $\gamma_{\theta_0}$ and $\tau_\theta$, $\gamma_{\theta_0}$ can be rewritten as $\gamma_{\theta_0} = \tau_\theta \Gamma_\theta$ with $\Gamma_\theta = -(d\theta/dA)_{\Omega^\cdot}(A_0/\theta^{\max}(A_0))$, a dimensionless parameter characterizing the steady response of the quantity $\theta$ to strain rate. Then, by combining Eqs. (2.84) and (2.86), the transfer function $T_{\theta^{\max}}(\omega)$ between $\hat{\theta}_1^{\max}(\omega)$ and $\hat{a}_1(\omega)$ is given by $T_{\theta^{\max}}(\omega) = T_{\text{steady}}^{\theta^{\max}|A_\theta}(\omega) T_{\text{unst}}^{\text{finite},\theta}(\omega)$. Gain and phase lag of $\theta^{\max}$ are expressed respectively by $G_{\theta^{\max}}(\omega) = 20log_{10}(|T_{\theta^{\max}}(\omega)| \,/\, |T_{\theta^{\max}}(\omega=0)|)$ and $\varphi_{\theta^{\max}}(\omega)$,

where:

$$\begin{cases} |T_{\theta^{\max}}(\omega)| = \dfrac{|a_1 p_\theta \theta_0^{\max}|}{A_0} \dfrac{1}{\sqrt{1+\eta(\omega)^2}} \dfrac{1}{\sqrt{1+\left(\frac{2\eta(\omega)\Gamma_\theta}{Da_\theta}\right)^2}} \\ \varphi_{\theta^{\max}}(\omega) = \tan^{-1}(\eta(\omega)) + \tan^{-1}(2\eta(\omega)\Gamma_\theta/Da_\theta) \\ \qquad\qquad + 2\eta(\omega)/Da_\theta \end{cases} \tag{2.89}$$

with $\eta(\omega) = \omega/(2A_0) = \pi f/A_0$ the Stokes number and $Da_\theta = A_0^{-1}\tau_\theta^{-1}$ the Damköhler number associated with $\theta$. From Eq. (2.89), it can be deduced that three non-dimensional parameters are responsible for the phase lag and damping of the response of $\theta$:

- $\eta$ compares the characteristic time associated to the strain rate $A_0$ to the imposed frequency $f$ and is responsible for the filtering of the flow structure. The damping response of all the quantities increases when $\eta$ increases.
- $Da_\theta$ is directly responsible for the phase lag and damping response due to the low chemical time scale of the analyzed quantity $\theta$. The lower $Da_\theta$ is, the more the response of $\theta^{\max}$ is phase-lagged and damped.
- $\Gamma_\theta$, which represents the steady response of the quantity $\theta$ to strain rate, also contributes to the damping response of $\theta$ with unsteady strain fluctuations. For high values of $\Gamma_\theta$, the damping response will be high.

This identified behavior is valid for all the quantities but is more significant in the case of species with large chemical characteristic time scales ($Da_\theta \ll 1$), which is the case of soot precursors and particles. Equation (2.89) allows the predictions of the unsteady response of $\theta$ from information on steady flames. Its validity will discussed, in particular for soot production, in Sec. 2.4.3.1.

## 2.4.2 Detailed simulations of soot production in unsteady laminar diffusion flames at imposed strain rate

### 2.4.2.1 Numerical configuration

A counterflow propane/air diffusion flame is considered here by varying the imposed strain rate $a(t)$ from an initial flame at $A_0 = 60$ s$^{-1}$. Ten frequencies and three amplitudes have been considered. Pure propane and pure air stream, both at 294 K are supplied through the two opposed nozzles at a distance $L =$ 12.7 mm, discretized with more than 400 points. This configuration corresponds to the configuration experimentally studied by Decroix and Roberts (2000) and Santoianni et al. (2001). For each studied frequency, ten signal periods are computed. Once the permanent regime is attained, the response of each variable is studied in terms of gain and phase lag.

### 2.4.2.2 PAH and soot particles response

Results for small strain rate fluctuations ($\alpha = 10\%$) are first considered here. Figure 2.25 (left) presents the unsteady response of the soot maximum volume fraction and pyrene ($A4$) maximum mass fraction (the smallest considered soot precursor) to the unsteady imposed strain rate during two oscillating cycles. Quantities have been normalized with their respective steady values at the lowest and highest strain rates for three frequencies. The higher the frequency, the more $f_V^{\max}$ and $Y_{A4}^{\max}$ fluctuations are dumped and phase-lagged. Looking at the results in the $a$-space (Fig. 2.25, right) enables a clear comparison with the quasi-steady solution (grey line). A quasi-steady response is observed at low frequency ($f = 0.1$Hz), while for higher frequencies, solutions step aside from the steady results.

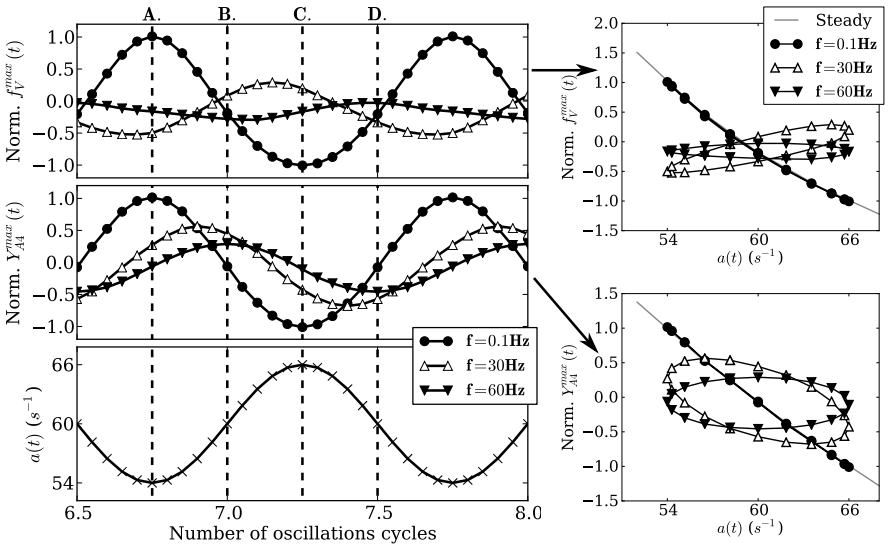


**Figure 2.25:** *Normalized response of soot maximum volume fraction ($f_V^{max}$), pyrene maximum mass fraction ($Y_{A4}^{max}$) to the unsteady imposed strain rate ($a(t)$).*

The temporal evolution of the PSD is also studied here by looking at the four instants **A.**,**B.**,**C.**,**D.** of Fig. 2.25 separated by 90° in one pulsation period. Results for three frequencies are presented in Fig. 2.25 together with the quasi-steady state at the spatial position $x^{\text{soot}}$, where soot volume fraction is maximum, close to the stagnation point. At each time, the PSD shows a bi-modal nature with one peak for small particles (generated by nucleation) and another for large aggregates (due to condensation and coagulation). In the quasi-steady case, from point **A.** to **C.** the characteristic flow time decreases (since $a(t)$ increases), so that particles have less time to coagulate. The position of the aggregates peak translates then towards smaller diameter values: the higher the strain rate, the smaller are the aggregates composing the soot popula-

tion. Inversely, from point **C.** to **A.**, the strain rate decreases, particles have the time to coagulate and bigger aggregates populate the PSD. The unsteady PSDs follow such dynamics, but their response is affected by the phase-lag already observed on the global $f_V$. Indeed, at $f = 5$Hz, the PSD responds in a quasi-steady way, whereas the phase-lag effect is more and more evident on PSD for higher frequencies. The response of the PSD is also more and more damped so that at $f = 60$Hz only small PSD fluctuations are observed between the four instants. For high oscillation frequencies, the PSD is observed to not oscillate anymore since the oscillations are completely damped.

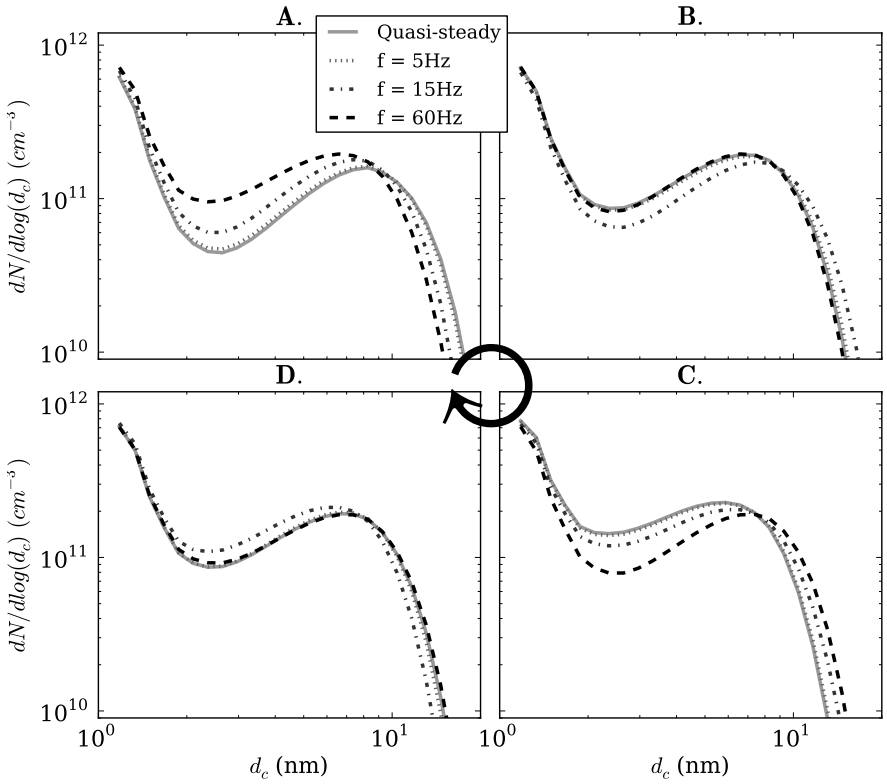


**Figure 2.26:** *Unsteady variations of the PSD at $f_V^{max}$ position.*

### 2.4.3 Unsteady dynamics of PAH and soot particles in laminar counterflow diffusion flames

#### 2.4.3.1 Comparison with analytical predictions

In order to understand the processes governing the PSD evolution, results for the different sections are now investigated.

Lines in Fig. 2.27 presents the response in terms of gain and phase lag of maximum temperature, $Y_{A2}^{\max}$, $Y_{A4}^{\max}$, maximum soot mass fraction of two sec-

tions (sections 12 and 16, whose mean diameter are indicated in Table 2.7) and $f_V^{\max}$. The response of precursors and soot is more phase-lagged and damped than temperature. Moreover, phase-lag and damping increases with their size (not shown for all precursors). Big particles are the main contributions to soot volume fraction, so that $f_V$ response is mainly governed by the last soot sections.

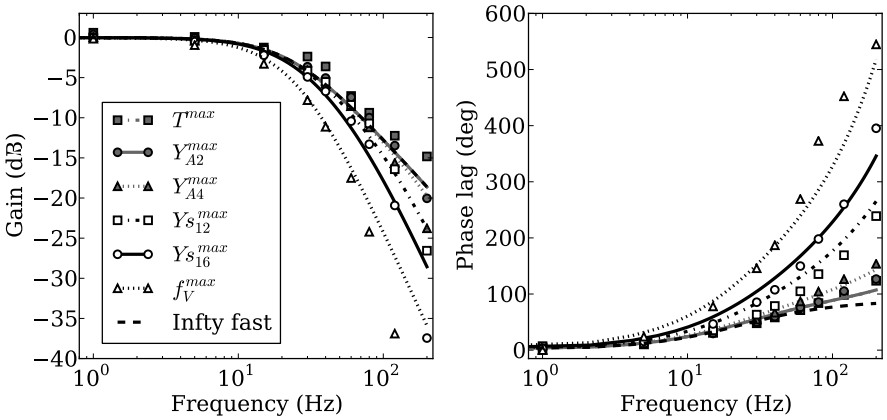


**Figure 2.27:** *Comparison between analytical model predictions (lines) and numerical results (symbols) of amplitude gain and phase lag for maximum temperature, naphtalene (A2) and pyrene (A4) maximum mass fractions, maximum mass fractions of the $12^{th}$, the $16^{th}$ soot sections and maximum soot volume fraction. Analytical results for $T^{max}$ and $Y_{A2}^{max}$ are superposed.*

A good agreement is obtained between the numerical results (lines) and the analytical model (symbols) described in Section 2.4.1.2. Discrepancies are mainly observed at high frequencies but the hierarchical behavior between temperature, soot precursors and soot sections is well predicted. This confirms that soot dynamics are mainly governed by the three parameters identified with the analytical model. In particular, soot response is mainly due to its slow chemistry compared to the flame.

To identify the main physical processes contributing to such a long chemical time, the characteristic time scales for nucleation ($\tau_{\text{nu}}$), condensation ($\tau_{\text{cond}}$), surface growth ($\tau_{\text{sg}}$) and coagulation ($\tau_{\text{coag}}$) have been estimated for different sections from the steady flame at $A_0$.
Indeed, by perturbing each volume fraction production rate relative to each phenomenon (ph) by a small value (typically 1%), the characteristic time scales $\tau_{\text{nu},i}$ for nucleation, $\tau_{\text{cond},i}$ for condensation, $\tau_{\text{sg},i}$ for surface growth, $\tau_{\text{ox},i}$ for oxidation and $\tau_{\text{coag},i}$ for coagulation can be expressed as:

$$\tau_{\text{ph},i} = \Delta\left[(\rho Y_{s,i}/\rho_s)^{\max}\right] / \Delta\left[(\dot{Q}_{\text{ph},i})^{\max}\right] \tag{2.90}$$

where $\Delta\left[(\dot{Q}_{\text{ph},i})^{\max}\right]$ corresponds to the variation of the peak volume fraction

production rate of the phenomenon for the $i^{\text{th}}$ section.

Table 2.7 presents these characteristic time scales normalized by the flame time scale ($\tau_T = 0.31$ ms) for five soot sections. All the characteristic time scales increase with the soot particle size, in particular for $\tau_{\text{cond}}$ and $\tau_{\text{coag}}$ that depend on the collisions rate. The particle number density of the last sections being smaller than for small particles sections, the number of particles available for collision is lower so that the characteristic time scales of collisional phenomena increases with the particle size.

The long characteristic time scale of $f_V^{\max}$, governing the phase-lag and damping of the unsteady response, is then mainly due to condensation and coagulation phenomena of the biggest particles.

| Section | $d_{c,i}^{\text{mean}}$ (nm) | $\frac{\tau_{\text{nu}}}{\tau_T}$ | $\frac{\tau_{\text{cond}}}{\tau_T}$ | $\frac{\tau_{\text{sg}}}{\tau_T}$ | $\frac{\tau_{\text{coag}}}{\tau_T}$ |
|---|---|---|---|---|---|
| 1 | 1.2 | 3.4 | 3.2 | 3.6 | - |
| 8 | 2.6 | - | 4.2 | 4.4 | 2.3 |
| 12 | 4.2 | - | 6.5 | 5.7 | 4.6 |
| 16 | 6.6 | - | 12 | 7.7 | 8.1 |
| 20 | 10 | - | 17 | 8.3 | 13 |

**Table 2.7:** *Comparison of normalized characteristic time scales of nucleation, condensation, surface growth and coagulation. $d_{c,i}^{mean}$ represents the mean collisional diameter of a soot particle in the $i^{th}$ section.*

In order to study the validity of the assumption on the induced delay time due to slow chemistry presented in Section 2.4.1.2, Fig. 2.28 presents the obtained numerical phase lag due to this delay time as a function of the expected one. This phase lag $\Delta\varphi$ is obtained by substracting to the obtained numerical phase lag $\varphi_{\theta^{\max}}^{\text{num}}(\omega)$ the theoretical phase lag of the equivalent steady strain rate $A_\theta$ of the variable of interest $\theta$:

$$\Delta\varphi = \varphi_{\theta^{\max}}^{\text{num}}(\omega) - \tan^{-1}(\eta(\omega)) - \tan^{-1}(2\eta(\omega)\Gamma_\theta/\text{Da}_\theta) \tag{2.91}$$

Good results are obtained for all the species and temperature, which confirms the representativity of the chosen variable ($\tau_\theta$). Nevertheless, some discrepancies exist and future investigations are still needed in order to define in a more precise way this delay time.

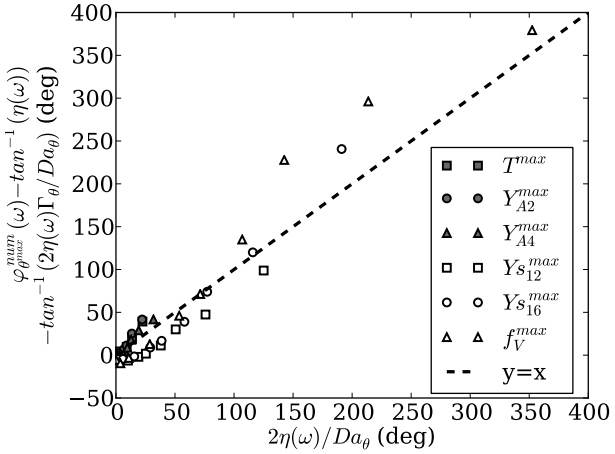


**Figure 2.28:** *Numerical results of the induced phase lag due to the delay time imposed by slow chemistry as a function of the expected ones.*

#### 2.4.3.2 Numerical results at high amplitudes

In order to study the soot dynamics at higher amplitudes, computations have been performed for amplitudes $\alpha$ of 30% and 60%. Table 2.8 compares the numerical results for the phase lag and amplitude gain of $Y_{A4}^{\max}$ and $f_V^{\max}$ for three amplitudes and three frequencies. The phase lag increases with the frequency in a similar way for all the amplitudes. The gain remains almost the same for $\alpha = 10\%$ and $\alpha = 30\%$, but decreases for $\alpha = 60\%$. The difference of the numerical behavior between $\alpha = 30\%$ and $\alpha = 60\%$ highlights the non-linear effects for such amplitudes, which cannot be described by the linear analytical model whose predictions do not depend on the perturbation amplitude.

| $f$ | $\theta$ | $\alpha = 10\%$ | | $\alpha = 30\%$ | | $\alpha = 60\%$ | |
|---|---|---|---|---|---|---|---|
| (Hz) | | $G_{\theta^{\max}}$ | $\varphi_{\theta^{\max}}$ | $G_{\theta^{\max}}$ | $\varphi_{\theta^{\max}}$ | $G_{\theta^{\max}}$ | $\varphi_{\theta^{\max}}$ |
| 30 | $A4$ | -4 | 54 | -4 | 53 | -5 | 56 |
| 30 | $f_V$ | -4 | 146 | -4 | 158 | -13 | 142 |
| 60 | $A4$ | -9 | 87 | -8 | 91 | -10 | 87 |
| 60 | $f_V$ | -14 | 269 | -14 | 287 | -24 | 256 |
| 120 | $A4$ | -16 | 126 | -16 | 134 | -18 | 130 |
| 120 | $f_V$ | -33 | 460 | -33 | 524 | -41 | 497 |

**Table 2.8:** *Numerical analysis of the impact of the strain fluctuation amplitude ($\alpha$) on the pyrene maximum mass fraction and soot maximum volume fraction gain (G in dB) and phase lag ($\varphi$ in deg).*

### 2.4.4 Conclusion on unsteady soot production behavior in pulsed laminar flames

Response of sooting propane-air counterflow diffusion flames to imposed strain rate harmonic oscillations have been numerically investigated with a detailed description for the gas and the solid phases. The unsteady behavior of soot particles and precursors production, as well as the PSD evolution, were studied both analytically and numerically. It has been observed that the higher the oscillation frequency is, the more PAHs and soot particles fluctuations are damped and phase-lagged so that unsteady solutions are farther and farther away from the quasi-steady state. The phase-lag and damping increase with the size of PAHs and soot particles.

An analytical model has been proposed to predict the observed phase lags and dampings assuming a linear behavior. Three non-dimensional parameters ($\eta$, $Da_\theta$ and $\Gamma_\theta$) govern the unsteady response. Soot particles are characterized by long time scales mainly due to condensation and coagulation phenomena. Indeed, compared to the gas species, their dynamics, particularly the additional identified phase lag, are mainly governed by the $Da_\theta$ parameter.

Therefore, models developed for numerical simulations of soot production in turbulent flames have to correctly reproduce these observed features in order to represent unsteady behaviors such as soot intermittency. On the one hand, these behaviors highlight the limits of flamelet regime assumption based on quasi-steady hypothesis, implying major complexities in modeling for turbulent calculations. In this sense, the presented results support the need for specific techniques (Xuan and Blanquart 2015) to account for PAHs response to unsteady strain rate fluctuations. On the other hand, the reduced models have to provide a good prediction of $\eta$, $Da_\theta$ and $\Gamma_\theta$ for PAHs and soot. As an example, representative soot precursors have to be chosen in terms of these three parameters in order to obtain the good unsteady behavior of soot production: large precursors dynamics (such as pyrene and coronen) have to be reproduced. The proposed analytical model will be very useful for the development of models that reproduce the dynamics of soot and their precursors in turbulent flames.

## 2.5 Discussion of the results

In this chapter, a sectional model enabling to describe soot particles size distribution in laminar flames has been developed. However, high variability of sectional methods exist in literature. Moreover, numerous uncertainties remain about the different processes governing soot particles evolution. Challenges in describing with a high accuracy the soot particles size distribution evolution are then discussed in this section.

Coupled with a detailed gas chemistry, the sectional approach has recently been widely used to study laminar 1-D or 2-D academical configurations (Colket et al. 1994; McEnally et al. 1998; Smooke et al. 1999; Wen et al. 2005; Netzell 2006; Marchal 2008; Dworkin et al. 2009; Echavarria et al. 2011; Sirignano et al. 2011; Blacha et al. 2012). The sectional model has also been used for the description of PAHs growth in some recent studies (Blacha et al. 2012; Eberle et al. 2015; Eberle et al. 2017). It has also been used in 3-D RANS calculations (Netzell et al. 2007; Aubagnac-Karkar et al. 2015) coupled with flamelet-based models for the gaseous phase.

Due to high uncertainties in physical and chemical processes description, these models can differ on several points:

- The gas phase chemistry used for the prediction of PAHs. Indeed, PAHs prediction remains an important challenge and no reference kinetic scheme is today recognized as the one enabling to correctly predict these aromatics concentrations in all kind of flames.
- The model used for nucleation (based on polymerization or dimerization assumptions, PAHs considered for the nucleation, ...). The exact chemical process of particles nucleation is not well understood, even if dimerization process is today recognized as the major process involved in soot particles nucleation. Some studies have also shown that this process can be reversible and this reversibility should be taken into account in our models (Eaves et al. 2015). Finally, sticking coefficients of this process are also unknown and a lot of different models have been proposed in the literature (Yapp et al. 2015; Wang et al. 2015).
- The collision regime and the corresponding collision efficiencies considered for describing condensation and coagulation phenomena.
- The chemical-based mechanism for surface growth and oxidation (HACA, HACA-RC,...). Indeed, the chemical mechanism for surface growth and oxidation processes is still not well defined and the impact of others radicals, like the methyl ($CH_3$) and ethynyl ($C_2H$) should be taken into account based on recent studies (Hwang and Chung 2001; Wang et al. 2015). Moreover, the modeling of the proportion of active sites parameter $\alpha$ is also still unknown.
- The description of soot particles geometry (spherical or fractal). For this point, very few studies have proposed a modeling of soot particles fractal geometry. In the work of Marchal (2008), a modification of the law governing the surface-volume relationship for a classical spherical particle has been proposed. This methodology is retained and improved in our study and the proposed model has been detailed in Section 2.2.3. However, Table 2.9 presents an overview of several studies that have investigated the value of the mean value of the primary particle diameter $d_p$ in flames. High variability of the value of $d_p$ can be observed from 5 to 60 nm. In-

deed, this value depends on multiple parameters as the flame type, the considered or the history of the soot aggregates. Numerous investigations are then required in order to correctly reproduce the evolution of this quantity.

| Publication | Combustible and comburant | Flame regime | $d_p$ [nm] |
|---|---|---|---|
| Lee et al. (1962) | $C_3H_8/C_2H_4/C_3H_6$ and air | Laminar diffusion flame | 20 – 40 |
| Prado et al. (1977) | Kerosene and air | Turbulent diffusion flame | 19 – 30 |
| Prado et al. (1981) | Propane and Oxygen | Laminar premixed flame | 15 – 26 |
| Harris and Weiner (1984) | Toluene/Ethylene and air | Laminar premixed flame | 20 – 25 |
| Samson et al. (1987) | Acetylene and air | Laminar diffusion flame | 20 – 30 |
| Zhang et al. (1988) | Methane and oxygen | Laminar premixed flame | 20 |
| Megaridis and Dobbins (1989) | Ethylene and air | Laminar diffusion flame | 30 – 37 |
| Köylü and Faeth (1994) | Acetylene and air | Turbulent diffusion flame | 47 |
| Köylü and Faeth (1994) | Propylène | Turbulent diffusion flame | 41 |
| Köylü and Faeth (1994) | Ethylene and air | Turbulent diffusion flame | 32 |
| Köylü and Faeth (1994) | Propane and air | Turbulent diffusion flame | 30 |
| Faeth and Köylü (1995) | Toluene and air | Turbulent diffusion flame | 51 |
| Faeth and Köylü (1995) | Benzene and air | Turbulent diffusion flame | 50 |
| Faeth and Köylü (1995) | N-heptane and air | Turbulent diffusion flame | 35 |
| Faeth and Köylü (1995) | Isopropanol and air | Turbulent diffusion flame | 31 |
| Köylü et al. (1997) | Ethylene and air | Flamme diffusion laminaire | 18 – 32 |
| Krishnan et al. (2000) | Butadiene and air | Turbulent diffusion flame | 42 |
| Krishnan et al. (2000) | Cyclohexane and air | Turbulent diffusion flame | 42 |
| Zhu et al. (2002) | Ethene and air | Laminar diffusion flame | 37 |
| Zhu et al. (2002) | Acetylene and air | Laminar diffusion flame | 51 |
| Hu et al. (2003) | Ethylene and air | Turbulent diffusion flame | 19 – 35 |
| Hu et al. (2003) | Acetylene and air | Turbulent diffusion flame | 17 – 34 |
| Zhao et al. (2005) | Ethylene and air | Laminar premixed flame | 20 |
| Williams et al. (2007) | Ethylene and air | Laminar diffusion flame | 36 |
| Williams et al. (2007) | Kerosene and air | Laminar diffusion flame | 41 |
| Jensen et al. (2007) | Kerosene JP-8 and air | Pool fire | 64 – 74 |
| Sachdeva and Attri (2008) | Kerosene and air | Laminar diffusion flame | 23 |
| Sachdeva and Attri (2008) | Hexane and air | Laminar diffusion flame | 42 |
| Abid et al. (2009) | Ethylene and air | Laminar premixed flame | 10–30 |
| Li et al. (2011) | Diesel and air | Diesel engine | 18–29 |
| Bladh et al. (2011) | Ethylene and air | Laminar premixed flame | 5-15 |
| Kook and Pickett (2011) | m-xylene/n-dodecane and air | Turbulent diffusion flame | 13 |
| Kook and Pickett (2011) | Jet-A and air | Turbulent diffusion flame | 16 |
| Menkiel et al. (2012) | Diesel and air | Diesel engine | 20–45 |
| Bescond et al. (2016) | Propane and air | Laminar diffusion flame | 15-36 |
| Bescond et al. (2016) | Ethylene and air | Laminar diffusion flame | 35 |

**Table 2.9:** *Summary of primary particles diameter measurements in literature (extracted and completed from Maugendre (2009)).*

To conclude, because of the large uncertainties that remain in each soot formation sub-model, it is very difficult to compare the results obtained with

different soot sectional models and it can not be expected to exactly reproduce the experimental measurements for all possible configurations. However, the tendencies can be compared and discussed.

## 2.6 Conclusion

The sectional model used in this thesis has been presented.
Correct gaseous phase modeling is needed in order to correctly predict global flame parameters, but also soot gaseous precursors and the species involved in surface growth and oxidation phenomena. The KM2 kinetic scheme, describing soot precursors formation until seven aromatic rings, has been identified as the one satisfying these criteria at a reasonable cost.
Then, the equations governing the developed sectional approach have been presented. In particular, an extension of the sectional method has been proposed in order to take into account fractal properties of soot particles, based on a assumed $S - V$ relationship for soot particles.

This model has then be validated with a good agreement in premixed laminar configurations at atmospheric and elevated pressures. In counterflow diffusion configurations, good predictions have been obtained for propane and methane fuels, but under-prediction by a factor five is obtained for ethylene-air configurations.

Important numerical models uncertainties still remain in soot particles formation modeling and the different origins of these uncertainties have been discussed in details. In particular, impact of different radicals have been proposed in literature in order to improve soot particles formation prediction in counterflow configurations.

Then, based on this sectional method, the unsteady behavior of soot particles and precursors production, as well as the PSD evolution, were studied both analytically and numerically. Three non-dimensional parameters, characterized mainly by the time scales involved in soot production, have been identified as the one governing the unsteady response of soot production.

Finally, an improvement of the understanding of soot particles formation processes and soot particles properties are required in order to both improve the quality and precision of modeling predictions.

# Part II

# Large Eddy Simulations of sooting flames

# Introduction

As explained in the first part of the manuscript, the prediction of soot emission is extremely challenging due to its complex nature, characterized by a strong coupling between flow parameters, flame characteristics and soot properties. This is even more difficult when studying soot production in turbulent flames, where the chemical scales underlying soot production compete with the turbulence scales (Xin and Gore 2005; Bisetti et al. 2012; Attili et al. 2014).

Therefore, the numerical prediction of soot requires adequate and precise models for the characterization of the turbulent behaviour of the flame as well of the different phenomena involved in soot production. Different strategies have been proposed in literature as a compromise between accuracy and computational cost.

On the one hand, Direct Numerical Simulations (DNS), providing a full description of all the temporal and spatial scales, and Large Eddy Simulations (LES), resolving only the most energetic scales, have been used to investigate turbulent soot production in academic configurations (Lignell et al. 2008; Attili et al. 2014; Arias et al. 2015) or more realistic flames (El-Asrag and Menon 2009; Mueller et al. 2013; Franzelli et al. 2015; Eberle et al. 2015; Koo et al. 2016), respectively. However, due to their high computational cost, these simulations rely on simplified description for the soot evolution, *i.e.* semi-empirical models (Leung et al. 1991; Lindstedt 1992) or methods of moments (Frenklach and Wang 1994; Blanquart and Pitsch 2007; Salenbauch et al. 2015; Wick et al. 2017), which usually do not provide access to the soot particles size distribution (PSD). Therefore, these approaches allow an adequate description of the spatial and temporal evolution of the flow and the flame, but not of the soot PSD. Nevertheless, method of moments can provide an accurate description of soot fractality at a low cost, by using bi-variate moments of the soot PSD in particles surface and volume spaces (Blanquart and Pitsch 2007; Mueller et al. 2009a; Mueller and Pitsch 2012). On the other hand, due to their high computational cost, the use of sectional methods such as the one presented in Chapters 1 and 2 has been limited to Reynolds Averages Navier Stokes (RANS) computations (Netzell et al. 2007; Fraioli et al. 2011; Aubagnac-Karkar et al. 2015). This RANS-sectional approach provides access to more details in soot

particles size distribution spatial evolution while loosing information on the flow and the flame, for which only ensemble-average statistics are available.

Here, we propose to employ the whole potential of both strategies, by combining an LES approach with a sectional model for the prediction of soot particles evolution.

In this context, the LES formalism is introduced in Chapter 3, by presenting the models for all unclosed terms of the filtered equations for the solid phase description. Then, a first application of the proposed LES formalism is presented in Chapter 4 in the study of an atmospheric turbulent jet ethylene-air flame. In Chapter 5, soot production in a confined pressurized ethylene-air flame is investigated. In both applications, soot particles size distributions evolutions are analyzed and physical and chemical processes leading to identified particles size distributions shapes are discussed.

# Chapter 3

# LES formalism for sooting turbulent flames based on a sectional approach

*Large-Eddy Simulation (LES) of sooting turbulent flames requires the resolution of transport equations for both gaseous and solid phases. In this section, the novel features, mainly concerning the solid phase treatment will be provided, since the description of the reactive gaseous phase relies on a classical LES formalism.*
*This formalism has been presented in the paper (Rodrigues et al. 2018) accepted for publication. The proposed formalism has been implemented into the AVBP code (Schonfeld and Rudgyard 1999), the solver retained in this thesis for all LES simulations as described in Appendix B.*

**Contents**

## 3.1 Filtered soot sectional equations

### 3.1.1 Separation of gaseous and solid contributions on the soot sectional source terms

#### Nucleation

The LES formalism will be presented in Sec. 3.1.2. However, in order to highlight the source terms dependency on the gaseous and solid characteristics, it is convenient to rewrite them as a product of two contributions. For nucleation, it writes:

$$\dot{q}_{\mathrm{nu},1} = \dot{q}^{\mathrm{gas}}_{\mathrm{nu},1}\dot{q}^{\mathrm{solid}}_{\mathrm{nu},1}, \tag{3.1}$$

where:

$$\begin{aligned}\dot{q}^{\mathrm{gas}}_{\mathrm{nu},1} &= \epsilon_{\mathrm{nu}}\frac{\sqrt{T}}{\rho}\left(\frac{3}{4\pi}\right)^{1/6}\sqrt{\frac{6k_b}{\rho_s}}4\sqrt{2}v_{\mathrm{d}}^{7/6}N_{\mathrm{d}}^2 \\ \dot{q}^{\mathrm{solid}}_{\mathrm{nu},1} &= 1\end{aligned} \tag{3.2}$$

#### Condensation

As for nucleation, the gaseous and the solid contributions for the condensation source term have to be separated as:

$$\dot{q}_{\mathrm{cond},i} = \dot{q}^{\mathrm{gas}}_{\mathrm{cond},i}\dot{q}^{\mathrm{solid}}_{\mathrm{cond},i} \tag{3.3}$$

with $\dot{q}^{\mathrm{gas}}_{\mathrm{cond},i} = \sqrt{T}N_d v_d/\rho$. Combining Eqs. (2.22) and (3.3), $\dot{q}^{\mathrm{solid}}_{\mathrm{cond},i}$ is expressed as:

$$\dot{q}^{\mathrm{solid}}_{\mathrm{cond},i} = \dot{q}^{\mathrm{gas}\to i,\mathrm{solid}}_{\mathrm{cond},i} + \dot{q}^{i-1\to i,\mathrm{solid}}_{\mathrm{cond},i} - \dot{q}^{i\to i+1,\mathrm{solid}}_{\mathrm{cond},i} \tag{3.4}$$

with:

$$\begin{aligned}\dot{q}^{\mathrm{gas}\to i,\mathrm{solid}}_{\mathrm{cond},i} &= \dot{q}^{\mathrm{gas}\to i}_{\mathrm{cond},i}/\dot{q}^{\mathrm{gas}}_{\mathrm{cond},i} \\ \dot{q}^{i-1\to i,\mathrm{solid}}_{\mathrm{cond},i} &= \dot{q}^{i-1\to i}_{\mathrm{cond},i}/\dot{q}^{\mathrm{gas}}_{\mathrm{cond},i} \\ \dot{q}^{i\to i+1,\mathrm{solid}}_{\mathrm{cond},i} &= \dot{q}^{i\to i+1}_{\mathrm{cond},i}/\dot{q}^{\mathrm{gas}}_{\mathrm{cond},i}.\end{aligned} \tag{3.5}$$

Therefore, $\dot{q}^{\mathrm{gas}\to i,\mathrm{solid}}_{\mathrm{cond},i}$, $\dot{q}^{i-1\to i,\mathrm{solid}}_{\mathrm{cond},i}$ and $\dot{q}^{i\to i+1,\mathrm{solid}}_{\mathrm{cond},i}$ only depend on the gaseous phase through $v_d$. As a first approximation for the computation of the filtered quantities that will be presented in Sec. 3.1.2, $\dot{q}^{\mathrm{gas}\to i,\mathrm{solid}}_{\mathrm{cond},i}$, $\dot{q}^{i-1\to i,\mathrm{solid}}_{\mathrm{cond},i}$ and $\dot{q}^{i\to i+1,\mathrm{solid}}_{\mathrm{cond},i}$ will be computed considering $v_d$ equal to $\widehat{v_d}$, defined by simplification of Eq. (2.18) as equal to:

$$\widehat{v_d} = 2\cdot\frac{\sum_{i=1}^{N_{\mathrm{PAH}}}\widetilde{\dot{Q}^{\mathrm{d}}_{\mathrm{PAH}_i}}}{\sum_{i=1}^{N_{\mathrm{PAH}}}\widetilde{\dot{Q}^{\mathrm{d}}_{\mathrm{PAH}_i}}/(2v_{\mathrm{PAH}_i})}. \tag{3.6}$$

### Surface growth and oxidation

In Eqs. (2.27) and (2.28), $k_{\text{sg}} = K_{\text{sg}}/\rho$, $k_{ox} = K_{\text{ox}}/\rho$ depend only on the gaseous phase. Then, as for nucleation and condensation, the source terms for surface growth and oxidation can be written as:

$$\begin{aligned} \dot{q}_{\text{sg},i} &= \dot{q}^{\text{gas}}_{\text{sg},i}\dot{q}^{\text{solid}}_{\text{sg},i} \\ \dot{q}_{\text{ox},i} &= \dot{q}^{\text{gas}}_{\text{ox},i}\dot{q}^{\text{solid}}_{\text{ox},i} \end{aligned} \tag{3.7}$$

with $\dot{q}^{\text{gas}}_{\text{sg},i} = k_{\text{sg}}$, $\dot{q}^{\text{gas}}_{\text{ox},i} = k_{\text{ox}}$. From Eq. (2.26), $\dot{q}^{\text{solid}}_{\text{sg},i}$ and $\dot{q}^{\text{solid}}_{\text{ox},i}$ are expressed as:

$$\begin{aligned} \dot{q}^{\text{solid}}_{\text{sg},i} &= \dot{q}^{\text{gas}\to i,\text{solid}}_{\text{sg},i} + \dot{q}^{i-1\to i,\text{solid}}_{\text{sg},i} - \dot{q}^{i\to i+1,\text{solid}}_{\text{sg},i} \\ \dot{q}^{\text{solid}}_{\text{ox},i} &= -\dot{q}^{i\to\text{gas},\text{solid}}_{\text{ox},i} + \dot{q}^{i+1\to i,\text{solid}}_{\text{ox},i} - \dot{q}^{i\to i-1,\text{solid}}_{\text{ox},i} \end{aligned} \tag{3.8}$$

with:

$$\begin{aligned} \dot{q}^{\text{gas}\to i,\text{solid}}_{\text{sg},i} &= \dot{q}^{\text{gas}\to i}_{\text{sg},i}/\dot{q}^{\text{gas}}_{\text{sg},i}, \quad \dot{q}^{i\to\text{gas},\text{solid}}_{\text{ox},i} = \dot{q}^{i\to\text{gas}}_{\text{ox},i}/\dot{q}^{\text{gas}}_{\text{ox},i}, \\ \dot{q}^{i-1\to i,\text{solid}}_{\text{sg},i} &= \dot{q}^{i-1\to i}_{\text{sg},i}/\dot{q}^{\text{gas}}_{\text{sg},i}, \quad \dot{q}^{i+1\to i,\text{solid}}_{\text{ox},i} = \dot{q}^{i+1\to i}_{\text{ox},i}/\dot{q}^{\text{gas}}_{\text{ox},i}, \\ \dot{q}^{i\to i+1,\text{solid}}_{\text{sg},i} &= \dot{q}^{i\to i+1}_{\text{sg},i}/\dot{q}^{\text{gas}}_{\text{sg},i}, \quad \dot{q}^{i\to i-1,\text{solid}}_{\text{ox},i} = \dot{q}^{i\to i-1}_{\text{ox},i}/\dot{q}^{\text{gas}}_{\text{ox},i}. \end{aligned} \tag{3.9}$$

### Coagulation

Equations (2.32) can be written as:

$$\begin{aligned} \beta^{\text{fm}}_{i,j} &= \beta^{\text{fm,gas}}_{i,j}\beta^{\text{fm,solid}}_{i,j} \\ \beta^{\text{c}}_{i,j} &= \beta^{\text{c1,gas}}_{i,j}\beta^{\text{c1,solid}}_{i,j} + \beta^{\text{c2,gas}}_{i,j}\beta^{\text{c2,solid}}_{i,j} \end{aligned} \tag{3.10}$$

where:

$$\begin{aligned} \beta^{\text{fm,gas}}_{i,j} &= \sqrt{T} \\ \beta^{\text{fm,solid}}_{i,j} &= \epsilon_{\text{coag}}\left(\frac{3}{4\pi}\right)^{1/6}\sqrt{\frac{6k_b}{\rho_s}} \\ &\quad \times \sqrt{\frac{1}{v_i^{\text{mean}}} + \frac{1}{v_j^{\text{mean}}}}(d_{c,i} + d_{c,j})^2 \\ \beta^{\text{c1,gas}}_{i,j} &= \frac{T}{\mu} \\ \beta^{\text{c1,solid}}_{i,j} &= \frac{2k_b}{3}(d_{c,i} + d_{c,j})\left(\frac{1}{d_{c,i}} + \frac{1}{d_{c,j}}\right) \\ \beta^{\text{c2,gas}}_{i,j} &= \frac{T\lambda_{\text{gas}}}{\mu} \\ \beta^{\text{c2,solid}}_{i,j} &= \frac{5.028\cdot k_b}{3}(d_{c,i} + d_{c,j})\left(\frac{1}{d^2_{c,i}} + \frac{1}{d^2_{c,j}}\right) \end{aligned} \tag{3.11}$$

with $\beta_{v,w}^{\mathrm{fm,gas}}$, $\beta_{v,w}^{\mathrm{c1,gas}}$ and $\beta_{v,w}^{\mathrm{c2,gas}}$ depending only on the gaseous phase quantities ($\mu$, $P$ and $T$).
The source term $\dot{q}_{\mathrm{coag},i}$ is expressed as:

$$\dot{q}_{\mathrm{coag},i} = \dot{q}_{\mathrm{coag},i}^{\mathrm{fm}} + \dot{q}_{\mathrm{coag},i}^{\mathrm{c}} = \dot{q}_{\mathrm{coag},i}^{\mathrm{fm}} + \dot{q}_{\mathrm{coag},i}^{\mathrm{c1}} + \dot{q}_{\mathrm{coag},i}^{\mathrm{c2}} \tag{3.12}$$

with $\dot{q}_{\mathrm{coag},i}^{\mathrm{fm}}$ the part of the coagulation source term which relies on a free molecular regime and $\dot{q}_{\mathrm{coag},i}^{\mathrm{c}}$ the part of the coagulation source term which relies on a continuum regime:

$$\begin{aligned}
\dot{q}_{\mathrm{coag},i}^{\mathrm{fm}} &= \dot{q}_{\mathrm{coag},i}^{\mathrm{fm,gas}}\, \dot{q}_{\mathrm{coag},i}^{\mathrm{fm,solid}} \\
\dot{q}_{\mathrm{coag},i}^{\mathrm{c1}} &= \dot{q}_{\mathrm{coag},i}^{\mathrm{c1,gas}}\, \dot{q}_{\mathrm{coag},i}^{\mathrm{c1,solid}} \\
\dot{q}_{\mathrm{coag},i}^{\mathrm{c2}} &= \dot{q}_{\mathrm{coag},i}^{\mathrm{c2,gas}}\, \dot{q}_{\mathrm{coag},i}^{\mathrm{c2,solid}}
\end{aligned} \tag{3.13}$$

with:

$$\begin{aligned}
\dot{q}_{\mathrm{coag},i}^{\mathrm{fm,gas}} &= \frac{\sqrt{T}}{\rho}, \quad & \dot{q}_{\mathrm{coag},i}^{\mathrm{fm,solid}} &= \dot{q}_{\mathrm{coag},i}^{\mathrm{fm}} / \dot{q}_{\mathrm{coag},i}^{\mathrm{fm,gas}} \\
\dot{q}_{\mathrm{coag},i}^{\mathrm{c1,gas}} &= \frac{T}{\mu\rho}, \quad & \dot{q}_{\mathrm{coag},i}^{\mathrm{c1,solid}} &= \dot{q}_{\mathrm{coag},i}^{\mathrm{c1}} / \dot{q}_{\mathrm{coag},i}^{\mathrm{c1,gas}} \\
\dot{q}_{\mathrm{coag},i}^{\mathrm{c2,gas}} &= \frac{T\lambda_{\mathrm{gas}}}{\mu\rho}, \quad & \dot{q}_{\mathrm{coag},i}^{\mathrm{c2,solid}} &= \dot{q}_{\mathrm{coag},i}^{\mathrm{c2}} / \dot{q}_{\mathrm{coag},i}^{\mathrm{c2,gas}}
\end{aligned} \tag{3.14}$$

### 3.1.2 Filtered transport equations

In the LES formalism, the filtered equation for $i^{\mathrm{th}}$ section soot mass fraction is obtained by applying a spatial filter to the Eq.(2.11):

$$\begin{aligned}
&\frac{\partial \overline{\rho}\widetilde{Y_{s,i}}}{\partial t} + \nabla\cdot(\overline{\rho}\widetilde{u_i}\widetilde{Y_{s,i}}) + \nabla\cdot\left(\overline{-\rho C_{\mathrm{th}}\frac{\nu}{T}\boldsymbol{\nabla} T Y_{s,i}}\right) \\
&= -\nabla\cdot\left(\overline{\rho\mathbf{u}\widetilde{Y_{s,i}}} - \overline{\rho}\widetilde{\mathbf{u}}\widetilde{Y_{s,i}}\right) + \rho_s\overline{\dot{Q}_{s,i}}
\end{aligned} \tag{3.15}$$

where $\bar{\cdot}$ and $\widetilde{\cdot}$ denote the filtering and the density-weighted filtering operations, respectively.
Several terms in Eq. (3.15) are unclosed:

- $\mathbf{I}: J_{s,i}^t = \overline{\rho\mathbf{u}\widetilde{Y_{s,i}}} - \overline{\rho}\widetilde{\mathbf{u}}\widetilde{Y_{s,i}}$ which represents the subgrid-scale $i^{\mathrm{th}}$ section soot flux. This flux is modeled using a gradient assumption:

$$J_{s,i}^t = -\overline{\rho} D_{s,i}^t \nabla\widetilde{Y_{s,i}} \tag{3.16}$$

where $D_{s,i}^t = \nu^{\mathrm{sgs}}/\mathrm{Sc}_{s,i}^{\mathrm{sgs}}$ is the $i^{\mathrm{th}}$ section soot turbulent diffusivity, $\nu^{\mathrm{sgs}}$ is the turbulent viscosity obtained from the Wale model (Nicoud and Ducros 1999), and $\mathrm{Sc}_{s,i}^{\mathrm{sgs}}$ is the subgrid Schmidt number taken equal to 0.6.

- **II** : $\overline{J_{s,i}}^{\text{th}} = \overline{-\rho C_{\text{th}} \frac{\nu}{T} \boldsymbol{\nabla} T Y_{s,i}}$ which represents the filtered thermophoresis flux closed as:

$$\overline{J_{s,i}}^{\text{th}} \approx -\overline{\rho} C_{\text{th}} \overline{\nu} \frac{\boldsymbol{\nabla} \widetilde{T}}{\widetilde{T}} \widetilde{Y_{s,i}} \tag{3.17}$$

- **III** : $\overline{\dot{Q}_{s,i}} = \overline{\rho} \widetilde{\dot{q}_{s,i}}$ which will be closed through the subgrid model presented after in Sec. 3.1.2. Following Eq. (2.12), it writes:

$$\widetilde{\dot{q}_{s,i}} = \widetilde{\dot{q}_{\text{nu},i}} + \widetilde{\dot{q}_{\text{cond},i}} + \widetilde{\dot{q}_{\text{sg},i}} + \widetilde{\dot{q}_{\text{ox},i}} + \widetilde{\dot{q}_{\text{coag},i}} \tag{3.18}$$

The filtered equation for $i^{\text{th}}$ section soot mass fraction finally reads as:

$$\begin{aligned} &\frac{\partial \overline{\rho} \widetilde{Y_{s,i}}}{\partial t} + \nabla \cdot \left( \overline{\rho} \widetilde{\mathbf{u}} \widetilde{Y_{s,i}} \right) + \nabla \cdot \left( -\overline{\rho} C_{\text{th}} \overline{\nu} \frac{\boldsymbol{\nabla} \widetilde{T}}{\widetilde{T}} \widetilde{Y_{s,i}} \right) \\ &= \nabla \cdot \left( \overline{\rho} \frac{\nu^{\text{sgs}}}{\text{Sc}_t} \boldsymbol{\nabla} \widetilde{Y}_{s,i} \right) + \rho_s \overline{\rho} \widetilde{\dot{q}_{s,i}} \end{aligned} \tag{3.19}$$

## 3.2 Subgrid model for soot source terms

In order to close the filtered soot source terms, the subgrid model developed for the hybrid method of moments (HMOM) in (Mueller and Pitsch 2011) is here derived for the sectional method.
In this model, a filtered quantity $\widetilde{\psi}(\xi_j, \sigma_i)$, where $\xi_j$ and $\sigma_i$ are gaseous and soot scalars ($Y_{s,i}$ for instance) respectively, is written with a joint subfilter PDF $\widetilde{P}(\xi_j, \sigma_i)$:

$$\begin{aligned} \widetilde{\psi}(\xi_j, \sigma_i) &= \int \int \psi(\xi_j, \sigma_i) \widetilde{P}(\xi_j, \sigma_i) d\xi_j d\sigma_i \\ &= \int \int \psi(\xi_j, \sigma_i) \widetilde{P}(\xi_j) P(\sigma_i | \xi_j) d\xi_j d\sigma_i \end{aligned} \tag{3.20}$$

As presented in Eq. (2.13), the soot source terms $\dot{q}_{\text{p},k}$ of a section $k$ can be written as a product of a first function depending only on the gaseous phase and a second function depending on the solid phase, such that the filtered soot source term is given by:

$$\widetilde{\dot{q}_{\text{p},k}}(\xi_j, \sigma_i) = \int \int \dot{q}_{\text{p},k}^{\text{gas}}(\xi_j) \dot{q}_{\text{p},k}^{\text{soot}}(\sigma_i) \widetilde{P}(\xi_j) P(\sigma_i | \xi_j) d\xi_j d\sigma_i \tag{3.21}$$

where the subscript $_{\text{p}}$ represents any subscript $_{\text{nu}}$, $_{\text{cond}}$, $_{\text{sg}}$, $_{\text{ox}}$, $^{\text{fm}}_{\text{coag}}$, $^{\text{c1}}_{\text{coag}}$ or $^{\text{c2}}_{\text{coag}}$.
Following Mueller and Pitsch (2012), under the independency assumption between gaseous and soot quantities, this conditional soot distribution can be

modeled by the corresponding marginal distribution:

$$\widetilde{\dot{q}_{\mathrm{p},k}} = \underbrace{\int \dot{q}^{\mathrm{gas}}_{\mathrm{p},k}(\xi_j)\widetilde{P}(\xi_j)d\xi_j}_{\widetilde{\dot{q}_{\mathrm{p},k}|_{\mathrm{gas}}}} \underbrace{\int \dot{q}^{\mathrm{soot}}_{\mathrm{p},k}(\sigma_i)P(\sigma_i)d\sigma_i}_{\widetilde{\dot{q}_{\mathrm{p},k}|_{\mathrm{soot}}}} \tag{3.22}$$

This assumption is valid if the time scales for the evolution of the thermo-chemical state are largely smaller than those of soot production source terms (Mueller and Pitsch 2012).
Then, the filtered soot source term reads:

$$\widetilde{\dot{q}_{\mathrm{p},k}} = \widetilde{\dot{q}_{\mathrm{p},k}|_{\mathrm{gas}}}\widetilde{\dot{q}_{\mathrm{p},k}|_{\mathrm{soot}}} \tag{3.23}$$

where the thermo-chemical and soot parts need to be completely independent. The formulation of soot source terms into gas and solid contributions is provided in Sec. 3.1.1.
The gaseous phase contribution $\widetilde{\dot{q}_{\mathrm{p},k}|_{\mathrm{gas}}}$ can be modeled with any approach classically developed for purely gaseous flames (Veynante and Vervisch 2002), which will be presented in Sec. 3.3.
The solid phase contribution is modeled through a double-delta distribution function including a "non-sooting" mode and a "sooting" mode (Mueller and Pitsch 2011):

$$P(\sigma_i) = \omega\delta(\sigma_i) + (1-\omega)\delta(\sigma_i - \sigma_i^*) \tag{3.24}$$

where $\omega$ is the subgrid soot intermittency and $\sigma_i^*$ the value of $\sigma_i$ for the sooting mode of the considered quantity. The filtered value of $\sigma_i$ is given by:

$$\begin{aligned} \widetilde{\sigma_i} &= \int \sigma_i P(\sigma_i)d\sigma_i = \sigma_i^*(1-\omega) \\ \Leftrightarrow\ \sigma_i^* &= \widetilde{\sigma_i}/(1-\omega) \end{aligned} \tag{3.25}$$

Then, the solid phase contribution can be expressed as:

$$\begin{aligned} \widetilde{\dot{q}_{\mathrm{p},k}|_{\mathrm{soot}}}(\sigma_i) &= (1-\omega)\dot{q}^{\mathrm{soot}}_{\mathrm{p},k}(\sigma_i^*) \\ &= (1-\omega)\dot{q}^{\mathrm{soot}}_{\mathrm{p},k}\left(\frac{\widetilde{\sigma_i}}{1-\omega}\right) \end{aligned} \tag{3.26}$$

Equation (3.25) yields the following expression for the subgrid soot intermittency $\omega$:

$$\omega = 1 - \frac{\overline{\sigma_i}^2}{\overline{\sigma_i^2}} \tag{3.27}$$

As in (Mueller and Pitsch 2011), the particles number density $N_{\mathrm{part}}$ is here chosen for the evaluation of $\omega$:

$$\omega = 1 - \frac{\overline{N_{\mathrm{part}}}^2}{\overline{N_{\mathrm{part}}^2}} \tag{3.28}$$

Then, in order to evaluate $\omega$, the filtered equations for $N_{\text{part}}$ and $N_{\text{part}}^2$ are added to the solid phase system of equations. The filtered equation for $\overline{N_{part}^2}$ is given as in (Mueller and Pitsch 2011):

$$\begin{aligned}
&\frac{\partial}{\partial t}\left(\overline{N_{\text{part}}^2}\right) + \nabla\cdot\left(\widetilde{\mathbf{u}}\overline{N_{\text{part}}^2}\right) \\
&= 2\overline{\rho}\widetilde{m_N\dot{N}_{\text{part}}} - \overline{N_{\text{part}}^2\nabla\cdot\mathbf{u}} - \overline{N_{\text{part}}^2\nabla\cdot\mathbf{v_T}} \\
&+ \nabla\cdot\left(-\overline{\mathbf{v_T}N_{\text{part}}^2}\right) - \nabla\cdot\left(\overline{\rho}\mathbf{u}\widetilde{\frac{N_{\text{part}}^2}{\rho}} - \overline{\rho}\widetilde{\mathbf{u}}\widetilde{\frac{N_{\text{part}}^2}{\rho}}\right)
\end{aligned} \tag{3.29}$$

with $m_N = N_{\text{part}}/\rho$ and $\dot{N}_{\text{part}}$ the particles number density source term. This equation is closed here in analogy with Eq. (3.19) as follows:

- **I** : $J^t_{s,N^2_{\text{part}}} = \overline{\rho}\widetilde{\left(\mathbf{u}\frac{N^2_{\text{part}}}{\rho}\right)} - \overline{\rho}\widetilde{\mathbf{u}}\widetilde{\left(\frac{N^2_{\text{part}}}{\rho}\right)}$, with:

$$\begin{aligned}
\overline{J_{s,N^2_{\text{part}}}}^t &= -\overline{\rho}D^t_{s,N^2_{\text{part}}}\boldsymbol{\nabla}\widetilde{\left(\frac{N^2_{\text{part}}}{\rho}\right)} \\
&= -\overline{\rho}D^t_{s,N^2_{\text{part}}}\boldsymbol{\nabla}\left(\frac{\overline{N^2_{\text{part}}}}{\overline{\rho}}\right)
\end{aligned} \tag{3.30}$$

  with $D^t_{s,N^2_{\text{part}}} = \nu^{\text{sgs}}/\text{Sc}^{\text{sgs}}_{N^2_{\text{part}}}$ and $\text{Sc}^{\text{sgs}}_{N^2_{\text{part}}} = 0.6$.
- **II** : $\overline{J_{s,N^2_{\text{part}}}}^{\text{th}} = \overline{\mathbf{v_T}N^2_{\text{part}}}$ with:

$$\overline{J_{s,N^2_{\text{part}}}}^{\text{th}} \approx -\overline{\rho}C_{\text{th}}\overline{\nu}\frac{\boldsymbol{\nabla}\widetilde{T}}{\widetilde{T}}\widetilde{\left(\frac{N^2_{\text{part}}}{\rho}\right)} = -\overline{\rho}C_{\text{th}}\overline{\nu}\frac{\boldsymbol{\nabla}\widetilde{T}}{\widetilde{T}}\frac{\overline{N^2_{\text{part}}}}{\overline{\rho}} \tag{3.31}$$

- **III** : $\overline{N^2_{\text{part}}\nabla\cdot\mathbf{u}}$ closed as in (Mueller and Pitsch 2011):

$$\overline{N^2_{\text{part}}\nabla\cdot\mathbf{u}} = \overline{N^2_{\text{part}}}\nabla\cdot\widetilde{\mathbf{u}} \tag{3.32}$$

- **IV** : $\overline{N^2_{\text{part}}\nabla\cdot\mathbf{v_T}} \approx \overline{N^2_{\text{part}}}\nabla\cdot\widetilde{\mathbf{v_T}}$ in the same as for the term **III**. $\nabla\cdot\widetilde{\mathbf{v_T}}$ is modeled by:

$$\nabla\cdot\widetilde{\mathbf{v_T}} \approx \nabla\cdot\left(-C_{\text{th}}\overline{\nu}\frac{\boldsymbol{\nabla}\widetilde{T}}{\widetilde{T}}\right) \tag{3.33}$$

- **V** : $\widetilde{m_N\dot{N}_{\text{part}}}$ which is closed with Eq. (3.20).

The final equation is given by:

$$\begin{aligned}
&\frac{\partial \overline{N_{\text{part}}^2}}{\partial t} + \nabla \cdot \left( \widetilde{\mathbf{u}} \overline{N_{\text{part}}^2} \right) = 2\overline{\rho} \widetilde{\dot{N}_{\text{part}} m_N} - \overline{N_{\text{part}}^2} \nabla \cdot \widetilde{\mathbf{u}} \\
&- \overline{N_{\text{part}}^2} \nabla \cdot \left( -C_{\text{th}} \overline{\nu} \frac{\boldsymbol{\nabla} \widetilde{T}}{\widetilde{T}} \right) + \nabla \cdot \left( C_{\text{th}} \overline{\nu} \frac{\boldsymbol{\nabla} \widetilde{T}}{\widetilde{T}} \overline{N_{\text{part}}^2} \right) \\
&+ \nabla \cdot \left( \overline{\rho} \frac{\nu^{\text{sgs}}}{\text{Sc}_t} \boldsymbol{\nabla} \left( \widetilde{\frac{N_{\text{part}}^2}{\rho}} \right) \right)
\end{aligned} \tag{3.34}$$

The filtered equation for $N_{\text{part}}$ can be derived similarly:

$$\begin{aligned}
&\frac{\partial \overline{N_{\text{part}}}}{\partial t} + \nabla \cdot \left( \widetilde{\mathbf{u}} \overline{N_{\text{part}}} \right) = \overline{\dot{N}_{\text{part}}} + \nabla \cdot \left( C_{\text{th}} \overline{\nu} \frac{\boldsymbol{\nabla} \widetilde{T}}{\widetilde{T}} \overline{N_{\text{part}}} \right) \\
&+ \nabla \cdot \left( \overline{\rho} \frac{\nu^{\text{sgs}}}{\text{Sc}_t} \boldsymbol{\nabla} \left( \widetilde{\frac{N_{\text{part}}}{\rho}} \right) \right)
\end{aligned} \tag{3.35}$$

The source term $\overline{\dot{N}_{\text{part}}}$ is decomposed into five source terms, one for each phenomenon involved in soot production:

$$\overline{\dot{N}_{\text{part}}} = \overline{\dot{N}_{\text{nu}}} + \overline{\dot{N}_{\text{cond}}} + \overline{\dot{N}_{\text{sg}}} + \overline{\dot{N}_{\text{ox}}} + \overline{\dot{N}_{\text{coag}}} \tag{3.36}$$

where for each phenomenon p (nucleation, condensation, surface growth, oxidation or coagulation), as the soot volume fraction density $q(v)$ is assumed constant inside each section, the corresponding source term is evaluated as:

$$\begin{aligned}
\overline{\dot{N}_{\text{p}}} &= \sum_{i=1}^{N_{\text{sect}}} \int_{v_i^{\text{min}}}^{v_i^{\text{max}}} \frac{\overline{\dot{Q}_{\text{p},i}}}{v_i^{\text{max}} - v_i^{\text{min}}} \frac{1}{v} dv \\
&= \sum_{i=1}^{N_{\text{sect}}} \frac{\overline{\dot{Q}_{\text{p},i}}}{v_i^{\text{max}} - v_i^{\text{min}}} \ln \left( \frac{v_i^{\text{max}}}{v_i^{\text{min}}} \right)
\end{aligned} \tag{3.37}$$

## 3.3 Subgrid models for gaseous quantities

In this section, the subgrid models for the filtered gaseous quantities are detailed. They concern both the purely gaseous quantities as well as the gaseous contribution to the filtered soot source terms highlighted in Eq. (3.22).

Concerning the different subgrid fluxes, they are modeled with classical gradient assumptions, based on the Wale model (Nicoud and Ducros 1999) for the turbulent viscosity, and fixed values of 0.6 for both the subgrid-scale Schmidt $\text{Sc}^{\text{sgs}}$ and Prandtl $\text{Pr}^{\text{sgs}}$ numbers.

Every gaseous thermochemical state is here described with the Flamelet/ Progress Variable (FPV) model (Pierce and Moin 2004), whose details are summarized for completeness. When neglecting heat losses, any gaseous thermochemical variable $\xi_j$ is obtained from solutions of steady non-premixed flamelet equations solved numerically for different strain rates allowing to describe the S-shape curve with both stable and unstable branches. Following the FPV approach, the different variables are then parametrized as a function of the mixture fraction $Z$ and a normalized progress variable $C$:

$$\xi_j^{\text{tab}} = \mathcal{F}(Z, C), \tag{3.38}$$

where $\mathcal{F}$ represents the relationship obtained from the solution of the steady flamelet equations.

Radiative heat losses are accounted for by following the procedure of Ihme and Pitsch (2008a), who have extended the classical FPV model to account for heat losses due to radiation (radiation FPV model). The flamelet database is then augmented with solutions of unsteady flamelets computed by imposing the radiative source term to steady initial flamelets. To parametrize these unsteady flamelets, a heat loss parameter $H$ is added to the parametrization:

$$\xi_j^{\text{tab}} = \mathcal{G}(Z, C, H) \tag{3.39}$$

where $\mathcal{G}$ represents the relationship obtained now with this new database.
The previous relationship is recast in terms of two quantities that uniquely identify each flamelet solution of the database: $\Lambda = C(Z_{\text{st}})$ and $\Phi = H(Z_{\text{st}})$, where $Z_{st}$ corresponds to the stoichiometric mixture fraction. Each gaseous thermochemical quantity can then be retrieved as:

$$\xi_j^{\text{tab}} = \mathcal{G}(Z, C, H) = \mathcal{G}^{\star}(Z, \Lambda, \Phi). \tag{3.40}$$

Each gaseous filtered scalar quantity $\widetilde{\xi}_j^{\text{tab}}$ is then expressed by:

$$\widetilde{\xi}_j^{\text{tab}} = \int \xi_j^{\text{tab}}(Z, \Lambda, \Phi)\widetilde{P}(Z, \Lambda, \Phi) dZ d\Lambda d\Phi \tag{3.41}$$

with $\widetilde{P}$, the density-weighted joint PDF. Equation (3.41) is then used to determine the gaseous part $\widetilde{\dot{q}_{s,k}|_{\text{gas}}}$ of Eq. (3.22).
As done by Ihme and Pitsch (2008a), we assume that the progress parameter $\Lambda$, the heat loss parameter $\Phi$ and the mixture fraction $Z$ are statistically independent. The joint PDF can then be expressed in terms of the marginal distributions of each parameter:

$$\widetilde{P}(Z, \Lambda, \Phi) = \widetilde{P}_Z(Z) P_{\Lambda}(\Lambda) P_{\Phi}(\Phi). \tag{3.42}$$

A $\beta$-PDF is used to model the mixture fraction distribution, implemented following the second-order numerical approach of Lien et al. (2009). The statistical distributions of the reaction progress and heat loss parameters are represented by a Dirac function. Then, the joint subfilter gaseous PDF can be expressed by:

$$\widetilde{P}(Z,\Lambda,\Phi) = \beta\left(Z;\widetilde{Z},S_Z\right)\delta\left(\Lambda-\widetilde{\Lambda}\right)\delta\left(\Phi-\widetilde{\Phi}\right), \tag{3.43}$$

where $S_Z$ is the mixture fraction segregation factor.
Except for the PAH concentration that requires a special treatment presented in Sec. 3.4, each gaseous thermochemical variable can then be retrieved in a precomputed 4-D table, and can be expressed as:

$$\widetilde{\xi}_j^{\,\mathrm{tab}} = \widetilde{\xi}_j^{\,\mathrm{tab}}(\widetilde{Z},S_Z,\widetilde{\Lambda},\widetilde{\Phi}) \equiv \widetilde{\xi}_j^{\,\mathrm{tab}}(\widetilde{Z},S_Z,\overline{C},\overline{H}). \tag{3.44}$$

To retrieve the variables of the table, $\widetilde{Z}$ is directly transported together with the other radiation FPV-state-variables: the variance of the mixture fraction $\widetilde{Z''^2}$, the enthalpy $\widetilde{h}$[1] and the progress variable $\widetilde{Y_C}$. Then, $S_Z$, $\overline{C}$ and $\overline{H}$ are evaluated as:

$$S_Z = \frac{\widetilde{Z''^2}}{\widetilde{Z}(1-\widetilde{Z})} \tag{3.45}$$

$$\overline{H} = \frac{\widetilde{h} - \widetilde{h^{\mathrm{rad}}}(Z,S_Z)}{\widetilde{h^{\mathrm{adiab}}}(Z,S_Z) - \widetilde{h^{\mathrm{rad}}}(Z,S_Z)} \tag{3.46}$$

$$\overline{C} = \frac{\widetilde{Y_C} - \widetilde{Y_C^{\mathrm{f}}}(Z,S_Z)}{\widetilde{Y_C^{\mathrm{eq}}}(Z,S_Z) - \widetilde{Y_C^{\mathrm{f}}}(Z,S_Z)} \tag{3.47}$$

where $h^{\mathrm{adiab}}$ is the enthalpy of the adiabatic flamelet, $h^{\mathrm{rad}}$ is the enthalpy of the flamelet presenting the maximum of radiation heat losses (which corresponds to the flame at the lowest strain rate in the stable branch of the S curve). $Y_C$ is the non-normalized progress variable defined as a weighted sum of species mass fractions with $Y_C^{\mathrm{eq}}$ its value for the lowest strain rate flamelet on the stable branch of the S curve and $Y_C^{\mathrm{f}}$ its frozen value when chemical reactions are neglected. The implementation methodology and validation of the radiation FPV model in the AVBP code is presented in Appendix C.

## 3.4 PAH model

Because of their long chemical time scales, PAHs may not lie on the flamelet manifold and can not be treated as the other gaseous characteristics. The same

[1] $\widetilde{h}$ corresponds to the enthalpy without considering compressible effects. Then, in AVBP, $\widetilde{h}$ corresponds to a transported "low-mach" enthalpy enabling to determine the corresponding non-dimensional $\overline{H}$ parameter in the table.

approach as Mueller and Pitsch (2012) is here used for modeling the unsteady effects of strain rate and transport on PAH production. The spatially-filtered transport equation for the lumped PAH mass fraction $\widetilde{Y_{\mathrm{PAH}}}$ is given by:

$$\begin{aligned}\frac{\partial\overline{\rho}\widetilde{Y}_{\mathrm{PAH}}}{\partial t}+\nabla\cdot\left(\overline{\rho}\widetilde{\mathbf{u}}\widetilde{Y}_{\mathrm{PAH}}\right)&=-\nabla\cdot\left(\overline{\rho\mathbf{u}\widetilde{Y_{\mathrm{PAH}}}}-\overline{\rho}\widetilde{\mathbf{u}}\widetilde{Y}_{\mathrm{PAH}}\right)\\&+\overline{\nabla\cdot\left(\rho D_{\mathrm{PAH}}\boldsymbol{\nabla}Y_{PAH}\right)}+\overline{\rho}\widetilde{\dot{Q}_{\mathrm{PAH}}}\end{aligned}\tag{3.48}$$

Several terms are unclosed in Eq. (3.48) and require some modeling efforts:

- **I** : $J^t_{\mathrm{PAH}}=\overline{\rho\mathbf{u}\widetilde{Y_{\mathrm{PAH}}}}-\overline{\rho}\widetilde{\mathbf{u}}\widetilde{Y_{\mathrm{PAH}}}$ closed as:

$$J^t_{\mathrm{PAH}}=-\overline{\rho}D^t_{\mathrm{PAH}}\nabla\widetilde{Y_{\mathrm{PAH}}}\tag{3.49}$$

  with $D^t_{\mathrm{PAH}}=\nu^{\mathrm{sgs}}/\mathrm{Sc}^{\mathrm{sgs}}_{\mathrm{PAH}}$ with $\mathrm{Sc}^{\mathrm{sgs}}_{\mathrm{PAH}}=0.6$,
- **II**:
  For the lumped species, the source term $\widetilde{\dot{Q}_{\mathrm{PAH}}}$ can be split into three different terms (Mueller and Pitsch 2012): the chemical production term ($\dot{Q}_{\mathrm{PAH},+}$), the chemical consumption term ($\dot{Q}_{\mathrm{PAH},-}$), which is linear with the species concentration, and the dimerization source term ($\dot{Q}_{\mathrm{DIM}}$), which is quadratic with the species concentration. The corresponding decomposition can be written as:

$$\begin{aligned}\widetilde{\dot{Q}_{\mathrm{PAH}}}=\widetilde{\dot{Q}_{\mathrm{PAH},+}}&+\widetilde{\left(\frac{\dot{Q}_{\mathrm{PAH},-}}{Y_{\mathrm{PAH}}}\right)Y_{\mathrm{PAH}}}\\&+\widetilde{\left(\frac{\dot{Q}_{\mathrm{DIM}}}{Y^2_{\mathrm{PAH}}}\right)Y^2_{\mathrm{PAH}}}\end{aligned}\tag{3.50}$$

  To close the second and third terms of this equation, the following relation between the transport equation model and the radiation FPV model is used (Mueller and Pitsch 2012):

$$\begin{aligned}\overline{\dot{Q}_{\mathrm{PAH}}}=\widetilde{\dot{Q}_{\mathrm{PAH},+}}^{\mathrm{tab}}&+\widetilde{\dot{Q}_{\mathrm{PAH},-}}^{\mathrm{tab}}\left(\frac{\widetilde{Y_{\mathrm{PAH}}}}{\widetilde{Y_{\mathrm{PAH}}}^{\mathrm{tab}}}\right)\\&+\widetilde{\dot{Q}_{\mathrm{DIM}}}^{\mathrm{tab}}\left(\frac{\widetilde{Y_{\mathrm{PAH}}}}{\widetilde{Y_{\mathrm{PAH}}}^{\mathrm{tab}}}\right)^2.\end{aligned}\tag{3.51}$$

  The lumped source terms from the table $\widetilde{\dot{Q}_{\mathrm{PAH},+}}^{\mathrm{tab}}$, $\widetilde{\dot{Q}_{\mathrm{PAH},-}}^{\mathrm{tab}}$, $\widetilde{\dot{Q}_{\mathrm{DIM}}}^{\mathrm{tab}}$ and the value of $\widetilde{Y_{\mathrm{PAH}}}^{\mathrm{tab}}$, are computed by summing their respective

values obtained for the $N_{\mathrm{PAH}}$ selected PAHs:

$$\begin{aligned}
\widetilde{\dot{Q}}^{\mathrm{tab}}_{\mathrm{PAH},+} &= \sum_{i=1}^{N_{\mathrm{PAH}}} \widetilde{\dot{Q}}^{\mathrm{tab}}_{\mathrm{PAH}_i,+} \\
\widetilde{\dot{Q}}^{\mathrm{tab}}_{\mathrm{PAH},-} &= \sum_{i=1}^{N_{\mathrm{PAH}}} \widetilde{\dot{Q}}^{\mathrm{tab}}_{\mathrm{PAH}_i,-} \\
\widetilde{\dot{Q}}^{\mathrm{tab}}_{\mathrm{DIM}} &= \sum_{i=1}^{N_{\mathrm{PAH}}} \widetilde{\dot{Q}}^{\mathrm{tab}}_{\mathrm{PAH}_i} \\
\widetilde{Y}^{\mathrm{tab}}_{\mathrm{PAH}} &= \sum_{i=1}^{N_{\mathrm{PAH}}} \widetilde{Y}^{\mathrm{tab}}_{\mathrm{PAH}_i}
\end{aligned} \tag{3.52}$$

- **III** : $\overline{\nabla \cdot (\rho D_{\mathrm{PAH}} \boldsymbol{\nabla} Y_{PAH})}$:
  In the limit of very large Reynolds number, the appropriate diffusion model used in the flamelet computation is a unity Lewis number model because of high turbulent diffusivities compared with the molecular ones (Peters 2000). Unity Lewis number has then been assumed for all the PAHs accordingly for the construction of the table given the target simulation which is a turbulent jet flame.
  Nonetheless, the study by Pitsch (Pitsch 2000) on differential diffusion in turbulent diffusion flames highlighted that such effects are not always negligible and are even significant in the close vicinity of the jet nozzle where the flow is weakly turbulent such as in the studied configuration. In such regions, one should then take into account the high Lewis numbers for PAHs. The production of PAHs and soot particles has indeed been shown to be sensitive to the PAHs and soot diffusion model (non-unity or unity Lewis number) in direct numerical simulations of a temporal mixing layer (Attili et al. 2016) and in RANS studies of turbulent jet diffusion flames (Kronenburg et al. 2000; Yunardi et al. 2008; Lalit et al. 2017). Non-negligible effects of PAHs high Lewis numbers in weakly turbulent zones can therefore also be expected in the large-eddy simulation of the considered jet flame close to the jet exit.
  Consequently, the choice of the diffusion model for PAHs can be strongly important and is not straightforward: unity Lewis model assumption everywhere or non-unity Lewis model assumption can lead to large errors in LES of sooting flames. Such an issue is a challenging task in the modeling community that remains to be tackled. An alternative compromise is considered here to partially account for differential diffusion effects by retaining the real molecular diffusivities $D_{\mathrm{PAH}_i}$ in the transport equations for PAHs:

$$\overline{\nabla \cdot (\rho D_{\mathrm{PAH}} \boldsymbol{\nabla} Y_{PAH})} = \nabla \cdot \left( \overline{\rho D_{\mathrm{PAH}}} \boldsymbol{\nabla} \widetilde{Y_{PAH}} \right) \tag{3.53}$$

The competition between molecular diffusion and turbulent transport is then captured at the resolved scales only. However, it should be noticed that an inconsistency appears since the flamelet table has been generated with unity Lewis numbers. This is tempered by the previously described relaxation model, which allows the PAHs deviation from the flamelet manifold.
Finally, since a lumped PAH is considered, the corresponding lumped diffusion coefficient $\overline{D_{\mathrm{PAH}}}$ is calculated as:

$$\overline{D_{\mathrm{PAH}}} = \frac{\overline{D_{\mathrm{PAH}_i}}\nabla Y_{\mathrm{PAH}_i}}{\nabla Y_{\mathrm{PAH}}}. \tag{3.54}$$

## 3.5 Radiative heat transfer modeling

Due to its high dependency on temperature, radiation plays an important role in jet flames (Ihme and Pitsch 2008a). Its role is even more significant in the case of sooting flames and the quality of the radiation model can have major effects on the prediction of soot and gaseous quantities (Tessé et al. 2004; Consalvi and Nmira 2016a). As a first approach, an optically-thin radiation model is used in the present parts. For the gaseous phase, Planck mean absorption coefficients are used (Barlow et al. 2001) and $CO_2$, $H_2O$ and CO are considered as the main contributing gaseous species to the radiative energy transfer. For the soot particles, they are considered as aggregates of non-overlapped spherical primary particles and the RDG/RDG-FA theory is applied to these primary particles without considering scattering (see Chapter 6, Section 6.2.2.7). A Planck mean absorption coefficient $\kappa_{\mathrm{soot}}^{\mathrm{Planck}}(T)$ (Modest 2013) is used with:

$$\kappa_{\mathrm{soot}}^{\mathrm{Planck}}(T) = 3.83\frac{C_0 f_V T}{C_2} \tag{3.55}$$

with $C_0 = \frac{36\pi ab}{(a^2-b^2+2)^2+4a^2b^2}$ and $C_2 = hc/k_B$ the second Planck constant. The refractive index of soot particles is taken equal to $m = a - ib = 1.57 - 0.56i$ (Smyth and Shaddix 1996) (value that is erroneously and frequently attributed to Dalzell and Sarofim (1969)).
Then, the total radiative source term $P^{\mathrm{R}}$ is expressed by:

$$P^{\mathrm{R}} = -4\sigma\left(\sum_i(\kappa_{\mathrm{Pl},i}p_i) + \kappa_{\mathrm{soot}}^{\mathrm{Planck}}\right)\widetilde{T}^4 \tag{3.56}$$

where $\sigma$ is the Stefan-Boltzmann constant, $\kappa_{\mathrm{Pl},i}$ is the Planck mean absorption coefficient of species $i$ calculated as in (Barlow et al. 2001) and $p_i$ is the partial pressure of species $i$. The calculation of these Planck mean absorption coefficients is presented in Chapter 6 and their evolution as a function of temperature in Appendix D, Sec. D.1.2.

Unsteady LES calculation enables to alleviate most of the issues of Turbulence-Radiation Interaction (TRI) (Coelho 2007; Coelho 2012) which is significant in RANS simulations. The remaining subgrid-scale TRI effects are neglected in the present study.

# Chapter 4

# LES of a turbulent diffusion flame

*In this chapter, the LES formalism presented in Chapter 3 is applied to the simulation of a turbulent jet diffusion ethylene-air flame. Temperature and species radial profiles are compared to experimental profiles. Concerning soot particles evolution, axial and radial profiles of mean and root mean square (RMS) of soot volume fraction are compared to experimental data.*
*Once the LES approach is validated, the objective of this chapter is to investigate soot production in turbulent flames thanks to the access to the full LES information on soot production phenomena. Soot formation is then analyzed through the study of the different source terms involved in soot production. The major contributors of soot production are then identified. Thanks to the coupled LES-sectional approach, information on spatial and temporal evolution of the PSD are numerically accessible in a turbulent flame simulation. Flame and soot dynamics are discussed in details, through the study of soot particles Lagrangian paths. In the current study, high fluctuations between one-peak and two-peak PSD shapes are observed.*
*Finally, an interpretation of the usual time soot intermittency index is proposed based on the full temporal data obtained for the particles size distribution. The results for the corresponding index is then compared with other indexes based on other variables representative of soot particles presence and the obtained differences between them are discussed.*

*This chapter refers to an article that has been accepted for publication to the journal Combustion and Flame (Rodrigues et al. 2018).*

Contents



## 4.1 Presentation of the configuration

The configuration chosen for the simulation is the turbulent non-premixed ethylene/air flame, which has been extensively characterized experimentally at Sandia (Zhang et al. 2011). This configuration corresponds to a turbulent jet with Reynolds $Re_D = 20\,000$, based on the fuel injector diameter of the main jet $D = 3.2$ mm. The corresponding bulk velocity is $v_{\text{fuel}} = 54.7$ m/s.
The main jet tube presents an outer diameter of 4.6 mm and is surrounded by another tube with an inner diameter of 15.2 mm, and an outer diameter of 19.1 mm. The outer tube features an insert having 64 holes on 3 rings. These 64 holes correspond to 64 pilot flames used for the stabilization of the flame and are fed by ethylene/air mixture with an equivalence ratio of $\phi = 0.9$. The global mass flow rate of the 64 pilot injectors is equal to $1.77 \times 10^{-4}$ kg/s and their total heat release corresponds to only 2% of the heat release of the main jet. The pilot flames size, number and spacing have been chosen such that they produce a uniform flow rate of hot products around the burner exit plane. Finally, a coflow of air at $v_{\text{air}} = 0.6$ m/s surrounds the whole pilot flames.
The inlet temperatures of all the flows, except the pilot, are equal to 294 K. For the pilot flame, an adiabatic flame temperature equal to 2296 K for the corresponding equivalence ratio has been imposed.

Different sets of experimental data are used for the comparison with numerical results:

- CARS temperature and $X_{O_2}/X_{N_2}$ measurements from (Kearney et al. 2015),
- PLIF OH and LII soot volume fractions measurements from (ISF3 2017),

- Axial profile of soot intermittency measurements from Shaddix et al. (2010).

## 4.2 Modeling and numerical setup

The lookup table is discretized with $100 \times 20 \times 100 \times 20$ grid points in the $\widetilde{Z}$, $S_Z$, $\overline{C}$ and $\overline{H}$ directions, respectively. The model presented in Chapter 3 was implemented in the code AVBP (Schonfeld and Rudgyard 1999). This parallel CFD code, developed at CERFACS and IFPEN, solves the three-dimensional compressible Navier-Stokes equations on unstructured meshes. The third-order in space and time finite element TTGC scheme (Colin and Rudgyard 2000) is retained for this simulation. Navier-Stokes Characteristic Boundary Conditions (NSCBC) (Poinsot and Lele 1992) are used to prescribe the boundary conditions. The Tabulated Thermochemistry for Compressible flows formalism (TTC) is used (Vicquelin et al. 2011). Flamelets, and hence the flamelet table, are computed with a low Mach-number assumption which results in neglecting compressible effects in the combustion model. This approximation is valid in the studied case. However, using the enthalpy given by the set of compressible transport equations directly in Eq. (C.10) of Appendix C would wrongly impress variations in the tabulated quantities (species mass fractions, $\cdots$) associated to the captured acoustic waves. Therefore, an additional equation for the enthalpy with a low-Mach number approximation is here transported. The corresponding field $\widetilde{h}$ is fed to Eq. (C.10). For the solid phase, 25 sections are transported to describe the particles size distribution describing particles with volumes comprised between $v^{\mathrm{MIN}} = 0.7$ nm$^3$ and $v^{\mathrm{MAX}} = 5 \times 10^9$ nm$^3$. The latter value is a compromise between accuracy and limited CPU over-cost, based on a convergence study on 1-D laminar flames showing that 25 sections are sufficient for the prediction of the soot volume fraction.

For the generation of the flamelet database used for the radiation FPV model, the detailed kinetic scheme KM2 (Wang et al. 2013) has been retained to solve the steady and unsteady equations for the 1-D counterflow flames with the REGATH package (Franzelli et al. 2013). The dimerization source term defined in Eq. (2.16) is added to each PAH chemical source term involved in dimerization process in order to take into account in the flamelet database, the PAH removal due to nucleation and condensation processes. Unity Lewis number diffusion model is used for the generation of the flamelet database. The progress variable $Y_C$ is chosen equal to

$$Y_C = \left( \frac{Y_{CO_2}}{W_{CO_2}} + \frac{Y_{H_2O}}{W_{H_2O}} + \frac{Y_{CO}}{W_{CO}} - 3\frac{Y_{CH_4}}{W_{CH_4}} \right) / \left( 1/W_{CO_2} + 1/W_{H_2O} + 1/W_{CO} - 3/W_{CH_4} \right), \tag{4.1}$$

such that it uniquely maps each flamelet. The methodology used for the generation of the table is presented in Appendix C.

Fully-developed pipe flow mean and RMS radial profiles have been obtained from a preliminary computation in order to impose the inlet turbulent boundary conditions, detailed in Appendix E.
The computational domain (Fig. 4.1) is composed of three inlets, the walls and one outlet. It extends to 312.5D downstream, 8D upstream of the nozzle and 94D in the radial direction. The 64 pilot flames are modeled with a single concentric flow with the uniform mass flow rate. The mesh contains 10M cells/1.7M nodes and the typical cell size at the jet exit is $\Delta x \approx 0.20$mm. This mesh has been validated on cold flow simulations in Appendix E based on literature data of Pope (2000) on round jets.

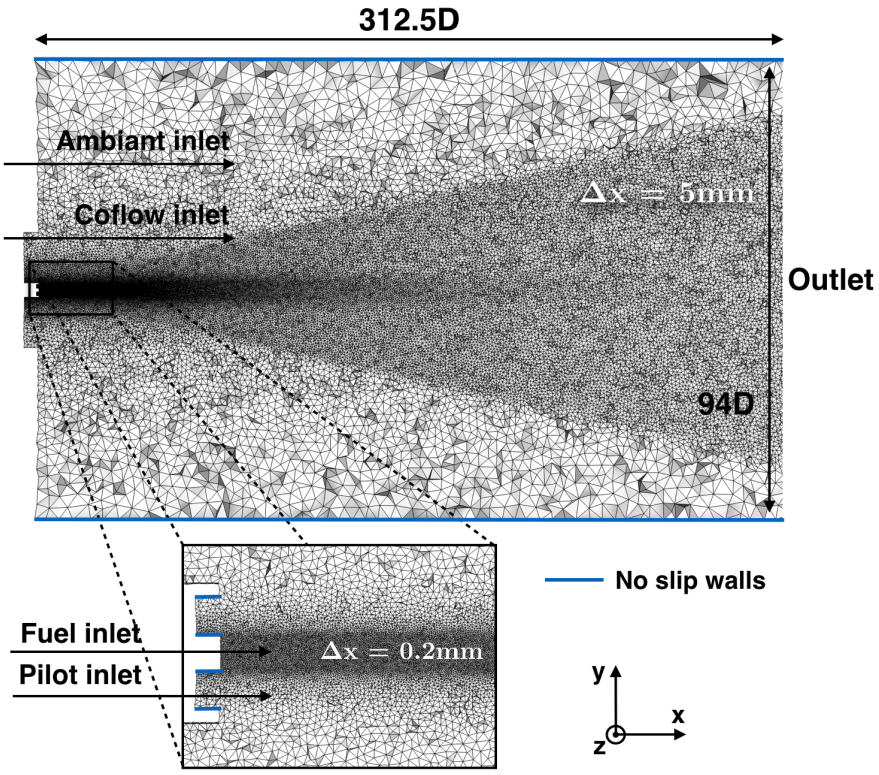


**Figure 4.1:** *Longitudinal cut of the cylindrical computational domain.*

This simulation has been performed using a Bull cluster equipped with Intel E5-2680 processors with a total computational time (including averaging time) of 750 000 CPU hours. The averaged fields have been computed over 250 ms of physical time.

## 4.3 Comparison with experiments

In order to validate the LES approach, the numerical results are compared to the available experimental data. Concerning the gaseous phase, Fig. 4.2 (top) shows a comparison of radial mean and root mean square (RMS) temperature profiles with experiments at $x/D = 134$ (Kearney et al. 2015). In Fig. 4.2 (bottom), results for mean and RMS of $X_{O_2}/X_{N_2}$ ratio are presented for the same height. Good prediction of the mixture and temperature is obtained. Small overestimation of temperature at the centerline is observed and peaks of radial temperature and $X_{O_2}/X_{N_2}$ ratio RMS are slightly underestimated. Several aspects can affect the quality of these results: the predicted turbulent mixing, the turbulent combustion model and also the radiation modeling (here, optically thin assumption) which is important because of its coupling with temperature. Moreover, it should be reminded that this set of experimental data (Kearney et al. 2015) comes from measurements in altitude where the pressure is about 15% lower than the one used in our numerical setup (1atm). The overall agreement is satisfactory and good predictions of the gaseous phase are essential for the prediction of the source terms of the solid phase evolution.

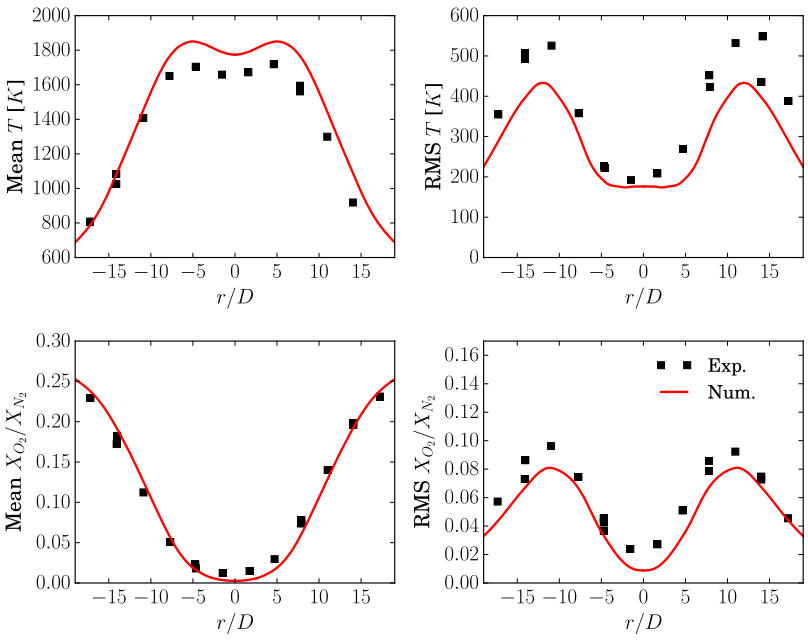


**Figure 4.2:** *Comparison of mean and RMS temperature (top) and* $\mathrm{X_{O_2}/X_{N_2}}$ *(bottom) radial profiles between numerical (line) and experimental results (symbols) at* $x/D = 134$. *Experimental data is from Kearney et al. (2015)*

In addition, Fig. 4.3 shows a comparison of mean OH radial profiles at different heights above the burner between predictions and measurements (ISF3 2017).

The experimental data being non-quantitative, experimental and numerical results are here normalized by their respective maximum values for each height above the burner. The obtained agreement confirms a good prediction of the position of the flame front and of the mean flame brush, necessary to correctly locate soot oxidation phenomena.

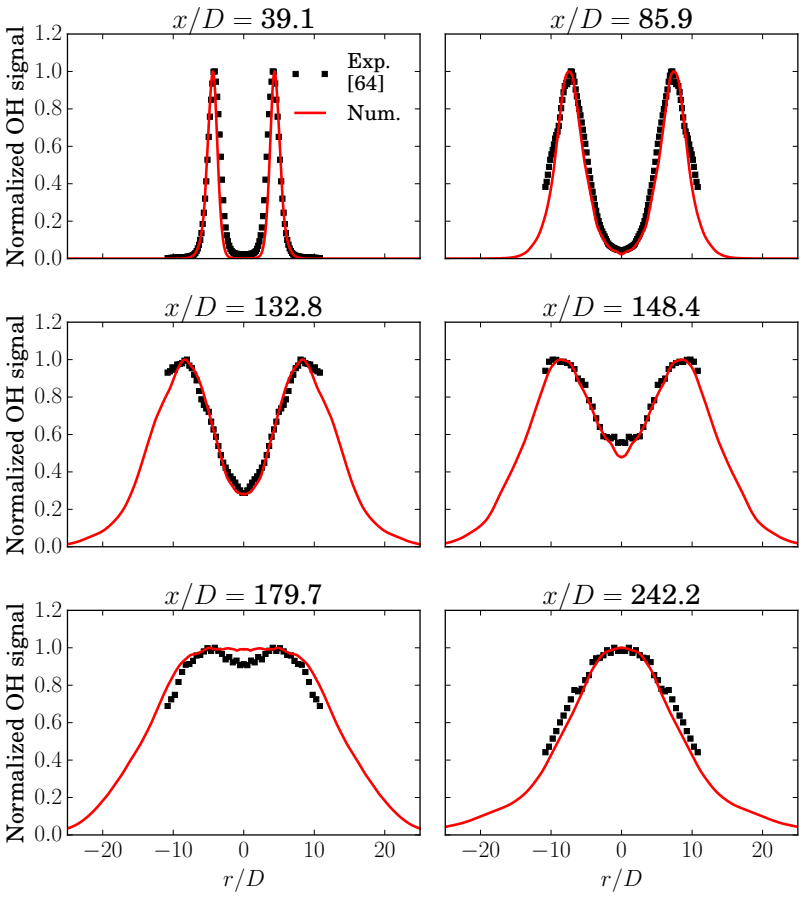


**Figure 4.3:** *Normalized mean OH radial profiles at different heights above the burner: numerical results (line) are compared to experiments (symbols). Experimental data is from ISF3 (2017).*

In order to validate the proposed approach for sooting turbulent flames, it is firstly possible to quantify the resolved temporal soot intermittency. This quantity is defined experimentally at each point as the probability of finding an instantaneous value of $f_V$ lower than 0.03 ppm[1]. Figure 4.4 shows a comparison of numerically-resolved soot intermittency and experimental probe-resolved

[1]It is important to notice that the temporal soot intermittency does not correspond to the subgrid intermittency previously defined in Eq. (3.28).

soot intermittency along the flame centerline as a function of the axial position. It can be seen that the model reproduces well this quantity even if numerical results seem slightly translated upstream. At $x/D > 150$ soot presence is detected experimentally whereas no more soot particles are obtained in the simulation. Globally, these results seem to confirm a good prediction of soot particles production dynamics.

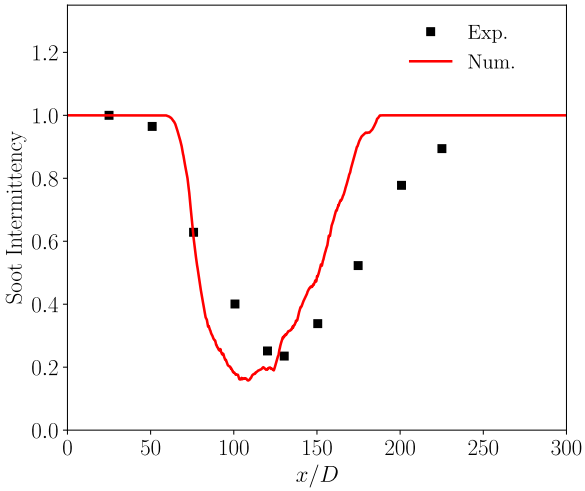


**Figure 4.4:** *Comparison of numerical (line) and experimental (symbols) soot intermittency axial profiles. Experimental data is from Shaddix et al. (2010).*

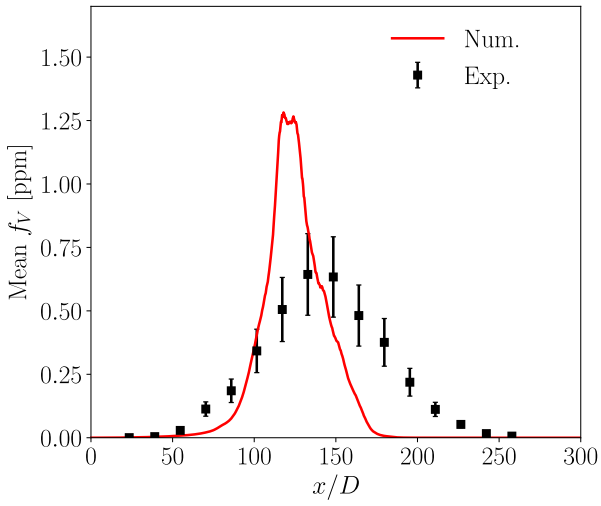


**Figure 4.5:** *Mean soot volume fraction axial profiles: comparison between experimental (symbols) and numerical (line) data. Experimental data is from ISF3 (2017).*

Axial mean soot volume fraction profile is compared with experiments in Fig. 4.5 (ISF3 2017). A reasonable agreement of soot production is obtained, but the

peak soot volume fraction is overestimated by a factor two. Soot destruction is also predicted too early compared to experiments. In literature, similar results on other sooting jet flames have already been observed by Mueller and Pitsch (2012), whereas a previous work based on the DQMOM model presented an underestimation of $f_V$ for the currently studied flame (Xuan and Blanquart 2015). As a consequence, it can be said that the present prediction of soot volume fraction is reasonable compared to the state-of-the-art in large eddy simulations of soot production.

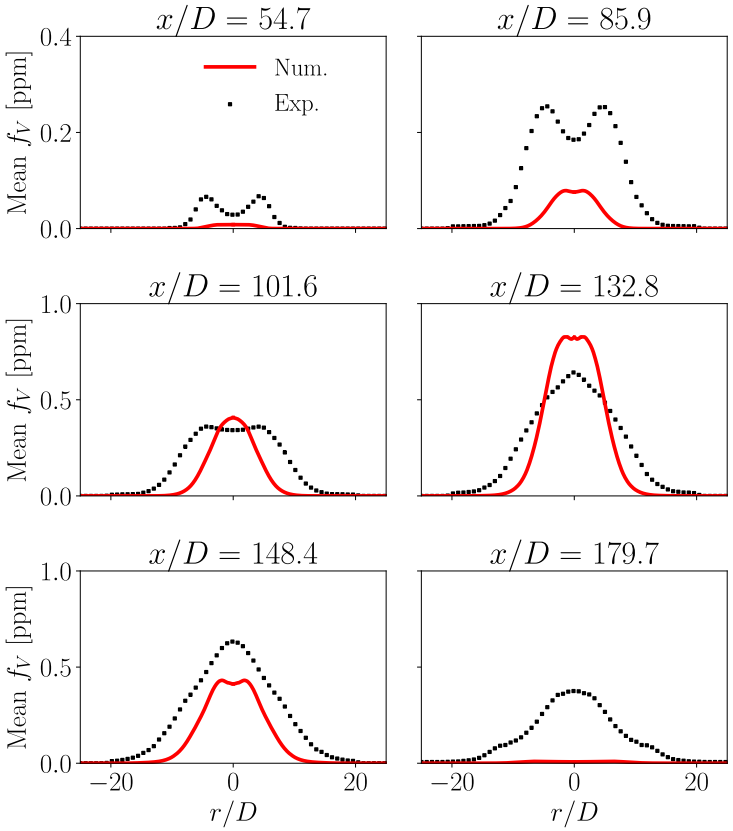


**Figure 4.6:** *Mean soot volume fraction radial profiles at different heights above the burner: comparison between experimental (symbols) and numerical (line) data. Experimental data is from ISF3 (2017).*

Figure 4.6 compares radial mean profiles for soot volume fraction at different heights above the burner. As for the axial profiles, an overestimation of soot volume fraction magnitude is obtained between x/D=110 and x/D=140. The width of the soot volume fraction zone is underpredicted.
Figure 4.7 compares relative radial RMS profiles of $f_V$ for the same heights. The relative radial RMS corresponds to the soot volume fraction RMS divided by the mean soot volume fraction. This comparison enables to focus only on the

prediction of high RMS zone of soot volume fraction production. Predictions of the magnitude and position of high relative RMS of soot production are quite reasonable compared to experiments. Then, it can be concluded that despite the discrepancies on soot volume fraction magnitude prediction, the temporal dynamics of soot production are well predicted.

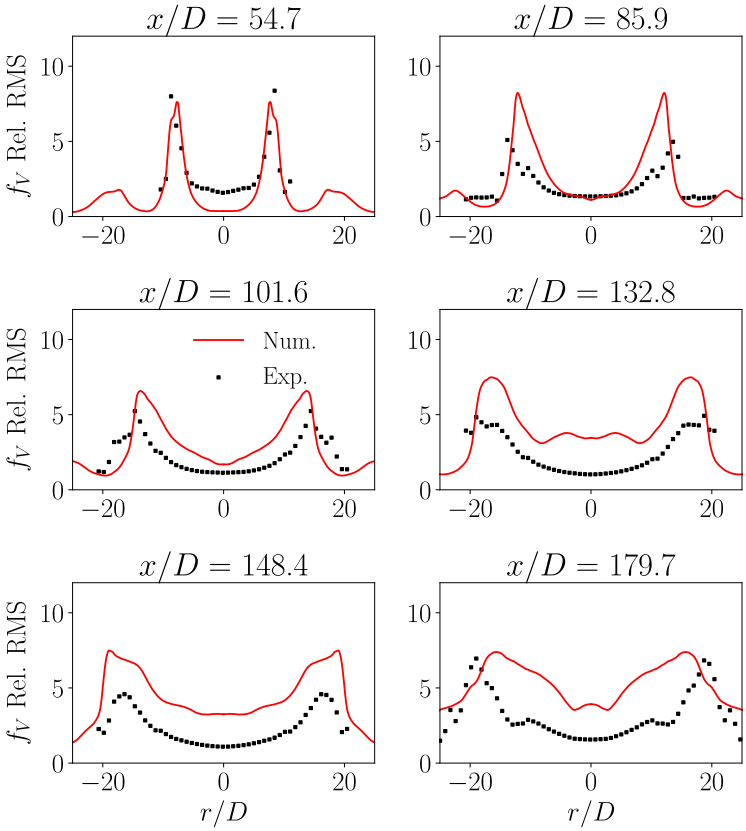


**Figure 4.7:** *Relative soot volume fraction RMS radial profiles at different heights above the burner: comparison between experimental (symbols) and numerical (line) data. Experimental data is from ISF3 (2017).*

In conclusion, despite the fact that errors in soot volume fraction magnitude and position predictions are still present with the proposed sectional method, this simulation corresponds to the state-of-the-art in terms of soot production prediction. In addition, it provides the access to the particles size distribution evolution, enabling new analysis of soot particles evolution in turbulent flames, which will be presented in next section.

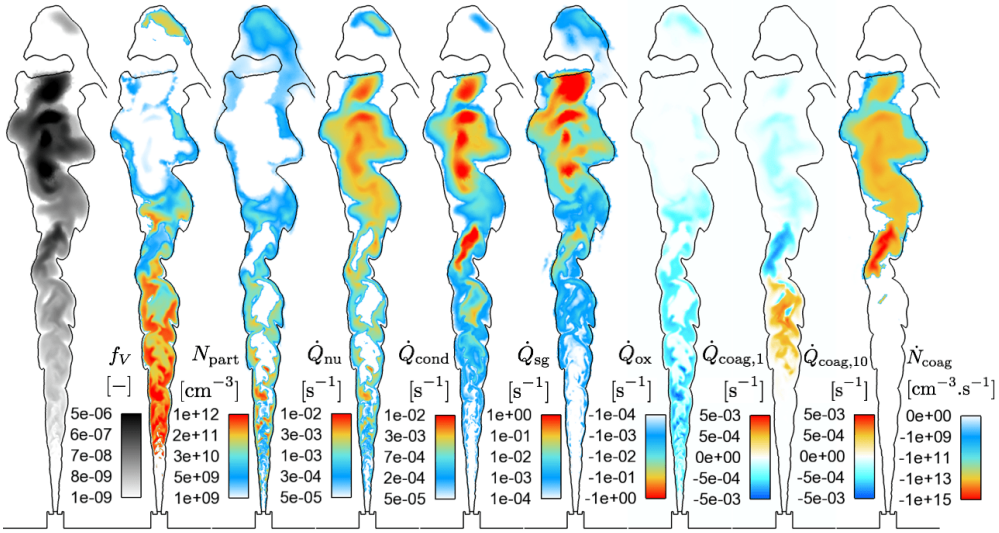


**Figure 4.8:** *From left to right: typical instantaneous fields of soot volume fraction, particles number density, nucleation, condensation, surface growth and oxidation volume source terms for all the sections, volume coagulation source term for the first and tenth section and number coagulation source term for all the sections. The iso-contour of mixture fraction at $Z_0$ (indicating the flame front) is shown in solid line.*

## 4.4 Numerical characterization of the evolution of the soot production in a turbulent flame

This section presents a characterization of soot production evolution in the studied non-premixed ethylene/air flame by analyzing all accessible information thanks to the coupling of the LES approach and the sectional method.

### 4.4.1 Global quantities

Figure 4.8 shows instantaneous fields of soot volume fraction $f_V$ and of particles number density $N_{\text{part}}$ (from the left). An iso-contour of mixture fraction at value $Z_0$ localizing the flame front is also shown with a solid line. It can be noticed that soot particles are always located on the rich side of the flame ($Z > Z_0$) close to the jet axis.
In order to understand the phenomena governing the $N_{\text{part}}$ and $f_V$ fields, Fig. 4.8 also presents the instantaneous total soot volume fraction source terms: nucleation $\dot{Q}_{\text{nu}}$, condensation $\dot{Q}_{\text{cond}}$, surface growth $\dot{Q}_{\text{sg}}$ and oxidation $\dot{Q}_{\text{ox}}$. Nucleation occurs at the bottom of the flame where PAHs concentrations are high due to very rich mixtures. Condensation occurs almost all over the flame, while surface growth and oxidation are more located downstream in the flame. It can be seen that maximum surface growth and oxidation source terms are at least two orders of magnitude higher than nucleation and condensation phenomena.

With the presented model and for the studied flame, surface reactivity source terms are the main contributors in soot volume fraction production. Surface growth occurs at the middle of the flame whereas oxidation is mainly present at the top of the flame, but also near the stoichiometric iso-contour where particles are oxidized. It is important to note that these observations are in contrast with studies in literature on similar flames. In the studies presented in (Bisetti et al. 2012; Mueller and Pitsch 2012), nucleation and condensation have been found to be the major processes involved in soot production. However, in other studies (El-Asrag et al. 2007; El-Asrag and Menon 2009), surface growth is found to be at least of the same order of magnitude as PAH-related soot growth pathways. In the current study, surface growth is identified to be the main process involved in soot particles growth. This variability in results can be due to the large diversity that exists between the different sub-models and constants used for each one of the soot formation processes in different works. At the same time, the investigated flames are also different and today there is no proof that a specific hierarchy exists between the numerous phenomena governing soot production common to all turbulent flames.

Coagulation does not alter the total volume source term, but it may be interesting to look at its effect in terms of section distribution. The coagulation source terms are presented in Fig. 4.8 for the first ($\dot{Q}_{\text{coag},1}$) and the tenth sections ($\dot{Q}_{\text{coag},10}$) of the soot particles size distribution, corresponding respectively to particles with mean volumes $v_1^{\text{moy}} = 0.9$ nm$^3$ and $v_{10}^{\text{moy}} = 4 \cdot 10^3$ nm$^3$. For the first section, soot coagulation source term is always negative because of the coagulation of the smallest particles to form bigger ones. For the tenth section, it is first positive because of the coagulation of soot particles from the smallest soot sections, then becomes negative because of the coagulation of the particles from the tenth section towards bigger soot sections.

The coagulation source term of the total number density $\dot{N}_{\text{coag}}$ calculated as in Eq. (3.37) is also presented in Fig. 4.8. Comparing the fields of $\dot{N}_{\text{coag}}$ and $N_{\text{part}}$, one can observe that the decrease of particles number density at the middle of the flame is linked to coagulation leading to the presence of big soot particles. As a consequence, condensation becomes more important than nucleation in this region, where particle diameters are much larger than the dimer diameter so that condensation rate (collision of one soot particle with a dimer particle) is higher than nucleation (collision of two dimer particles).

In conclusion, in the present simulation we observe that the particle number density is higher at the bottom of the flame where nucleation process is important and decreases downstream due to the coagulation phenomenon. On the contrary, soot volume fraction increases along the axial position mainly due to surface growth and then decreases up to the tip of the flame where soot particles are oxidized due to the presence of OH radical.

In order to confirm the tendencies observed on the instantaneous fields, Fig. 4.9 gives a representation of the localization of the total nucleation, condensation, surface growth and oxidation source terms. The colored region corresponds to

the zone where the mean source term is higher than 25% of its maximum value. The location of the PAH, $C_2H_2$, and OH mass fractions are also indicated. Nucleation and condensation source terms are linked to the presence of PAHs, and condensation occurs higher in the flame than nucleation (Fig. 4.9**a**). Indeed, as explained previously, soot nucleation is less probable than condensation once the size of the soot particles and, consequently, the number of big particles are high enough.
Concerning surface growth (Fig. 4.9**b**) and oxidation (Fig. 4.9**c**) phenomena, as expected, they are linked to the presence of $C_2H_2$ and OH species, respectively, and to the presence of big particles since these phenomena depend on the particle surface.
Figure 4.10 presents the normalized mean fields of the soot coagulation source terms for several selected sections. For the first section (Fig. 4.10**a**), soot particles always coagulate by forming bigger particles so that the source term is negative everywhere. For sections 5 (Fig. 4.10**b**) and 10 (Fig. 4.10**c**), two regions can clearly be identified, corresponding to the coagulation of smaller particles to form particles in the corresponding section (in red) and the coagulation of the soot particles of the section towards bigger soot particles (in blue). For higher soot sections (Fig. 4.10**d-e**), the mean coagulation source term is positive so that coagulation from smaller soot sections predominates compared to coagulation towards bigger sections.

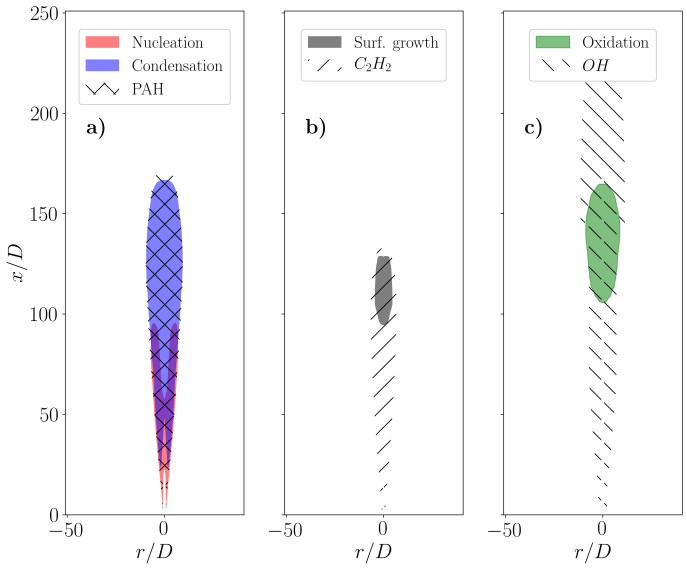


**Figure 4.9:** ***a)*** *Nucleation and condensation presence indexes related to the presence of PAH precursors;* ***b)*** *Surface growth index related to the presence of* $C_2H_2$ *species;* ***c)*** *Oxidation index related to the presence of* OH *species.*

These first analyses illustrate the physical richness obtained through the pro-

posed sectional approach. Before exploring the results in details, it is important to identify where the subgrid soot model may affect the results. For this, the mean subgrid soot intermittency $\omega$ is presented in Fig. 4.10**f**. When $\omega$ is near one, the subgrid model for the soot quantities is active, whereas when $\omega$ is closed 0, the soot quantities are resolved on the grid and the effect of the soot subgrid model is negligible. It can be observed that starting from $x/D = 50$, $\omega$ is lower than 0.1. As a consequence, the analysis will be performed in the following only for $x/D > 50$, where results are expected to be only slightly affected by the soot subgrid model.

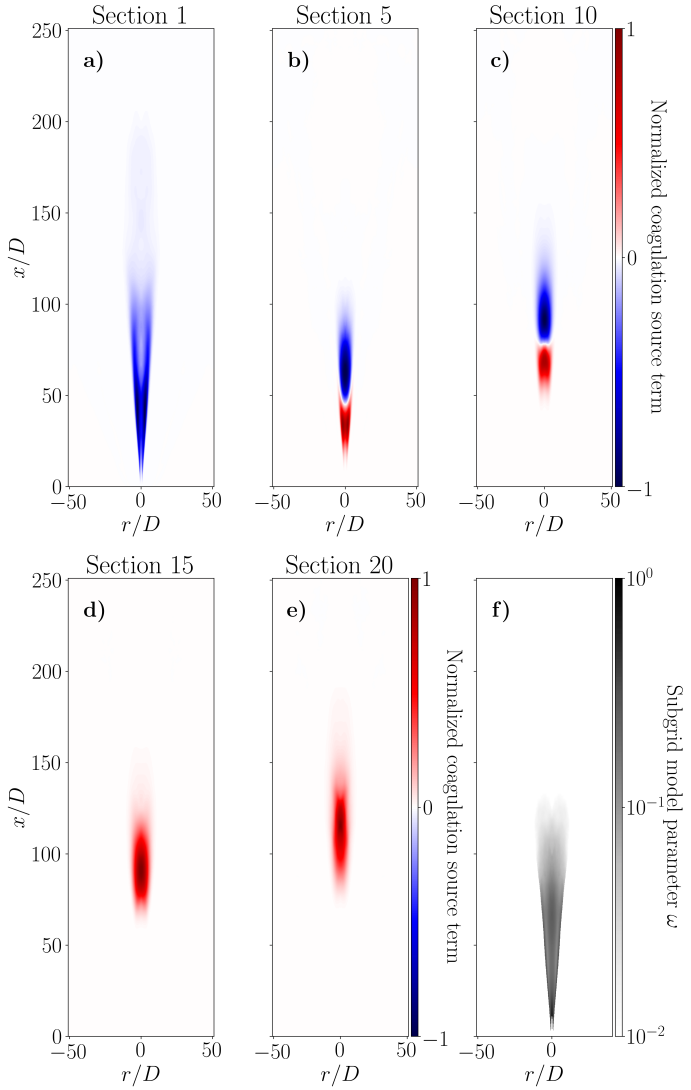


**Figure 4.10:** ***a)-e)*** *Normalized mean fields of soot coagulation source term for different soot sections;* ***f)*** *mean field of soot subgrid model parameter* $\omega$

### 4.4.2 Mean particles size distributions

As already mentioned, the sectional method provides access to the PSD information that can be used to characterize particle formation and evolution along the flame. For this, Fig. 4.11 shows mean particles size distributions of soot particles at the centerline for different selected heights above the burner: $(\mathrm{d}N/\mathrm{dlog}(d_a))_i = 3\ln(10)q_i$. For $x/D < 75$, the PSD presents one peak. Downstream, more particles are found in higher soot sections and a two-peak distribution is observed.[2] These results are qualitatively in agreement with the experimental tendencies only very recently observed in similar flames (Boyette et al. 2017; Chowdhury et al. 2017).

Details of the different source terms involved for each section are shown in Fig. 4.12 for the same six heights.

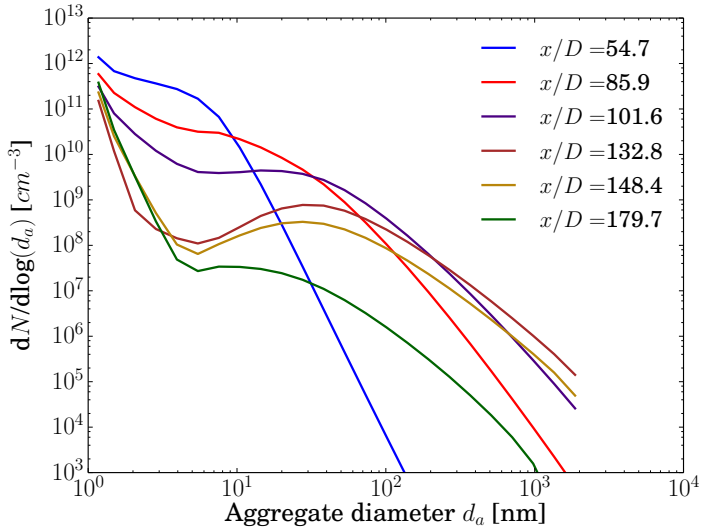


**Figure 4.11:** *Mean particles size distribution of soot particles at the centerline for different selected heights above the burner.*

For $x/D = 54.7$, all the phenomena involved in soot production present almost the same order of magnitudes. Only small particles are present and, as mentioned before, the particles size distribution presents a one-peak shape corresponding to the nucleation of the smallest soot particles. At $x/D = 85.9$, surface growth is the main phenomena involved in soot production. Oxidation and coagulation are also present and a two-peak shape of the PSD starts to be observed. The second peak of this two-peak PSD shape is more and more shifted toward bigger diameters mainly because of the surface growth

[2]The particles size distribution is considered as a one-peak shape when the PSD is monotone, and as a two-peak shape elsewhere.

and the coagulation of soot particles downstream in the flame. Then, between $x/D = 101.6$ and $x/D = 148.4$, a transition between the relative contributions of surface growth and oxidation is observed. Oxidation process is more and more important and at $x/D = 179.7$, soot particles are totally oxidized.
Important physical processes information can then be captured with the presented approach enabling to understand the predicted mechanism of soot evolution in this flame.

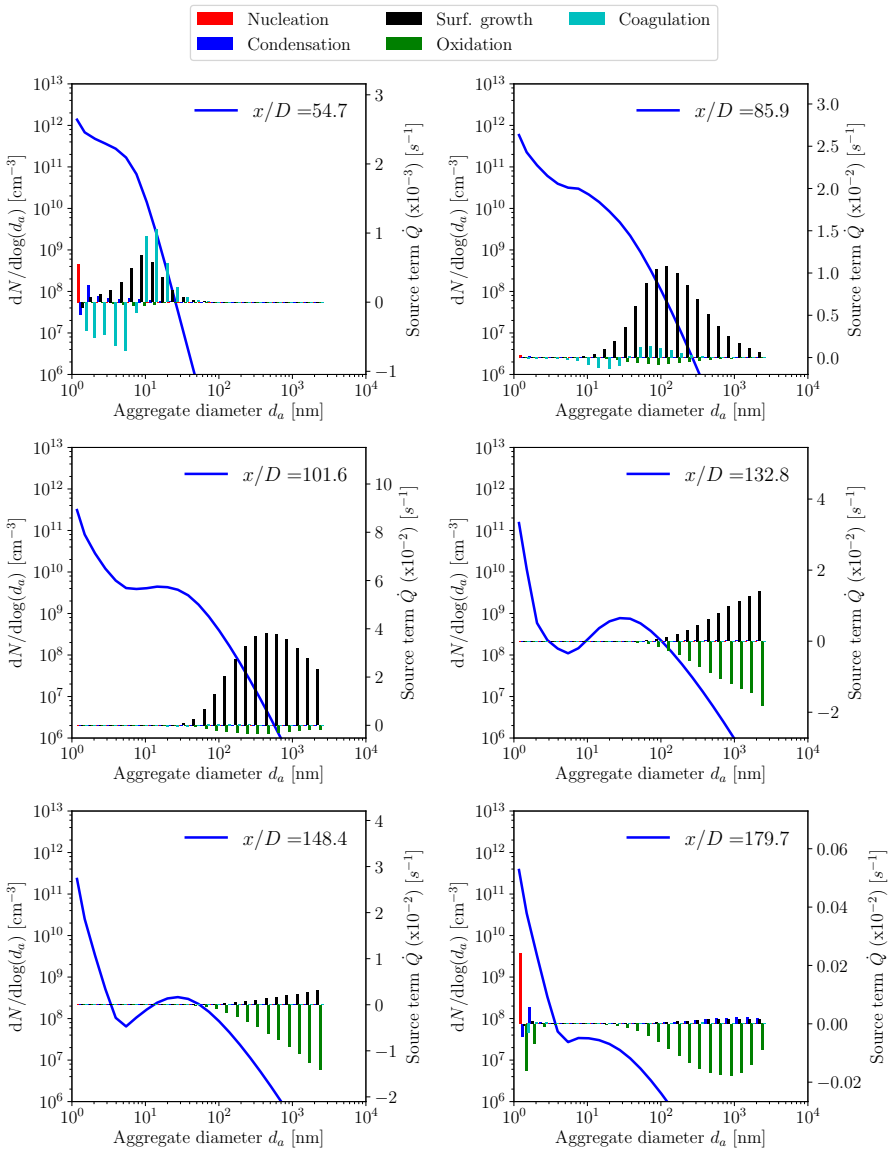


**Figure 4.12:** *Mean particles size distributions and details of mean soot sections source terms at the jet centerline for different selected heights above the burner.*

A representation of the mean soot particles size distribution shape along the flame is given in Fig. 4.13. Blue region corresponds to the zone where in average the PSD presents one peak whereas red region corresponds to the region where the PSD presents two peaks. Then, at the bottom of the flame, the PSD presents a one-peak shape whereas a two-peak PSD shape is observed downstream of the flame.

### 4.4.3 Dynamic evolution of the PSD

#### 4.4.3.1 PSD shape dynamics

The coupling of an LES approach with a soot sectional method provides unique information on the temporal evolution of the soot PSD in the flame. As an example, the temporal evolution of the PSD at $x/D = 85.9$ (at the centerline) is presented in Fig. 4.14**a** showing high fluctuations with time from one-peak to two-peak shapes.

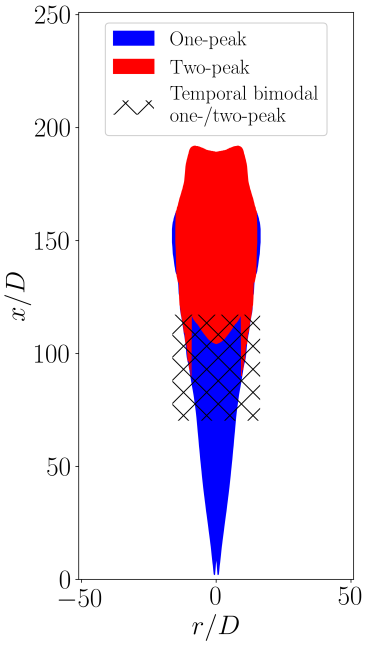


**Figure 4.13:** *Index of the structure of the particles size distribution (one-peak, two-peak and temporal bimodality).*

The same phenomena can conveniently be represented by looking at the probability density function (pdf) for each diameter, presented in Fig. 4.14**b** for the same position. The presented pdf is rescaled for each value of the aggregate diameter. Then, for each diameter, black points correspond to the most probable value of the particles size distribution function, whereas light grey points correspond to less probable values of the PSD. Looking at the pdf in Fig. 4.14**b**,

the signature of a temporal bimodal behavior of the PSD is identified by the presence of two most probable values for small sections.

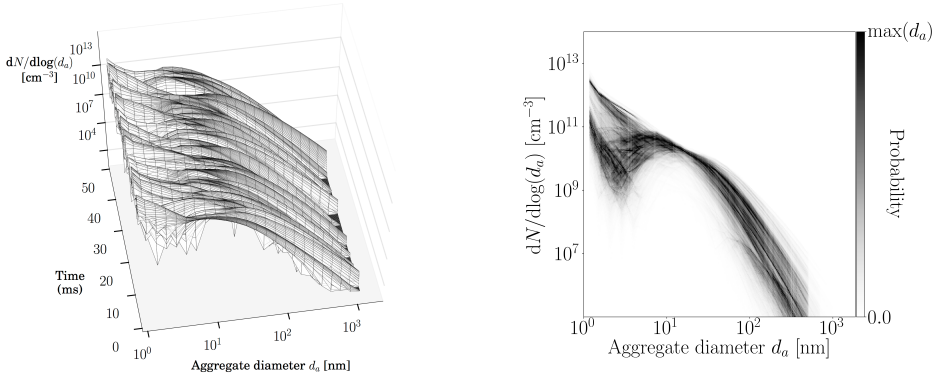


(a) Temporal evolution of the PSD for $x/D = 85.9$

(b) Probability density function of the PSD for $x/D = 85.9$. For each diameter $d_a$, the colorbar is normalized between 0 and the maximum probability $\max(d_a)$ for this diameter.

**Figure 4.14:** *Unsteady evolution of particles size distribution of soot particles at the centerline for* $x/D = 85.9$.

In order to analyze the evolution of the structure of the PSD with time, Fig. 4.15 presents the probability density functions of particles size distributions for twelve different selected heights at the jet centerline:

- Important fluctuations of the first peak of the PSD are observed from $x/D = 53.1$ to $x/D = 62.5$ above the burner (Fig. 4.15**a-d**). However, there is no temporal bimodality and the PSD presents always a one-peak shape.
- From $x/D = 70.3$ to $x/D = 101.6$ (Fig. 4.15**e-i**), regular transitions between one-peak and two-peak PSD shapes can be observed. At $x/D = 101.6$ (Fig. 4.15**i**),, strong oscillations of the particles size distribution are observed. Soot volume fraction is the highest in the flame and the second peak of the particles size distribution is shifted towards big soot particles. The strong oscillations explain also the high RMS observed at these heights in Fig. 4.7. A very large spanning of PSD values is observed for big sections, increasing with the height above the burner.
- For the heights $x/D = 132.8$ and $x/D = 148.4$ (Fig. 4.15**j-k**), there is no temporal bimodality anymore. The PSD always presents a two-peak shape but the second peak is lower than in the previous heights because of the oxidation process that has already started. Compared to the second peak of the PSD, lower fluctuations of the first peak are observed. The spanning of values of the PSD increases until $x/D \approx 150$.
- At $x/D = 179.7$ (Fig. 4.15**l**), as previously observed, big soot particles are almost totally oxidized. Only small soot particles remain at this height

above the flame.
This analysis confirms the presence of a large region (presented in hatched in Fig. 4.13) where a temporal bimodal behavior is observed due to transition from a one-peak shape region located at the bottom of the flame and a two-peak shape zone downstream.

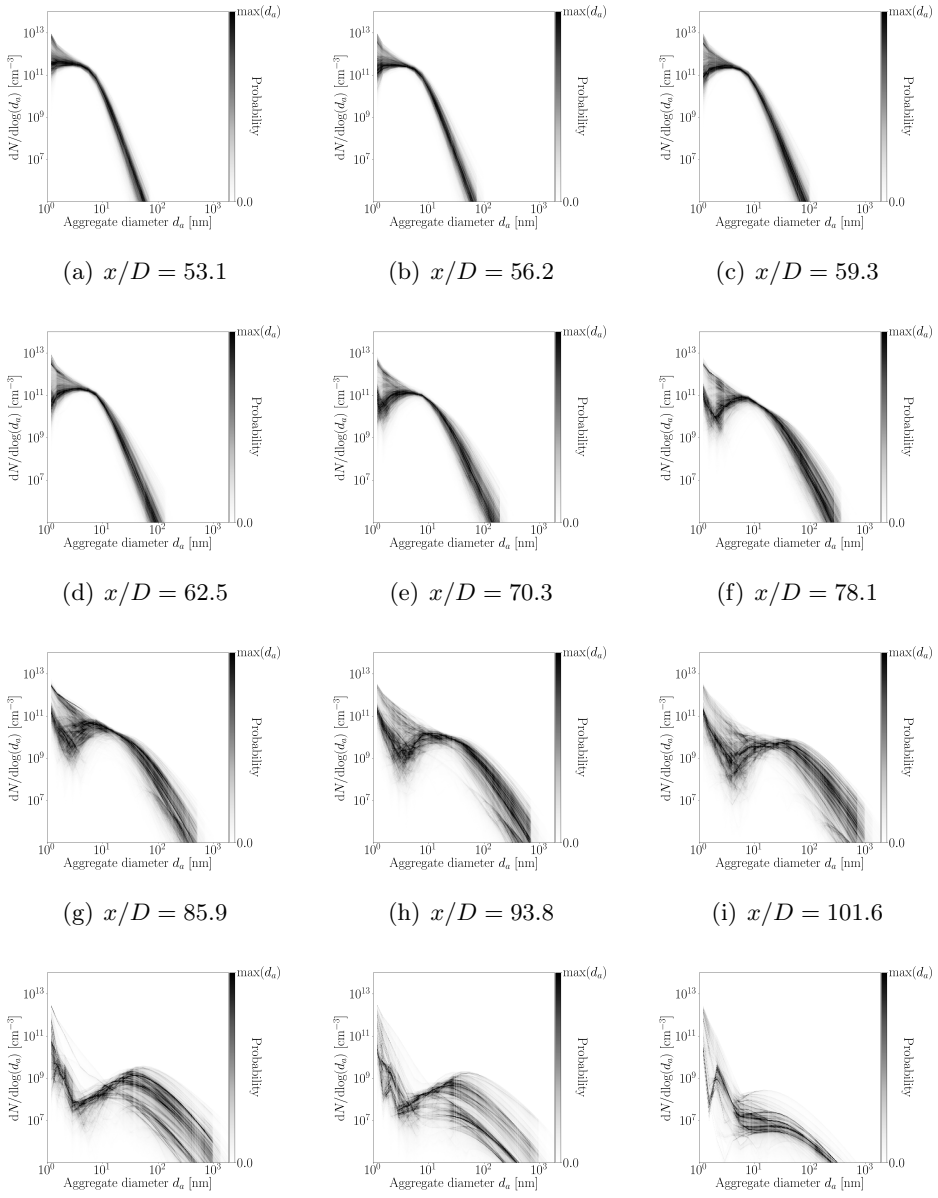


(a) $x/D = 53.1$ (b) $x/D = 56.2$ (c) $x/D = 59.3$

(d) $x/D = 62.5$ (e) $x/D = 70.3$ (f) $x/D = 78.1$

(g) $x/D = 85.9$ (h) $x/D = 93.8$ (i) $x/D = 101.6$

(j) $x/D = 132.8$ (k) $x/D = 148.4$ (l) $x/D = 179.7$

**Figure 4.15:** *Probability density functions of particles size distributions of soot particles at the centerline for twelve selected heights above the burner.*

#### 4.4.3.2 Role of the particles history on the PSD

In order to understand the origin of the PSD fluctuations, scatter plots of particles size distribution are plotted in Fig. 4.16 (left) colored by the value of the mixture fraction at three different heights.

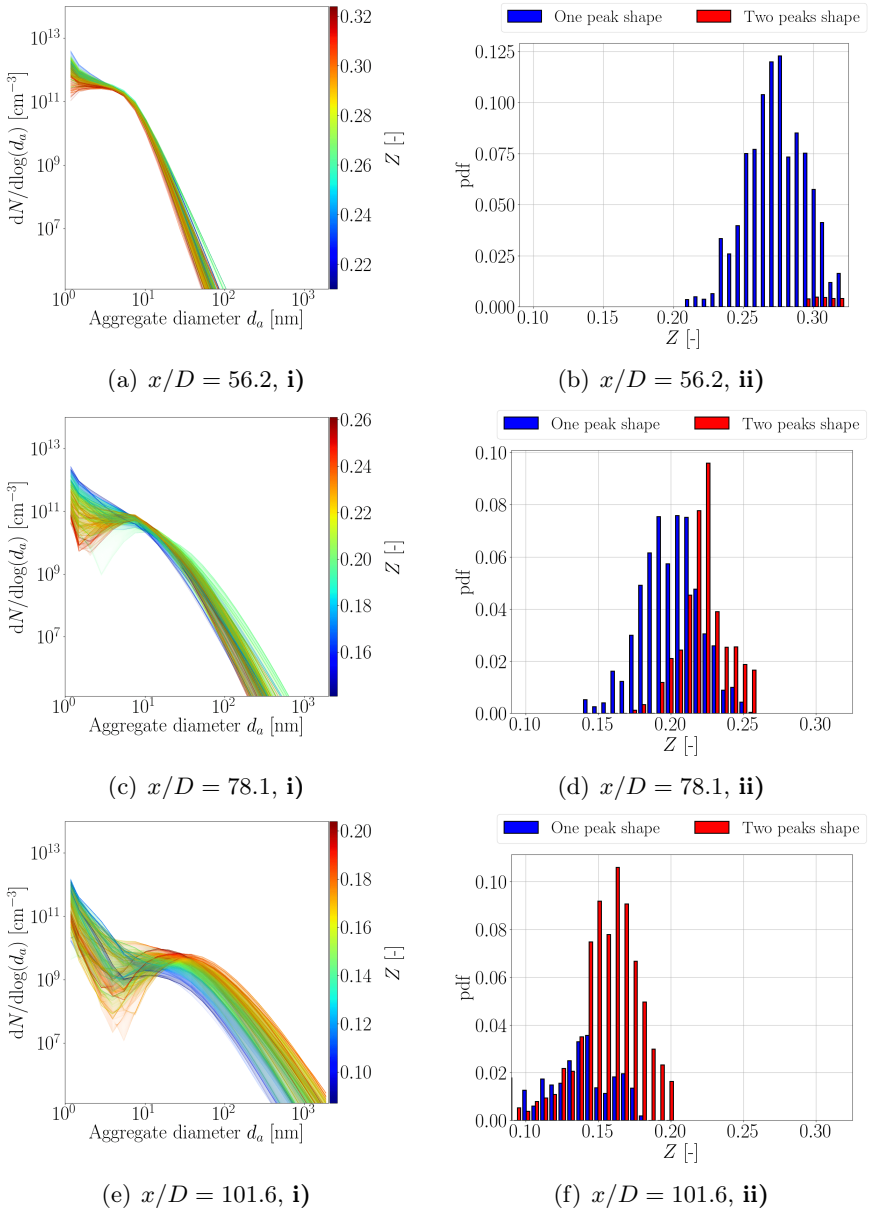


(a) $x/D = 56.2$, **i)** (b) $x/D = 56.2$, **ii)**

(c) $x/D = 78.1$, **i)** (d) $x/D = 78.1$, **ii)**

(e) $x/D = 101.6$, **i)** (f) $x/D = 101.6$, **ii)**

**Figure 4.16:** *For different heights above the burner:*
***i)*** *left, Scatter plots of particles size distributions colored by the value of instantaneous mixture fraction,*
***ii)*** *right, Probability density functions of the mixture fraction conditioned by the particles size distribution shape.*

It is first observed that depending on the position, the PSD does not have the same shape for a given value of the mixture fraction $Z$. However, it can be observed that at a fixed position in the temporal bimodal zone ($x/D = 78.1$ and $x/D = 101.6$), the PSD tends to present a one-peak PSD shape in leaner pockets whereas a two-peak PSD shape is observed in richer pockets. This is confirmed by looking at the corresponding probability density functions of mixture fraction in Fig. 4.16 (right), which have been conditioned by the shape of the particles size distribution. It is again observed that two populations coexist for $70 < x/D < 110$: a two-peak PSD shape in the richer pockets and a one-peak PSD shape in the leaner pockets. However, it can be concluded that the PSD-shape is not univocally governed by the mixture fraction and it seems that the particle history plays a role on the instantaneous PSD at a given flame point.

In order to confirm the role of particle history, a set of Eulerian instantaneous fields has been post-processed in order to extract Lagrangian trajectories representative of soot particles. Two Lagrangian trajectories issued from the center of the ethylene tube exit have been extracted at two different instants for a total Lagrangian time of 14 ms each (Fig. 4.17). These trajectories have been computed taking into account both the fluid and the soot particles thermophoretic velocities, and can then be considered as tracers of small reactors moving at the velocity $\widetilde{\mathbf{u}} + \widetilde{\mathbf{v}_{\text{th}}}$. In this representation, turbulent transport and chemical/collisional source terms are then considered as source terms of the reactors. Their projected trajectories are represented together with an instantaneous field of soot volume fraction $f_V$ and the sets of data presented hereafter refer to the corresponding extracted Eulerian fields at each position and time for each Lagrangian trajectory. The first trajectory (solid purple line in Fig. 4.17**a**) ends up in a one-peak shape particles size distribution at $x/D = 76.9$ $D$, Fig. 4.17**b**, solid line. The second trajectory (dashed purple line in Fig. 4.17**a**) ends up in a two-peak shape particles size distribution (dashed line) at $x/D = 92.8$ D, Fig. 4.17**c**, dashed line.
The corresponding source terms are plotted in Fig. 4.17**b-c** with the particles size distribution for the final Lagrangian time of the trajectory ($\tau_f = 14$ ms). Looking at the final values of the source terms, the two trajectories end with two different soot formation process steps. For the first trajectory, all the source terms have the same order of magnitude. Nucleation and condensation are still important processes of the soot particles evolution. For the second trajectory, nucleation and condensation are still active processes (even if they are not visible in Fig. 4.17**c** because of the difference of magnitudes between the different soot formation processes), but the main contributors of soot particles evolution at the final position are the surface reactivity processes (surface growth and oxidation). Their order of magnitude per section is one order ($\approx 10^{-2}$ s$^{-1}$) higher than the ones obtained for the first trajectory ($\approx 10^{-3}$ s$^{-1}$).
As we mentioned before, surface growth and oxidation are the main contributors in this simulation. It was also noted that these phenomena are highly linked to

the presence of $C_2H_2$ for surface growth and OH for oxidation processes (Fig. 4.9), so that such behavior is expected to be linked to the evolution of these quantities along the particle trajectories.
To verify that, the evolution of the Lagrangian temporal mean mass fraction of $C_2H_2$, i.e. $1/\tau \int_0^\tau Y_{C_2H_2}(\tau')d\tau'$ and Lagrangian temporal mean mass fraction of OH, i.e. $1/\tau \int_0^\tau Y_{OH}(\tau')d\tau'$ are represented respectively in Fig. 4.18**a** and Fig. 4.18**b**. The corresponding evolution of the mixture fraction along the trajectory is plotted in Fig. 4.18**c**. Finally, the Lagrangian time integral of the sum of surface growth and oxidation source terms, i.e. $\int_0^\tau (\dot{Q}_{sg}(\tau') + \dot{Q}_{ox}(\tau')d\tau'$, is plotted in Fig. 4.18**d**. For all these figures, the solid lines correspond to the first trajectory resulting in a one-peak PSD shape, whereas the dashed lines correspond to the second trajectory resulting in a two-peak PSD shape. First, it can be observed that for $C_2H_2$ mass fraction, both trajectories follow quite the same evolution (Fig. 4.18**a**). However, at the end, the first particle trajectory will reach a leaner mixture region compared to the second trajectory (cf. Fig. 4.18**c**), where the OH mass fraction is high (cf. Fig. 4.18**b**). The resulting evolution of the Lagrangian time integral of the sum of the surface growth and oxidation source terms is then affected by these processes. Indeed, it can be seen in Fig. 4.18**d**, that an equilibrium between surface growth and oxidation processes is observed for the first trajectory (in solid line), whereas for the second one, surface growth process evolution increases faster than the oxidation process, enabling particles to grow and therefore to have a higher rate of coagulation. In this case, as surface growth boosts the coagulation of soot particles and nucleation is still an active process, particles are finally distributed in a two-peak PSD shape.
The particles size distribution is then strongly affected by the local gaseous conditions encountered by the particles along their trajectories.

Two other Lagrangian trajectories are studied in Fig.4.19. Both are issued from the fuel injector and their projected trajectories are plotted in Fig. 4.19**a**. However, the first trajectory (in solid lines) ends up with a one-peak PSD shape with a total integrated Lagrangian time $\tau_f = 10.7$ ms, whereas the second one (in dashed lines) ends up with a two-peak PSD shape with a total integrated Lagrangian time $\tau_f = 12.4$ ms. Here, the total Lagrangian time is different for the two trajectories but the final position coincides ($x/D = 78.1$). One trajectory results in a one-peak PSD shape (Fig. 4.19**b**) and the other one in a two-peak PSD shape (Fig. 4.19**c**). Their corresponding final soot sectional source terms are also plotted in Fig. 4.19**b-c** (bars). For both trajectories, at the end, surface growth and coagulation are the main contributors of soot particles evolution. The same orders of magnitude for the final source terms are obtained for both trajectories. However, as the total integrated Lagrangian time $\tau_f$ of the second trajectory is higher than the first one, the particles following the second trajectories spend more time in regions where surface growth is

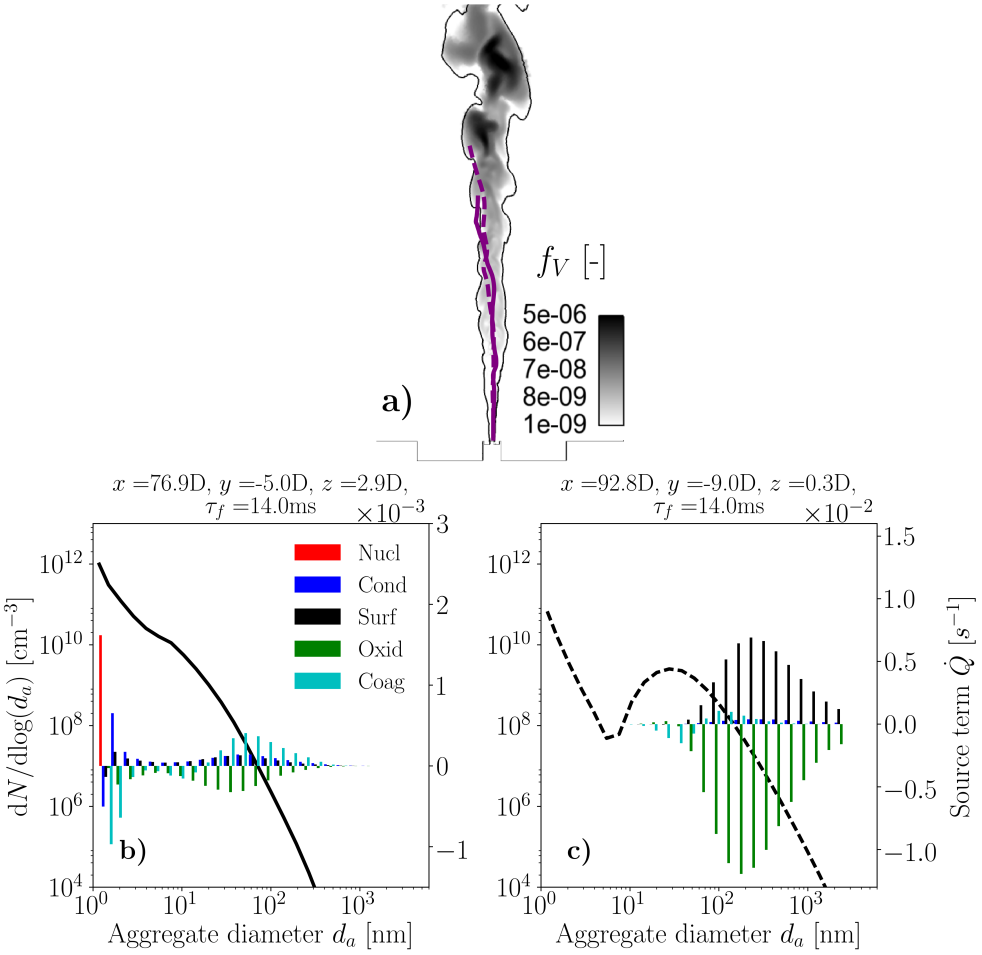


**Figure 4.17:** *Final particles size distributions (lines) and final soot sectional source terms (bars) of two Lagrangian trajectories issued from the center of the jet and with a total Lagrangian time of 14 ms resulting in a one-peak (**b**)) and two-peak (**c**)) PSD shapes. The projected trajectories (in solid purple line for the the trajectory resulting in a one-peak shape and in dashed line for the trajectory resulting in a two-peak shape) are represented with an instantaneous field of soot volume fraction $f_V$ (**a**)).*

active so that a two-peak PSD is finally observed. This analysis is confirmed by looking at the evolution of the Lagrangian time integral of the sum of the surface growth and oxidation source terms (Fig. 4.20**d**), which is linked to the evolution of the Lagrangian temporal mean mass fraction of $C_2H_2$ (Fig. 4.20**a**), of the Lagrangian temporal mean mass fraction of OH (Fig. 4.20**b**) and of the mixture fraction (Fig. 4.20**c**). This quantity evolves in the same way for both trajectories, but as the first trajectory Lagrangian time is shorter than that of the second trajectory, the total accumulated soot mass is lower than the second one, resulting then in a one-peak shape PSD. The total integrated path time of soot history plays also a role in the evolution of the PSD at a fixed position

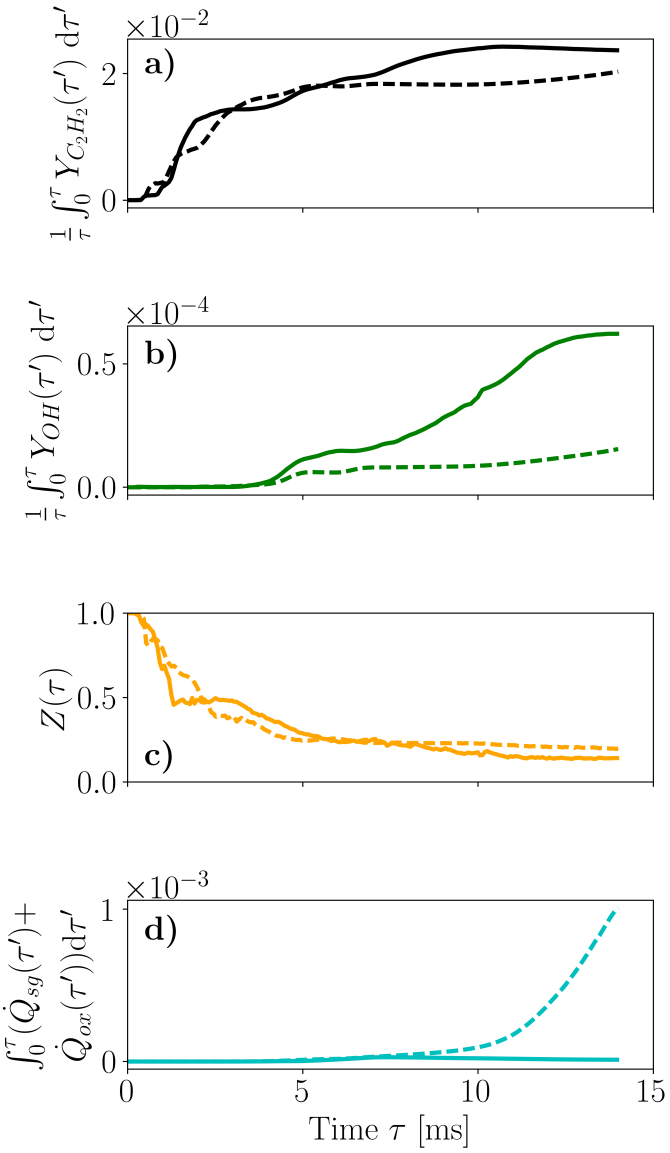


**Figure 4.18:** *Lagrangian temporal mean mass fraction of* $C_2H_2$*, Lagrangian temporal mean mass fraction of* OH*, mixture fraction* $Z$*, and Lagrangian time integral of the sum of the surface growth and oxidation source terms evolutions for the trajectories of Fig. 4.17 resulting in a one-peak PSD shape (solid lines) and in a two-peak PSD shape.*

in the flame.

Overall, it can be concluded that the particles history, i.e. the succession of the chemical and collisional phenomena experienced by the soot population along its trajectory in the flame (mainly driven by turbulence), is responsible for the

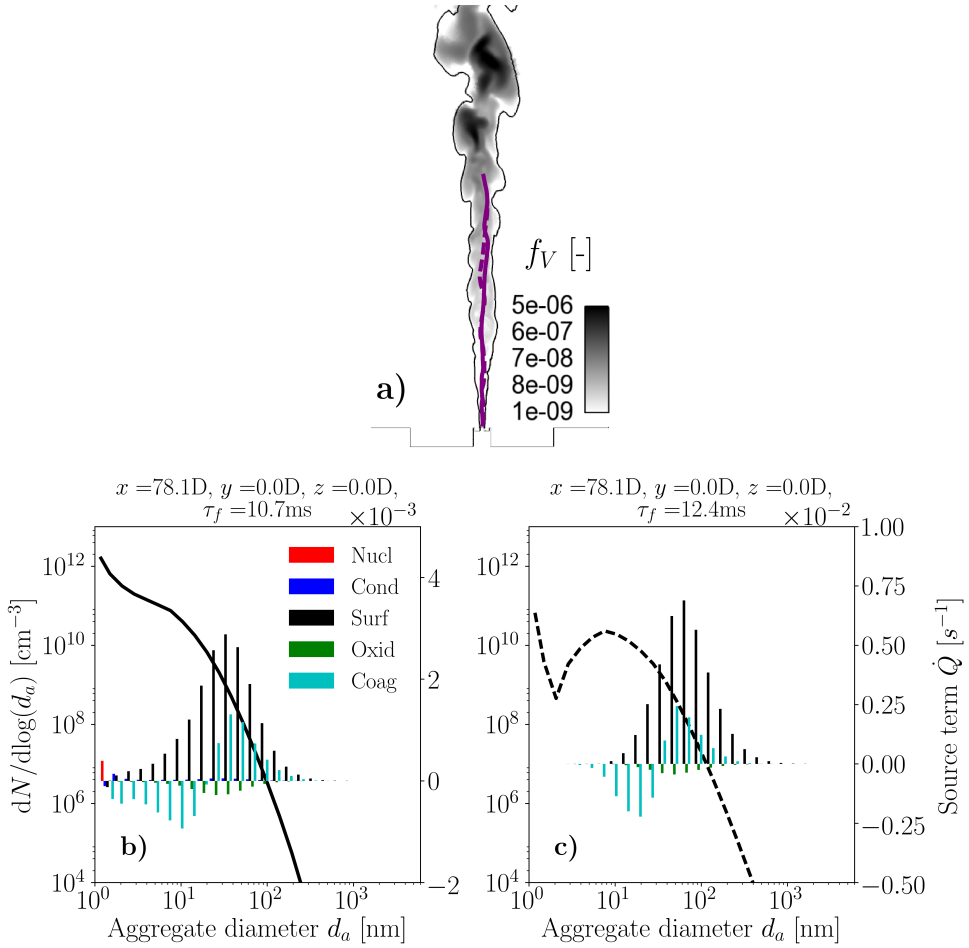


**Figure 4.19:** *Projected trajectories, in solid purple line for the the trajectory resulting in a one-peak shape and in dashed line for the trajectory resulting in a two-peak shape, are represented with an instantaneous field of soot volume fraction $f_V$ (**a**). Final particles size distributions (lines) and final soot sectional source terms (bars) of two Lagrangian trajectories issued from the jet and resulting in a one-peak (**b**) and two-peak (**c**) PSD shapes at the same position.*

high temporal fluctuations observed in the PSD shapes.

## 4.5 Soot presence indexes

Having access to full information on soot quantities in the numerical simulations, it may be interesting to interpret the experimental soot intermittency index in light of the numerical observations. Due to experimental constraints, this quantity is measured by fixing a threshold $\epsilon_{f_V}$ chosen in (Shaddix et al. 2010) as $\epsilon_{f_V} = 0.03$ ppm so that if $f_V$ is lower than $\epsilon_{f_V}$, it is considered that no soot is observed. Therefore, the soot intermittency index, indicating the

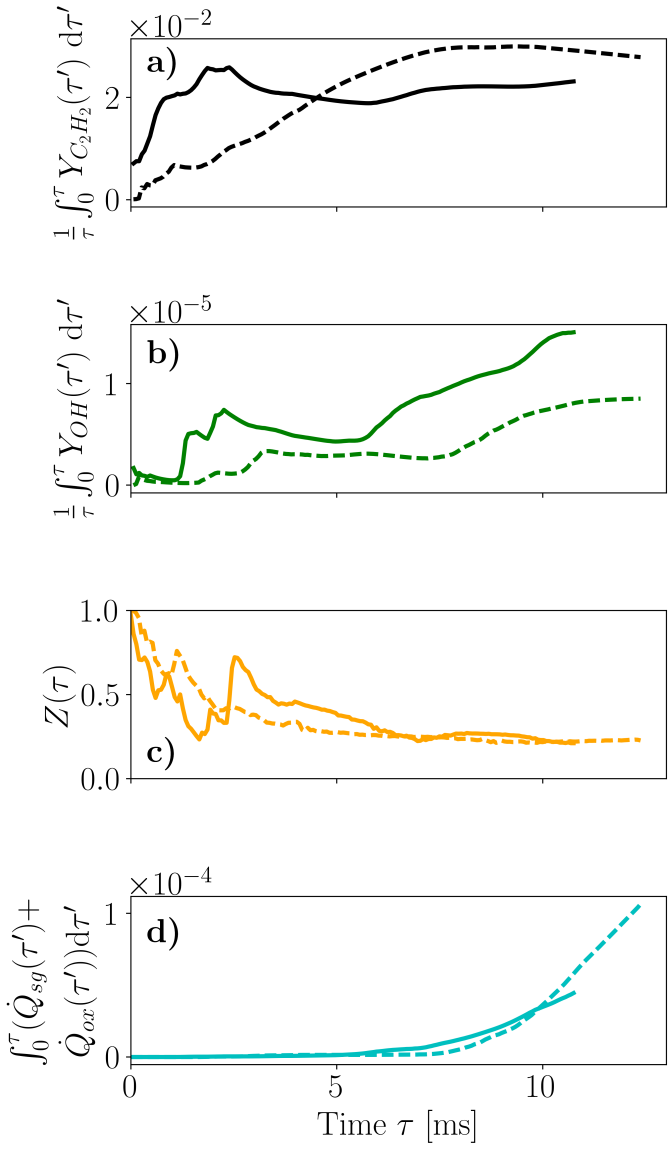


**Figure 4.20:** *Lagrangian temporal mean mass fraction of* $C_2H_2$*, Lagrangian temporal mean mass fraction of* OH*, mixture fraction* $Z$*, and Lagrangian time integral of the sum of the surface growth and oxidation source terms evolutions for the trajectories of Fig. 4.19 resulting in a one-peak PSD shape (solid lines) and in a two-peak PSD shape (dashed lines).*

probability of having (0) or not having (1) soot, may be affected by the value of $\epsilon_{f_V}$. In order to investigate this point, the numerical mean soot index is plotted in Fig. 4.21, while retaining the same threshold. At the bottom of the flame, a very low probability of having soot particles is observed, while high

probability is obtained between $x/D = 75$ and $x/D = 175$.

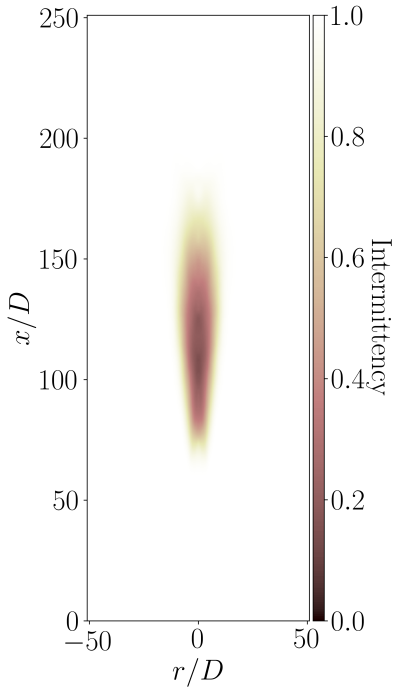


**Figure 4.21:** *Mean field of resolved temporal soot intermittency.*

In addition, Fig. 4.22 presents the temporal evolution of the PSD shape for two selected heights in the transition region ($x/D = 78.1$ and $x/D = 93.8$). A value of one corresponds to a two-peak PSD shape whereas a value of zero corresponds to a one-peak PSD shape. Grey regions correspond to instants where the classical soot intermittency index i.e. $f_V > 0.03$ppm indicates that soot particles are present. High intermittency is observed in soot presence and two-peak PSD shape signals. These results point out the existence of a strong correlation for this flame between the two-peak PSD shape criterion and this definition of soot intermittency index, i.e. that for this specific threshold only two-peak populations of soot are detected.

In order to confirm this correlation, a two-peak PSD shape index is defined as the probability of having (1) or not having (0) a two-peak PSD (Fig. 4.23) and compared with the experimental and numerical results for the classical definition of soot intermittency. As previously observed, a correlation between soot presence and two-peak PSD shape is verified. This can be easily explained by the fact that in the investigated flow configuration, it has been observed that when the simulated soot volume fraction is above the experimental threshold (0.03 ppm), the PSD generally presents a two-peak shape, whereas a one-peak

PSD shape is generally obtained for low values of soot volume fraction ($f_V$), below the experimental threshold.

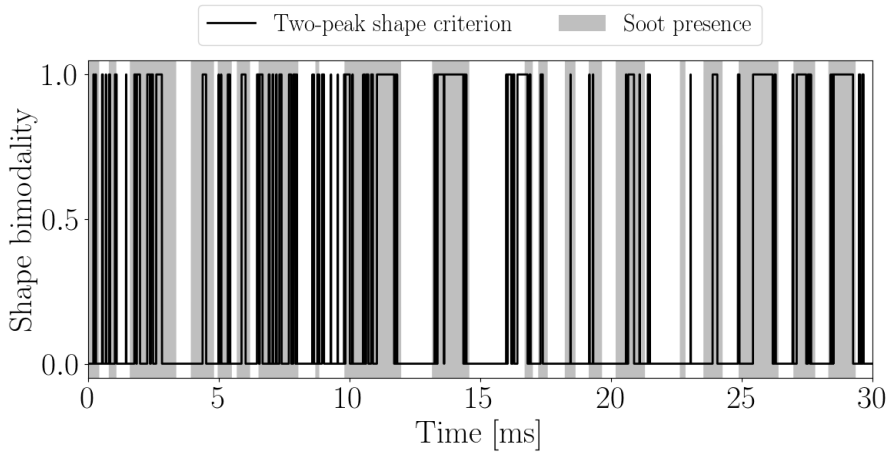


(a) $x/D = 78.1$

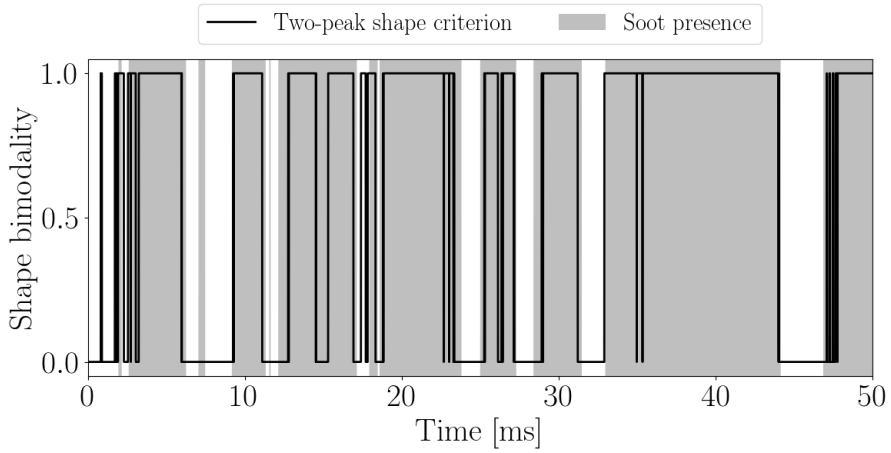


(b) $x/D = 93.8$

**Figure 4.22:** *Time evolution of shape bimodality criterion for two selected heights above the burner. A value of 1 corresponds to a two-peak shape, whereas 0 corresponds to a one-peak shape. Soot presence index is indicated in grey filled regions.*

In addition, a new index based on the probability of having the particles number density $N_{\text{part}}$ below an arbitrary threshold of $4 \cdot 10^{11}$ cm$^{-3}$ has been calculated and is presented in Fig. 4.23. This definition is representative of the zones where soot particles are numerous and is not related to the mass of soot particles. It can be observed that this indicator does not show the same soot presence zones as the other ones. Indeed, with the classical definition of global soot intermittency, no soot presence is detected below $x/D = 60$ while the indicator based on $N_{\text{part}}$ clearly shows a zone where lots of (small) soot particles are

present.
Therefore, due to the experimental threshold, the soot intermittency identifies regions where soot volume fraction is high enough to be measured, and, for this specific configuration, is strongly correlated with presence of a two-peak PSD. However, it is important to note that this observation may vary depending on the studied configuration, and that at this stage no causality between two-peak PSD and soot intermittency can be stated.

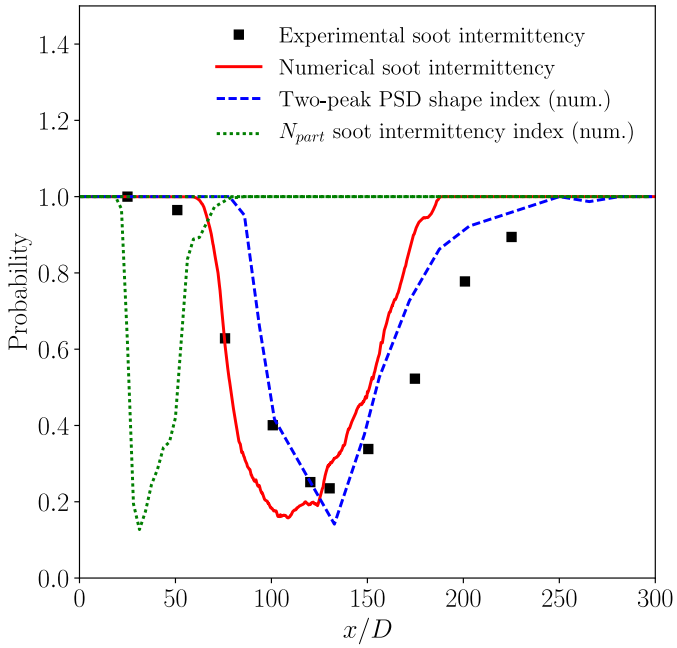


**Figure 4.23:** *Comparison between experimental intermittency index, numerical soot intermittency index, two-peak PSD shape index and soot intermittency index based on $N_{part}$. Experimental data is from Shaddix et al. (2010).*

## 4.6 Conclusion

A Large Eddy Simulation approach has been developed for sooting turbulent non-premixed flames in Chapter 3. It is based on:

- a soot sectional description validated in laminar premixed and diffusion flames at Chapter 1,
- the Radiation Flamelet/Progress Variable for turbulent combustion model including heat losses due to gas phase and soot particles radiation,
- a relaxation model for PAHs evolution description enabling to capture the slow chemistry of soot precursors evolution,
- a soot subgrid model based on a presumed subfilter PDF approach previously developed for the hybrid method of moments, adapted to the

sectional model at 3.

The model is applied in this chapter to the simulation of a jet ethylene-air diffusion flame. A good agreement with experiments is obtained between numerical profiles of mean and RMS temperature and non-quantitative OH profiles compared. Concerning soot evolution, good predictions of soot position and soot volume fraction are obtained. Good dynamics of soot evolution production are also achieved. Indeed, soot intermittency is well predicted compared to experiments, which allows to be confident of the soot particles dynamics description. Once validated, the numerical results have been used to analyze the soot source terms. Surface reactivity of soot particles has been identified as the most important contributions to the total soot mass production and destruction. These observations differ from previous studies. Indeed, depending on the model used to describe the solid phase, previous studies of Bisetti et al. (2012); Mueller and Pitsch (2012) have found that PAH-related soot growth pathways were the major contributor of soot production in this kind of flames but, others (El-Asrag et al. 2007; El-Asrag and Menon 2009) have found that surface and PAH-related growth pathways were responsible in a similar way of soot particles growth. Further fundamental studies are therefore still necessary. Since it is impossible today to say if there really exists a hierarchy among the different processes for all turbulent flames and which model is capable to reproduce it.

In addition, to characterize soot production in turbulent flames:

- Soot particles size distributions have been analyzed thanks to the validated sectional model. A one-peak PSD shape is first observed for $x/D < 70$ whereas a two-peak PSD shape is observed higher in the flame. Once the two-peak shape is obtained and before total oxidation at $x/D \approx 180$, the second peak of the PSD distribution is shifted to bigger soot particles along the flame.
- The temporal evolution of the PSD has been characterized at different positions of the flame. It has been shown that it is subjected to strong fluctuations, whose spanning increases with the height above the burner. In addition, a temporal bimodal region is identified at $70 < x/D < 110$, where both one-peak and two-peak PSD shapes can be observed. By analyzing Lagrangian trajectories, it has been shown that soot history, i.e. the succession of the chemical and collisional phenomena experienced by the soot population along the flame, is responsible for such bimodal behavior.
- Finally, the role of the experimental threshold for the definition of the intermittency index has been investigated. It has been shown that for this configuration, the intermittency index, which is linked to the zones where $f_V$ is high, mainly localizes the presence of a two-peak PSD shape, while it neglects the presence of small particles, generally correlated with the particle number density $N_{\text{part}}$.

# Chapter 5

# LES of a confined pressurized burner

*In this chapter, the proposed turbulent model for soot production developed in Chapter 3 is applied to a confined pressurized non-premixed turbulent ethylene-air flame.*
*The first objective of this simulation is the study of turbulent soot production in a confined burner representative of aero engine combustors at a laboratory scale. The second objective is to study the impact of heat losses on flame stabilization and soot production in such combustors. These two objectives are tackled by comparing simulations considering first, adiabatic conditions, and second, radiative heat losses (optically thin radiation model) and heat exchange by wall conductive fluxes (by imposing measured temperature quartz windows profiles). Based on this analysis, the need for adequate and precise models for heat losses are justified.*
*Finally, differences in soot production behaviors and particles size distributions with the ones obtained by the simulation of the turbulent jet diffusion flame in Chapter 4 are studied and discussed.*

## Contents



## 5.1 Presentation of the configuration

The burner, experimentally studied at DLR (Geigle et al. 2013; Geigle et al. 2015; Geigle et al. 2015; Geigle et al. 2017; Nau et al. 2017), consists of three concentric flows. The combustion chamber geometry is shown in Fig. 5.1. Air at room temperature is supplied to the combustor through a central (diameter 12.3 mm) and an annular nozzle (inner diameter 14.4 mm, outer diameter 19.8 mm). The air flows are fed from separate plenums. Radial swirlers consist of 8 channels (width of 4.2 mm, height of 5.4 mm) for the central nozzle and 12 channels (width of 3.2 mm, height of 4.5 mm) for the annular nozzle.

Gaseous fuel ($C_2H_4$) is injected in between the two air flows through 60 straight channels ($0.5 \times 0.4$ mm$^2$) forming a concentric ring. Thus, the fuel positioning mimics the atomizing lip between swirled air flows as used for spray flames. The exit planes of the fuel and air flows are located at the level of the combustion chamber inlet, being defined as height $h = 0$ mm. The combustion chamber measures 120 mm in height and has a square section of $68 \times 68$ mm$^2$. Four quartz windows (127 mm $\times$ 59 mm $\times$ 3 mm) are mounted between four water-cooled metal posts yielding large optical access of 51.4 mm $\times$ 120 mm to the flame. Finally, secondary oxidation air is injected through 4 transversal inlets at a height $h = 80$ mm.

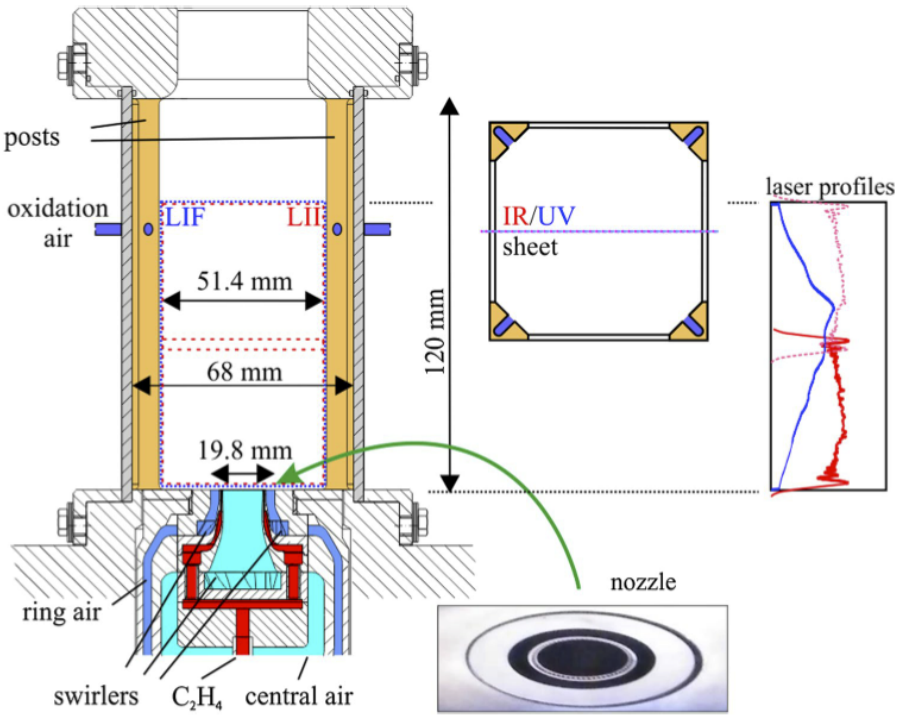


**Figure 5.1:** *Burner geometry (from Geigle et al. (2015))*

The burner including the cooling system was designed for operation at approximately 10 kW/bar thermal power. The flow rates applied for the considered operating condition, given in standard liters per minute (slpm), are shown in Table 5.1.

| $p$ [bar] | $\Phi$ | $P$ [kW] | $Q_{\mathrm{air,c}}$ [slpm] | $Q_{\mathrm{air,r}}$ [slpm] | $Q_{\mathrm{fuel}}$ [slpm] | $Q_{\mathrm{oxi}}$ [slpm] | $Q_{\mathrm{air,c}}/Q_{\mathrm{air}}$ | $Q_{\mathrm{oxi}}/Q_{\mathrm{air}}$ | $\Phi_{\mathrm{global}}$ | $P_{\mathrm{global}}$ [kW] |
|---|---|---|---|---|---|---|---|---|---|---|
| 3.0 | 1.2 | 32.2 | 140.8 | 328.5 | 39.3 | 187.4 | 0.3 | 0.4 | 0.86 | 38.6 |

**Table 5.1:** *Flame parameters of the studied case (flow rates are referenced at STP conditions: 1.013bar and 273K).*

The equivalence ratio $\Phi$ and thermal power $P$ were calculated from the primary air flow rate $Q_{\mathrm{air}}$ as a sum of central ($Q_{\mathrm{air,c}}$) and ring air ($Q_{\mathrm{air,r}}$), whereas the global equivalence ratio $\Phi_{\mathrm{global}}$ and the global thermal power $P_{\mathrm{global}}$ were calculated from the total air flow rate, $Q_{\mathrm{air}} + Q_{\mathrm{oxi}}$ (where $Q_{oxi}$ corresponds the secondary oxidation air flow rate). The variable amount of oxidation air is given as fraction $Q_{\mathrm{oxi}}/Q_{\mathrm{air}}$. The air split ratio is defined as the ratio of central air to the total combustion air $Q_{\mathrm{air,c}}/Q_{\mathrm{air}}$. Note that due to the excess fuel the value for $P$ is purely a function of the combustion air mass flow rate whereas $\Phi_{\mathrm{global}}$ changes to lean after injection of oxidation air and thus $P_{\mathrm{global}}$ depends on the fuel mass flow rate.

Comprehensive validation data obtained by several laser diagnostics is available for each operating point. In the present work, the following measurements are used for model validation: velocity components by stereo-PIV (Particle Image Velocimetry) (Geigle et al. 2017), temperature by CARS (Coherent Anti-Stokes Raman) (Geigle et al. 2015), soot volume fraction by Laser-Induced Incandescence (LII) (Geigle et al. 2013), OH by Laser-Induced Fluorescence (LIF) (Geigle et al. 2013), and wall temperatures by Laser-Induced Phosphorescence (LIP) (Nau et al. 2017).

It is important to notice that based on Laser Induced Incandescence (LII) measurements (Geigle et al. 2013), soot volume fraction is low in this configuration with a maximum time-averaged soot volume fraction of approximatively 30p̃pb. This value is twenty times lower than the soot volume fraction magnitude observed in the turbulent jet flame studied in Chapter 3. That is why soot particles are not expected to play an important role on thermal radiation for this configuration compared with gas phase contribution.

## 5.2 Numerical set-up

### 5.2.1 Geometry, boundary conditions and numerical grid

Figure 5.2 presents the geometry used for the calculations. In Fig. 5.2 (a), the different parts of the geometry are shown: the primary injection system composed of two swirled air injectors (central and ring) and the fuel injector between them; the combustion chamber with the secondary air injections at a distance of 80 mm from the primary injectors exit; and finally, a fictitious ambient air environment enabling to impose a far pressure boundary condition for the system. Figure 5.2 (b) illustrates more precisely each one of these inlets, especially the three different inlets composing the primary injection and the four secondary air injections.

Temperature, scalar values and velocities are imposed at the inlets, while pressure is imposed at the outlet. Navier-Stokes Characteristic Boundary Conditions (NBCBC) (Poinsot and Lele 1992) are used to prescribe the boundary conditions at the inlets and outlets. Adiabatic and slip boundary conditions are imposed at the walls of the injectors. For the combustion chamber walls, a wall law model (Jaegle et al. 2010) is used for determination of temperature and velocities near the walls.

The numerical grid contains 40.5 millions of tetrahedra cells and 7.15 millions of nodes. Mesh refinement has been considered in the flame region and near the secondary air injections. The smallest cell size is located in the fuel injectors, with 6 cells in the fuel injector 0.4 mm width, leading to a smallest cell size of

approximatively 60 $\mu$m. Figure 5.3 presents the numerical grid in this refined region.

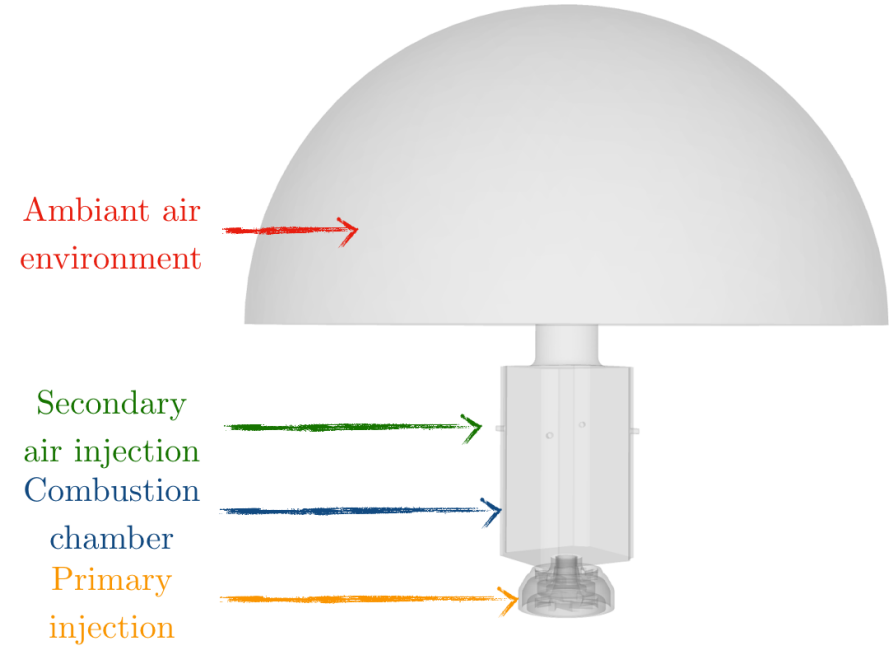


(a) Global view

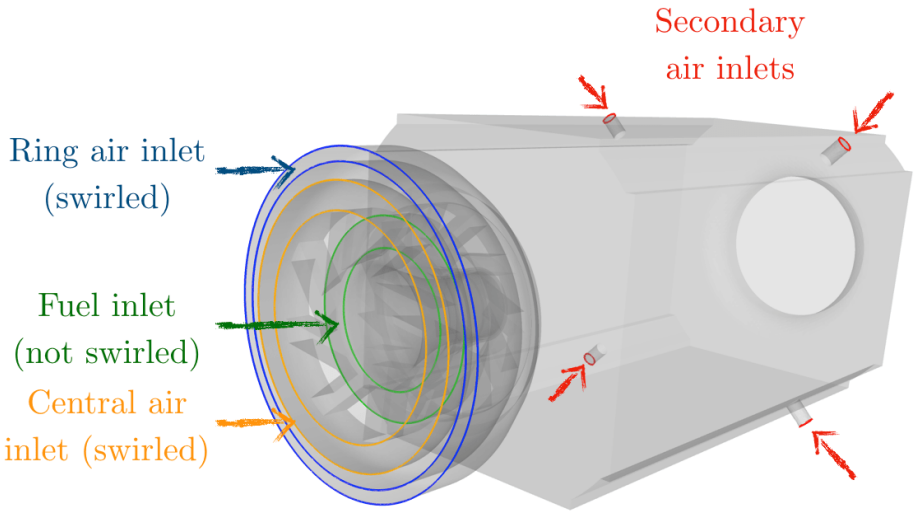


(b) Inlets

**Figure 5.2:** *Geometry used in the numerical simulations*

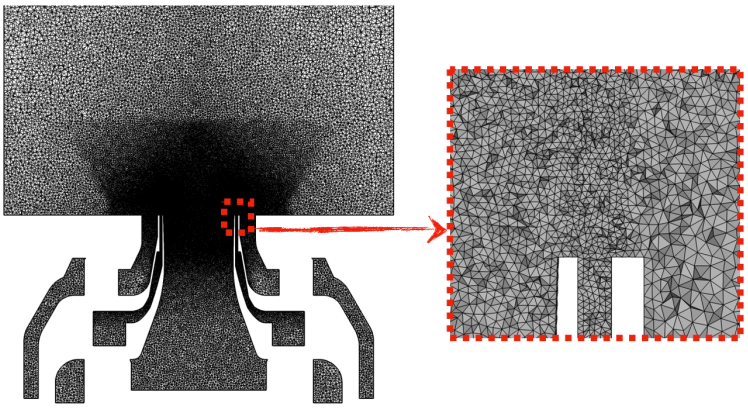

**Figure 5.3:** *Numerical grid: local refinements near injectors.*

### 5.2.2 Modeling

The same numerical modeling as the one used in the simulation of the jet diffusion flame presented in Chapters 3 and 4 has been considered. As the pressure is different, a new flamelet database at 3 atm has been generated for the RFPV model and the LES soot production modeling. The corresponding lookup table is discretized with $100 \times 20 \times 100 \times 20$ grid points in the $\widetilde{Z}$, $S_Z$, $\overline{C}$ and $\overline{H}$ directions, respectively. The third-order in space and time finite element TTGC scheme (Colin and Rudgyard 2000) is retained for this simulation. The more recent SIGMA subgrid model (Nicoud et al. 2011) is here used instead of the Wale model (Nicoud and Ducros 1999), previously considered in Chapter 4, in order to access correctly the subgrid stresses in such swirled flow.

Several numerical cases, called R$l$W$m$S$n$, are considered depending on the description of thermal radiation, wall boundary conditions and soot description. Radiation models R0 and R1 respectively correspond to cases without considering radiation and with an optically thin assumption (OTA), respectively. For the wall treatment, adiabatic (W0) and wall imposed temperature (W1) are considered at the combustion chamber walls. These imposed temperatures are extrapolated from the measurements of quartz windows centerline temperature measurements from Nau et al. (2017) considering uniform temperature in the spanwise direction for a given height. At the bottom walls, a constant temperature estimated equal to 650 K has been considered. Cases without considering soot formation (S0) and considering the soot sectional LES formalism (S1) developed in Chapter 3 are also considered. All these cases are referenced in Table 5.2. The cost for the simulation of the case R0W0S1 is 400 000 CPU hours on Intel E5-2590V3 cores for an averaging time of statistics $\tau = 40$ ms. The relative costs of the others simulations are gathered in Tab. 5.2.

| Case | Gaseous Description | Radiation Modeling | Walls Treatment | Soot Description | Rel. Cost |
|---|---|---|---|---|---|
| **COLD** | - | None | None | None | 0.15 |
| **R0W0S1** | KM2+RFPV | Adiab. | Adiab. | Sectional | 1.0 |
| **R1W0S0** | KM2+RFPV | OTA | Adiab. | None | 0.25 |
| **R1W1S1** | KM2+RFPV | OTA | Imposed Temp. | Sectional | 1.03 |

**Table 5.2:** *Definition of the different numerical cases.*

Figure 5.4 presents the temperature field imposed for the quartz windows boundary condition for the case R1W1S1. It is based on LIP measurements (Nau et al. 2017) along the axis of the quartz window ($y = 0$). The bottom wall is imposed at 650 K based on DLR communication.

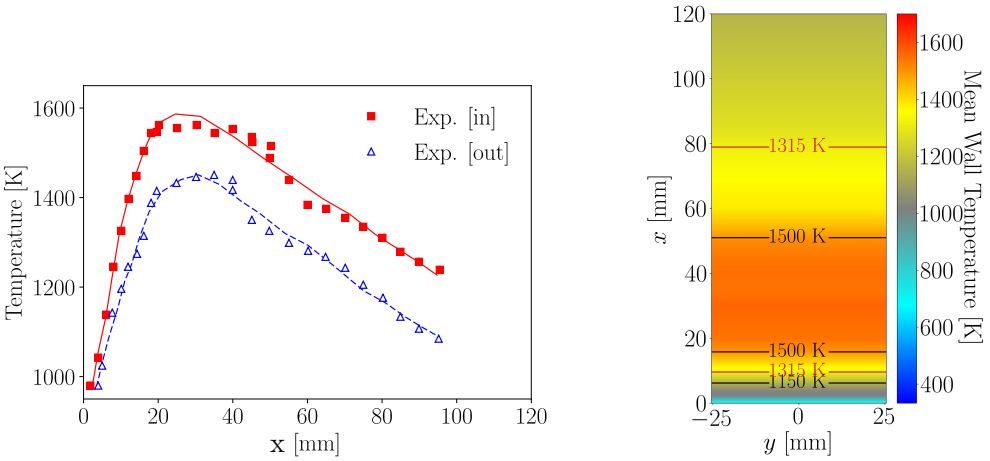


(a) Internal (in) and external (out) faces experimental axial temperature profiles of the quartz windows (from Nau et al. (2017))

(b) Imposed temperature field at the quartz windows surfaces

**Figure 5.4:** *Definition of the quartz windows temperature boundary condition for the case R1W1S1.*

## 5.3 Cold case

Figure 5.5 presents a comparison of the numerical and experimental velocity fields colored by tangential velocity for the COLD numerical case referenced in Tab. 5.2. Velocity vectors based on the axial and radial components of the velocity fields are also compared. A good agreement is obtained between numerical and experimental fields. The inner recirculating zone is also indicated with an iso-line of null-axial velocity. A good agreement is also obtained between experimental and numerical recirculating zones.

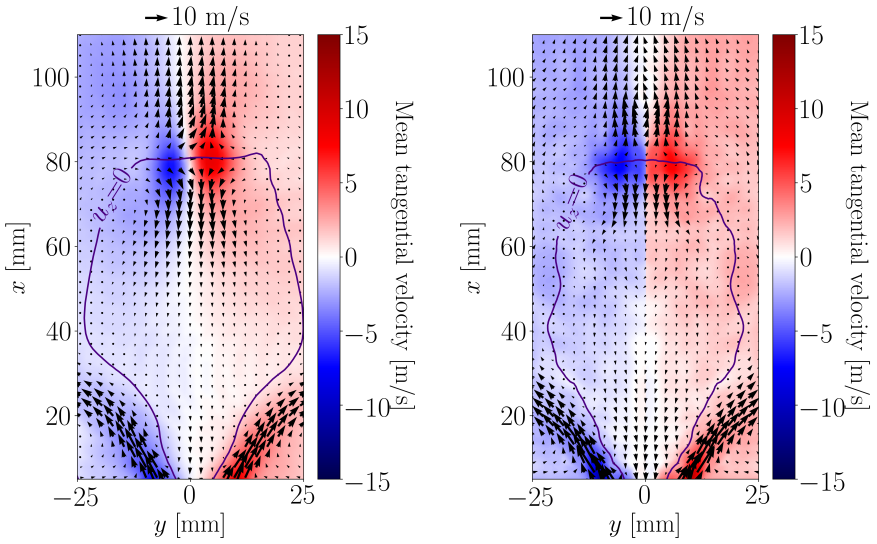


(a) Experimental field (Geigle et al. 2017) (b) Numerical field

**Figure 5.5:** *Cold case: comparison of experiment and numerical velocity fields colored by tangential velocities. Arrows correspond to the velocity vectors based on the axial and radial velocity vector components. The arrow at the top of the figure corresponds to a velocity of 10 m/s.*

Figure 5.6 compares respectively the axial, radial and tangential profiles between numerical predictions and experiments.
Up to $x = 26$ mm, a good agreement with experiments is obtained. However, for $x = 71$ mm and near the secondary air jets, it can be observed that differences between numerical predictions and experiments are more pronounced. In this region, the opposite secondary air jets collide and generate a stagnation flow. The flow then splits into one part that goes to the top of the chamber and another one that moves upstream. The difference at $x = 71$ mm is due to an underestimation of the part of the flow moving upstream as seen in Fig. 5.5 as well. The error could be attributed to a non-ideal jet alignment in the experiment and to an effect of the coarsening mesh in the 2$^{\text{nd}}$ half of the chamber.

## 5.4 Reactive case

### 5.4.1 Velocity

In this section, reactive flow experimental velocity fields are compared to numerical results obtained for the different cases of Table 5.2.
Figure 5.7 shows the comparison of experimental and numerical fields of tangential velocities. Arrows correspond to the velocity vectors based on the axial and radial velocity vector. The numerical field corresponds to the case R1W1S1. Two series of measurements are presented: the sum of correlations method

(SoC) enabling to have a global view of the velocity fields and the field of view (FoV) method, which is more accurate but only enables to access a smaller part of the velocity fields. According with DLR communication, numerical results will be compared to the FoV measurements. The purple isoline corresponds to the line where null axial velocity is observed and enables to identify the inner and outer recirculating zones.

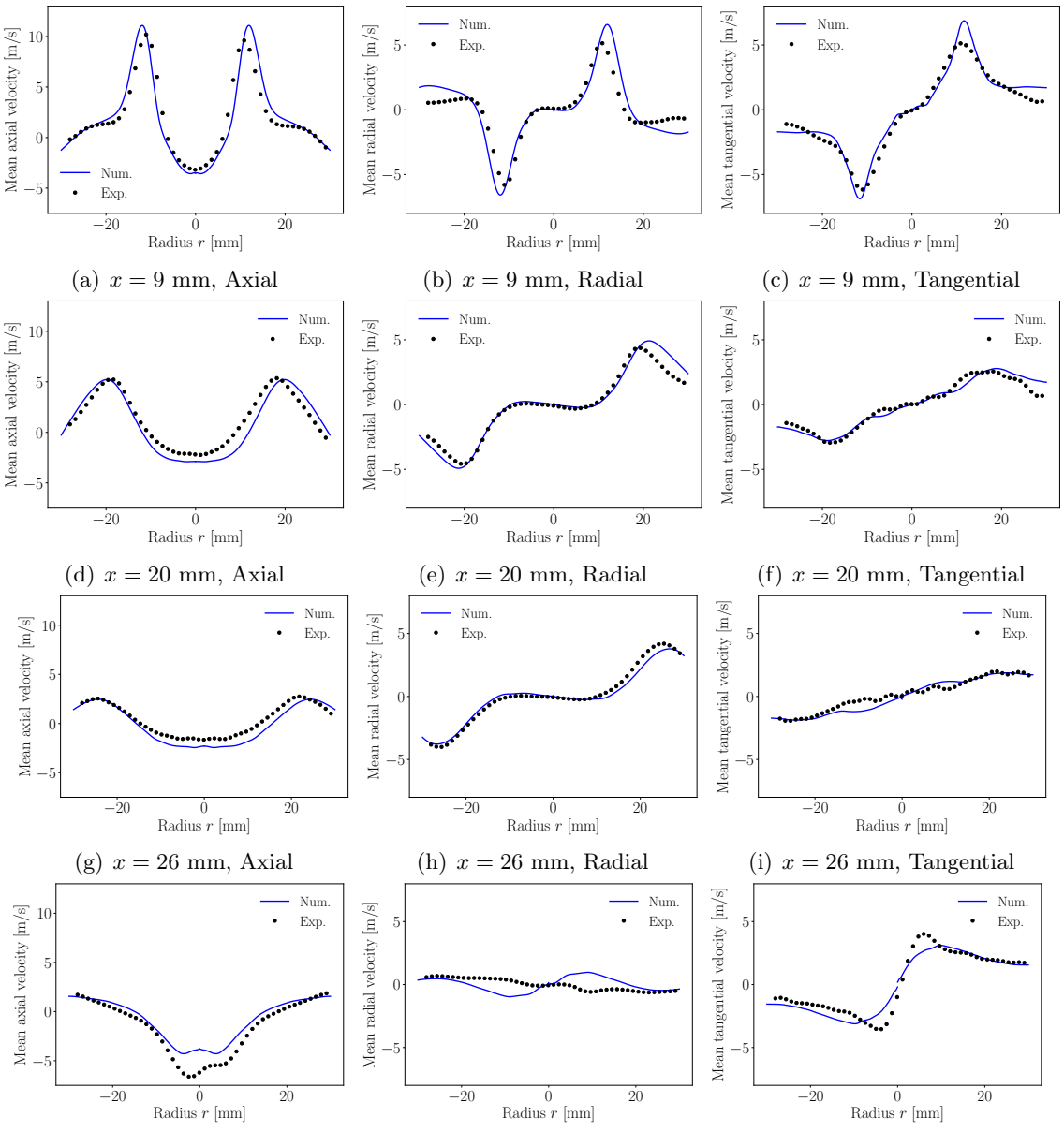


(a) $x = 9$ mm, Axial (b) $x = 9$ mm, Radial (c) $x = 9$ mm, Tangential

(d) $x = 20$ mm, Axial (e) $x = 20$ mm, Radial (f) $x = 20$ mm, Tangential

(g) $x = 26$ mm, Axial (h) $x = 26$ mm, Radial (i) $x = 26$ mm, Tangential

(j) $x = 71$ mm, Axial (k) $x = 71$ mm, Radial (l) $x = 71$ mm, Tangential

**Figure 5.6:** *Comparison of axial, radial and tangential velocity profiles at different heights above burner, compared with PIV measurements (Geigle et al. 2017).*

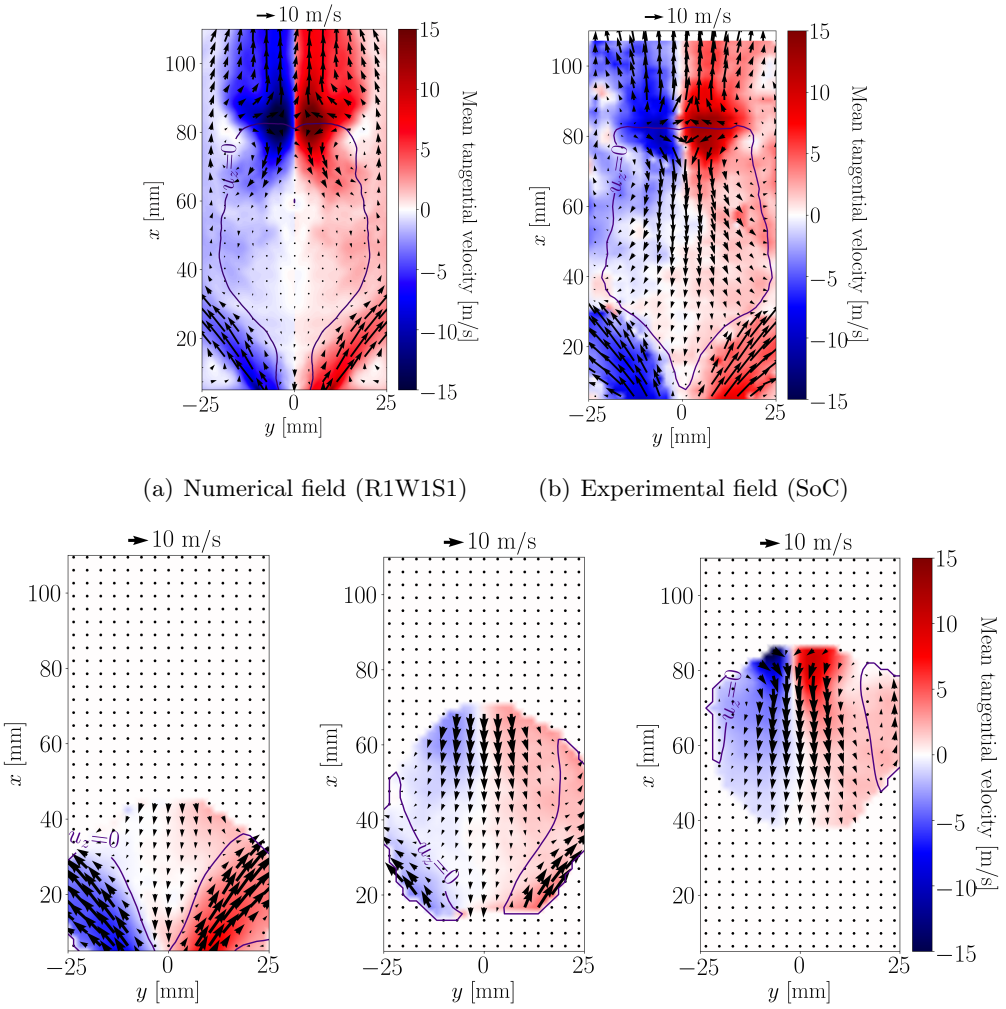


(a) Numerical field (R1W1S1) (b) Experimental field (SoC)

(c) Experimental field (FoV bottom) (d) Experimental field (FoV middle) (e) Experimental field (FoV top)

**Figure 5.7:** *Reactive case: comparison of experimental and numerical fields of tangential velocities. Arrows correspond to the velocity vectors based on the axial and radial velocity vector components. The arrow at the top of the figures corresponds to a velocity of 10 m/s. The two types of experimental measurements are represented: the sum of correlation method (SoC) and field of view methods (FoV) for each method (data are from Geigle et al. (2017) and communication from DLR)*

A fair general agreement is obtained for the velocity fields and the recirculating zone. A major discrepancy is however observed for the inner recirculating zone which is more intense in the experimental measurements compared to numerical predictions. This can be explained by the numerical difficulty on predicting correctly the splitting of secondary air injection, and the corresponding air momentum that goes downstream the combustor.

Figure 5.8 compares the predicted velocity fields for the three studied cases with the experimental measurements (field of view and sum of correlations). A good general agreement is obtained for the considered heights where the flow stabilizes. Stronger discrepancies are obtained with the case R0W0S1, which predicts a narrower inner recirculating zone compared to experiments and the other simulated cases (see Figs. 5.8 (d) and (g)). Intensity of the inner recirculating zone at the selected heights are generally slightly under-predicted compared with experiments.

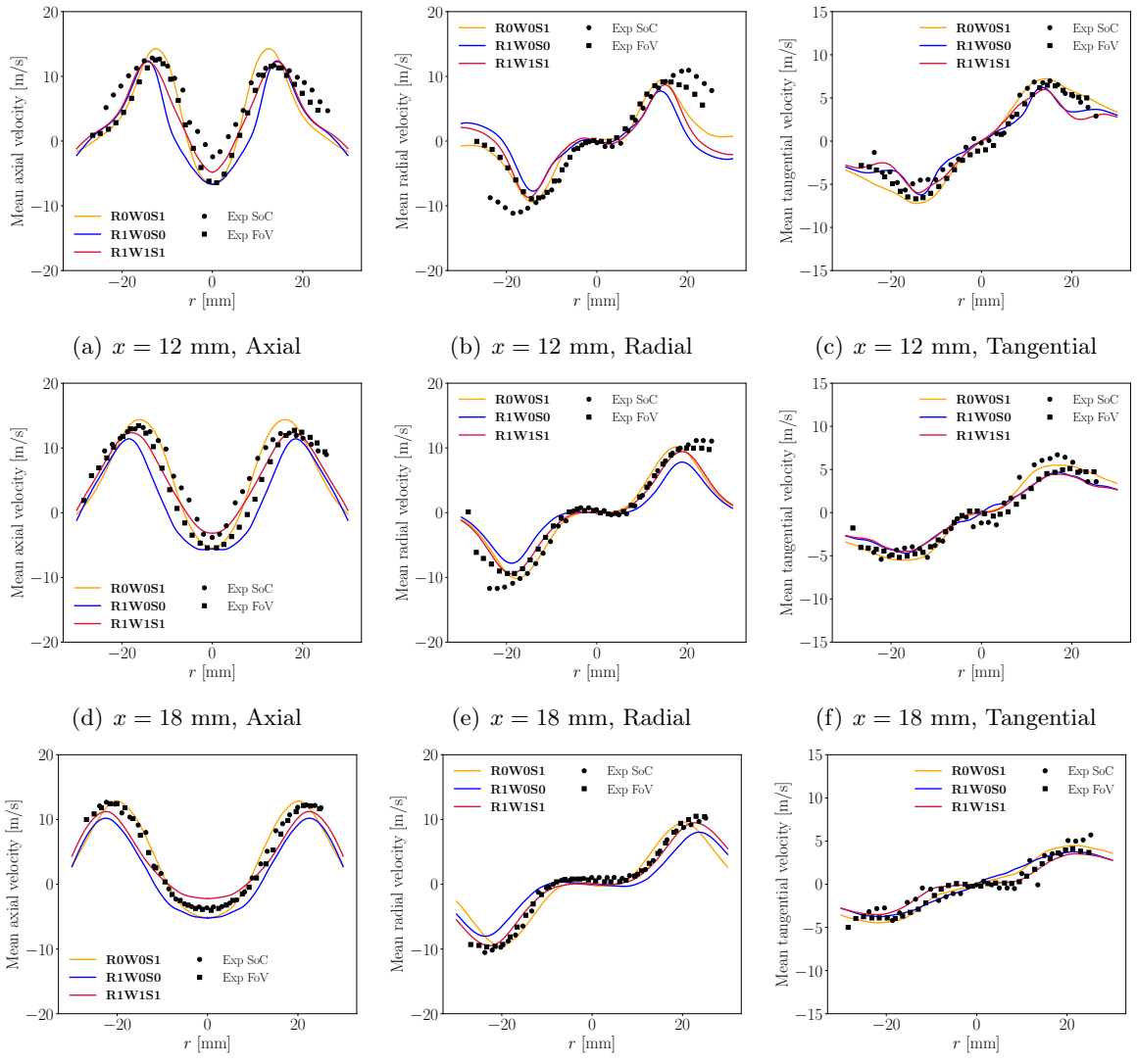


(a) $x = 12$ mm, Axial (b) $x = 12$ mm, Radial (c) $x = 12$ mm, Tangential

(d) $x = 18$ mm, Axial (e) $x = 18$ mm, Radial (f) $x = 18$ mm, Tangential

(g) $x = 24$ mm, Axial (h) $x = 24$ mm, Radial (i) $x = 24$ mm, Tangential

**Figure 5.8:** *Reactive case: comparison of numerically predicted axial, radial and tangential velocity profiles at different positions above burner with PIV FoV and SoC measurements (Geigle et al. 2017).*

### 5.4.2 Temperature fields

Figure 5.9 compares the predicted instantaneous temperature fields between the different cases. Impacts of heat losses can be observed on flame stabilization position, flame shape but also burnt gases temperature:

- Cold gases from secondary air inlets are entrained in the inner recirculation zone (IRZ). Thus, a mixing between these cold air gases and the hot burnt gases from combustion is observed and a lower temperature in the IRZ is obtained.
- The same flame stabilization height is obtained for the cases R1W0S0 and R1W1S1. The flame stabilizes in the injector for the adiabatic case (case R0W0S1) whereas it stabilizes in the chamber when radiation is accounted for (cases R1W0S0 and R1W1S1).
- In high temperature regions, a decrease of temperature is obtained when considering radiative heat losses (R1W0S0) compared to the adiabatic case.
- A decrease of temperature near walls, mainly in the outer recirculating zone (ORZ), is obtained when considering wall heat losses (R1W1S1).

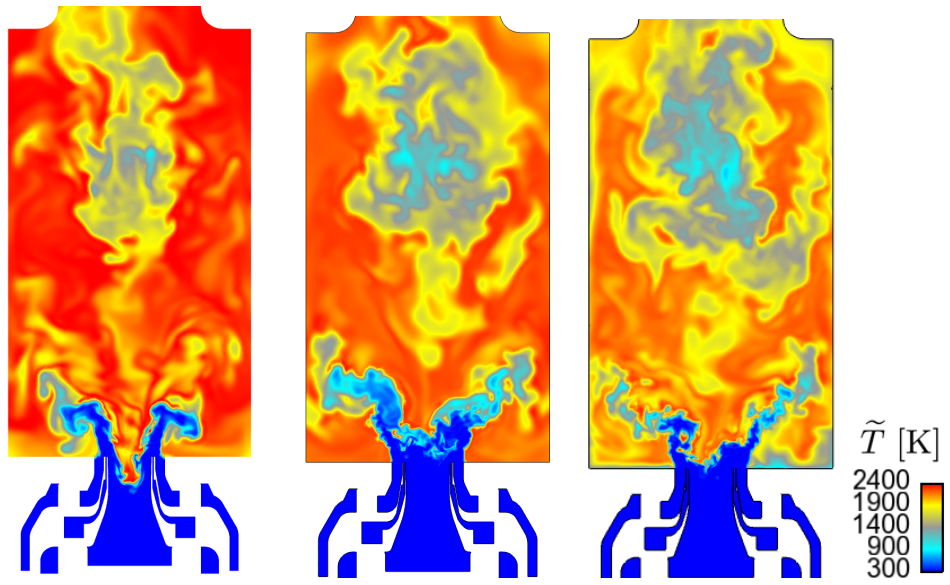


(a) Case R0W0S1 (b) Case R1W0S0 (c) Case R1W1S1

**Figure 5.9:** *Instantaneous fields of temperature*

Figure 5.10 compares the predicted mean temperature fields between the different cases. Similar features as in instantaneous fields are observed:

- Lower temperatures in the inner recirculation zones due to the entrainment in this region of the cold air injected through the secondary air oxidation inlets.

- A decrease of temperature when considering radiative heat losses with the optically thin radiation model (R1W0S1).
- Isothermal boundary conditions decrease temperature in the outer recirculating zones (R1W1S1).

Moreover, different flame opening are observed for the three studied cases. The opening angle of the swirled flame is higher in the case accounting for radiative heat losses (R1W0S0) compared with the case that not considers any heat losses (R0W0S1). The flame stabilizes also more downstream in this case. When taking also into account wall heat losses (R1W1S1), the mean flame position is nearly the same and its opening angle is even more higher.

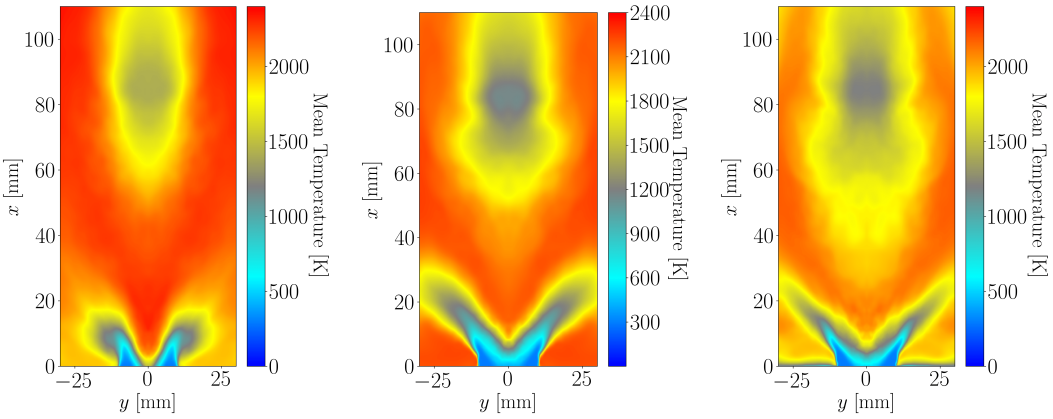


(a) Case R0W0S1 (b) Case R1W0S0 (c) Case R1W1S1

**Figure 5.10:** *Mean fields of temperature.*

Figure 5.11 compares the axial profiles ($y = 0$) of temperature of the different cases with experimental measurements. For all cases, temperature increases at the flame front near x = 0 mm. The experimental mean position of the flame front is located between x = 0 mm and x = 12 mm. This flame position is well retrieved for the cases considering heat losses (cases R0W1S1 and R1W1S1) compared with the adiabatic case (case R0W0S1), which predicts a flame position too upstream in the combustion chamber anchoring inside the swirling injector. At higher heights, due to secondary air injection of cold air, burnt gases mix with recirculating leaner and cooler pockets of burnt gases. Then, the mixture axial temperature decreases until x = 80 mm corresponding to the position of the secondary cold air injection. At higher heights, near combustor exit, this mixture mixes with burnt gases not cooled by the secondary cold air injection and coming from the sides of the combustion chamber. Then, the axial temperature increases again. The overall axial temperature is overestimated

by approximatively 100 K compared with experimental measurements in case R0W0S1. In case R1W0S1, the optically-thin radiation model implies an important decrease of axial temperature due to radiative heat losses. Considering also wall heat losses, the axial temperature decreases again and is underestimated by approximatively 100 K compared with the experimental data for $x \in$ [15 mm, 60 mm]. One can suggest that this underestimation can be explained by the overestimation of radiative heat losses when using the optically thin radiation model.

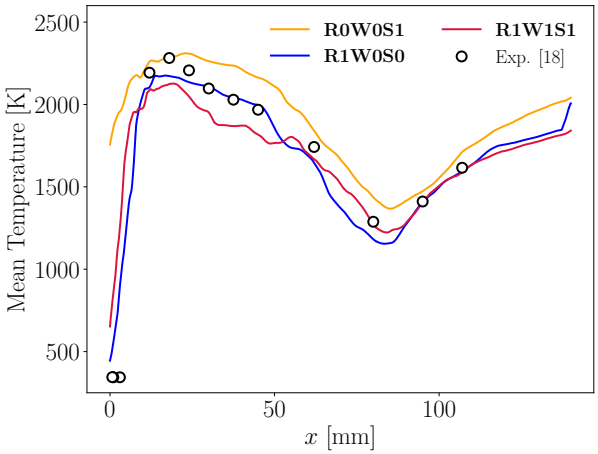


**Figure 5.11:** *Comparison of axial mean temperature profiles with experiments (Geigle et al. 2015).*

In order to study closely the impact of heat losses, Fig. 5.12 compares the radial profiles of mean temperature of the different cases with experimental measurements. At all different heights, radiative heat losses accounted for in cases R1W0S0 and R1W1S1 enable to have a good prediction of mean temperature. Near wall temperature is controlled by wall heat losses. Except for $x = 1$ mm, the hierarchical behavior between the three cases is again retrieved: temperature is higher for the case R0W0S1 which does not account for heat losses compared with case R1W0S0 that accounts for radiative heat losses. This last case presents near wall temperatures higher than the ones obtained in case R1W1S1, which accounts also for wall heat losses. Compared with experiments, a good general agreement is obtained for the case R1W1S1. Near bottom wall ($x = 1$ mm: Fig. 5.12 (a)), temperature is slightly overestimated for the case R1W1S1 compared with experimental measurements. In case R1W0S0, only radiative heat losses are considered and temperature is largely overestimated. In case R0W0S1, the temperature is lower than in case R1W0S0 as flame anchors in this region for case R0W0S1 whereas only burnt gases are present in this region for case R1W0S0. Uncertainties on the thermal boundary condition imposed at the bottom wall (considered here at 650 K, but with an uncertainty of $\pm$ 100 K as estimated by DLR) can explain the remaining deviation for

case R1W1S1. For $x = 18$ mm, the radial profiles cross the flame: the mean flame brush is well predicted at this position for the case R1W0S0 whereas it is underpredicted for the case R1W1S1.

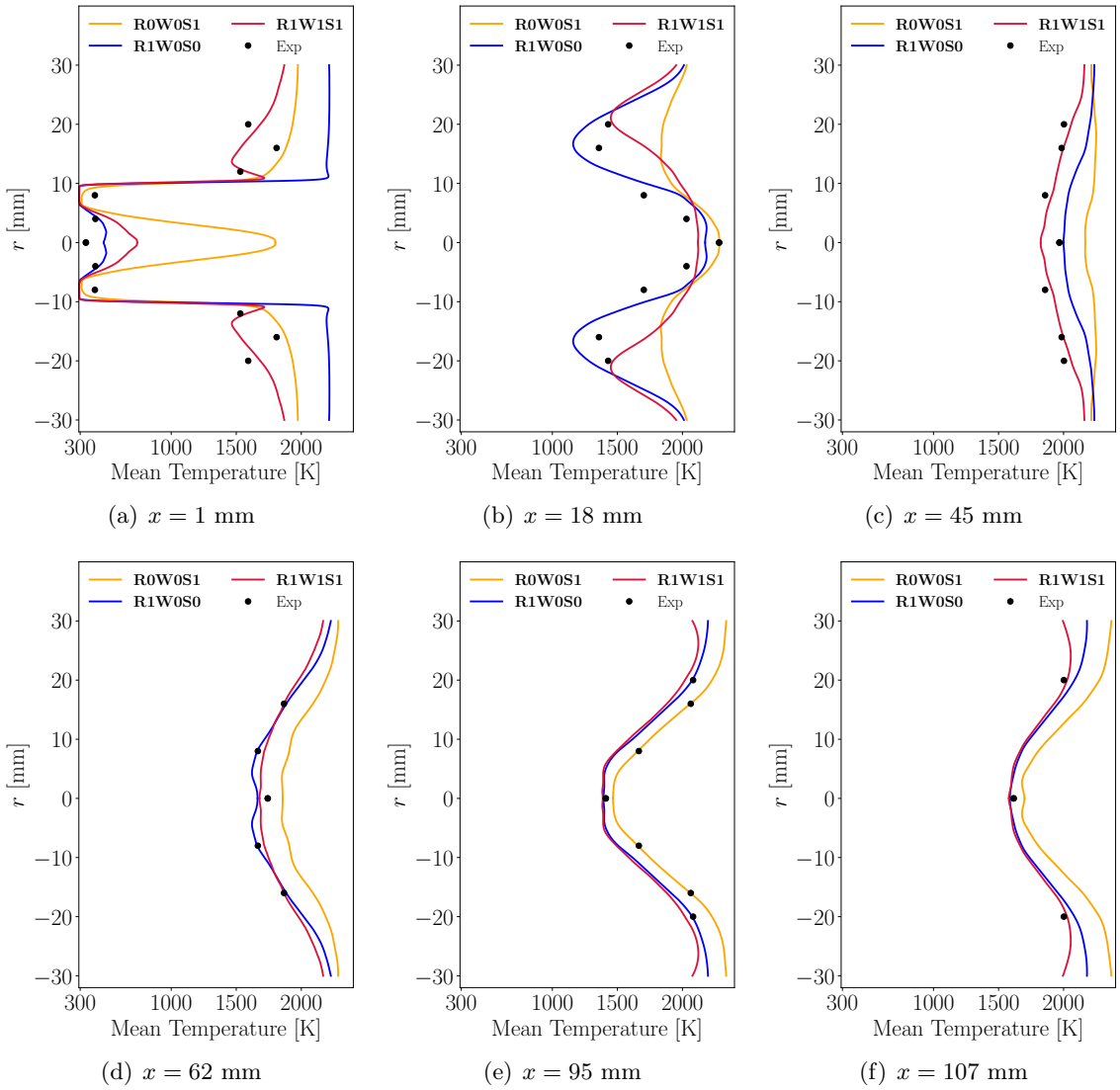


(a) $x = 1$ mm (b) $x = 18$ mm (c) $x = 45$ mm

(d) $x = 62$ mm (e) $x = 95$ mm (f) $x = 107$ mm

**Figure 5.12:** *Comparison of radial mean temperature profiles with experiments.*

Finally, the models used for heat transfer description have a strong impact on temperature fields, flame stabilization and flame shape. The models considered here for the three studied cases are quite simple (optically thin radiation model and imposed wall temperature) and precise model are then required in order to correctly describe flame properties. Results with more advanced models will be investigated in Chapters 8 and 9.

### 5.4.3 Analysis of combustion regime

In order to identify regions where combustion occurs and to validate the description of these regions, Fig. 5.13 compares the normalized experimental OH* chemiluminescence field with the predicted normalized mean heat release field. This comparison is known to work in premixed flames. While the validity of this comparison has not been demonstrated in diffusion combustion regimes, it is considered here as a first indicator for comparison. Mean flame broadening is under-predicted in the case R0W0S1 and is slightly upstream compared to experiments. In the case R1W0S0, the mean flame broadening is over-predicted and important heat release can be observed near lateral walls, whereas it is not observed experimentally. Finally, in the case R1W1S1, heat release position and broadening is well retrieved and wall heat losses prevent near wall heat release observed in the case R1W0S0, which considered only radiative heat losses.

Even if ethylene and air are not premixed before injection in this configuration, the combustion does not correspond necessarily to a diffusion regime. The combustion regime can be determined looking at flame indexes, such as the Takeno index $I_{\text{Takeno}}$ defined as:

$$I_{\text{Takeno}} = \left. \frac{\nabla Y_{O_2} \cdot \nabla Y_{C_2H_4}}{\left|\nabla Y_{O_2}\right| \cdot \left|\nabla Y_{C_2H_4}\right|} \right|_{\dot{\omega}_{Y_C} > \epsilon} \tag{5.1}$$

$\dot{\omega}_{Y_C}$ corresponds to the progress variable source term (representative of the heat release rate) and $\epsilon = 0.1$ s$^{-1}$ is here chosen in order to only consider positions where combustion occurs, masking then values where only mixing occurs.
The Takeno index $I_{\text{Takeno}}$ indicates the combustion regime: for a value near 1, gradients of fuel and oxidant are aligned and a premixed combustion is identified; for a value near -1, gradients of fuel and oxidant are opposed and a diffusion type of combustion is identified. Figure 5.14 presents the time-averaged Takeno index for the different cases.

Different combustion regimes coexist in this particular flame. First, near the injectors exit, a diffusion combustion regime is observed: burning of reactants is observed without their preliminary mixing. Downstream, reactants are sufficiently mixed to burn in a premixed regime. This regime reveals to be predominant for the primary combustion. As the equivalence ratio based on the primary injection is rich, unburnt hot gases still remain after this first combustion step. They react in a diffusion-like combustion regime downstream when encountering flow coming from secondary injection. By comparing the three numerical simulations, it can be observed that when not considering heat losses, the flame stabilization is different and diffusion combustion regime is more pronounced compared with the two other cases. Let us note that the chosen flamelet model (RFPV) to describe gaseous chemistry is a diffusion flame model. In light of the

observed combustion regime with both premixed and diffusion regimes, future studies should consider an hybrid approach to describe such a complex regime.

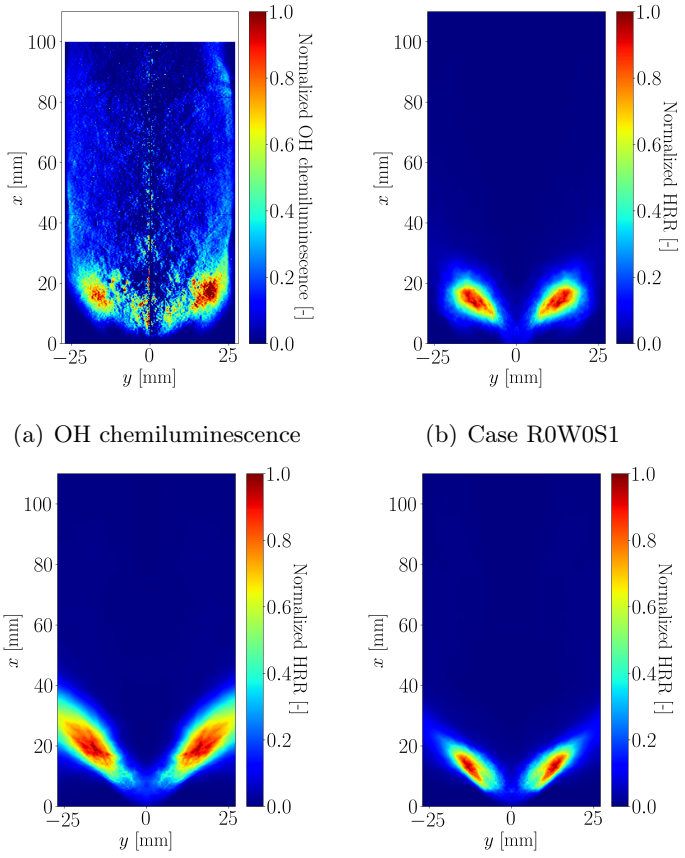


(a) OH chemiluminescence (b) Case R0W0S1

(c) Case R1W0S0 (d) Case R1W1S1

**Figure 5.13:** *Comparison between normalized experimental Abel deconvoluted OH* chemiluminescence and predicted normalized mean heat release rate fields.*

Figure 5.15 presents different scatter plots of temperature as a function of mixture fraction $Z$. From Figs. 5.15 (a) to (c), scatter plots of temperature over all the numerical domain are presented. The richest mixtures present a cold temperature, which denotes a mixing between pure fuel and air without any reaction. This premixing occurs upstream the flame. In leaner mixtures (including lean, stoichiometric and some rich conditions), the scatterplots span from the fresh gases temperature to the bunt gases temperature. Hence, combustion occurs for mixture fraction below a given threshold. This threshold is different between the different cases. For the case R0W0S1, combustion occurs until values of about $Z \approx 0.25$. For cases R1W1S1 and R1W0S0, this threshold is approximatively equal to $Z \approx 0.2$ and $Z \approx 0.15$ respectively. This is in agreement with flame stabilization localization: the more upstream the flame stabilizes, the less reactants are mixed before combustion and the more rich

reactants are burnt.

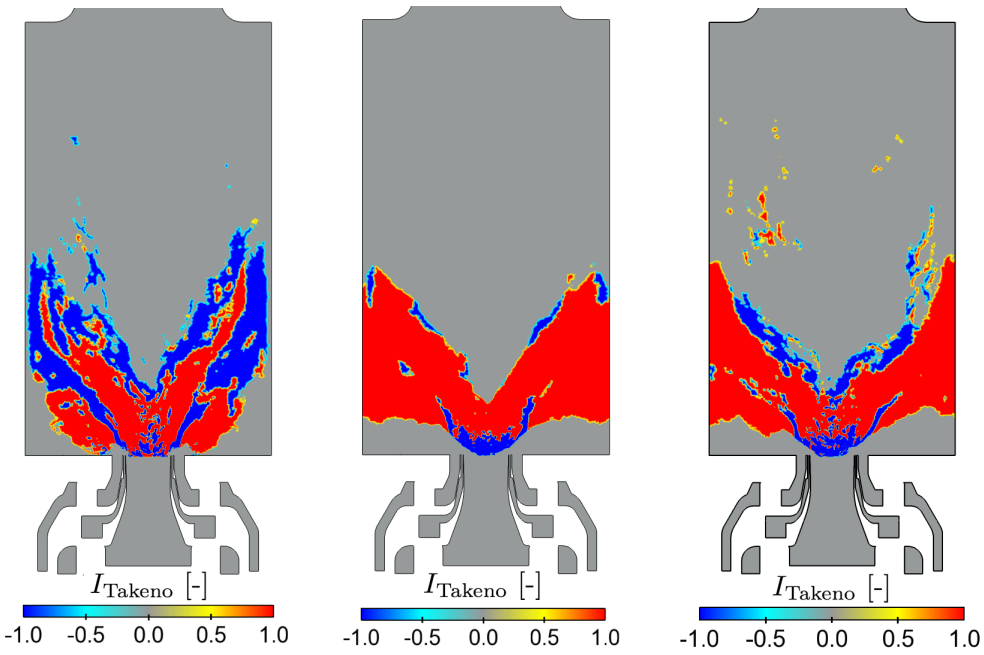


(a) Case R0W0S1 (b) Case R1W0S0 (c) Case R1W1S1

**Figure 5.14:** *Time-averaged Takeno index conditioned by progress variable source term presence for the different cases.*

From Figs. (d) to (e), the same scatter plots but conditioned by the Takeno index and with transparency controlled by the respective volume of the considered points are plotted: red color corresponds to an identified premixed combustion regime, blue color corresponds to an identified diffusion combustion regime and gray color corresponds to identified mixing (corresponding to regions where the progress variable source term is lower than $\epsilon$). In order to distinguish the different combustion regimes, these scatter plots are presented for $x \in [0\text{ mm}, 30\text{ mm}]$ in Figs. 5.15 (g) to (i), for $x \in [30\text{ mm}, 60\text{ mm}]$ in Figs. 5.15 (j) to (l) and for $x \in [60\text{ mm}, 120\text{ mm}]$ in Figs. 5.15 (m) to (p), without considering the identified mixing regions.
In the first region (presented in Figs. 5.15 (g) to (i) for $x \in [0\text{ mm}, 30\text{ mm}]$), a diffusion-like combustion regime is mainly observed in case R1W0S0. Indeed, the Takeno index indicates a diffusion-like regime and diffusion branches are identified in the temperature scatter plots. In cases R1W0S0 and R1W1S1, temperatures varying from 300 K and 2400 K in the flammability region are observed. For these points, the Takeno index indicates a premixed-like combustion regime. Then, the combination of premixed and diffusion-like combustion regimes are observed in these regions. In particular, in the case R1W0S0, premixed combustion regime is clearly predominant. This may be due do a more effective mixing between reactants before combustion.

In the second region (presented in Figs. 5.15 (j) to (l) for $x \in [30\text{ mm}, 60\text{ mm}]$), based on the same analysis, diffusion-like combustion regime are observed in cases R0W0S1 and R1W1S1 and premixed-like combustion regime is observed in case R1W0S0. These observations are in agreement with discussion of Fig. 5.14. Impact of heat losses due to radiation can be observed by comparing the scatter plots of the cases R1W0S0 and R1W1S1 with the one obtained for the case R0W0S1: a decrease of maximum temperature is noticed.
Finally, in this last region (presented in Figs. 5.15 (m) to (p) for $x \in [60\text{ mm}, 120\text{ mm}]$), the same combustion regimes of the second region are identified. In this region, impact of wall heat losses can also be identified with a decrease of burnt gases temperature. Indeed, burnt gases with a mixture fraction $Z \approx 0.6$ and a temperature varying from 1300 to 2300 K are observed in the case R1W1S1 in Fig. 5.15 (o) whereas for this mixture fraction, temperatures below 2200 K are not observed in cases R0W0S1 (Fig. 5.15 (m)) and R1W0S0 (Fig. 5.15 (n)). The same effect is observed for ($x \in [60\text{ mm}, 120\text{ mm}]$), where the temperature varies between 700 K and 2300 K in case R1W1S1 for $Z \approx 0.6$. This range of temperature corresponds to the temperature of the bottom wall, imposed in this simulation at 650 K.

### 5.4.4 Analysis of temperature probability density functions

Further analysis of temperature predictions can be done by looking at comparison between numerically-predicted and experimentally-measured temperature probability density functions (pdf). It is important to notice that experimental measurements are averaged through the corresponding probe volume, and that numerical results correspond to the resolved LES scales. Figure 5.16 presents the positions of the different probes used during the calculation and where the temperature probability density functions have been computed.

Figures 5.17 and 5.18 present the comparison between the experimentally-measured *pdf* and the numerically-predicted ones for the three studied cases. In a general manner, impact of radiative and wall heat losses can clearly be identified comparing each numerical simulation: the best agreement is generally obtained for the case considering both radiative and wall heat losses.

Looking at the axial probes near $x = 0$ mm (Figs 5.17 (a) and (b)), the experimental data show mainly the presence of cold gases with a temperature below 500 K. This corresponds to fresh gases, indicating that the flame is stabilized downstream this height. The adiabatic case R0W0S1 however presents a larger span of temperature with a large probability of hot burnt gases. This is consistent with the observed lower flame stabilization height in this case. On the other hand, the other two cases with heat losses (R1W0S1 and R1W1S1) most likely exhibit fresh gases at the considered location. This is also consistent with the outlined effects of heat losses on retrieving the correct flame position.

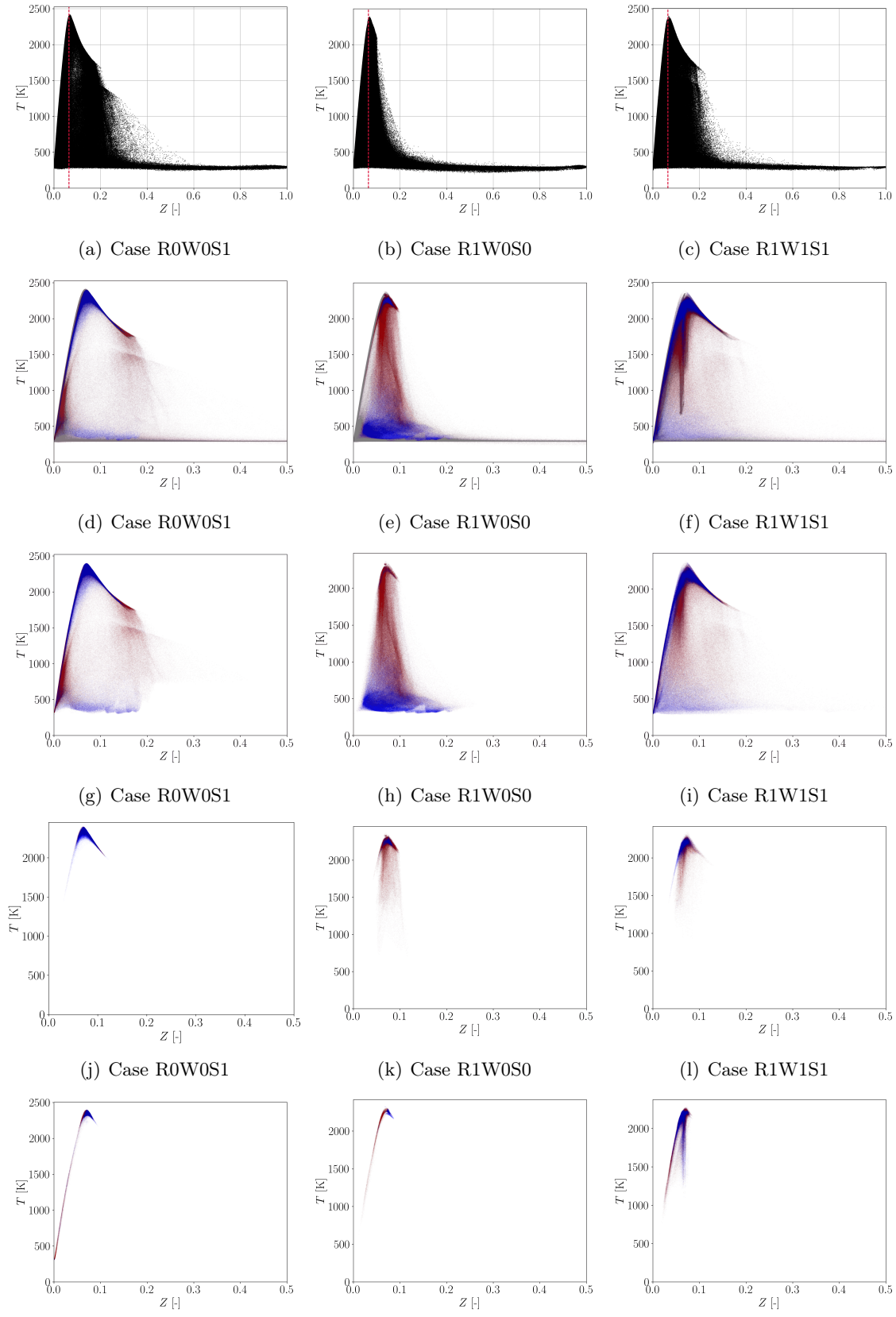


(a) Case R0W0S1 (b) Case R1W0S0 (c) Case R1W1S1

(d) Case R0W0S1 (e) Case R1W0S0 (f) Case R1W1S1

(g) Case R0W0S1 (h) Case R1W0S0 (i) Case R1W1S1

(j) Case R0W0S1 (k) Case R1W0S0 (l) Case R1W1S1

(m) Case R0W0S1 (n) Case R1W0S0 (o) Case R1W1S1

**Figure 5.15:** *For the three studied cases, scatter plots for instantaneous solutions of: temperature for Fig. (a) to (c), temperature colored by the respective value of Takeno index for Figs. (d) to (f) for all the volume, temperature colored by the respective value of Takeno index for Figs. (g) to (i) for* $x > 0$ *mm and* $x < 30$ *mm, temperature colored by the respective value of Takeno index for Figs. (j) to (l) for* $x > 30$ *mm and* $x < 60$ *mm, temperature colored by the respective value of Takeno index for Figs. (m) to (p) for* $x > 60$ *mm and* $x < 120$ *mm.*

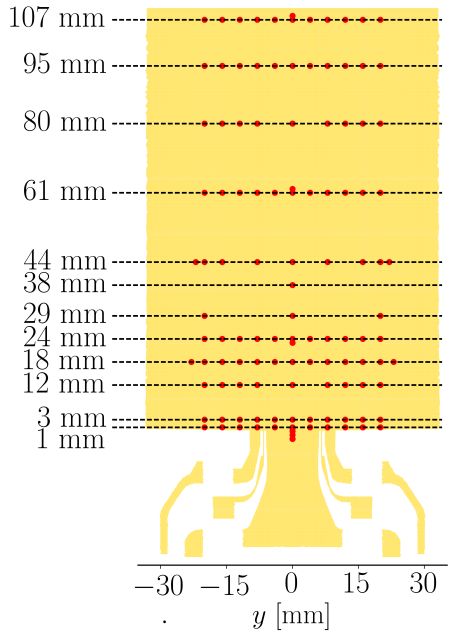


**Figure 5.16:** *Position of the different probes during the calculation*

More downstream on the centerline, for $x \in [12\text{ mm}, 18\text{ mm}]$ (Figs 5.17 (c) and (d)), the temperature is always under-predicted compared with experiments. This region corresponds to the second zone of diffusion combustion regime where rich hot gases burn with the secondary air injection. Indeed, the equivalence ratio based on primary injection is globally rich. Then, after the first step of primary rich combustion, these hot burnt gases burn with secondary air injections, which, in the experimental data, can lead to temperatures higher than 2500 K (surprisingly, higher than the adiabatic flame temperature computed for premixed reactants at 300 K). Under-estimation of temperature when accounting for heat losses can also be due to an overestimation of radiative heat losses as the coarse optically thin radiation model is used in these simulations. Further downstream on the centerline (Figs 5.17 (e) to (j)), radiative and wall heat losses enable to retrieve very well experimental measurements.
Looking now at probes near combustion chamber walls (at $y = 20$ mm in Fig. 5.18), heat losses enable also to retrieve good temperatures *pdfs*. Temperatures *pdfs* at $y = 8$ mm in Fig. 5.18, corresponding to points between the combustion chamber centerline and walls, are also well retrieved when considering radiative and wall heat losses.
Finally, the probe at $x = 18$ mm and $y = 20$ mm (Fig. 5.18 (b)) corresponds to a position where the front flame is intermittently present and not present. The temperature broadening at this position is very well retrieved for the cases considering radiative heat losses, whereas it is underestimated for the adiabatic case. Mean temperature is also overestimated for the adiabatic calculation at this point.

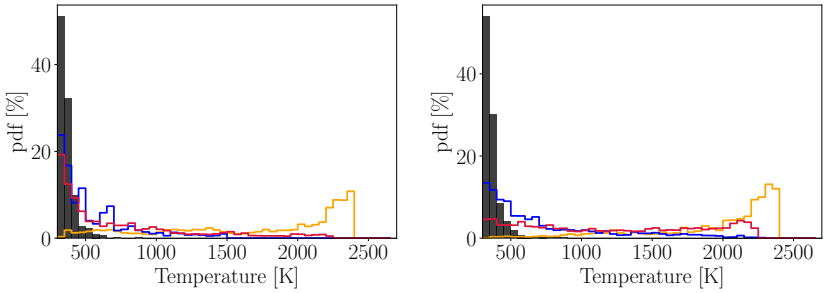


(a) $x = 0$ mm, $y = 0$ mm




(b) $x = 3$ mm, $y = 0$ mm

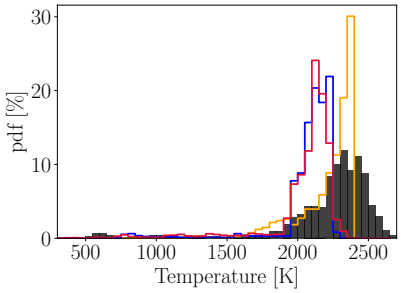


(c) $x = 12$ mm, $y = 0$ mm

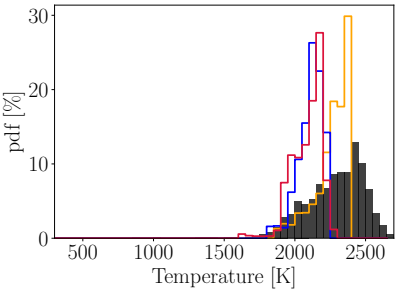


(d) $x = 18$ mm, $y = 0$ mm

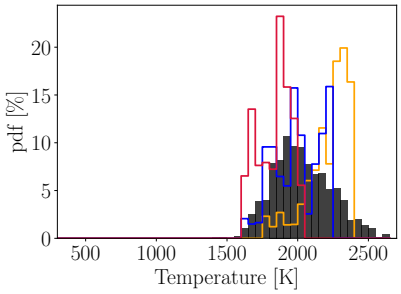


(e) $x = 37$ mm, $y = 0$ mm

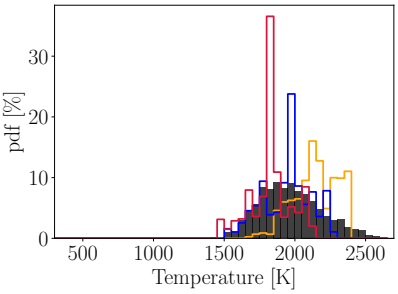


(f) $x = 45$ mm, $y = 0$ mm

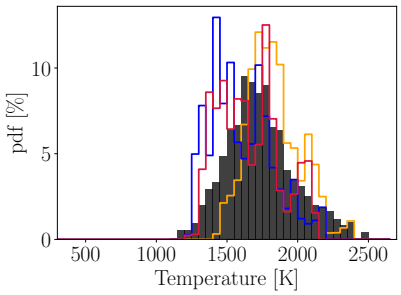


(g) $x = 62$ mm, $y = 0$ mm

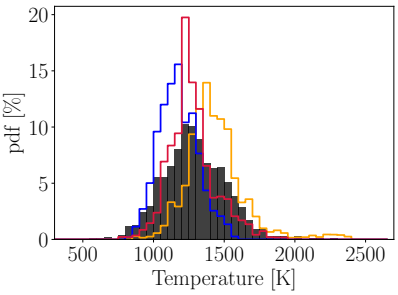


(h) $x = 80$ mm, $y = 0$ mm

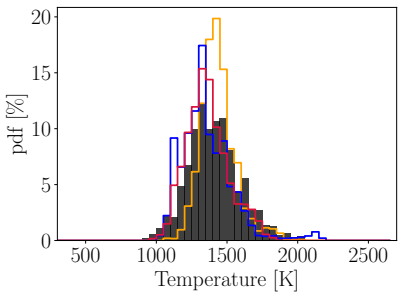


(i) $x = 95$ mm, $y = 0$ mm

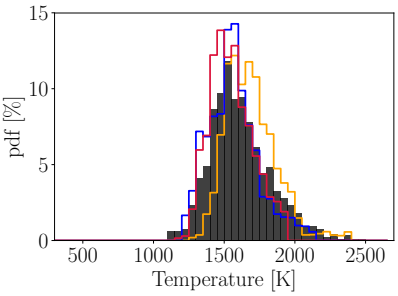


(j) $x = 107$ mm, $y = 0$ mm

**Figure 5.17:** *Comparison of numerically-predicted temperature probability density functions with experiments for probes located in the axis of the combustion chamber. Black histograms correspond to experimental data. Orange, blue and red curves correspond to numerically-predicted data for the R0W0S1, R1W0S1 and R1W1S1 cases, respectively.*

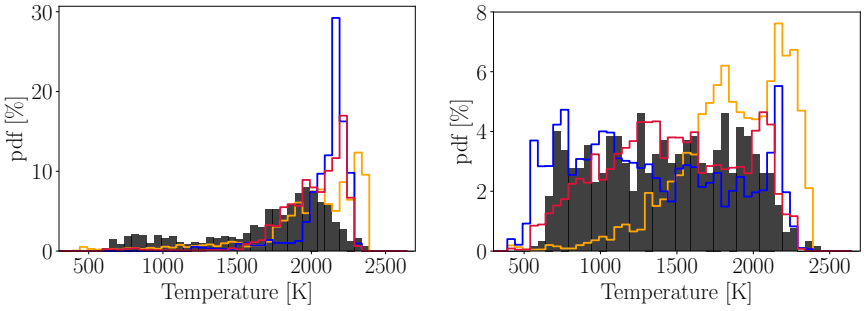


(a) $x = 18$ mm, $y = 8$ mm




(b) $x = 18$ mm, $y = 20$ mm

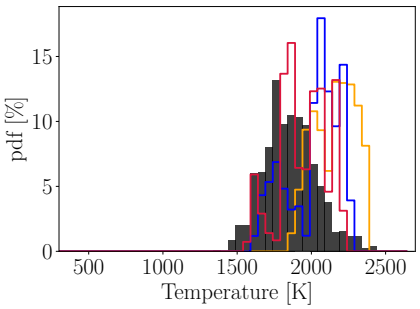


(c) $x = 45$ mm, $y = 8$ mm

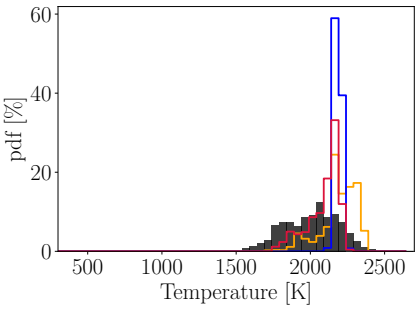


(d) $x = 45$ mm, $y = 20$ mm

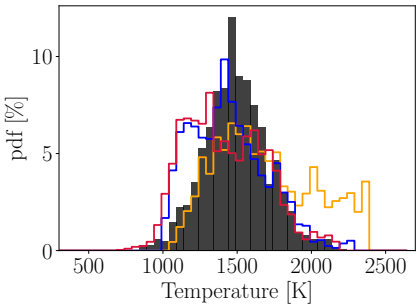


(e) $x = 80$ mm, $y = 8$ mm

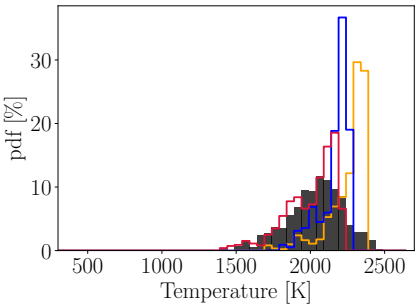


(f) $x = 80$ mm, $y = 20$ mm

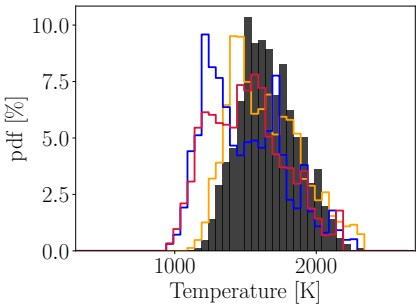


(g) $x = 95$ mm, $y = 8$ mm

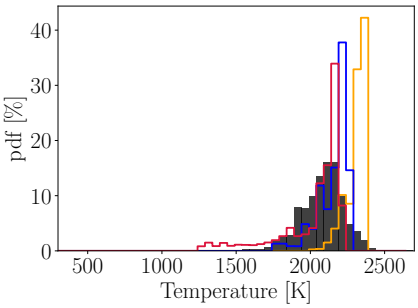


(h) $x = 95$ mm, $y = 20$ mm

**Figure 5.18:** *Comparison of numerically-predicted temperature probability density functions with experiments for probes located at $y = 8$ mm and $y = 20$ mm. Black histograms correspond to experimental data. Orange, blue and red curves correspond to numerically-predicted data for the R0W0S1, R1W0S1 and R1W1S1 cases, respectively.*

### 5.4.5 PAH fields

This subsection compares the fields of soot precursors between the cases where soot production has been predicted: cases R0W0S1 and R1W1S1. Figure 5.19 presents the normalized mean $C_2H_2$ fields, and Figs. 5.20, 5.21, and 5.22 present respectively the normalized mean fields for the A2, A4 and A6 soot precursors. For each one of these fields, black color is used for values lower than 5% of the maximum value.

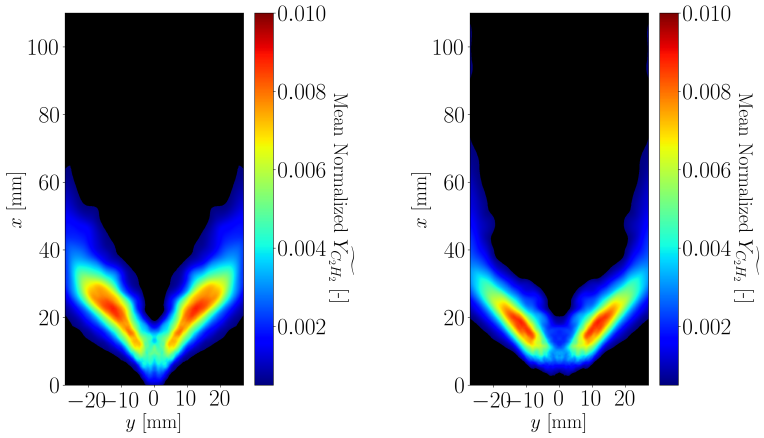


(a) Case R0W0S1 (b) Case R1W1S1

**Figure 5.19:** *Mean $\widetilde{Y_{C_2H_2}}$ predicted fields.*

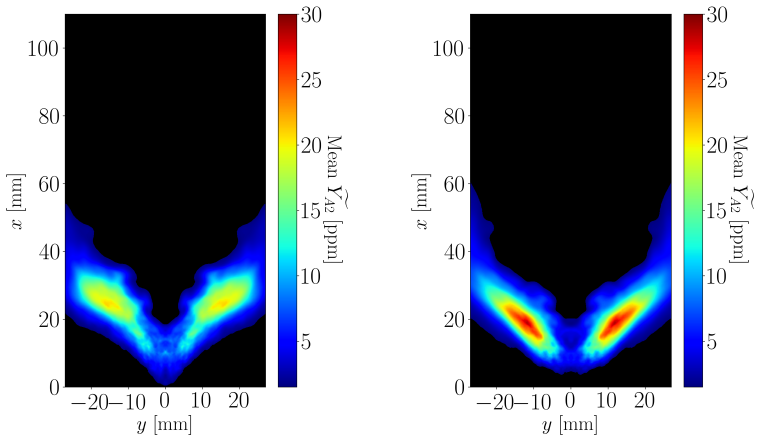


(a) Case R0W0S1 (b) Case R1W1S1

**Figure 5.20:** *Mean $\widetilde{Y_{A2}}$ predicted fields.*

It can be observed that big soot precursors (A4 and A6) are localized downstream of the flame whereas small soot precursors are present closer to the

burner inlet. Taking into account these big soot precursors is then important in order to retrieve soot particles nucleation all along the chamber. Radiative and wall heat losses also impact soot precursors production as their localization are different. Indeed, even if the maximum mean values of each soot precursor is the same for the two considered cases, soot precursors are present in larger zones for the adiabatic case compared with the case accounting for radiative and wall heat losses.

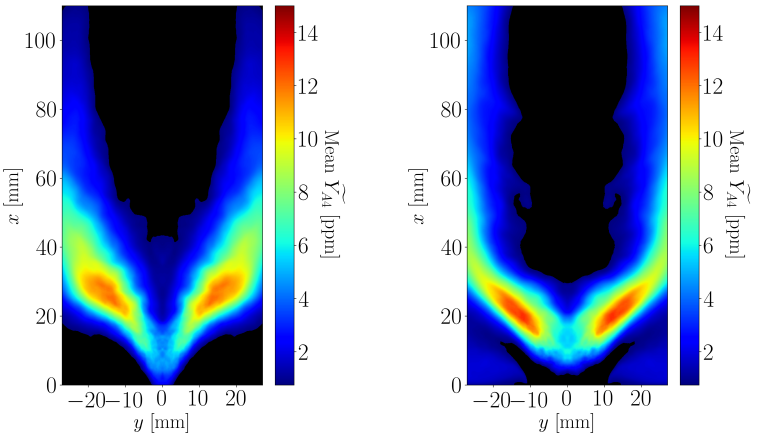


(a) Case R0W0S1 (b) Case R1W1S1

**Figure 5.21:** *Mean $\widetilde{Y_{A4}}$ predicted fields.*

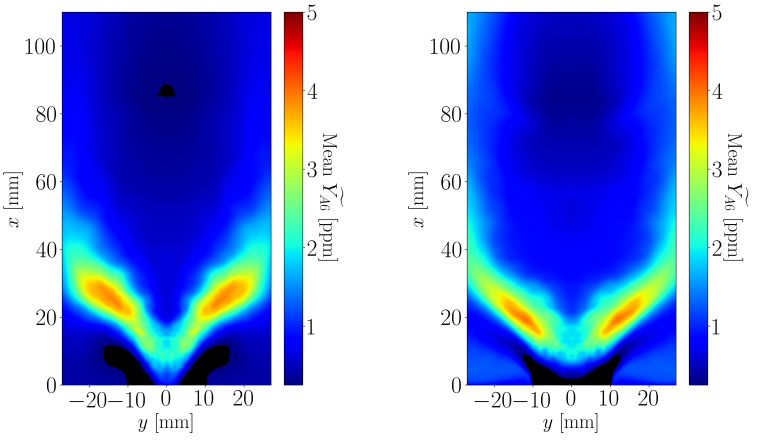


(a) Case R0W0S1 (b) Case R1W1S1

**Figure 5.22:** *Mean $\widetilde{Y_{A6}}$ predicted fields.*

Figure 5.23 presents PAH Laser Induced Fluorescence (LIF) fields measurements for the studied case, together with mean soot presence regions represented by the red continuous contour. The chosen detection range (300 to 350

nm) corresponds to small, i.e. two- to four-ring PAH (i.e. $A_2$ to $A_4$). Comparing then mean $\widetilde{Y_{A_2}}$ (Fig. 5.20) and $\widetilde{Y_{A_4}}$ (Fig. 5.21) with Fig. 5.23, one can observe that an higher prediction fidelity is obtained with the case R1W1S1, which account for heat losses, compared with the case R0W0S1, especially at the wings of the flame opening and in the outer recirculation zones.

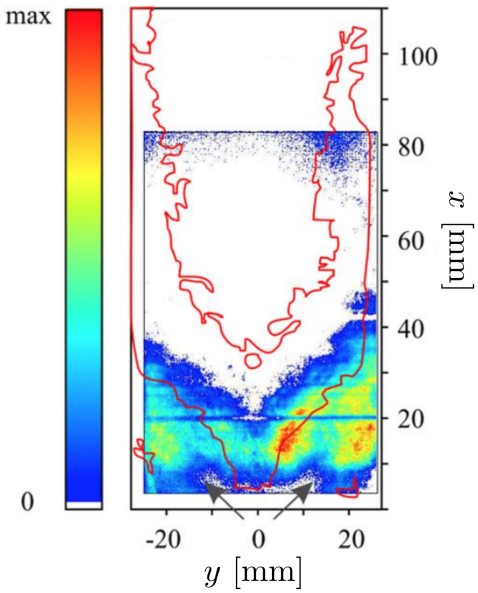


**Figure 5.23:** *Average distribution of PAH measured by Laser Induced Fluorescence (LIF), extracted from Geigle et al. (2015). The red continuous contour represents the soot distribution (regions where mean soot volume fraction is higher than 0.1ppb).*

### 5.4.6 Soot fields

#### 5.4.6.1 Mean soot volume fraction fields

Figure 5.24 presents a comparison between mean soot volume fraction experimental and numerically predicted fields for the R0W0S1 and the R1W1S1 cases. For both cases, a good localization of soot volume fraction is obtained. Concerning soot volume fraction magnitude, it is under-predicted by approximatively a factor of two in the case R0W0S1 and by a factor of four in the case R1W1S1. Figure 5.25 presents the numerical predictions of mean soot volume fraction obtained in literature for the same configuration. Then, compared to the state-of-the-art soot predictions in turbulent configurations, predicting soot volume fraction by a factor two is a good general agreement.

Strong impact of heat losses on soot magnitude can also been observed with a decrease of soot volume fraction in presence of heat losses by a factor two. This can be explained by the fact that in presence of heat losses, soot precursors are

stabilized upstream in the combustor, where the residence time for nucleation and condensation processes is lower, but also that soot precursors production decrease with heat losses. This tendency of soot volume fraction decreasing with the increase of heat losses has already been observed in Mehta et al. (2010) and Reddy et al. (2015a) in turbulent flames.

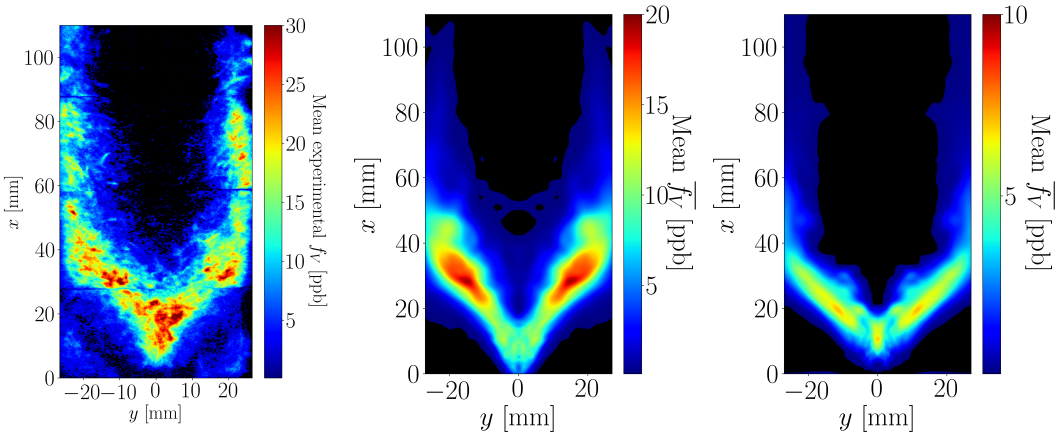


(a) Experimental field (b) Case R0W0S1 (c) Case R1W1S1

**Figure 5.24:** *Comparison of experimentally measured and numerically predicted mean soot volume fraction fields*

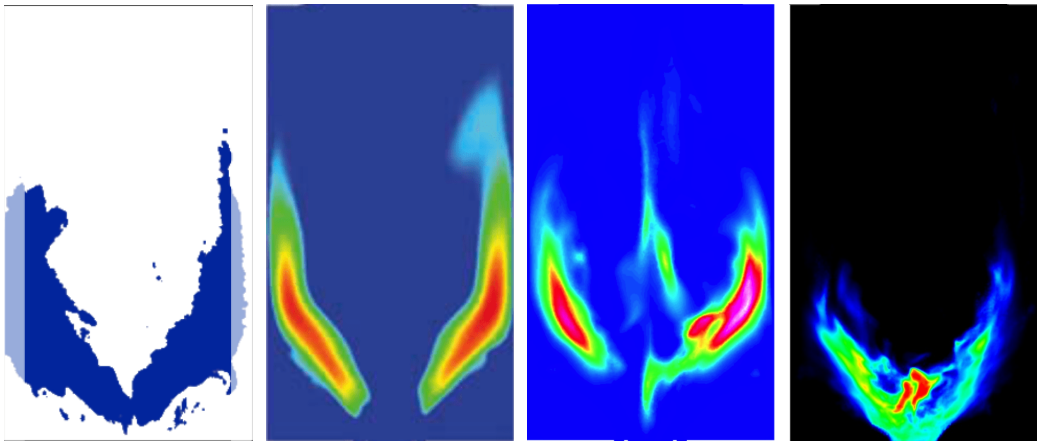

(a) Franzelli et al. (2015) (b) Eberle et al. (2015) (c) Koo et al. (2016) (d) Wick et al. (2017)

**Figure 5.25:** *Numerical predictions of mean soot volume fraction field in literature for the same configuration. Numerically predicted peak soot volume fraction are, from left to right, equal to 0.2 ppb, 500 ppb, 6 ppb and 7 700 ppb.*

Finally, it is also important to notice that soot volume fraction magnitude in this configuration is two orders of magnitude lower than the one obtained in the jet diffusion flame studied in Chapter 4. Differences in soot particles residence times, soot particles evolution processes but also in global equivalence ratio may explain such a difference.

#### 5.4.6.2 Particles size distribution function

The probability density functions (PDF) of particles size distribution have been also computed at the position of the probes, indicated in Fig. 5.16. Figure 5.26 presents the corresponding PDF at different positions for the case R1W1S1.

For all the considered positions, the PSD presents a one-peak shape. Based on observations done in Chapter 4, the residence time in locally rich zones may be too small to obtain a two-peak PSD shape.
Strong differences in PSD fluctuations are observed between the different positions. In regions of flame front spatial fluctuations (Fig. 5.26 **(a)**, **(b)**, **(d)**, **(e)**, **(g)**, **(h)**, **(j)**, **(m)**, **(p)**), high fluctuations of soot particles size distributions are observed. This is directly linked to the instantaneous presence or not of gaseous soot precursors in this corresponding region. For all other positions, few fluctuations of the PSD are noticed.

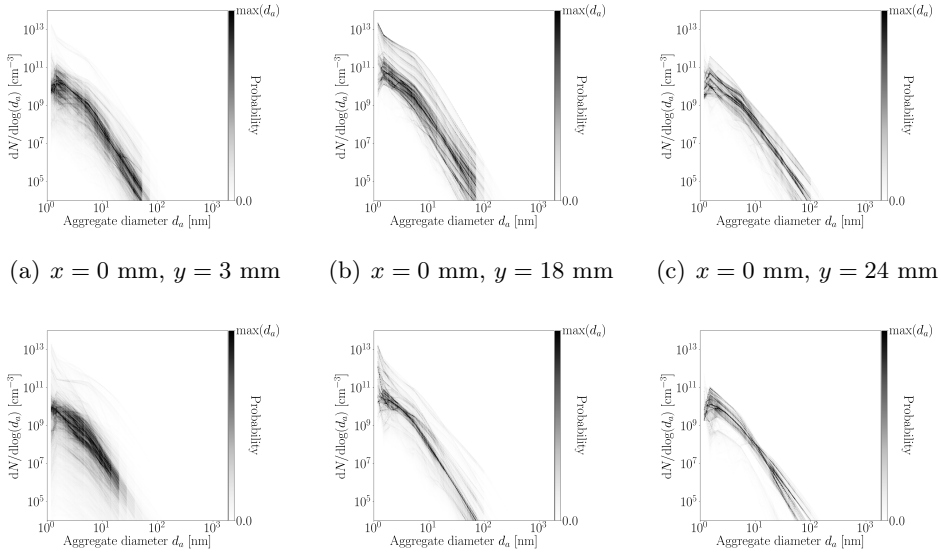


(a) $x = 0$ mm, $y = 3$ mm (b) $x = 0$ mm, $y = 18$ mm (c) $x = 0$ mm, $y = 24$ mm

(d) $x = 4$ mm, $y = 3$ mm (e) $x = 4$ mm, $y = 18$ mm (f) $x = 4$ mm, $y = 24$ mm

**Figure 5.26:** *Probability density functions of particles size distribution at different positions in the burner.*

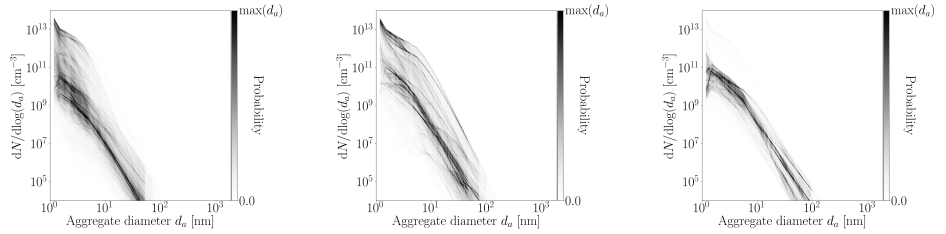


(a) $x = 8$ mm, $y = 12$ mm (b) $x = 8$ mm, $y = 18$ mm (c) $x = 8$ mm, $y = 24$ mm

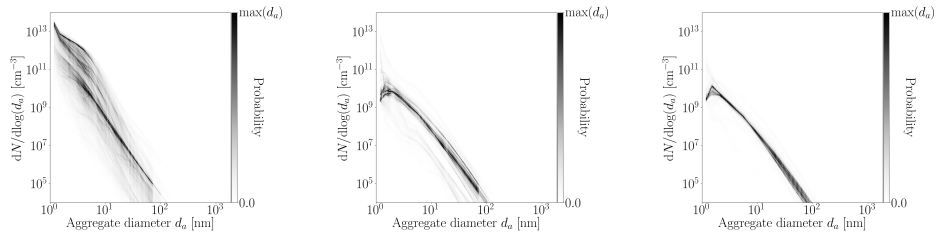


(d) $x = 16$ mm, $y = 24$ mm (e) $x = 16$ mm, $y = 45$ mm (f) $x = 16$ mm, $y = 62$ mm

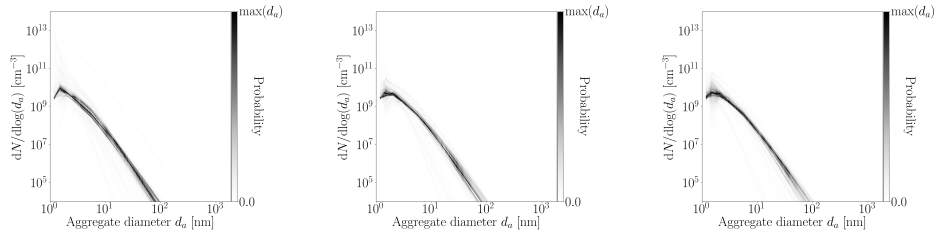


(g) $x = 16$ mm, $y = 80$ mm (h) $x = 16$ mm, $y = 95$ mm (i) $x = 16$ mm, $y = 107$ mm

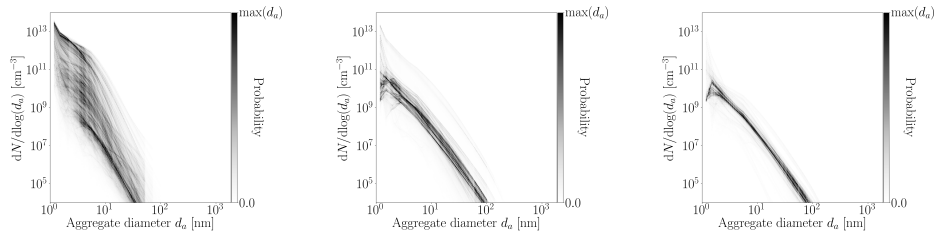


(j) $x = 20$ mm, $y = 24$ mm (k) $x = 20$ mm, $y = 45$ mm (l) $x = 20$ mm, $y = 62$ mm

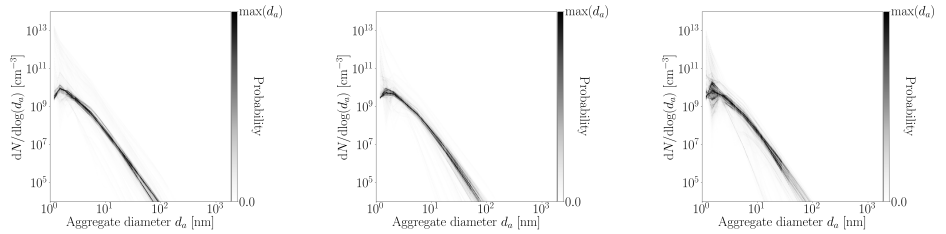


(m) $x = 20$ mm, $y = 80$ mm (n) $x = 20$ mm, $y = 95$ mm (o) $x = 20$ mm, $y = 107$ mm

**Figure 5.26:** *Probability density functions of particles size distribution at different positions in the burner.*

### 5.4.7 Analysis of soot production

In Fig. 5.27, mean source terms of soot production are plotted.

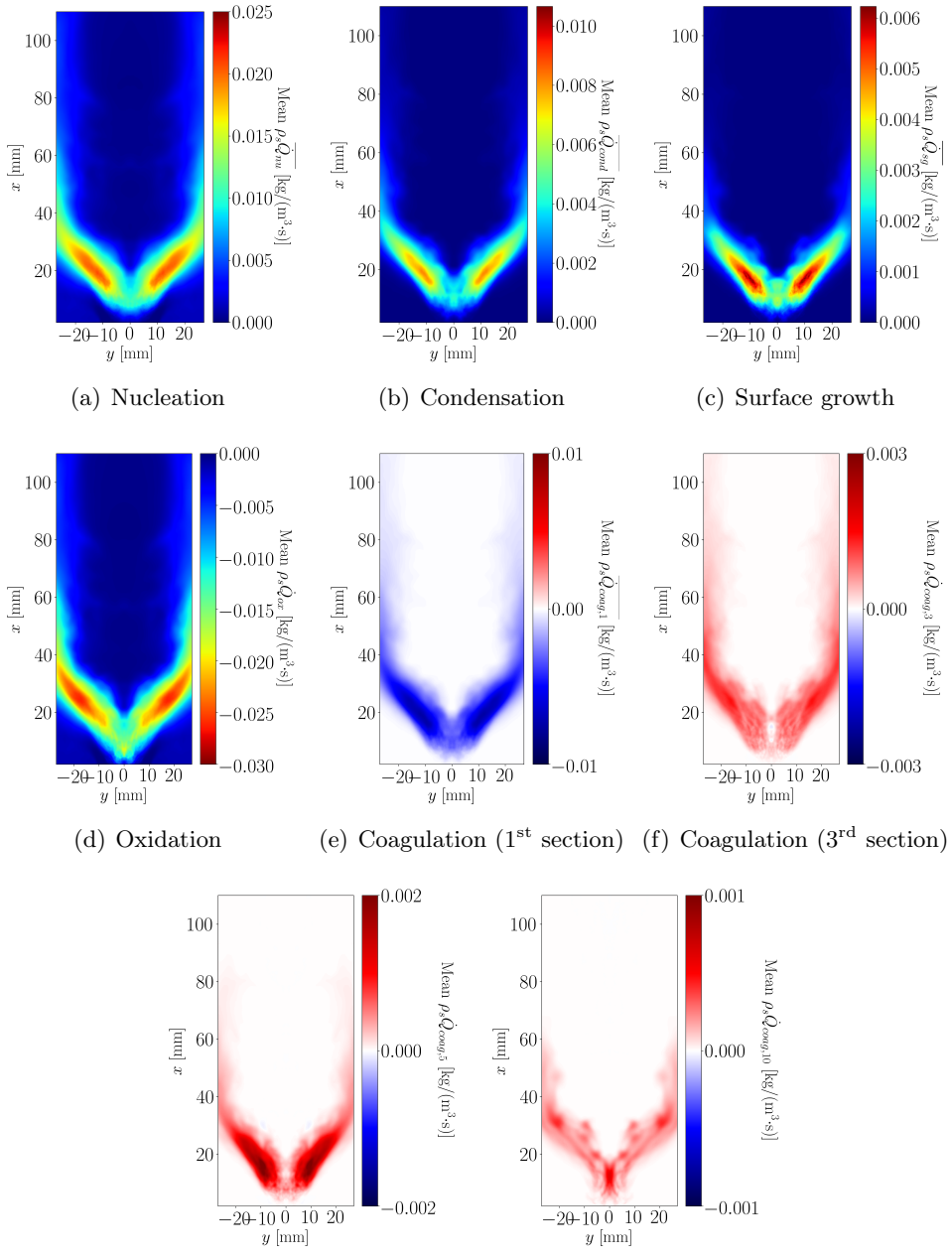


(a) Nucleation (b) Condensation (c) Surface growth

(d) Oxidation (e) Coagulation (1st section) (f) Coagulation (3rd section)

(g) Coagulation (5th section) (h) Coagulation (10th section)

**Figure 5.27:** *Mean soot source terms of nucleation, condensation, surface growth, oxidation and coagulation (for the 1$^{st}$, 3$^{rd}$, 5$^{th}$ and 10$^{th}$ sections).*

In this configuration, nucleation and condensation are the two main contributors of soot production. Surface growth participates with a source term four times lower than nucleation. On the other hand, high oxidation is observed, and an important part of soot production by nucleation and condensation is oxidized. Looking at coagulation fields, one can see that coagulation source term is negative for the first section, whereas it is mainly positive for all the other sections.

This is in contrast with the results of Chapter 4 where intermediate sections presented regions with positive and negative source terms. This can be explained by lower residence time scales of soot particles and then the absence of a two-peak shape in the PSD. Indeed, coagulation rate scales with the product of the particles number density of each section. Due to the one-peak shape of the PSD, sections corresponding to big soot particles present a particles number density lower than the one of smaller sections. Then, these sections present a lower coagulation probability towards bigger soot sections compared with the probability of small particles coagulating towards these sections. Finally, particles mainly grow by surface growth and condensation and high oxidation is observed in this configuration, due to the overall lean conditions.

Figure 5.28 presents a representative view of soot particles according to their size. Particles are gathered by groups of 5 sections, and the field is colored for values higher than 2 % of their maximum values.

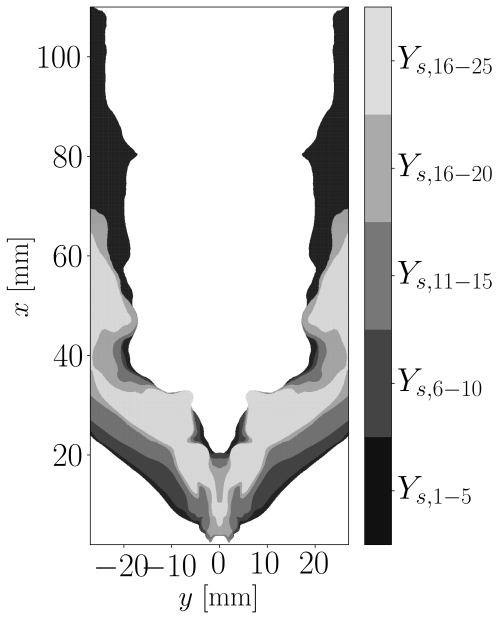


**Figure 5.28:** *Presence of soot particles according to their size.*

Linking this figure with Fig. 5.24, which presents the soot volume fraction fields, one can link the high soot volume fraction regions with regions where all size of particles are present. In the wings, only small soot particles are present. This is in agreement with the presence of mainly nucleation and condensation source terms in this region (Fig. 5.27).

## 5.5 Conclusion

In this chapter, the turbulent sooting flame model described in Chapter 3 has been employed to simulate a pressurized confined turbulent sooting ethylene-air. Impact of heat losses has been analyzed by comparing simulations without heat losses, simulations considering only radiative heat losses and simulations considering both radiative and wall heat losses.

Considering radiative heat losses even with a coarse approximation such as the optically thin assumption seems to enable to correctly retrieve the flame stabilization. A strong impact of heat losses is observed on all the combustion chamber, with large temperature decrease between calculations with heat losses and calculations with adiabatic assumption. Unless temperature is under-estimated when considering radiative heat losses with the optically thin radiation model, radiative and wall heat losses have also enabled to retrieve good temperature dynamics when comparing predicted temperature probability density functions with experimental CARS measurements. Then, the models used for heat transfer description have a strong impact on temperature fields, flame stabilization and flame shape. The models considered here for the three studied cases are quite simple (optically thin radiation model and imposed experimental centerline wall temperature). Using optically thin radiation model generally overestimates radiation heat losses and imposed centerline mean wall temperature is not appropriate in regions far from the centerline of the quartz windows and does not account for walls temperature dynamics. Then, it would be interesting to evaluate the impact of more precise models on the description of flame properties. This is the objective of the third part of this manuscript.

Soot production has also been investigated and compared with LII experimental measurements of soot volume fraction. For the three studied cases, good soot production localization has been obtained compared with experiments. Analyzing the different pathways of soot physical and chemical mechanisms, soot production through PAH pathways (nucleation and condensation) has been recognized as the major contributors whereas soot oxidation controls soot particles depletion. Soot oxidation has been revealed to be very important in this configuration due to the overall lean operating condition.

Particles size distributions dynamics have also been analyzed in this configura-

tion for the numerical simulation accounting for radiative and wall heat losses. By contrast with the PSD observed in Chapter 4, for all the considered points in the combustion chamber, the particles size distribution presents a one-peak PSD shape. High fluctuations of this PSD is observed for regions near the flame front, whereas very small fluctuations have been observed downstream the flame position. Very few big particles (with diameter higher than 10 nm) are observed in this configuration: soot particles do not grow through surface growth due to very localized $C_2H_2$ region presence and only slightly coagulate due to low residence time scales inside the combustion chamber.

Finally, heat losses modify soot production. Two main mechanisms may imply such modification. First, flame shape is modified and therefore soot precursors position is modified when considering heat losses. Second, residence time is altered when considering radiative and wall heat losse, which may lead to a decrease of soot volume fractions. Compared with literature, state of the art prediction of soot magnitude is achieved with a discrepancy factor lower than four.

# Part III

# Multi-physics simulations of sooting flames

# Introduction

In the second part of the manuscript, soot production has been studied in turbulent jet and confined swirled flames by developing a dedicated LES formalism. Heat losses have also been accounted for in such simulations and important impact of both radiative and wall heat transfers on flame stabilization and soot production has been identified for the confined swirled configuration. However, in these simulations, simple radiation models have been considered in order to assess such radiative heat losses. For the confined swirled configuration, wall heat losses relied on imposed measured boundary temperature fields from the centerline profile.

In highly emitting and absorbing medium such as turbulent highly sooting flames, radiation reabsorption must be accounted for and the optically-thin radiation model used in part II is a drastic simplification. Determining properly this absorption contribution on total radiative power requires the resolution of the Radiative Transfer Equation (RTE) and a description of the radiative properties of gaseous and solid phases. In part III, the RTE will be solved for the two turbulent flames studied in part II. Chapter 6 presents the different models for radiative properties and the different numerical methods that can be used in order to solve the RTE. The methodology considered here (Monte-Carlo), as well as the radiative properties modeling of the gaseous phase (cK model) and the solid phase (non-scattering RDG theory) and their recent developments are presented. In Chapter 7, a coupled Monte-Carlo resolution - LES simulation of the sooting jet turbulent flame studied in Chapter 4 is presented and the associated radiative transfer is analyzed in details.

Conjugate heat transfer (CHT) simulations enable to estimate wall temperatures instead of relying on temperature measurements. Predicting such wall temperature enables also to prevent some potential wall damages. However, a good prediction of wall temperatures remains a real challenge in turbulent configurations. Chapter 8 presents the strategy used in this thesis to predict wall temperatures at an affordable cost. This methodology is applied to the simulation of the pressurized combustion chamber studied in Chapter 5 while neglecting radiative effects. Prediction of wall temperatures are compared to measurements in order to evaluate the quality of the chosen methodology. Fi-

nally, in Chapter 9, a fully-coupled simulation of the confined pressurized burner investigated in Chapter 5 is presented accounting for emitted and reabsorbed radiation and conjugate heat transfer. Analysis of the different heat transfers and their impact is carried out by comparing the different simulation cases.

# Chapter 6

# Detailed radiation modeling in turbulent sooting flames

*In this chapter, the radiative transfer and its governing equation (the radiative transfer equation: RTE) is presented. The different approaches to model gaseous and soot particles radiative properties are presented, with a focus on the ones used in this thesis: ck (correlated-k) methods for gas and Rayleigh approximation for soot particles. Different ways of solving the RTE are briefly discussed and the retained Monte Carlo approach is presented. Different sampling methods are discussed and the concept of Quasi Monte Carlo sampling is introduced. The gains obtained with this approach are discussed. Then, the reciprocity principle in radiation is explained and discussion about the different Monte Carlo approaches (reciprocal or not) are discussed, while justifying the choice of the Emission Reciprocity Method (ERM) approach. Finally, the code used in the simulations of Chapters 7 and 9 is presented and its coupling with the CFD solver AVBP through the Open-Palm library is explained.*

*It should then be noticed that the general methods enabling to model radiative transfers in sooting flames are introduced, but not all of them are used in the presented works. Sections 6.1, 6.2.1.5, 6.2.1.6, 6.2.1.7, 6.2.2.4, 6.2.2.5, 6.4, 6.5, and 6.6 contain the minimum details of the methods used in the following chapters.*

## Contents

## 6.1 Introduction to radiative transfer

Radiative heat transfer differs from the two other modes conduction and convection as it is caused by electromagnetic waves. The interactions length scales are also different between these three phenomena. Indeed, conductive and convective heat transfers correspond to short-range interactions and partial differential equations are generally used to describe them. By contrast, radiative heat transfer corresponds to long-range interactions and the entire enclosure of the system needs to be considered in order to describe the local energy conservation, resulting into an integro-differential equation.

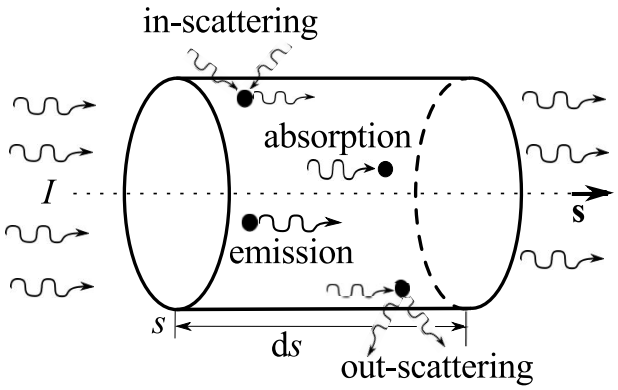


**Figure 6.1:** *Schematic description of radiation energy evolution (Extracted from (Zhang 2013)).*

When considering an energy ray of wavenumber $\nu$ with a corresponding radiative intensity $I'_\nu$ which travels over a distance $ds$ in the direction $\mathbf{u}$, its energy can be modified through three mechanisms, as seen in the schematic of Fig. 6.1. First, energy can be absorbed by the crossed media with an absorption coefficient $\kappa_\nu$. Second, in the case of local thermodynamic equilibrium (LTE) which is assumed in this thesis, the media can emit energy with the same probability of absorption, leading to an emission coefficient $\kappa_\nu$. Finally, a part of the initial intensity can be scattered in another direction with a scattering coefficient $\sigma_\nu$.

The Radiative Transfer Equation (RTE) for a media of refractive index $n$ can then be written as:

$$\begin{aligned}\frac{dI'_\nu}{ds} = &- \underbrace{\kappa_\nu I'_\nu}_{\text{Absorption}} - \underbrace{\sigma_\nu I'_\nu}_{\text{Scattering}} \\ &+ \underbrace{\kappa_\nu n^2 \, I^\circ_\nu}_{\text{Emission by the media}} + \underbrace{\frac{\sigma_\nu}{4\pi}\int_{4\pi} p_\nu(\mathbf{u}', \mathbf{u}, s) I'_\nu(\mathbf{u}', s) d\Omega'}_{\text{Received scattering}}\end{aligned} \tag{6.1}$$

where $I'_\nu(\mathbf{u}', s)$ is the local intensity traveling in the direction $\mathbf{u}$ and $p_\nu(\mathbf{u}', \mathbf{u}, s)$ is the *phase function* and corresponds to the probability that a ray in the direction $\mathbf{u}'$ will be scattered in the direction $\mathbf{u}$ at the local position $s$. $d\Omega'$ corresponds to the infinitesimal solid angle of integration. $I^\circ_\nu$ corresponds to the blackbody spectral emissive intensity expressed through the *Planck's law*:

$$I^\circ_\nu(T) = \frac{2\pi h c_0^2 \nu^3}{n^2 \left[ e^{\frac{h\nu}{k_b T}} - 1 \right]} \tag{6.2}$$

where $h$ and $k_b$ are respectively the Planck's and Boltzmann's constants, and $c_0$ the speed of light in vacuum.
Knowing the radiative intensity $I'_\nu(\mathbf{u}, s)$ for all the wavelengths $\nu$, directions $\mathbf{u}$ and positions $s$, one can first compute the radiative heat flux vector $\mathbf{q}^R$:

$$\begin{aligned}\mathbf{q}^R &= \int_{\nu=0}^{\infty} \mathbf{q}^R_\nu d\nu \\ &= \int_{\nu=0}^{\infty} d\nu \int_{4\pi} I'_\nu(\mathbf{u}, s)\mathbf{u} d\Omega\end{aligned} \tag{6.3}$$

The volumetric radiative power added in the gaseous energy equation at a local position $\mathbf{r}$ is obtained through:

$$\begin{aligned}P^{\mathrm{R}} &= -\nabla \cdot \mathbf{q}^R \\ &= -\int_{\nu=0}^{\infty} d\nu \int_{4\pi} \mathrm{div}\left[ I'_\nu(\mathbf{u}, s)\mathbf{u} \right] d\Omega\end{aligned} \tag{6.4}$$

Then, using Eq. (6.1), the radiative power $P_R$ can be expressed as:

$$P^{\mathrm{R}} = -\int_{\nu=0}^{\infty} \left[ \left( 4\pi\kappa_\nu I^\circ_\nu - \int_{4\pi} \beta_\nu I'_\nu d\Omega + \quad \frac{\sigma_\nu}{4\pi}\int_{4\pi} p_\nu(\mathbf{u}', \mathbf{u}, s) d\Omega \right) \right] d\nu \tag{6.5}$$

where $\beta_\nu = \kappa_\nu + \sigma_\nu$ is the total extinction.

If the medium is non-scattering ($\sigma_\nu = 0$), this equation is simplified and is expressed as:

$$P^{\mathrm{R}} = \underbrace{\int_{\nu=0}^{\infty} \left[ \kappa_\nu \int_{4\pi} I'_\nu d\Omega \right] d\nu}_{\text{absorbed power}} - \underbrace{4\pi \int_{\nu=0}^{\infty} \kappa_\nu I^{\circ}_\nu d\nu}_{\text{emitted power}} \tag{6.6}$$

where contributions of absorbed power ($P^a$) and emitted power ($P^e$) can be identified.

The radiative flux $\varphi^R(s,t)$ is obtained as:

$$\varphi^R(s,t) = \mathbf{q}^R \cdot \mathbf{n} = \int_{\nu=0}^{\infty} d\nu \int_{4\pi} I'_\nu(s,\mathbf{u}) \mathbf{n} \cdot \mathbf{u} d\Omega \tag{6.7}$$

where $\mathbf{n}$ is the unity vector normal to the wall.

## 6.2 Radiative properties

### 6.2.1 Gaseous phase radiative properties

In the following, several ways of describing the radiative properties, from the reference ones (line-by-line databases) to the more simplified ones (WSGG models) are described. Models enabling a compromise between cost and accuracy are also presented (narrow-band or ck models), and the ck model, chosen for the simulations of Chapters 7 and 9 is presented in details.

#### 6.2.1.1 Line-by-line databases

Several line-by-line spectral database providing detailed high-resolution line spectra are available for the major gaseous species. The most comprehensive one, named HITRAN (Rothman et al. 2009), provides the detailed spectra for 31 species.

Unfortunately, only spectral lines that are not negligible at room temperature are considered in this database. However, at higher temperatures, certain lines become more important and this database becomes not adequate for the determination of the spectral properties at these temperatures. Extensions of this database were then first derived by Rivière et al. (1995) for $H_2O$ and by Scutaru et al. (1993) for $CO_2$, including the spectral lines corresponding to these "hot lines". Extended database has finally been integrated by Rothman et al. (2010) in the HITEMP database.

Generally, the high resolution spectra calculation is not affordable in practical 3-D calculations, but it provides a reference solution in academical configurations, enabling to determine the accuracy of the simplified models presented hereafter.

#### 6.2.1.2 WSGG models

The weighted-sum-of-grey-gases (WSGG) model consists of replacing the integral of spectral properties by a summation over a set of $K$ grey gases, enabling to simulate the properties of the non-grey gas. It has been first introduced by Hottel and Sarofim (1967) for zonal methods of RTE resolution, and then extended to any solution method of the RTE by Modest (1991).

This approach can be easily described in the case of a uniform column of gas of temperature $T$. Indeed, if the medium is grey, *i.e* $\kappa_\nu = \kappa = \text{const.}$, the emittance of the isothermal gas $\epsilon(s,T)$ function of this abscissa $s$ and temperature $T$ writes:

$$\begin{aligned}\epsilon(T,s) &= \frac{\int_0^{+\infty}(1-e^{-\kappa_\nu s})I_\nu^\circ(T)d\nu}{\int_0^{+\infty}I_\nu^\circ(T)d\nu} \\ &= \frac{\int_0^{+\infty}(1-e^{-\kappa s})I_\nu^\circ(T)d\nu}{\int_0^{+\infty}I_\nu^\circ(T)d\nu} = 1-e^{-\kappa s}\end{aligned} \tag{6.8}$$

The idea is to assume that for a non-grey isothermal gas, the emittance can be written as a *weighted sum of grey gases*:

$$\epsilon(T,s) = \sum_{k=0}^{K}\omega_k(T)\left(1-e^{-\kappa_k s}\right) \tag{6.9}$$

where for each grey gas band $k$, $\kappa_k$ is the corresponding constant absorption coefficient and $\omega_k(T)$ is the weights of the corresponding grey gas. These weight are empirical functions of temperature (local medium temperature or wall temperature). Both parameters are independent from the local position. As for an infinitely thick medium, absorptance (and therefore emittance) is equal to one, the sum of weighting coefficients must verify:

$$\sum_{k=1}^{K}\omega_k(T) = 1 \tag{6.10}$$

Then, according to Modest (1991), the total radiative $I(s)$ intensity can be calculated as:

$$I'(s) = \sum_{k=1}^{K} I'_k(s) \tag{6.11}$$

where $I'_k(s)$ correspond the radiative intensity of the grey gas band $k$, verifying the RTE of a grey gas:

$$\frac{dI_k(s)}{ds} = \kappa_k\left(\omega_k(T)\frac{\sigma T^4}{\pi} - I_k(s)\right) \tag{6.12}$$

Even if this approach is an important approximation of the gas radiative properties, and can lead to large errors in extremely complicated media, it has been largely used from simple configurations (Mesyngier and Farouk 1996; Yu et al. 2000) to the description of more complex ones (Kuhlert and Renz 1998; Bressloff 1999; Omori et al. 2000) with good results compared to more detailed descriptions.

Initially, this method was based on empirical weights $\omega_k(T)$. Then, as the WSGG model can be seen as a box model, where $\omega_k(T)$ corresponds to the fraction of the emissive power spectrum where the absorption coefficient equals $\kappa_k$, Denison and Webb (Denison and Webb 1993; Denison and Webb 1995b; Denison and Webb 1995a; Denison and Webb 1995c) extended the WSGG method by computing the values of $\omega_k(T)$ from line by line databases. This approach is called the Spectral-Line-based Weighted-sum of grey gases (SLW). Other sets of parameters enabling to account for overlapping gas bands (Solovjov and Webb 2000b) in mixtures and soot were later developed (Solovjov and Webb 2000a). Riviere et al. (Rivière et al. 1996; Pierrot et al. 1999; Pierrot et al. 1999) developed a similar approach (the ADF: Absorption Distribution Function approach) for 1-D mixture of $CO_2$ and $H_2O$ for various temperatures and concentrations of both gases.

#### 6.2.1.3 Total emissivity approaches

An estimation of the flux emitted by a homogeneous isothermal gas mass at temperature $T$ can be useful to estimate the order of magnitude of the radiative flux in a given application. A total emissivity $\epsilon(T)$ is defined as:

$$\epsilon(T) = \frac{1}{\sigma T^4} \int_{\nu=0}^{+\infty} \pi \epsilon'_\nu(T) I^\circ_\nu(T) d\nu = \frac{1}{\sigma T^4} \int_{\nu=0}^{+\infty} \pi \left(1 - e^{-\kappa_\nu L}\right) I^\circ_\nu(T) d\nu \quad (6.13)$$

where L is a characteristic dimension of the studied application.

The value of the total emissivity can be computed from other radiative properties description. For a quick estimation, it has also been tabulated for different species, as for $CO_2$ and $H_2O$ by Hottel and Sarofim (1967). When considering a mixture of several species with overlapping bands, similar approaches have been developed by Hottel and Sarofim (1967); Felske and Tien (1974).

The incoming radiative flux at walls is finally estimated as $\epsilon(T)\sigma T^4$. For a complex system, the major simplifications of this approach are:

- it considers only an homogeneous isothermal gas system,
- it is based on a representative length scale $L$ of the complex domain,
- it considers black walls: then, wall to wall radiative exchanges are not accounted for.

Nonetheless, this approach can be used for engineering sizing calculations in order to estimate the order of magnitude of such radiative transfers.

#### 6.2.1.4 Statistical Narrow-Band (SNB) models

In SNB models, the spectrum is divided into bands of size $\Delta\nu$ sufficiently narrow to consider a constant value of the Planck's law inside each band, but sufficiently large to include a large number of absorption lines allowing a statistical treatment of absorption coefficient from these lines. Several other assumptions are needed to construct the model:

- the center of the $N$ absorption rays inside each interval $\Delta\nu$ is supposed to have a random position inside the interval $\Delta\nu$,
- each one of the $N$ rays of the considered interval are supposed to belong to an infinite series of identical rays, positioned in a very large number of consecutive intervals of width $\Delta\nu$ (representative set),
- the $N$ rays of the interval have the same profiles (Lorentz, Doppler or Voigt) and their different widths $\gamma_m$ can be represented by a mean width $\overline{\gamma}$ (in the following, only the Lorentz broadening will be considered in order to illustrate the construction of the SNB models),
- the intensities $S$ of the $N$ rays follow a presumed distribution $P(S)$.

In the case of a homogeneous isothermal column of length $l$, temperature $T$, pressure $p$ with only one absorbing species with a molar fraction $x$, the mean transmissivity of a column $\overline{\tau'}^{\Delta\nu}$ can be retrieved by a statistical model, like the one of Malkmus (1967):

$$\overline{\tau'}^{\Delta\nu} = \exp\left\{-\frac{\overline{\beta}}{\pi}\left[\sqrt{1+2xpl\frac{\overline{k}}{\overline{\beta}}}-1\right]\right\} \qquad (6.14)$$
$$\overline{\beta} = 2\pi\overline{\gamma}/\overline{\delta}$$

where $\overline{k}(T)$ represents the ratio of the mean intensity of the lines by the mean spacing of the lines, $\overline{\delta}(T)$ represents the lines characteristic spacing and $\overline{\gamma}$ represents the average width of the lines. $\overline{k}(T)$ and $\overline{\delta}(T)$ are generally tabulated as a function of temperature and the considered spectral interval (Ludwig 1973; Rivière and Soufiani 2012), whereas $\overline{\gamma}$ is given by analytical laws function of the absorbant species, the temperature, the pressure and the concentrations of the different species in the medium (Soufiani and Taine 1997).

When considering a non isothermal column with only one absorbing species, one can first divide the heterogeneous column into $N_c$ homogeneous isothermal elements, each one characterized by a length $l_j$, conditions $(T_j, p_j, x_{ji})$ and parameters $(\overline{k}(T_j), 1/\overline{\delta}(T_j), \overline{\gamma}(T_j, p_j, x_{ji}))$. Then, it is necessary to model the spectral correlations between the different isothermal elements. The classical *Curtis-Godson* approximation is presented here (a detailed review of the

different approximations in literature can be found in Young (1977)). The considered approximation is the one classically used in combustion, because of its high accuracy in this kind of configurations at high temperature (less than 5% of error). It consists on introducing an extensive quantity $u$ characterizing the composition of the column of length $l$:

$$u = \int_0^l x_i(s)p(s)ds \tag{6.15}$$

Then, equivalent parameters $\overline{\kappa_e}$ and $\overline{\beta_e}$ are defined as:

$$\begin{aligned} \overline{k_e}u &= \int_0^l x_i(s)p(s)\overline{k}(s)ds \\ \overline{\beta_e}\ \overline{k_e}u &= \int_0^l x_i(s)p(s)\overline{k}(s)\overline{\beta}(s)ds \end{aligned} \tag{6.16}$$

The idea is then to consider an equivalent isothermal column parametrized by $\overline{k_e}$ and $\overline{\beta_e}$. The corresponding mean transmissivity of the column is then given by:

$$\overline{\tau_i'}^{\Delta\nu} = \exp\left\{ -\frac{\overline{\beta_e}}{\pi}\left[\sqrt{1+2xpl\frac{\overline{k_e}}{\overline{\beta_e}}}-1\right]\right\} \tag{6.17}$$

Finally, considering a medium with $N$ absorbing gases, the mean transmissivity of a column of this medium is given by:

$$\overline{\tau'}^{\Delta\nu} = \prod_{i=1}^{N} \overline{\tau_i'}^{\Delta\nu} \tag{6.18}$$

This model can be also extended when $P$ different kind of small particles are also present in the medium. The transmissivity of a column of this medium is in this case expressed by:

$$\overline{\tau'}^{\Delta\nu} = \prod_{i=1}^{N} \overline{\tau_i'}^{\Delta\nu} \prod_{p=1}^{P} \overline{\tau_p'}^{\Delta\nu} \tag{6.19}$$

with $\tau_p'$, the transmissivity across the column for each particles kind $p$.
This expression is based on the assumption of statistical independency of the spectral distributions of the absorption coefficients of the different species and of the considered particles.

Finally, the radiative transfer equation for a non-scattering media is solved for each narrow-band $\Delta\nu$ based on its transmissivity-formulated expression (valid only considering black walls):

$$I_\nu'(\mathbf{u}, s) = I_\nu'(\mathbf{u_0}, 0)\tau_{0s}' + \int_0^s I_\nu^\circ\left[T(s')\right]\frac{\partial\tau_{\nu,s's}'}{\partial s'}ds'. \tag{6.20}$$

#### 6.2.1.5 ck models

This approach is the one retained for the calculations in this thesis. Details of the construction of the gas radiative properties database are given below.

##### 6.2.1.5.1 Preliminary : $k-$distribution method in a uniform media

The first step in a narrow-band $k-$distribution method is to consider bands of size $\Delta\nu$ sufficiently small to assume that Planck functions are constant, as for SNB models. By doing so, in order to retrieve the different radiative quantities, only the knowledge of the distribution function of the absorption coefficient inside these intervals $\Delta\nu$ is needed.

In the $k-$distribution method, the basic idea is to compute Eqs. (6.6) and (6.7) by considering the integral over the values taken by the absorption coefficient $\kappa_\nu$ instead of considering it over the wavenumber $\nu$. Then, noting $f(k)dk$ the fraction of $\Delta\nu$ for which the absorption coefficient $\kappa_\nu$ takes values between $k$ and $k+dk$, the average transmissivity $\overline{\tau}^{\Delta\nu}(l)$ over the band $\Delta\nu$ of a uniform column of size $l$ writes:

$$\overline{\tau}^{\Delta\nu}(l) = \frac{1}{\Delta\nu}\int_{\Delta\nu}\exp(-\kappa_\nu l)d\nu = \int_{k=0}^{+\infty} f(k)\exp(-kl)dk \tag{6.21}$$

This change of variable can be applied to any quantity $F$ that depends on $\kappa_\nu$:

$$\overline{F} = \frac{1}{\Delta\nu}\int_{\Delta\nu} F(\kappa_\nu)d\nu = \int_{k=0}^{+\infty} f(k)F(k)dk \tag{6.22}$$

$f(k)$ can be computed analytically by dividing the spectrum into $N$ intervals of size $\delta_{\nu_i}$ such that $\kappa_\nu$ is a monotonic function inside each interval. As illustrated in Fig. 6.2, on each interval $[\nu_i, \nu_i+\delta_{\nu_i}]$, $\kappa_\nu$ can be estimated as:

$$\kappa_\nu = \kappa_{\nu_i} + \left|\frac{d\kappa_\nu}{d\nu}\right|_i (\nu-\nu_i) \text{ for} \nu \in [\nu_i, \nu_i+\delta_{\nu_i}] \tag{6.23}$$

Then, noting $k_{\min,i}$ and $k_{\max,i}$ respectively the minimum and maximum values of $\kappa_\nu$ inside the $i^{\text{th}}$ interval, for $k \in [k_{\min,i}, k_{\max,i}]$, the quantity $d\nu_i$ of the $i^{\text{th}}$ interval for which the absorption coefficient $\kappa_\nu$ takes values between $k$ and $k+dk$ is equal to:

$$d\nu_i = dk\left|\frac{d\kappa_\nu}{d\nu}\right|_i \tag{6.24}$$

Summing the contribution of all the bands, one obtains:

$$f(k)dk = \frac{1}{\Delta\nu}\sum_{i=1}^{N} d\nu_i = \sum_{i=1}^{N}\frac{dk}{\Delta\nu}\left|\frac{d\kappa_\nu}{d\nu}\right|_i [H(k-k_{\min,i}) - H(k-k_{\max,i})] \tag{6.25}$$

where $H$ is the Heaviside function.

$f(k)$ is then given by:

$$f(k) = \sum_{i=1}^{N} \frac{1}{\Delta\nu} \left| \frac{d\nu}{d\kappa_\nu} \right|_i [H(k - k_{\min,i}) - H(k - k_{\max,i})] \tag{6.26}$$

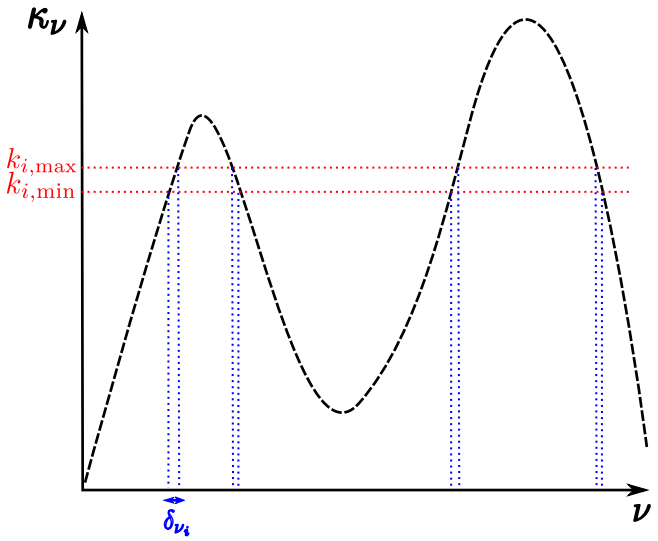


**Figure 6.2:** *Principle of k-distribution method. $f(k)dk$ corresponds to the sum of the intervals $\delta_{\nu_i}$ divided by $\Delta\nu$.*

#### 6.2.1.5.2 ck method in practical conditions with non-uniform media

The problem of the $k-$ distribution method in a non-uniform media is that spectral lines are very dynamic. As a consequence, very noisy functions $f(k)$ can be obtained, which are then hardly integrable.

To deal with these difficulties, the correlated$-k$ (ck) approach introduces the cumulative distribution function $g(k)$, defined as:

$$g(k) = \int_0^k f(k')dk'. \tag{6.27}$$

This function $g(k)$ is defined as a monotonic increasing function from $[k_{\min}, k_{\max}]$ to $[0, 1]$, where $k_{\min}$ and $k_{\max}$ are the minimum and maximum values of $\kappa_\nu$ inside the interval $\Delta\nu$. It corresponds to the probability that the absorption coefficient takes a value lower than $k$. As it is a monotonic increasing function, it exists a reciprocal function $k(g)$ at each point $s$ of the medium. This reciprocal function represents the absorption coefficient reordered by increasing

values, and can be easily computed from high-resolution line-by-line databases.

In the ck method, the average transmissivity of a nonuniform column is then approximated as:

$$\begin{aligned}\overline{\tau}^{\Delta\nu} &= \frac{1}{\Delta\nu}\int_{\Delta\nu}\exp\left[-\int_0^l \kappa_\nu(s)ds\right]d\nu \\ &\approx \int_0^1 \exp\left[-\int_0^l k(g,s)ds\right]dg\end{aligned} \tag{6.28}$$

Figure 6.3 presents a comparison between $k$ and cumulative $k$-distributions for $CO_2$ at different conditions. While $k$-distributions present a very erratic and noisy spectrum, smooth variations of the cumulative $k$-distributions are observed: more robust integration methods can then be applied with this method.

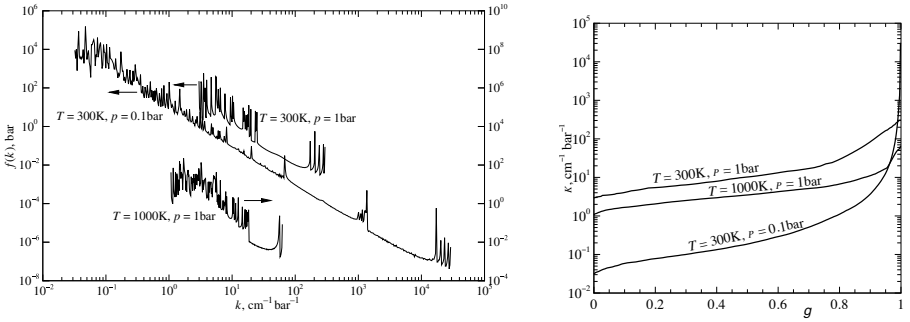


(a) $k$ distributions for $CO_2$ at different conditions.

(b) $k$-values as a function of cumulative $k$-distribution $g$ for $CO_2$ at different conditions.

**Figure 6.3:** *Comparison between k distribution and corresponding cumulative k-distributions for* $CO_2$ *at different conditions.*

It has been shown that the approximation of Eq. (6.28) is reasonable when one of the following conditions are fulfilled (Goody and Yung 1995):

- The media is optically thin (at all frequencies),
- The absorption spectrum can be put in the similar form (called "scaling approximation"): $\kappa_\nu(\mathbf{r}') = \eta(\nu)\Phi(\mathbf{r}')$. Then, the spectra reordering is carried out from a unique transformation of the wave number space, which does not depend on the position. Equation (6.28) is then rigorous.

This last condition is generally satisfied in atmospheric studies with small temperature gradients (Taine et al. 1999).

Using generally Gaussian-type quadrature, the average intensity $\overline{I}_{\nu_b}$ of the band

can be computed as:

$$\overline{I}_{\nu_b}(s) = \sum_{j=1}^{N} \omega_j I_{g_j}(s) \tag{6.29}$$

where $g_j$ and $\omega_j$ are the quadrature points and weights respectively, and $N$ is the quadrature order.
The intensity $I_{g_j}$ for a quadrature point $g_j$ in a non-scattering medium verifies then:

$$\frac{\partial I_{g_j}}{\partial s}(\mathbf{u}, s) = \; k(g_j, s) \left[ I^{\circ}_{\nu_b}(s) - I_{g_j}(s) \right]. \tag{6.30}$$

However, in our applications, several species absorb simultaneously in the same spectral bands. In this case, as for SNB models, we can assume that the spectra of these species are uncorrelated over each narrow band and therefore, the mean transmissivity of a mixture column in the narrow band of size $\Delta\nu_b$ can be approximated by the multiplication of the mean transmissivities of the species over the same narrow band.

For two species with absorption coefficient $k_1(g_i, s)$ and $k_2(g_i, s)$ at the quadrature points $(g_i)_{i=1,N}$, the transmissivity of a mixture column between $s = 0$ and $s = l$ writes:

$$\begin{aligned} \overline{\tau}^{\Delta_{\nu_b}} &= \left\{ \sum_{i=1}^{N} \omega_i \exp\left[ - \int_0^l k_1(g_i, s) ds \right] \right\} \left\{ \sum_{j=1}^{N} \omega_j \exp\left[ - \int_0^l k_2(g_j, s) ds \right] \right\} \\ &= \sum_{i=1}^{N} \sum_{j=1}^{N} \omega_i \; \omega_j \exp\left\{ - \int_0^l \left[ k_1(g_i, s) + k_2(g_j, s) \right] ds \right\} \end{aligned} \tag{6.31}$$

This expression corresponds to an $N^2$-point quadrature with the weights $\omega_i \omega_j$. Given that the RTE is linear with the mean radiative intensity $\overline{I}_{\nu_b}$ and with the mean transmissivities for each narrow band $[\nu_b, \nu_b + \Delta\nu_b]$, $\overline{I}_{\nu_b}$ satisfies:

$$\overline{I}_{\nu_b}(s) = \; \sum_{i=1}^{N} \sum_{j=1}^{N} \omega_i \omega_j I_{g_i, g_j}(s) \tag{6.32}$$

Thus, the radiative transfer equation for a couple of quadrature points $(g_i, g_j)$ is the following:

$$\frac{\partial I_{g_i, g_j}}{\partial s}(s) = \left( k_1(g_i, s) + k_2(g_j, s) \right) \left[ I^{\circ}_{\nu_b}(s) - I_{g_i, g_j}(s) \right] \tag{6.33}$$

The absorption coefficient of the mixture is then well described, but the calculation cost increases with the number of species: for two species, a $N^2$-point quadrature is needed for each narrow band, and a $N^m$-point quadrature would be necessary for $m$ species. Therefore, in our computations, only $CO_2$ and $H_2O$ will be taken into account in order to have an affordable computational cost, as they have largely higher absorption coefficients compared with other species in combustion (see Appendix D.1).

#### 6.2.1.6 Link with mean absorption coefficients

The use of mean absorption coefficient over all wavelength spectrum can be adequate in two specific cases:

1. When the medium is optically thin (i.e. when the mean free path for radiative transfer is very big compared to the physical dimensions of the system), absorption phenomenon can be neglected and the radiative power can be expressed as:

$$P^{\mathrm{R}} = -4\kappa_{\mathrm{Pl}}\sigma T^4 \tag{6.34}$$

where $\kappa_{\mathrm{Pl}}$ is the Planck mean absorption coefficient calculated as:

$$\kappa_{\mathrm{Pl}} = \frac{\int_{\nu=0}^{\infty} \kappa_\nu I_\nu^\circ(T) d\nu}{\int_{\nu=0}^{\infty} I_\nu^\circ(T) d\nu} = \frac{\int_{\nu=0}^{\infty} \kappa_\nu I_\nu^\circ(T) d\nu}{\sigma/\pi T^4}. \tag{6.35}$$

This model can be used when the medium is optically thin for all the wavelengths. When the medium is composed of combustion burnt gases (mainly $CO_2$ and $H_2O$), even if this hypothesis is widely used in combustion community, this hypothesis is not verified as reabsorbed radiative power is generally not negligible.

2. When the medium is optically thick (i.e. when the mean free path for radiative transfer is very small compared to the physical dimensions of the system), a diffusion approximation can be used. The corresponding radiative thermal conductivity $\lambda_R$ can be expressed as a function of the Rosseland mean absorption coefficient $\kappa_R$:

$$\lambda_R = \frac{16\sigma n^2 T^3}{3\kappa_R} \tag{6.36}$$

where $\kappa_R$ is computed as:

$$\frac{1}{\kappa_R} = \frac{\pi}{\sigma T^3} \int_{\nu=0}^{\infty} \frac{1}{\kappa_\nu} \frac{\partial I_\nu^\circ(T)}{\partial T} d\nu \tag{6.37}$$

In Appendix D.1.2, mean Planck absorption coefficients of the major species in combustion are given. The origin of the database used in our calculation is also detailed.

#### 6.2.1.7 Retained gaseous radiative properties

In the following chapters, two different models will be used and compared:

- the crude optically thin radiation model that considers the medium composed of burnt gases as optically thin for all the wavelengths,
- a detailed model implying the resolution of the RTE for the different wavelengths: the narrow-band ck model. This choice yields an accurate description of radiative transfer. While the approach is expensive, when associated with a Monte Carlo solver (Sec. 6.4), it becomes affordable nowadays in 3-D unsteady simulations.

### 6.2.2 Soot particles radiative properties

#### 6.2.2.1 Overview of soot radiative properties

When a photon passes close to a soot particle, this photon can by absorbed or scattered. The scattering is mainly due to diffraction, and, as the particles index is different from that of air, refraction and reflection. This scattering can be of two different types. When the mean distance $a$ between soot particles is equal or smaller than wavelength $\lambda$, the scattering by one particle can be affected by the presence of surrounding particles: this case is called *dependent scattering*. In the other case, when $a \gg \lambda$, the scattering is *independent* and the cloud of particles does not impact the scattering.

The radiative properties of spherical soot particles of diameter $d$ depend on three nondimensional parameters (Modest 2013): the complex index of refraction $m = n - ik$ (with $n$ and $k$ respectively the real and imaginary parts of the refraction index $m$), the nondimensional size parameter $x = \pi d/\lambda$ and the ratio of the mean distance of soot particles with the wavelength $\lambda$: $a/\lambda$.

Figure 6.4 shows the results of the study of Tien and Drolen (1987), which indicates the different types of particles and their class of nondimensional parameters. It can be observed that for soot particles, generally, $f_v < 10^{-4}$ and $a/\lambda \gg 1$, indicating that *dependent scattering effects* can be neglected. Moreover, the nondimensional parameter $x$ is generally very small compared to 1. This characteristic is fundamental in the construction of the models that will be presented hereafter.
Classically, *scattering cross-section* $C_{\text{sca}}$ and *absorption cross-section* $C_{\text{abs}}$ are used in order to quantify scattering and absorption phenomena. Extinction, gathering absorption and scattering is then expressed towards the *extinction cross-section* $C_{\text{ext}}$, defined as:

$$C_{\text{ext}} = C_{\text{abs}} + C_{\text{sca}} \tag{6.38}$$

To quantify these phenomena with nondimensional parameters, efficiency fac-

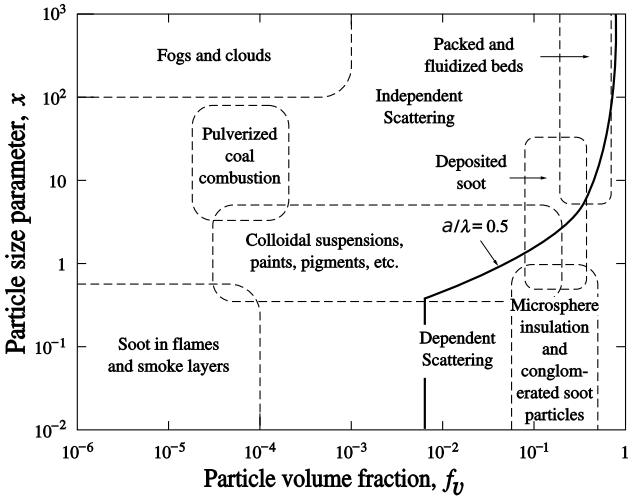


**Figure 6.4:** *Scattering regime map for independent and dependent scattering as a function of size nondimensional parameter $x = \pi d/\lambda$ (extracted from Modest (2013), based on the work of Tien and Drolen (1987)) .*

tors $Q$ for each of these phenomena are introduced. They correspond to the ratio of the cross-section with the projected surface area of a particle sphere:

$$\begin{aligned} &\textit{Absorption efficiency factor} && Q_{\text{abs}} = 4C_{\text{abs}}/(\pi d^2) \\ &\textit{Acattering efficiency factor} && Q_{\text{scat}} = 4C_{\text{sca}}/(\pi d^2) \\ &\textit{Extinction efficiency factor} && Q_{\text{ext}} = 4C_{\text{ext}}/(\pi d^2) \\ &\text{with:} && Q_{\text{ext}} = Q_{\text{abs}} + Q_{\text{sca}}. \end{aligned} \tag{6.39}$$

As studied in details by Okyay (2016), it has been demonstrated that for particles with primary diameter $d_p$ lower than 1 $\mu m$ (which is the case on our calculations), the scattering of soot particles can be neglected and does not impact the extinction coefficients. Therefore, in the following, scattering will be neglected and relations (6.38) and (6.39) become:

$$\begin{aligned} C_{\text{sca}} \ll C_{\text{abs}} \quad &\Rightarrow C_{\text{ext}} \approx C_{\text{abs}} \\ Q_{\text{sca}} \ll Q_{\text{abs}} \quad &\Rightarrow Q_{\text{ext}} \approx Q_{\text{abs}} \end{aligned} \tag{6.40}$$

Knowing the particles number density $n(d)$ of soot particles as a function of their diameter $d$, one can obtain the corresponding absorption coefficient of the soot particles $\kappa_{\lambda,\text{soot}}$:

$$\kappa_{\lambda,\text{soot}} = \int_0^{+\infty} C_{\text{abs}}(d)n(d)\mathrm{d}d = \frac{\pi}{4}\int_0^{+\infty} Q_{\text{abs}}(d)n(d)d^2\mathrm{d}d \tag{6.41}$$

#### 6.2.2.2 Soot particles index

Soot complex index of refraction is of important consideration as it plays a role in all radiation phenomena (scattering, diffraction and absorption).

Figure 6.5 presents a comparison of the complex soot index of refraction measurements in literature. It can be observed that a significant variability exists in these data and, therefore a large uncertainty of soot radiative properties can be expected.

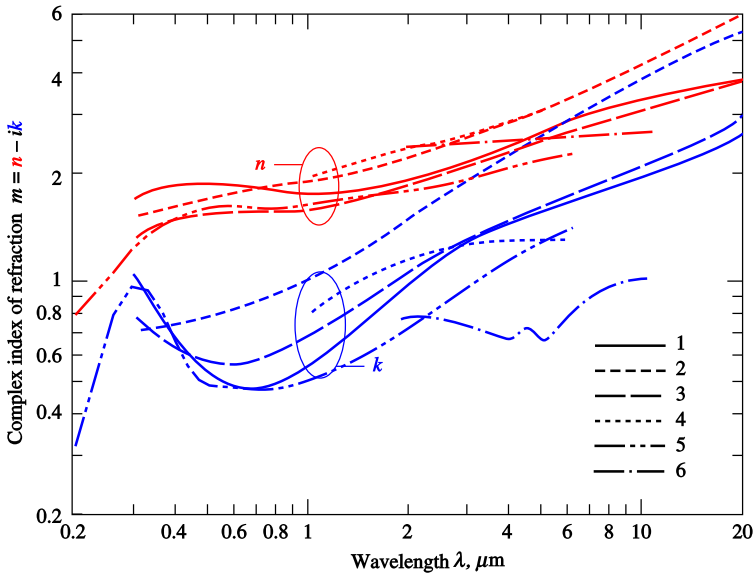


**Figure 6.5:** *Comparison of soot complex index of refraction from different studies (extracted and adapted from Modest (2013)): n the real part and k the imaginary part. Data comes from:* ***1****: Lee and Tien (1981) (polystyrene and plexiglas soot),* ***2****: Stull and Plass (1960) (amorphous carbon),* ***3****: Dalzell and Sarofim (1969) (propane soot),* ***4****: Howarth et al. (1966) (pyrographite at 300K),* ***5****: Chang and Charalampopoulos (1990) (propane soot),* ***6****: Felske et al. (1984) (propane soot).*

This information is also necessary when doing measures of soot volume fraction in flames by laser extinction. Indeed, it plays a role in the refractive index function, defined hereafter in Eq.(6.49). Important uncertainties have therefore to be expected in the soot volume fraction measurements provided in literature. Generally, in combustion community, a constant value of this refractive index is used. The most frequently value used for this refractive index is $m = 1.57 - 0.56i$, as explained by Smyth and Shaddix (1996).

For wavelength range $0.4 \leq \lambda \leq 30\mu m$, Chang and Charalampopoulos (1990)

have provided polynomial fits of $n$ and $k$ as a function of the wavelength $\lambda$:

$$\begin{aligned} n &= 1.811 + 0.1263\ln\lambda + 0.027\ln^2\lambda + 0.0417\ln^3\lambda \\ k &= 0.5821 + 0.1213\ln\lambda + 0.2309\ln^2\lambda - 0.01\ln^3\lambda \end{aligned} \tag{6.42}$$

This polynomial fit corresponds to the data of study 5 presented in Fig. 6.5. Even if it exists a large uncertainty in these parameters, we will consider only these two commonly set of parameters in the simulations of Chapters 7 and 9:

1. $m(\lambda) = m = 1.57 - 0.56i$,
2. $m(\lambda) = n(\lambda) - k(\lambda)i$ from Eq.(6.42).

#### 6.2.2.3 Mie theory

Mie theory is based on the exact solution of the radiative properties for an isolated sphere placed in vacuum (Hulst and van de Hulst 1957), and subject to an incident plane electromagnetic wave of wavelength $\lambda$. The corresponding solutions for the extinction and scattering efficiencies are:

$$\begin{aligned} Q_{\text{ext}} &= \frac{2}{x^2}\sum_{l=1}^{+\infty}(2l+1)\mathcal{R}e(a_l + b_l) \\ Q_{\text{sca}} &= \frac{2}{x^2}\sum_{l=1}^{+\infty}(2l+1)(|a_l|^2 + |b_l|^2) \end{aligned} \tag{6.43}$$

where the Mie series coefficient $a_l$ and $b_l$ are obtained from Ricatti-Bessel functions $\psi_l(x)$ and $\zeta_l(x)$:

$$\begin{aligned} a_l &= \frac{\psi_l'(mx)\psi_l(x) - m\psi_l(mx)\psi_l'(x)}{\psi_l'(mx)\zeta_l(x) - m\psi_l(mx)\zeta_l'(x)} \\ b_l &= \frac{m\psi_l'(mx)\psi_l(x) - \psi_l(mx)\psi_l'(x)}{m\psi_l'(mx)\zeta_l(x) - \psi_l(mx)\zeta_l'(x)} \end{aligned} \tag{6.44}$$

with $x = \pi d/\lambda$ the nondimensional size parameter and $m$ the complex refractive index.

For low values of $l$, the detailed expressions of $\psi_n$, $\psi_n'$, $\zeta_n$, $\zeta_n'$, $a_n$ and $b_n$ can be found in literature (Deirmendjian et al. 1961; Wiscombe 1980). Powerful computational algorithms (Mätzler 2002) have also been developed enabling to precisely determine these absorbing and scattering efficiencies.

#### 6.2.2.4 Rayleigh theory

Rayleigh theory comes from the results of the Mie theory, in case of small particles, *i.e* $x = \pi d/\lambda \ll 1$ (Bohren and Huffman 2008). It can then be

demonstrated that scattering and absorption efficiencies write:

$$\begin{aligned} Q_{\text{sca}} &= \frac{8}{3}\left|\frac{m^2-1}{m^2+2}\right|^2 x^4 \\ Q_{\text{abs}} &= -4\mathcal{I}m\left\{\frac{m^2-1}{m^2+2}\right\} x \end{aligned} \tag{6.45}$$

For soot particles with $m = 1.57 - 0.56i$, one obtains: $Q_{\text{sca}} \approx 2.49x^4$ and $Q_{\text{abs}} \approx -1.04x$.
Then, for soot particles, as $k \neq 0$ (with $k$ the imaginary part of the refractive index $m$) and $x \ll 1$ (implying $x^4 \ll x$), $Q_{\text{ext}} \approx Q_{\text{abs}}$. We retrieve then the fact that scattering is negligible compared to absorption for small particles such as soot particles in Rayleigh's regime.

Then, the absorption coefficient can be calculated as:

$$\begin{aligned} \kappa_{\lambda,\text{soot}} &= \int_0^{+\infty} Q_{\text{abs}} \frac{\pi d^2}{4} n(d)\mathrm{d}d \\ &= -\mathcal{I}m\left\{\frac{m^2-1}{m^2+2}\right\} \int_0^{+\infty} \left(\frac{\pi d}{\lambda}\right) \pi d^2 n(d)\mathrm{d}d \end{aligned} \tag{6.46}$$

Moreover, the soot volume fraction $f_V$ writes:

$$f_V = \int_0^{+\infty} \left(\frac{\pi d^3}{6}\right) n(d)\mathrm{d}d \tag{6.47}$$

Then, the soot absorption coefficient can be written directly as a function of the soot volume fraction $f_V$, the index of soot particles $m$ and the wavelength $\lambda$:

$$\kappa_{\lambda,\text{soot}} = -\mathcal{I}m\left\{\frac{m^2-1}{m^2+2}\right\} \frac{6\pi f_V}{\lambda} = \frac{36\pi nk}{(n^2-k^2+2)^2+4n^2k^2} \frac{f_V}{\lambda} \tag{6.48}$$

In soot literature, the refractive index function $E(m)$ is commonly introduced:

$$E(m) = -\mathcal{I}m\left\{\frac{m^2-1}{m^2+2}\right\} = \frac{6nk}{(n^2-k^2+2)^2+4n^2k^2} \tag{6.49}$$

Then, soot absorption coefficient can be expressed as a function of $E(m)$, $\lambda$ and $f_V$:

$$\kappa_{\lambda,\text{soot}} = \frac{6\pi E(m) f_V}{\lambda} \tag{6.50}$$

For $m = 1.57 - 0.56i$, one obtains respectively: $E(m) = 0.260$ and $\kappa_{\lambda,\text{soot}} = 4.89 f_V/\lambda$. Figure 6.6 compares the evolution of soot absorption coefficient with

wavelength considering Rayleigh theory with constant refractive index ($m = 1.57 - 0.56i$) and with wavelength-dependent refractive index from Eq. (6.42). A good consistency for the order of magnitude of both models is obtained.

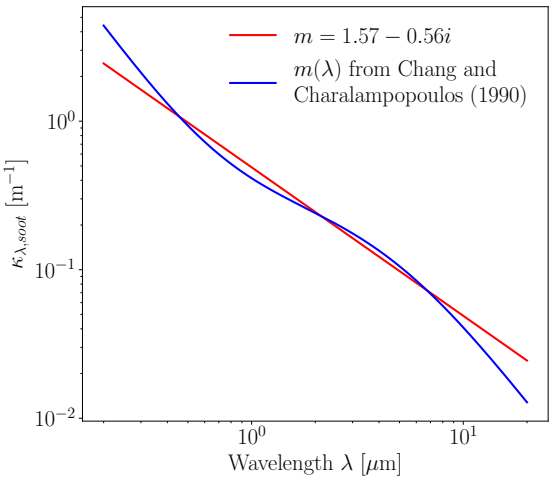


**Figure 6.6:** *Evolution of soot absorption coefficient with wavelength considering Rayleigh theory. Values obtained with constant refractive index ($m = 1.57 - 0.56i$) and wavelength-dependent refractive index from Eq. (6.42) are compared.*

Figure 6.7 summarizes the corresponding variations of $E(m)$ with the wavelength $\lambda$, computed based on the values of the real and imaginary parts of the soot particles refractive index $m$ referenced on different studies. The important uncertainties on the value of the optical index of soot particles, which depends on the fuel, their structure (spherical or aggregate), but also their surface condition, lead then to important variability ($\pm 50\%$) of the values of $E(m)$, which are used in laser extinction measurements for the determination of the soot volume fraction $f_V$. Moreover, these laser extinction measurements are generally used as calibration measures for LII measurements of soot volume fraction in turbulent flames. Then, precision of LII measurements are also impacted by such uncertainties.

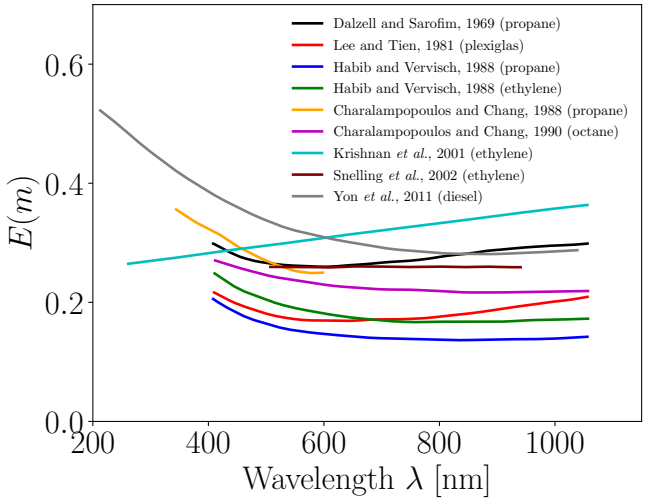


**Figure 6.7:** *Comparison of dependence of $E(m)$ with excitation wavelength $\lambda$, extracted and adapted from Mouton (2014) . The data sets are extracted from multiple studies analysing the evolution of $E(m)$ with wavelentgh for various fuels (Dalzell and Sarofim 1969; Lee and Tien 1981; Habib and Vervisch 1988; Charalampopoulos and Chang 1988; Chang and Charalampopoulos 1990; Krishnan et al. 2001; Snelling et al. 2002; Yon et al. 2011)*

#### 6.2.2.5 Planck mean soot absorption coefficient based on Rayleigh theory

If $n$ and $k$ are considered independent of the wavelength $\lambda$, the Planck mean absorption coefficient $\kappa_{\text{soot}}^{\text{Pl}}$ for soot particles is equal to:

$$\begin{aligned}\kappa_{\text{soot}}^{\text{Pl}}(T) &= \frac{1}{\sigma/\pi T^4}\int_0^{+\infty}\kappa_{\nu,\text{soot}}(T)I_\nu^\circ(T)d\nu \\ &= \frac{\sum_{n=1}^{+\infty}24/n^5}{\sum_{n=1}^{+\infty}6/n^4}\frac{C_0 f_V T}{C_2} = 3.83\frac{C_0 f_V T}{C_2}\end{aligned} \tag{6.51}$$

with $C_2 = hc/k_B$ is the second Planck constant and $C_0 = 6\pi E(m)$.
When considering wavelength dependent complex refractive index from Eq. (6.42), simple analytical expression can not be obtained, but numerical integration can be done. Figure 6.8 provides a comparison of the Planck mean absorption from Eq. (6.51) with $m = 1.57 - 0.56i$ and the one obtained when considering wavelength dependent complex refractive index, both considering a soot volume fraction of $f_V = 10^{-7}$. It can be observed that wavelength dependent soot refractive index does impact the Planck mean absorption coefficient, up to 10% at very high temperatures.

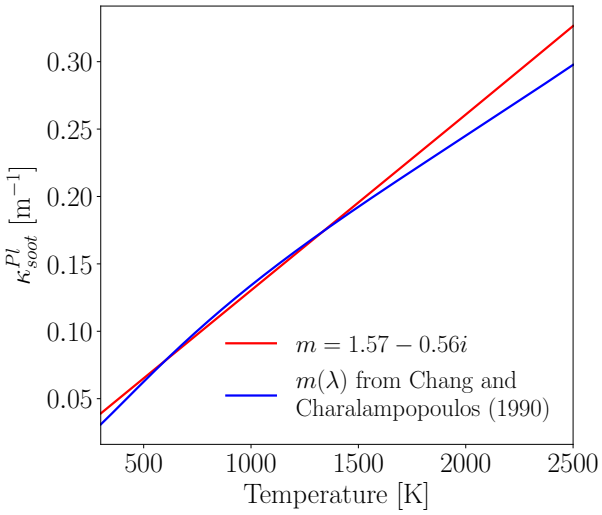


**Figure 6.8:** *Comparison of obtained Planck mean soot absorption coefficient as function of temperature when considering a constant index* $m = 1.57 - 0.56i$ *for soot particles and a wavelength dependent one from Eq.*(6.42).

Mie theory is limited only to spherical or spheroidal objects. Rayleigh theory corresponds to a particular case of Mie theory, only valid for small spherical objects. More complex methods are required for computing the real properties of soot fractal aggregates. RDG-FA and DDA methods, introduced hereafter, are some of them.

#### 6.2.2.6 RDG theory

The RDG (*Rayleigh-Debye-Gans*) theory applied on a spherical particle is based on two main assumptions:

- $|m-1| \ll 1$,
- $x|m-1| \ll 1$, where $x = \pi d/\lambda$.

where $d$ is the diameter of a soot spherical particle.

When these two main assumptions are verified, it can be demonstrated that the same expressions for soot absorption coefficient that the ones of the Rayleigh regime for a spherical particle are retrieved (Bohren and Huffman 2008).

The RDG theory is generally also applied for soot aggregates composed of $n_p$ primary particles with the same primary diameter $d_p$.
To apply the RDG theory on such aggregate, the following conditions must be verified:

- $|m-1| \ll 1$,
- $x_p|m-1| \ll 1$, where $x_p = \pi d_p/\lambda$.

When these conditions are satisfied, it is considered that no radiative interactions exist between the different primary particles composing a soot aggregate. The absorption cross section $C_{\text{abs,agg}}$ of one aggregate is directly derived from results of RDG theory and is expressed as (Köylü and Faeth 1993; Bohren and Huffman 2008):

$$C_{\text{abs,agg}} = n_p C_{\text{abs,p}} \tag{6.52}$$

where $C_{\text{abs,p}}$ is the absorption cross section of a small spherical primary particle:

$$C_{\text{abs,p}} = -\,\pi x_p d_p^2 \mathcal{I}m\left\{\frac{m^2-1}{m^2+2}\right\} \quad where \quad x_p = \pi d_p/\,\lambda. \tag{6.53}$$

#### 6.2.2.7 RDG-FA theory

The RDG-FA (*Rayleigh-Debye-Gans for Fractal Aggrates*) extends this approach to the study of fractal aggregates. It has been first proposed by Dobbins and Megaridis (1991) and the idea is to correct the simple expression obtained from RDG scattering with additional terms, enabling to take into account radiative properties of soot aggregates depending on their overlapping, necking or even coating (Yon et al. 2015; Liu et al. 2016). These phenomena are results of the different chemical and physical processes that soot particles can undergo. Figure 6.9 illustrates each one of these phenomena.

RDG-FA is also used for the study of scattering properties of soot aggregates (Yon et al. 2014). More rigorous techniques like IEFS or DDA (introduced briefly hereafter) are then used to test the accuracy limits of this approach or bring new improvements (Farias et al. 1996).

As explained previously, here we will not consider the part of the RDG-FA concerning scattering, as it is generally negligible for the particles found in our applications. We will consider that soot aggregates are composed of $n_p$ spherical and not overlapped primary particles with a primary diameter $d_p$. Necking and coating phenomena will also be neglected. When considering only absorption, and when the previous conditions are verified, RDG and RDG-FA are equivalent. Thus, knowing the distribution of aggregates and their corresponding number of primary particles $n_p$ and diameters $d_p$, one can obtain their corresponding radiative properties.

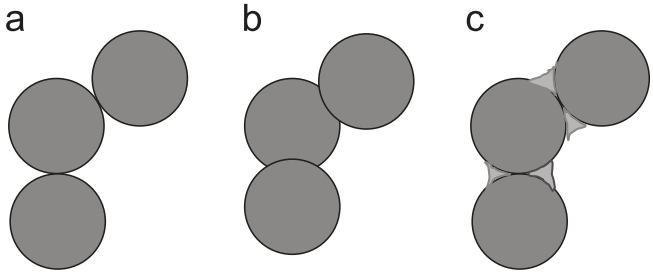


Schematic illustrating (a) point-touch, (b) overlapping, and (c) necking between neighbouring primary particles of a soot aggregate.

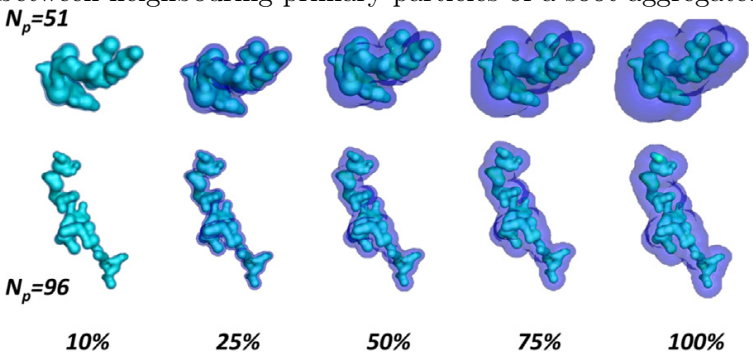


Graphical illustration of two soot aggregates with different levels of coating thickness from 10% to 100% of the primary particle diameter

**Figure 6.9:** *Illustration of soot aggregates overlapping, necking and coating phenomena (extracted from Liu et al. (2016)).*

In fact, for the only considered absorption phenomenon, Eq. (6.52) is identical to Eq. (6.50) even considering aggregates of spherical primary particles:

$$
\begin{aligned}
\kappa_{\lambda,\text{soot}} &= \int_0^{+\infty} C_{\text{abs,agg}}(d) n(d) \mathrm{d}d \\
&= \int_0^{+\infty} n_p(d) C_{\text{abs,p}}(d) n(d) \mathrm{d}d \\
&= -\int_0^{+\infty} 6\pi/\lambda \; \mathcal{I}m \left\{ \frac{m^2-1}{m^2+2} \right\} \underbrace{n_p(d)\pi(d_p(d))^3/6}_{v(d)} n(d) \mathrm{d}d \\
&= -6\pi/\lambda \; \mathcal{I}m \left\{ \frac{m^2-1}{m^2+2} \right\} \int_0^{+\infty} v(d) n(d) \mathrm{d}d \\
&= -6\pi/\lambda \; \mathcal{I}m \left\{ \frac{m^2-1}{m^2+2} \right\} \int_0^{+\infty} q(d) \mathrm{d}d \\
&= -6\pi/\lambda \; \mathcal{I}m \left\{ \frac{m^2-1}{m^2+2} \right\} f_V \\
&= \frac{6\pi E(m) f_V}{\lambda}
\end{aligned}
\tag{6.54}
$$

In fact, the description of soot aggregates properties by RDG-variant models only differs in their approximation of scattering.

In their study, Farias et al. (1996) and coworkers compare the accuracy of the RDG-FA classical method with the integral equation formulation for scattering (IEFS) reference calculations for numerically generated aggregated with number of primary particles varying from $n_p = 16$ to $n_p = 256$. The studied aggregates are fractal-like aggregates that are representative of those obtained with the diffusion-limited cluster-cluster aggregation (DLCCA) algorithm with a fractal dimension $D_f = 1.8$, but no overlapping or necking is considered. Figure 6.10 presents deviation contours of the RDG-FA absorption cross sections results compared with the results obtained from the IEFS technique, depending on the value of the parameters $n_p$, $m$ and $x_p = \pi d_p/\lambda$. Considering $m = 1.57 - 0.56i$, the corresponding value of $|m - 1|$ is approximatively 0.8. Moreover, generally in gas-turbine applications, $d_p < 100$nm and the the wavelength of interest $\lambda$ is greater than 500nm. Then, $x_p$ is generally very small compared to unity, and does not exceed the value of 0.5. Looking at Fig. 6.10, it can then be concluded that, generally, RDG-FA theory estimates the absorption coefficient of the considered aggregates with an error lower than 10%. It can also be observed that the error increases with the number of primary particles $n_p$, and therefore with the size of the aggregate.

It is important to notice that strong assumptions are present in this model, especially with the assumption of no radiative interactions between the different primary particles composing a soot aggregate, and the hypothesis of no overlapping and no necking. However, some primary studies show that complex aggregates absorption properties can be retrieved by RDG-FA method by correctly adding correction factors to this theory (Yon et al. 2014; Yon et al. 2015).

#### 6.2.2.8 Towards detailed radiative properties: DDA approach and impact of soot morphology in their radiative properties

In their study, Yon et al. (2015) also show that when soot aggregates present necking and overlapping, their scattering and absorption coefficients significantly decrease at near UV and increase at longer wavelengths. Necking and overlapping, among other geometric characteristics of soot aggregates, must then be taken into account in order to correctly predict their absorption coefficient.

In order to obtain radiative properties of very complex soot aggregates (with overlapping or necking), complex numerical and analytical techniques are required: IEFS (Farias et al. 1996; Eymet et al. 2002), GMM (Liu and Snelling 2008), T-matrix (Mishchenko et al. 2013) or DDA (Yon et al. 2014) are some

of them. Only DDA will be detailed here as it is the one that can simulate arbitrary geometries, such as soot complex aggregates (Okyay 2016).

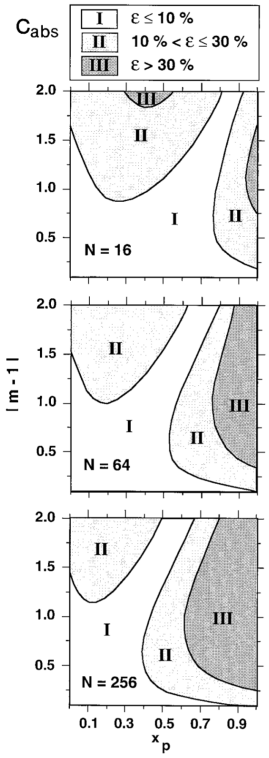


**Figure 6.10:** *Percent deviation contours for the accuracy domains of the RDG-FA approximation for predicting the absorption cross sections of DLCCA aggregates depending on their number of primary aggregates ($n_p$ but noted $N$ in the present figure), the nondimensional size parameter $x_p = \pi d_p/\lambda$, and the refractive index $m$. The fractal dimension of $D_f$ of all considered aggregates is approximatively 1.8 (representative of soot aggregates). The figure is extracted from the work of Farias et al. (1996).*

The DDA approach has been firstly proposed by Purcell and Pennypacker (1973) and further developed by Draine (1988), Draine and Goodman (1993), Enguehard (2009) and Lallich (2009). It consists of discretizing the studied object, subject to an incident electromagnetic field, into $N$ dipole elements verifying two conditions: the size of the volume elements should be smaller compared to the attenuation length of the incident wave inside the material, and, the path difference of the incident electromagnetic field inside the volume element should be negligible. These conditions imply that (Draine 1988): $2\pi|m|\delta/\lambda < 1$, where $\delta$ is the characteristic size of each dipole. Each dipole being polarized under the effect of the external electromagnetic field, the absorption and scattering cross sections can be obtained by solving the dipole-dipole interaction matrix expressed as a function of the incident illuminating electromagnetic field and the fields emitted by each one of the dipoles (Okyay 2016).

Using this approach, Okyay (2016) and coworkers have computed the radiative properties of two real soot aggregates reconstructed by tomography. Their reconstructions are presented in Fig. 6.11. The left figure, called "small aggregate" presents an extent of approximatively 300nm, whereas the other one, called "big aggregate" presents an extent of approximatively 1.5$\mu$m.

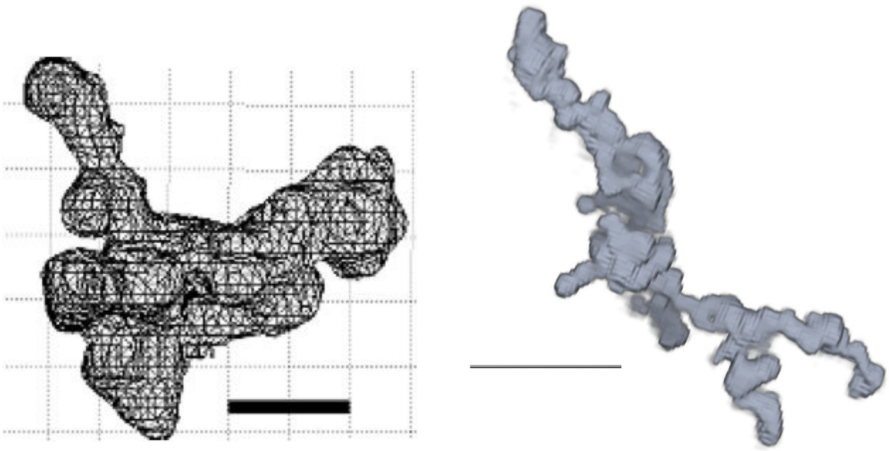

(a) Small aggregate (scale bar corresponds to 100nm)

(b) Big aggregate (scale bar corresponds to 500nm)

**Figure 6.11:** *Reconstructed geometries of the two aggregates studied in the work of Okyay (2016).*

Figure 6.12 presents the calculated absorption cross sections of these aggregates using the DDA approach (legend "TOMO"). In this study, the idea was to compare the quality of the different approaches that have been presented in the previous paragraphs for the prediction of soot aggregates radiative properties. Figure 6.12 compares the reference solutions ("TOMO") with the results from the Mie theory considering only one equivalent spherical particle ("Mie $R_{veq}$"), Mie theory considering $N_p$ primary particles of radius $r_p = d_p/2$, RDG-FA classical theory, and DDA theory applied on DLCCA point-contact reconstructed aggregates. For all these cases, the absorption cross section is underestimated for both aggregates. The last comparison is done by generating with a modified version of the DLCCA method, soot particles aggregates with overlapping (the coefficient $C_p$ is defined at the ratio between the distance separating the center of two adjacent primary particles with the diameter of a primary particle $d_p$). It can be observed that DDA calculations on these aggregates enable to retrieve the value of the radiative properties obtained for the tomographic reconstructed aggregates.

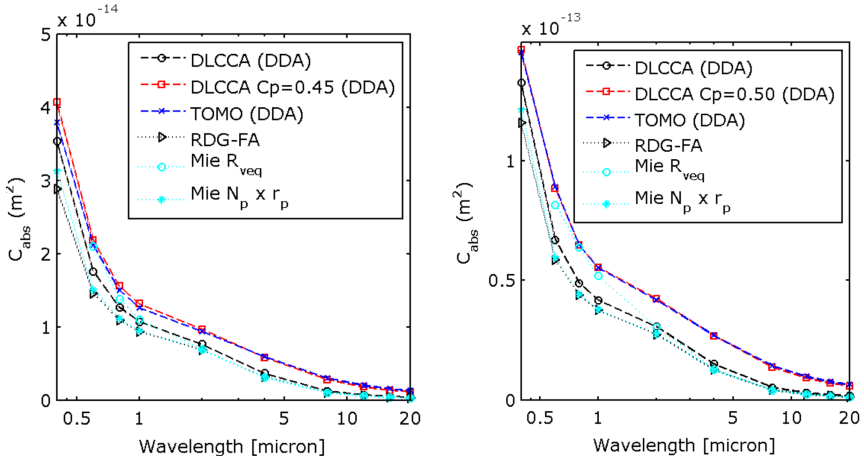


(a) Small aggregate (b) Big aggregate

**Figure 6.12:** *Absorption cross sections calculations of the two considered aggregates by Okyay (2016).*

These results illustrate the impact of overlapping on the radiative properties of soot, but also the large uncertainty that remains on soot particles properties. As they can be found as aggregates in combustion applications, simple Rayleigh theory can not be rigorously applied, and further studies are still required in order to describe precisely the radiative properties of soot particles.

In the present works, as a first approach, no scattering and the Rayleigh regime applied to primary particles composing soot aggregates will be considered for the soot particles radiative properties. In fact, as explained previously, when neglecting scattering, the same absorption coefficient formula is obtained while considering a soot aggregate as an equivalent sphere verifying the Rayleigh regime or RDG assumption, or aggregates composed of spherical primary particles verifying the Rayleigh regime (RDG/RDG-FA assumptions). In future works, more complex radiative properties as the one obtained from DDA calculations can be envisaged thanks to the sectional model presented in Part I, which allows for a specific expression per size of aggregates.

## 6.3 Resolution methods of the Radiative Transfer Equation (RTE)

Describing radiative properties of gas and soot is a first step in considering resolution of the radiative transfer equation in presence of both phases. However, the resolution of the RTE is quite challenging and different techniques have been developed. In the next paragraphs, the different resolution methods will be presented briefly.

As we have seen previously in Eq. (6.6), the radiative power is expressed as an integral dependent on numerous variables: the wavenumber $\nu$ and the azimuthal angle $\psi$ and the polar angle $\theta$ parametrizing the solid angle $\Omega$. To compute this integral, several methods can be found in the literature:

- Spherical Harmonics Approximation (**PN**) where the directional intensity $I'_\nu$ is expressed in the orthonormal spherical harmonics basis $Y_l^m(\theta, \psi)$:

$$\int_{\Omega=0}^{4\pi} Y_l^m Y_{l'}^{m'*} d\Omega = \delta_{mm'}\delta_{ll'} \tag{6.55}$$

  where the symbol $^*$ corresponds to the conjugate complex number.
  The radiative intensity $I'_\nu(\mathbf{r}, \mathbf{u})$ depends then separately on $\mathbf{r}$ and $\mathbf{u}$ and is expressed as:

$$I'_\nu(\mathbf{r}, \mathbf{u}) = \sum_{r=0}^{\infty} \sum_{m=-l}^{+l} A_{l\nu}^m(\mathbf{r}) Y_l^m(\theta, \psi) \tag{6.56}$$

  where $A_{j\nu}^m(\mathbf{r})$ are the unknown fields. Based on the fast convergence of the spherical harmonics basis with $\mathbf{u}(\theta, \psi)$, this method allows then to solve at a lower cost the RTE by only computing the first components of the basis (for the $P_1$ method, the development is done until $l = 1$, for $P_3$ method, until $l = 3$, ...). The drawback is the computational cost needed to increase the accuracy of the method (increasing the development order increases drastically the computational time).
- Discrete Ordinates Method (**DOM**) where the integrals over the directions are replaced by numerical quadratures. The quadrature points correspond to the discrete ordinates and the radiative intensity at each point is obtained by progressing point-by-point in each discrete ordinate direction,
- Finite Volume Method (**FVM**) where the space is subdivided into control volumes and the solid angle $4\pi$ is divided into a finite number of control angles. The direction intensity at each node is then obtained by integrating the RTE over a control volume and a control angle,
- Monte-Carlo Method (**MC**) where the RTE is solved statistically. In this approach, photons are emitted following probability density functions for the directions and the wavelength. The progression of each photon is tracked until it has no more energy or it exits the system. The main advantage of this method is that the cost does not depend on the dimensions of the problem (here the directions and the wavelength). However, in its classical utilisation, its convergence rate is low and follows typically a $1/\sqrt{N}$-law where N is the number of photon bundles.
- Ray tracing methods, which solves the RTE in a deterministic way by discretizing the space of directions and wavelength and by emitting one

photon for each direction and each wavelength.

To accurately determine the value of the radiative power, the Monte-Carlo method has therefore three main advantages:

1. Its cost does not depend on the dimension of the integration variables. Therefore, given the number of integration variables, it can be more suitable for radiation power evaluation compared with more deterministic methods like FVM or DOM.
2. Monte-Carlo methods enable to account for detailed spectral radiative properties, such as the ck narrow-band model in a much cheaper way. Indeed, the RTE is only solved for some spectral bands determined by the Monte Carlo algorithm instead of being solved for each spectral band in FVM or DOM.
3. It enables then to obtain an error control of the convergence. Increasing the number of photon bundles enables to reduce the estimation error of the radiative power, which can be also estimated.

As mentioned before, in the following, only Monte Carlo type methods will be considered. A variant, the Quasi Monte-Carlo method, which is a quasi-probabilistic method will be also presented.

## 6.4 Monte Carlo resolution of the RTE

### 6.4.1 Monte Carlo general principle

The general Monte Carlo integration deals with the integration of multidimensional integrals such as:

$$I = \int_V f(\mathbf{x}) \frac{d\mathbf{x}}{V} \equiv E[f] \tag{6.57}$$

where $\Omega$ is the volume of integration equal to $V = \int_V d\mathbf{x}$.

In the naive Monte Carlo approach, $I$ is approximated by sampling randomly and uniformly $N$ points on $\Omega$: $\mathbf{x_1}, \mathbf{x_2}, ..., \mathbf{x_N}$. $I$ is then statistically estimated through the estimator $\widehat{I}_N$:

$$I \approx \widehat{I}_N = \frac{1}{N} \sum_{i=1}^{N} f(\mathbf{x_i}) \tag{6.58}$$

Indeed, the law of large numbers ensures that: $\lim_{N \to +\infty} \widehat{I}_N = I$.

The quality of the estimation of $I$ is impacted by the intrinsic standard deviation $\sigma_{\text{intrinsic}}$ of the estimator, calculated through the unbiased estimate of the

variance:

$$\sigma_{\text{intrinsic}} \equiv \sigma(f) \approx \frac{1}{N-1}\sum_{i=1}^{N}\left(f(\mathbf{x_i}) - E[f]\right)^2 \tag{6.59}$$

Indeed, the central limit theorem states that the convergence of the standard deviation of the estimator samples $\sigma(\widehat{I}_N)$, which is a metric of the error between $\widehat{I}_N$ and $I$, follows the law:

$$\sigma(\widehat{I}_N) \approx \frac{\sigma_{\text{intrinsic}}}{\sqrt{N}}. \tag{6.60}$$

which decreases with a $\mathrm{N}^{-1/2}$ law, and does not depend on the number of dimensions of the integral.

In the following sections, this principle is applied to the calculation of the radiative power $P_i$ at each cell $i$, based on its integral formulation in (6.6) which can be written as

$$P_i = \int_{\nu=0}^{\infty}\int_{4\pi}\left[\kappa_\nu\left(I'_\nu - I^\circ_\nu\right)\right]d\Omega d\nu \tag{6.61}$$

### 6.4.2 Monte Carlo methods for the resolution of the RTE

In classical Monte Carlo (Forward Method: **FM**), the radiation computational domain is discretized into $N_v$ and $N_f$ isothermal finite cells of volume $V_i$ and faces of area $S_i$ respectively. Neglecting scattering, the radiative power in any cell $i$ is written as the sum of the part of the emitted powers of all the other cells $j$ absorbed by the cell $i$ ($P^{\text{ea}}_{ji}$) minus the emitted power from the cell $i$:

$$P_i^{\text{FM}} = \sum_{j=1}^{N_v+N_f} P^{\text{ea}}_{ji} - P^e_i \tag{6.62}$$

Fig. 6.13 illustrates how $P^{\text{ea}}_{ij}$, the energy emitted by the differential volume $dV_i$, transmitted by the media and absorbed by $dV_j (= dA_j \times ds_j)$ is computed. It is expressed by:

$$P^{\text{ea}}_{ij} = \int_{\nu=0}^{+\infty} P^{\text{ea}}_{\nu,ij}d\nu \tag{6.63}$$

with:

$$P^{\text{ea}}_{\nu,ij} = (4\pi\kappa_\nu(T_i)I^\circ_\nu(T_i)dV_i) \times \left(\frac{dA_j}{4\pi r^2}\right) \times (\tau_{\nu,r}) \times \ (\kappa_\nu(T_j)ds_j) \tag{6.64}$$

and where $I^\circ_\nu(T_i)$ is the equilibrium spectral intensity at temperature $T_i$, $r$ the distance between $dV_i$ and $dV_j$, $\kappa_\nu$ the spectral absorption coefficient and $\tau_{\nu,r}$

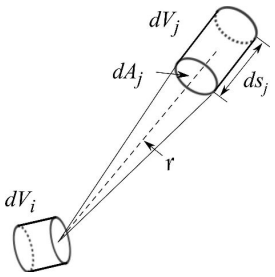


**Figure 6.13:** *Radiative exchange between two differential volume elements. (Extracted from Zhang (2013)).*

the transmissivity of the column between the differential volumes $dV_i$ and $dV_j$.

In the classical Monte Carlo method, at each point of the domain $i$, the direction and the wavelength $\nu_n$ of the photon bundle $n$ are randomly chosen by following their corresponding probability density functions (detailed later). A large number of optical shots are then issued from the cells. Statistical estimation $\widehat{P}_i$ of $P_i$ is obtained by summing the contributions of the $N_i$ shots:

$$\begin{aligned}\widehat{P}_i &= \left(\frac{1}{N_i}\sum_{n=1}^{N_i}\sum_{j=1}^{N_v+N_f}\delta_{ijn}P^{\mathrm{ea}}_{ji\nu_n}\right) - P^e_i \\ &= \frac{1}{N_i}\sum_{n=1}^{N_i}\left[\sum_{j=1}^{N_v+N_f}\delta_{ijn}P^{\mathrm{ea}}_{ji\nu_n} - P^e_i\right]\end{aligned} \tag{6.65}$$

where $\delta_{ijn}$ equals 1 if the bundle $n$ emitted by cell $i$ crosses cell $j$, 0 otherwise.

Then, as explained in Section 6.4.1, the convergence is ensured by the law of large numbers and the central limit theorem states that the convergence of such statistically process measured by the sample standard deviation $\sigma(\widehat{P}_i)$ follows the law:

$$\sigma(\widehat{P}_i) \approx \frac{\sigma_{\mathrm{intrinsic}}}{\sqrt{N_i}} \tag{6.66}$$

where $\sigma_{\mathrm{intrinsic}}$ is the intrinsic population standard deviation and $N_i$ is the number of evaluations of the estimator.

### 6.4.3 Reciprocity Principle

The radiative power of any cell $i$ can also be written as the sum of the exchange powers $P_{ij}^{\text{exch}}$ between $i$ and all the other cells $j$, *i.e.*:

$$P_i = \sum_{j=1}^{N_v+N_f} P_{ij}^{\text{exch}} = -\sum_{j=1}^{N_v+N_f} P_{ji}^{\text{exch}} \tag{6.67}$$

For volume cells, $P_{ij}^{\text{exch}}$ is defined as:

$$P_{ij}^{\text{exch}} = P_{ji}^{\text{ea}} - P_{ij}^{\text{ea}} = \int_{\nu=0}^{\infty} (P_{\nu,ji}^{\text{ea}} - P_{\nu,ij}^{\text{ea}}) d\nu \tag{6.68}$$

where $P_{\nu,ji}^{\text{ea}}$ is the spectral radiative power emitted by the volume $i$ and absorbed by the volume $j$, introduced in Eq. (6.64).
Equation (6.64) can be rewritten as:

$$\frac{P_{\nu,ij}^{\text{ea}}}{I_\nu^\circ(T_i)} = \tau_{\nu,r}\kappa_\nu(T_i)\kappa_\nu(T_j)\frac{dV_i dV_j}{r^2} \tag{6.69}$$

Similarly, $P_{\nu,ji}^{\text{ea}}$ is expressed as:

$$\frac{P_{\nu,ji}^{\text{ea}}}{I_\nu^\circ(T_j)} = \tau_{\nu,r}\kappa_\nu(T_i)\kappa_\nu(T_j)\frac{dV_i dV_j}{r^2} \tag{6.70}$$

Then, noting that right sides of the two last equations are identical, one can obtain the following relation between $P_{\nu,ij}^{\text{ea}}$ and $P_{\nu,ji}^{\text{ea}}$:

$$\frac{P_{\nu,ij}^{\text{ea}}}{I_\nu^\circ(T_i)} = \frac{P_{\nu,ji}^{\text{ea}}}{I_\nu^\circ(T_j)} \tag{6.71}$$

This corresponds to the so-called *reciprocity principle*, enabling then to rewrite the exchanged power $P_{\nu,ij}^{\text{exch}}$ between $i$ and $j$ as:

$$P_{\nu,ij}^{\text{exch}} = P_{\nu,ji}^{\text{ea}} - P_{\nu,ij}^{\text{ea}} = \tau_{\nu,r}\kappa_\nu(T_i)\kappa_\nu(T_j)\left[I_\nu^\circ(T_j) - I_\nu^\circ(T_i)\right]\frac{dV_i dV_j}{r^2} \tag{6.72}$$

Writing $\frac{dV_j}{r^2} = ds_j d\Omega_i$, with $d\Omega_i$ the corresponding solid angle at which $dA_j$ is seen from $dV_i$, $P_{\nu,ij}^{\text{exch}}$ can be expressed as:

$$P_{\nu,ij}^{\text{exch}} = \tau_{\nu,r}\kappa_\nu(T_i)\kappa_\nu(T_j)ds_j\left[I_\nu^\circ(T_j) - I_\nu^\circ(T_i)\right]dV_i d\Omega_i \tag{6.73}$$

Integrating $P_{\nu,ij}^{\text{exch}} d\nu$ over all the optical paths issued from $i$ and crossing $j$, and over all the frequencies $\nu$, the total exchanged power $P_{ij}^{\text{exch}}$ between $i$ and $j$ is expressed as:

$$P_{ij}^{\text{exch}} = \int_{\nu=0}^{\infty} \kappa_\nu(T_i)\left[I_\nu^\circ(T_j) - I_\nu^\circ(T_i)\right]\int_{V_i}\int_{4\pi} A_{ij\nu} d\Omega_i dV_i d\nu, \tag{6.74}$$

where:

$$A_{ij\nu} = \sum_{m=1}^{N_p} \tau_\nu(\mathrm{BF}_m)\alpha_{jm\nu} \tag{6.75}$$

and $N_p$ represents the total number of crossing of the cell $j$ by a given optical path issued from the cell $i$.

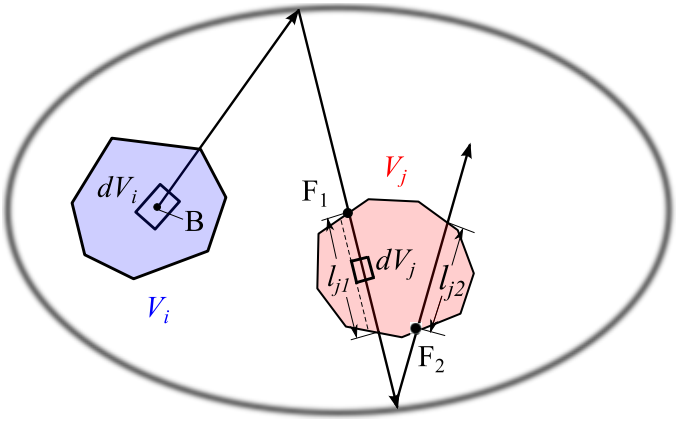


**Figure 6.14:** *Representation of an optical path issued from a cell $i$ and crossing a cell $j$.*

For the $m$-th crossing of the cell $j$ by an optical path issued from $i$, $\tau_\nu(\mathrm{BF}_m)$ is the spectral transmissivity between the source point B in cell $i$ and the inlet point $\mathrm{F}_m$ in the cell $j$ of the corresponding path, accounting for all the of the optical path on walls. For an optical path issued from B and crossing in its path until $\mathrm{F}_m$ Q volume points $\mathrm{P}_{qm}$ and R opaque walls points $\mathrm{W}_{rm}$ presenting a spectral emissivity $\epsilon_{r\nu}$, the transmissivity $\tau_\nu(\mathrm{BF}_m)$ writes:

$$\tau_\nu(\mathrm{BF}_m) = \tau_\nu(\mathrm{BP}_{1m}) \left( \prod_{q=1}^{Q} \tau_\nu(\mathrm{P}_{qm}\mathrm{P}_{q+1m}) \right) \left( \prod_{r=1}^{R} (1-\epsilon_{r\nu}) \right) \tau_\nu(\mathrm{P}_{Qm}\mathrm{F}_m) \tag{6.76}$$

$\alpha_{jm\nu}$ is the spectral absorptivity of the optical path corresponding column inside the cell $j$ for the $m$-th crossing (see Fig. 6.14):

$$\alpha_{jm\nu} = 1 - \exp\left[-\kappa_\nu(T_j) l_{jm}\right] \tag{6.77}$$

If $j$ corresponds to an opaque wall surface, $\alpha_{jm\nu} = \epsilon_{j\nu}$ where $\epsilon_{j\nu}$ is the wall spectral emissivity of the cell $j$.

Finally,

- For a volume cell, the radiative power $P_i$ of a cell $i$ is given by:

$$P_i = \sum_{j=1}^{N_{ij}} P_{ij}^{\text{exch}} \tag{6.78}$$

- For surface cells, the radiative flux integrated on the surface area $S_i$ is noted $\Phi_i$ and is given by:

$$\Phi_i = \sum_{j=1}^{N_{ij}} \Phi_{ij}^{\text{exch}} \tag{6.79}$$

  where the exchanged flux $\Phi_{ij}^{\text{exch}}$ between a surface cell $i$ of surface $S_i$ and a volume cell $j$ is given by

$$\Phi_{ij}^{\text{exch}} = \int_0^{+\infty} \epsilon_{i\nu} \left[ I_\nu^\circ(T_j) - I_\nu^\circ(T_i) \right] \int_{S_i} \int_{4\pi} A_{ij\nu} \cos(\theta_i) \mathrm{d}\Omega_i \mathrm{d}S_i \mathrm{d}\nu \tag{6.80}$$

where $A_{ij\nu}$ accounts for all the paths between emission from any point of the cell (or face in case of a wall) $i$ and absorption in any point of the cell (or face) $j$, after transmission, scattering and possible wall reflections along the paths (Tessé et al. 2002). $\theta_i$ is the angle of the path with the surface normal $S_i$.

### 6.4.4 The different classical and reciprocal methods

Based on Eqs. (6.78) and (6.79), several Monte Carlo formulations can be implemented and used for the calculation of the estimated radiative power $\widehat{P}_q$ at cell $q$:

- the classical Forward Method (**FM**), where only the information of the power transported in the forward direction of every optical path is taken into account,
- the classical Backward Method (**BM**), where optical paths are issued from the point of the calculated radiative power and absorbed power from the emitted powers of all the points crossed by the optical paths is calculated,
- the Emission-based Reciprocity Method (**ERM**) where optical paths are issued from the point of the calculated local radiative power, and information based on reciprocity principle is taken into account,
- the Absorption-based Reciprocity Method (**ARM**), which is another reciprocal formulation, where the local radiative power of the cell $q$ is computed through the exchanged powers of all the optical paths issued from all the system cells crossing the cell $q$.

Their principles are illustrated in Fig. 6.15 and are briefly detailed in the following. They can be classified by groups of Forward and Backward Methods, as well as non reciprocal and reciprocal methods, as summarized in Table 6.1.

| | Forward | Backward |
|---|---|---|
| **Non reciprocal** | FM | BM |
| **Reciprocal** | ARM | ERM |

**Table 6.1:** *Monte Carlo resolution methods of the Radiative Transfer Equation.*

#### 6.4.4.1 Foward Method (FM)

As illustrated in Fig. 6.15 (top left), in the Forward Method, for calculating the radiative power of a cell $q$, we generate all the optical paths from all the cells $i$, and then, the balance between absorption and emission in this cell is done at the cell $q$ considering all the optical paths originating from all the cells $i$, that have crossed the cell $q$. The corresponding radiative power $\widehat{P}_q^{\mathrm{FM}}$ is calculated as:

$$\widehat{P}_q^{\mathrm{FM}} = \sum_{i=1}^{N_v+N_f} \widehat{P}_{iq}^{\mathrm{ea}} - P_q^e \tag{6.81}$$

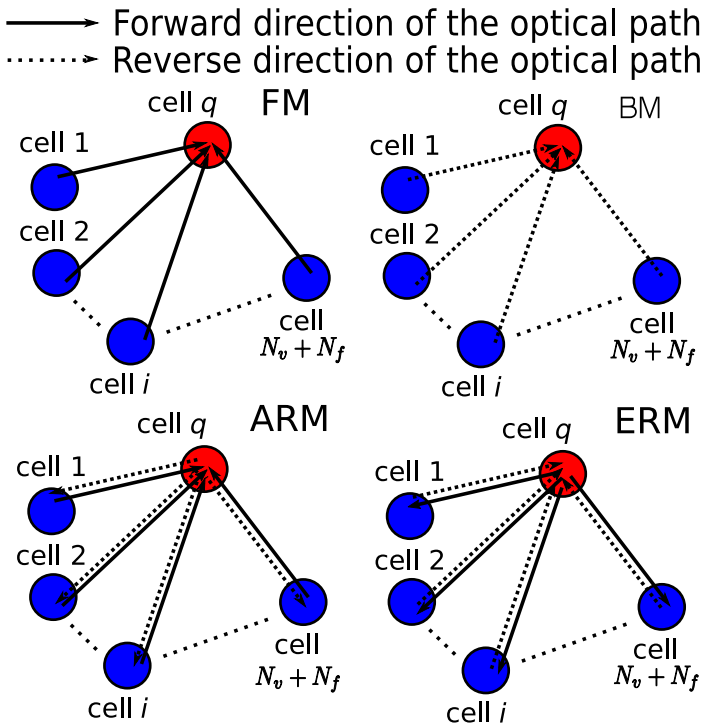


**Figure 6.15:** *Principle of calculation of the radiative power in the cell q in the FM, BM, ERM and ARM (extracted and adapted from Tessé et al. (2002)).*

#### 6.4.4.2 Backward Method (BM)

As illustrated in Fig. 6.15 (top right), in the Backward Method, for calculating the radiative power of a cell $q$, we generate only optical paths from the cell $q$, and the absorbed power from emitted powers from all the other cells $i$ crossed by the optical paths are accounted for. The corresponding radiative power $\widehat{P}_q^{\mathrm{BM}}$ is calculated as:

$$\widehat{P}_q^{\mathrm{BM}} = \sum_{i=1}^{N_v+N_f} \widehat{P}_{iq}^{\mathrm{ea}} - P_q^e \tag{6.82}$$

The expression of the radiative power at the cell $q$ is the same as the one obtained for FM but the optical paths are only issued from the cell $q$ of interest.

#### 6.4.4.3 Absorption-based Reciprocity Method (ARM)

In this first reciprocal formulation, illustrated in Fig.6.15 (bottom left), the radiative power of the cell $q$ is also calculated based on all the optical paths that have been emitted from all the cells $i$ of the domain, but, it is computed based on the exchanged powers between the cell $q$ and the cells that have emitted the optical paths. The statistical estimation of the radiative power of the cell $q$ is written as:

$$\widehat{P}_q^{\mathrm{ARM}} = \sum_{i=1}^{N_v+N_f} -\widehat{P}_{iq}^{\mathrm{exch}} \tag{6.83}$$

However, in contrast with the FM, the emitted power $P_q^e$ of the cell $q$ is then statistically reconstructed and not exactly computed. From the reciprocity principle, it can be computed as (Tessé et al. 2002):

$$P_q^e = \sum_{i=1}^{N_v+N_f} \lim_{N_i \to +\infty} \frac{P_i^e}{N_i} \sum_{n=1}^{N_{iq}} \frac{I^\circ_{\nu_n}(T_q)}{I^\circ_{\nu_n}(T_i)} \sum_{m=1}^{N_p} \tau_{\nu_n}(\mathrm{BF}_m)\alpha_{jm\nu} \tag{6.84}$$

where $N_p$ represents the total number of crossing of the cell $q$ by a given optical path issued from the cell $i$.

#### 6.4.4.4 Emission-based Reciprocity Method (ERM)

In this second reciprocal formulation (illustrated in Fig.6.15 (bottom right)), the principle of exchanged powers is also used, but for computing the radiative power of the cell $q$, as for the Backward Method, the optical paths are only issued from this same cell $q$. Indeed, only the exchanged powers between the cell $q$ and the other cells from the opticals paths originating from this same cell

$q$ are necessary to compute the radiative power $P_q$ of the cell $q$.

From the reciprocity principle, the radiative power of the cell $q$ in ERM is then expressed as:

$$\widehat{P}_q^{\mathrm{ERM}} = \sum_{j=1}^{N_v+N_f} \widehat{P}_{qj}^{\mathrm{exch}} \tag{6.85}$$

Finally, substituting Eq. (6.65) into Eq. (6.85), the final expression of $\widehat{P}_q^{\mathrm{ERM}}$ as it is computed in the presented simulations writes:

$$\widehat{P}_q^{\mathrm{ERM}} = \frac{P_q^e}{N_q} \sum_{n=1}^{N_q} \sum_{m=1}^{M_n} \left[ \frac{I^\circ_{\nu_n}(T_m)}{I^\circ_{\nu_n}(T_q)} - 1 \right] \tau_{\nu_n}(\mathrm{BF}_m) \alpha_{jm\nu} \tag{6.86}$$

where $m = 1$ designates the cell $q$ and $m = M_n$ the last cell crossed by the $n$-th optical path originating from the cell $q$.
In a general way, the use of the reciprocity principle like in ARM and ERM, allows to ensure that the exchange power between two cells at the same temperature is rigorously equal to zero, whereas this property is only statistically verified with the FM. In practice, this property results in more accurate results than those obtained using more conventional techniques, like the FM for the calculation of radiative powers (Tessé et al. 2002).

Here, the advantage of ERM is that, in contrast with ARM and FM, it is not necessary to compute all the optical paths from all the system cells in order to compute the radiative power of the cell $q$. Then, one can only compute the points of interest in the domain at a reduced cost.

### 6.4.5 Probability density functions for the ERM method

The ERM method has been used for the majority of the calculations carried out in this thesis. This section details the corresponding probability density functions used to determine the directions and the wavenumber of each photon bundle in the Monte Carlo method.

Introducing the power per unit volume $P_i^e(T_i)$ in the volume $V_i$:

$$P_i^e(T_i) = 4\pi \int_{\nu=0}^{\infty} \kappa_\nu(T_i) I^\circ_\nu(T_i) d\nu, \tag{6.87}$$

Eq. (6.78) can be written as:

$$\begin{aligned} P_{ij}^{\text{exch}} &= P_i^e(T_i) \int_{\nu=0}^{\infty} \left[ \frac{I_\nu^\circ(T_j)}{I_\nu^\circ(T_i)} - 1 \right] \int_{4\pi} \frac{\kappa_\nu(T_i) I_\nu^\circ(T_i)}{P_i^e(T_i)} A_{ij\nu} d\Omega_i d\nu \\ &= P_i^e(T_i) \int_{\nu=0}^{\infty} \left[ \frac{I_\nu^\circ(T_j)}{I_\nu^\circ(T_i)} - 1 \right] \int_{4\pi} A_{ij\nu} f_i(\Delta, \nu) d\Omega_i d\nu \end{aligned} \tag{6.88}$$

where $A_{ij\nu}$ is defined in Eq. (6.75), $f_i(\Delta, \nu)$ is the joint PDF, with $\Delta$ the direction and $\nu$ the wavenumber of the emitted bundle.

$f_i(\Delta, \nu)$ can be separated in two independent parts:

$$\begin{aligned} & f_i(\Delta, \nu) d\Omega_i d\nu = f_{\Delta_i}(\Delta) d\Omega_i f_{\nu_i}(\nu) d\nu, \\ \text{with: } & \begin{cases} f_{\Delta_i}(\Delta) = 1/(4\pi) \\ f_{\nu_i}(\nu) = \dfrac{\kappa_\nu(T_i) I_\nu^\circ(T_i)}{\int_0^\infty \kappa_\nu(T_i) I_\nu^\circ(T_i)} \end{cases} \end{aligned} \tag{6.89}$$

Moreover, in spherical coordinates, the direction $\Delta$ is determined by the azimuthal angle $\psi$ and the polar angle $\theta$. The *pdf* for the direction $f_{\Delta_i}(\Delta)$ is then rewritten as:

$$\begin{aligned} & f_{\Delta_i}(\Delta) d\Omega_i = \frac{1}{4\pi} d\Omega_i = \frac{\sin(\theta_i)}{2} d\theta_i \frac{1}{2\pi} d\psi_i = f_{\theta_i}(\theta_i) d\theta_i f_{\psi_i}(\psi_i) d\psi_i \\ \text{with: } & \begin{cases} f_{\theta_i}(\theta_i) = \sin(\theta_i)/2 \\ f_{\psi_i}(\psi_i) = 1/(2\pi) \end{cases} \end{aligned} \tag{6.90}$$

Finally, the photon bundles will be determined according to these three *pdf* (one for $\nu_i$, one for $\theta_i$ and one for $\psi_i$), enabling to determine all their characteristics. Note that in the presented calculations, radiative power $P^{\text{R}}$ is computed locally at the nodes of the computational domain. Therefore, it is not necessary to randomly select a point in the volume of each cell to compute a cell-averaged value.

For the determination of the wavenumber $\nu$, the azimuthal angle $\psi$ and the polar angle $\theta$, three numbers $R_\nu$, $R_\theta$ and $R_\psi$ are randomly sorted between 0 and 1, and the corresponding angles are determined such that:

$$\begin{aligned} R_\nu &= \int_0^\nu f_\nu(\nu') d\nu' \\ R_\theta &= \int_0^\theta f_\theta(\theta') d\theta' \quad \Leftrightarrow \quad \theta = \cos^{-1}(1 - 2R_\theta) \\ R_\psi &= \int_0^\psi f_\psi(\psi') d\psi' \quad \Leftrightarrow \quad \psi = 2\pi R_\psi \end{aligned} \tag{6.91}$$

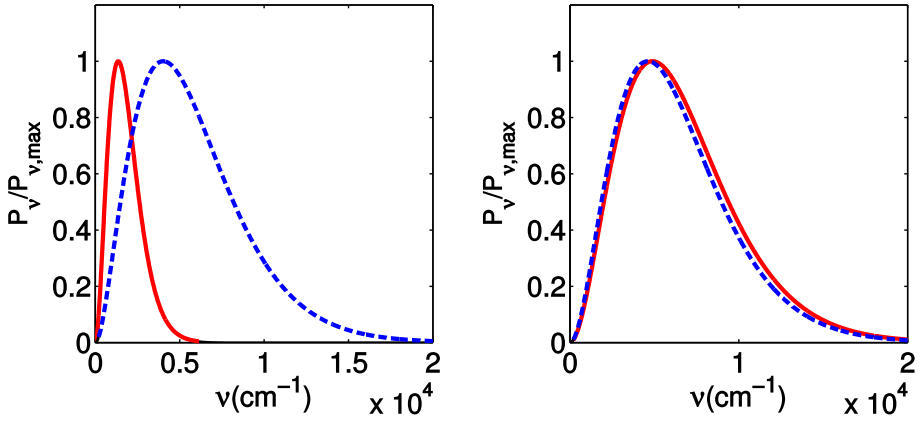


(a) Point at 700 K (b) Point at 2500 K

**Figure 6.16:** *Spectral emitted (in red solid lines) and absorbed power (in blue dashed lines) for different cells of the case studied by Zhang et al. (2012)*

### 6.4.6 Optimized Emission-based Reciprocity Method (OERM) and Importance Sampling

The ERM convergence becomes difficult in regions where emission and absorption phenomena coexist. Indeed, in heterogenous configurations in terms of temperature and composition, the absorption spectra of a given point can be very different compared to the emission spectra of the originating point of the photon.

This has been studied by Zhang et al. (2012) in the case of homogeneous composition but heterogeneities in temperature. In this case, channel flows with temperature profiles varying from 500 K to 2 500 K have been studied. It has been shown that the absorption spectra of a local point at 700 K comes mainly from the hot regions (2 500 K), therefore local absorption and emission spectra are clearly different, as illustrated in Fig. 6.16 **a)** in the case of a grey gas. However, in the very hot region, the two spectra are mainly the same as illustrated in Fig. 6.16 **b)**, because these regions mainly reabsorb the energy coming from nearby hot regions at approximatively the same temperature.

Then, it was proposed to modify the *pdf* used to sample the wavelength frequency. The idea is to use the so-called *Importance Sampling* principle in order to sample on the frequencies of interest, *i.e* the ones where the exchanged powers are the most important. In their study, Zhang et al. (Zhang et al. 2012) proposed to sample the frequency based on the emission-*pdf* of the hottest

region $f_{\nu_i}^{\mathrm{OERM}}(\nu)$:

$$f_{\nu_i}^{\mathrm{OERM}}(\nu) = \frac{\kappa_\nu(T_{\max}) I_\nu^\circ(T_{\max})}{\int_0^\infty \kappa_\nu(T_{\max}) I_\nu^\circ(T_{\max})} \tag{6.92}$$

Then, equation (6.88) becomes in this case:

$$\begin{aligned} P_{ij}^{\mathrm{exch}} =& P_i^e(T_{\max}) \int_{\nu=0}^{\infty} \frac{\kappa_\nu(T_i) I_\nu^\circ(T_i)}{\kappa_\nu(T_{\max}) I_\nu^\circ(T_{\max})} \left[ \frac{I_\nu^\circ(T_j)}{I_\nu^\circ(T_i)} - 1 \right] \\ & \int_{V_i} \int_{4\pi} A_{ij\nu} f_{V_i}(\mathrm{B}) dV_i f_{\Delta_i}(\Delta) d\Omega_i f_{\nu_i}^{\mathrm{OERM}}(\nu) d\nu \end{aligned} \tag{6.93}$$

Actually, in case of a heterogeneous composition of the gases, which is the case in our configurations, this methodology is not appropriate because the absorption coefficient $\kappa_\nu(X_{\mathrm{m}}, f_{V,\mathrm{m}}, T_{\max}, P_{\mathrm{m}})$ (where $X_{\mathrm{m}}$, $f_V, \mathrm{m}$ and $P_{\mathrm{m}}$ are the composition, soot volume fraction and pressure at the position where temperature is maximum and equal to $T_{\max}$) can favour spectral bands that do not correspond to the local absorption and emission. To correct this effect, the following spectral *pdf* $f_{\nu_i}^{\mathrm{OERM2}}(\nu)$ is introduced:

$$f_{\nu_i}^{\mathrm{OERM2}}(\nu) = \frac{\kappa_\nu(T_i) I_\nu^\circ(T_{\max})}{\int_0^\infty \kappa_\nu(T_i) I_\nu^\circ(T_{\max})}, \tag{6.94}$$

where $\kappa_\nu(T_i)$ and $I_\nu^\circ(T_{\max})$ correspond respectively to the local absorption coefficient of the cell $i$ and the spectral intensity at the maximum temperature of the domain $T_{\max}$. The exchanged power $P_{ij}^{\mathrm{exch}}$ between the cells $i$ and $j$ can then be written as:

$$\begin{aligned} P_{ij}^{\mathrm{exch}} =& P_i^{e,\max} \int_{\nu=0}^{\infty} \frac{I_\nu^\circ(T_i)}{I_\nu^\circ(T_{\max})} \left[ \frac{I_\nu^\circ(T_j)}{I_\nu^\circ(T_i)} - 1 \right] \\ & \int_{V_i} \int_{4\pi} A_{ij\nu} f_{V_i}(\mathrm{B}) dV_i f_{\Delta_i}(\Delta) d\Omega_i f_{\nu_i}^{\mathrm{OERM2}}(\nu) d\nu \end{aligned} \tag{6.95}$$

where $P_i^{e,\max}$ corresponds to a pseudo-emission based on the radiative intensity at $T_{\max}$. It is calculated as:

$$P_i^{e,\max} = 4\pi V_i \int_{\nu=0}^{\infty} \kappa_\nu(T_i) I_\nu^\circ(T_{\max}) d\nu \tag{6.96}$$

To illustrate the impact of the choice of this pdf and therefore the impact of using "Important Sampling" techniques, Fig. 6.17 presents a 1-D simple heterogeneous test case at atmospheric pressure. In this test case, two absorbing species are considered: $CO_2$ and $H_2O$. Their concentrations vary, from 0.0 at

walls to 0.5 at the middle for $H_2O$, and from 0.5 at walls to 0.0 at the middle for $CO_2$ whereas temperature varies from 500 K to 2500 K in the volume. The mesh is discretized into 401 regularly spaced points. Profiles of temperature, $X_{H_2O}$ and $X_{CO_2}$ are respectively plotted in Fig. 6.17 **a)**, **b)** and **c)**. The corresponding emitted power is also presented in Fig. 6.17 **d)**.

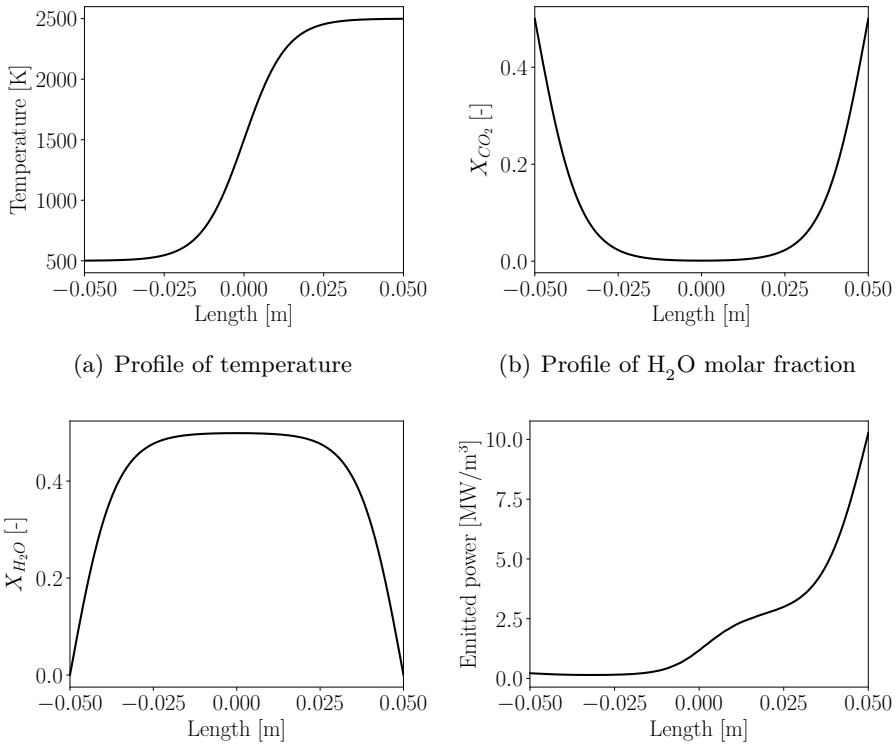


(a) Profile of temperature

(b) Profile of $H_2O$ molar fraction

(c) Profile of $CO_2$ molar fraction

(d) Profile of Emitted power

**Figure 6.17:** *Studied 1-D case for the comparison of ERM, OERM and OERM2.*

For this test case, the radiative power is calculated through the classical Monte Carlo technique with a criterion of convergence fixed to 1% for the radiative power using the RAINIER code presented in the next section. Another convergence criterion is also retained in order to avoid infinite number of samplings in regions where radiative power is near zero: if the statistical error (RMS) of the radiative power at a given point is lower than 1 000 $W/m^3$, the point is considered converged. The three frequency sampling methods are here compared: ERM, OERM and OERM2. Figure 6.18 **a)** presents the results for the radiative power calculation for the different techniques. The corresponding relative statistical error of the estimator is presented Fig. 6.18 **b)**. As each method carries out calculations until convergence, it can be observed first that the three methods predict approximatively the same value of the radiative power. Concerning

convergence, the relative RMS criterion (1%) is also respected for the majority of points except for the points where the radiative power is zero, which is also expected.

In order to compare the efficiency of each of the three methods, the profile of ray samples number for each point of the mesh is presented in Fig. 6.18 **c)**. For very hot regions, the three methods reveal to be quasi-identical in terms of number of samples necessary to converge the radiative power. This is expected since in these regions, $f_\nu^{\mathrm{ERM}}(\nu) \approx f_\nu^{\mathrm{OERM}}(\nu) \approx f_\nu^{\mathrm{OERM2}}(\nu)$. In the regions where the radiative power is near zero, the process is stopped through maximum number of sampling points or minimum radiative power RMS. Finally, in the cold regions near walls and where the three *pdf* are the most different, the number of samples necessary to converge with OERM2 technique is approximatively one half order of magnitude lower than OERM, which is one half order of magnitude lower than ERM. This is due to the use of the intensity at maximal temperature which is responsible for the maximum exchange energy (for OERM and OERM2 techniques) and the use of a local absorption coefficient (in the case of OERM2), which is most representative of the wavelengths of absorption at each point. For intermediate zones, OERM2 is better or as good as ERM technique. Then, in overall, the OERM2 technique is well adapted for calculation of radiative powers in such heterogeneous domains.
Table 6.2 compares the computational times obtained for the radiative power calculation for the three compared methods. These calculations were all done with 24 processors. It can be observed that an important gain in computational time can be obtained using these important sampling techniques, especially using the OERM2 technique.

| | ERM | OERM | OERM2 |
|---|---|---|---|
| Time [s] | 18 934 | 3 881 | 49 |

**Table 6.2:** *Comparison of computational time of the studied case with 24 processors.*

### 6.4.7 Quasi Monte Carlo methods

The application of Quasi Monte-Carlo methods for the resolution of the RTE in the RAINIER code results from a collaborative work with L. Palluotto's and N. Dumont's PhD theses. This work has been presented at the ASME Turbo Expo 2017 and the corresponding conference paper can be found in Appendix D, Section .

#### 6.4.7.1 Principle

The idea of the Quasi Monte Carlo (QMC) method is to use a new cubature rule that looks like a Monte Carlo method: this quasi-random (also called

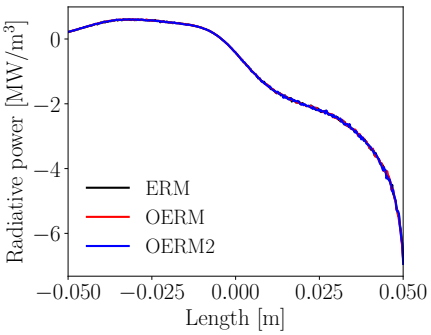


(a) Profile of calculated radiative power

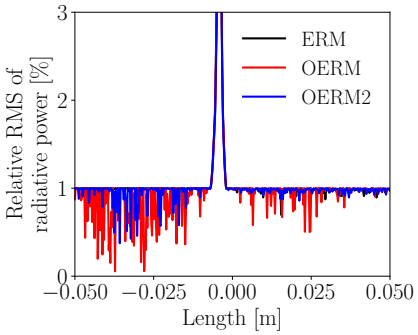


(b) Profile of relative RMS of radiative power calculation

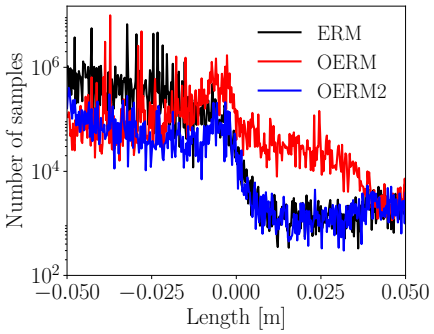


(c) Profile of ray samples number

**Figure 6.18:** *Comparison of ERM, OERM and OERM2 for the estimation of the radiative power.*

low-discrepancy) sampling consists on using pseudo-random low-discrepancy sequences, whose points are distributed in a way to provide better uniformity. The Sobol sequence is here used and its construction results from Joe and Kuo (2008). The Quasi Monte-Carlo terminology refers to the use of this alternative sampling method in order to evaluate multivariate integration, as it is the case for the Radiative Transfer Equation (RTE).

Figure 6.19 illustrates the better uniformity of the Quasi-Monte Carlo sampling compared to the Monte Carlo one, for the sampling of the azimuthal angle $\psi$ and the polar angle $\theta$ following the pdf of Eq. (6.90).

The advantage of this method is the enhancement of the convergence rate (Hlawka 1961). Indeed, with this method, it has been shown that the convergence of the standard deviation follows the law:

$$\sigma(P_i) \propto \frac{1}{N_i} \tag{6.97}$$

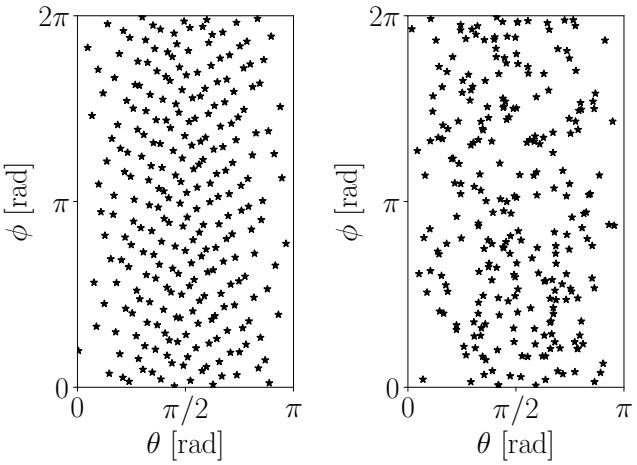


**Figure 6.19:** *Comparison of the sampling of polar ($\theta$) and azimuthal angle ($\psi$) following the pdf of Eq. (6.90) using a Sobol sequence (left) and a classic purely random sequence (right).*

where $N_i$ is the total number of bundles issued from a point $i$, instead of the classical $1/\sqrt{N}$-law for Monte-Carlo.
To asses the error estimation of this method, it is in practice necessary to use a Randomized Quasi Monte-Carlo (Lemieux 2009). To do so, in the context of radiation simulations, $n$ packages are considered: within each of these packages, a low discrepancy sequence of $N_i/n$ points is used, while the $n$ sequences of the packages are randomized using an I-binomial scrambling (Tezuka and Faure 2003). Then, one can benefit from the faster convergence rate of Quasi Monte-Carlo within each package and have an estimation of the error using the variance between the packages, as it is done for classical Monte-Carlo methods.

#### 6.4.7.2 Comparison of methods

Figure 6.20 **a)** presents the comparison of classical Monte Carlo and Quasi Monte Carlo determination accuracy of the integral $3\int_0^1 x^2 dx = 1$. Figure 6.20 **b)** shows the evolution of the standard deviation of the estimator with sampling number for the evaluation of this same integral. It can be clearly observed that the convergence of the Quasi Monte Carlo methods is faster than the convergence of Monte Carlo ones. Moreover, the decrease law of the standard deviation with sampling number ($\propto 1/\sqrt{N}$ for Monte Carlo and $\propto 1/N$ for Quasi Monte Carlo) is also retrieved.

The same case as the one presented in Fig. 6.17 is now studied using QMC sampling technique. Table 6.3 compares the computational times between MC and QMC sampling techniques for the three variants of emission-based reciprocity methods: ERM, OERM and OERM2. It can clearly be observed that

QMC enhances largely the convergence speed in the 1-D case. This can be explained by looking at the number of samples needed at each point to converge the radiative power (Fig. 6.21), which is approximatively one order of magnitude lower in QMC method compared to MC method.

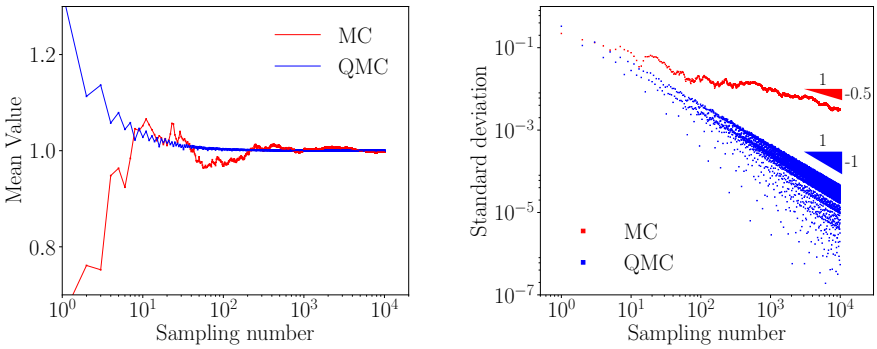


(a) Evolution of estimation of $3\int_0^1 x^2 dx$ as a function of sampling number

(b) Evolution of standard deviation with sampling number

**Figure 6.20:** *Comparison of MC and QMC convergence for the estimation of* $3\int_0^1 x^2 dx$.

| | ERM | OERM | OERM2 |
|---|---|---|---|
| Time [s] - **MC** | 18 934 | 3 881 | 49 |
| Time [s] - **QMC** | 320 | 25.7 | 5.0 |

**Table 6.3:** *Comparison of computational times of the studied case with 24 processors between MC and QMC methods.*

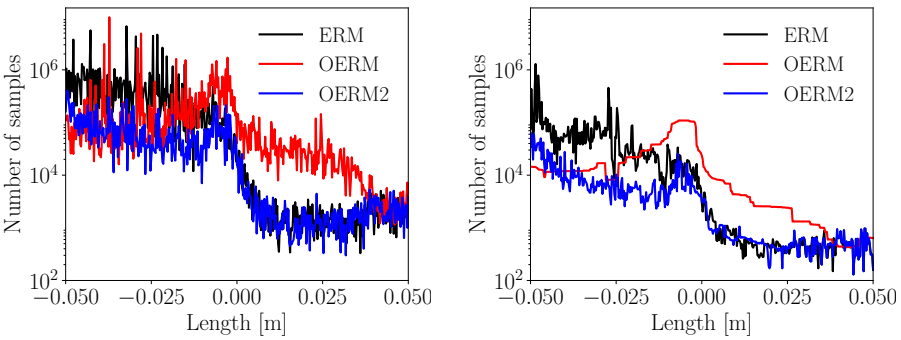


(a) Profile of sampling number (MC method)

(b) Profile of sampling number (QMC method)

**Figure 6.21:** *Comparison of MC and QMC convergences for the 1-D case presented in Fig. 6.17 for the three emission-based reciprocity methods: ERM, OERM and OERM2.*

As it clearly enhances the convergence rate of the estimators while preserving the possibility of error estimation, this method will be retained in the coupled simulations.

## 6.5 RAINIER code

### 6.5.1 Presentation of the code

RAINIER is an in-house code developed at EM2C laboratory (Zhang 2011; Refahi 2013; Zhang 2013; Koren 2016). It solves the radiative transfer equation using Monte-Carlo formalism. ERM, OERM and OERM2 techniques can be used for the choice of the frequency sampling technique. Monte Carlo or Quasi-Monte Carlo sampling techniques are also implemented and validated.

RAINIER solves the radiative transfer equation for each point of any type of unstructured mesh and can then be coupled with any CFD code. The principle is based on the emission of a large number of photon bundles for each volume (or surface) point where the radiative power (or the heat flux) may be computed.

Thanks to the use of the ERM-like technique and the loading of all the mesh and data fields by all the processors, the code can also be largely parallelized. Tests of scalability have been performed up to 1920 processors and are presented in Fig. 6.22. The test has been performed on a Bull cluster equipped with Intel E5-2690 processors on a test case containing 8 millions of cells. A very good scalability is obtained, enabling then the computation of radiative power in a large number of cores and the possibility of doing high-fidelity coupled simulations with largely parallelized solvers.

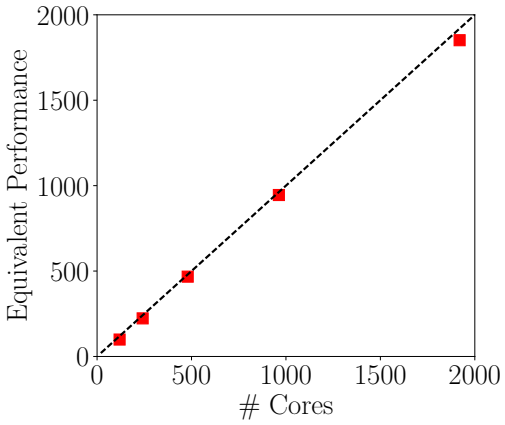


**Figure 6.22:** *Scalability of the RAINIER radiative solver with number of cores. Points correspond to the calculated points, dashed line corresponds to the ideal performance.*

### 6.5.2 Implementations realized during this thesis

During this thesis, several implementations have been realized in the RAINIER code:

- Soot radiative properties based on constant or wavelength-dependent soot refractive index,
- Adding of spectral bands to accurately handle black wall and soot emission from 300 to 2500 K,
- Backward Monte Carlo method, whose utilization is detailed in Chapter 7,
- Co-implementation of the Quasi Monte Carlo sampling technique and OERM2 method for importance samplings,
- Directional probes for estimation of incoming radiative fluxes over a reduced solid angle, as detailed in Appendix D, and used in Chapter 7,
- Calculations over reduced set of points defined by geometric domains or threshold values of radiative participating species,
- Possibility to solve the RTE with Monte-Carlo sampling of the solid angle directions and deterministic resolution over the wavelength space,
- Coupling with the AVBP flow solver and AVTP wall heat transfer solver.

## 6.6 Coupling with the flow solver

### 6.6.1 The Open-palm library

The open-source OpenPALM coupler (Duchaine et al. 2015) co-developed at Cerfacs and Onera has been used in order to couple the codes used for the multi-physics simulations carried out during this thesis. This library can be divided into three dedicated parts: PALM, CWIPI and PrePALM.

The PALM library handles the parallel communications and the launching/exit of the different coupled applications. It acts as an interface: each code sends its data to PALM which then dispatches the information (Buis et al. 2006).

The CWIPI library handles the parallel interpolation of data in the eventually not conforming different meshes used by the applications (Refloch et al. 2011). A minimization of the global cost of the parallel communications is done through the optimization of the communication graph created by CWIPI.

The PrePALM application is a Graphical User Interface (GUI) enabling to create easily a coupling between different codes. Links and communications between the different codes are created through this interface which then creates the coupled applications using the PALM library and if necessary the CWIPI library. Figure 6.23 illustrates this GUI with the coupling of three codes: a flow solver (AVBP), a heat transfer equation solver in solids (AVTP) and a

radiation solver (RAINIER). This case corresponds to the coupled calculation done and presented in Chapter 9.

### 6.6.2 Communications

Figure 6.24 illustrates the coupling scheme between the flow solver (**AVBP**) and the radiation solver (**RAINIER**). After each coupling time step $\Delta t_{\text{cpl}}$, the two solvers exchange information:

- the flow solver sends the fields of temperature $T$, pressure $P$, soot volume fraction $f_V$ and species molar fractions $X_k$,
- the radiative solver sends the field of radiative power $P^{\text{R}}$ computed from those flow fields for the next time step.

Thanks to the Open-palm library, these communications are done at a low cost and the fields can be interpolated between the two different unstructured meshes used by the flow and radiation solvers.

### 6.6.3 Determination of coupling time step

In order to simplify the communications and to avoid too intrusive implementations, the coupling time step $\Delta t_{\text{cpl}}$ is chosen proportional to the flow time step $\Delta t_f$:

$$\Delta t_{\text{cpl}} = n_{\text{cpl}} \Delta t_f \tag{6.98}$$

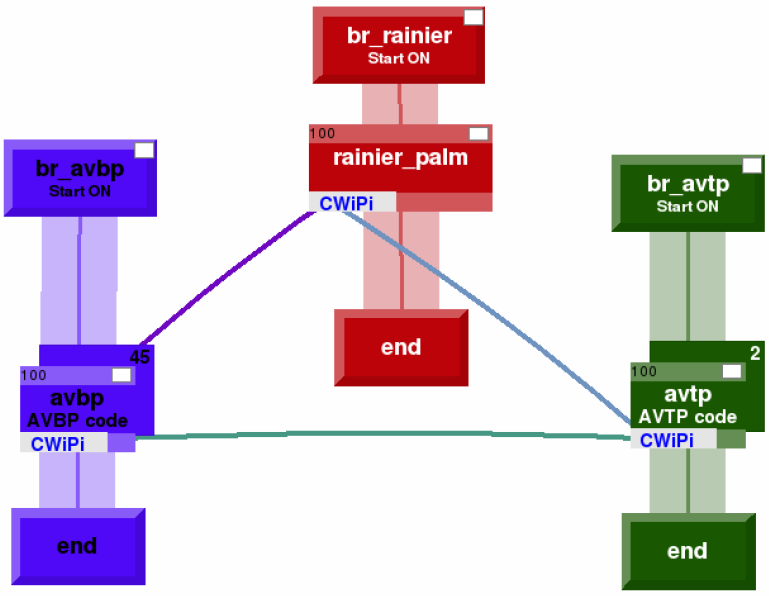


**Figure 6.23:** *Exemple of OpenPalm coupled configuration extracted from the GUI PrePalm. The lines correspond to the communications (which can be in both directions) between the different codes.*

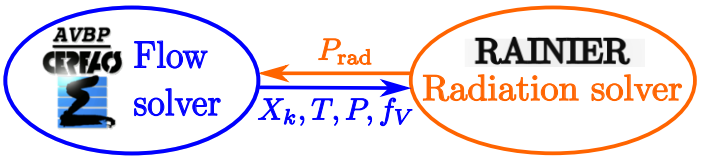


**Figure 6.24:** *Scheme of coupling between flow solver (**AVBP**) and radiative solver (**RAINIER**).*

For the coupling between radiation and fluid, the coefficient of proportionality $n_{\text{cpl}}$ between these two time steps is determined by fixing the corresponding error in the exchanged fields due their evolution between two coupling time steps equal to the convergence criteria of the Monte Carlo radiation solver. $n_{\text{cpl}}$ is then fixed and $\Delta t_{\text{cpl}}$ varies according to $\Delta t_f$. An example of the determination of this parameter is given next chapter in the coupled simulation of jet diffusion flame.

## 6.7 Conclusion

The radiative transfer equation has been presented. It is an integro-differential equation which depends on six variables: the direction ($\Delta = (\theta, \psi)$ in spherical coordinates, the position ($\mathbf{r}(x, y, z)$ in cartesian coordinates), and the wavelength $\lambda$ (or wavenumber $\nu$). In this equation, gas and soot particles impact the radiative intensity through their corresponding absorption coefficients. $CO_2$ and $H_2O$ are the main participating species in radiative properties of gas combustion products. Their radiative properties strongly vary with frequency and require then dedicated modeling strategies. Different approaches have been presented (line-by-line, WSGG, SLW, SNB, ck) and the ck method has been chosen for its facility of implementation, its accuracy, and its relatively reasonable cost when only two absorbing gaseous species are considered.

The modeling of soot particles radiative properties is extremely complex and challenging. For small spherical particles, the Rayleigh approximation is good enough. However, for fractal aggregates of soot particles, which are not spherical anymore, and with sizes that are lower but of the same order of magnitude than radiation wavelength of interest for hot products of combustion, this approximation is no more accurate. The interpenetration of soot particles composing soot aggregates increases greatly the absorption coefficient of such soot aggregates. A lot of uncertainties still exist today and very sophisticated methods are necessary in order to obtain these radiative properties, which depend on multiple properties of the soot aggregates and their environment. The current models used for soot prediction in turbulent flames via LES solvers can not provide all these informations. For these reasons, in our applications, combined with the fact that it can be easily implemented together with the gaseous species ck model, the RDG/RDG-FA's theory applied to aggregates

composed of supposed spherical primary particles and neglecting scattering (which is equivalent to Rayleigh's theory) is considered in this PhD thesis. Future works should consider scattering effects in RDG-FA's theory in order to investigate their impacts on total radiative transfers.

The integro-differential form of the RTE leads to difficulties for the resolution of this equation and multiple methods have been developed. Here, the chosen method is the Monte-Carlo Method (MCM). This method has multiple advantages: first, it is easy to be implemented for the study of complex configurations; second, the precision of the computation can be statistically estimated and therefore the uncertainty of the obtained results can be quantified; third, it is well adapted to the study of six-variable dependency of the RTE because its cost does not depend on the number of dimensions of the problem. However, in order to obtain statistically converged results, the computational cost is generally very high. To face this problem, several improvements of the classical MCM have been implemented. First, the use of Quasi-Monte Carlo methods as sampling generator increases the convergence speed. Combined with randomization methods, both the increase of convergence speed due to the use of Sobol sequences and the possibility to estimate the uncertainty of a computation in Monte Carlo are conserved. Secondly, importance sampling using appropriate *pdf* for wavenumber sampling (OERM and OERM2) has been used in order to reduce the variance of the estimator and therefore decrease the computational time of calculations even further.

# Chapter 7

# LES of a turbulent sooting jet flame coupled with radiative energy transfer

*Part of this chapter has been submitted to the Eurotherm CTRPM-VI 2018 conference (Rodrigues et al. 2018).*

*Gas and soot radiative transfer in a turbulent sooting flames are studied in an ethylene-air jet diffusion flame, previously investigated in Chapter 4 with simplified assumptions on radiative transfer. The computation is based on a coupled Monte-Carlo - Large Eddy Simulation. The developed sectional model presented in Chapter 3 is used for soot particles description. The radiative transfer equation is solved using a Quasi Monte-Carlo method with a cK model describing gas radiative properties and the RDG's theory assumption for soot particles properties, as presented in Chapter 6. The numerical results are compared to experimental data on radiative intensity measured along the flame height. The different radiative contributions (emission-absorption, gas-soot) are then analyzed to study the nature of the radiative energy transfer in the investigated flame. Scale-resolved Turbulence Radiative Interactions (TRI) are finally analyzed and discussed.*

## Contents



# 7.1 Introduction

In industrial burners and combustion chambers, heat exchanges are of multiple types: conduction, convection and radiation. In presence of soot particles, radiation heat transfer can become very important and must therefore be controlled in order to either preserve the materials used in combustors or to maximize efficiently heat exchange in certain industrial applications. The use of modeling is therefore necessary in order to understand and predict such heat exchanges in practical systems.

The modeling of gaseous combustion products evolution along with their thermal radiation has been studied in literature and more and more predictive simulations have been achieved (Coelho 2004; Coelho 2007; Wang et al. 2008; Poitou et al. 2012). Nevertheless, taking into account the contribution of soot particles in the radiative heat transfer of turbulent flames, which is generally encountered in industrial applications, requires the modeling of these particles evolution and of the complex coupling that exists between soot, turbulence and thermal radiation.

To do so, Tessé et al. (2004) proposed a RANS modeling of turbulent sooting jet diffusion flame coupled with a Monte Carlo radiation solver. For soot particles description, an empirical model enabling to estimate soot volume fraction evolution has been used.Wang et al. (2005) have also proposed RANS coupled simulations based on an empirical model for soot particles evolution. In this study, the resolution of the radiative transfer equation (RTE) is based on the spherical harmonics method. Pal et al. (2011) have compared coupled RANS modeling of turbulent jet sooting diffusion flame with spherical harmonics method, DOM method and Monte Carlo methods in terms of accuracy and cost. Again, an empirical model for soot particles is used in order to retrieve a good agreement with experimental measurements. Mehta et al. (2010) have also considered a coupled approach between RANS for turbulence description and Monte Carlo resolution of the RTE. For the description of soot particles, a detailed validated soot model based on a method of moments has been retained. More recently, Consalvi and co-authors (Consalvi and Nmira 2016b; Consalvi and Nmira 2017) have investigated turbulent sooting jet diffusion flames based on RANS calculations, finite volume method for the RTE resolution and a semi-empirical model for soot particles predictions.

Compared to RANS modeling, large eddy simulations (LES) enable to capture the turbulence radiation interactions (TRI) at the LES mesh scale (Poitou et al. 2008; Roger et al. 2011; Poitou et al. 2012). Gupta et al. (2013) proposed such approach for the investigation of luminous flames coupled with a Monte Carlo method for the resolution of the RTE. However, the used empirical model for soot particles providing the soot volume fraction as a function of the local equivalence ratio lacks physical description of soot production. Lecocq et al. (2014) have also investigated soot radiation in coupled LES simulations based on a DOM solver of the RTE and a semi-empirical model for soot predictions.

In the previous works, different radiative properties have been considered in coupled simulations: grey/total emissivities (Snegirev 2004; Saji et al. 2008), WSGG (Snegirev 2004; Saario et al. 2005; Guedri et al. 2011; Reddy et al. 2015b; Centeno et al. 2016), ck (Liu et al. 2004; Tessé et al. 2004; Wang et al. 2005; Liu et al. 2011; Demarco et al. 2013; Hernández et al. 2013; Consalvi and Nmira 2016b; Consalvi and Nmira 2017) or line-by-line (Mehta et al. 2010) for burnt gases and grey (Saji et al. 2008), WSGG (Snegirev 2004; Saario et al. 2005; Guedri et al. 2011; Reddy et al. 2015b; Centeno et al. 2016) or spectrum-resolved Rayleigh theory (or RDG/RDG-FA theory neglecting scattering) (Liu et al. 2004; Tessé et al. 2004; Wang et al. 2005; Liu et al. 2011; Demarco et al. 2013; Hernández et al. 2013; Mehta et al. 2010; Consalvi and Nmira 2016b; Consalvi and Nmira 2017) for soot particles.

In the present study, an LES of a turbulent jet diffusion flame is carried out with an advanced modeling of the solid phase based on the sectional model of

Chapter 1 describing the evolution in size of the soot particles. The radiative transfer equation is solved with the Monte-Carlo solver described in Chapter 6. Detailed gas radiative properties are considered based on a narrow band cK model while the soot properties are described by RDG-FA's theory neglecting scattering. Such a coupled simulation represents the first large-eddy simulation based on a sectional model for soot particles description and coupled with a Monte Carlo radiation solver. While several uncertainties still remain, this is a state-of-the-art achievement in respect to the retained numerical solver and to the modelling choices. The temperature and soot volume fraction profiles are compared with the experimental profiles to validate the predictions of the simulation for the gaseous and solid phases. The corresponding predictions of the gaseous and solid phases are compared with the calculation of Chapter 4 based on the optically thin radiation model and another calculation without radiation heat losses. The predicted radiative intensity is also validated by comparing numerical results with experiments.
Contributions of participating gaseous species and soot particles on total radiative powers are analyzed. Spectral radiative exchanges between gas and soot solid phases are investigated and the impact of reabsorption on total radiative exchanges for both phases and depending on the band wavenumber is detailed.

Finally, let us outline that all analyses are carried out with the LES resolved fields. Effects of subgrid turbulent-radiation interactions (subgrid TRI) have indeed been neglected. Impact of the captured TRI on both gas and soot phase radiative contributions are discussed by studying the radiative powers fields with and without considering TRI.

## 7.2 Configuration

The configuration studied in this chapter is the same as the one studied in Chapter 4 and corresponds to a turbulent non-premixed flame fed with pure ethylene which has been characterized experimentally at Sandia (ISF3 2017). It corresponds to a turbulent jet with Reynolds $\mathrm{Re}_D = 20\,000$, based on the fuel injector of the main jet $D = 3.2$ mm.

Compared with Chapter 4 where the optically thin radiation model is considered (with no resolution of the radiative transfer equation), the radiative transfer equation is here solved based on a Quasi Monte-Carlo method with a cK model describing gas radiative properties and the RDG-FA's theory for soot particles absorption properties, as presented in Chapter 6.

## 7.3 Numerical modeling

### 7.3.1 LES modeling of gaseous and solid phases

The LES modeling of gaseous and solid phases presented in Chapter 4 is here considered for the coupled simulations.

### 7.3.2 Radiation model

#### 7.3.2.1 Radiative properties

For gaseous species, as described in Chapter 6, only the radiative properties of $CO_2$ and $H_2O$ species are considered (the contribution of other species in this kind of flames being at least one order of magnitude lower than those of these two species (Rivière and Soufiani 2012)). The radiative properties are modeled through a narrow-band approach: the cK model (Goody and Yung 1995) based on updated parameters due to Riviere and Soufiani (Rivière and Soufiani 2012). These parameters have been generated for applications at atmospheric pressure in temperature range 300-4000 K. They are based on the CDSD-4000 database for $CO_2$ absorption spectra (Rothman et al. 2010) and HITEMP 2010 $H_2O$ absorption spectra (Tashkun and Perevalov 2011). For $H_2O$, 44 spectral bands, with widths varying from 50 $cm^{-1}$ to 400 $cm^{-1}$, are considered between 150 $cm^{-1}$ and 9200 $cm^{-1}$. $CO_2$ absorbs radiation in only 17 of these bands. The cK database is made of 7-points Gauss quadrature per band for each gaseous component, leading to 1022 pseudo-spectral points, since 49 quadrature points are used in the 17 overlapping bands.

For the radiation of soot particles, 93 spectral bands have been introduced between 150 and 29 000 $cm^{-1}$, of which 44 are common to the gas. This enables to capture correct effect of soot absorption coefficient for temperatures from 300 K up to 2500 K. The maximum (simulated) primary particle diameter $d$ encountered in the considered flame is around 20 nm. Then the size parameter $x = 2\pi d\nu$ is lower than 0.1 for all the considered wavenumbers. While the retained soot sectional approach allows to describe some features of the soot morphology, such effects in radiative transfer are neglected in this manuscript and will have to be incorporated in future studies, as discussed in Chapter 6. Using the RDG/RDG-FA theory for soot aggregates' radiative properties, the soot absorption coefficient $\kappa_\nu^{soot}$ of a cloud of soot particles and aggregates is equivalent to the one obtained from Rayleigh's theory (Modest 2013): $\kappa_\nu^{soot} = C_0 f_V \nu$ with $C_0 = \frac{36\pi nk}{(n^2-k^2+2)^2+4n^2k^2}$, where $m = n - ik$ corresponds to the complex index of refraction of soot particles, taken as equal to $m = 1.57 - 0.56i$ (Smyth and Shaddix 1996), $\nu$ is the wavenumber (in $m^{-1}$) and $f_V$ is the soot volume fraction. For the computation of the total extinction by soot particles, scattering by the soot particles is neglected as it is negligible compared to absorption according to RDG theory for the considered index of refraction.

#### 7.3.2.2 Monte Carlo resolution of the Radiative Transfer Equation

The reciprocal formalism is used here in order to solve the radiative transfer equation. The exchanged power between two cells $i$ and $j$ is given by:

$$P_{ij}^{\text{exch}} = \int_{\nu=0}^{+\infty} \kappa_\nu(T_i)\left[I_\nu^\circ(T_j) - I_\nu^\circ(T_i)\right] \int_{4\pi} A_{ij\nu} d\Omega d\nu \tag{7.1}$$

$A_{ij\nu}$ accounts for all the paths between emission from the node $i$ and absorption in any point of the cell $j$, after transmission, scattering and possible wall reflections along the paths. The total radiative power of a cell $i$ is computed as: $P_i = \sum_j P_{ij}^{\text{exch}}$. The Emission-based Reciprocity Method (ERM) method is used here in order to compute the radiative power of each cell (Tessé et al. 2002). For calculation of the radiative intensities at the measurement probe locations, as they are placed in cold regions, the Optimized Emission-based Reciprocity Method (OERM2) is used in order to converge efficiently the Monte-Carlo simulation. The mean radiative intensity $I_q^{\text{R}}$ at a probe location $q$ which will be compared to the experimental data is directly linked to the directive radiative flux of a domain face $q$ ($\Phi_q^{\Omega_1}$) over the solid angle $\Omega_1$ through:

$$I_q^{\text{R}} = 1/\Omega_1 \cdot \Phi_q^{\Omega_1} = 1/\Omega_1 \cdot \int_0^\infty d\nu \int_{\Omega_1} I'_\nu(\mathbf{u},\mathbf{r})(\mathbf{u}\cdot\mathbf{n})\mathrm{d}\Omega \tag{7.2}$$

Using the OERM2 method, $\Phi_q^{\Omega_1}$ is evaluated as:

$$\begin{aligned}\Phi_q^{\Omega_1} &= \sum_{j=1}^{N_f+N_v} \Phi_{qj}^{\Omega_1,\text{exch}} \\ &= \sum_{j=1}^{N_f+N_v} \left[\left(1-\left(1-\frac{\Omega_1}{2\pi}\right)^2\right)\sigma T_{\max}^4 \int_{\nu=0}^\infty \frac{I_\nu^\circ(T_q)}{I_\nu^\circ(T_{\max})}\left[\frac{I_\nu^\circ(T_j)}{I_\nu^\circ(T_q)}-1\right]\right. \\ &\quad \left.\int_{\Omega_1} A_{ij\nu} f_{\Omega_q}^{\text{wall}}(\Omega) f_{\nu_q}(\nu, T_{\max}) d\Omega d\nu\right]\end{aligned} \tag{7.3}$$

with:

$$f_{\nu_q}(\nu, T_{\max}) = \frac{I_\nu^\circ(T_{\max})}{\int_{\nu=0}^\infty I_\nu^\circ(T_{\max})d\nu},\ f_{\Omega_q}^{\text{wall}}(\Omega)d\Omega = f_{\theta_q}^{\text{wall}}(\theta)d\theta f_{\psi_q}^{\text{wall}}(\psi)d\psi$$

$$\text{and } \begin{cases} f_{\theta_q}^{\text{wall}}(\theta) = \dfrac{2\cos(\theta)\sin(\theta)}{1-(1-\Omega_1/2\pi)^2} \\ f_{\psi_q}^{\text{wall}}(\psi) = 1/(2\pi) \end{cases} \tag{7.4}$$

$\kappa_\nu(T_{\max})$ corresponds to the absorption coefficient of the point at maximum temperature and $I_\nu^\circ(T_{\max})$ its respective equilibrium intensity.

### 7.3.3 Numerical codes and coupling

For the fluid solver (AVBP), the same numerical setup as the one presented in Chapter 4 is considered.

The in-house RAINIER code solves the radiative transfer equation in unstructured meshes with a Monte Carlo method. A Randomized Quasi Monte-Carlo (Lemieux 2009) based on Sobol low-discrepancy sequences (Joe and Kuo 2008) is used for random numbers generation in order to increase the efficiency of the classical Monte Carlo Method (Palluotto et al. 2017). The ERM method (Tessé et al. 2002) is used for the calculation of the radiative power, and the OERM2 method (Zhang et al. 2012) is used for the calculation of the radiative directive fluxes at the probe positions.

Both codes AVBP and RAINIER are coupled using the Open-palm library (Buis et al. 2006). The radiative power field is updated based on the temperature, $X_{CO_2}$, $X_{H_2O}$ and soot volume fractions fields provided by the LES solver every $N_{\text{ite}}$ iterations of the flow solver in order to preserve a relative error lower than 3% on the computed radiative power and temperature fields.

In order to determine the value of $N_{\text{ite}}$, two parameters, $\alpha_1(N)$ and $\alpha_2(N)$, are defined as L2 error norms of the radiative power and temperature fields:

$$\begin{aligned}\alpha_1(N) &= \sqrt{\int_V \left|T_{i_0+N} - T_{i_0}\right|^2 dV} \Bigg/ \sqrt{\int_V \left|T_{i_0}\right|^2 dV} \\ \alpha_2(N) &= \sqrt{\int_V \left|P^{\text{R}}_{i_0+N} - P^{\text{R}}_{i_0}\right|^2 dV} \Bigg/ \sqrt{\int_V \left|P^{\text{R}}_{i_0}\right|^2 dV}\end{aligned} \tag{7.5}$$

where $V$ corresponds to the computational domain, $T_{i_0}$ and $P^{\text{R}}_{i_0}$ correspond respectively to the temperature and radiative power fields at a reference iteration $i_0$ of the fluid solver and $T_{i_0+N}$ and $P^{\text{R}}_{i_0+N}$ correspond respectively to the temperature and radiative power fields at iteration $i_0 + N$. All the fields are obtained in a preliminary study where the AVBP and RAINIER codes are coupled at each iteration.

Figure 7.1 presents the evolution of $\alpha_1(N)$ and $\alpha_2(N)$ parameters with the number of iterations of the fluid solver $N$. The coupling iterations number $N_{\text{ite}}$ satisfying 3% of relative error is $N_{\text{ite}} = 65$, and is chosen here in the coupled simulation. The time step of the LES solver is limited by the acoustic time scale (CFL criterion) and yields $\Delta t \approx 6.5 \times 10^{-8}$ s. The coupling period of the coupled simulation is then $\Delta t_{\text{cpl}} = 65\Delta t = 4.2 \times 10^{-6}$ s.

### 7.3.4 Numerical setup and CPU cost

This simulation has been performed using a cluster equipped with Intel E5-2680 processors with a total computational time (including averaging time) of 1,500 thousands of CPU hours on the OCCIGEN cluster provided by CINES and GENCI (allocation 2017-A0022B10159). The averaged fields have been computed over 250 ms of physical time. The repartition of processors between both codes is presented in Tab. 7.1: the CPU cost is then nearly equally distributed between the two codes.

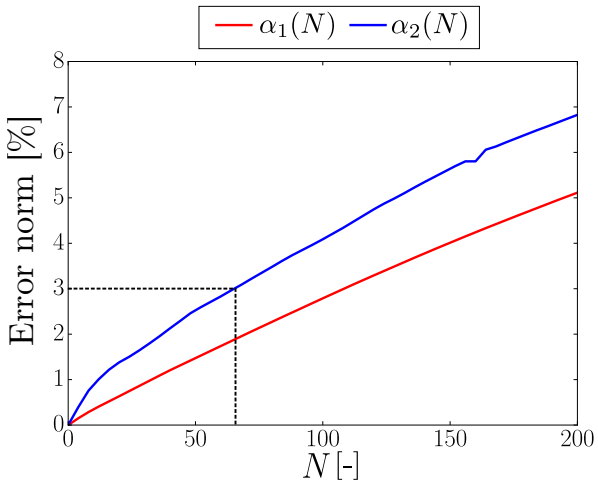


**Figure 7.1:** *Evolution of L2 error norms of the temperature and radiative power fields at fluid solver iteration $i_0 + N$ based on temperature and radiative power fields at fluid solver iteration $i_0$.*

| Codes | AVBP | RAINIER |
|---|---|---|
| Number of processors | 1120 | 1092 |

**Table 7.1:** *CPUs repartition between AVBP and RAINIER codes.*

Finally, Tab. 7.2 compares the relative CPU costs of this simulation (MC) and the simulation of Chapter 4 considering soot particles formation and radiation through the optically thin model, with a simulation which does not consider radiation nor soot particles formation (ADIAB). The latter is considered as reference for CPU cost.

| Case | Soot description | Radiation description | Rel. CPU cost |
|---|---|---|---|
| ADIAB | None | None | 1.0 |
| OPT | Sectional | Optically thin radiation model | 4.1 |
| MC | Sectional | Monte-Carlo resolution of the RTE | 8.2 |

**Table 7.2:** *Relative CPU costs of the studied cases.*

## 7.4 Numerical results and validation

In the following, gaseous and soot profiles predictions with the coupled simulation are compared with experiments and two other computations: one not considering radiation and soot particles formation (ADIAB) and the other one considering an optically thin radiation model for both gaseous and solid phases (OPT, Chapter 4).

### 7.4.1 Instantaneous fields

Figure 7.2 presents, from left to right, instantaneous fields of radiative power accounting for only gas contribution $P^{\mathrm{R}}_{\mathrm{gas}}$, temperature $T$, $CO_2$ and $H_2O$ molar fractions ($X_{CO_2}$ and $X_{H_2O}$ respectively), radiative power accounting for both gas and soot contributions $P^{\mathrm{R}}$ and soot volume fraction $f_V$. Please note that the color scales of images of $P^{\mathrm{R}}$ and $P^{\mathrm{R}}_{\mathrm{gas}}$ are not linear to highlight the field heterogeneity.

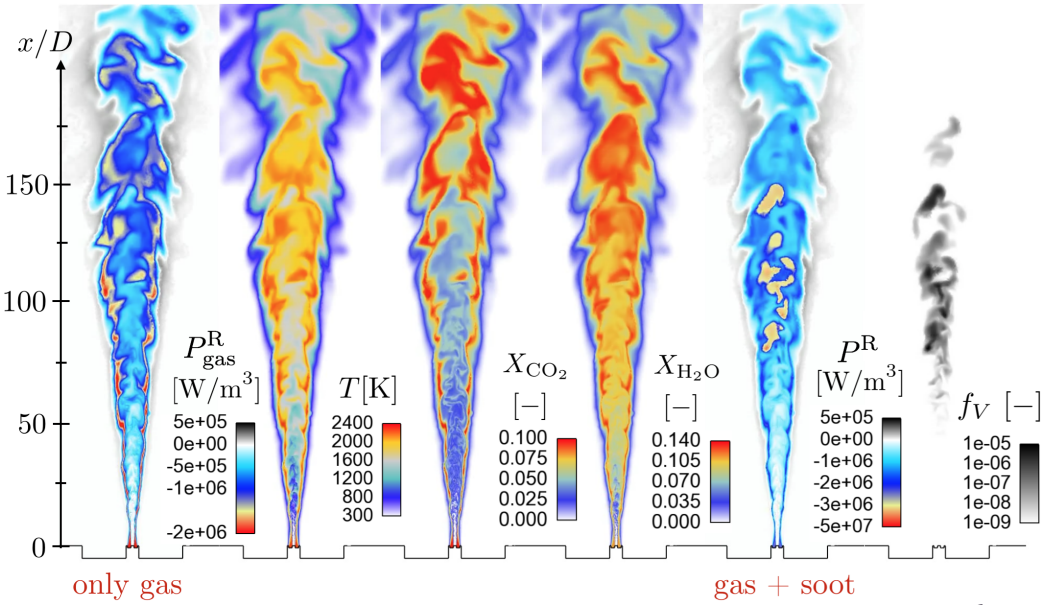


**Figure 7.2:** *Instantaneous fields of, from left to right, radiative power accounting for only gas contribution, temperature,* $CO_2$ *and* $H_2O$ *molar fractions, radiative power accounting for both gas and soot contributions and soot volume fraction.*

Without considering soot contribution to radiation, the radiative power is linked to high temperature regions combined with $CO_2$ and $H_2O$ presence, which corresponds to mixtures close to stoichiometric conditions. Soot particles are present in richer regions and maximum instantaneous soot volume fraction is nearly 10 ppm. Then, radiative power resulting from soot particles is located also in richer regions compared with radiative power resulting from only the gas phase. Moreover, when accounting for soot particles, due to high levels of

soot volume fraction, radiative power is at least one order of magnitude than the one obtained when considering only radiation from gas phase. Finally, radiative power is positive in lean regions near stoichiometry, corresponding to regions with low temperature (below 1000 K) where absorbed power from $CO_2$ and $H_2O$ is higher than emitted power.

Figure 7.3 presents the instantaneous fields of radiative power and emitted power. The same range in colormaps is used in both fields and it can be observed an important difference between these two fields in terms of their corresponding values. Indeed, integrating the total radiative power, respectively only the emitted power over all the computational domain, one obtains respectively 6.4 kW and 13 kW. Then, approximatively half of the emitted power is reabsorbed inside the computational domain, justifying the need to solve the Radiative Transfer Equation in such configuration and outlining the inadequacy of the optically thin radiation model which neglects such reabsorption phenomenon.

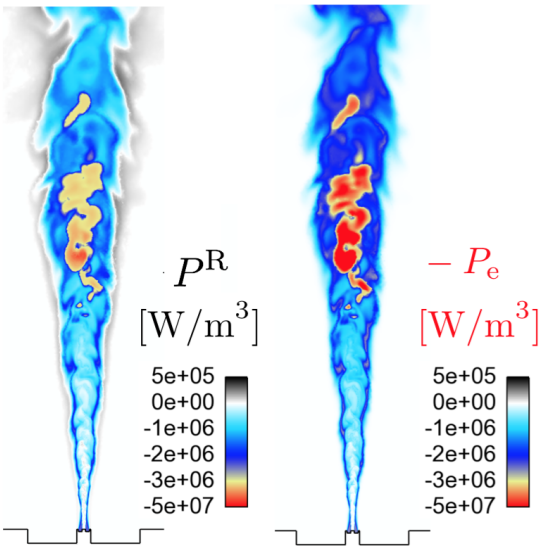


**Figure 7.3:** *Instantaneous fields of radiative power ($P^R$) and emitted power ($P^e$) of the coupled simulation.*

### 7.4.2 Mean temperature and species profiles

Figure 7.4(a) presents the evolution of predicted axial temperature profiles for the three simulation cases. While for the first part of the flame, the temperature profiles are quite similar, the downstream temperature decrease is largely impacted by the hypothesis done for thermal radiation. The lowest decrease rate is obtained for the computation without radiation whereas the highest decrease rate is obtained for the computation with the optically thin radiation model. This is due to the impact of radiation heat losses in the burnt gases. The coupled simulation, which accounts for reabsorption, presents lower radiation heat losses and therefore, an intermediate temperature decrease rate.

Figure 7.4(b) presents a comparison between the three computations with experiments of Kearney et al. (Kearney et al. 2015) of mean and RMS radial temperature profile obtained at $x/D = 134$.

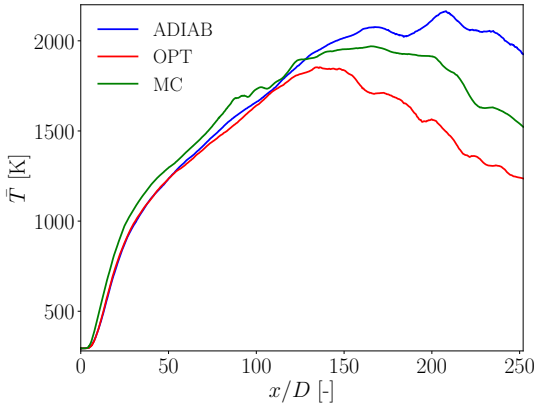


(a) Axial numerical temperature profile

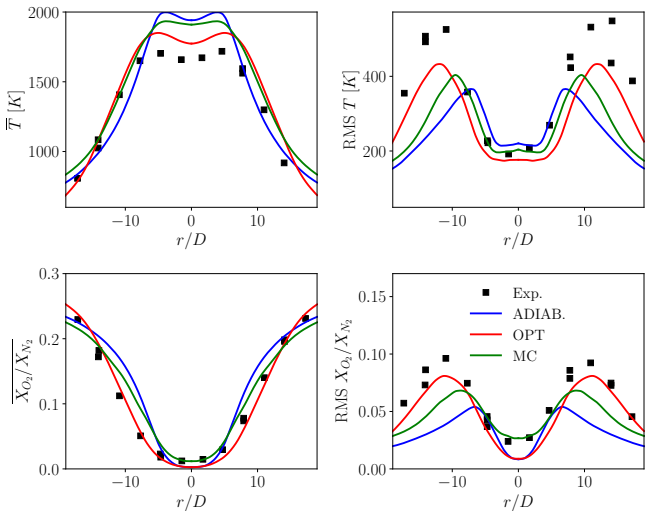


(b) Comparison between experimental and numerical radial temperature and $X_{O_2}/X_{N_2}$ mean and RMS profiles at $x/D = 134$.

**Figure 7.4:** *Mean temperature and species profiles for the different studied cases. Results obtained with adiabatic hypothesis (ADIAB), optically thin (OPT, Chapter 4) and coupled Monte-Carlo (MC) are respectively represented in blue, red and green solid lines. Experimental data from Kearney et al. (2015) are presented in black squares.*

It is important to remind that these experiments have been carried out in Albuquerque, where ambient pressure is equal to 0.84 bar, 17% lower than the pressure used in the computation (1.01325 bar). The soot volume fraction, soot intermittency and radiative intensity measurements by Shaddix et al. (ISF3 2017) have been done at Livermore, where ambient pressure is equal to 1 atm. That is why, a 1 atm pressure has been used for the simulation. Nonetheless, the

hierarchy between the three computations is again observed, with the highest temperature and lowest temperature for the computations without radiation and with the optically thin radiation model, respectively. Unfortunately, the pressure difference prevents any definitive conclusion between experimental and measurements and numerical results.
Mean and RMS results for the $X_{O_2}/X_{N_2}$ ratio are also presented for the three computations and compared with experimental measurements. For all these quantities, a reasonable agreement is observed.

### 7.4.3 Soot volume fraction profiles

Figure 7.5 (a) presents a comparison of axial soot volume fraction profiles with experiments for two different simulations: the coupled simulation with detailed radiation modeling, and the one considering the optically thin radiation model of Chapter 4. Figure 7.5 (b) compares the axial profiles of soot intermittency for both computations. First, for both quantities and for both computations, a good agreement between predictions and experimental data is observed, as noticed in Chapter 4. Secondly, it can be observed that detailed radiation modeling impacts only slightly these results compared to results obtained with optically thin radiation model: for the case with detailed radiation modeling, soot oxidation is predicted slightly later than in the optically thin radiation computation case. Achieving significantly better soot predictions is then not related here to radiation modeling, but is rather impacted by large uncertainties that remain in soot modeling as discussed in Chapter 4.

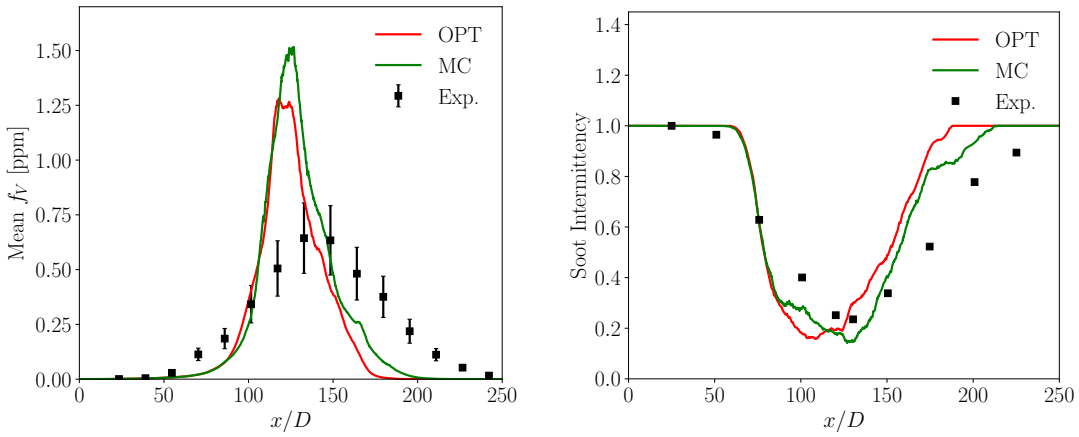


(a) Soot volume fraction axial profile

(b) Soot intermittency axial profile

**Figure 7.5:** *Impact of radiation modeling on soot volume fraction predictions. OPT (Chapter 4) and MC are respectively represented in red and green solid lines. Experimental data from ISF3 (2017) are presented in black squares.*

### 7.4.4 Radiative intensity profiles

Experimental measurements of radiative intensity profiles have been carried out at Livermore (where pressure is 1 atm). Figure 7.6 illustrates the measurement principle. Radiation from the flame over a small solid angle $\Omega = 1.065 \times 10^{-4}$ sr is collected by a radiometer at different positions in the axis of the flame $x/D = 50$, $x/D = 100$, $x/D = 135$ and $x/D = 175$) and for each one of this height above the burner, radial radiative intensities are obtained by collecting radiation paths at different positions shifted from the axis of the flame (see flame cross section in Fig. 7.6).

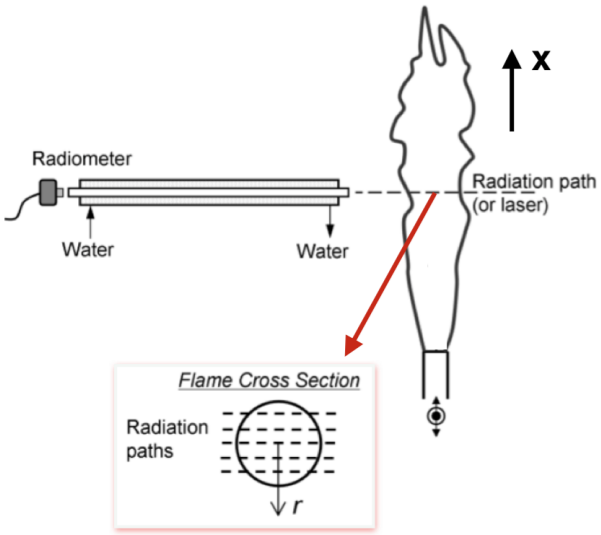


**Figure 7.6:** *Radiative intensity measurement principle (from communication of C. Shaddix (ISF3 2017).*

Figure 7.7(a) compares the axial profile of radiative intensity profiles (Eq. 7.2) with these experimental measurements. Blue solid lines correspond to gaseous contribution from $CO_2$ and $H_2O$ species whereas red solid lines correspond to the total contribution when taking into account both gaseous and solid phases. Figure 7.7(b) presents the radial profiles of experimental radiative intensities, numerical radiative intensities with total contribution (gaseous and soot contributions in red solid line), numerical intensities taking into account only gaseous contribution (in blue solid lines) at different heights above the burner ($x/D = 50$, $x/D = 100$, $x/D = 135$ and $x/D = 175$). It can be observed that for the results with the total contribution, a good agreement with the experiments of ISF3 (2017) is observed. Comparing these results with those obtained for only the gaseous contribution, one can see that soot particles are important contributors of the axial directive intensity for this flame. The discrepancies with the experimental results are mainly due to the differences observed in soot predictions. Indeed, for the heights where soot volume frac-

tion profiles are well predicted ($x/D = 135$ and $x/D = 175$), good predictions in radial profiles of radiative intensities are also obtained. The predictions are globally in a reasonable agreement with experimental measurements.

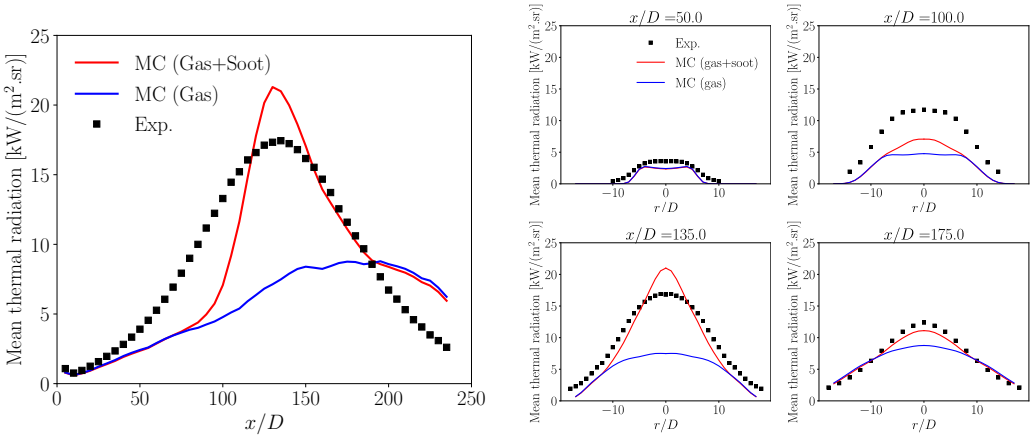


(a) Axial profile (b) Radial profiles

**Figure 7.7:** *Comparison between experimental radiative intensity profiles from ISF3 (2017) and numerical predictions. The contribution of only gaseous phase is plotted in blue, whereas total contribution is plotted in red.*

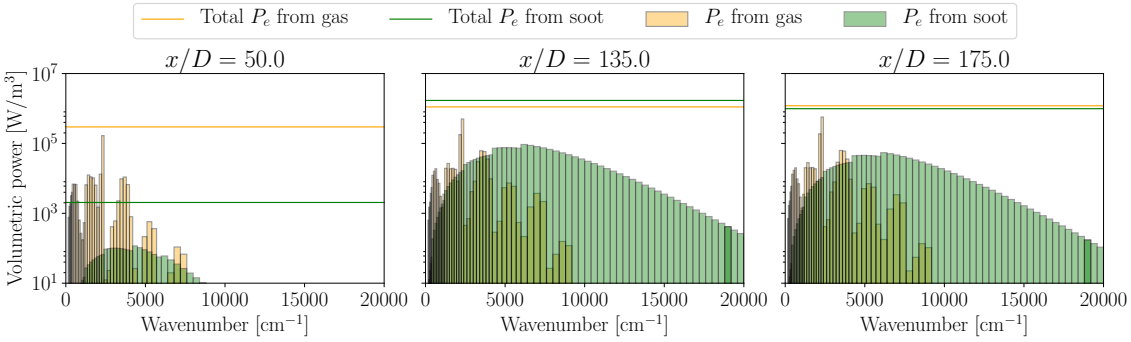


**Figure 7.8:** *Comparison of spectral emitted volumetric power from gas (in orange) and soot (in green) at the centerline for different heights. Total emitted power over all the spectrum is represented in orange solid line for gas and in green solid line for soot.*

Figure 7.8 presents the spectral distribution of volumetric emitted power from soot and gas at different heights of the jet centerline. Reported values are band-averaged in the considered set of narrow bands. The horizontal lines denote the total emitted power from soot and gas at the considered heights. The gas emission spectrum is highly dynamic and composed of very intense bands at low wavenumbers whereas the soot emission spectrum is continuous and is more intense for high wavenumbers. Moreover, depending on the position, the major

contributor in emitted power can be either gas or soot particles. Then, gas and soot particles spectra present different characteristics and diverse radiative behaviours can be expected depending on the considered position in the flame.

## 7.5 Absorption and emission contributions on radiative power

Figure 7.9 presents the fields of the mean emitted power and full radiative power for the coupled simulation. The high value of the radiative power at the between $x/D = 100$ and $x/D = 150$ correspond to the presence of a high soot volume fraction. It can be observed that radiative power is largely reduced by re-absorption phenomenon. Indeed, integrating the radiative and emitted powers over all the volume, one finds respectively, 5.7kW of total radiative power and 12kW of emitted power. Then, more than a half of the emitted radiative power is reabsorbed within the medium as already noticed on an instantaneous field previously.

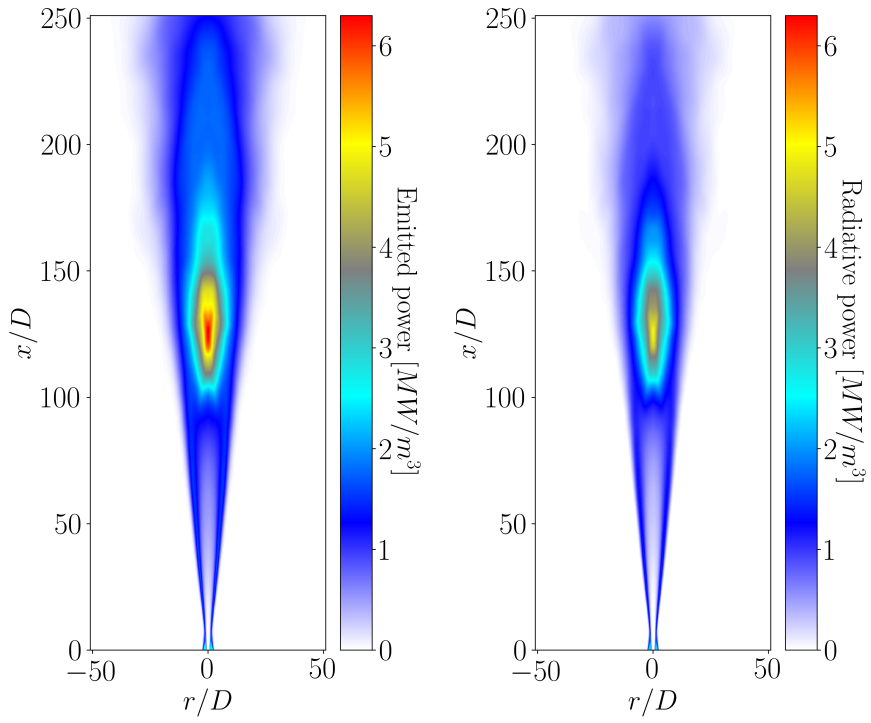


(a) Mean emitted power $P^e$

(b) Mean radiative power $-P^{\mathrm{R}} = -(P^a - P^e)$

**Figure 7.9:** *Fields of mean emitted power and radiative power for the coupled computation.*

In order to investigate the role of gaseous participating species and soot particles in the total volume integrated radiative power, four separate computations have been carried out for one representative instantaneous 3-D field obtained from the coupled simulation and taking into account emission and absorption of both gas and solid phases (computation Ref.): one considering only gas emission and gas absorption (computation GEGA), one considering only gas emission and soot absorption (computation GESA), one considering only soot emission and gas absorption (computation SEGA) and one considering only soot emission and soot absorption (computation SESA). For these computations, as the role of soot particles and gaseous participating species are not symmetric in emission and absorption, the ERM method is not appropriate and a backward Monte Carlo method is used instead. For the calculation of the transmissivity of the optical path, both phases are always considered.

Table 7.3 presents the corresponding total volume-integrated emitted power ($P_e$), absorbed power ($P_a$) and radiative power ($P^{\mathrm{R}}$) for the four computations, compared with the reference computation, where gaseous and soot contributions are considered for both emission and absorption (case **Ref.**). For this instantaneous solution, several observations can be done:

- Approximatively 56% (6.06 kW out of 10.86 kW) of the emitted power from the gaseous phase is reabsorbed by the gaseous phase,
- Less than 0.3% (0.03 kW out of 10.86 kW) of the emitted power from the gaseous phase is reabsorbed by the soot phase,
- Approximatively 10% (0.13 kW out of 1.27 kW) of the emitted power from the soot phase is reabsorbed by the soot phase,
- Less than 2% (0.02 kW out of 1.27 kW) of the emitted power from the soot phase is reabsorbed by the gaseous phase,
- Even if for regions of high soot volume fraction soot particles are the major contributors of radiative transfer, soot particles only account for 19 % of the total volume integrated radiative power (1.12 kW out of 5.89 kW).

**Table 7.3:** *Gaseous and soot contribution on emitted $P_e$ and absorbed $P_a$ powers.*

| Case | Ref. | GEGA | GESA | SESA | SEGA |
|---|---|---|---|---|---|
| $P_e$ [kW] | 12.13 | 10.86 | 10.86 | 1.27 | 1.27 |
| $P_a$ [kW] | 6.24 | 6.06 | 0.03 | 0.13 | 0.02 |
| $P^{\mathrm{R}}$ [kW] | -5.89 | -4.80 | -10.83 | -1.14 | -1.25 |

Reabsorption phenomenon ($P_a$) is then more important for the gaseous phase (see Ref. and GEGA cases). Reabsorption only slightly modifies soot total contribution to radiative power (see SESA and SEGA cases). Moreover, very small interactions are observed between soot particles and gaseous species in terms of radiative transfer. Indeed, soot only slightly absorbs gaseous emission

(case GESA), and gas absorbs little of soot emission (case SEGA). The corresponding spectral volume-integrated emission and absorption of the different cases are presented in Fig. 7.10. As expected, the Ref. case shows that 2 cK bands are the major contributors of gaseous emissions (from 2000 to 2500 $cm^{-1}$). For these bands, important gas absorption is also observed. For soot particles, soot absorption coefficient presents a continuous wide band spectrum and lower reabsorption for soot particles is observed (SESA case). Finally, gaseous reabsorption from soot emission is negligible and is only observed for the two bands mostly responsible for gaseous emissions (SEGA case).

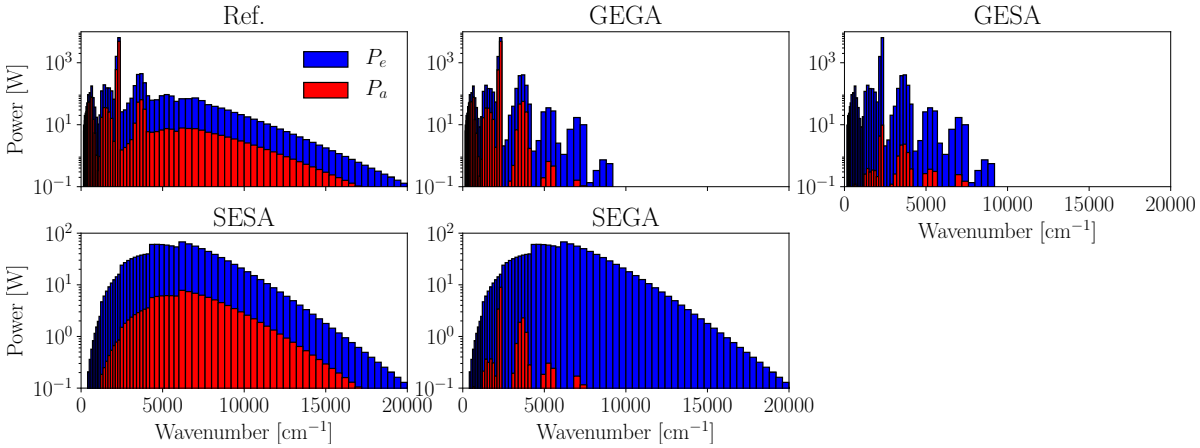


**Figure 7.10:** *Spectral emitted and absorbed volume-integrated powers for the instantaneous representative solution. Results correspond to the reference case taking into account gas and soot particles emission and absorption and the four other studied cases: GEGA, GESA, SEGA and SESA.*

It can then be concluded that the radiative exchanges between gas and solid phases are negligible. Concerning gaseous and soot reabsorption, one can interpret these results by looking at the optical thicknesses for each spectral band at different positions above the burner. To do so, for each height $x$ above the burner, we define the transmissivity $\tau_\nu(x)$ as $\tau_\nu(x) = \exp\left(-\int_{y=-\infty}^{+\infty} \kappa_\nu(y, z=0)dy\right)$, where $\kappa_\nu$ is the local absorption coefficient.

Figure 7.11 presents the corresponding transmissivities at three different heights above the burner: $x/D = 62.5$, $x/D = 125.0$ and $x/D = 187.5$. For the range of temperature [300 K, 1 900 K] observed in the flame, the wavenumbers participating to the radiative heat transfer are comprised between 150 $cm^{-1}$ and 13 000 $cm^{-1}$, with at least 95% of the radiative power represented by the range [150 $cm^{-1}$,10 000 $cm^{-1}$]. Then, only the range [150 $cm^{-1}$,10 000 $cm^{-1}$] is considered in this figure. The limit of an optically thin medium ($\tau_\nu \approx e^{-0.1}$) is also presented with a dashed line. For all these three heights, transmissivities taking into account gas, soot and gas+soot contributions are plotted.

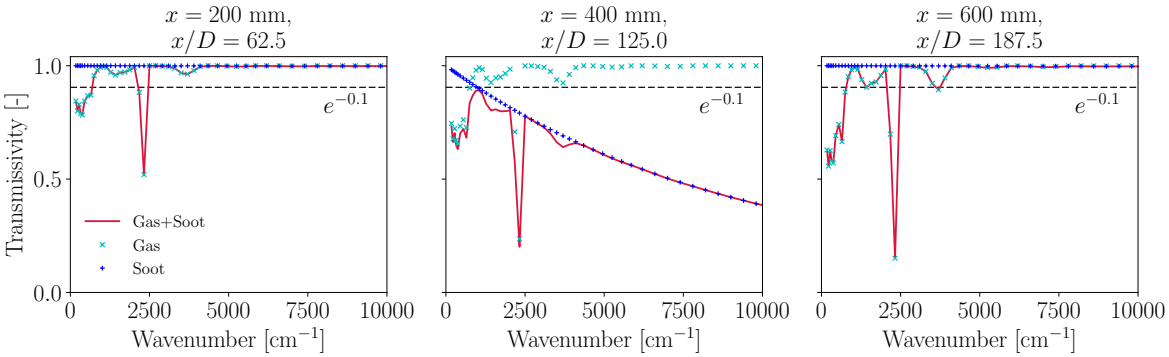


**Figure 7.11:** *Spectral transmissivities across the flame for different heights above the burner. Gaseous and soot contributions are also presented. The horizontal dashed line denotes the limit of the optically thin medium.*

First, concerning gas emissions, it can be observed that two $CO_2$ bands (corresponding to wave numbers between 2175 and 2475 cm$^{-1}$) highly contributing to gas emission present transmissivities largely lower than $e^{-0.1}$, explaining then why for these two bands, reabsorption is significative, and therefore, total gas reabsorption is important.

Secondly, it can be seen that soot particles have a strong influence at $x/D = 125.0$ where soot volume fraction is maximum. The transmissivity across soot particles decreases with the wavenumber. However, it can be observed that the optical thickness of soot particles is lower than those of the two highly contributing bands. This explains why only 10 % of the soot emitted power is reabsorbed.

## 7.6 Study of Turbulence Radiation Interactions

Figure 7.12 presents a comparison between mean field of radiative power issued from the coupled simulation (same as Fig. 7.9 (b) with a different color scale) and the one obtained from the resolution of the RTE based on mean fields of temperature, pressure, $CO_2$ and $H_2O$ molar fractions and soot volume fraction. This simulation correspond to the results that one should obtain when neglecting turbulent-radiation interactions (TRI). Comparing these two fields, one can observe that when accounting for large-scale turbulent-radiation interactions (solved with the coupled approach), radiative power in region of soot presence ($-10 < r/D < 10$ and $100 < x/D < 175$) is largely reduced.

Integrating both fields over the computational domain, one finds respectively 5.7 kW for the coupled simulation and 5.0 kW for the simulation based on the mean fields of temperature, pressure, $CO_2$ and $H_2O$ molar fractions, and soot volume fraction. Then, a non-negligible impact of turbulence-radiation

interactions is demonstrated. This justifies the interest in unsteady coupled simulations based on LES approach in order to capture correctly the large-scale turbulent-radiation interactions.

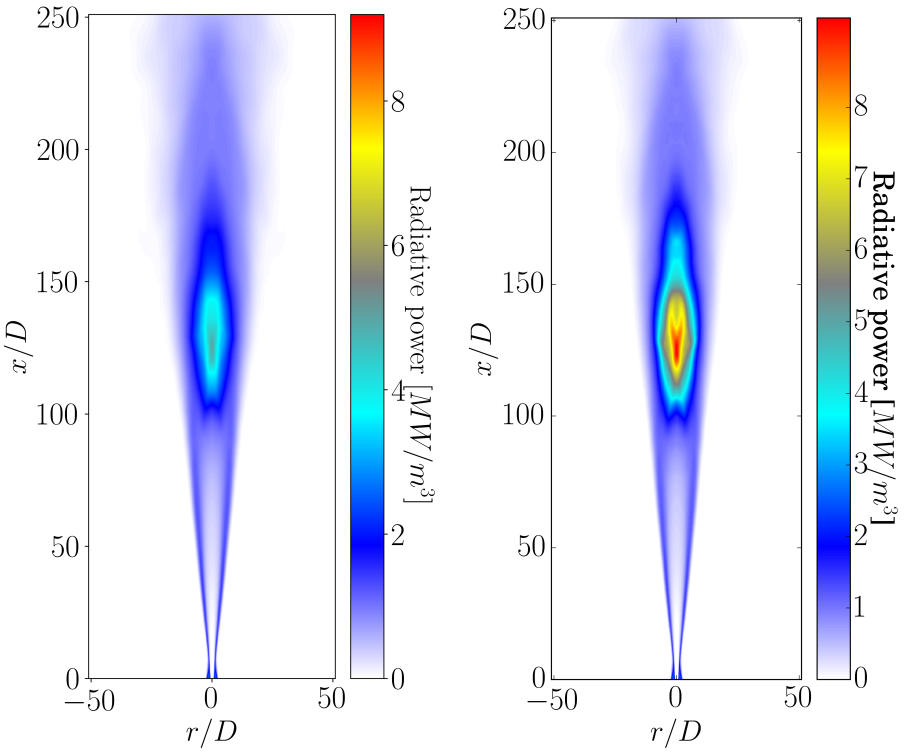


(a) Mean radiative power (b) Radiative power based on mean fields

**Figure 7.12:** *Comparison between mean field of radiative power issued from the coupled simulation (left) and the one obtained from the resolution of the RTE based on mean fields of temperature, pressure,* $CO_2$ *and* $H_2O$ *molar fractions and soot volume fraction (right).*

Figure 7.13 compares the radiative intensity profiles in these two cases, when considering only gas contribution and when considering both gas and solid phase contributions in radiative heat transfers.

Looking at the blue curves comparing gas radiative intensities, turbulent-radiative interactions increase mean radiative intensities in gas phase, as already observed in literature (Tessé et al. 2004; Coelho 2007; Pal et al. 2011; Poitou et al. 2012; Coelho 2012). Looking at total contribution when accounting for soot particles contribution to the radiative power, one can observe that turbulent-radiative interactions in fact largely decrease radiative intensities. Therefore, TRI effects increase the radiative power contribution from gas while it decreases the one from soot particles. This observation is confirmed by the work of Consalvi and

Nmira (2016a); Consalvi and Nmira (2017) where soot absorption coefficient-Planck function correlation and absorption turbulence-radiation interactions have been studied in turbulent diffusion flames. Their negative correlations have been demonstrated, which yields a decrease in radiative power.

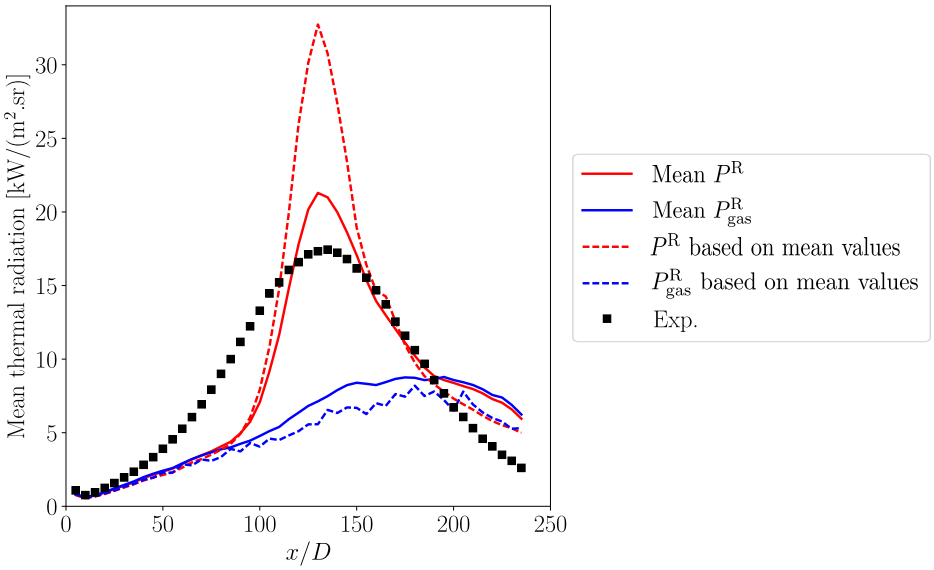


**Figure 7.13:** *Comparison between experimental radiative intensity profiles, the ones obtained with coupled simulation accounting for gas phase (solid blue line) and both gas and solid phases (solid red line) and the ones obtained solving the radiative transfer equation based on the mean fields of pressure, temperature,* $CO_2$ *and* $H_2O$ *molar fractions and soot volume fraction accounting for gas phase (dashed blue line) and both gas and solid phases (dashed red line).*

## 7.7 Conclusion

A coupled simulation of an ethylene/air jet diffusion flame combining large-eddy simulation with a detailed sectional model and a detailed Monte Carlo resolution of the radiative transfer equation has been proposed in this chapter. Good predictions in terms of temperature, species and soot volume fraction have been obtained compared to experiments. Axial and radial profiles of radiative intensity have also been compared with measurements obtained with a radiometer. An overall good agreement is observed.

The total soot particles volume-integrated radiative power is responsible for 19% of the total radiative heat transfer from the flame. In regions of high soot volume fraction ($\approx 1$ ppm), the major contribution to the radiative power comes from soot particles. Discrepancies between radiative intensity predictions and experiments are mainly observed for these regions and are therefore linked to

discrepancies observed in soot volume fraction predictions.

Impacts of reabsorption phenomena have also been investigated. Strong reabsorption is observed with approximatively half of the emitted radiative power reabsorbed. Depending on their respective transmissivities and therefore their optical thicknesses, the different gas bands contribute in a different way to the total absorbed radiative power. For several of them and the ones that contribute the most, the optically thin medium assumption is not valid and reabsorption must be considered. Therefore, for this atmospheric flame, gas radiation cannot be described by the optically thin radiation model which is yet widely used in the combustion community. Concerning soot particles, the optically thin medium is not valid at high wavenumbers for regions with high values of soot volume fraction. Finally, very small radiative interactions between gas and solid phases are observed due to the small overlapping of their absorption coefficient spectrum.

Nevertheless, several uncertainties remain in soot particles radiative properties. In recent studies, the morphology of soot fractal aggregates has been shown to drastically increase soot particles absorption coefficient (Yon et al. 2015; Okyay 2016) compared with those predicted with the RDG's theory for aggregates composed of non-overlapped spherical primary particles. Future work will be to consider these complex radiative soot particles properties in order to investigate their impact on total radiative power of sooting flames.

All results have neglected subgrid-scale TRI while most of TRI effects are believed to be captured on the resolved scales. Such effects investigated in Poitou et al. (2008) and Roger et al. (2011) will have to be considered in future works. Nonetheless, the present results allow to investigate resolved TRI at the LES mesh scale. A positive turbulent-radiative interaction for radiative power resulting from gas phase and a negative turbulent-radiative interaction for radiative power resulting from soot particles have been demonstrated. It will be valuable to carry out further analysis of the generated data to study the usual assumptions and models used to close TRI effects in a RANS context.

# Chapter 8

# Simulation of a confined pressurized sooting flame while accounting for conjugate heat transfer

*In this chapter, the multi-physics framework dealing with coupled turbulent sooting flame and conjugate heat transfer simulations is presented. The Hybrid Cell Neumann Dirichlet methodology used in this work is presented and its implementation on the AVBP/AVTP framework is detailed. Then, a conjugate heat transfer simulation of the DLR burner is presented with the objective of predicting the quartz window temperature. The corresponding prediction and its comparison with experimental measurements are analyzed. Causes of high quartz windows temperature are studied by studying the cause of wall fluxes. The impact of heat losses on flame stabilization and soot production are finally discussed.*

## Contents

## 8.1 Introduction

The use of large-eddy simulations (LES) is becoming more and more popular in industrial applications to attain high-fidelity predictions of turbulent flows. In the meantime, predicting wall heat flux distribution and wall temperatures as early as possible in the design stage has become a key issue in several industrial applications in order to avoid extreme heat fluxes loading in the materials. To do so, one needs to account for conjugate heat transfer (CHT) which couples the flow simulation to heat conduction within solid parts of the system. That is why the corresponding multi-physics problems are now also studied in combination with high-fidelity approaches (Duchaine et al. 2009; Kuhn et al. 2010; Tiselj et al. 2013) such as LES or direct numerical simulations (DNS) when affordable. In reactive flow simulations, the necessary accounting for realistic temperature boundary conditions has recently yielded to several studies where conjugate heat transfer is studied with either LES in turbulent flows (Jaure et al. 2013; Berger et al. 2016; Kraus et al. 2018; Koren et al. 2018) or DNS in laminar flows (Mari et al. 2016; Miguel-Brebion et al. 2016).

In these coupled multi-physics simulations, dedicated numerical solvers are generally considered to treat the different physical phenomena in order to avoid waste of computational resources due to the different characteristic time scales between the different physical phenomena. Indeed, heat diffusion in a solid has generally a time scale which is higher by several orders of magnitude than the one of a fluid. This can lead to a large amount of CPU resources wasted to solve heat conduction in the solid when using a unique solver for both fluid and solid.
Classical LES or DNS solver are then used in the fluid domain and a dedicated heat transfer equation solver is used in the solid domain. A partitioned coupled approach is considered: both solvers compute their own temporal iterations (noted $n_s$ and $n_f$ for the solid and the fluid solvers, respectively) with their own time step (noted $\Delta t_s$ and $\Delta t_f$ for the solid and fluid solvers, respectively) until a physical time corresponding to the prescribed coupling time step: $\Delta t_{\text{cpl}} = n_s \Delta t_s = n_f \Delta t_f$. Traditionally, $n_s$ and $n_f$ are generally imposed by the user before the computation. The choice of this parameter has an impact on both the accuracy of the temporal integration (with large errors if $\Delta t_{\text{cpl}}$ is too high) and the computational cost (with large waste of CPU resources if $\Delta t_{\text{cpl}}$ is too low).

As the computational domain is split into two sub-domains (the fluid and walls), boundary conditions at the interface must be provided. Decomposition methods are generally considered when steady conjugate heat transfer is considered (Quarteroni and Valli 1999). The steady solution on the whole domain is achieved iteratively using classical methods, such as Neumann-Dirichlet, Dirichlet-Dirichlet and Neumann-Neumann coupling techniques (Roux and Ga-

raud 2009; Henshaw and Chand 2009; Errera and Chemin 2013).
When considering unsteady conjugate heat transfer, as the solid and fluid solvers advance in time in their own between each coupling time step, temperature and heat flux cannot be maintained continuous at the interface and discontinuity of temperature and heat flux at the solid-fluid interface must be treated. Methods based on their steady variant have been considered in the literature. The Dirichlet-Dirichlet (respectively Neumann-Neumann) coupling approach is based on a prescribed boundary temperature (resp. heat flux) as a boundary condition between each coupling time step, implying different heat fluxes (resp. temperatures) on both sides. The boundary temperature (resp. heat flux) is modified after each coupling time step in order to obtain a continuous heat flux (resp. temperature) at the fluid-solid interface. These two strategies are generally numerically unstable, and the classical Neumann-Dirichlet approach or a more general formulation involving a Robin condition is generally considered instead (Cubasch et al. 1992; Voss and Sausen 1996; Lunkeit et al. 1996; Duchaine et al. 2009; He and Oldfield 2010; He 2013; Jaure et al. 2013; Radenac et al. 2014): the flow solver uses a Dirichlet temperature boundary condition while the solid solver considers a Neumann heat flux boundary condition, ensuring then a temperature and heat flux continuity at each coupling time step. Indeed, as long as the ratio $\rho_f c_{p,f} \Delta x_f / \rho_s c_s \Delta x_s$ (with $\rho_f$ and $\rho_s$ the solid and fluid densities, $c_{p,f}$ and $c_s$ the fluid and solid heat capacities, and $\Delta x_f$ and $\Delta x_s$ the space discretization on the fluid and solid sides of the interface respectively) is lower than the unity, this coupling technique is stable (Giles 1997). This condition is generally fulfilled in gas-wall CHT applications due to higher density of the solid compared to the fluid.

However, in all these traditional methods, the coupling period is a parameter which is adjusted in each coupling time step depending on the strength of wall-fluid interactions. In the methodology developed by Koren et al. (2017c); Koren et al. (2017a), a modified Neumann-Dirichlet coupling method, the *Hybrid-Cell Neumann Dirichlet* (HCND) approach, has been proposed in order to determine automatically and dynamically the coupling time step. Besides, the main advantages of this HCND coupling methodology are:

- The coupling is energy conservative over a coupling period,
- The coupling methodology is *self-adaptive*: the time step is automatically determined by controlling through a PID controller the numerical integration error,
- The control of the numerical integration error enables to ensure the numerical stability of the coupling procedure,
- The numerical accuracy of the coupling method is controlled through the prescribed tolerance,
- An acceleration method has also been developed in order to accelerate artificially the transient slow heat conduction in the solid parts of such coupled simulations, without impacting the signal properties of the wall

temperature and heat flux fluctuations.

The principle of the HCND methodology and its acceleration method is presented in the following in section 8.2. Then, the work done for its implementation in the AVBP/AVTP framework is presented in section 8.3. Finally, the application of this methodology for the study of the conjugate heat transfer in the DLR combustion chamber studied in Chapter 5 is presented in section 8.4.

## 8.2 HCND methodology

The Hybrid Cell Neumann Dirichlet (HCND) methodology has been firstly proposed by Koren et al. (2017c). It is based on an energy balance on hybrid fluid-solid cells rather than the classical Neumann-Dirichlet approach (Duchaine et al. 2009; Jaure et al. 2013). Next section presents the principle of this hybrid cell. Then, the equations solved in order to obtain the mean wall temperature field and its corresponding fluctuations are presented.

### 8.2.1 Hybrid Cell principle

Figure 8.1 illustrates the hybrid cell principle. It is based on a conforming mesh at walls between fluid and solid parts and the hybrid cell is composed by a fluid cell and the corresponding solid cell.

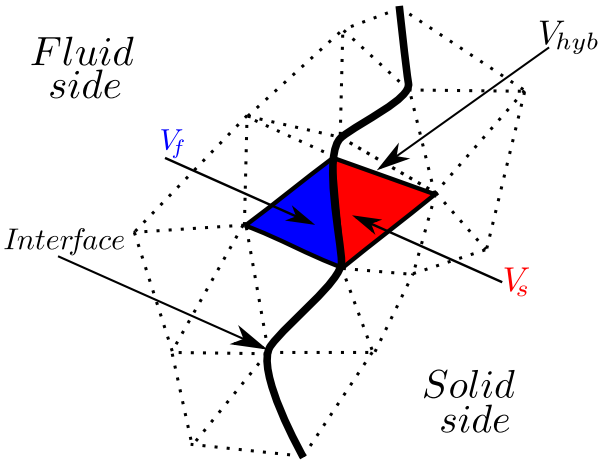


**Figure 8.1:** *Fluid and solid domains used for a coupled simulation. Dashed triangles represent the mesh and both grey triangles represent the two cells which make the hybrid cell around the interface (from (Koren et al. 2017c)).*

The corresponding energy balance equation for the hybrid cell enthalpy $H_{\text{hyb}}$

writes:

$$\frac{dH_{\text{hyb}}}{dt} = -\sum_{j=1}^{n_{\text{face}}} A_j \phi_{\mathbf{j}} \cdot \mathbf{n}_{\text{ext,j}} \tag{8.1}$$

where $n_{\text{face}}$, $A_j$, $\phi_{\mathbf{j}}$ and $\mathbf{n}_{\text{ext,j}}$ correspond to the the number of internal faces of the hybrid cell, the surface of the $j^{\text{th}}$ face, the total heat flux at the face $j$ and the outgoing normal to the face $j$ (exiting the fluid domain), respectively.

Noting $\Phi_{\mathbf{f}}$ and $\Phi_{\mathbf{s}}$ the fluxes integrated over all internal hybrid cell faces of the fluid and of the solid respectively, the right hand side of the Eq. (8.1) can be written as:

$$-\sum_{j=1}^{n_{\text{face}}} A_j \phi_{\mathbf{j}} \cdot \mathbf{n}_{\text{ext,j}} = -\Phi_{\mathbf{f}} - \Phi_{\mathbf{s}} \tag{8.2}$$

Being the enthalpy extensive, the left hand side of the Eq. (8.1) is expressed by:

$$\frac{dH_{\text{hyb}}}{dt} = \int_{V_f} \rho_f c_{p,f} \frac{dT_{\text{bnd}}}{dt} dV + \int_{V_s} \rho_s c_s \frac{dT_{\text{bnd}}}{dt} dV \tag{8.3}$$

where $V_f$ and $V_s$ are the volumes of the fluid and solid parts of the hybrid cell respectively. $c_{p,f}$ corresponds to the heat capacity at constant pressure of the fluid and $c_s$ corresponds to the heat capacity of the solid, assumed incompressible.
Neglecting spatial variations of thermo-physical properties in each subcell during a given time step, the equation for the boundary temperature $T_{\text{bnd}}$:

$$\frac{dT_{\text{bnd}}}{dt} = -\frac{\Phi_f + \Phi_s}{\rho_f c_{p,f} V_f + \rho_s c_s V_s} \tag{8.4}$$

Note that, generally, $\Phi_f$ represents the convective ($\Phi_{\text{conv}}$) and radiation fluxes ($\Phi_{\text{rad}}$) on the fluid side, whereas $\Phi_s$ corresponds to the solid conductive ($\Phi_{\text{cond}}$) flux:

$$\begin{cases} \Phi_f = \Phi_{\text{conv}} + \Phi_{\text{rad}} \\ \Phi_s = \Phi_{\text{cond}} \end{cases} \tag{8.5}$$

Then, when using this methodology, Dirichlet boundary conditions are employed in both solvers.The ordinary differential equation (Eq. (9.1)) is solved through an Adams-Bashforth time integration scheme (Hairer et al. 1993) and the obtained boundary temperature $T_{\text{bnd}}$ at each hybrid cell is imposed as boundary condition of each code.

In fact, generally, $\rho_s c_s V_s$ is several orders of magnitudes higher than $\rho_f c_{p,f} V_f$. Then, Eq. (9.1) can be approximated as:

$$\frac{dT_{\text{bnd}}}{dt} \approx -\frac{\Phi_{f,\text{bnd}} + \Phi_{s,\text{bnd}}}{\rho_s c_s V_s} \tag{8.6}$$

This equation corresponds exactly to the equation solved by the heat transfer equation solver for determining the boundary temperature to apply when using a classical Neumann-Dirichlet approach. Then, as long as $\rho_s c_s V_s \gg \rho_f c_{p,f} V_f$, the HCND approach provides the same evolution of the boundary temperature than the classical Neumann-Dirichlet approach.
However, compared with the classical Neumann-Dirichlet approach, the fact of solving Eq. (9.1) separately enables to control the coupling time step $\Delta t_{\text{cpl}}$ with any classical controller used for such an ordinary differential equation. The chosen time step control methodology is detailed in the following paragraph.

### 8.2.2 Time step control

The methodology developed by Koren et al. (2017c) is based on a self-adaptive coupling frequency of the different codes used for the unsteady coupled conjugate heat transfer simulations. Based on control theory (Gustafsson et al. 1988; Hairer et al. 1993), different variables are introduced in order to control the coupling time step $\Delta t_{\text{cpl}}$ based on a target error tolerance $\eta$:

$$\begin{aligned} C &= \log\left(\Delta t_{\text{cpl}}\right) \\ \theta &= \log(\epsilon) - \log(\eta) \end{aligned} \tag{8.7}$$

where $C$ is an actuator which influences $\theta$, the variable that is controlled. $\epsilon$ and $\eta$ correspond respectively to the numerical error and the prescribed error tolerance. The variation of $C$ is expressed through a general PID (Proportional-Integral-Derivative) controller:

$$-\dot{C}(t) = K_P \dot{\theta}(t) + K_I\ \theta(t) + K_D \ddot{\theta}(t) \tag{8.8}$$

where $K_P$, $K_I$ and $K_D$ are respectively the proportional, integral and derivative control gains. Solving Eq. (8.8), one obtains the optimal next coupling time step at time $n+1$ based on the PID controller:

$$\Delta t_{\text{opt}} = \Delta t^n_{\text{n,cpl}} \left(\frac{\eta}{\epsilon_{n-1}}\right)^{-\alpha} \left(\frac{\eta}{\epsilon_n}\right)^{\beta} \left(\frac{\eta}{\epsilon_{n-2}}\right)^{\gamma} \tag{8.9}$$

where:

$$\alpha = K_P + 2K_D, \quad \beta = K_P + K_I + K_D, \quad \gamma = K_D \tag{8.10}$$

and $\epsilon_{n-1}$, $\epsilon_n$ and $\epsilon_{n+1}$ correspond to the error for at $n-1$, $n$, $n+1$ coupling communications step. $\Delta t^n_{\text{n,cpl}}$ corresponds to the coupling time step of the $n^{\text{th}}$

coupling. The values of $K_P$, $K_I$ and $K_D$ are chosen in order to obtain the best precision and the smoothest evolution of the time step size (Gustafsson et al. 1988; Söderlind 2003). The values of parameters $\alpha$, $\beta$ and $\gamma$ are given in Table 8.1 as a function of the order $k$ of the integration scheme. A first order integration scheme is considered for all the presented calculations.

| $\alpha(k+1)$ | $\beta(k+1)$ | $\gamma(k+1)$ |
|---|---|---|
| $1/9$ | $1/18$ | $1/18$ |

**Table 8.1:** *Coefficients of the PID controller (from Söderlind (2003)).*

### 8.2.3 Accelerated variant of the method

#### 8.2.3.1 Fluid and solid characteristic time scales in practical CHT simulations

In many applications, an issue with the CHT simulation of unsteady flows is the very slow conduction characteristic time scale in the solid parts. Then, the physical time required to attain the permanent regime is not affordable. To deal with this issue, the physical transient regime is generally accelerated artificially in order to attain the permanent regime (which is still unsteady in pulsated or turbulent configurations) with an affordable cost (Duchaine et al. 2009; He and Oldfield 2010; He 2013; Errera and Chemin 2013; Jaure et al. 2013; Duchaine et al. 2013; Berger et al. 2016). Among these works, two main approaches can be encountered. The first approach considers the coupling of an unsteady flow solver with a steady solid heat transfer solver (Errera and Chemin 2013). It enables to obtain the mean fields in the solid with a very low computational cost but does not give access to the fluctuations of temperature and heat flux in the solid parts of the computational domain. The second one is the desynchronization method (Duchaine et al. 2009; Jaure et al. 2013; Duchaine et al. 2013; Berger et al. 2016). In this approach, the physical times of each code are not synchronized and the flow solver simulated a physical time of $\Delta t_{\text{cpl}}$ while the solid heat transfer solver simulated a physical time of $\alpha \Delta t_{\text{cpl}}$ with $\alpha \approx 100 - 1000$. The permanent regime, mean temperatures and mean heat flux fields are achieved in an efficient way, but the signal unsteadiness of the temperature and heat fluxes is not preserved. Indeed, this approach has two main drawbacks : the fluctuations frequencies perceived by the solid are modified and the amplitudes of heat loads are generally wrongly amplified. In practice, the codes could no longer be desynchronized once the permanent regime is achieved but this introduces yet another transient slow process.

Here, the accelerated technique developed by Koren et al. (2017a) that enables to conserve the perturbations signal integrity is considered. The main characteristics of this accelerated method are:

- It conserves the HCND benefits in terms of automatic coupling time step

determination and integration error control.
- It accelerates the time needed to attain the permanent regime in the solid side.
- It conserves the steady-state fluctuations signal properties in terms of amplitudes and frequencies spectrum.

This section presents its principle. Its implementation and validation in the AVBP/AVTP framework will be presented in section 8.3.

#### 8.2.3.2 Equations for mean and fluctuating fields

The accelerated method is based on the resolution of the heat transfer equation for both the mean and fluctuating fields of solid temperature. Next paragraphs summarize the corresponding equations and boundary conditions in this methodology.

**Separation of variables for the mean and fluctuating temperature fields:**

Conduction heat transfer being a linear phenomenon (*i.e.* all the operators in the corresponding heat transfer equation are linear) the temperature field can be split into two contributions: a mean temperature field ($\widehat{T}_s$) and a fluctuating one ($T'_s$) verifying the following equations:

$$T_s = \widehat{T}_s + T'_s \tag{8.11}$$

$$0 = \nabla \cdot \left( \lambda_s \nabla \widehat{T}_s \right) \tag{8.12}$$

$$\rho_s c_s \frac{\partial T'_s}{\partial t} = \nabla \cdot \left( \lambda_s \nabla T'_s \right) \tag{8.13}$$

For these two latter equations, boundary conditions need to be provided. They are explained in the next paragraph.

**Boundary conditions**

For the mean component $\widehat{T}$, a Neumann-type boundary condition is used. The imposed value is the mean heat flux from the fluid side $\widehat{\phi}_{f,\mathrm{bnd}}$, computed as:

$$\widehat{\Phi}_{f,\mathrm{bnd}} = \frac{1}{\tau} \int_0^\tau \Phi_{f,\mathrm{bnd}}(t) dt \tag{8.14}$$

where $\tau$ is the computing time.

Once the averaged wall heat flux is converged, the mean solid temperature is also converged since a steady equation is solved. Then, the permanent regime of the solid field is reached in an accelerated way, as it will converge only after several flow characteristic time scale, instead of the characteristic time scales of the solid ($\tau_s = L_s^2/a_s$ where $L_s$ and $a_s$ correspond respectively to the solid length scale and the solid thermal diffusivity). $\tau_s$ is generally higher then the flow characteristic time scale because of the lower thermal diffusivity of solid compared with that of the fluid.

For the fluctuating component $T'_s$, following the HCND method, a Dirichlet boundary condition is used at the interface between solid and fluid. This boundary condition corresponds to the fluctuating boundary temperature $T'_{\text{bnd}}$ at the interface and is advanced in time using the hybrid cell interface model combined with the coupling time step control presented in 8.2.2:

$$\frac{dT'_{\text{bnd}}}{dt} = -\frac{\Phi'_f + \Phi'_s}{\rho_f c_{p,f} V_f + \rho_s c_s V_s} \tag{8.15}$$

In the presented accelerated approach, the fluxes used in the interface model correspond to the conductive fluctuating heat flux provided by the unsteady heat transfer solver ($\phi'_{\text{s,bnd}}$) and the fluctuating heat flux in the fluid side, computed as:

$$\Phi'_{f,\text{bnd}} = \Phi_{f,\text{bnd}} - \widehat{\Phi}_{f,\text{bnd}} \tag{8.16}$$

For the initialization, the fields of mean temperature for the mean and fluctuating field are set to:

$$\begin{aligned} &\widehat{T}_s(t=0,x) = T_s(t=0,x) \\ &T'_s(t=0,x) = 0. \end{aligned} \tag{8.17}$$

#### 8.2.3.3 Limits due to non-linear boundary conditions

At an uncoupled solid interface, several boundary conditions can coexist for:

- A Dirichlet condition with an imposed temperature: $T = T_{\text{wall}}$.
- A Neumann condition with a constant flux $\phi = \phi_0$ towards the exterior,
- A mixed condition with conducto-convective flux $\phi = h(T - T_{\text{exch}})$, where the heat transfer coefficient $h$ can depend on local temperature $T$ and time $t$, and $T_{\text{exch}}$ is the exchange temperature.
- A boundary condition with a radiative boundary condition $\phi = \epsilon\sigma\left(T^4 - T_\infty^4\right)$ where $\sigma$ is the Stefan constant and $\epsilon$ is the wall emissivity, which can depend on the local temperature.

To illustrate the treatment of boundary conditions in case of the accelerated method, we will take the case of the mixed boundary condition:

$$\phi = \phi_0 + h(T - T_{\text{exch}}) + \epsilon\sigma(T^4 - T_\infty^4) \tag{8.18}$$

where $h$ and $\epsilon$ are assumed constant spatially and temporally.

Then, the boundary condition $\overline{\phi}$ to be applied for the mean solid temperature solver is:

$$\overline{\phi} = \phi_0 + h(\overline{T} - T_{\text{exch}}) + \ \epsilon\sigma(\overline{T^4} - T_\infty^4) \tag{8.19}$$

However, as information about the value of $\overline{T^4}$ are not known, therefore, the following boundary condition is imposed:

$$\widehat{\phi} = \phi_0 + h(\widehat{T} - T_{\text{exch}}) + \epsilon\sigma(\widehat{T}^4 - T_\infty^4) \tag{8.20}$$

where $\widehat{T}$ corresponds to the field verifying the Eq. (8.12) with the boundary condition presented in Eq. (8.20). It does not correspond exactly to the mean temperature field $\overline{T}$ of the computation, which cannot be obtained when non-linear boundary conditions as the one presented here are imposed to the system.

Then the boundary condition $\phi'$ used for the calculation of the *pseudo-fluctuation* $T'$ is:

$$\begin{aligned}
\phi' &= \phi - \widehat{\phi} \\
&= h(T - \widehat{T}) + \epsilon\sigma(T^4 - \widehat{T}^4) \\
&= h(\widehat{T} + T' - \widehat{T}) + \ \epsilon\sigma((\widehat{T} + T')^4 - \widehat{T}^4) \\
&= hT' + \epsilon\ \sigma(4\widehat{T}^3T' + 6\widehat{T}^2T'^2 + 4\widehat{T}T'^3 + T'^4)
\end{aligned} \tag{8.21}$$

However, as the sum of Eqs. (8.12) and (8.13) corresponds to the exact equation verified by the temperature field, and also the sum of the equations (8.20) and (8.21) verifies the correct flux, the temperature field is well retrieved by computing $T = \widehat{T}\ + T'$.

## 8.3 HCND: and validation in AVBP/AVTP framework

### 8.3.1 The AVTP solver and implementation methodology

The Open-palm library is again used in order to couple the different presented codes together and exchange information. In the following, the implementation of the Hybrid Cell Neumann-Dirichlet (HCND) approach in AVBP-AVTP will be presented in the non-accelerated and accelerated cases.

#### 8.3.1.1 The AVTP solver

The code AVTP (Jaure et al. 2013) is used to solve the unsteady heat conduction within the solid walls with a spatial second-order Galerkin diffusion scheme (Donea and Huerta 2003) and a first-order backward Euler scheme time integration. The resolution of the implicit system is done with a parallel matrix free conjugate gradient method (Frayssé et al. 2005).

#### 8.3.1.2 Non-accelerated HCND method

The quick interface temperature solver and time-step controller is duplicated in AVBP and AVTP, simplifying greatly the communications exchange scheme.

Figure 8.2 represents the communication exchanges between the different codes for the non-accelerated HCND method. The same approach as the one done by Koren (2016) with flow and solid YALES2 solvers is considered. At each coupling time step, the following communications are done:

1. Codes send to each other information about instantaneous flux and heat capacity of their corresponding part of the hybrid cells. In the same communication, the fluid solver also sends its current integrating time step ($\Delta t_f$) to the solid solver.
2. Each code solves the temperature ODE for each hybrid cell and determine the corresponding next coupling time step. The effective next time step is finally determined considering first the minimum time step of all the hybrid cells ODEs determined by each local controller, and second, considering the maximum multiple $n_f$ of the fluid solver time step $\Delta t_\mathrm{f}$ that is lower than the minimum time step of all the hybrid cells ODEs. That is why the fluid solver also sends its time step to the solid solver, such that it can also determines the appropriate next coupling time step.
3. Then, the number of iterations to be done by the fluid solver before the next exchanged communication is determined and both codes solve their corresponding equations.

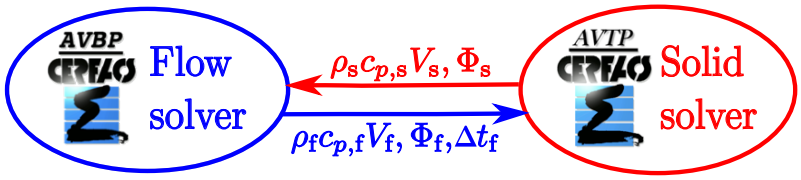


**Figure 8.2:** *Scheme of the interface model for coupled unsteady conjugate radiation heat transfer.*

#### 8.3.1.3 Accelerated HCND method

Instead of having two instances of AVTP to solve the steady and unsteady heat transfer equations as in Koren PhD thesis (Koren 2016) and as presented in Fig.

8.3 (a), a single instance of the code AVTP is here used. Again, this simplifies greatly the communications scheme and AVTP is modified to solve sequentially the steady and unsteady heat equations. The validation of the implementation of AVTP steady version is detailed in the next section.

Figure 8.3 (b) represents the communication exchanges between the different codes for the accelerated HCND method. The exchanges are based on the same communications scheme of the non-accelerated case, but other information are exchanged. The corresponding communications are:

1. As for the non-accelerated case, the fluid solver sends information about heat capacity, flux and time step. The solid solver handles the calculation and storage of the mean fluid and solid fluxes ($\overline{\Phi_\mathrm{f}}$ and $\overline{\Phi_\mathrm{s}}$ respectively) at the fluid-solid interface and sends information about the heat capacity, flux, fluxes and time step. In particular, it sends back the mean fluxes in the fluid solver side back to the fluid solver and the solid side fluctuating fluxes,
2. Both solvers compute or have information about the fluctuating fluxes of each solver and compute the next coupling time step.
3. The fluid solver continues its iterations, while the solid solver solves both the mean temperature $\widehat{T_s}$ based on the mean fluid flux (with a classical Neumann boundary condition) and the fluctuating temperature $T_s\prime$ based on the HCND energy balance of the fluctuating fluxes.

### 8.3.2 Validation of AVTP steady variant

A steady formulation of the heat transfer equation solver has been implemented in the AVTP solver in order to implement the HCND methodology. This is mainly based on a reformulation of the implicit system to solve in the solver.

The small validation case corresponding to a 2-D case is represented in Fig. 8.4. It corresponds to a square with a side length equal to 1 m. The solid thermal conductivity is considered equal to 1 W/m/K. The mesh contains 100 points in both directions. Adiabatic conditions are considered on the left and right sides of the domain. An isothermal boundary condition $T_\mathrm{top} = 1000$ K is considered at the top of the domain. For the bottom of the domain, four cases are considered:

- (a): An isothermal boundary condition with a bottom temperature $T_\mathrm{bottom} = 300$ K,
- (b): A flux boundary condition with an outgoing bottom flux $\phi_\mathrm{bottom} = 500$ W/m$^2$ for which the bottom temperature expected value is $T_\mathrm{bottom} = 500$ K,
- (c): A convective-type boundary condition with $\phi_\mathrm{bottom} = h_\mathrm{bottom}(T_\mathrm{bottom} - T_\mathrm{air})$, with an exchange coefficient $h_\mathrm{bottom} = 1$ W/m$^2$/K and an exchange temperature $T_\mathrm{air} = 300$ K for which the bottom temperature expected

value is $T_{\text{bottom}} = 650$ K,

- (d): A mixed radiative-convective-type boundary condition with $\phi_{\text{bottom}} = h_{\text{bottom}}(T_{\text{bottom}} - T_{\text{air}}) + \epsilon\sigma(T^4_{\text{bottom}} - T^4_{\infty})$ with $h_{\text{bottom}} = 1$ W/m$^2$/K, $T_{\text{air}} = 300$ K, $\epsilon = 0.25$ and $T_\infty = 300$ K for which the bottom temperature expected value is $T_{\text{bottom}} = 440.6$ K.

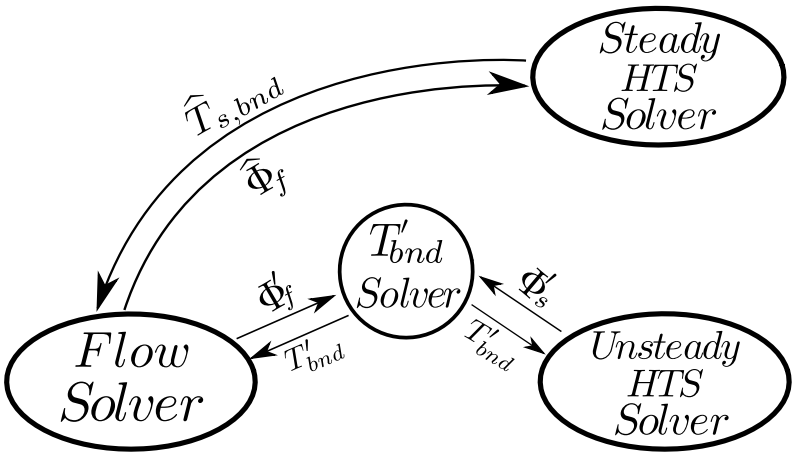


(a) Accelerated HCND coupling scheme in Koren (2016)

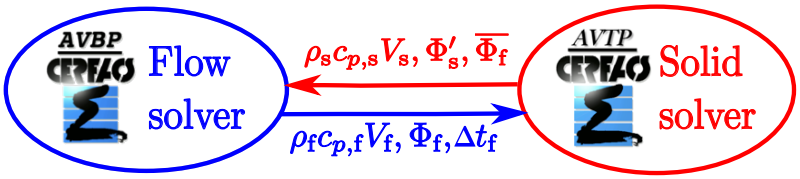


(b) Considered accelerated HCND coupling scheme

**Figure 8.3:** *Scheme of the interface model for coupled accelerated unsteady conjugate radiation heat transfer.*

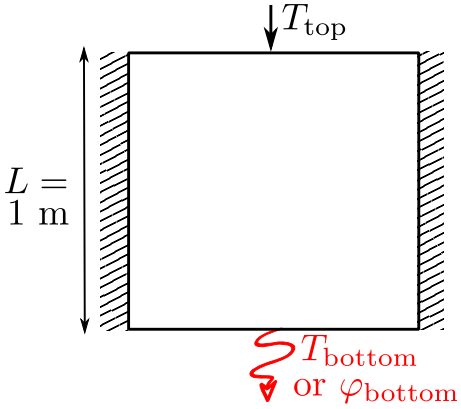


**Figure 8.4:** *Validation configuration of the AVTP steady variant.*

Figure 8.5 presents the corresponding results for the four cases, obtained using the AVTP steady variant. For all the cases, the good temperature at the bottom of the quartz is retrieved, validating the implementation.

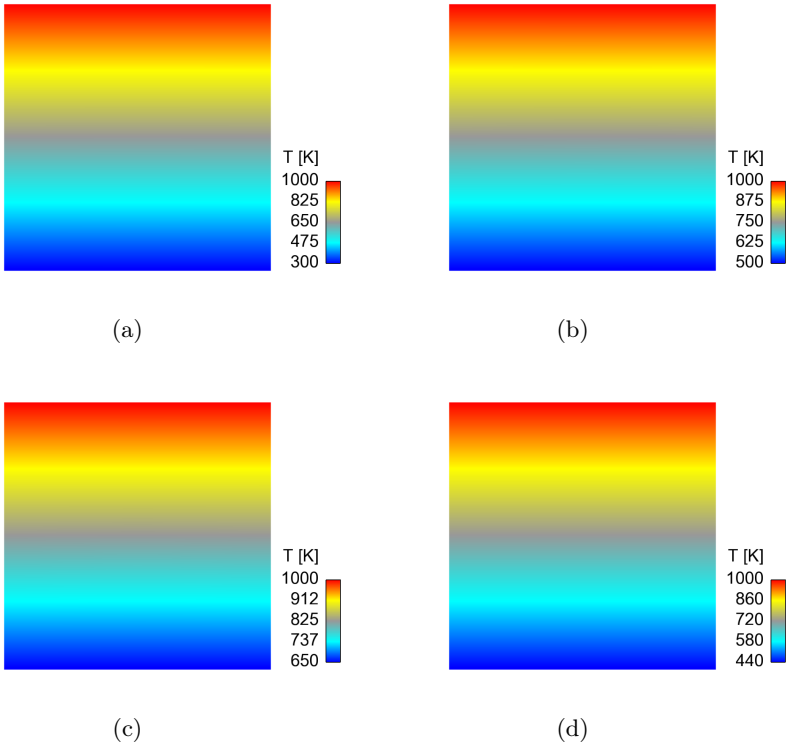


**Figure 8.5:** *Temperature fields of the validation cases for the implementation of the AVTP steady variant.*

### 8.3.3 1-D and unsteady validation test case

The validation test case studied by Koren et al. (2017c) has been here considered to validate the implementation of the method in the AVBP-AVTP framework. As AVBP handles ideal gases, the density handles ideal gases, the density depends on the temperature which prevents comparison with Koren's results with the incompressible YALES2 solver. This test case therefore allows to verify the correct behaviour of the methodology, once implemented in the AVBP/AVTP framework.

Fig. 8.6 illustrates this 1-D configuration. Two different domains are considered: a fluid part from $x = -L_f$ to $x = 0$ and a solid part from $x = 0$ to $x = L_s$. The density, heat capacity and thermal conductivity are respectively noted $\rho_f$, $c_{p,f}$ and $\lambda_f$ for the fluid part and $\rho_s$, $c_s$ and $\lambda_s$ for the solid part.

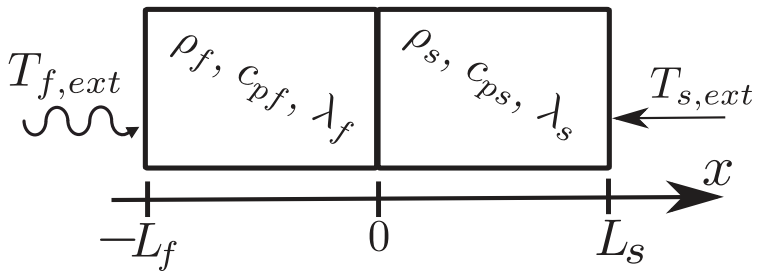


**Figure 8.6:** *One-dimensional test case configuration. The length $L_f$ of the fluid part is 1 mm while the length $L_s$ of the solid part is 1 mm.*

Table 8.2 summarizes the different thermodynamical properties used for this one-dimensional case. For boundary conditions, a constant temperature $T_{s,\text{ext}} = 293$ K is imposed at the right side of the domain ($x = L_s$), while a fluctuating temperature $T_{f,\text{ext}}(t)$ is imposed at the left side ($x = -L_f$):

$$\begin{aligned} T_{f,\text{ext}}(t) &= T_0\,(1 + 0.1\sin(2\pi f_{\text{ext}} t)) \quad \text{for } t > 0, \\ T_{f,\text{ext}}(t) &= T_{\text{ini}} \qquad\qquad\qquad\qquad\quad \text{for } t = 0. \end{aligned} \tag{8.22}$$

with $T_{\text{ini}} = 293$ K, $T_0 = 500$ K and $f_{\text{ext}} = 100$ Hz.

| Solid part | | Fluid part | |
|---|---|---|---|
| $\rho_s$ | 8510.0 | $\rho_f$ | 2.4 |
| $c_s$ | 439.0 | $c_{p,f}$ | 8913.0 |
| $\lambda_s$ | 11.7 | $\lambda_f$ | 0.810 |

**Table 8.2:** *Properties of the mediums considered in the one-dimensional HCND test case in SI units: density, heat capacity and thermal conductivity. The fluid density corresponds to its value at (293+500)/2 = 396.5 K.*

Then, once the steady state attained, the mean temperature at the boundary surface $T_{\text{bnd}}$ should fluctuate around the mean value $\overline{T_{\text{bnd}}}$:

$$\overline{T_{\text{bnd}}} = \frac{T_s \frac{\lambda_s}{L_s} + T_0 \frac{\lambda_f}{L_f}}{\frac{\lambda_s}{L_s} + \frac{\lambda_f}{L_f}} \tag{8.23}$$

For the values of thermal conductivities presented in Table 8.2, the theoretical value of $\overline{T_{\text{bnd}}}$ is then 306.4 K.

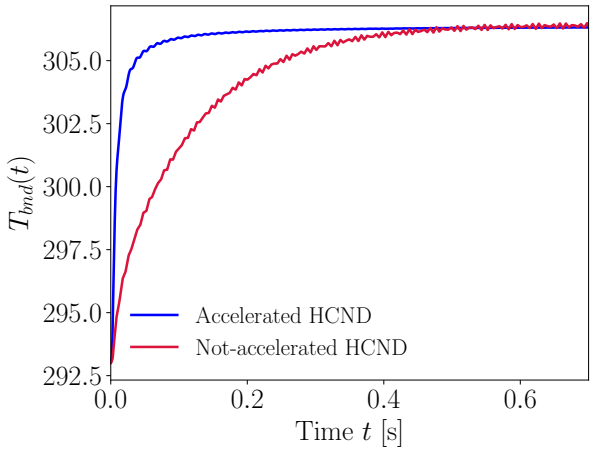


**Figure 8.7:** *Evolution of boundary temperature $T_{bnd}(t)$ with time t with the accelerated and non-accelerated HCND technique.*

Figure 8.7 presents the evolution of the boundary temperature $T_{\text{bnd}}(t)$ as a function of time $t$ for both the accelerated and non-accelerated HCND techniques. The asymptotic temperature of both cases is consistent with the theoretical value of 306.4 K. Moreover, the physical time required to converge towards the stationary solution is largely decreased with the accelerated technique.
Considering the characteristic diffusive time scales of fluid and solid, $\tau_f = L_f^2/D_f = (L_f^2\rho_f c_{p,f})/\lambda_f = 0.026$ s and $\tau_s = L_s^2/D_s = (L_s^2\rho_s c_s)/\lambda_s = 0.32$ s respectively, the solid characteristic diffusive time scale controls the non-accelerated transient problem. This time scale is retrieved as the characteristic time scale of the non-accelerated HCND curve in Fig. 8.7. The accelerated method enables to constrain the problem to only the fluid characteristic time scale $\tau_f$. This behavior is also well retrieved for the blue curve in Fig. 8.7.

Finally, a significant CPU cost saving to reach the permanent regime is obtained thanks to this accelerated technique.

Figure 8.8 illustrates the evolution of the coupling time step $\Delta t_{cpl}$ normalized by the fluid solver time step $\Delta t_f$, depending on the chosen tolerance $\eta$ for the resolution of the ODEs at the interface. As in the work of Koren et al. (2017c), it can be observed that the coupling time step evolves according to a frequency which is twice that of the exterior perturbation, due to the absolute value used to estimate the error done at each coupling time step. It can also be observed that when decreasing the tolerance, the coupling time step given by the proportional–integral–derivative (PID) controller decreases. A decrease of approximatively one order of magnitude of this coupling time step is observed when dividing the tolerance by 100, which also corresponds to what has been observed by Koren et al. (2017c).

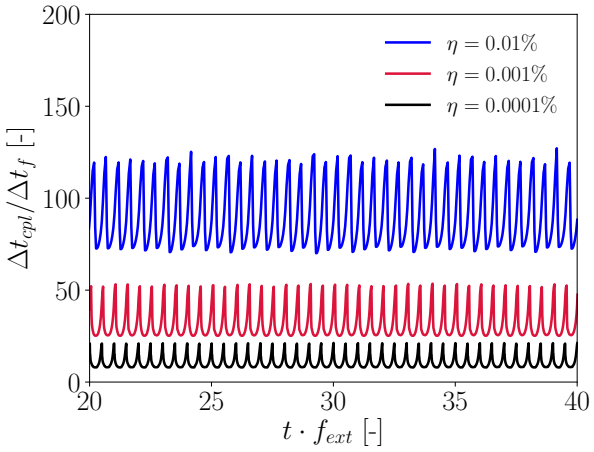


**Figure 8.8:** *Evolution of boundary temperature coupling time step $\Delta t_{cpl}$ with time $t$, depending on chosen tolerance $\eta$.*

The implementation and simplification (see Figs. 8.2 and 8.3) of the HCND accelerated and non-accelerated coupling scheme inside the AVBP/AVTP framework are validated. Next section describes the application of this methodology to a conjugate heat transfer simulation of the DLR burner in order to predict the quartz wall temperature field and compare it to experimental data.

## 8.4 Coupled LES of a confined sooting flame with wall heat transfer

### 8.4.1 Geometry and thermal environment of the considered case

The configuration studied here is the same as the one studied in Chapter 5. Table 8.3 summarizes the operating conditions. In this chapter, the thermal environment of the overall combustion chamber is studied in details in order to predict the quartz wall temperatures.

| $p$ | $\Phi$ | $P_{\text{primary}}$ | $Q_{\text{air,c}}$ | $Q_{\text{air,r}}$ | $Q_{\text{fuel}}$ | $Q_{\text{oxi}}$ | $\frac{Q_{\text{air,c}}}{Q_{\text{air}}}$ | $\frac{Q_{\text{oxi}}}{Q_{\text{air}}}$ | $\Phi_{\text{global}}$ | $P_{\text{global}}$ |
|---|---|---|---|---|---|---|---|---|---|---|
| [bar] | [-] | [kW] | [slm] | [slm] | [slm] | [slm] | [-] | [-] | [-] | [kW] |
| 3 | 1.2 | 32.2 | 140.8 | 328.5 | 39.3 | 187.4 | 0.3 | 0.4 | 0.86 | 38.6 |

**Table 8.3:** *Considered operating point: Pressure, $p$, volume flow rates for air through burner (central and ring), $Q_{air,c}$ and $Q_{air,r}$, fuel, $Q_{fuel}$, oxidation air through secondary air inlet, $Q_{oxi}$, primary and global equivalence ratios, $\Phi$ and $\Phi_{global}$, primary and global thermal powers, $P$ and $P_{global}$, and fractions $Q_{air,c}/Q_{air}$ and $Q_{oxi}/Q_{air}$ with $Q_{air} = Q_{air,c} + Q_{air,r}$. Flow rates are referenced to 1.013 bar and 273 K.*

Figure 8.9 presents this thermal environment. Optical access in the combustion chamber is provided through four separate quartz windows of thickness $e_1 = 3$ mm on each side. The whole combustion chamber is surrounded by a stainless steel pressure housing and optical access to the combustion chamber is guaranteed through four external quartz. Cooling of the internal quartz is established through multiple transversal laminar air jets at each side of the quartz windows, as illustrated in Fig. 8.10.

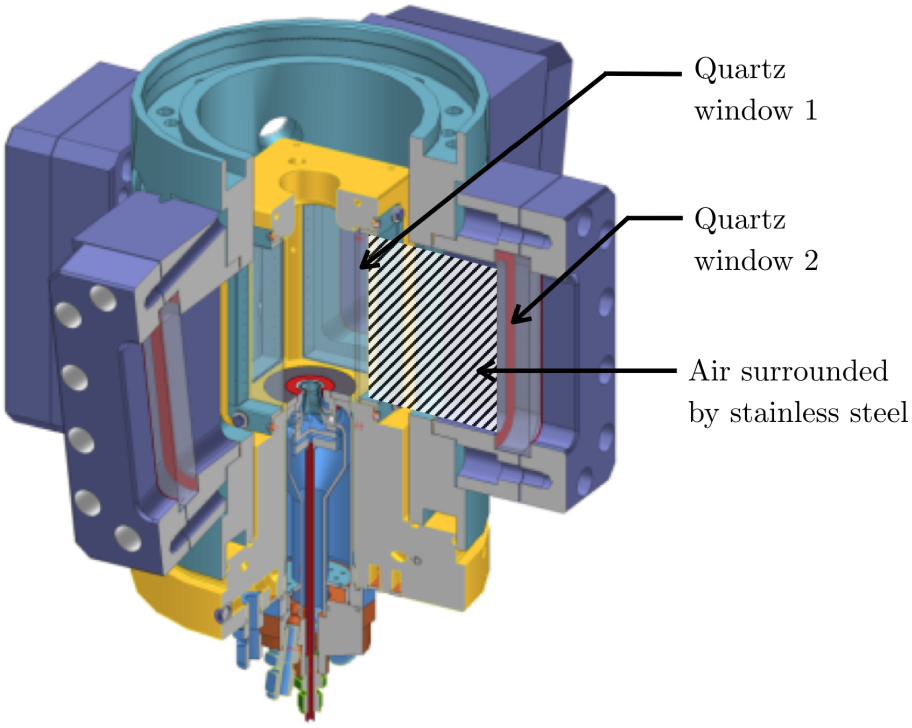


**Figure 8.9:** *Design of burner, combustion chamber and optical module of pressure housing.*

The quartz windows of this combustion chamber are fixed through four copper posts at each corner, which are cooled at 333 K. The bottom of the combustion chamber is composed of stainless steel cooled at 650 K. Inner and outer quartz walls temperatures have been measured using laser induced phosphorescence technique (LIP) (Nau et al. 2017). The corresponding axial temperatures are given in Fig. 8.11.

The geometry used for the fluid domain is the same used for the uncoupled simulations in Chapter 5. Concerning the solid part, only the geometry composed by the four combustion chamber quartz windows and the four copper posts are considered. Figure 8.12 illustrates the considered geometry for the conjugate

heat transfer simulation.

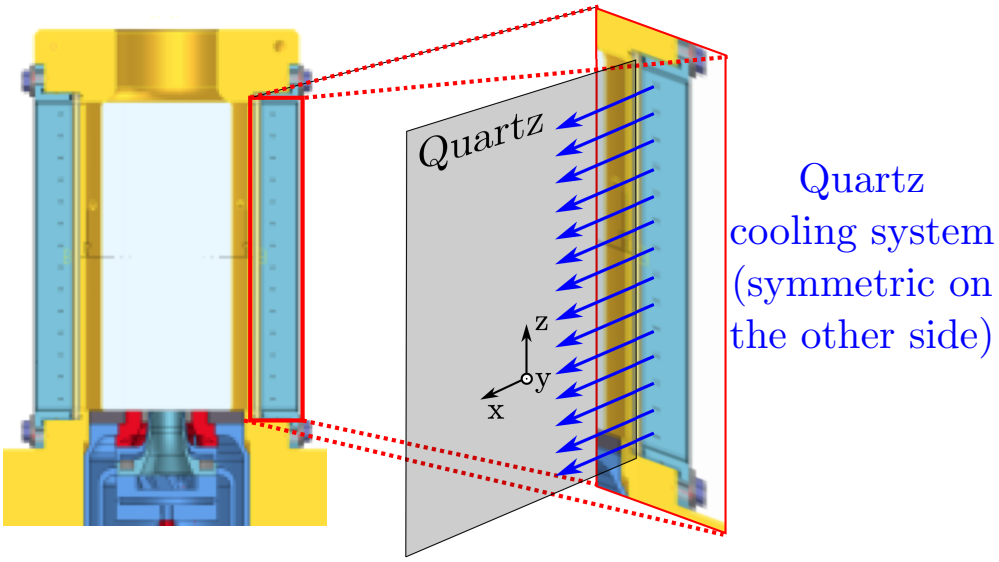


**Figure 8.10:** *Combustion chamber quartz cooling system (from ISF communication ISF3 (2017) )*

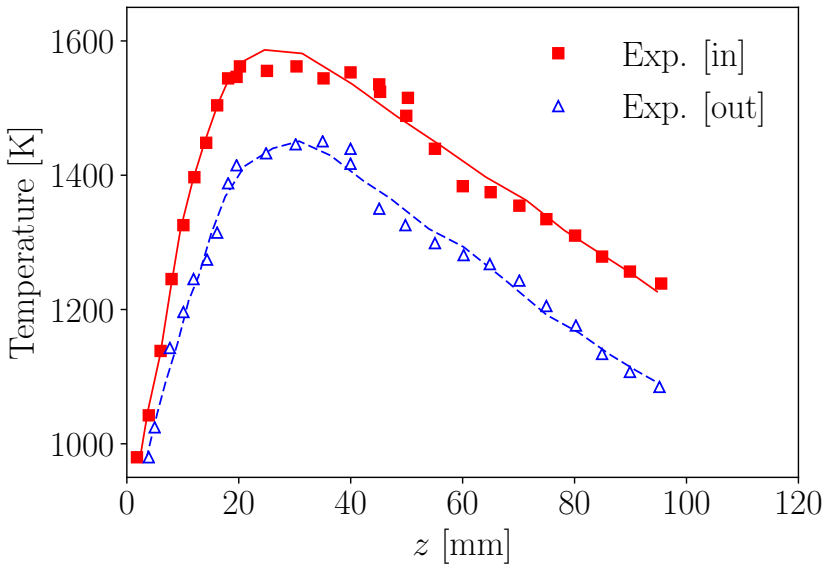


**Figure 8.11:** *Experimental measured axial temperature profiles at the inner and outer faces of the combustion chamber quartz (from Nau et al. (2017)).*

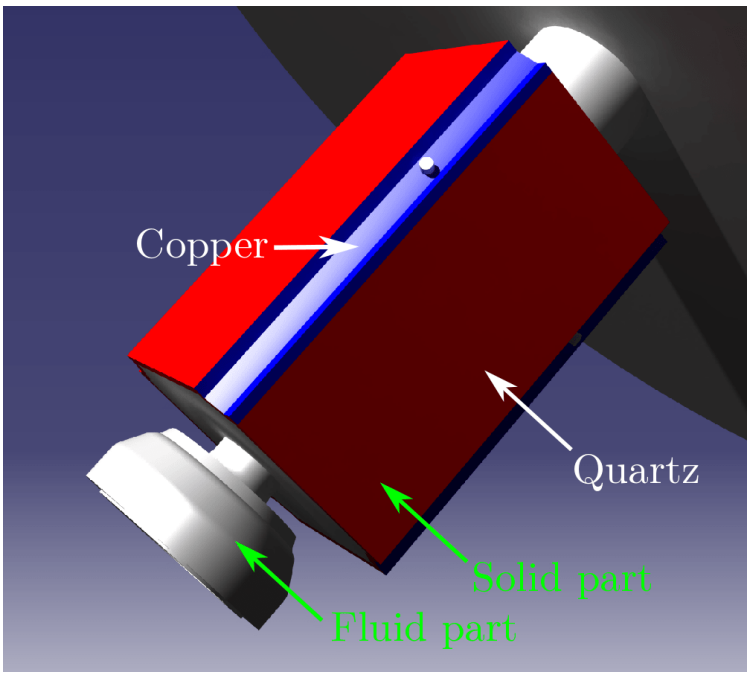


**Figure 8.12:** *Considered geometry for the conjugate heat transfer simulation.*

### 8.4.2 Numerical set-up and physical modelling

#### 8.4.2.1 Mesh

A longitudinal cut of the meshes used in the coupled conjugate heat transfer simulation is presented in Fig. 8.13.

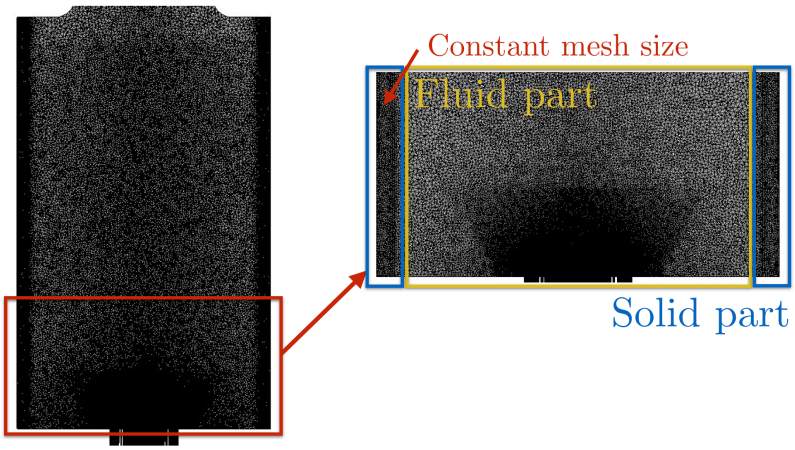


**Figure 8.13:** *Longitunal cuts of the meshes used in the coupled conjugate heat transfer simulations.*

Table 8.4 summarizes the properties of these different meshes: the mesh for the fluid part presents the same properties as the one used in the simulations in Chapter 5, except for refinements for mesh conforming near walls. Concerning the solid mesh, a tetrahedra mesh has been realized with a constant cell size equal to 0.375 mm, leading to 8 points in the quartz width. The two meshes are also conforming at their boundaries in order to apply the HCND methodology.

| Domain | Fluid | Solid |
|---|---|---|
| Mesh type | Tetrahedra | Tetrahedra |
| Number of nodes | 8 millions | 3.1 millions |
| Number of cells | 44.6 millions | 15.7 millions |
| Smallest cell characteristic size [mm] | 0.08 | 0.375 |

**Table 8.4:** *Details on the meshes used in the conjugate heat transfer simulation*

#### 8.4.2.2 Modelling of reactive flow

For the reactive flow and soot modeling, the same models and numerical methods described in Chapter 5 are considered, which are briefly:

- the RFPV model (Pierce and Moin 2004; Ihme and Pitsch 2008a) combined with the LES soot production modeling (Rodrigues et al. 2018),
- the third-order in space and time finite element TTGC scheme (Colin and Rudgyard 2000),
- and the SIGMA subgrid model (Nicoud et al. 2011).

Unless for the coupled walls for which the boundary condition is handled by the accelerated HCND method and where wall laws developed by Jaegle et al. (2010) are considered, the same boundary conditions as the one considered in Chapter 5 are considered.

#### 8.4.2.3 Physical properties of copper

The following density $\rho_{\text{copper}}$ and thermal conductivity $\lambda_{\text{copper}}$ have been used for the copper:

$$\begin{aligned} \rho_{\text{copper}} &= 8960 \text{ kg/m}^3 \\ \lambda_{\text{copper}} &= 401.0 \text{ W/(m.K)} \end{aligned} \tag{8.24}$$

By contrast with the density and thermal conductivity of copper, the heat capacity is highly dependent of temperature: a polynomial fit as a function of temperature $T$ provided by White and Collocott (1984) has been used. The

heat capacity $c_{\text{copper}}(T)$ of copper is expressed as:

$$c_{\text{copper}}(T) = 323.015 + 82.0936 \cdot \left(\frac{T}{T_0}\right) + 24.8305 \cdot \left(\frac{T}{T_0}\right)^2 + 3.45565 \cdot \left(\frac{T}{T_0}\right)^3 \tag{8.25}$$

with $T_0 = 293$ K.

#### 8.4.2.4 Physical properties of quartz

**Thermodynamical properties**

The density of quartz is taken constant and equal to 2200 kg/m$^3$. For the heat capacity of quartz, measurements from Sosman (1927) are represented in Fig. 8.14. A polynomial fit, valid for $T \in [20\text{K}, 2000\text{K}]$, has been done. The quartz heat capacity $c_{\text{q}}(T)$ used in our calculations is then expressed as:

$$c_{\text{q}}(T) = -62.8778 + 1148.41 \cdot \left(\frac{T}{T_0}\right) - 468.192 \cdot \left(\frac{T}{T_0}\right)^2 + 119.116 \cdot \left(\frac{T}{T_0}\right)^3 - 21.6623 \cdot \left(\frac{T}{T_0}\right)^4 + 2.56091 \cdot \left(\frac{T}{T_0}\right)^5 - 0.1314654 \cdot \left(\frac{T}{T_0}\right)^6 \tag{8.26}$$

with $T_0 = 293$ K.

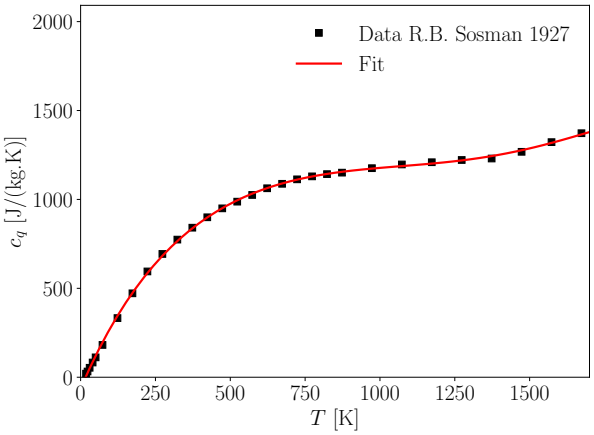


**Figure 8.14:** *Heat capacity of quartz. Symbols comes from data of Sosman (1927)*

Quartz thermal conductivity strongly varies with temperature. This information is generally not given by the quartz manufacturers. In a recent study

(Combis et al. 2012), its dependency with temperature has been characterized based also on data from Heraeus manufacturer (Heraeus 2016). The data from this manufacturer are reported in Fig. 8.15 and a polynomial fit of this data has been done. In our calculations, the conductivity $k_q(T)$ of the quartz is then defined as:

$$\frac{k_q(T)}{k^0} = a_0 + a_1\left(\frac{T}{T_0}\right) + a_2\left(\frac{T}{T_0}\right)^2 + a_3\left(\frac{T}{T_0}\right)^3 \tag{8.27}$$

with: $a_0 = 0.97980$, $a_1 = -0.10063$, $a_2 = 0.13677$, $a_3 = -0.011744$, $T_0 = 293$ K and $k^0 = k_q(293\text{ K}) = 1.38$ W/m/K.

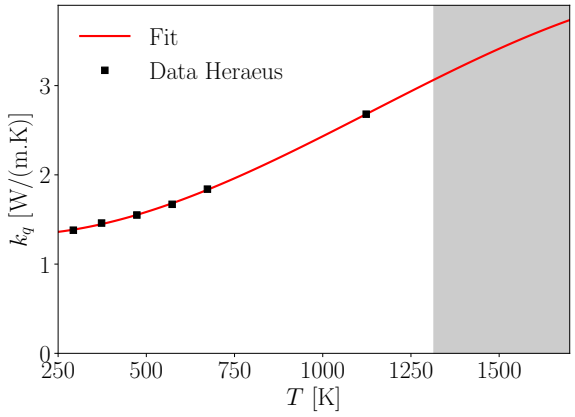


**Figure 8.15:** *Thermal conductivity of quartz. Symbols are due to Heraeus (2016)*

### Radiative properties

A band model describing the spectral transmittance of the quartz slab has been realized in order to correctly describe the radiative properties of the quartz viewing windows. Details of this band model are given in Appendix F.

From this band model, a total emissivity has been determined. This emissivity $\overline{\epsilon^{\text{slab}}}(T)$ is expressed as a function of the temperature $T$ as:

$$\begin{aligned}\overline{\epsilon^{\text{slab}}}(T) = 0.72517 &+ 0.54384\cdot\left(\frac{T}{T_0}\right) - 0.39988\cdot\left(\frac{T}{T_0}\right)^2 \\ &+ 0.10231\cdot\left(\frac{T}{T_0}\right)^3 - 0.013100\cdot\left(\frac{T}{T_0}\right)^4 \\ &+ 8.4328\cdot10^{-4}\cdot\left(\frac{T}{T_0}\right)^5 - 2.1722\cdot10^{-5}\cdot\left(\frac{T}{T_0}\right)^6\end{aligned} \tag{8.28}$$

with $T_0 = 293$ K.

#### 8.4.2.5 External thermal boundary condition at quartz surfaces

A modeling of the combustion chamber external thermal environment is required in order to provide a correct boundary condition at quartz surfaces. Through a detailed study of the overall thermal environment presented in Appendix F, a simplified model has been retained for the external boundary condition. The flux boundary condition at the quartz outer surface $\phi^{\text{out}}(x,z)$ is given by:

$$\begin{aligned}\phi^{\text{out}}(x,z) = &\underbrace{\overline{\epsilon^{\text{slab}}}(T_{\text{out}}(x,z))\sigma T_{\text{out}}(x,z)^4 - \overline{\epsilon^{\text{slab}}}(T_3)\sigma T_3^4}_{\text{radiative transfer}} \\ &+ \underbrace{h_1(x,z)(T_{\text{out}}(x,z) - T_{\text{in}}^{\text{air}})}_{\text{conducto-convective transfer}}\end{aligned} \tag{8.29}$$

where:

- $x$ and $z$ correspond respectively to the transverse and axial coordinates respectively (see Fig. 8.10),
- $\sigma$ is the Stefan-Boltzmann constant,
- $T_3 = 313$ K is the pressure housing stainless steel temperature,
- $T_{\text{in}}^{\text{air}} = 313$ K is the air temperature inside the pressure housing,
- $T_{\text{out}}(x,z)$ is the temperature field of the quartz external face,
- $h_1(x,z)$ corresponds to the conducto-convective transfer coefficient correlated to the quartz cooling system. As detailed in Appendix F, the quartz walls are cooled through multiple transverse laminar air jets. These air jets are modeled through an equivalent wall jet, for which the heat transfer coefficient $h_1(x,z)$ is computed as:

$$h_1(x,y) = h_1(x_1,y) = \text{Nu}_1(x_1,y)\lambda_t^{\text{air}}(T_{\text{film}}(x_1,y))/(x_1 + l_{\text{th}}) \tag{8.30}$$

  where $x_1 = l - |x|$ is the transverse distance to the quartz edge: $l$ is the transverse length of the quartz, $T_{\text{film}}(x_1,y) = (T_{\text{film}}(x_1,y) + T_{\text{in}}^{\text{air}})/2$ is the film temperature and $\lambda_t^{\text{air}}(T_{\text{film}}(x_1,y))$ is air thermal conductivity at the temperature $T_{\text{film}}(x_1,y)$. $l_{\text{th}}$ corresponds to the distance between the thermal origin and the quartz edge. Its expression is detailed in Appendix F. Finally, the Nusselt number $\text{Nu}_1(x_1,y)$ is expressed as:

$$\text{Nu}_1(x_1,y) = 0.345\text{Pr}(T_{\text{film}})^{0.34}\text{Re}_{e_{\text{eq}}}^{0.75}\left(\frac{x + l_{\text{th}}}{e_{\text{eq}}}\right)^{1/4} \tag{8.31}$$

  where $e_{\text{eq}}$ is the equivalent wall jet thickness $e_{\text{eq}}$ and $\text{Re}_{e_{\text{eq}}}$ is the Reynolds number based on this wall jet thickness.

Both the impact of the cooling system and radiative transfer leaving the quartz wall are then modeled with the expression of this boundary condition.

#### 8.4.2.6 Other thermal boundary conditions

The walls of the copper metallic posts will be considered isothermal at 333 K. Without more information, the top of the quartz windows has been considered at the same temperature. The temperature at the bottom of the quartz is considered equal to 650 K: the temperature imposed to the bottom of the combustion chamber.

#### 8.4.2.7 Codes coupling parameters

Table 8.5 presents the cores repartition that have been considered for this configuration. Then, the coupled simulation considering conjugate heat transfer at the quartz windows only increases by 9% the cost of the simulation compared with the non-coupled simulation of Chapter 5 (LES accounting for soot, wall heat losses through imposed wall temperatures based on centerline quartz windows measurements and optically thin radiation model), for an overall of 450 000 CPU hours.

| Code | AVBP | AVTP | PALM |
|---|---|---|---|
| Nb. of cores | 2576 | 223 | 1 |

**Table 8.5:** *Cores repartition for the coupled simulation presented in this chapter.*

For the coupling scheme, a relative tolerance $\eta$ of 1% of the fluctuating temperature has been considered together with an absolute tolerance $a_{\text{tol}}$ of 0.02 K (fluctuations of temperature lower than 0.02 K are not considered for the calculation of the next time coupling step $\Delta t_{\text{cpl}}$). This criterion has been added in order to avoid erratic small time steps imposed by the HCND method due to very small numerical fluctuations of the wall temperature. Figure 8.16 shows the typical evolution of $\Delta t_{\text{cpl}}/\Delta t_{\text{cfl}}$ ratio during 3 ms of physical time, with $\Delta t_{\text{cfl}} \approx 2.5 \times 10^{-8}$ s. The coupling time step $\Delta t_{\text{cpl}}$ evolves between 160 and 200 times the value of the acoustic time step $\Delta t_{\text{cfl}}$ according to unsteady fluxes evolution resulting from the turbulent reactive flow inside the combustion chamber. Then, the average value of the coupling time step is $\Delta t_{\text{cpl}} \approx 4.5$ $\mu$s.

### 8.4.3 Results of the coupled CHT simulation

In this section, a calculation accounting for soot production and conjugate heat transfer will be considered. However, no radiation will be taken into account in order to determine only the impact of wall heat losses. In the following, by consistency with the nomenclature defined in Chapter 5, this case will be designated as the **R0W2S1** case (**W2** corresponding to coupled conjugate heat transfer simulation). Let us outline that the case R1W2S1 (LES accounting for soot, conjugate heat transfer and optically thin radiation model) is also not considered because it is physically wrong and inconsistent: gases and soot

radiation emission would exit the combustion chamber without any absorption at the walls.

#### 8.4.3.1 Instantaneous fields

Figure 8.17 presents instantaneous fields of temperature and heat conductivity for the solid part of the domain. The four copper posts are maintained at 333 K. Concerning quartz windows, zones of high temperature are observed at the bottom of the quartz, and quartz temperature decreases with the height above the burner: the temperature varies between 333 K and 1650 K over all the quartz domain. This large heterogeneity in temperature leads to a large heterogeneity in terms of quartz thermal conductivity, which varies from 1.3 W/m/K up to 3.5 W/m/K. Appropriate description of the quartz conductivity is then required in order to estimate correctly conductive fluxes at the combustion chamber quartz windows.

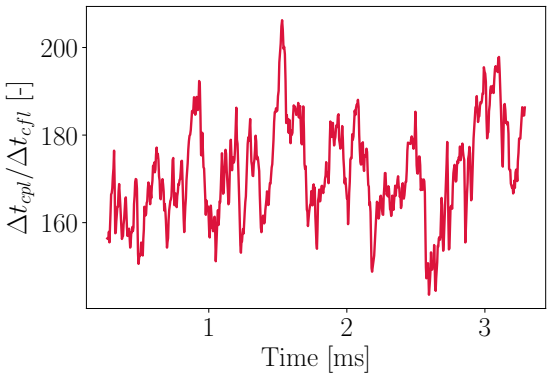


**Figure 8.16:** *Evolution of $\Delta t_{cpl}/\Delta t_{cfl}$ ratio over 3 ms of physical time.*

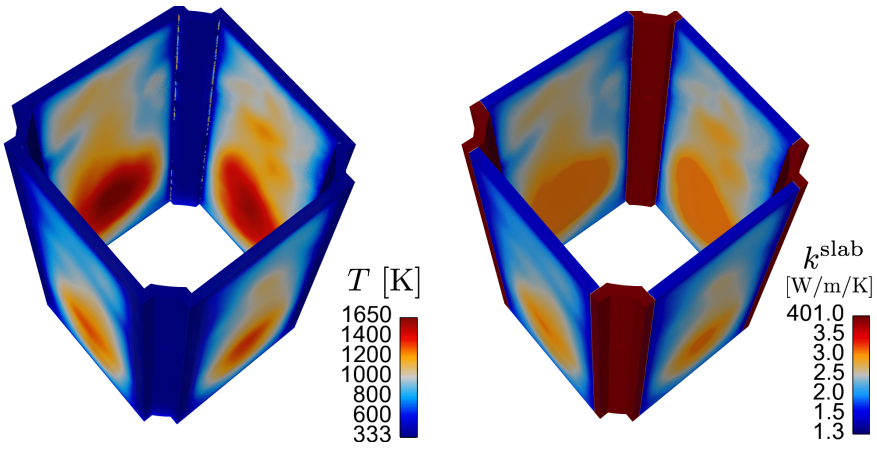


(a) Temperature $T$ (b) Heat conductivity $\lambda$

**Figure 8.17:** *Solid domain: Instantaneous fields for the coupled CHT simulation.*

Figure 8.18 presents instantaneous fields of fluid axial velocity, together with wall temperature (Fig. 8.18(a)) and with wall conductive heat flux (Fig. 8.18(b)). At the regions where the swirled flow reaches the wall with axial velocities, high values of conductive heat flux are obtained, leading to high values of wall temperatures, and consequently high values of conductive fluxes inside the quartz. Figure 8.18(c) presents the fluid temperature field together with the quartz wall temperature field. Then, downstream of the flame, in regions of low quartz temperature, the burnt gases are cooled and large heterogeneities in wall fluid temperature are observed.

Figure 8.19 presents 3-D instantaneous volume renderings of the normalized progress variables together with wall temperature (Fig. 8.19(a)) and wall conductive heat fluxes (Fig. 8.19(b)). As stated previously, it can be observed that regions with high conductive fluxes are observed where the swirled flow impinges the wall, leading then to high wall temperature values.

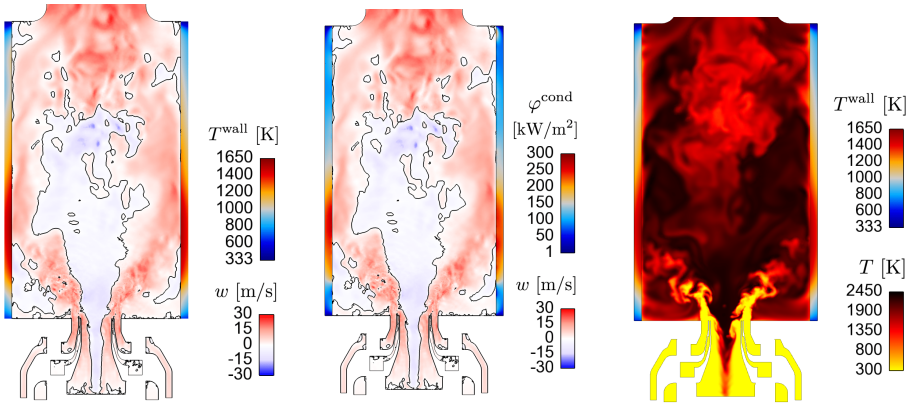


(a) Fluid axial velocity field and wall temperature field

(b) Fluid axial velocity field and wall conductive heat flux field

(c) Fluid temperature field and wall conductive heat flux field

**Figure 8.18:** *2-D instantaneous views of the fluid and solid domains.*

### 8.4.3.2 Mean wall temperature fields

Figure 8.20 presents a comparison of the inner and outer quartz window wall axial temperatures obtained with the conjugate numerical simulation and the experimental ones. An excellent prediction of quartz temperature in the first part of the window inner face (until $x = 40$ mm). This agreement is quite satisfactory given the employed high-fidelity models based on LES and conjugate heat transfer. At the top, an under-prediction of the quartz temperature by approximatively 100 K is observed, which is explained by a not-well defined temperature boundary condition at the top of the quartz used in the current calculations. Finally, the overestimation of the difference between the window face temperatures indicates that the simulated incoming total wall flux or the

external cooling are too large compared to experiments.

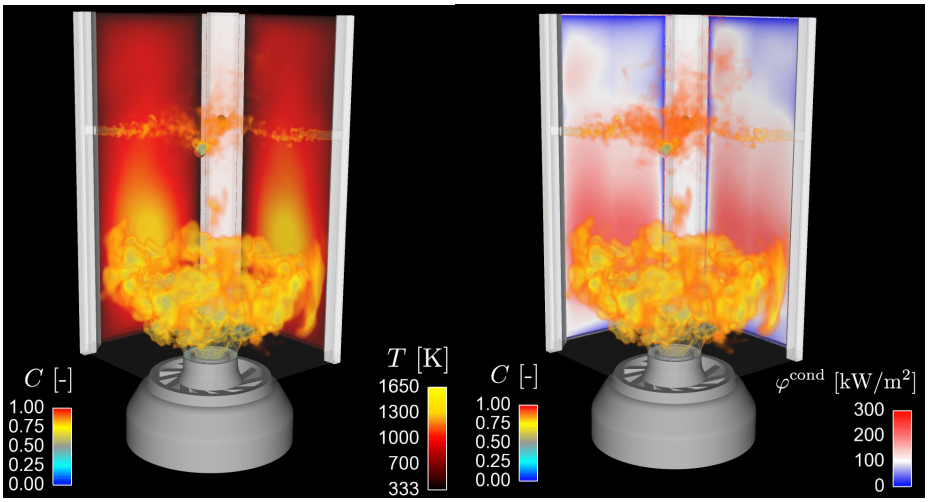


(a) Normalized progress variable volume rendering of the fluid domain, wall temperature field

(b) Normalized progress variable volume rendering of the fluid domain, wall conductive heat flux field

**Figure 8.19:** *3-D instantaneous views of the fluid and solid domains.*

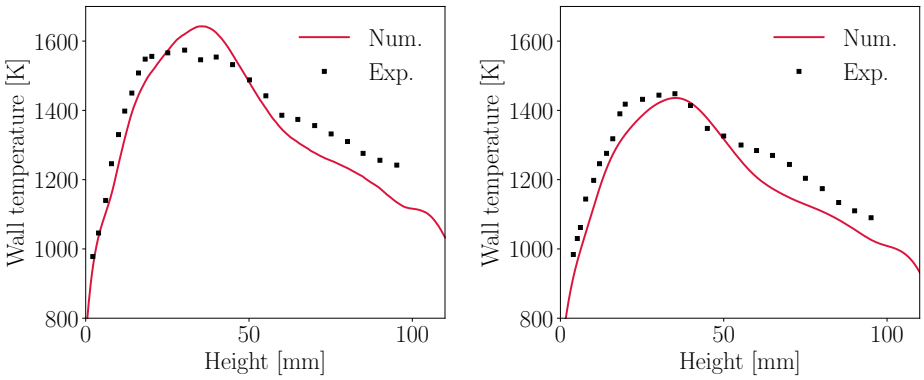


(a) Inner face

(b) Outer face

**Figure 8.20:** *Comparison between numerical and experimental quartz window axial temperature profiles. The experimental measurements are from Nau et al. (2017).*

Figure 8.21 presents the corresponding mean fields of temperature for the quartz inner (Fig. 8.21(a)) and outer (Fig. 8.21(b)) faces. Iso-lines of temperature are also presented. The red isoline corresponds to the quartz annealing temperature. Important gradients of temperature over all the quartz surface can be noticed, which can lead to important thermal stresses. It can also be observed that wall temperature exceeds annealing quartz temperature in both inner and external wall sides. Figure. 8.21(c) illustrates the regions were windows were damaged experimentally: the inner line corresponds to the surface damage at

the outer side whereas the outer line corresponds to the window damage in the inner side of the combustion chamber quartz. A link between these two regions can clearly be observed. Then, the conjugate heat transfer simulation enables to retrieve quite faithfully the experimental damaged regions of the quartz.

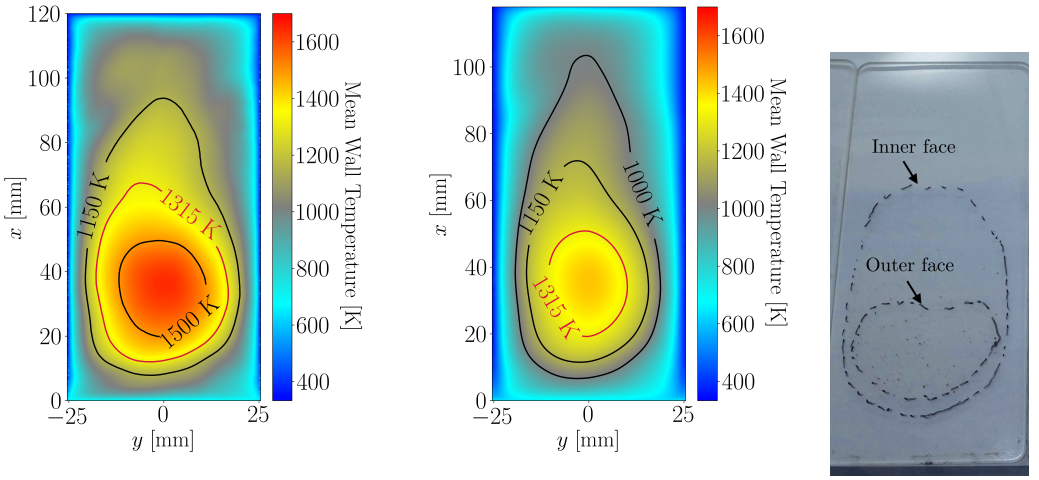


(a) Inner face

(b) Outer face

(c) Quartz window experimental damaged zones

**Figure 8.21:** *Numerical fields of the inner and outer faces quartz window temperature. The red isoline corresponds to the quartz annealing temperature.*

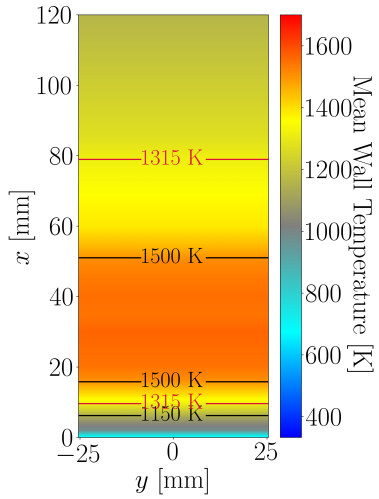


**Figure 8.22:** *Wall temperature field based on axial wall temperature measurements of Nau et al. (2017) imposed as boundary condition of case R1W1S1 .*

Figure 8.22 presents the wall temperature field imposed as boundary condition of the case R1W1S1. This field has been constructed extrapolating the data from measurements of Nau et al. (2017) in the transverse direction. It can be observed that the CHT simulation (case R0W2S1) enables to have more informations about transverse evolution of the temperature within the quartz, which are more representative of quartz window experimental damaged zones.

#### 8.4.3.3 Impact of CHT on flame shape, flame stabilization and temperature profiles

In order to study the impact of conjugate heat transfer on flame stabilization, the results of this simulation (case R0W2S1) will be compared with the following two other cases:

- Case R0W0S1 corresponding to no radiation heat losses, and no wall heat losses,
- Case R1W1S1 corresponding to optically thin radiation heat losses and, wall heat losses imposed with isothermal boundary condition from centerline profile measurements.

For both cases, soot production is accounted for.

Figure 8.23 presents the obtained temperature fields for the three considered cases. Heat losses drive the flame stabilization height and opening. The same flame opening is observed for the cases R1W1S1 and R0W2S1 whereas a lower flame opening is observed for the case R0W0S1, which does not consider heat losses. However, on the centerline, the mean flame position for the conjugate heat transfer case is similar to the one obtained for the adiabatic case. Looking at the comparison of the instantaneous fields of temperatures between these three cases in Fig. 8.24, it can be observed that the case R0W2S1 presents the more upstream position of the flame inside the injector. This highlights that radiation heat losses participate in driving the mean flame tip position for this flame, as described in Chapter 5.

Figure 8.25 presents a comparison of axial temperature profiles for the cases R0W0S1, R1W1S1 and R0W2S1.
For all cases, temperature increases at the flame front near $x = 0$ mm. The experimental mean position of the flame front is located between $x = 0$ mm and $x = 12$ mm. For $x < 12$ mm, the temperature RMS is higher than 500 K representing high temperature fluctuations due to the local dynamics of the flame front. Then, the mixture temperature is decreased until $x = 80$ mm corresponding to the position of the secondary cold air injection. At higher heights, the temperature increases again.
The impact of different heat losses can be identified by comparing different cases.

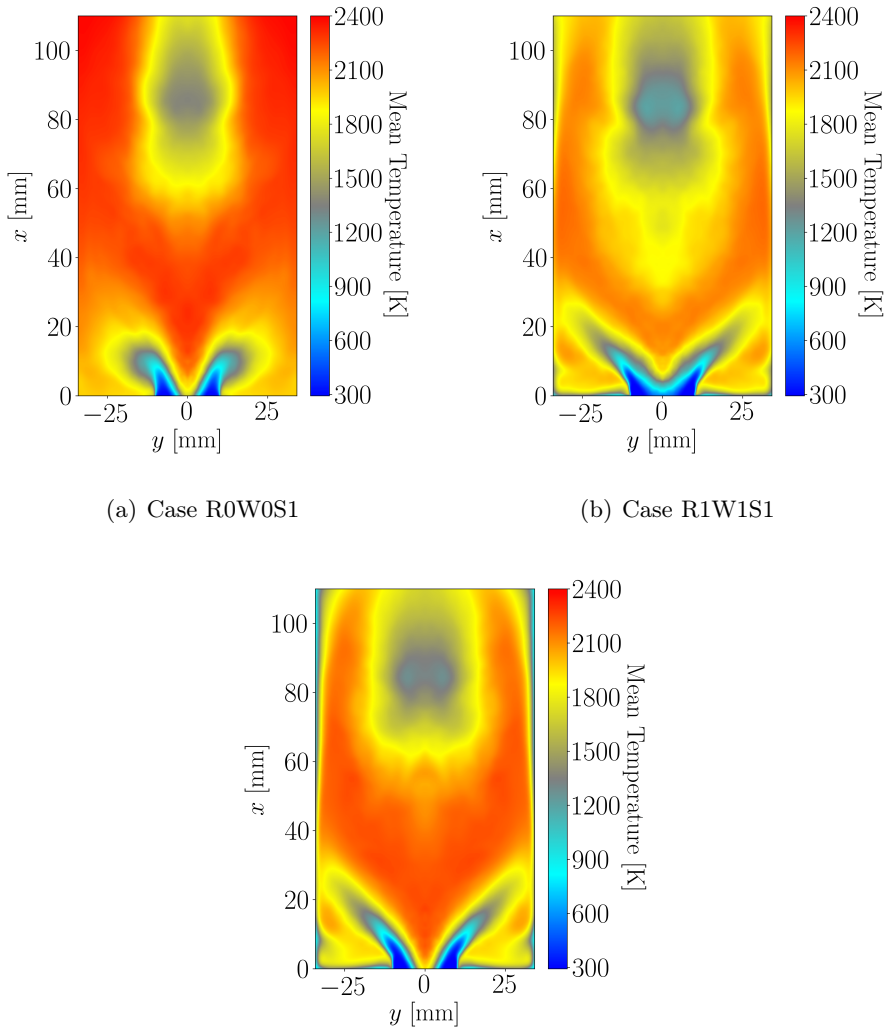


(a) Case R0W0S1

(b) Case R1W1S1

(c) Case R0W2S1

**Figure 8.23:** *Comparison between R0W0S1, R1W1S1 and R0W2S1 mean temperature fields.*

In case R1W1S1, the optically-thin radiation model implies an important decrease of axial temperature due to radiative heat losses which underestimate the experimental data for $x \in [15\text{ mm}, 60\text{ mm}]$. In case R1W0S0, wall heat losses are not accounted for and temperature is higher for $x \in [15\text{ mm}, 60\text{ mm}]$ than in case R1W1S1. The best agreement is obtained for this case, but it is important to notice that it does not take into account wall heat losses and overestimated radiative heat losses through the optically thin radiation model.

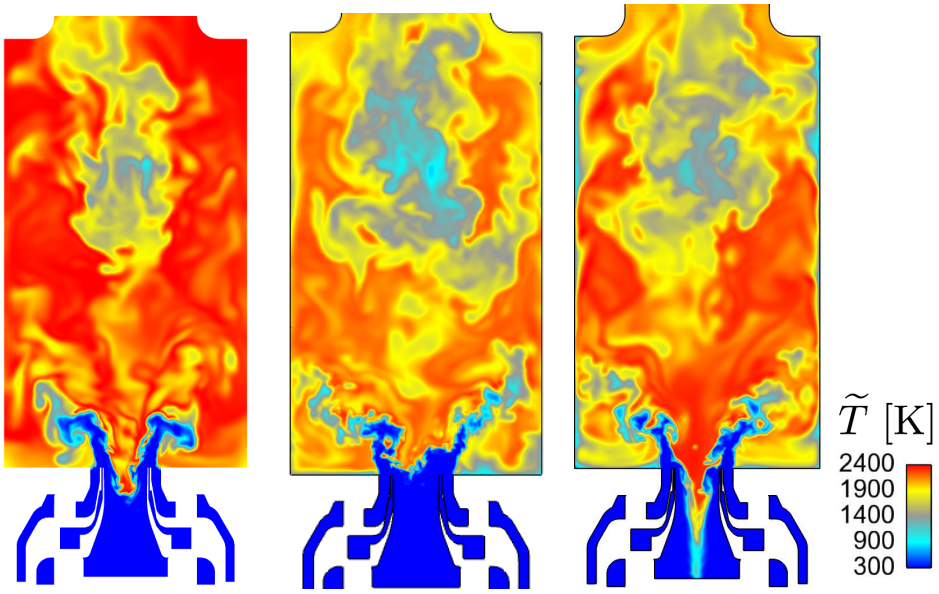


(a) Case R0W0S1 (b) Case R1W1S1 (c) Case R0W2S1

**Figure 8.24:** *Comparison between R0W0S1, R1W1S1 and R0W2S1 instantaneous temperature fields.*

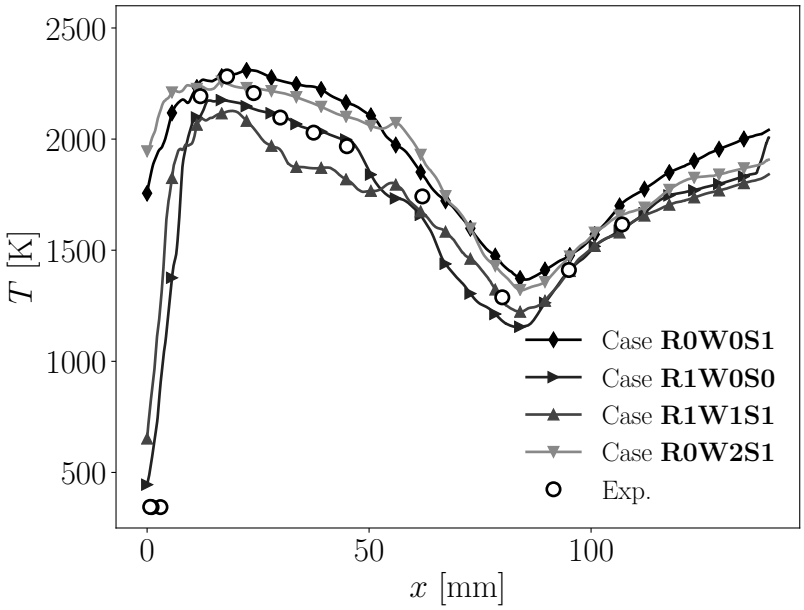


**Figure 8.25:** *Comparison between R0W0S1, R1W1S1, R0W2S1 axial temperature profiles and experimental measurements of Geigle et al. (2015).*

Moreover, compared to cases R0W0S1 and R0W2S1 that predict a flame that anchors inside the swirling injector, the mean flame position is well reproduced in R1W0S1 and R1W1S1, which shows a better agreement with experiments at the for $x < 5$ mm. The temperature in the cases R0W0S1 and R0W2S1 is higher than in R1W0S0 and R1W1S1 but is also higher than experimental measurements between $x = 40$ mm and $x = 70$ mm.
Thus, as reminded previously, radiative heat losses seems to drive the flame stabilization position in the present configuration. But, accounting for wall heat losses and considering an optically thin radiation model would overestimate total heat losses, and a more accurate description of thermal radiation must be used in order to predict the experimental data. This is the topic of the Chapter 9.

#### 8.4.3.4 Impact of CHT on soot production

Figure 8.26 compares the mean fields of soot volume fraction for the three cases with the experimental LII measurements of Geigle et al. (2015).

For all cases, soot production position is well retrieved compared with experimental data. Soot magnitude is underestimated with a factor varying from 2 to 5 depending on the modeling of radiative and wall heat losses.
Soot magnitude is therefore dependent on heat losses modeling: the highest soot magnitude level is obtained for case R0W0S1 which neglects all heat losses, whereas the lowest soot magnitude level is obtained for case R1W1S1 which accounts for wall heat losses and overestimates radiation heat losses. The magnitude of soot volume fraction is intermediate for case R0W2S1. This tendency of soot volume fraction decreasing with the increase of heat losses has already been observed in Mehta, Haworth, and Modest (2010); Reddy, De, and Yadav (2015a) in turbulent flames and will deserve additional analysis in future works.

#### 8.4.3.5 Wall heat fluxes

Figure 8.27 (left) presents the mean conductive heat flux obtained from the CHT simulation for the inner face. Maximum wall conductive heat flux is observed in the region $x \in$ [30 mm,50 mm], where the burnt gases flow impacts the quartz window. Then, wall conductive heat flux decreases downstream and upstream of this region. Impact of the swirled flow rotation can also be observed looking at the dissymetry of the conductive heat flux: the swirled flow impacts at a lower position of the quartz in the right side compared to the left side. Previous studies also have observed this behavior in similar swirled flows (Koren et al. 2017b).

Figure 8.27 (right) presents the obtained wall $y+$ field at the quartz windows boundary surfaces. As the boundary surface mesh is uniform, and neglecting

variations of viscosity, the highest values of $y+$ correspond to regions with the highest values of wall shear stresses. Besides, $y+$ field presents values higher than 2 in all the regions justifying the use of wall laws at the quartz windows boundary surfaces.

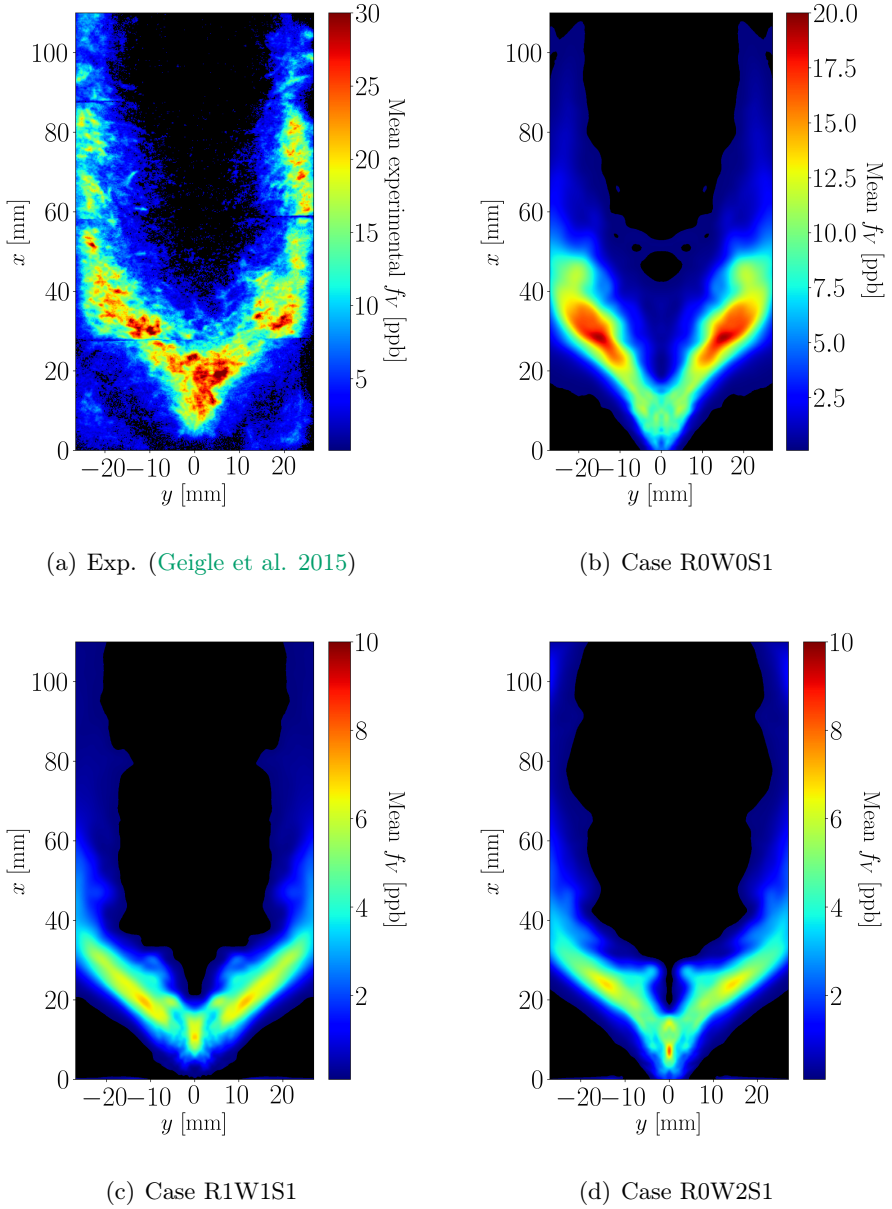


(a) Exp. (Geigle et al. 2015)

(b) Case R0W0S1

(c) Case R1W1S1

(d) Case R0W2S1

**Figure 8.26:** *Comparison between experimental measurements, R0W0S1, R1W1S1 and R0W2S1 fields of soot volume fraction.*

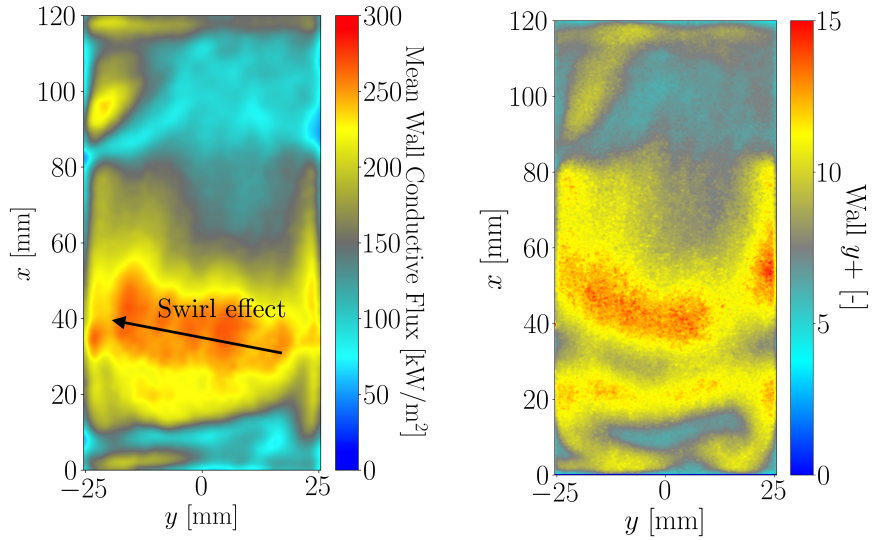


**Figure 8.27:** *Left: Numerical field of the inner mean conductive flux. Right: Numerical field of wall y+.*

#### 8.4.3.6 Energy balance

The macroscopic balance of sensible enthalpy writes:

$$\underbrace{\int_{\text{outlet-inlet}} \rho h_s \mathbf{u} \cdot \mathbf{dS}}_{\textbf{(I)}} + \underbrace{\int_{\text{walls}} \phi_{\textbf{cond,bnd}} \cdot \mathbf{dS}}_{\textbf{(II)}} = \underbrace{\dot{\Omega}}_{\textbf{(III)}} \tag{8.32}$$

The global balance of sensible enthalpy involves the outlet and inlet convective fluxes **(I)**, the integrated wall conductive flux **(II)** and the integrated heat release rate **(III)**. For this coupled case, the heat release (38.6 kW) is redistributed in the following manner:

- Fluid thermal energy (term **(I)**): 32.4 kW (84%),
- Convective wall heat losses (term **(II)**): 6.2 kW (16 %).

By comparison, the convective wall heat losses are equal to 1.6 kW in the case R1W1S1. This difference can be explained by lower temperatures of burnt gases due to high radiative heat losses with the optical thin radiation model, but also an underestimation of convective wall heat losses due to the extrapolation of the axial wall temperatures in the transverse directions which largely overestimates the quartz windows temperatures near the corners.

## 8.5 Conclusion

In this chapter, the general methodology for treating Conjugate Heat Transfer in combustion chambers has been presented. The HCND methodology initially developed by Koren et al. (2017c) and its corresponding accelerating technique have been detailed. The validation of the implementation of this methodology in the AVBP-AVTP framework has been presented. Compared with the approach done in Koren's thesis, the coupling scheme has been simplified and only one instance of AVTP and AVBP are used in order to deal with the accelerated HCND technique.

Then, based on this methodology, a conjugate heat transfer simulation of the DLR burner realized on AVBP and AVTP codes by using a model for external thermal boundary condition at solid walls has been presented. External wall temperature profiles have been compared with experimental LIP measurements.

For this configuration, good predictions of axial wall temperatures have been obtained. High conductive heat fluxes are observed at the region of jet impingement on the walls. These high conductive heat fluxes result in high temperatures of the quartz windows in this region, higher than the annealing temperature. The corresponding region corresponds well with regions where deformation of quartz has been observed experimentally, showing that the proposed coupling technique is able to predict such risks. Besides, the unsteady heat loads captured by LES are not described by steady conjugate heat transfer analyses, such thermal variations on the solid parts of industrial systems could provide valuable information on high-cycle thermal fatigue.

Finally, it has been observed that heat losses description impacts the flame stabilization. In the presented coupled simulation which does not consider radiation, the flame stabilizes upstream compared with experiments. However, the good flame position is obtained when taking into account radiation through the optically-thin radiation model. On the other hand, this optically-thin radiative model overestimates the radiation heat losses and underestimates temperature compared with experiments. Then, proper radiation modeling is required in this configuration. Next chapter will present a fully coupled strategy in order to describe turbulent combustion with heat losses, taking into account conjugate heat transfer but also the resolution of the Radiative Transfer Equation. Modification in wall heat fluxes, wall temperature, and soot formation will finally be discussed and compared with the coupled simulation presented in this chapter.

# Chapter 9

# Multi-physics simulation of a confined pressurized sooting flame

*In Chapter 5, the DLR burner has been investigated and important impacts of both radiative and wall heat losses have been identified in flame stabilization, flame properties and soot particles formation. In Chapter 8, conjugate heat transfers inside this burner have been investigated demonstrating the capability of the methodology in predicting the temperature walls temperature. In Chapter 7, impact of radiation description in radiative intensities of a jet diffusion flame have been investigated. Solving the RTE instead of considering a simple optically thin radiation model enabled to predict with a good precision the radiative intensities of such flames.*

*The first objective in this chapter is to demonstrate the capability of multi-physics simulations to predict both good flame properties and soot production and heat transfers inside such pressurized confined burner. A fully-coupled AVBP/AVTP/RAINIER simulation framework is therefore developed and presented. This framework is based on the HCND methodology presented in Chapter 8 where radiative fluxes at walls are additionally accounted for. The multi-physics simulation of the DLR burner investigated in this chapter is then based on an LES modeling of the turbulent combustion and soot production, a conjugate heat transfer modeling with quartz temperature prediction and a coupled Monte-Carlo resolution of the RTE for the determination of the radiative power and fluxes. Detailed modeling of quartz windows radiative properties is also considered and presented.*

*Finally, the second objective in this chapter is to study the impact of radiative heat losses in wall temperature predictions. Results are compared with the uncoupled simulations and the conjugate heat transfer simulation of Chapter 8. Impact on flame stabilization and soot production are also investigated.*

## Contents



## 9.1 Introduction

In practical burners and combustion chambers, heat losses due to radiation and wall heat transfer impact flame stabilization (Nogenmyr et al. 2013; Guiberti et al. 2015; Tay-Wo-Chong et al. 2016), gaseous pollutant emissions (Ihme and Pitsch 2008a; Lamouroux et al. 2014) and soot production (Mehta et al. 2010; Reddy et al. 2015a).

In a fully predictive approach, determining these phenomena requires to compute the combustor walls temperature as well. At high pressure and in the presence of soot particles, radiative heat transfer becomes more important and

must also be accounted for. Multi-physics simulations are therefore necessary in order to correctly assess the effects of these different heat transfer mechanisms inside the combustion chamber.

To develop accurate and high-fidelity tools for multi-physics simulations of turbulent flows, large-eddy simulations (LES) are more and more considered. Coupled wall-fluid simulations designated as conjugate heat transfer (CHT) computations have been carried out in combustion chambers (Jaure et al. 2013) and turbomachine applications (Duchaine et al. 2009; Duchaine et al. 2013; Fadl and He 2017). Separately, radiation modeling in coupled simulations has been considered in different studies (Jones and Paul 2005; Lecocq et al. 2014; Poitou et al. 2012; Gupta et al. 2013).
Fully-coupled simulations accounting for both CHT and thermal radiation have been achieved only recently (Berger et al. 2016; Koren et al. 2017b) while including comparisons to experimental data.

## 9.2 Numerical setup

### 9.2.1 AVBP/AVTP/RAINIER coupling framework

#### 9.2.1.1 Adaptation of the HCND metholodogy

In order to account for the radiative flux with the HCND methodology presented in Chapter 8, each hybrid cell balance of energy is modified and written as:

$$\frac{dT_{\text{bnd}}}{dt} = -\frac{\Phi_{\text{conv}} + \Phi_{\text{rad}} + \Phi_{\text{cond}}}{\rho_f c_{p,f} V_f + \rho_s c_s V_s} \tag{9.1}$$

with:

$$\begin{aligned}
\Phi_{\text{conv}} &= \sum_{j=1}^{n_{\text{face}}} A_j \ \phi_{\mathbf{conv}} \cdot \mathbf{n}_{\text{ext,j}} \\
\Phi_{\text{rad}} &= \sum_{j=1}^{n_{\text{face}}} A_j \ \phi_{\mathbf{rad}} \cdot \mathbf{n}_{\text{ext,j}} \\
\Phi_{\text{cond}} &= \sum_{j=1}^{n_{\text{face}}} A_j \ \phi_{\mathbf{cond}} \cdot \mathbf{n}_{\text{ext,j}}
\end{aligned} \tag{9.2}$$

and where:

- $n_{\text{face}}$ is the number of internal faces of the hybrid cell,
- $A_j$ is the surface of the $j^{\text{th}}$ face,
- $\mathbf{n}_{\text{ext,j}}$ is the outgoing normal to the face $j$ (exiting the fluid domain),
- $\phi_{\mathbf{conv}}$ is the convective flux computed by the flow solver (AVBP),

- $\phi_{\mathbf{rad}}$ is the active part of the radiative flux on the quartz windows, characterized by their spectral absorptance $A_\nu^{\text{slab,model}}$, reflectance $A_\nu^{\text{slab,model}}$ and transmittance $T_\nu^{\text{slab,model}}$, whose calculation are detailed in this Chapter. As the quartz material is semi-transparent, the total flux $\varphi_{\mathbf{rad}}$ defined in Chapter 6 in Eq. (6.7) also accounts for transparent bands which do not interact directly with the solid parts' heat transfer. Thus, the flux $\phi_{\mathbf{rad}}$ is the part of $\varphi_{\mathbf{rad}}$ accounting for absorption and emission but not transmission. To compute it, the following modifications of the RAINIER code are done:
  - At the quartz windows, Eq. (6.80) of Chapter 6 is modified in order to take into account the spectral absorptance $A_\nu^{\text{slab,model}}$ of the quartz windows:

$$\begin{aligned}\Phi_{ij}^{\text{exch}} = &\int_0^{+\infty} A_\nu^{\text{slab,model}} \left[I_\nu^\circ(T_j) - I_\nu^\circ(T_i)\right] \\ &\int_{S_i}\int_{4\pi} A_{ij\nu}\cos(\theta_i)\mathrm{d}\Omega_i\mathrm{d}S_i\mathrm{d}\nu\end{aligned} \tag{9.3}$$

  - Equation (6.76) of Chapter 6 is modified in order to take into account semi-transparent properties of quartz windows. Then, for an optical path issued from a point B and crossing in its path until a point $\mathrm{F}_m$ Q volume points $\mathrm{P}_{qm}$, R opaque walls points presenting a spectral emissivity $\epsilon_{rm\nu}$, T semi-transparent wall points with a spectral reflectance $R_\nu^{\text{slab,model}}$, the transmissivity $\tau_\nu(\mathrm{BF}_m)$ writes:

$$\begin{aligned}\tau_\nu(\mathrm{BF}_m) = &\tau_\nu(\mathrm{BP}_{1m}) \prod_{q=1}^{Q} \tau_\nu(\mathrm{P}_{qm}\mathrm{P}_{q+1m}) \\ &\prod_{r=1}^{R}(1-\epsilon_{r\nu}) \prod_{t=1}^{T}(R_\nu^{\text{slab,model}})\tau_\nu(\mathrm{P}_{Qm}\mathrm{F}_m)\end{aligned} \tag{9.4}$$

  - Exchanged powers between cells (or wall faces) $i$ and the walls of the surrounding laboratory ambiant room for the quartz windows transparent bands are also considered. In the computation of these exchanged powers, the spectral transmittance $T_\nu^{\text{slab,model}}$ of the quartz windows is then taken into account.
- $\phi_{\mathbf{cond}}$ is the conductive flux computed by the solid solver (AVTP).

$\Phi_{\text{conv}}$, $\Phi_{\text{rad}}$, $\Phi_{\text{cond}}$ are then the integrated fluxes over all internal hybrid cell faces.

#### 9.2.1.2 Communication scheme

In the same way, in order to couple the three codes (AVBP, AVTP and RAINIER), the communications scheme presented in Chapter 8 is modified. Figure 9.1 presents the general communication scheme between the three solvers for a non-accelerated coupled simulation.

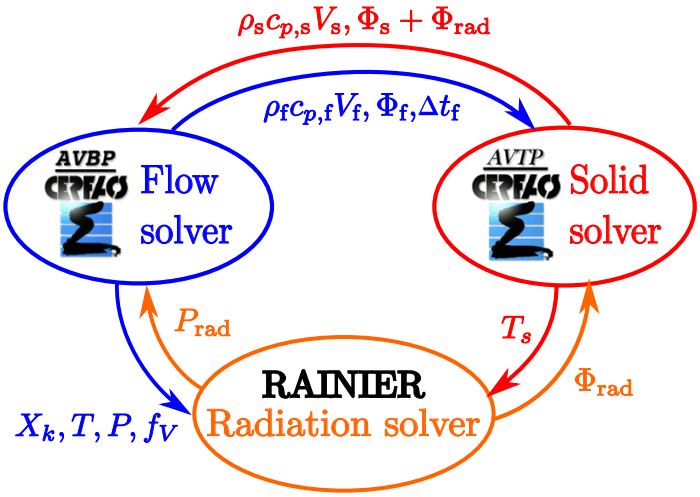


**Figure 9.1:** *Communication scheme between the three solvers.*

At each coupling time step, the following communications are done:

1. The radiation solver sends the radiative power field $P^R$ to the flow solver and radiative fluxes $\Phi_{rad}$ to the solid solver. It receives information about species concentration, temperature, pressure and soot volume fraction from the flow solver as well as wall temperature from the solid solver for next radiative power and fluxes calculations.
2. The flow solver sends information about heat capacity, fluid heat flux at the hybrid cell fluid surfaces $\Phi_f$ and fluid times step to the solid solver. The solid solver sends heat capacity, solid and radiative heat fluxes at the hybrid cell boundaries $\Phi_s + \Phi_{rad}$ to the fluid solver.
3. The fluid and solid solvers have informations about fluctuating fluxes and can determine the next coupling time step $\Delta t_{cpl}$ following the HCND approach.
4. Each code solves it's own system of equations until the next coupling time step of the three codes.

When considering an accelerated coupled simulation, the modifications of the communication scheme are the same as the one presented in Chapter 8 with the calculations by the solid solver of the mean radiative and fluid fluxes.

### 9.2.2 Modeling of the DLR burner

#### 9.2.2.1 Investigated cases and CPU cost

Several numerical cases R$n$W$m$S1 are considered depending on the description of thermal radiation and wall boundary conditions. They correspond to simulations detailed in previous chapters and to the new multi-physics one. Radiation models R0, R1 and R2 respectively correspond to cases without considering radiation, with an optically-thin assumption (OTA) and with a Monte Carlo (MC) resolution of the radiative transfer equation. For the wall treatment, adiabatic (W0), imposed wall temperature (W1: Imposed Temp.) and conjugate heat transfer (W2: CHT) cases are considered. In all these simulations, soot production is considered (S1). The corresponding nomenclature is reminded in Tab. 9.1. The cost for the simulation of the R0W0 case is 400 000 CPU hours on Intel E5-2690V3 cores for an averaging time of statistics $\tau = 40$ ms. The relative costs of the other simulations are gathered in Tab. 9.1.

| Case | Radiation model | Wall treatment | Rel. CPU cost | Detailed in |
|---|---|---|---|---|
| R0W0S1 | None | Adiab. | 1 | Chapter 5 |
| R1W1S1 | OTA | Imposed Temp. | 1.03 | Chapter 5 |
| R0W2S1 | None | CHT | 1.12 | Chapter 8 |
| R2W2S1 | MC | CHT | 2.30 | Here |

**Table 9.1:** *Nomenclature used for the different simulated cases and CPU costs.*

Table 9.2 presents the cores repartition that has been considered for the configuration R2W2S1 in order to optimize the waiting time of each code. Indeed, the cores repartition must be well balanced between the three solvers. The coupled simulation considering conjugate heat transfer from the quartz windows and thermal radiation (case R2W2S1) increases by 123% the cost of the simulation compared with the non-coupled simulation (case R1W1S1), for an overall of 920 000 CPU hours.

| **Code** | **AVBP** | **AVTP** | **RAINIER** | **PALM** |
|---|---|---|---|---|
| Nb. of cores | 1288 | 112 | 1399 | 1 |

**Table 9.2:** *Cores repartition for the coupled simulation R2W2S1.*

The cases R0W0S1 and R1W1S1 have been already analyzed in Chapter 5 and the case R0W2S1 in Chapter 8 and are now compared with the case R2W2S1 in order to study the impact of detailed radiation modeling.

#### 9.2.2.2 Modeling of reactive turbulent flow and heat conduction in combustor walls

For the reactive flow and soot modeling, the same models and numerical methods described in Chapters 5 and 8 are considered, which are briefly:

- the RFPV model (Pierce and Moin 2004; Ihme and Pitsch 2008a) combined with the LES soot production modeling (Rodrigues et al. 2018),
- the third-order in space and time finite element TTGC scheme (Colin and Rudgyard 2000),
- and the SIGMA subgrid model (Nicoud et al. 2011).

Unless for the coupled walls for which the boundary condition is handled by the accelerated HCND method accounting for radiative fluxes, the same boundary conditions as the one considered in Chapter 8 are considered.

For the combustor walls, the same modeling of Chapter 8 is considered:

- Copper posts with constant density and thermal conductivity defined in Eq. (8.24) and temperature dependent heat capacity defined in Eq. (8.25).
- Quartz windows with constant density of 2200 kg/m$^3$ and temperature dependent heat capacity and thermal conductivity, defined in Eqs. (8.26) and (8.27) respectively.

#### 9.2.2.3 Boundary conditions of the different solvers

For the fluid and solid solvers, the same boundary conditions as the one used in Chapter 8 are used:

- For the copper metallic posts, they are considered isothermal at 333 K. Without more information, the top of the quartz windows has been considered at the same temperature. The temperature at the bottom of the quartz is considered equal to 650 K: the temperature imposed to the bottom of the combustion chamber.
- As for Chapter 8, the model developed in Appendix F has been retained for the external boundary condition. The flux boundary condition at the quartz surface $\phi^{\text{out}}(x,z)$ is given by:

$$\begin{aligned}\phi^{\text{out}}(x,z) = \overline{\epsilon^{\text{slab}}}(T_{\text{out}}(x,z))\sigma T_{\text{out}}(x,z)^4 - \overline{\epsilon^{\text{slab}}}(T_3)\sigma T_3^4 \\ + h_1(x,z)(T_{\text{out}}(x,z) - T_{\text{in}}^{\text{air}})\end{aligned} \tag{9.5}$$

  where:
  - $x$ and $z$ correspond respectively to the transverse and axial coordinates respectively (see Fig. 8.10),
  - $\sigma$ is the Stefan-Boltzmann constant,
  - $T_3 = 313$ K is the pressure housing stainless steel temperature,

- $T_{\text{in}}^{\text{air}} = 313$ K is the air temperature inside the pressure housing,
- $T_{\text{out}}(x, z)$ is the temperature field of the quartz external face,
- $h_1(x, z)$ corresponds to the conducto-convective transfer coefficient correlated to the quartz cooling system.
- $\overline{\epsilon^{\text{slab}}}(T)$ corresponds to the total emissivity of the quartz slab at temperature T

Details of the calculation of $h_1(x, z)$ are given in Chapter 8 and Appendix F. Both the impact of the cooling system and radiative transfer leaving the quartz wall are then modeled with the expression of this boundary condition.

Concerning the radiative solver, the following boundary conditions are considered within the fluid domain:

- Inlets and oulets are considered as non-reflecting with a far-field temperature equal to 300 K,
- The bottom chamber is considered opaque with an emissivity equal to 0.6,
- The copper posts are considered opaque with an emissivity equal to 0.87 (emissivity of oxidized copper).

The quartz windows are considered as semi-transparent. Next sections describe how their corresponding properties are taken into account as boundary conditions of the radiative solver.

#### 9.2.2.4 Quartz radiative properties modeling

Many laboratory-scale combustors are equipped with viewing windows to allow characterization of the reactive flow. One must take care of the semi-transparent nature of such windows. While absent in industrial systems, these windows, often present in laboratory-scale models, can strongly modify the internal and external radiative heat transfer. Surprisingly, this effect on the combustor heat transfer has not been thoroughly investigated. In fact, the validation of coupled CFD simulation with thermal radiation has mainly been involved with unconfined flames (Modest and Haworth 2016) mostly because of the usually unknown wall temperature in confined configurations. Applications to confined combustor with opaque boundaries as in Zhao et al. (2013) require to provide the wall emissivity which can be quite uncertain depending on the type and state of the material. To the best of our knowledge, only a couple of studies from French research groups have investigated combustors enclosed with viewing windows (Gonçalves dos Santos et al. 2008; Poitou et al. 2011; Poitou et al. 2012; Koren et al. 2017b). The windows' properties were either not detailed or a fixed averaged total emissivity was specified (Poitou et al. 2011; Koren et al. 2017b).

The spectral band model of quartz window radiative properties presented in Appendix F is considered here. However, in contrast with the treatment done for

the solid solver, this band model is used as detailed spectral radiative properties for the radiative transfer equation solver. Figure 9.2 presents the corresponding spectra of transmittance $T_\lambda^{\text{slab,model}}$, reflectance $R_\lambda^{\text{slab,model}}$ and absorptance $A_\lambda^{\text{slab,model}}$ of the 3-mm quartz window slab.

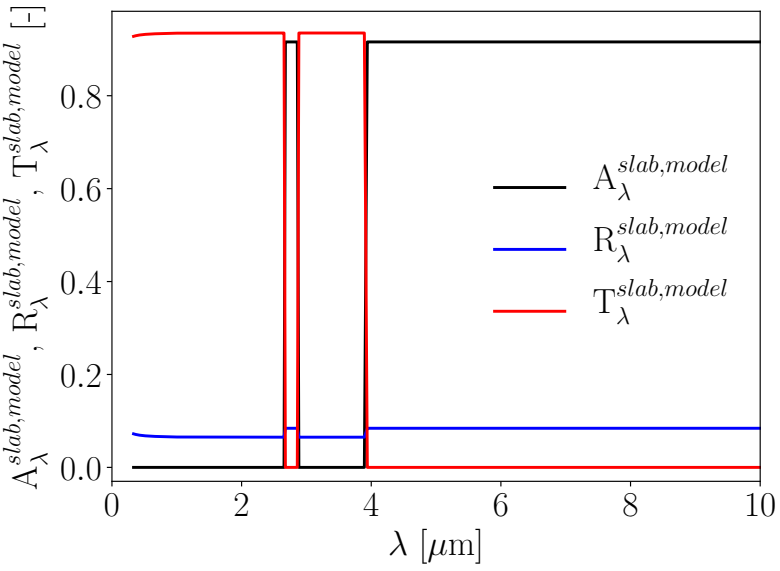


**Figure 9.2:** *Transparent and non-transparent spectral band model for a 3-mm thickness Corning HPFS 7980 quartz.*

In practice, in order to consider these detailed quartz radiative properties, for a ray with a wavelength $\lambda$ incoming at a quartz surface[1]:

- $T_\lambda^{\text{slab,model}}$ is the percentage of its energy leaving the domain exchanging energy with the infinite temperature $T_\infty = 300$ K,
- $A_\lambda^{\text{slab,model}}$ is the percentage of its energy absorbed when exchanging energy with the local quartz temperature $T_{\text{wall}}$,
- $R_\lambda^{\text{slab,model}} = (1 - T_\lambda^{\text{slab,model}} - A_\lambda^{\text{slab,model}})$ is the percentage of its energy which is diffusively reflected.

For the calculation of the fluxes $\phi_{\mathbf{rad}}$ that account for the active part of radiative fluxes on the quartz windows, i.e. the part that is not transmitted without any absorption, detailed spectral emissivities are also considered based on the $A_\lambda^{\text{slab,model}}$ spectrum (Eq. (9.3) with $\nu = 1/\lambda$).

#### 9.2.2.5 Gas and soot particles radiative properties

For the gas phase, only the radiative properties of $CO_2$ and $H_2O$ species are considered. They are modeled through a narrow-band approach: the cK model

[1] The RAINIER solver actually solves the RTE considering the wavenumber $\nu = 1/\lambda$

(Goody and Yung 1995) based on updated parameters of Rivière and Soufiani (2012), as presented in Chapters 6 and 7.

For the soot particles radiation, the size parameter $x = 2\pi d_p/\lambda$ is lower than 0.1 for all the considered wavenumbers. The RDG theory applied for aggregates of non-overlapped spherical particles presented in Chapter 6 is applied for the computation of the soot particles absorption coefficient, as already done in Chapter 7. The refractive index $m = 1.57-0.56i$ is considered for soot particles.

#### 9.2.2.6 RTE Monte-Carlo resolution and error control

The randomized Quasi Monte-Carlo method (Lemieux 2009) based on Sobol low-discrepancy sequences (Joe and Kuo 2008) is used for random numbers generation in order to increase the efficiency of the classical Monte-Carlo Method (Palluotto et al. 2017). The ERM method (Tessé et al. 2002) is used for the calculation of the radiative power and radiative fluxes. In order to be able to realize the simulation at a reasonable cost, the computational domain corresponds to the same as the one used for the AVBP code but with coarser cell sizes, leading to 12.7 millions of cells and 2.4 millions of node. It is indeed considered that this mesh enables to capture the radiative exchange length scales.
A statistical relative error of maximum 5% on wall radiative fluxes and radiative power calculation has been considered in the Monte-Carlo algorithm. In order to enhance convergence, points where radiative power is low are not converged with this accuracy. Indeed, if the RMS of the radiative power estimator is lower than 75 kW/m$^3$ (i.e. 3% of maximum radiative power), the corresponding radiative power is considered as converged, since its weight in the final results are considered negligible. In the same way, if the RMS of the radiative flux estimator is lower than 1 kW/m$^2$ (i.e. 3% of maximum radiative flux) the corresponding radiative flux is considered as converged.

## 9.3 Results

### 9.3.1 Impact of radiative heat losses description on flame stabilization

Figure 9.3 presents the averaged temperature fields for four different cases (see Tab. 9.1).

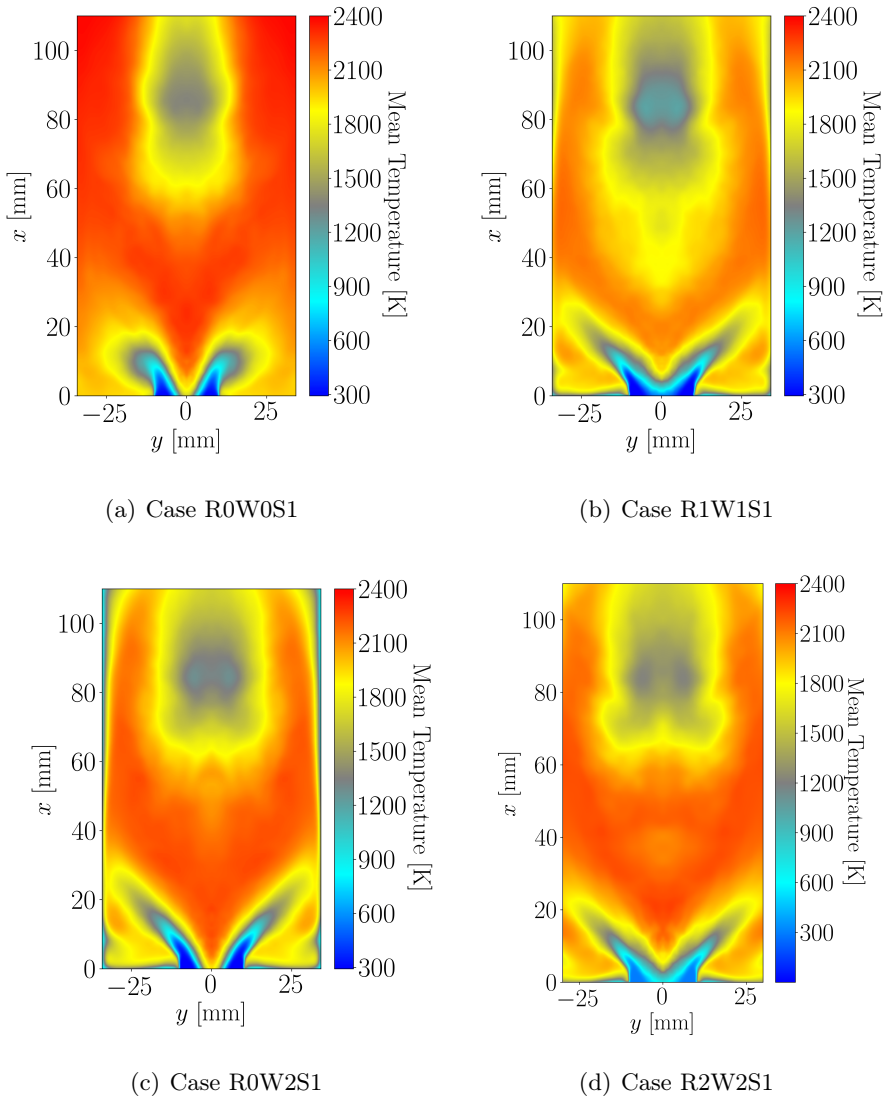


(a) Case R0W0S1

(b) Case R1W1S1

(c) Case R0W2S1

(d) Case R2W2S1

**Figure 9.3:** *Comparison between R0W0S1, R1W1S1, R0W2S1 and R2W2S1 mean temperature fields.*

Looking at the centerline, it can be observed that cases which account for radiation (cases R1W1S1 and R2W2S1) describe a mean flame position of the flame outside of the burner injectors, whereas cases which do not account for radiation (cases R0W0S1 and R0W2S1) describe a mean flame position inside the burner injectors. Then, radiation heat losses drive the flame stabilization position.

Looking at the mean flame opening, roughly the same opening is obtained for the cases R0W2S1 and R2W2S1. This opening is higher than in case R0W2S1, which is also higher than case R0W0S1. Then, the different heat losses tend to

increase the mean flame opening.

The comparison between R0W0S1, R1W1S1, R0W2S1 and R2W2S1 instantaneous temperature fields in Fig. 9.4 confirms these analyses. It can also be observed an hierarchy on the burnt gases temperature fields. The hottest burnt gases temperature is observed for the case R0W0S1 which does not account for heat losses. Then, the second hottest burnt gases temperature is observed for the case R2W2S1 which accounts for wall heat losses. The third hottest burnt gases temperature is obtained for the case R2W2S1 which accounts also for detailed radiative heat losses. Finally, the coldest burnt gases temperature is obtained for the case R1W1S1 which accounts for wall heat losses through imposed boundary temperature and overestimates radiative heat losses with the optically-thin radiation model.

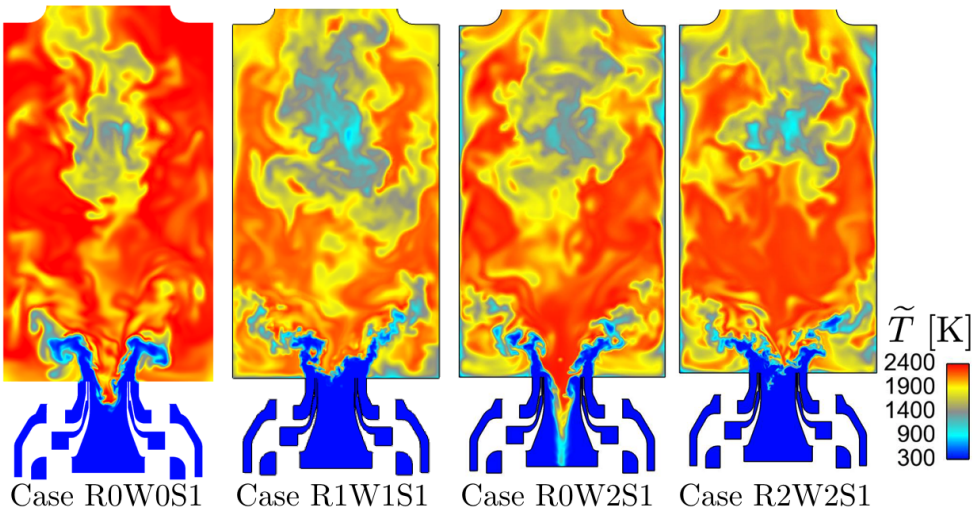


**Figure 9.4:** *Comparison between R0W0S1, R1W1S1, R0W2S1 and R2W2S1 instantaneous temperature fields.*

Figure 9.5 presents a comparison of axial profiles of temperature obtained by the different studied cases with experimental measurements. Figure 9.6 presents radial profiles of temperature at different positions above the burner: $x = 1$ mm, $x = 24$ mm and $x = 107$ mm.

Looking at the axial profiles, impact of different heat losses can be identified. As already discussed in Chapter 8, comparing the case R0W0S1 with the case R0W2S1, a decrease of axial temperature by approximatively 50 K can be noticed. Near the walls, the decrease of temperature due to wall heat losses attain 400 K as it can be observed in the radial profiles of temperature for $x =$ 107 mm. The same conclusions of Fig. 9.4 can be observed about the hierarchy of the different cases. In the case R1W1S1, the optically-thin radiation model

implies an important decrease of axial temperature due to radiative heat losses. Compared with the two previous cases, flame stabilizes more downstream on the centerline and temperature profiles at this position reproduce well the flame experimental position located between $x = 3$ mm and $x = 12$ mm. However, far above the burner, temperature is under-estimated compared with experiments.

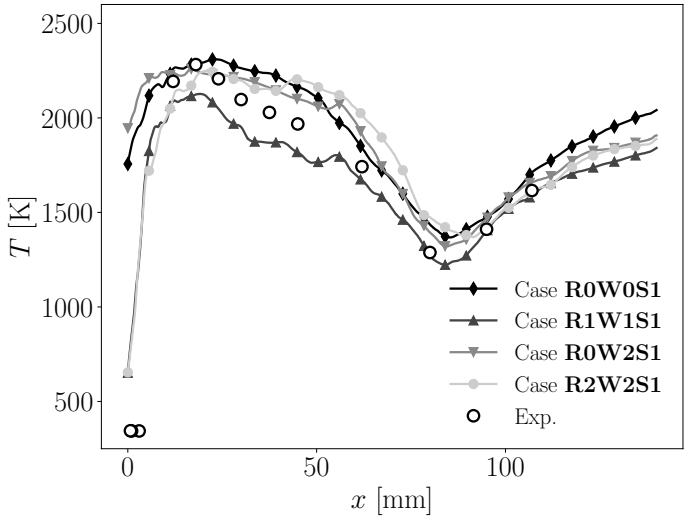


**Figure 9.5:** *Comparison of predicted axial temperature profiles for the different cases with experimental measurements (Geigle et al. 2013).*

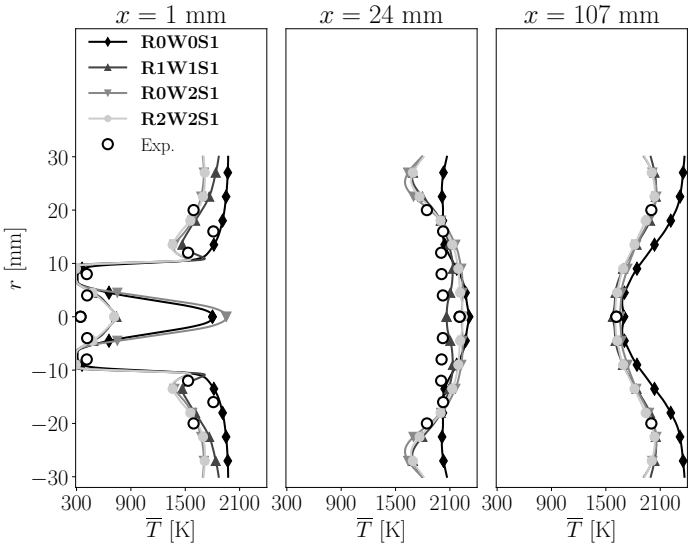


**Figure 9.6:** *Comparison of predicted radial temperature profiles for the different cases with experimental measurements (Geigle et al. 2013).*

In the coupled simulation relative to the case R2W2S1, reabsorption is taken

into account in the calculation of the radiative power. Therefore, temperature is higher than in the case R1W1S1, but it is higher than experimental measures between $x = 40$mm and $x = 70$mm. For all other positions, temperature profiles are in agreement with experimental measurements. Flame stabilization is also well retrieved as for the case R1W1S1. Moreover, as it will be detailed in Section 9.3.3, measured wall temperatures are well retrieved in the coupled simulation and impact of wall heat losses on flame stabilization in the cases R2W2S1 and R1W1S1 can be considered as the same. This confirms that radiative heat losses seem to drive the mean flame stabilization position in the centerline in the presented simulations.

### 9.3.2 Impact of heat losses on soot production

Figure 9.7 presents a comparison of the different soot volume fraction fields with the experimental result due to Geigle et al. (2013).

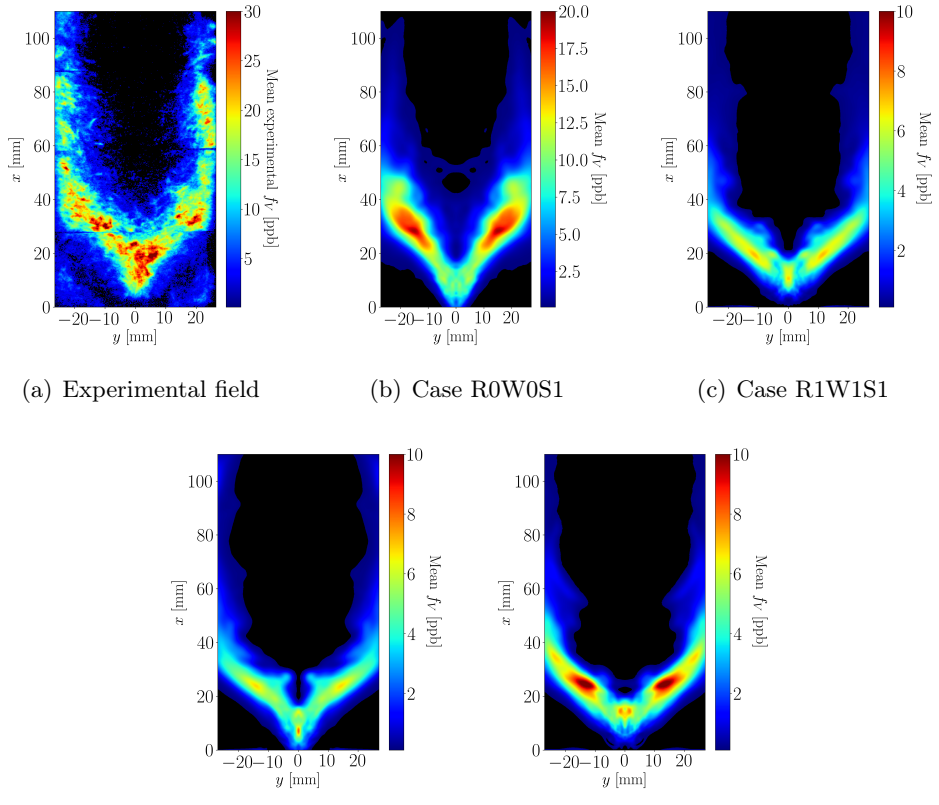


(a) Experimental field (b) Case R0W0S1 (c) Case R1W1S1

(d) Case R0W2S1 (e) Case R2W2S1

**Figure 9.7:** *Comparison between soot volume fraction measurements (Geigle et al. 2013) and numerical predictions for different cases.*

For all the cases, soot production position is well retrieved compared with experimental data. Soot magnitude is predicted with a factor varying from 2 to 5 depending on the modeling of radiative and wall heat losses. Indeed, soot magnitude reveals to be dependent on heat losses modeling: the highest soot magnitude level is obtained for the case R0W0S1 which neglects heat losses, whereas the lowest soot magnitude level is obtained for the case R1W1S1 which accounts for wall heat losses and overestimates radiation heat losses. For the case R2W2S1 which accounts for reabsorption, the magnitude of soot volume fraction is higher than the case R1W1S1 but lower than the case R0W0S1, validating then the general tendency of soot volume fraction decrease with the increase of heat losses, as already observed in literature (Mehta et al. 2010; Reddy et al. 2015b).

### 9.3.3 Quartz windows temperature

Figure 9.8 presents a comparison of wall temperature prediction and experimental LIP measurements (Nau et al. 2017) of the inner and outer faces of the combustion chamber quartz.

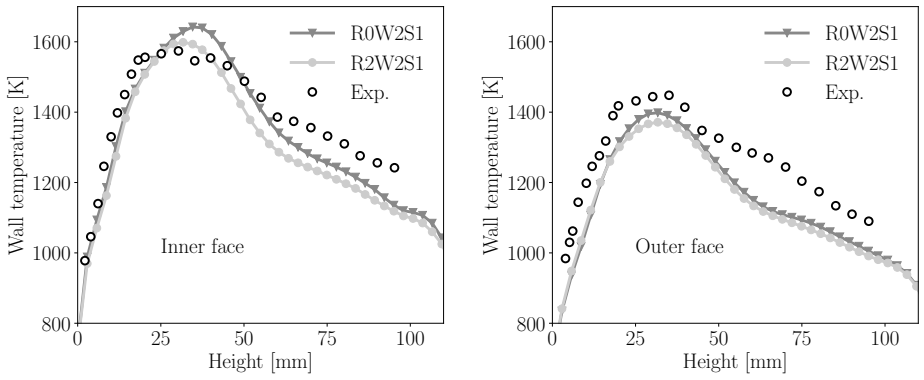


(a) Inner face (b) Outer face

**Figure 9.8:** *Comparison between wall temperature predictions and experimental LIP measurements (Nau et al. 2017).*

A good general agreement can be observed for both cases. It can be observed that radiative effects tend to decrease the highest temperature leading to a very good prediction of quartz temperature in the first part of the quartz (until $x = 40$ mm). For highest heights, an under-prediction of quartz temperature is observed by approximatively 100 K. This misprediction can be explained by a non-well defined temperature at the top of the quartz, used in the current calculations.
Figure 9.9 presents the inner and outer quartz temperatures for the two coupled simulations (cases R0W2S1 and R2W2S1). Important temperature gradients

are observed over all the quartz surface, which can lead to important thermal stresses. The red-isoline corresponds to $T_{\text{wall}} = 1315$ K, which is the annealing temperature. It is important to remind that the regions where quartz temperature is higher than this annealing temperature correspond to regions where degradation of quartz has been observed experimentally (see Fig. 8.21 (c)), demonstrating then the capacity of the methodology in predicting such risks.

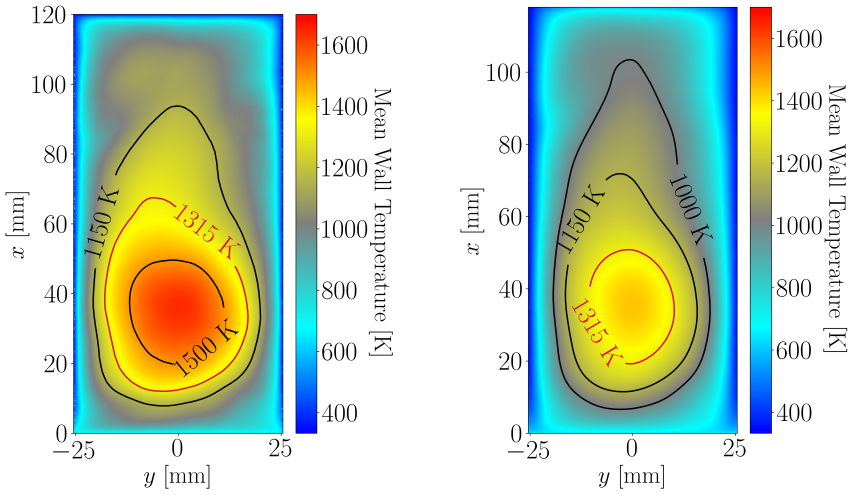


(a) Inner wall temperature, R0W2S1 case (b) Outer wall temperature, R0W2S1 case

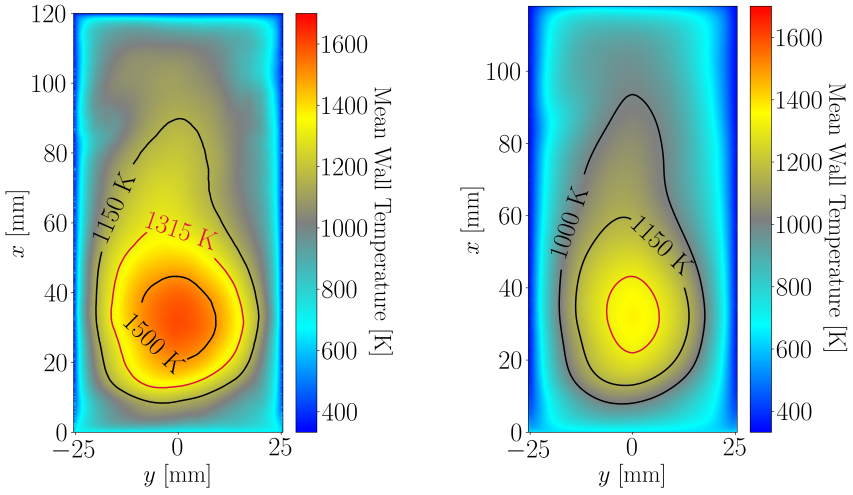


(c) Inner wall temperature, R2W2S1 case (d) Outer wall temperature, R2W2S1 case

**Figure 9.9:** *Comparison of wall temperatures fields between cases R0W2S1 and R2W2S1.*

### 9.3.4 Wall fluxes

#### 9.3.4.1 Inner wall fluxes

Figure 9.10 presents the contributions of radiative and convective heat exchanges on total fluxes $\phi_{\text{tot}}^{\text{in}}$ at the quartz inner face for the two coupled cases: R0W2S1 and R2W2S1. The total fluxes $\phi_{\text{tot}}$ can be decomposed on:

$$\phi_{\text{tot}}^{\text{in}} = \phi_{\text{conv}}^{\text{in}} + \phi_{\text{rad}}^{\text{in}} \tag{9.6}$$

where:

- $\phi_{\text{conv}}^{\text{in}} = \phi_{\mathbf{conv}} \cdot \mathbf{n_{ext}}$ is the normal quartz window convective flux from gaseous flow that induces a conductive flux predicted by the wall law in LES ($\mathbf{n_{ext}}$ corresponds to the outgoing combustion chamber normal),
- $\phi_{\text{rad}}^{\text{in}} = \phi_{\mathbf{rad}} \cdot \mathbf{n_{ext}}$ is the normal quartz window radiative flux with $\phi_{\mathbf{rad}}$ computed as in Eq. (9.3).

Total fluxes corresponds then to the sum of radiative and convective fluxes in case R2W2S1, whereas it corresponds to only the convective flux in case R0W2S1.

Several observations can be made:

- Negligible differences can be noticed between the total flux of the case R0W2S1 (which is identical to the convective flux) and the convective flux of the case R2W2S1. Therefore, radiation effects do not alter near wall convective fluxes for this configuration.
- For the total flux of the case R2W2S1, contribution of radiative flux is at least one order of magnitude lower than that of convective fluxes. Radiative fluxes are negative high temperature regions and positive in low temperature regions. Therefore, they tend to homogenize quartz temperature by decreasing the highest temperatures and increasing the lowest temperatures.

This latter observation is illustrated looking at the axial (at $y = 0$ mm) mean total fluxes at the inner face of the quartz window for both cases in Fig. 9.11. In both cases, the same increase of total flux is observed until $x \approx 30$ mm. However, for $x > 30$ mm, total fluxes in both cases decrease until $x = 110$ mm but with different slopes. As radiative fluxes tend to homogenize the temperature inside the quartz windows, a lower slope is observed in case R2W2S1 than in case R0W2S1.

Figure 9.12 presents the repartition of this total axial flux between convective and radiative fluxes. It can be observed that radiative fluxes correspond to maximum 15% of the total conductive flux, negatively or positively. Therefore, convective fluxes are responsible for most of the total conductive flux inside

the quartz windows while radiative flux homogenize the corresponding wall temperature.

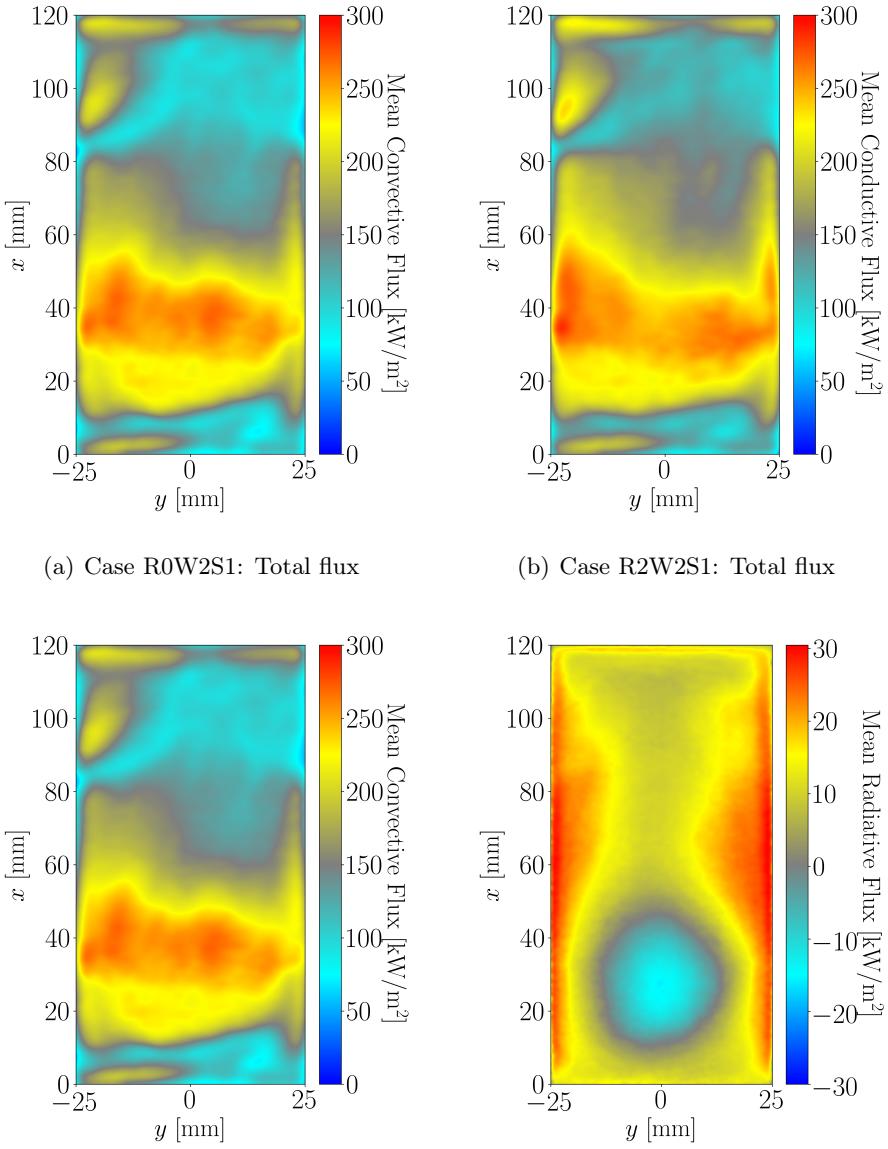


(a) Case R0W2S1: Total flux

(b) Case R2W2S1: Total flux

(c) Case R2W2S1: Convective flux

(d) Case R2W2S1: Radiative flux

**Figure 9.10:** *Comparison of heat fluxes at the inner face of a quartz window for the cases R0W2S1 and R2W2S1.*

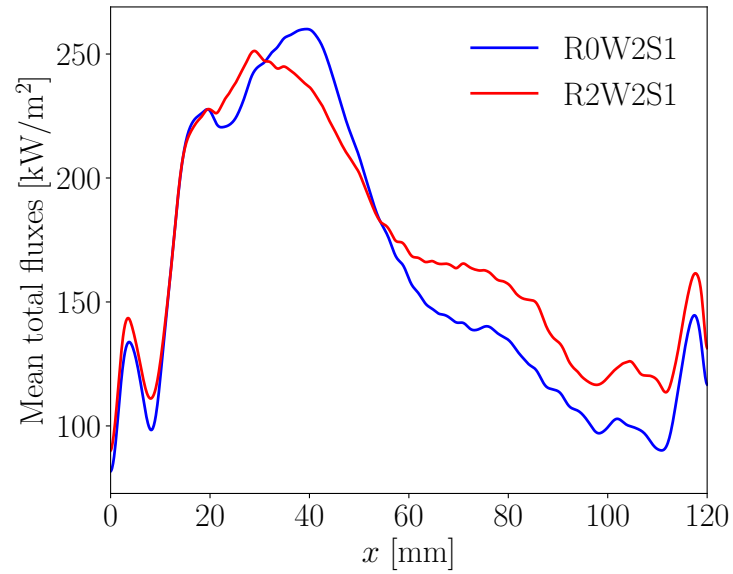


**Figure 9.11:** *Comparison of axial (at $y = 0$ mm) mean total (convective+radiative) fluxes at the inner face of a quartz window between case R0W2S1 and case R2W2S1.*

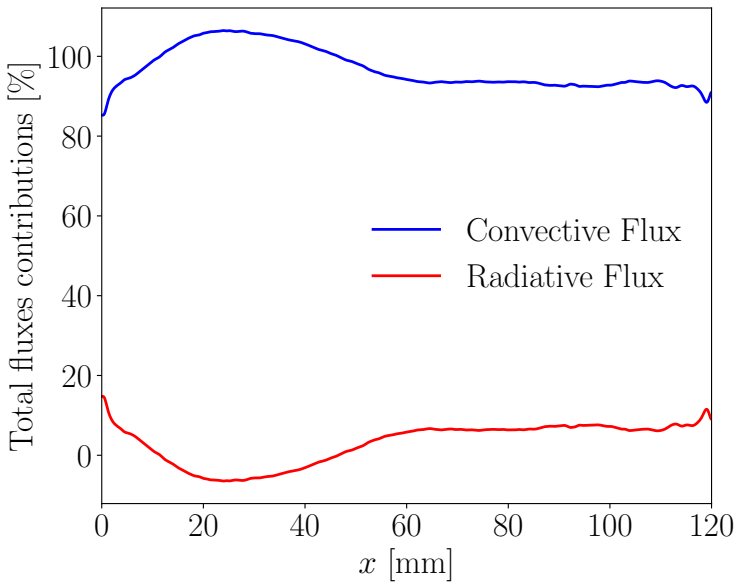


**Figure 9.12:** *Repartition of the total axial (at $y = 0$ mm) flux between convective and radiative fluxes for case R2W2S1.*

#### 9.3.4.2 Outer wall fluxes

Figure 9.14 presents the contributions of radiative and convective heat exchanges on total fluxes $\phi^{\text{out}}$ at the quartz outer faces for the two coupled cases: R0W2S1 and R2W2S1. In both cases, both fluxes are considered and the total fluxes can be decomposed on:

$$\phi^{\text{out}} = \phi^{\text{out}}_{\text{conv}} + \phi^{\text{out}}_{\text{rad}} \tag{9.7}$$

where:

- $\phi^{\text{out}}_{\text{conv}}$ corresponds to the conducto-convective transfer with the quartz cooling systems (wall jets) defined in Eqs. (8.29) and (8.30) of Chapter 8.
- $\phi^{\text{out}}_{\text{rad}}$ corresponds to the radiative flux at the quartz windows external surface, defined in Eqs. (8.28) and (8.29) of Chapter 8.

Several observations can be made:

- Radiative fluxes are strongly linked with the outer face quartz windows temperature fields. Then, as for temperature, the radiative flux is higher in case R0W2S1 than in case R2W2S1.
- Impact of wall jets cooling can be analyzed looking at the convective fluxes in Figs. 9.16 (a) and (b). Convective fluxes are higher near the copper posts at the outlets of the wall jets. Then, they decrease until the center of the quartz. Moreover, as the temperature field, the convective flux is not symmetrical: it is higher in the left side than in the right side due to higher temperatures in the left side of the quartz windows (swirl effects).

Figure 9.13 presents a comparison of axial (at $y = 0$ mm) mean convective, radiative and total (convective+radiative) fluxes at the outer face of a quartz window between case R0W2S1 and case R2W2S1. As already observed, all fluxes decrease in case R2W2S1 compared to case R0W2S1 as temperature of the quartz windows outer faces are lower in this case.

Moreover, in both cases, the convective fluxes represent approximatively two thirds of the total fluxes whereas radiative fluxes represent one third of the total fluxes. Averaging these profiles with the axial position, one finds 160 kW/m$^2$ (respectively 145 kW/m$^2$) for the total flux, 109.8 kW/m$^2$ (respectively 100.3 kW/m$^2$) for the convective flux and 50.6 kW/m$^2$ (respectively 44.7 kW/m$^2$) for the radiative flux for the case R0W2S1 (respectively R2W2S1). These values can be compared with the pre-analysis done in Appendix F where averaged values of 150.4 kW/m$^2$, 104.6 kW/m$^2$ and 45.8 kW/m$^2$ were obtained for the total, convective and radiative fluxes respectively. Good consistency is then obtained between the pre-analysis and the results obtained from the 3-D coupled simulations.

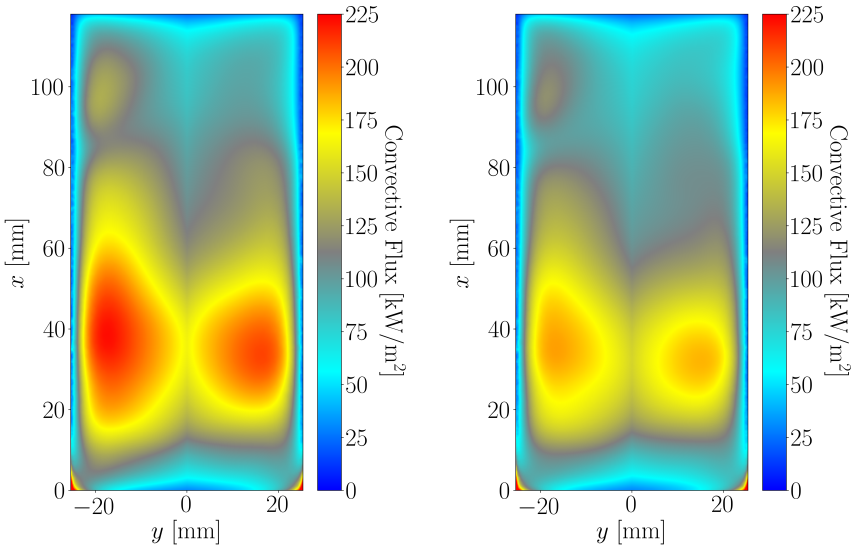


(a) Case R0W2S1: Convective flux

(b) Case R2W2S1: Convective flux

(c) Case R0W2S1: Radiative flux

(d) Case R2W2S1: Radiative flux

**Figure 9.13:** *Comparison of heat fluxes at the outer face of a quartz window for the cases R0W2S1 and R2W2S1.*

Figure 9.15 presents the total emissivities of the quartz windows outer faces for both cases. In both cases, due to the semi-transparent properties of quartz windows and their corresponding variations with quartz windows external surface temperature (Eq. (8.28)), huge variations of total emissivities can be observed with value near 1.0 in cold regions near copper posts and values of 0.2 in the

hottest regions. Small variations are observed between cases R0W2S1 and R2W2S1 with a slightly lower outer wall emissivity in case R0W2S1 than in case R2W2S1 in the hottest regions due to higher quartz temperatures in this case.

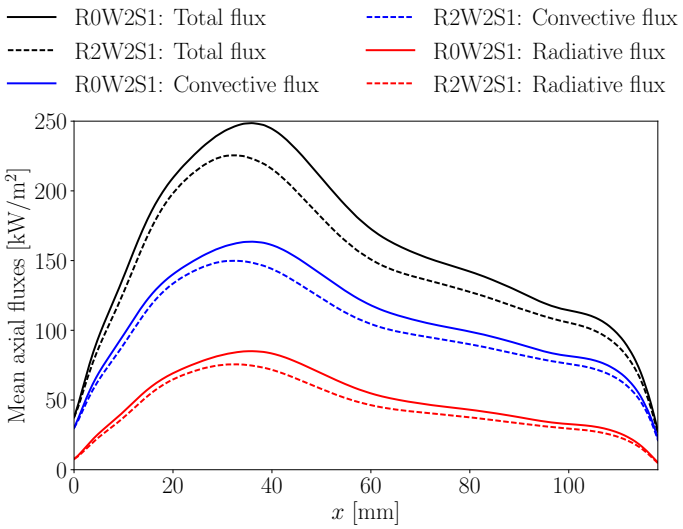


**Figure 9.14:** *Comparison of axial (at $y = 0$ mm) mean convective, radiative and total (convective+radiative) fluxes at the outer face of a quartz window between case R0W2S1 and case R2W2S1.*

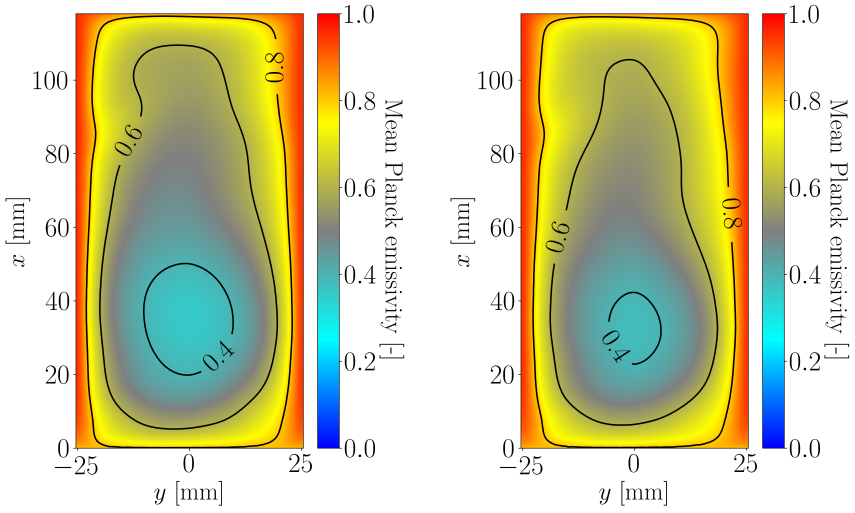


(a) Case R0W2S1 (b) Case R2W2S1

**Figure 9.15:** *Mean Planck emissivities of the quartz windows outer faces in cases R0W2S1 and R2W2S1.*

Figure 9.16 presents the repartition of longitudinal total flux between convective and radiative fluxes at the outer face of the quartz window for case R2W2S1 and several transverse positions: $y = -15$ mm, $y = 0$ mm and $y = 15$ mm. It should be noticed the proportion of each flux is here represented by its corresponding filled region, which is different from the representation used in Fig. 9.14.

As already observed in Fig. 9.14 for $y = 0$ mm, corresponding to regions with higher temperatures, radiative fluxes represent approximatively one third of the total outgoing flux. However, the proportion of radiative flux on the total flux decreases when getting closer to the copper posts, as observed in Figs. 9.14 (b) and (c) for respectively two positions: $y = -15$ mm and $y = 15$ mm. This is due to two main reasons:

- The decrease of the temperature of the quartz windows face when getting close to the copper posts decreases the weight of radiative flux on total fluxes as it scales with the power four of temperature and the convective flux nearly varies linearly with the temperature,
- The convective fluxes increase when getting closer of the copper posts as the wall jet cooling is more efficient near wall jets exit.

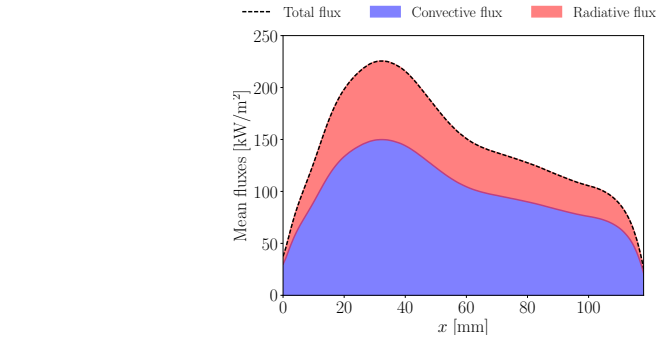


(a) $y = 0$ mm

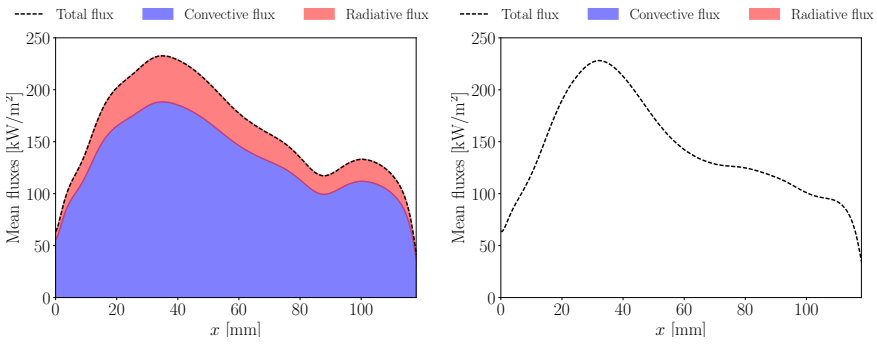


(b) $y = -15$ mm

(c) $y = 15$ mm

**Figure 9.16:** *Repartition of longitudinal total flux between convective and radiative fluxes at the outer face of the quartz window for case R2W2S1 and for several transverse positions: $y = -15$ mm, $y = 0$ mm and $y = 15$ mm.*

Finally, it can be observed again that, as the temperature field, the repartition of fluxes is not symmetrical relative to $y = 0$ plane and different repartitions are obtained for $y = -15$ mm and $y = 15$ mm.

### 9.3.5 Radiative heat transfers inside the combustion chamber

Figure 9.17 compares the radiative powers instantaneous fields between cases R1W1S1 and R2W2S1.

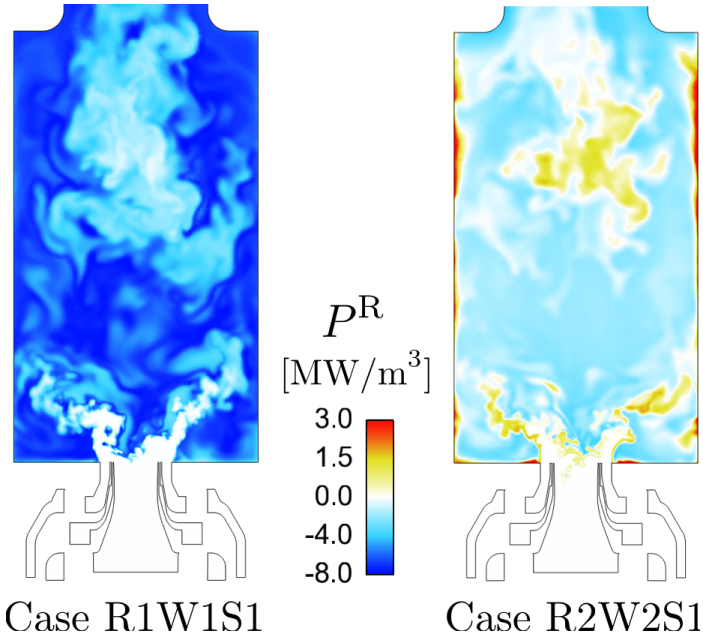


**Figure 9.17:** *Comparison between radiative powers instantaneous fields of cases R1W1S1 and R2W2S1.*

In case R1W1S1, the optically thin radiation model is considered and reabsorption phenomenon is neglected. Therefore, the radiative power is negative. In case R2W2S1, detailed radiation modeling is considered and reabsorption phenomenon is considered. At any point, if the absorbed power is higher than the emitted power, the radiative power is positive. This is observed in three main regions: near the walls where the hot burnt gases are cooled down due to wall heat losses, in the mixing region with secondary cold air injection where hot burnt gases are diluted with cold secondary air injections, and near the flame front where cold gases are preheated through radiative transfers. These different behaviors of the radiative power are not described with the optically thin radiation model in the case R1W1S1. In all the other regions, high impact of the reabsorption phenomenon is also observed and the optically thin radiation model largely overestimates the magnitude of the radiative power. Finally, in both cases, a high axial absolute value of radiative power is obtained for the hot burnt gases near the flame front, explaining the important role of radiative

heat losses in governing the mean flame stabilization position, as discussed in Figs. 9.3 and 9.4.

Figure 9.18 presents the mean emitted, absorbed and total radiative powers over longitudinal slices of height of 3 mm, over all the fluid domain for the case R2W2S1. In a general manner, strong reabsorption is observed at all positions with 78% of the emitted power reabsorbed in the volume. In the secondary oxidation zone (heights between 60 mm and 100 mm), reabsorption is more important than local emitted power: the cold burnt gases reabsorb energy emitted from hot burnt gases at higher temperature localized between 20 mm and 60 mm above the burner. The radiative power is then positive in this region and cold burnt gases are reheated by radiative heat transfers.

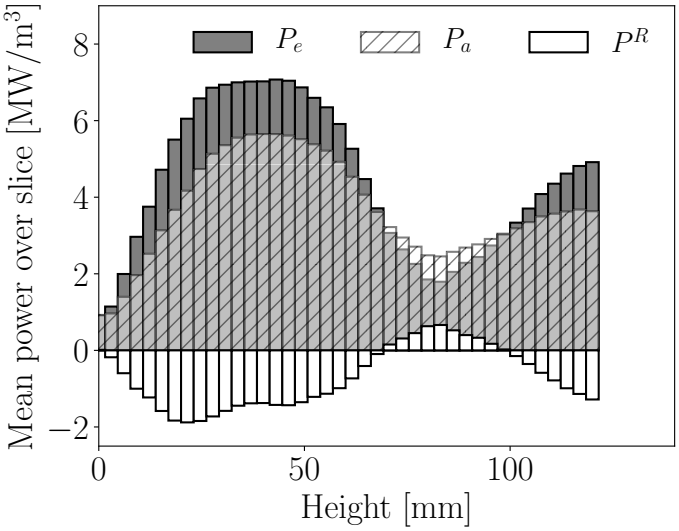


**Figure 9.18:** *Mean emitted, absorbed and total powers per axial slices of the fluid domain.*

Figure 9.19 presents the mean emitted absorbed and total radiative powers transverse profiles at different heights above burner inlets. For all the positions, absorbed power near the walls is higher than emitted power. Then, the radiative power in these regions is positive and gas temperature is heated through radiative heat losses. At the centerline, near the flame front region ($x$ = 20mm), the absolute radiative power is maximum and as already stated before, it drives the mean flame position. Looking at higher heights above the burner ($x$ = 40 mm and $x$ = 60 mm), the gap between emitted and absorbed power decreases and at $x$ = 80 mm, corresponding to the region of burnt gases cooled by the secondary cold air injection, the absorbed power is higher than the emitted power. At $x$ = 100 mm, the axial radiative power is nearly zero, and the emitted becomes bigger than the absorbed power at $x$ = 120 mm as the

temperature of the burnt gases increase (see Fig. 9.5). In a general way, it is again observed that for all the heights, re-absorption phenomenon is important and corresponds to at least 50% of the local emitted power.

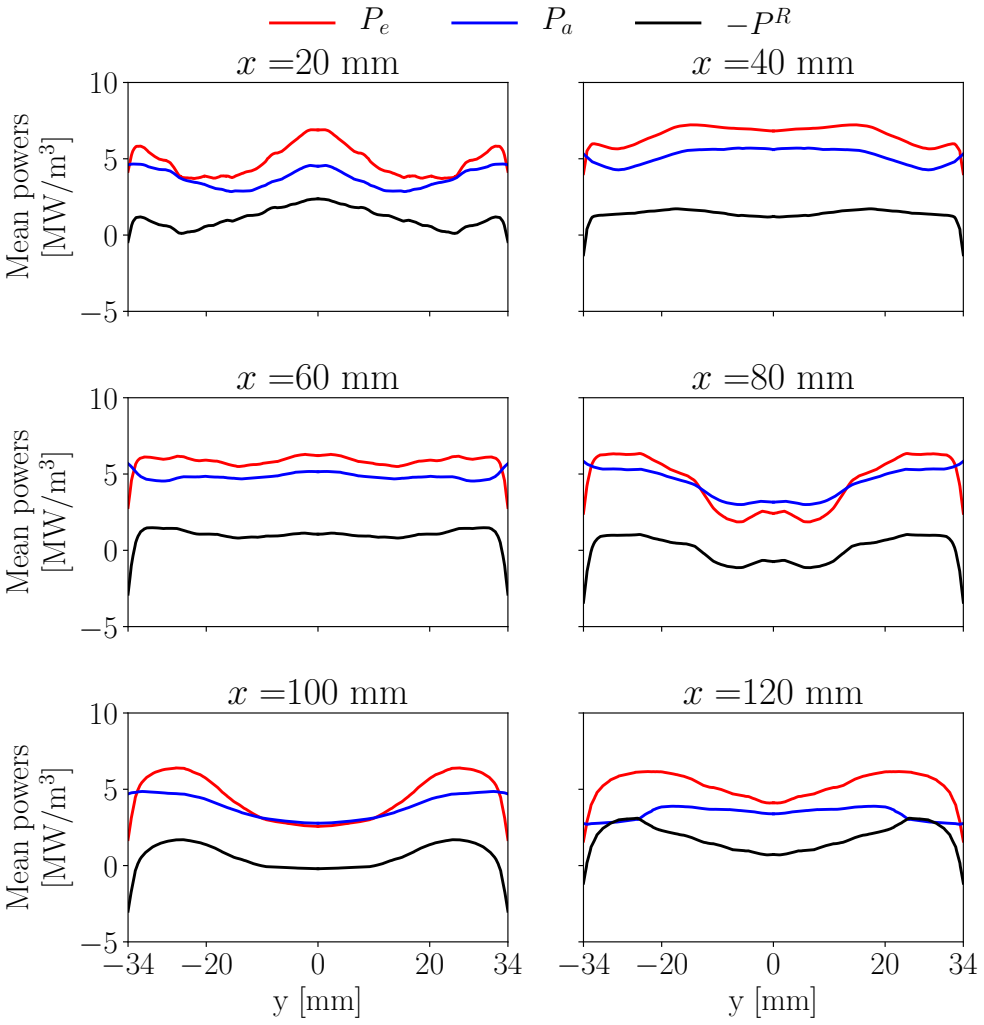


**Figure 9.19:** *Mean emitted, absorbed and total radiative powers transverse profiles at different heights above burner inlets.*

In order to correctly quantify the origin of such absorption, the RTE is solved for each wavelength deterministically (but using Quasi Monte-Carlo approach for the solid angle directions) for one instantaneous solution. Figure 9.20 presents the corresponding total emitted, absorbed and total radiative powers for each band of the cK+Rayleigh/RDG database. It can be observed that the major part of emitted power comes from two bands around 2 500 cm$^{-1}$. These two bands correspond to high $CO_2$ absorption coefficients and high optical thicknesses. Indeed, 90.6 % of the power emitted by these bands is reabsorbed.

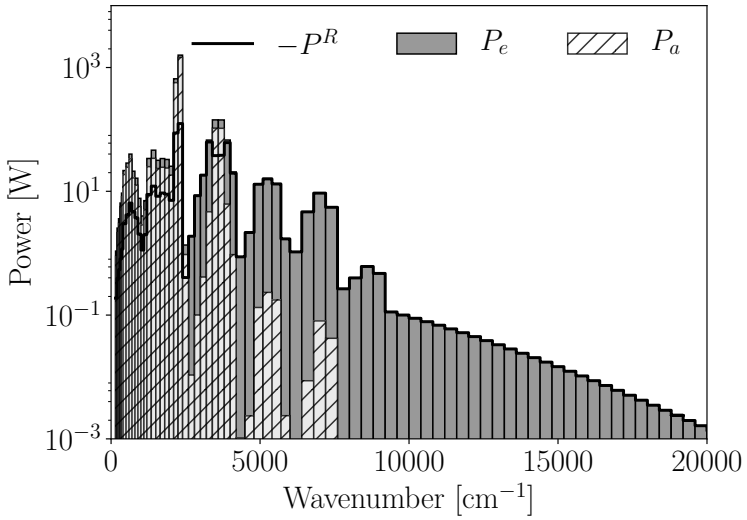


**Figure 9.20:** *Spectral emitted, absorbed and total radiative powers.*

Figure 9.21 presents the spectral proportion of the emitted (Fig. 9.21(a)) and radiative (Fig. 9.21(b)) powers. It can be observed that the major band that initially contributes for approximatively 50 % of total emitted power only accounts for 20 % of the total radiative power. Then, bands around 3 500 cm$^{-1}$ that originally contribute for approximatively 3 % of the emitted power represent 10 % of the total radiative power. Consequently, reabsorption phenomena, based on the optical thicknesses of the different bands, redistributes the role of the different bands on total radiative heat transfer, justifying the need of solving the RTE for all the wavelengths of the radiative spectrum.

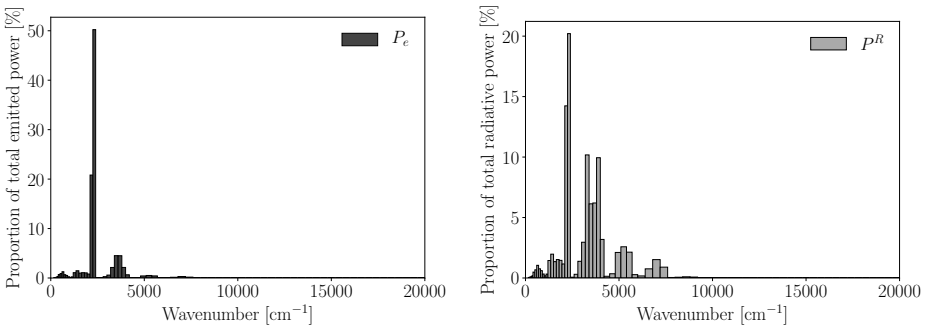


(a) Emitted power

(b) Radiative power

**Figure 9.21:** *Spectral proportion of total emitted and radiative powers.*

Figure 9.22 presents a comparison between instantaneous emitted radiative powers fields from gas (Fig. 9.22 (a)) and solid (Fig. 9.22 (b)) phases, noted $P_e^{\text{gas}}$ and $P_e^{\text{soot}}$ respectively. Fig. 9.22 (c) presents the ratio of the emitted

power from soot particles over the total emitted power. It can be observed that soot particles have a negligible role on emitted radiative powers. Indeed, integrating the radiative power from gas and soot particles over all the domain, one obtains 3.1 kW and 4 W respectively.

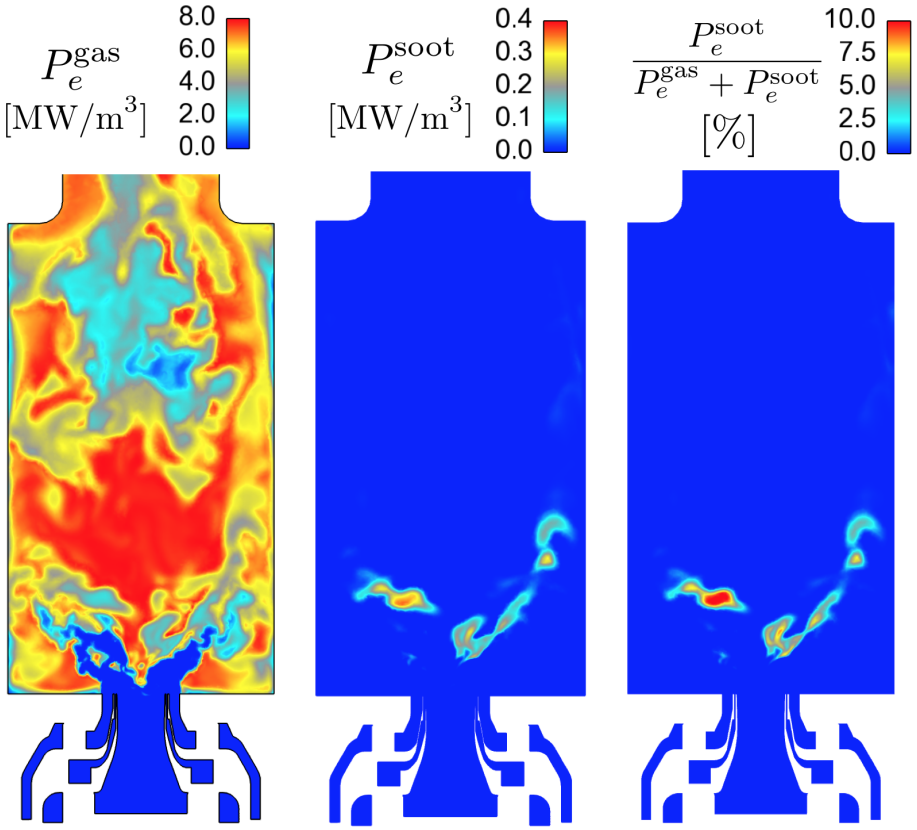


(a) Emitted power from gas (b) Emitted power from soot (c) Ratio of emitted power from soot

**Figure 9.22:** *Comparison between instantaneous emitted radiative powers from gas and soot phases.*

Knowing the maximum instantaneous soot volume fraction which is approximatively 0.1 ppm, and based on Eq. (6.54) of Chapter 6 of the soot absorption coefficient, the maximum instantaneous spectral soot absorption coefficient $\kappa_{\nu,\text{soot}}^{\max}$ on the spectral range of interest ($\nu \in [150\ \text{cm}^{-1}, 20\,000\ \text{cm}^{-1}]$) can be obtained: $\kappa_{\nu,\text{soot}}^{\max} \approx 0.98\ \text{m}^{-1}$. For a characteristic dimension $L = 0.1$ m of the combustion chamber, the minimum radiative transmissivity due to soot particles presence is then equal to $\exp(-\kappa_{\nu,\text{soot}}^{\max} L) = 91\%$. Thus, radiation from soot particles can be considered as optically thin. This is also observed in Fig. 9.20 where negligible reabsorption is observed for $\nu > 10\,000\ \text{cm}^{-1}$, corresponding to spectral bands where only soot particles emit.

### 9.3.6 Energy global balances

#### 9.3.6.1 Combustor energy balance

When considering radiative heat losses, the macroscopic balance of sensible enthalpy writes:

$$\underbrace{\int_{\text{outlet-inlet}} \rho h_s \mathbf{u} \cdot \mathbf{dS}}_{\textbf{(I)}} + \underbrace{\int_{\text{walls}} \phi_{\textbf{cond,bnd}} \cdot \mathbf{dS}}_{\textbf{(II)}} + \underbrace{\int_V -P^{\text{R}} \text{d}V}_{\textbf{(III)}} = \underbrace{\dot{\Omega}}_{\textbf{(IV)}} \tag{9.8}$$

This global balance of sensible enthalpy is done between the inlets of the numerical computational domain and the outlet of the top of the combustion chamber (the hemispherical domain representing the surrounding atmosphere is not accounted for).
It involves the outlet and inlet convective fluxes **(I)**, the integrated wall conductive flux **(II)**, the integrated radiative power **(III)** and the integrated heat release rate **(IV)**. Table 9.3 summarizes the value of the different terms of this energy balance for four different cases. For the coupled case R2W2S1, the heat release (38.6 kW) is redistributed in the following manner:

- Fluid thermal energy (term **(I)**): 31.6 kW (82%),
- Convective wall heat losses (term **(II)**): 6.3 kW (16%),
- Radiative heat losses (term **(III)**): 0.7 kW (2%).

| Case | **(I)** | **(II)** | **(III)** | **(IV)** |
|---|---|---|---|---|
| R0W0S1 | 38.6 | - | - | 38.6 |
| R1W1S1 | 33.8 | 1.6 | 3.2 | 38.6 |
| R0W2S1 | 32.4 | 6.2 | - | 38.6 |
| R2W2S1 | 31.6 | 6.3 | 0.67 | 38.6 |

**Table 9.3:** *Energy balances of the different coupled studied cases. All powers are expressed in kW.*

Then, compared to the conjugate heat transfer simulation R0W2S1, the convective heat transfer remains approximatively the same. The radiative contribution of case R2W2S1 is reduced compared to case R1W1S1 due to the strong reabsorption phenomenon. Finally, in case R0W0S1, no heat losses are considered and all the heat release is redistributed into fluid thermal energy. The radiative contribution is always at least one order of magnitude lower than the one of the convective heat flux. The fact that term **(III)** is positive confirms that, for both cases R1W1S1 and R2W2S1, thermal radiation introduces heat losses that decrease the achieved amount of fluid thermal energy characterized by term **(I)**.

#### 9.3.6.2 Balance of radiative transfer

The radiative contribution can be split into different parts corresponding surface integrals of the radiative flux $\varphi_{\mathbf{rad}}$:

$$\begin{aligned}\underbrace{\int_V -P^{\mathrm{R}}\mathrm{d}V}_{\textbf{(III)}} &= \int_V \nabla\cdot\varphi_{\mathbf{rad}}dV \\ &= \underbrace{\int_{\text{inlet+outlet}} \varphi_{\mathbf{rad}}\cdot\mathbf{dS}}_{\textbf{(IIIa)}} + \underbrace{\int_{\text{opaque walls}} \varphi_{\mathbf{rad}}\cdot\mathbf{dS}}_{\textbf{(IIIb)}} \\ &\quad + \int_{\text{quartz windows}} \varphi_{\mathbf{rad}}\cdot\mathbf{dS}\end{aligned} \tag{9.9}$$

On the semi-transparent viewing windows, one must distinguish the active radiative flux on the solid material $\phi_{\mathbf{rad}}$ from the total flux $\varphi_{\mathbf{rad}}$ that is partially transmitted:

$$\begin{aligned}\textbf{(III)} = \ \textbf{(IIIa)} \ + \ \textbf{(IIIb)} \ + \ &\underbrace{\int_{\text{quartz windows}} \phi_{\mathbf{rad}}\cdot\mathbf{dS}}_{\textbf{(IIIc)}} \\ &+ \underbrace{\int_{\text{quartz windows}} (\varphi_{\mathbf{rad}}-\phi_{\mathbf{rad}})\cdot\mathbf{dS}}_{\textbf{(IIId)}}\end{aligned} \tag{9.10}$$

The radiative term **(III)** is then made of four parts:

- the term **(IIIa)** corresponds to the absorbed and emitted radiation at the inlet and outlet far-fields,
- the term **(IIIb)** corresponds to the absorbed and emitted radiation at the opaque walls of the combustion chamber (bottom and top of the chamber, copper posts)
- the term **(IIIc)** corresponds to the absorbed and emitted radiation at the quartz windows.
- the term **(IIId)** corresponds to the thermal radiation passing through the quartz windows in the transparent bands.

In the presented simulation (case R2W2S1), the contributions **(IIIa)**, **(IIIb)**, **(IIIc)** and **(IIId)** are equal to 0.03 kW, 0.08 kW, 0.25 kW and 0.31 kW, respectively. The sum of contributions **(IIIa)** + **(IIIb)** + **(IIIc)** is equal to 0.36 kW. Hence, approximatively half of the internal radiation (**(IIId)** = 0.31 kW out of **(III)** = 0.67 kW) is leaving the combustion chamber through transparent bands of the quartz windows. This justifies the need for accounting for accurate description of quartz windows semi-transparent properties.

#### 9.3.6.3 Quartz windows energy balance

Figure 9.23 presents the definition of fluxes in order to determine the energy balance of one quartz window.

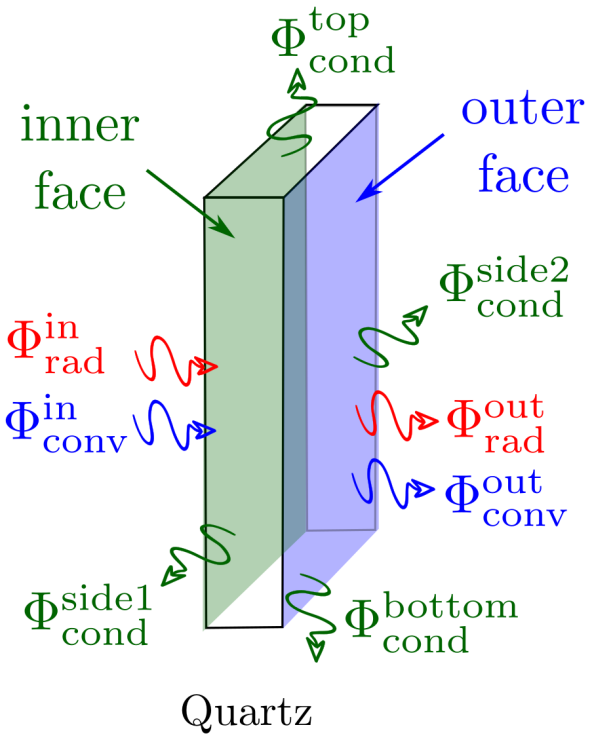


**Figure 9.23:** *Definition of integrated fluxes for quartz energy balance.*

$\Phi^{in}_{conv}$ and $\Phi^{in}_{rad}$ correspond to the integrated radiative and convective fluxes at the inner face of the quartz window, respectively computed by the AVBP and RAINIER codes:

$$\begin{aligned} \Phi^{in}_{conv} &= \int_{\text{inner face}} \phi^{in}_{conv} dS \\ \Phi^{in}_{rad} &= \int_{\text{inner face}} \phi^{in}_{rad} dS \end{aligned} \tag{9.11}$$

$\Phi^{out}_{conv}$ and $\Phi^{out}_{rad}$ correspond to the integrated radiative and convective fluxes at the outer face of the quartz window:

$$\begin{aligned} \Phi^{out}_{conv} &= \int_{\text{outer face}} \phi^{out}_{conv} dS \\ \Phi^{out}_{rad} &= \int_{\text{outer face}} \phi^{out}_{rad} dS \end{aligned} \tag{9.12}$$

Finally, $\Phi_{\text{cond}}^{\text{top}}$, $\Phi_{\text{cond}}^{\text{bottom}}$, $\Phi_{\text{cond}}^{\text{side1}}$ and $\Phi_{\text{cond}}^{\text{side2}}$ correspond to the conductive fluxes at each side of the quartz window, respectively at $x = 120$ mm, $x = 0$ mm, $y = 25$ mm and $y = -25$ mm.

The quartz window energy balance writes:

$$\Phi_{\text{conv}}^{\text{in}} + \Phi_{\text{rad}}^{\text{in}} = \Phi_{\text{conv}}^{\text{out}} + \Phi_{\text{rad}}^{\text{out}} + \Phi_{\text{cond}}^{\text{top}} + \Phi_{\text{cond}}^{\text{bottom}} + \Phi_{\text{cond}}^{\text{side1}} + \Phi_{\text{cond}}^{\text{side2}} \tag{9.13}$$

Table 9.4 presents the corresponding energy balance of one quartz in cases R0W2S1 and R2W2S1.

| | R0W2S1 | R2W2S1 |
|---|---|---|
| $\Phi_{\text{conv}}^{\text{in}}$ | 1.06 | 1.07 |
| $\Phi_{\text{rad}}^{\text{in}}$ | - | 0.06 |
| **Total in** | **1.06** | **1.13** |
| $\Phi_{\text{conv}}^{\text{out}}$ | 0.75 | 0.68 |
| $\Phi_{\text{rad}}^{\text{out}}$ | 0.19 | 0.17 |
| $\Phi_{\text{cond}}^{\text{top}}$ | 0.04 | 0.09 |
| $\Phi_{\text{cond}}^{\text{bottom}}$ | -0.03 | 0.00 |
| $\Phi_{\text{cond}}^{\text{side1}}$ | 0.05 | 0.09 |
| $\Phi_{\text{cond}}^{\text{side2}}$ | 0.06 | 0.10 |
| **Total out** | **1.06** | **1.13** |

**Table 9.4:** *Quartz energy balance for cases R0W2S1 and R2W2S1. All integrated fluxes are expressed in kW.*

The incoming convective flux is roughly the same in cases R0W2S1 and R2W2S1. In case R2W2S1, the incoming radiative flux is computed and is positive when integrating over all the quartz. Then, the total incoming flux is higher in case R2W2S1 than in case R0W2S1. The following energy redistributions can be observed:

- In both cases, the major part of the integrated flux over the inner face is redistributed to the outer face: 89% (0.94 kW out of 1.06 kW) for the case R0W2S1 and 75% (0.85 kW over 1.13 kW) for the case R2W2S1. This validates the approach done in Appendix F for the external thermal boundary condition modeling of the quartz window outer surface,
- In both cases, the contribution of the outgoing flux through the top surface is small: 4% (0.04 kW out of 1.06 kW) for the case R0W2S1 and 8% (0.09 kW over 1.13 kW) for the case R2W2S1. The underestimated temperature applied on the top surface is then unlikely to explain the remaining mismatch between experimental and numerical profiles in Fig. 9.8.
- 7% (0.08 kW out of 1.06 kW) and 16% (0.19 kW out of 1.13 kW) of the total integrated flux is redistributed through the other faces (bottom and sides) for the cases R0W2S1 and R2W2S1 respectively,
- The redistribution of the total integrated flux over the outer face is similar in both cases: 23% (0.19 kW out of 0.94 kW) and 20% (0.17 kW out of

0.85 kW) through convective fluxes and 77% (0.75 kW out of 0.94 kW) and 80% (0.69 kW out of 0.94 kW) through radiative fluxes for the cases R0W2S1 and R2W2S1 respectively.

## 9.4 Conclusion

A multi-physics simulation of a confined pressurized ethylene/air flame has been investigated combining:

- an LES modeling of turbulent combustion and soot production using a sectional approach,
- a conjugate heat transfer modeling with the recently developed HCND coupling approach to adapt the coupling period,
- and a Monte-Carlo resolution of radiative transfer with gases and soot spectral properties.

In comparison to Chapter 8 which only accounted for the first two solvers, the radiative transfer equation has been here additionally solved numerically. Detailed radiation modeling is seen to be important in order to correctly describe flame stabilization on the centerline and the temperature field. Important reabsorption is observed in all the fluid domain. This phenomenon is enhanced by the elevated pressure (3 bar). Absorption has been shown to be responsible of a redistribution of the different emitting bands in total radiative transfer. The emission from the most important emitting bands, presenting important radiative absorption coefficient are optically thick and their total contribution in radiative transfer is then largely reduced. Optically thin bands, representing a lower proportion of the total emitted power, have therefore an enhanced role in the total radiative transfer. Moreover, detailed spectral radiative properties of quartz windows have been identified as important in order to correctly determine the radiative fluxes in such laboratory-scale combustion chambers. Indeed, roughly half of the total wall radiative flux passes through the transparent bands of the quartz windows. All these conclusions justify the need for the resolution of the Radiative Transfer Equation in such configurations.

Concerning soot particles, their small impact on total radiative transfers has been demonstrated for the considered setup and operating condition. It is due to the small magnitude of soot volume fraction compared with the jet diffusion flame studied in Chapter 7. Nonetheless, an important impact of radiative heat losses description on soot production has been demonstrated with a decrease of soot volume fraction when overestimating radiative heat losses through the optically thin radiation model.

Finally, several perspectives of this study can be identified. First, concerning the DLR test rig, there are still some small discrepancies between wall tem-

perature measurements and numerical predictions (as observed in Fig. 9.8). Several possible causes and modeling improvements could be investigated: an effect of downstream mesh coarsening; an impact of the retained wall laws; radiative effects in such wall laws (Zhang et al. 2013a; Zhang et al. 2013b); an improved external heat transfer modeling at the outer face of the quartz window thanks to a CFD simulation of the external flow induced by the cooling films in the pressure housing. Secondly, in the presented coupled approach, the coupling time step $\Delta t_{\text{cpl}}$ is only controlled at the boundary interface between the fluid and solid domains. However, radiative power has an impact over all the computational domain and future work is needed in order to control the coupling time step with domain-based criteria. This has been done with an *a priori* approach in Chapter 7 but an automatic control should also be derived for coupled simulations with thermal radiation.

# Conclusion

The global objective of this thesis was to develop a numerical high fidelity modeling of soot production and heat transfer in turbulent combustion chambers. In the context of predicting the thermal loads and pollutants formation, the more general goal was to evaluate the capacity of such high fidelity models to predict them. To do so, four main axes have been investigated: the detailed modeling of soot production in laminar configurations, the development of an LES formalism for soot production in turbulent flames, the detailed modeling of radiative transfers in turbulent sooting flames and finally, the development of a coupled multi-physics framework for the study of turbulent sooting flames accounting for conjugate heat transfer and radiative transfers.

In next paragraphs, for these four axes, the main achievements and limits of the different works presented in this thesis are analyzed and the different perspectives/improvements are discussed.

## Major achievements and perspectives

### Modeling of soot production in laminar flames

A sectional model for soot production based on state-of-the-art understanding of soot physical and chemical processes has been proposed. Validation of the proposed model for soot volume fraction and particles size distributions prediction has been carried out against state-of-the-art measurements of such quantities in burner stabilized stagnation laminar premixed flames. Validation of the proposed model has also been investigated for pressurized laminar premixed flames and atmospheric counterflow diffusion flame. Uncertainties in soot particle formation processes in such counterflow flames, as the HACA mechanism lead to an under-prediction of soot volume fraction in such flames. Further investigations of these uncertainties are required in order to assess good prediction of soot production in such configurations.

The proposed model has then been used in order to study unsteady dynamics of PAHs and soot production when submitted to harmonic strain rate oscillations. Large chemical time scales of precursors and soot particles formation

were identified. Consequently, particular behavior of soot production response has been highlighted: the higher the oscillation frequency compared to local strain rate, the more PAHs and soot particles fluctuations are damped and phase-lagged. This phase-lag and damping has been identified to increase with the chemical time scale, and therefore the size of PAHs and soot particles. An analytical model has finally been proposed in order to predict such observed phase lags and dampings, assuming a linear response of these quantities. This analytical model can be easily used for the study of soot production response to harmonic oscillations. As a further perspective, this analytical model can be used in order to understand and/or model PAHs and soot particles formation behavior in more complex turbulent flames, where a wide range of frequencies and strain rates can be encountered.

### Development of an LES formalism based on the sectional method for soot production in turbulent flames

In order to transpose the detailed modeling of soot production proposed in the above laminar framework, a dedicated LES formalism based on a sectional method enabling to describe soot particles formation in turbulent configurations has been proposed. The model uses the non adiabatic FPV approach and a subgrid model for soot production is adapted to the proposed sectional method.

Then, the first LES of a jet diffusion flame based on the sectional method for soot production has been realized. The predictions revealed to be at the state-of-the-art of soot production in such turbulent configurations. Surface reactivity processes (surface growth and oxidation) were identified to be the major processes governing soot production in this configuration. Particles size distributions (PSD) in such diffusion sooting flame have been analyzed in details: (i) strong fluctuations of the particles size distribution and strong intermittency of soot production have been identified all along the flame, (ii) regions with a high probability of a one-peak or a two-peak PSD shape have been identified, but also regions with highly frequent transitions between these two PSD shapes, (iii) effects of history on final PSD shape have been investigated and surface growth together with agglomeration/coagulation phenomena have been identified as major contributors of a final two-peak PSD shape.

The proposed methodology has also been applied to soot prediction in a confined pressurized burner. Good overall predictions of soot volume fraction presence and magnitude have been achieved. In this configuration, the PSD has been always identified with a one-peak shape. By contrast with the jet diffusion flame, PAHs-related pathways (nucleation and condensation) are identified to be the major pathways of soot production in this configuration. Finally, impact of heat losses due to radiation and wall heat transfers has been identified on both flame stabilization and soot production.

Several studies are however necessary in order to further increase the fidelity of such simulations. First, impact of high PAHs Schmidt numbers in laminar zones of such turbulent flames has not been assessed even if important impact on soot production has been identified in canonical counterflow diffusion flames. Second, assessment of a soot subgrid model enabling to confidently model the unclosed subgrid terms of the proposed LES formalism for soot production must be realized.

### Detailed modeling of radiative transfers in turbulent sooting flames

Soot particles and gaseous radiative contributions in radiative transfers have been investigated. A methodology has been developed in order to couple a Monte Carlo resolution of the Radiative Transfer Equation and an LES of turbulent combustion with the developed LES formalism for soot production. Then, capacity of such methodology to predict radiative intensities of sooting turbulent flames has been investigated and a good prediction of these radiative fluxes has been demonstrated in the case of a turbulent jet diffusion flame, enabling to assess soot particles contribution on total radiative transfers of such flames.

Gas and soot particles radiative interactions have been quantified. Due to separate spectral bands of burnt gases (mainly $CO_2$ and $H_2O$) and soot particles, small interactions between gas (respectively soot) emitted energy and soot (respectively gas) absorbed energy have been observed. Due to their highly dynamic spectrum with highly absorbing bands compared to the continuous and wideband soot particles radiative spectrum, gaseous radiative reabsorption has been identified as the main contributor of total reabsorption in the two considered configurations: the Sandia flame (atmospheric ethylene-air diffusion flame) and the DLR burner (pressurized ethylene-air confined and swirled flame). Turbulence and radiative transfers interactions have finally been investigated in the turbulent jet flame. Due to high intermittency in soot production, high turbulence radiative interactions from soot particles have been identified and quantified.

The role of soot in thermal radiation was shown to be very different in the two considered configurations: significant in the Sandia flame and negligible in the DLR burner. To further clarify this difference, Figure 13 illustrates the evolution of total emissivity $\epsilon^{\text{gas+soot}}$ of a flame accounting for $CO_2$, $H_2O$ and soot particles, as a function of the soot volume fraction $f_V$ and the pressure $P$. This total emissivity is calculated as:

$$\epsilon^{\text{gas+soot}} = \frac{\pi \int_{\nu=0}^{+\infty} (1 - e^{-\kappa_\nu^{\text{gas+soot}} L}) d\nu}{\sigma T^4} \tag{9.14}$$

where $\kappa_\nu^{\text{gas+soot}}$ is the absorption coefficient based on Rainier ck database for $CO_2$ and $H_2O$ and RDG regime for soot aggregates' primary particles (function of the pressure $P$, the temperature $T$ and the molar fractions of $CO_2$ and $H_2O$), $T$ is the characteristic flame temperature and $L$ is the characteristic mean beam length.

In Fig. 13, a characteristic flame temperature $T = 1800$ K, a characteristic length $L = 10$ cm, $CO_2$ and $H_2O$ molar fractions of 0.1 are considered. The plotted total emissivity increases moderately with pressure and strongly with soot volume fraction for $f_V > 10^{-6}$. This highlights the well-known and expected impact of soots in thermal radiation, the so-called luminous radiation. Points corresponding to the pressure and maximum mean soot volume fraction of the Sandia jet flame and DLR burner are indicated in this figure. While exhibiting a sooting flame, the magnitude of soot volume fraction in the DLR burner is at least one order of magnitude lower than in the Sandia flame. This limitation is due to the moderate equivalence ratio where soot are formed in the confined combustor. Unfortunately, other operating conditions with significantly higher equivalence ratios generate strong soot deposition on the viewing wondows, preventing any visualization or LASER diagnostics on the flame. Due to its high soot volume fraction, the total emissivity in the Sandia jet flame is higher than the one of the DLR burner by a factor 3, explaining the high impact of soot in radiative fluxes for the Sandia jet flame.

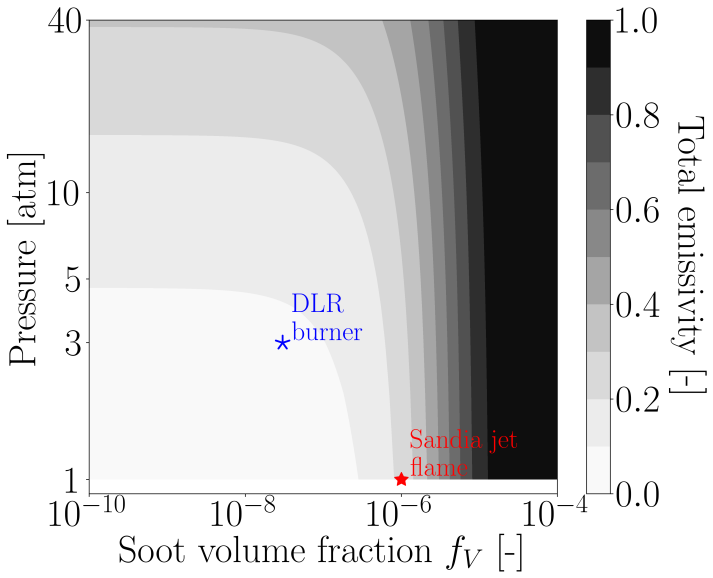


**Figure 13:** *Evolution of total emissivity from gaseous and solid phases with soot volume fraction $f_V$ and pressure $P$ calculated. Points corresponding to the pressure and maximum mean soot volume fraction of the Sandia jet flame and DLR burner are indicated. Parameters: $T = 1800$ K, $L = 10$ cm, $X_{CO_2} = X_{H_2O} = 0.1$.*

Figure 14 presents the evolution of the ratio between soot-only emissivity and gas+soot emissivity with pressure $P$ and soot volume fraction $f_V$. The total emissivities are calculated based on the same hypothesis of the ones used for Fig. 13. The contour plot confirms that soot particles have a very negligible impact on radiative transfers for the DLR burner case, whereas a high impact of soot particles is observed in the Sandia jet flame with a maximum ratio value of 0.85.

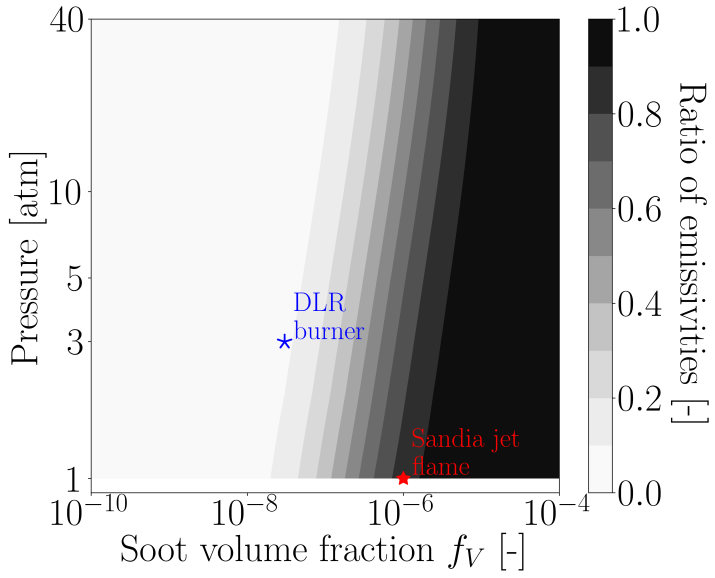


**Figure 14:** *Evolution of evolution of the ratio between soot-only emissivity and gas+soot emissivity with pressure $P$ and soot volume fraction $f_V$. Points corresponding to the pressure and maximum mean soot volume fraction of the Sandia jet flame and DLR burner are indicated. Parameters: $T = 1800$ K, $L = 10$ cm, $X_{CO_2} = X_{H_2O} = 0.1$.*

With the selected parameters in the emissivity computation, a soot magnitude level of 0.1 ppm can be identified as a minimum threshold in order to consider an effect of soot particles in total radiative transfers for a flame at 1 atm. This minimum threshold is seen to increase with pressure. It appears then necessary to distinguish sooting flames as the one in the DLR burner from sooting flames with active luminous radiation as in industrial gas turbines and combustion chambers where local soot volume fractions are high. Let us outline nevertheless that the DLR configuration is a state-of-the-art setup identified today by the international scientific community (ISF workshops) as the closest configuration to many realistic gas turbines due to its characteristics: swirled flow, non-premixed injection, pressurized (3 bar). Figures 13 and 14 reveal that there still remains a gap between realistic high-power gas turbines where luminous radiation is known to be significant (Lefebvre 1984) and laboratory-scale con-

figurations. Interestingly, the DLR setup can be considered as a way to study soot formation in an open loop without soot radiation interacting actively with the other phenomena in the combustor, including ultimately the soot formation itself.

All numerical results have neglected subgrid-scale turbulence-radiation interactions as most of TRI effects are believed to be captured on the resolved scales. Such effects investigated in Poitou et al. (2008) and Roger et al. (2011) will have to be investigated in the future works.

As soot particles can have an important contribution on total radiative transfers, improvements of both soot modeling and soot radiative properties description in such turbulent configuration remain necessary in order to improve the accuracy of computed radiative transfers.

### Coupled multi-physics framework for the study of turbulent sooting flames accounting for conjugate heat and radiative transfers

As pointed out in Chapter 5, heat losses due to wall heat transfer and radiation impact flame stabilization, gas temperature, and consequently gaseous pollutant emissions and soot production. In order to account for such effects without imposing experimental measured temperature boundary conditions, a coupled multi-physics framework accounting for conjugate and radiative transfers of turbulent sooting flames has been proposed. Detailed modeling of transfers through semi-transparent quartz windows used in a laboratory-scale combustor has also been assessed.

This framework has been employed for the simulation of the DLR confined pressurized burner and its capacity to predict mean wall temperatures, flame stabilization and soot production. Good predictions of all these quantities have been obtained. The high fidelity coupled approach is quite promising for predicting thermal loads in combustors. However, in order to predict soot particles impact on such thermal loads, confined configurations presenting higher levels of soot volume fraction are needed to be investigated, as explained in Chapter 9 and in the analyses of Figs. 13 and 14.
Perspectives to further increase the fidelity of the multiphysics simulation of the DLR burner include the improvements previously cited and additionally the ones mentioned in Chapter 9: impact of wall models and external heat transfer modeling.

### Acknowledgments

The following institutions and people are acknowledged for their support:

- The Air Liquide, CentraleSupélec and CNRS Chair on oxycombustion and heat transfer for energy and environment and the OXYTEC project, grant ANR-12-CHIN-001 of the French Agence Nationale de la Recherche for their financial support,
- GENCI for their granting access to the CINES, TGCC and IDRIS HPC resources for a total amount of approximatively 6.5 millions of CPU hours,
- HPC resources from the "Mésocentre" computing center of CentraleSupélec and Ecole Normale Supérieure Paris-Saclay supported by CNRS and Région Île-de-France (http://mesocentre.centralesupelec.fr/),
- Dr. C. Shaddix for providing experimental data and useful discussions about the Sandia jet flame,
- Dr. K.P. Geigle and the DLR for providing experimental data and useful discussions about the DLR burner.

# Appendix A

# Supplemental materials on soot modeling

**Contents**

# A.1 Supplemental materials on the soot sectional model

## A.1.1 Details on the HACA-RC mechanism source terms

### A.1.1.1 Reaction rates of the HACA-RC mechanism

The rate of each reaction of the HACA-RC mechanism presented in Table 1.4 can be expressed as:

$$\begin{aligned}
q_1 &= k_{1f}[C_{n_C}H][H] - k_{1b}[C^*_{n_C}][H_2] \\
q_2 &= k_{2f}[C_{n_C}H][OH] - k_{2b}[C^*_{n_C}][H_2O] \\
q_3 &= k_{3f}[C^*_{n_C}][H] - k_{3b}[C_{n_C}H] \\
q_4 &= k_{4f}[C^*_{n_C}][C_2H_2] - k_{4b}[C^*_{n_C}C_2H_2] \\
q_5 &= k_{5f}[C^*_{n_C}C_2H_2] - k_{5b}[C_{n_C+2}H][H] \\
q_6 &= k_{6f}[C^*_{n_C}][O_2] \\
q_{6'} &= k_{6'f}[C^*_{n_C}C_2H_2][O_2] \\
q_7 &= k_{7f}[C_{n_C}H][OH]
\end{aligned} \tag{A.1}$$

For $q_1$ to $q_{6'}$, the reactions constants $k_{if}$ and $k_{ib}$ are calculated from the Arrhenius law (of the form $A \cdot T^{\beta} \cdot e^{-E_a/RT}$).

For the reaction constant $k_{7f}$, it is determined through its efficiency $\gamma_{OH}$. This efficiency is defined as (El-Leathy et al. 2002):

$$\gamma_{OH} = \frac{4w_{ox}}{[OH]\mathbf{C}\bar{v}_{OH}} \tag{A.2}$$

where:

- $\mathbf{C}$, the number of sites at the surface of soot particles,
- [OH], the concentration of hydroxyl radicals,
- $w_{ox}$, the oxidation reaction rate per unit surface,
- $\bar{v}_{OH} = \sqrt{\frac{8RT}{\pi W_{OH}}}$, the equilibrium mean velocity of OH.
- $W_{OH}$, the molar weight of the OH species.

On the other hand, as $\mathbf{C} = N_A[C_{n_C}H]$, and given that a radical site has a surface assumed equal to $s_{C_2}$ (surface of two carbon atoms), the following relation can be obtained for $q_7$:

$$q_7 = s_{C_2} w_{ox} = \frac{\gamma_{OH}}{4} s_{C_2} N_A \left(\frac{8RT}{\pi W_{OH}}\right)^{\frac{1}{2}} [C_{n_C}H][OH] \tag{A.3}$$

Then, $k_{7f}$ can be expressed as a function of temperature $T$ :

$$k_{7f} = \frac{\gamma_{OH}}{4} s_{C_2} N_A \left(\frac{8RT}{\pi W_{OH}}\right)^{\frac{1}{2}} \tag{A.4}$$

### A.1.1.2 Expression of the radical active sites concentrations $C^*_{n_C}$ and $C^*_{n_C}C_2H_2$

$C^*_{n_C}C_2H_2$ is considered as a quasi-stationary species (Mauss et al. 1994). Then, based on chemical reactions of Tab. 1.4, it verifies the following relations:

$$\begin{aligned}
&\frac{d[C^*_{n_C}C_2H_2]}{dt} = 0 \\
\Leftrightarrow\ & k_{4f}[C^*_{n_C}][C_2H_2] - k_{4b}[C^*_{n_C}C_2H_2] - k_{5f}[C^*_{n_C}C_2H_2] \\
& + k_{5b}[C_{n_C+2}H][H] - k_{6'f}[C^*_{n_C}C_2H_2][O_2] = 0 \\
\Leftrightarrow\ & [C^*_{n_C}C_2H_2] = \frac{k_{4f}[C_2H_2]}{k_{4b}+k_{5f}+k_{6'f}[O_2]}[C^*_{n_C}] \\
& + \frac{k_{5b}[H]}{k_{4b}+k_{5f}+k_{6'f}[O_2]}[C_{n_C+2}H] \\
\Leftrightarrow\ & [C^*_{n_C}C_2H_2] = B[C^*_{n_C}] + D[C_{n_C}H]
\end{aligned} \tag{A.5}$$

with:

$$\begin{cases}
B = \dfrac{k_{4f}[C_2H_2]}{k_{4b}+k_{5f}+k_{6'f}[O_2]} \\
D = \dfrac{k_{5b}[H]}{k_{4b}+k_{5f}+k_{6'f}[O_2]}
\end{cases} \tag{A.6}$$

with the hypothesis that $C_{n_C+2}H \approx C_{n_C}H$.

$C^*_{n_C}$, $C^*_{n_C+2}$ and $C^*_{n_C-2}$ represent the radical active sites and are considered as equivalent. The quasi-stationary hypothesis for these quantities, as assumed by Mauss et al. (1994), writes:

$$\begin{aligned}
&\frac{d[C^*_{n_C}]}{dt} + \frac{d[C^*_{n_C+2}]}{dt} + \frac{d[C^*_{n_C-2}]}{dt} = 0 \\
\Leftrightarrow\ & k_{1f}[C_{n_C}H][H] + k_{2f}[C_{n_C}H][OH] - k_{1b}[C^*_{n_C}][H_2] - k_{2b}[C^*_{n_C}][H_2O] \\
& - k_{3f}[C^*_{n_C}][H] + k_{3b}[C_{n_C}H] - k_{4f}[C^*_{n_C}][C_2H_2] + k_{4b}[C^*_{n_C}C_2H_2] \\
& - k_{6f}[C^*_{n_C}][O_2] + k_{6'f}[C^*_{n_C}C_2H_2][O_2] + k_{6f}[C^*_{n_C}][O_2] \\
& + k_{7f}[C_{n_C}H][OH] = 0 \\
\Leftrightarrow\ & (k_{1f}[H] + k_{2f}[OH] + k_{3b} + k_{7f}[OH])[C_{n_C}H] \\
& + [C^*_{n_C}C_2H_2](k_{6'f}[O_2] + k_{4b}) \\
& = (k_{1b}[H_2] + k_{2b}[H_2O] + k_{3f}[H] + k_{4f}[C_2H_2])[C^*_{n_C}]
\end{aligned} \tag{A.7}$$

Combining the results obtained in the latter equations for $[C^*_{n_C}C_2H_2]$ with Eq.

(A.5), one obtains:

$$\begin{aligned}
&(k_{1f}[H] + k_{2f}[OH] + k_{3b} + k_{7f}[OH])[C_{n_C}H] + (k_{6'f}[O_2] \\
&+ k_{4b})\frac{k_{4f}[C_2H_2]}{k_{4b} + k_{5f} + k_{6'f}[O_2]}[C^*_{n_C}] \\
&+ (k_{6'f}[O_2] + k_{4b})\frac{k_{5b}[H]}{k_{4b} + k_{5f} + k_{6'f}[O_2]}[C_{n_C+2}H] \\
&= (k_{1b}[H_2] + k_{2b}[H_2O] + k_{3f}[H] + k_{4f}[C_2H_2])[C^*_{n_C}]
\end{aligned} \tag{A.8}$$

In the same way, $C_{n_C+2}H$ and $C_{n_C}H$ are considered equivalent. Then, the following equation is verified:

$$\begin{aligned}
&\left(k_{1f}[H] + k_{2f}[OH] + k_{3b} + k_{7f}[OH] + k_{5b}[H]\left(1 - \frac{k_{5f}}{k_{4b} + k_{5f} + k_{6'f}[O_2]}\right)\right)[C_{n_C}H] \\
&= [C^*_{n_C}]\left(k_{1b}[H_2] + k_{2b}[H_2O] + k_{3f}[H] + k_{4f}[C_2H_2] - k_{4f}[C_2H_2]\left(1 - \frac{k_{5f}}{k_{4b} + k_{5f} + k_{6'f}[O_2]}\right)\right) \\
\Leftrightarrow\quad &[C^*_{n_C}] = \frac{k_{1f}[H] + k_{2f}[OH] + k_{3b} + k_{7f}[OH] + k_{5b}[H]\left(1 - \frac{k_{5f}}{k_{4b}+k_{5f}+k_{6'f}[O_2]}\right)}{k_{1b}[H_2] + k_{2b}[H_2O] + k_{3f}[H] + k_{4f}[C_2H_2]\frac{k_{5f}}{k_{4b}+k_{5f}+k_{6'f}[O_2]}}[C_{n_C}H]
\end{aligned} \tag{A.9}$$

Finally, combining Eq.(A.5) and Eq.(A.9), the following expression can be obtained for $[C^*_{n_C}]$ and $[C^*_{n_C}C_2H_2]$:

$$\begin{cases}
[C^*_{n_C}] = A[C_{n_C}H] \\
[C^*_{n_C}C_2H_2] = AB[C_{n_C}H] + D[C_{n_C}H] = (AB + D)[C_{n_C}H]
\end{cases} \tag{A.10}$$

where $A = \frac{k_{1f}[H]+k_{2f}[OH]+k_{3b}+k_{7f}[OH]+k_{5b}[H]\left(1-\frac{k_{5f}}{k_{4b}+k_{5f}+k_{6'f}[O_2]}\right)}{k_{1b}[H_2]+k_{2b}[H_2O]+k_{3f}[H]+k_{4f}[C_2H_2]\frac{k_{5f}}{k_{4b}+k_{5f}+k_{6'f}[O_2]}}$ and, B and D are defined in Eq. (A.6).

### A.1.1.3 Expression of surface growth and oxidation source terms

Finally, the surface growth and oxidation reaction rates for the section $i$ can be written as:

$$\begin{aligned}
\dot{q}_{sg,i} &= \left(A[C_2H_2]k_{4f} - k_{4,b}(AB + D)\right)[C_{n_C}H] = K_{sg}[C_{n_C}H]_i \\
\dot{q}_{O_2,i} &= k_{6f}[O_2](A(1 + B) + D)[C_{n_C}H] = K_{O_2}[C_{n_C}H]_i \\
\dot{q}_{OH,i} &= k_{7f}[OH][C_{n_C}H] = K_{OH}[C_{n_C}H]_i
\end{aligned} \tag{A.11}$$

where $[C_{n_C}H]_i$ is obtained through Eq. (1.30) replacing the integral from $v = 0$ to $v = +\infty$ by an integral between $v = v_i^{\min}$ and $v = v_i^{\max}$.

### A.1.2 Additional results on premixed flames

The flames studied by Abid et al. (2008) have the same equivalence ratio as the one studied by Camacho et al. (2015), but the methodology for the experimental sampling of soot particles is different.

For the soot volume fraction, two different techniques have been employed: the *Thermocouple Particle Densitometry* (**TPD**), which perturbs only slightly the flow, and the "Tubular-probe sampling technique" coupled with a *Scanning Mobility Particle Sizer* (**SMPS**) which as discussed in Chapter 1 is an intrusive method, which perturbs the flow but enables access to the soot particles size distributions.

Abid et al. (2008) have shown that these two measurements are consistent if the measurements obtained with the **SMPS** technique are shifted by +0.35 cm. The numerical results presented hereafter will consider this shift for the comparison with experimental measurements.

Several configurations have been experimentally studied by modifying the inlet velocity of the cold gas, and therefore the residence time of soot particles. The considered configurations are summarized in Table A.1.

| Case | Cold gas velocity [at 298K and in cm/s] |
|---|---|
| C1 | 13 |
| C2 | 10 |
| C3 | 8 |
| C4 | 6.53 |
| C5 | 5.5 |

**Table A.1:** *Experimental configurations studied by Abid et al. (2008).*

#### A.1.2.1 Soot volume fraction, Particles number density and particles size distributions

For the *C1 flame*, the comparisons between numerical predictions and experimental measurements for the soot volume fraction and particles number density and for the particle size distributions are respectively presented in Fig. A.1 and Fig. A.2.

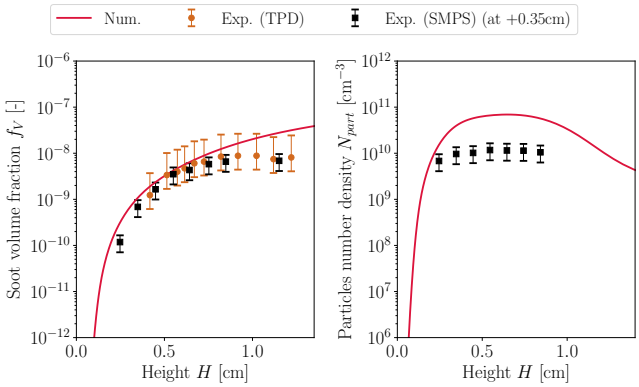


**Figure A.1:** *C1 flame: comparisons between numerical predictions and experimental measurements of the soot volume fraction and particles number density.*

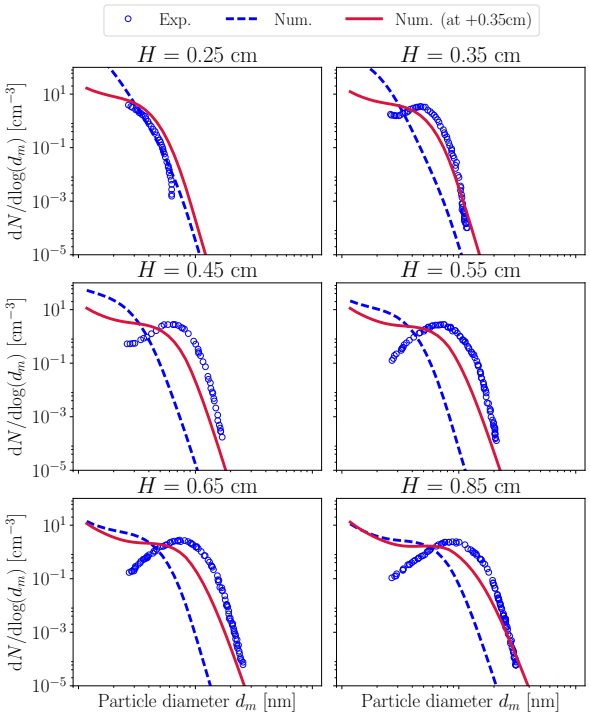


**Figure A.2:** *C1 flame: comparisons between numerical predictions and experimental measurements of the particle size distributions.*

For the *C2 flame*, the comparisons between numerical predictions and experimental measurements for the soot volume fraction and particles number density and for the particle size distributions are respectively presented in Fig. A.3 and Fig. A.4.

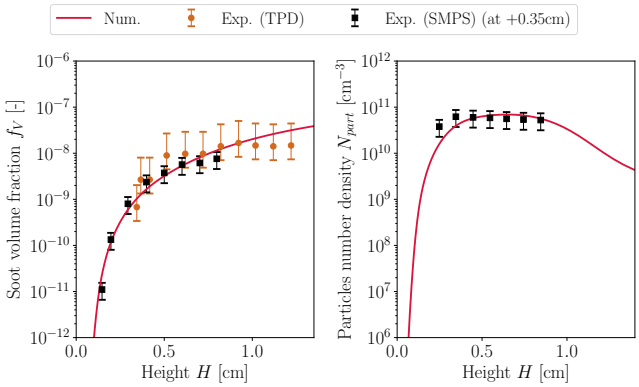


**Figure A.3:** *C2 flame: comparison of numerical predictions and experimental measurements of the soot volume fraction and particles number density.*

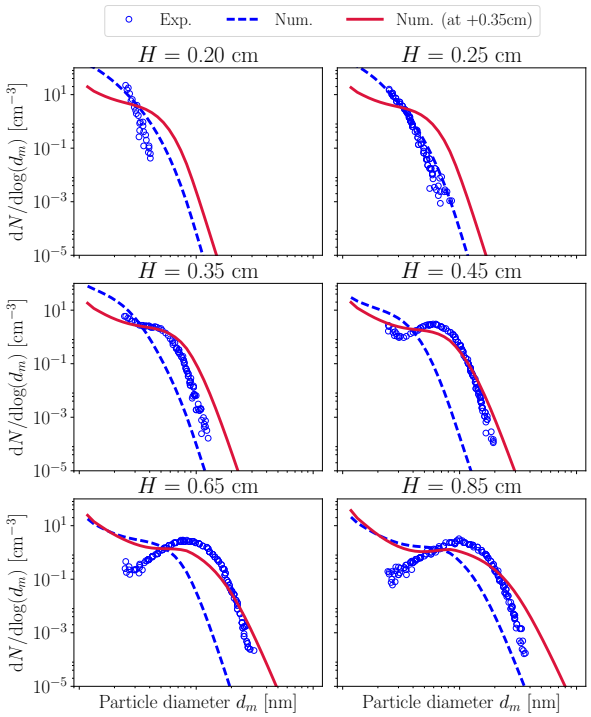


**Figure A.4:** *C2 flame: comparisons between numerical predictions and experimental measurements of the particle size distributions.*

For the *C3 flame*, the comparisons between numerical predictions and experimental measurements for the soot volume fraction and particles number density and for the particle size distributions are respectively presented in Fig. A.5 and Fig. A.6.

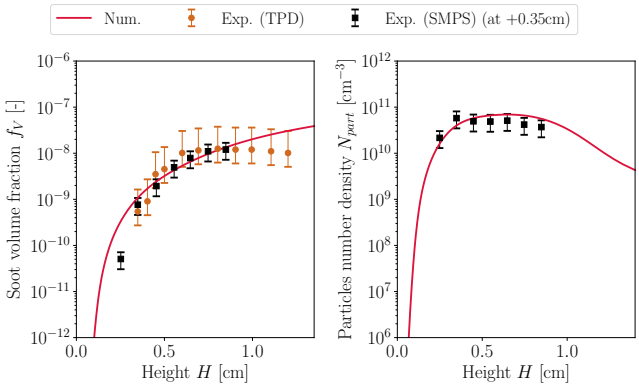


**Figure A.5:** *C3 flame: comparisons between numerical predictions and experimental measurements of the soot volume fraction and particles number density.*

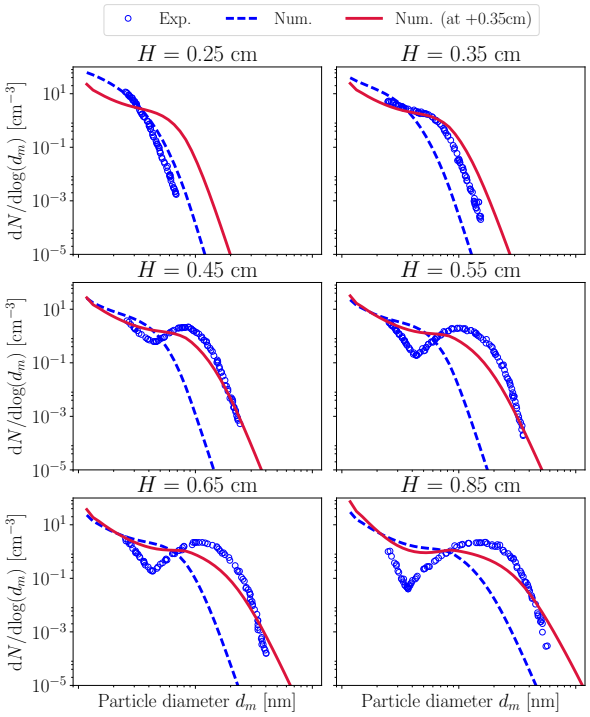


**Figure A.6:** *C3 flame: comparisons between numerical predictions and experimental measurements of the particle size distributions.*

For the *C4 flame*, the comparisons between numerical predictions and experimental measurements for the soot volume fraction and particles number density and for the particle size distributions are respectively presented in Fig. A.7 and Fig. A.8.

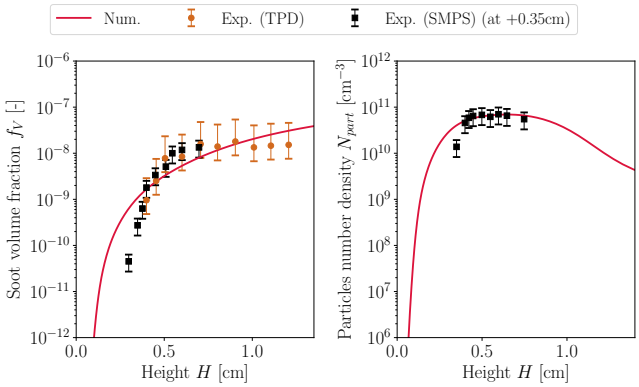


**Figure A.7:** *C4 flame: comparisons between numerical predictions and experimental measurements of the soot volume fraction and particles number density.*

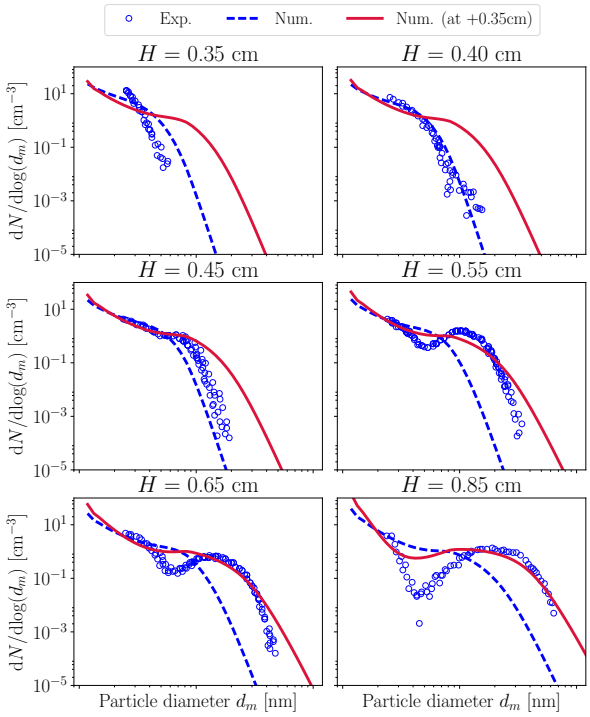


**Figure A.8:** *C4 flame: comparisons between numerical predictions and experimental measurements of the particle size distributions.*

For the *C5 flame*, the comparison between numerical predictions and experimental measurements for the soot volume fraction and particles number density and for the particle size distributions are respectively presented in Fig. A.9 and Fig. A.10.

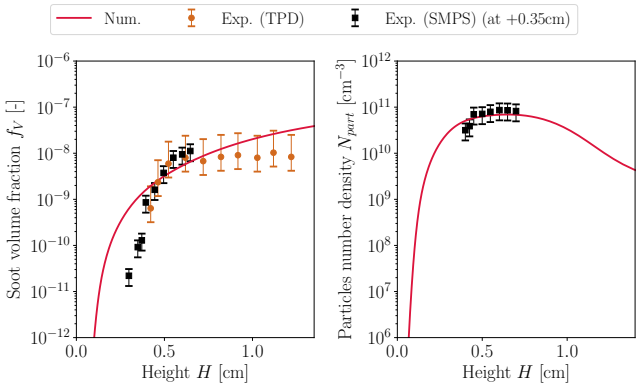


**Figure A.9:** *C5 flame: comparisons between numerical predictions and experimental measurements of the soot volume fraction and particles number density.*

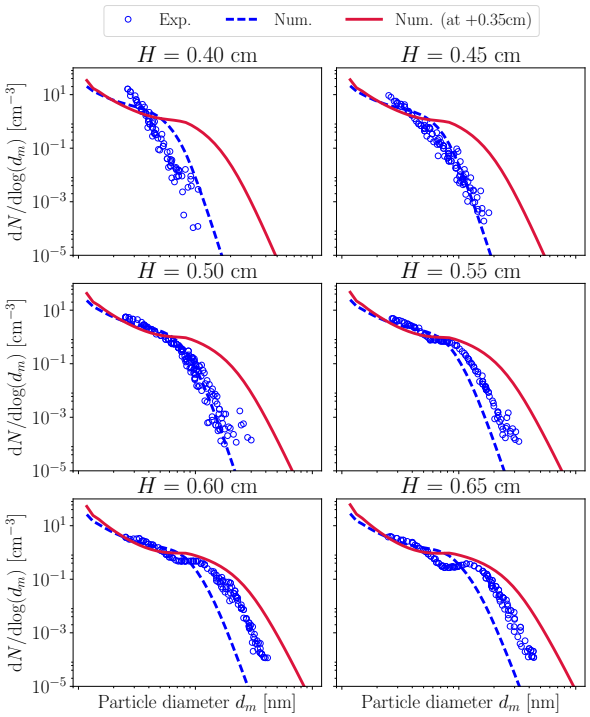


**Figure A.10:** *C5 flame: comparisons between numerical predictions and experimental measurements of the particle size distributions.*

### A.1.2.2 Conclusions

For all the flames, a good agreement is obtained for the global quantities (soot volume fraction and particles number density).

Concerning soot particles size distributions, a good agreement is obtained from C2, C3, C4 flames by shifting the results by +0.35 cm, as proposed by Abid et al. (2008). However, for C1 and C5 flames, particles growth seem to be predicted too slow and too fast respectively. It is important to notice that, as it has been seen in Chapter 2, a systematic shift does not precisely take into account the impact of the flow perturbation by the sampling technique. Indeed, the impact of the sampling technique depends not only on the sampling volume flow rate, but also the local properties of the flow near the probing orifice, which depend on the studied case.

## A.2 Numerical modeling methods proposed in literature

The different categories of models and methods enabling to describe soot particles evolution have been presented and compared in Chapter 1, Section 1.4. In this section of the Appendix, some of the different methods existing in literature are detailed.

### A.2.1 Empirical models

#### A.2.1.1 Tesner model

This model has been developed by Tesner et al. (1971); Tesner et al. (1971) from soot particles measurements in laminar hydrocarbon/hydrogen flames. In this model, the concentrations $\gamma$ of active sites involved in the soot particles formation process and the concentration of soot particles $N_{\text{part}}$ are assumed to verify the following coupled equations:

$$\begin{cases} d\gamma/dt = \gamma_0 + (f-g)\gamma - g_0 N\gamma \\ dN_{\text{part}}/dt = (a - bN_{\text{part}})\gamma \end{cases} \tag{A.12}$$

where $a$, $b$, $f$, $g$, $g_0$ are empirical constants and, $\gamma_0 = \Gamma_0 e^{-E_a/RT}$ corresponds to the spontaneous production rate of active particles which depends on temperature through an Arrhenius law. In their studies, Tesner el al. showed that keeping almost constant the parameters $a$, $b$, $f$, $g$, $g_0$ and adjusting the value of $\Gamma_0$ and the activation energy $E_a$, the model was able to correctly reproduce the soot evolution in laminar co-flow diffusion flames of the different studied hydrocarbon/hydrogen flames.

Further developments extended this model in oder to generalize the approach accounting for the $C/H$ ratio of the burning hydrocarbon (Magnussen 1989), but also accounting for diverse flame parameters (such as the Reynolds number in turbulent configurations) (Lopez-Parra and Turan 2007).

#### A.2.1.2 Moss model

Moss et al. (1989) proposed a two-equation model describing the nucleation, coagulation and surface growth processes. Soot mass fraction $Y_s = \rho_s f_V/\rho$ and particles number density concentration $m_N = N_{\text{part}}/\rho$ are assumed to follow the corresponding transport equations:

$$\begin{aligned} \nabla\cdot(\rho\,(\mathbf{u}+\mathbf{v_T})\,Y_s) &= \underbrace{\gamma(Z)m_N}_{\text{surf. growth}} + \underbrace{\delta(Z)}_{\text{nucleation}} \\ \nabla\cdot(\rho\,(\mathbf{u}+\mathbf{v_T})\,m_N) &= \underbrace{\alpha(Z)}_{\text{nucleation}} - \underbrace{\beta(Z)m_N^2}_{\text{coagulation}} \end{aligned} \tag{A.13}$$

where $\alpha(Z)$, $\beta(Z)$, $\gamma(Z)$ and $\delta(Z)$ depend on the local mixture fraction $Z$. They are expressed as:

$$\begin{aligned} \alpha &= C_\alpha \rho^2 T^{1/2} X_c \exp\left(-T_\alpha/T\right) \ ; \quad \beta = C_\beta T^{1/2} \\ \gamma &= C_\gamma \rho^2 T^{1/2} X_c \exp\left(-T_\gamma/T\right) \ ; \quad \delta = C_\delta \alpha \end{aligned} \tag{A.14}$$

where $X_c$ is the fuel mole fraction. $C_\alpha$, $C_\beta$, $C_\gamma$ and $C_\delta$ are empirical constants fitted as well as activation temperatures $T_\alpha$ and $T_\gamma$ based on the experimental results.

Using this model and fitting the numerical constants, Moss et al. (1989) have shown that a correct prediction of soot volume fraction evolution was achievable but since the oxidation phenomena is not taken into account in this model, it fails to describe soot volume fraction decreasing due to this process.

#### A.2.1.3 Kennedy model

In their work, Kennedy et al. (1990) proposed a two-equation simple model that is able to reproduce reasonably well the evolution of soot volume fraction and soot particles number density in a laminar ethylene/air co-flow diffusion flame, experimentally studied by Santoro et al. (1983). The following stationary equations for soot mass fraction $Y_s$ and particles number density concentration $m_N$ are solved:

$$\begin{aligned} \nabla \cdot \left(\rho \left(\mathbf{u} + \mathbf{v_T}\right) Y_s \ \right) &= \nabla \cdot \left(\rho D_s \ \nabla Y_s\right) + \rho\dot{\omega_n} + \rho\dot{\omega_g} - \rho\dot{\omega_o} \\ \nabla \cdot \left(\rho \left(\mathbf{u} + \mathbf{v_T}\right) m_N\right) &= \nabla \cdot \left(\rho D_s \ \nabla m_N\right) + \rho\dot{\omega_i} - \rho\dot{\omega_c} \end{aligned} \tag{A.15}$$

where:

- $\dot{\omega_n}$, $\dot{\omega_g}$ and $\dot{\omega_o}$ are the rates of soot volume formed by nucleation and surface growth and removed by oxidation, respectively.
- $\dot{\omega_i}$ is the particle inception rate and $\dot{\omega_c}$ is the particle coagulation rate.

In this model, $\dot{\omega_n}$ and $\dot{\omega_i}$ are assumed constant, whereas $\dot{\omega_g}$ and $\dot{\omega_o}$ are expressed as a function of the soot particles surface density (estimated equal to $f_V^{2/3}$) and a correction function depending on the local mixture fraction. $\dot{\omega_c}$ is expressed through the Smoluchowski equation assuming a monodisperse aerosol.

Comparing the results with experimental measurements, Kennedy et al. showed that by adjusting adequatly the mixture fraction dependent correction functions of the surface growth and oxidation source terms, they were able to reproduce well the soot volume fraction evolution on such laminar diffusion flame.

#### A.2.1.4 Said model

The model proposed by Said et al. (1997) consists on two equations. The first one describes the behavior of an intermediate species $I$, which derives from

the fuel, and can be transformed into soot if not oxidized previously. $I$ is then created by fuel decomposition, and destroyed by oxidation and by soot formation. The evolution of this intermediate species mass fraction $Y_I$ and of the soot mass fraction $Y_s$ is described through the following equations:

$$\begin{aligned}\frac{DY_I}{Dt} &= k_A Y_{\text{fuel}} Y_{\text{ox}}^{\alpha} \exp\left(-T_{A1}/T\right) - k_B\ Y_I Y_{\text{ox}}^{\beta} \exp\left(-T_{A2}/T\right) - k_I(T) Y_I \\ \frac{DY_s}{Dt} &= k_s(T) Y_I - \frac{k_{\text{ox}}}{\rho_s d_s} Y_{\text{ox}} Y_s P T^{-1/2} \exp\left(-T_{A3}/T\right)\end{aligned} \tag{A.16}$$

where $Y_{\text{fuel}}$ and $Y_{\text{ox}}$ are respectively the mass fractions of fuel and oxidant species, $P$ corresponds to the pressure. The other parameters are constants, fitted based on experimental results.

This model has been coupled with the Borghi Euler-Lagrange approach (Borghi 1988) for the modeling of turbulence interactions and applied for the simulation of both laminar and turbulent diffusion configuration with good predictions.

#### A.2.1.5 Zhubrin model

The model proposed by Zhubrin (2009) is different from the others as it is based only on algebraic equations for the prediction of soot emissions in flames. Based on atoms conservations principles, the model predicts the local amount of soot as a function of the number $x$ and $y$ of fuel carbon and hydrogen atoms, respectively, and the local mixture fraction. An adaptation of the algebraic relations for four identified zones in combustion (lean-mixture zone, intermediate zone, fuel-rich zone and sooting zone) has been proposed in order to increase the robustness of the model, and the model has been validated against experimental measurements detailed in Lockwood and Van Niekerk (1995).

### A.2.2 Semi-empirical models

#### A.2.2.1 Leung model

In the semi-empirical model proposed by Leung et al. (1991), later improved by Lindstedt (1994) and Lindstedt and Louloudi (2005), the soot mass fraction $Y_s$ and the particles number density concentration $m_N$ are modeled through the following transport equations:

$$
\begin{aligned}
\frac{\partial \rho m_N}{\partial t} \quad &+ \ \nabla \cdot (\rho(\mathbf{u}+\mathbf{v_T})m_N) = \underbrace{\frac{2}{C_{\min}} N_A k_1(T)\ [\mathrm{C_2H_2}]}_{\text{nucleation}} \\
&\underbrace{- 2C_a \left(\frac{6M_\mathrm{C}}{\pi\rho_s}\right)^{1/6} \left(\frac{6k_bT}{\rho_s}\right)^{1/2} (\rho m_N)^{11/6} \left(\frac{\rho Y_s}{\rho_s}\right)}_{\text{coagulation}} \\
\frac{\partial \rho Y_s}{\partial t} \quad &+ \ \nabla \cdot (\rho(\mathbf{u}+\mathbf{v_T})Y_s) = \underbrace{k_1(T)[\mathrm{C_2H_2}]W_\mathrm{C}}_{\text{nucleation}} \\
&+ \underbrace{k_2(T)W_{\mathrm{C_2H_2}} f(S) W_\mathrm{C}}_{\text{surf. growth}} - \underbrace{(k_3(T)[\mathrm{O_2}] + k_4(T)X_\mathrm{OH})SW_\mathrm{C}}_{\text{oxidation}}
\end{aligned}
\tag{A.17}
$$

where $C_a$ and $C_{\min}$ are constants of the model and $W_\mathrm{C}$ and $W_{\mathrm{C_2H_2}}$ correspond to the molar weight of one carbon and acetylene molecule respectively.

Each reaction rate $k_i(T)$ is expressed through an Arrhenius law: $k_i = A_i T^{\beta_i} e^{-T_i/T}$. For the surface growth and oxidation source terms in the soot mass fraction equation, $S$ corresponds to the total soot surface per unit volume of gas, and is evaluated from a monodisperse spherical soot particles assumption: $S = (\rho m_N)\pi d_p^2$ with $d_p$ the mean soot particle diameter evaluated as: $d_p = 6/\pi(Y_s/(\rho_s m_N))^{1/3}$. Finally, the function $f(S)$ in the surface growth term is proposed in order to integrate aging effects that can lead to a decay of soot surface reactivity and is modeled as: $f(S) = \sqrt{S}$.

The model differs from the model proposed by Brookes and Moss (1999) from the values of the empirical constants and by the fact that $f(S)$ varies as a square root function of the total soot surface whereas Brookes and Moss (1999) propose a linear dependency.

Initially, in the first model proposed by Leung et al. (1991), acetylene was considered as the precursor for soot particles nucleation (leading to the nucleation term in Eq. (A.17)). In the improvements done by Lindstedt (1994), the benzene ($A_1$) has been considered as the precursor of soot nucleation, enabling to validate the model in propane/air and ethylene/air counterflow diffusion flames without modifications of the model.

Due to its relative low cost and its easy coupling with turbulence models, while being based on an exhaustive description of the processes involved in soot production, this model is largely used in the modeling of sooting turbulent flames.

### A.2.2.2 Brookes and Moss model

The model proposed by Brookes and Moss (1999) is an improvement of the empirical model of Moss et al. (1989). It is based on a two-equation model where the soot particles number density $N_{\text{part}}$ and the soot mass fraction $Y_s$ are modeled through the following transport equations:

$$\begin{aligned}
\frac{DN_{\text{part}}}{Dt} &= \underbrace{aN_A\left(\frac{X_{C_2H_2}P}{RT}\right)^l e^{-21100/T}}_{\text{nucleation}} - \underbrace{\left(\frac{24RT}{\rho_s N_A}\right)^{1/2} d_p^{1/2} N_{\text{part}}^2}_{\text{coagulation}} \\
\frac{D(\rho Y_s)}{Dt} &= \underbrace{W_P\ a\left(\frac{X_{C_2H_2}P}{RT}\right)^l e^{-21100/T}}_{\text{nucleation}} \\
&\quad + \underbrace{b\left(\frac{X_{C_2H_2}P}{RT}\right)^m e^{-12100/T}\cdot\left[(\pi N_{\text{part}})^{1/3}\left(\frac{6M}{\rho_s}\right)^{2/3}\right]^\alpha}_{\text{surf. growth}} \\
&\quad - \underbrace{4.2325\frac{X_{OH}P}{RT}\sqrt{T}(\pi N_{\text{part}})^{1/3}(6M/\rho_s)^{2/3}}_{\text{oxidation}}
\end{aligned} \tag{A.18}$$

where $a$, $l$, $b$, $m$ and $\alpha$ are model constants. $W_P$ corresponds to the molar weight of an incipient soot particle, assumed to be composed of 12 carbon atoms in this model version. $d_p$ corresponds to the mean diameter of soot particle calculated as $d_p = (6M/(\pi N_{\text{part}}))^{1/3}$. $X_{C_2H_2}$ and $X_{OH}$ correspond respectively to the acetylene and hydroxyl radical concentrations.

It differs from the initial version of the model as it includes oxidation phenomena modeling, but also by the fact that nucleation and surface growth are dependent on the acetylene concentration and not the fuel one. The number of active sites available at a soot particle surface is also modeled as a linear function of the soot particles surface. This latter dependency is verified by comparison with experimental results. Finally, a dependence of the source terms with the pressure is introduced.

This model is employed for the simulation of a methane-air jet turbulent diffusion flame at elevated pressure and good results are obtained (Brookes and Moss 1999).

## A.2.3 Kinetic models

Richter et al. (2005) proposed a detailed kinetic modeling of soot particles formation based on:

- a detailed gas kinetic scheme for the prediction of soot gaseous precursors (PAH) up to coronene ($A_7$) with 275 species and 1102 elementary

reactions,

- 20 classes of soot particles size, called **"BINs"**, which are part of the global kinetic mechanism. For each class of BIN, surface growth, oxidation and coagulation phenomena are modeled through equivalent solid phase reactions. Nucleation is modeled through reactions leading to the formation of the first BIN (BIN1). For BINs, a total of 5552 reactions describes particle growth and dynamics.

This model has been validated for prediction of soot formation in premixed benzene/oxygen/argon premixed burner stabilized flames (Richter et al. 2005).

A similar approach, proposed by Saggese et al. (2015) has been developed and validated for the description of the PSD in laminar ethylene/oxygen/argon flames. In this work, the model differs from the one proposed initially by Richter et al. (2005) by taking into account the fractal behavior of soot particles for BINs corresponding to a diameter higher than 13 nm.

### A.2.4 Methods of moments

#### A.2.4.1 DQMOM

The Direct Quadrature Method of moments (Marchisio and Fox 2005; Blanquart and Pitsch 2009) closure of the source term is accomplished by approximating the PSD by a series of delta functions. For each couple $(x, y)$, the moment $M_{x,y}^{\mathrm{DQMOM}}$ is given by:

$$M_{x,y}^{\mathrm{DQMOM}} = \sum_{k=1}^{P} N_k V_k^x S_k^y \tag{A.19}$$

where $N_k$ are the weights of the delta functions and $V_k$ and $S_k$ are the abscissas of the delta functions in the bi-variate state-space. $P$ is the total number of delta functions used in the approximation.

This method is derived from the original Quadrature Method of Moments (QMOM) (McGraw 1997; Marchisio et al. 2003) where the PSD is also approximated by a series of delta functions, and the moments are approximated by Gauss quadrature. The weights and locations of the delta functions are determined through the product-difference algorithm (Gordon 1968), which can be costly and is not applicable in the case of bi-variate moments. To overcome this difficulty, in DQMOM, transport equations are solved directly for the weights and locations of the delta functions. Then, a linear system is inverted in order to retrieve the source terms for the transport equations of the weights and locations of the delta functions from the source terms of the classical moment transport equations. The difficulty of this method arises when two or more delta functions are too closely spaced, because of the ill-conditioning of the linear system.

#### A.2.4.2 MOMIC

In the Method of Moments with Interpolative Closure (MOMIC) (Frenklach and Harris 1987; Frenklach 2002; Mueller et al. 2009b; Selvaraj et al. 2016), the closure of the source terms is accomplished through polynomial interpolations of the logarithm of the known solved moments. For a bi-variate volume-surface description of the particles, the interpolation is given by:

$$M_{x,y}^{\mathrm{MOMIC}} = \exp\left(\sum_{r=0}^{R}\sum_{k=0}^{r} a_{r,k} x^k y^{r-k}\right) \tag{A.20}$$

where $R$ is the order of the polynomial interpolation. $a_{r,k}$ are constants to be determined from the set of known moments by taking the logarithm of Eq. (A.20) and inverting the obtained linear system. These parameters can then pre-computed *a priori* and stored to reduce the computational cost. However, the number of moments to solve is fixed by the chosen order $R$, and the number of additional moments to compute highly increases with the value of $R$.

#### A.2.4.3 HMOM

Generally, in rich flames presenting soot, the PSD is bimodal because of the persistent nucleation. The first mode corresponds to the small nucleated particles whereas the second mode corresponds to the larger particles. Mueller et al. (2009a) has studied the capability of the previous methods to capture this soot PSD particular shape. In particular, they have shown that:

- MOMIC is always well-defined but it fails to capture the influence of small particles in the prediction of the mean quantities of the distribution. Therefore, the bimodal shape is not well retrieved with this closure,
- DQMOM retrieves naturally the bimodal PSD with a virtually first fixed mode at the nucleated size. However, the linear system to invert is often ill-conditioned, which makes the method impractical.

The authors proposed a new methodology: the hybrid method of moments (HMOM) which combines the two previous methods: the MOMIC standard interpolation in addition of a fixed delta function at the nucleated size. The corresponding moments $M_{x,y}$ are closed as:

$$M_{x,y}^{\mathrm{HMOM}} = N_0 V_0^x S_0^y + \exp\left(\sum_{r=0}^{R}\sum_{k=0}^{r} a_{r,k} x^k y^{r-k}\right) \tag{A.21}$$

where $N_0$ is the weight of the delta function, which is transported, and $V_0$ and $S_0$ are the fixed location of the peak corresponding to the nucleated particles.

Even if it does not provide access to a detailed PSD, this method is largely used for the simulation of sooting turbulent flames, because of its reasonable cost and robustness while conserving the capacity of capturing the bimodality of the particle size distribution.

#### A.2.4.4 Other models

Other models based on the same principle of the DQMOM have been investigated in the literature. Among them, one may cite:

- The Extended Quadrature Method of Moments (EQMOM) (Yuan et al. 2012; Madadi-Kandjani and Passalacqua 2015; Nguyen et al. 2016). In this model, different types of kernel are used instead of simple Dirac functions, as for instance, log-normal kernel density functions which are well suited for describing the PSD (the support of the PSD being $\mathbb{R}_0^+$) or beta kernel functions if the support is bounded (i.e. the minimum and maximum soot volume particle are well defined). These methods require more sophisticated inverting methods but can largely decrease the errors in closure of source terms with a reduced set of moments. They enable also to reconstruct the particle size distribution. A variant of these methods, the CQMOM (Yuan and Fox 2011) is expressed as a function of bi-variate moments but does not enable to reconstruct the PSD.
- The Extended Conditional Quadrature Method of Moments (ECQMOM) which has been proposed by Salenbauch et al. (2015) by combining EQMOM and CQMOM methods in an elegant way. The surface of a soot particle is represented through a Dirac delta function conditioned by the kernels and weights of the EQMOM on the volume space, enabling then to have detailed information of the particle size distribution.

### A.2.5 Stochastic methods

In their work, Mitchell and Frenklach (1998); Balthasar and Kraft (2003); Balthasar and Frenklach (2005) used stochastic Monte Carlo algorithms in order to solve the soot population balance equation. However, in these works, when comparing with experimental measurements, the gas phase chemistry was solved separately in a deterministic classical way and the corresponding chemical species profiles were used as inputs of the stochastic soot solver. Therefore, no retroaction of soot particles evolution on the gas phase through surface growth and oxidation processes were taken into account.

Celnik et al. (2007) was the first to propose a stochastic Monte Carlo approach to predict soot particles evolution coupled with an ODE solver for the gas phase. An operator splitting technique is used to separately solve the two parts of the coupled problem. The corresponding model has been validated for soot predictions in perfectly stirred reactors (PSR) and plug-flow reactors (PFR).

# Appendix B

# Soot sectional model implementation validation in AVBP

**Contents**



## B.1 Validation of the laminar soot sectional model in AVBP and comparison with REGATH solutions

For the validation case of the sectional model, a 1-D premixed $C_2H_4$/air flame with an equivalence ration of $\phi = 2.1$ is solved with the REGATH code. The inlet temperature is set to 298 K.

The FPI tabulation (Gicquel et al. 2000) technique is used in order to generate the table, and the progress variable defined as $Y_C = Y_{\text{CO}} + Y_{\text{CO}_2}$ is used. Unity lewis model is used for all the species diffusion coefficients. The KM2 mechanism (Wang et al. 2013) is used.

For the tabulation, the consumption of PAHs by dimerization is taken into account and the corresponding values of the PAHs are tabulated and used in AVBP for the calculation of the number of dimers, and consequently, the nucleation and condensation source terms. In the same way, the mass fractions of all the species involved in the HACA-RC growth mechanism are tabulated and used then to compute the corresponding source terms of surface growth and oxidation phenomena.

Figure B.1 presents a comparison between AVBP and REGATH calculations. The REGATH calculation presents 2690 points, whereas two meshes have been employed in AVBP: the first one with 2690 corresponds to exactly the same mesh as the one used in REGATH, and the second one with 1340 points represents a mesh with two times less points. For all calculations 50 sections have been used for the discretization of the PSD and both calculations in AVBP have been done using the TTGC convective scheme.

For the gaseous phase, profiles of temperature, progress variable $Y_C$ and hear release rate are compared. For both meshes in AVBP, the values obtained in REGATH are well retrieved.

For the solid phase, profiles of the soot volume fraction $f_V$, the particles number density $N_{\text{part}}$, soot mass fractions of the first ($Y_{s,1}$), the tenth ($Y_{s,10}$) and the twentieth ($Y_{s,20}$) section are compared. It can be observed that the results obtained by the REGATH code are well retrieved for the exact same mesh as the one used in REGATH, which validates the implementation, but some differences appear with the coarser mesh.

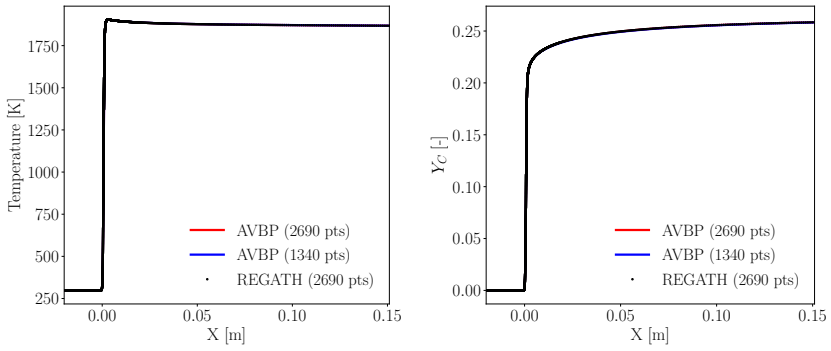


(a) Temperature




(b) Progress variable $Y_C$

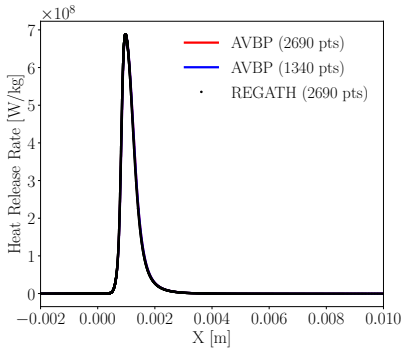


(c) Heat Release Rate

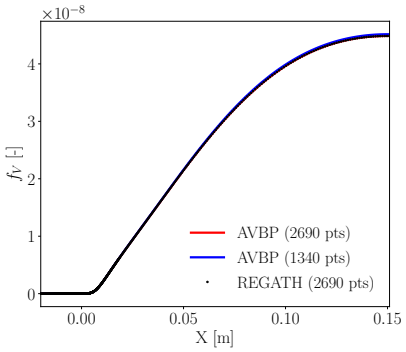


(d) Soot volume fraction

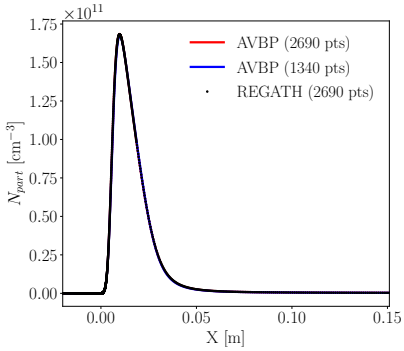


(e) Particles number density

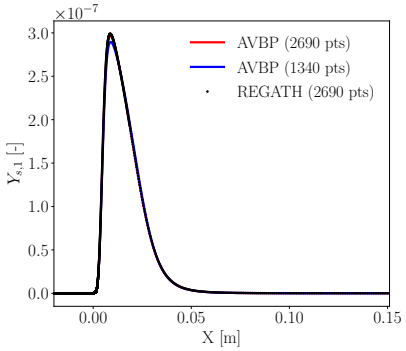


(f) Fisrt section mass fraction

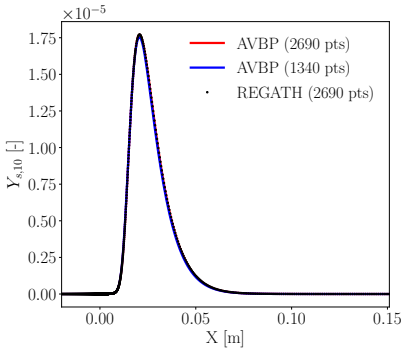


(g) Tenth section mass fraction

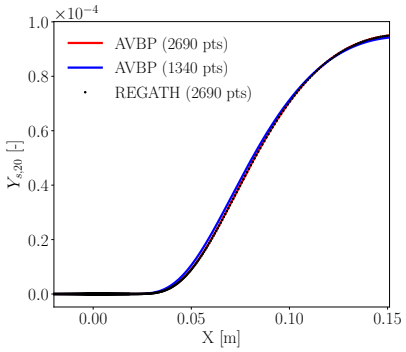


(h) Twentieth section mass fraction

**Figure B.1:** *Comparison of profiles of temperature, progress variable, heat release rate, soot volume fraction, particles number density and soot section mass fractions between REGATH and AVBP calculations.*

Figure B.2 presents for the same calculations the comparison of the obtained PSD at four different positions in the flame: $x = 0.04$ mm, $x = 0.08$ mm, $x = 0.12$ mm and $x = 0.16$ mm. Again, it can be observed that the PSD obtained by REGATH are well retrieved when using the same mesh in AVBP. Some differences appear for the coarser mesh used in AVBP.

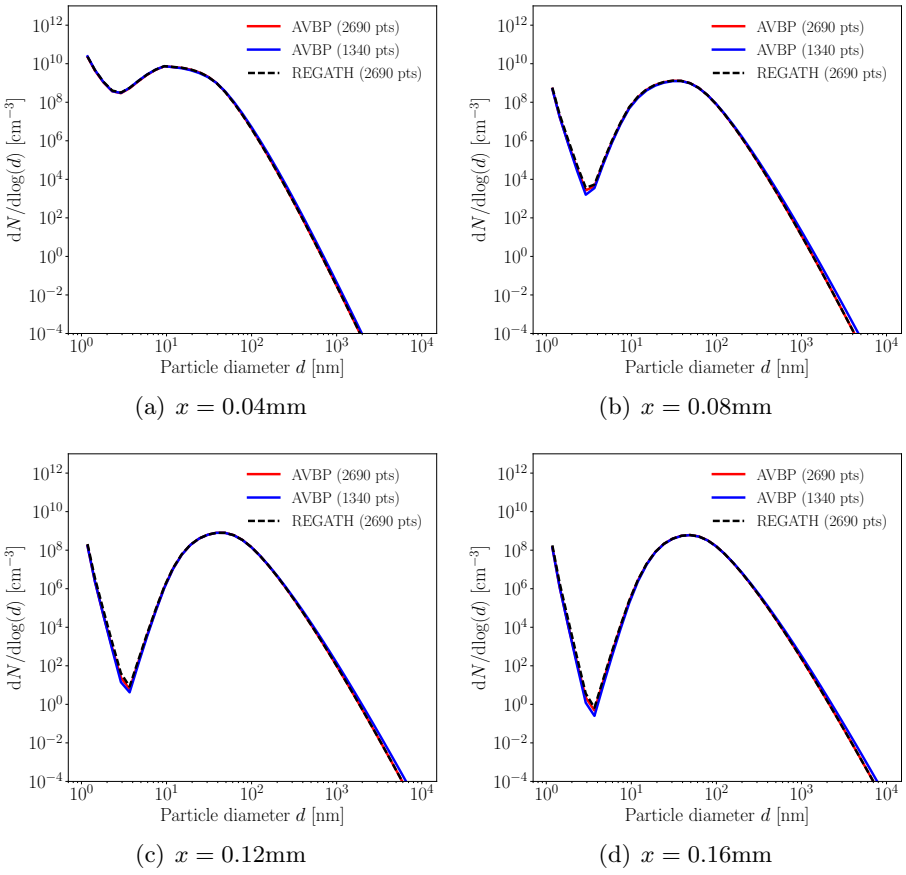


(a) $x = 0.04$mm (b) $x = 0.08$mm

(c) $x = 0.12$mm (d) $x = 0.16$mm

**Figure B.2:** *Comparison of obtained particles size distributions between AVBP and REGATH calculations at four different positions in the flame.*

## B.2 Implementation of lumped PAHs

In this section, the implementation and validation of the models for lumped PAHs developed respectively by Mueller and Pitsch (2012) and Xuan and Blanquart (2014) are presented. This latter model has not been used however in 3-D calculations because of its increase of computational cost, but increases accuracy of PAHs dynamics description compared with the former one.

### B.2.1 Global lumped PAH

In this model developed by Mueller and Pitsch (2012), a lumped PAH representative of all the PAHs involved in nucleation process is considered. Its mass fraction $Y_{\mathrm{PAH}}$ is obtained solving the following transport equation:

$$\frac{\partial \rho Y_{\mathrm{PAH}}}{\partial t} + \frac{\partial \rho u_i Y_{\mathrm{PAH}}}{\partial x_i} = \frac{\partial}{\partial x_i}\left(\rho D_{\mathrm{PAH}} \frac{\partial Y_{\mathrm{PAH}}}{\partial x_i}\right) + \dot{m}_{\mathrm{PAH}} \tag{B.1}$$

where $D_{\mathrm{PAH}}$ is the considered diffusion coefficient for the lumped PAH and $\dot{m}_{\mathrm{PAH}}$ its source term taking into account gaseous production, gaseous consumption and consumption by the dimerization process.
Then, the corresponding equation solved in the context of turbulence becomes:

$$\begin{aligned} &\frac{\partial \overline{\rho}\widetilde{Y_{\mathrm{PAH}}}}{\partial t} + \frac{\partial \overline{\rho}\widetilde{u_i}\widetilde{Y_{\mathrm{PAH}}}}{\partial x_i} \\ &= \frac{\partial}{\partial x_i}\left(\overline{\rho}\ \widetilde{u_i}\widetilde{Y_{\mathrm{PAH}}} - \overline{\rho u_i}\widetilde{Y_{\mathrm{PAH}}}\right) + \frac{\partial}{\partial x_i}\left(\overline{\rho}\ \overline{D_{\mathrm{PAH}}}\frac{\partial \widetilde{Y_{\mathrm{PAH}}}}{\partial x_i}\right) + \overline{\dot{m}_{\mathrm{PAH}}} \end{aligned} \tag{B.2}$$

The model is based on a relaxation model for the PAH source term. Indeed, as presented in Chapter 2, PAHs production and consumption have their own dynamics which can be different from that of the flame and its corresponding manifolds ($\widetilde{Z}$,$\widetilde{Y_C}$,...). To take into account this behavior, the source term is relaxed based on the current value of the PAH mass fraction $\widetilde{Y_{\mathrm{PAH}}}$. Then, as the PAH gaseous consumption scales linearly with its concentration, and the PAH consumption by dimerization process scales quadratically with its concentration, the filtered $\overline{\dot{m}_{\mathrm{PAH}}}$ source term is written as:

$$\overline{\dot{m}_{\mathrm{PAH}}} = \overline{\dot{m}_+}^{\mathrm{tab}} + \overline{\dot{m}_-}^{\mathrm{tab}}\left(\frac{\widetilde{Y_{\mathrm{PAH}}}}{\widetilde{Y_{\mathrm{PAH}}}^{\mathrm{tab}}}\right) + \overline{\dot{m}_D}^{\mathrm{tab}}\left(\frac{\widetilde{Y_{\mathrm{PAH}}}}{\widetilde{Y_{\mathrm{PAH}}}^{\mathrm{tab}}}\right)^2 \tag{B.3}$$

where $\overline{\dot{m}_+}^{\mathrm{tab}}$, $\overline{\dot{m}_-}^{\mathrm{tab}}$ and $\overline{\dot{m}_D}^{\mathrm{tab}}$ correspond respectively to the tabulated PAH gaseous production, gaseous consumption and dimerization consumption source terms. $\widetilde{Y}^{\mathrm{tab}}_{\mathrm{PAH}}$ corresponds to the tabulated value of the PAH.

Here, the implementation of this model is validated through the same 1-D flame used in Section B.1 but in this case a lumped PAH is used and the nucleation and condensation processes are calculated through the value of this lumped PAH. Unity lewis assumption is used for all the gaseous species.
In this case, as the flow is steady and laminar, the source term follows its tabulated value:

$$\dot{m}_{\mathrm{PAH}} = \dot{m}_+^{\mathrm{tab}} + \dot{m}_-^{\mathrm{tab}} + \dot{m}_D^{\mathrm{tab}} \tag{B.4}$$

and the transported value must be equal to its transported one: $Y_{\mathrm{PAH}} = Y^{\mathrm{tab}}_{\mathrm{PAH}}$.

Figure B.3 presents a comparison of the transported lumped PAH with its tabulated value. The two results are identical, validating the implementation of the approach.

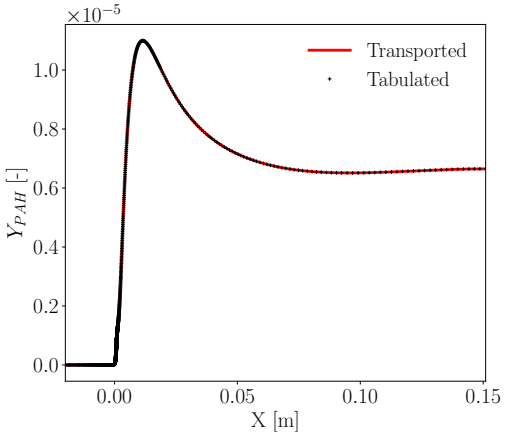


**Figure B.3:** *Comparison of the transported PAH value and tabulated PAH value for the global lumped PAH*

### B.2.2 Multiple lumped PAHs

Here, the validation of the implementation of the approach developed by Xuan and Blanquart (2014) is presented. In this study, Xuan et al. have considered that each class of PAH has its own dynamic, and then, the transport of each PAH class is needed in order to retrieve the good dynamics of their production in turbulent configurations.

Here, we have generalized this approach and according to the KM2 kinetic scheme, the following steps of PAHs production are considered, from the smaller to the bigger PAH:

$$\begin{aligned} &A_1 \leftrightarrow A_2 \leftrightarrow A_3 \leftrightarrow A_4 \\ &\leftrightarrow \text{BAPYR } (A_5) \leftrightarrow \text{BGHIPER } (A_6) \leftrightarrow \text{CORONEN}(A_7) \end{aligned} \tag{B.5}$$

Following Xuan and Blanquart (2014), for each $\text{PAH}_j$, the following transport equation is solved for its mass fraction $\widetilde{Y_{\text{PAH}_j}}$:

$$\begin{aligned} &\frac{\overline{\rho}\widetilde{Y_{\text{PAH}_j}}}{\partial t} + \frac{\partial \overline{\rho}\widetilde{u_i}\widetilde{Y_{\text{PAH}_j}}}{\partial x_i} \\ &= \frac{\partial}{\partial x_i}\left(\overline{\rho}\,\widetilde{u_i}\widetilde{Y_{\text{PAH}_j}} - \overline{\rho}\widetilde{u_i Y_{\text{PAH}_j}}\right) + \frac{\partial}{\partial x_i}\left(\overline{\rho}\,\overline{D_{\text{PAH}_j}}\frac{\partial \widetilde{Y_{\text{PAH}_j}}}{\partial x_i}\right) + \overline{\dot{m}_{\text{PAH}_j}} \end{aligned} \tag{B.6}$$

where $D_{\text{PAH}_j}$ corresponds to the diffusion coefficient of the species $\text{PAH}_j$ and

$\dot{m}_{\mathrm{PAH}_j}$ corresponds to its source term.

In the considered set of PAHs, and for the proposed sectional model, the first PAHs ($A_1$, $A_2$ and $A_3$) are not involved in the dimerization process, and only gaseous consumption and gaseous production source terms have to be considered for the calculation of their source term. For the other PAHs, dimerization process is included in the calculation of the global source term.

Moreover, as all these PAHs are transported, the production of each class of $\mathrm{PAH}_j$ is here corrected taking into account the transported value of the smaller previous $\mathrm{PAH}_{j-1}$ according to the scheme of PAHs production (see B.5). Then, the source term for each PAH writes:

- For the first PAH ($A_1$):

$$\overline{\dot{m}_{A_1}} = \overline{\dot{m}_{A_1,+}}^{\mathrm{tab}} + \overline{\dot{m}_{-}}^{\mathrm{tab}} \left( \frac{\widetilde{Y_{A_1}}}{\widetilde{Y_{A_1}}^{\mathrm{tab}}} \right) \tag{B.7}$$

- For the other PAHs for which no inception is considered ($A_2$ and $A_3$):

$$\overline{\dot{m}_{\mathrm{PAH}_j}} = \overline{\dot{m}_{\mathrm{PAH}_j,+}}^{\mathrm{tab}} \left( \frac{\widetilde{Y_{\mathrm{PAH}_{j-1}}}}{\widetilde{Y_{\mathrm{PAH}_{j-1}}}^{\mathrm{tab}}} \right) + \overline{\dot{m}_{-}}^{\mathrm{tab}} \left( \frac{\widetilde{Y_{\mathrm{PAH}_j}}}{\widetilde{Y_{\mathrm{PAH}_j}}^{\mathrm{tab}}} \right) \tag{B.8}$$

- Finally, for the other PAHs for which inception is considered ($A_4$, $A_5$, $A_6$ and $A_7$:

$$\begin{aligned} \overline{\dot{m}_{\mathrm{PAH}_j}} = \overline{\dot{m}_{\mathrm{PAH}_j,+}}^{\mathrm{tab}} \left( \frac{\widetilde{Y_{\mathrm{PAH}_{j-1}}}}{\widetilde{Y_{\mathrm{PAH}_{j-1}}}^{\mathrm{tab}}} \right) + \overline{\dot{m}_{-}}^{\mathrm{tab}} \left( \frac{\widetilde{Y_{\mathrm{PAH}_j}}}{\widetilde{Y_{\mathrm{PAH}_j}}^{\mathrm{tab}}} \right) \\ + \overline{\dot{m}_{D}}^{\mathrm{tab}} \left( \frac{\widetilde{Y_{\mathrm{PAH}_j}}}{\widetilde{Y_{\mathrm{PAH}_j}}^{\mathrm{tab}}} \right)^2 \end{aligned} \tag{B.9}$$

In laminar configurations, as for the global lumped PAH case, the corresponding source terms are respectively:

- For a $\mathrm{PAH}_j$ with no inception considered:

$$\dot{m}_{\mathrm{PAH}_j} = \dot{m}^{\mathrm{tab}}_{\mathrm{PAH}_j,+} + \dot{m}^{\mathrm{tab}}_{\mathrm{PAH}_j,-} \tag{B.10}$$

- For a $\mathrm{PAH}_j$ with inception considered:

$$\dot{m}_{\mathrm{PAH}_j} = \dot{m}^{\mathrm{tab}}_{\mathrm{PAH}_j,+} + \dot{m}^{\mathrm{tab}}_{\mathrm{PAH}_j,-} + \dot{m}^{\mathrm{tab}}_{\mathrm{PAH}_j,D} \tag{B.11}$$

And the transported values must be equal to the tabulated ones.

Figure B.4 presents a comparison of the transport of the PAH classes with their tabulated value. The two results are identical, validating the implementation of the approach.

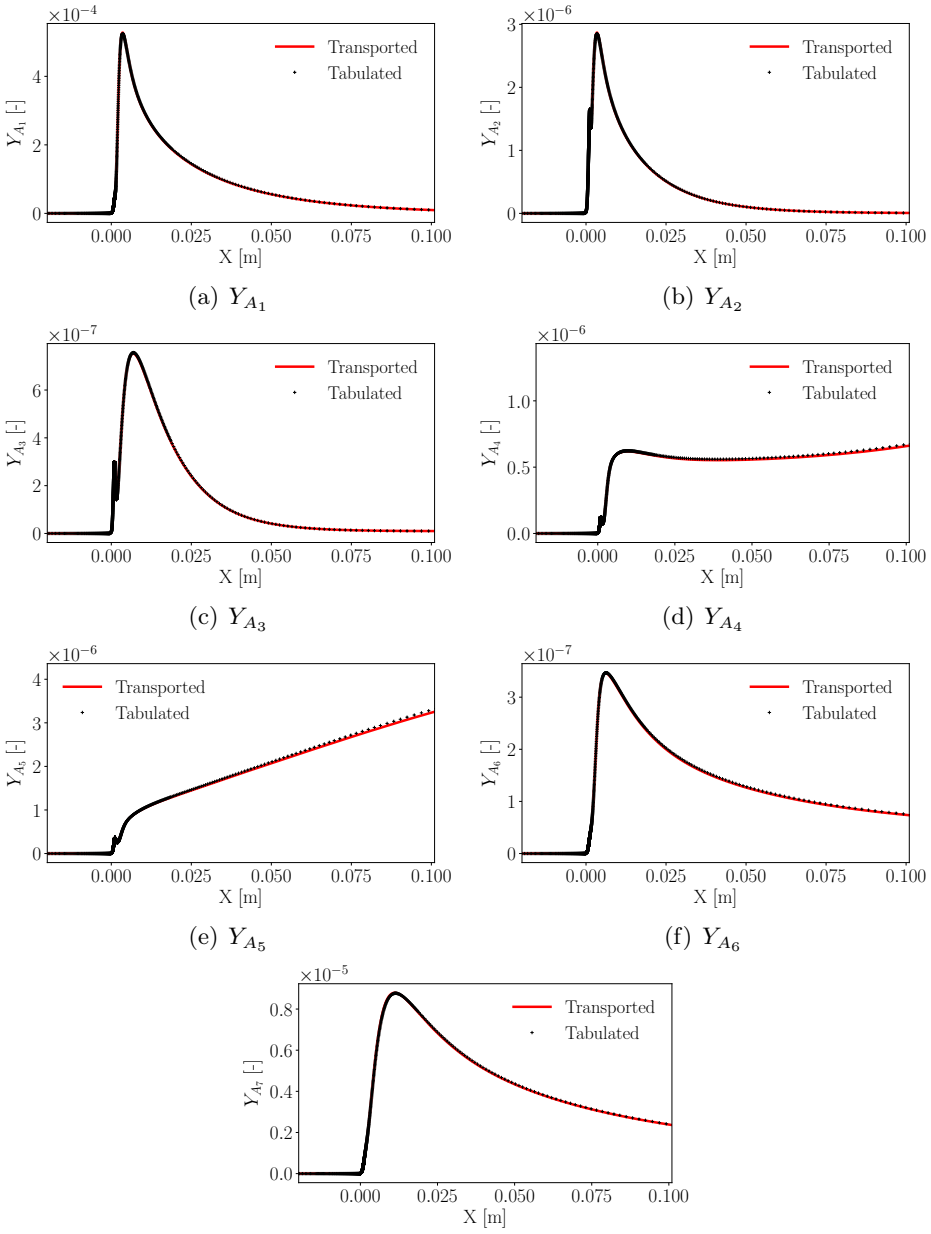


(a) $Y_{A_1}$ (b) $Y_{A_2}$ (c) $Y_{A_3}$ (d) $Y_{A_4}$ (e) $Y_{A_5}$ (f) $Y_{A_6}$ (g) $Y_{A_7}$

**Figure B.4:** *Comparison of the transported PAHs profiles and tabulated PAHs profiles for the multiple lumped PAHs approach*

## B.3 Implementation of the soot subgrid model

### B.3.1 Transport of $N_{\mathbf{part}}$ and $N^2_{part}$

As detailed in Chapter 3, the implemented subgrid model issued from the works of Mueller and Pitsch (2011) is based on the transport of $N_{\text{part}}$ and $N^2_{\text{part}}$. Their laminar transport equations are respectively:

- For $N_{\text{part}}$:

$$\frac{\partial N_{\text{part}}}{\partial t} + \nabla \cdot ((\mathbf{u} + \mathbf{v_T}) N_{\text{part}}) = \dot{N}_{\text{part}} \tag{B.12}$$

  where $\mathbf{v_T}$ is the thermophoretic velocity and $\dot{N}_{\text{part}}$ the particles number density source term expressed as in Eq. (3.37).
- For $N^2_{\text{part}}$:

$$\frac{\partial N^2_{\text{part}}}{\partial t} + \nabla \cdot \left( (\mathbf{u} + \mathbf{v_T}) N^2_{\text{part}} \right) = 2 N_{\text{part}} \dot{N}_{\text{part}} - N^2_{\text{part}} \nabla \cdot (\mathbf{u} + \mathbf{v_T}) \tag{B.13}$$

In fact, in theory, the transport of $N_{\text{part}}$ is not necessary as it can be recomputed from the transported values of each section $Y_{s,i}$, but in order to conserve the same numerical treatment between $N_{\text{part}}$ and $N^2_{\text{part}}$ (specially for the artificial viscosity), their values are also transported.

Figure B.5 presents a comparison of the transported values of $N_{\text{part}}$ and $N^2_{\text{part}}$ with the values computed from the sectional model (i.e. from the values of the $Y_{s,i}$ mass fractions). A good agreement is obtained, validating the transport of these two variables.

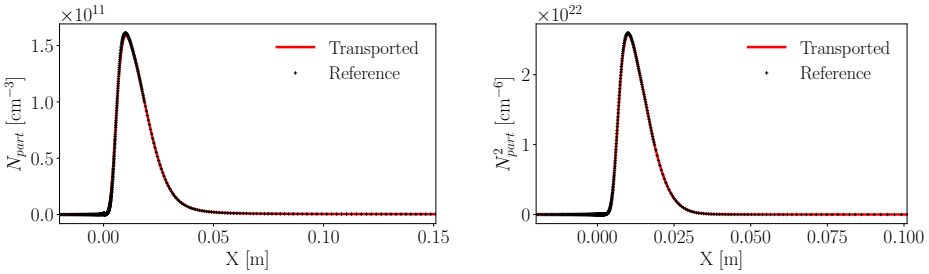


(a) $N_{\text{part}}$ (b) $N^2_{\text{part}}$

**Figure B.5:** *Comparisons of the transported $N_{part}$ and $N^2_{part}$ profiles with the profiles calculated from the sectional variables $Y_{s,i}$ (called "Reference")*

### B.3.2 Definition of the soot subgrid intermittency $\omega$ and calculation of filtered quantities

In a turbulent context, the corresponding filtered equations of $\widetilde{N_{\text{part}}}$ and $\widetilde{N^2_{\text{part}}}$ are respectively:

- For $\overline{N_{\text{part}}}$:

$$\begin{aligned}&\frac{\partial}{\partial t}\left(\overline{N_{\text{part}}}\right)+\nabla\cdot\left(\widetilde{\mathbf{u}}\overline{N_{\text{part}}}\right)\\&=\overline{\rho}\widetilde{\dot{m}_N}+\nabla\cdot\left(-\overline{\mathbf{v_T}N_{\text{part}}}\right)+\nabla\cdot\left(\overline{\rho}\widetilde{\mathbf{u}}\frac{\widetilde{N_{\text{part}}}}{\rho}-\overline{\rho}\mathbf{u}\frac{\widetilde{N_{\text{part}}}}{\rho}\right)\end{aligned}\tag{B.14}$$

- For $\overline{N_{\text{part}}^2}$:

$$\begin{aligned}&\frac{\partial}{\partial t}\left(\overline{N_{\text{part}}^2}\right)+\nabla\cdot\left(\widetilde{\mathbf{u}}\overline{N_{\text{part}}^2}\right)\\&=2\overline{\rho}\widetilde{m_N\dot{N}_{\text{part}}}-\overline{N_{\text{part}}^2\nabla\cdot\mathbf{u}}-\overline{N_{\text{part}}^2\nabla\cdot\mathbf{v_T}}\\&+\nabla\cdot\left(-\overline{\mathbf{v_T}N_{\text{part}}^2}\right)+\nabla\cdot\left(\overline{\rho}\widetilde{\mathbf{u}}\frac{\widetilde{N_{\text{part}}^2}}{\rho}-\overline{\rho}\mathbf{u}\frac{\widetilde{N_{\text{part}}^2}}{\rho}\right)\end{aligned}\tag{B.15}$$

It should be noted that $\overline{N_{\text{part}}^2}\neq\overline{N_{\text{part}}}^2$. The subgrid model developed by Mueller and Pitsch (2011) is based on this difference and the subgrid model parameter $\omega$ is defined as:

$$\omega=1-\frac{\overline{N_{\text{part}}}^2}{\overline{N_{\text{part}}^2}}\tag{B.16}$$

Then, as developed in Chapter 3 (Eq. (3.25)), the value for the sooting mode $\sigma_i^*$ of each quantity $\widetilde{\sigma}_i$ is calculated as:

$$\sigma_i^*=\widetilde{\sigma}_i/(1-\omega)\tag{B.17}$$

From a numerical point of view, and to avoid infinite numbers, a threshold $\epsilon$ has been considered such that:

- If $\omega<1-\epsilon$, the soot subgrid model is active and $\sigma_i^*=\widetilde{\sigma}_i/(1-\omega)$
- If $\omega>1-\epsilon$, which happens when $\frac{\overline{N_{\text{part}}}^2}{\overline{N_{\text{part}}^2}}\approx 0$, it is considered that very few soot particles are present and the subgrid model is not applied: $\sigma_i^*=\widetilde{\sigma}_i$.

The threshold value has been fixed equal to $\epsilon=10^{-3}$.

# Appendix C

# FPV table generation and validation

**Contents**



## C.1 Methodology for the generation of the table in the presented simulations

In the following subsections, the methodology of the generation of the radiation-flamelet progress variable tables used in this work is presented. The curves will correspond to the table used in Chapter 4 where air and fuel are considered at $T_f = 298$K and at atmospheric pressure.

### C.1.1 Generation of flamelets

For the generation of the flamelet database, strain-imposed counterflow non-premixed flames are considered with air and ethylene at $T_f = 298$K and $p = 1$ atm as reactants. Unity lewis diffusion model is used and the KM2 kinetic

scheme is considered (Wang et al. 2013). The continuation technique based on the curvilinear abscissa parametrized by the temperature and the strain rate and proposed by Kee et al. (1989); Nishioka et al. (1996) is used in order to generate the stable and unstable branches of the flamelet databse.

The corresponding so-called "S-curve" presenting the stable and unstable branch is presented in Fig. C.1. The extinction limit $\epsilon^{\text{ext}}$ of the ethylene-air flame is found to be equal to $\epsilon^{\text{ext}} = 1308\text{s}^{-1}$, which is consistent with results found in previous studies (Sarnacki et al. 2012).

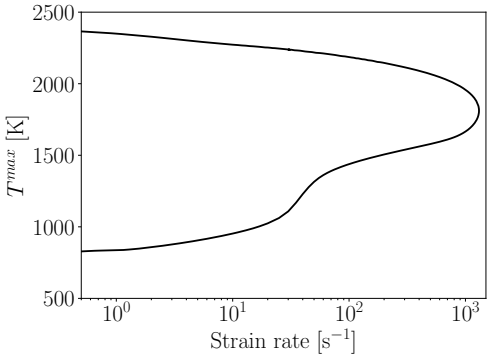


**Figure C.1:** *"S-curve": Evolution of the maximal temperature $T^{max}$ with the flamelet strain rate.*

### C.1.2 Tabulation methodology

For the generation of the FPV table, a progress variable characterizing the progress of reaction must be defined. Generally, this progress variable $Y_C$ is defined as a linear combination of the major products of combustion.

The most common definitions in literature of progress variable have been tested for the set of flamelets obtained from the generation of the $S$-curve and the evolution of these progress variables with the mixture fraction $Z$ for each flamelet is presented Fig. C.2. They correspond respectively to:

- Figure C.2 (a): $Y_C = Y_{H_2O} + Y_{CO_2}$ proposed by Pierce and Moin (2004)
- Figure C.2 (b): $Y_C = Y_{CO} + Y_{CO_2}$ proposed by Fiorina et al. (2003); Fiorina et al. (2005a); Fiorina et al. (2005b)
- Figure C.2 (c): $Y_C = Y_{H_2O} + Y_{CO_2} + Y_{CO} + Y_{H_2}$ proposed by Ihme and Pitsch (2008b)
- Figure C.2 (d): $Y_C = Y_{H_2O}/W_{H_2O} + Y_{CO_2}/W_{CO_2} + Y_{CO}/W_{CO}$ proposed by van Oijen and de Goey (2002).

For all these definitions of the progress variable, and for the chosen kinetic scheme (KM2) with fuel and air both at $T_f = 298\text{K}$ and $p = 1\text{atm}$, it can be observed that there is no bijection between a couple of $(Y_C, Z)$ and the flamelet

database.

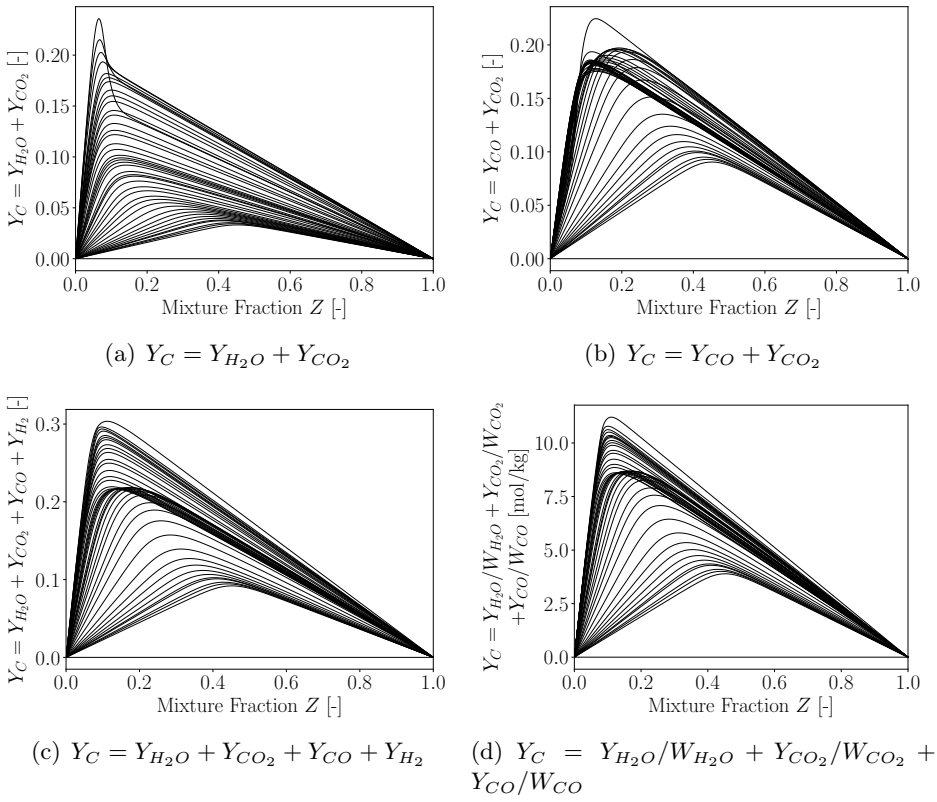


(a) $Y_C = Y_{H_2O} + Y_{CO_2}$

(b) $Y_C = Y_{CO} + Y_{CO_2}$

(c) $Y_C = Y_{H_2O} + Y_{CO_2} + Y_{CO} + Y_{H_2}$

(d) $Y_C = Y_{H_2O}/W_{H_2O} + Y_{CO_2}/W_{CO_2} + Y_{CO}/W_{CO}$

**Figure C.2:** *Evolution of the different definitions of the progress variable $Y_C$ proposed in literature as a function of the mixture fraction $Z$.*

In this work, in order to be able to use this flamelet database obtained from the generation of the $S-curve$, a new progress variable has been proposed:

$$Y_C = \frac{Y_{H_2O}/W_{H_2O} + Y_{CO_2}/W_{CO_2} + Y_{CO}/W_{CO} - 3Y_{CH_4}/W_{CH_4}}{1/W_{H2O} + 1/W_{CO_2} + 1/W_{CO} + 3/W_{CH_4}} \tag{C.1}$$

The addition of $CH_4$ species is justified by the fact that its reactivity has an impact in the unstable branch of the $S-curve$ presented in Fig. C.1. Indeed, it can be observed that around the extinction limit of methane-air flame (which is a at approximatively at $\epsilon = 400\text{s}^{-1}$) an increase of the maximum temperature is observed in the unstable branch due to the reactivity of the $CH_4$-air mixture. This causes the production of combustion products ($CO_2$ and $H_2O$). This behavior justifies the subtraction of the $CH_4$ mass fraction in the progress variable definition in order to conserve a well-defined progress variable, even in the unstable branch.

Figure C.3 shows the evolution of this progress variable $Y_C$ with the mixture fraction $Z$ for each flamelet of the $S-curve$ database. It can be observed that a bijectivity is obtained with the proposed progress variable. Then, each flamelet can be identified by defining the value of the progress variable at a given fixed $Z_0$. This parameter is noted $\Lambda$:

$$\Lambda = Y_C(Z_0) \tag{C.2}$$

Here, $Z_0$ is chosen equal to 0.064. In Fig. C.3, each flamelet is colored according to their corresponding value of $\Lambda$.

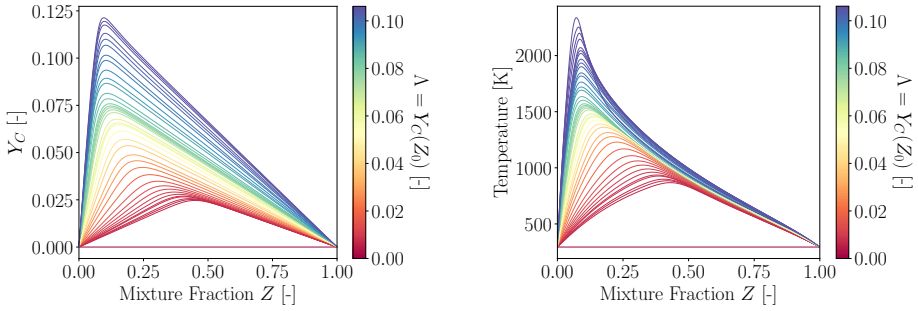


(a) Evolution of $Y_C$ with $Z$ for each flamelet

(b) Evolution of $T$ with $Z$ for each flamelet

**Figure C.3:** *Evolutions of the progress variable ($Y_C$) and temperature ($T$) with the mixture fraction for each flamelet, identified by the parameter $\Lambda$*

### C.1.3 $\beta$-pdf model

As detailed in Chapter 3, a $\beta - pdf$ model is used for the closure of the source term in the $Z$-space. Any filtered quantity $\widetilde{\phi}$ writes:

$$\widetilde{\phi} = \int_0^1 \phi(Z)\widetilde{P}(Z)dZ \tag{C.3}$$

with $\widetilde{P}(Z)$ the probability of finding $Z$, assumed to follow a $\beta$-pdf:

$$\widetilde{P}(Z) = \frac{Z^{\alpha-1}(1-Z)^{\beta-1}dZ}{\int_0^1 Z^{\alpha-1}(1-Z)^{\beta-1}dZ} \tag{C.4}$$

where the parameters $\alpha$ and $\beta$ of the $\beta$-pdf are defined by:

$$\alpha = \widetilde{Z}\left(\frac{1}{S_Z} - 1\right); \quad \beta = \alpha\left(\frac{1}{\widetilde{Z}} - 1\right); \quad S_Z = \frac{Z_v}{\widetilde{Z}(1-\widetilde{Z})} \tag{C.5}$$

with $\widetilde{Z}$ the mass-weighted average of the mixture fraction, $S_Z$ the mixture fraction segregation factor and $Z_v$ the variance of the mixture fraction.

In the implementation used here in the tables generation, for the calculation of each filtered value $\widetilde{\phi}$, the variable $\phi(Z)$ is approximated by a series of quadratic segments. For each interval $n$, $\phi(Z)$ is approximated by a parabola:

$$\text{For } Z \in [Z_n, Z_{n+1}],\ \phi(Z) = a_n + b_n Z + c_n Z^2 \tag{C.6}$$

with $a_n$, $b_n$ and $c_n$, coefficients calculated such that the approximation is correct at each discretization point $Z_n$.

Then, the integration of $\widetilde{\phi}$ on each sub-interval is calculated following the approach of Lien et al. (2009):

$$\begin{aligned}\int_{Z_n}^{Z_{n+1}} (a_n + b_n Z + c_n Z^2)\widetilde{P}(Z)dZ &= a_n \left[I_{Z_{n+1}}(\alpha,\beta) - I_{Z_n}(\alpha,\beta)\right] \\ &+ b_n \frac{B(\alpha+1,\beta)}{B(\alpha,\beta)} \left[I_{Z_{n+1}}(\alpha+1,\beta) - I_{Z_n}(\alpha+1,\beta)\right] \\ &+ c_n \frac{B(\alpha+2,\beta)}{B(\alpha,\beta)} \left[I_{Z_{n+1}}(\alpha+2,\beta) - I_{Z_n}(\alpha+2,\beta)\right]\end{aligned} \tag{C.7}$$

where $B$ and $I_Z$ are respectively the complete and regularized incomplete $\beta$ functions.

To illustrate the results obtained with a $\beta - pdf$ subgrid model based on the segregation factor $S_Z$ of the mixture fraction, Fig. C.4 shows the evolution of the filtered temperature $\widetilde{T}$ and filtered progress variable $\widetilde{Y_C}$ with the weight-averaged mixture fraction $\widetilde{Z}$ for different values of the segregation factor $S_Z$:

- For $S_Z = 0$, the variance $Z_v$ is null and $\widetilde{\phi}(\widetilde{Z}) = \phi(Z)$,
- For $S_Z = 1$, the mixture between gases at $Z = 0$ and $Z = 1$ is predominant, and the value of $\widetilde{\phi}$ follows a linear variation as a function of $\widetilde{Z}$ between its value $\phi(0)$ at $Z = 0$ and $\phi(1)$ at $Z = 1$.

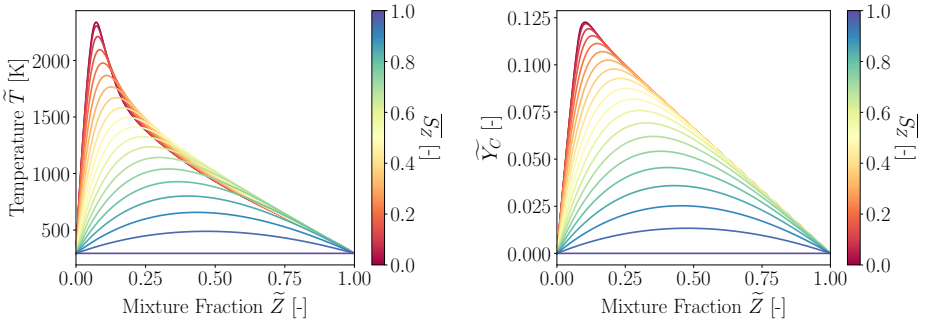


(a) $\widetilde{T}$ (b) $\widetilde{Y_C}$

**Figure C.4:** *Evolution of the filtered temperature $\widetilde{T}$ and the filtered progress variable $\widetilde{Y_C}$ as a function of the mixture fraction $\widetilde{Z}$ for a flamelet corresponding to a stain rate of $\epsilon = 1.5s^{-1}$ in the stable branch.*

### C.1.4 Enthalpy defect

In order to take into account heat losses and therefore to generate a radiation flamelet progress variable (RFPV) table, the procedure initially proposed by Ihme and Pitsch (2008a) has been used. For each flamelet of the FPV dataset, unsteady calculation are done by adding a radiative source term (which accounts for the optically thin radiation of $CO$, $CO_2$ and $H_2O$ species) and starting from the steady flamelet without radiation source term. During this unsteady calculation, intermediate unsteady flamelets are stored as a part of the RFPV flamelet dataset. Each one of these unsteady flamelets are parametrized through a parameter $\Phi$ corresponding to the value of enthalpy at a chosen mixture fraction $Z_0$:

$$\Phi = H(Z_0). \tag{C.8}$$

Figure C.5 illustrates the obtained unsteady flamelets from the steady adiabatic flamelet corresponding to a strain rate $\epsilon = 0.15\text{s}^{-1}$ in the stable branch. In these figures, each unsteady flamelet is colored by its corresponding value of the $\Phi$ parameter.

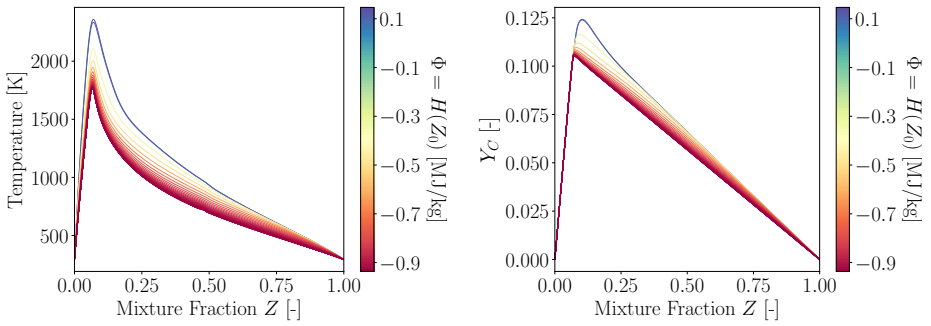


(a) Temperature $T$ (b) Progress variable $Y_C$

**Figure C.5:** *Impact of enthalpy defect on the profiles of temperature and progress variable of the lowest-strained flame of the stable branch ($\epsilon = 0.15s^{-1}$).*

Then, each flamelet of the RFPV database is parameterized by a unique set of parameters $(\Lambda, \Phi)$.

### C.1.5 Non-dimensional parameters used for the tabulation

As previously explained in Chapter 3, the tabulation is done as a function of non-dimensional parameters: the mixture fraction $Z$, the non-dimensional progress variable $\overline{C}$, the segregation factor $S_Z$ and the non-dimensional enthalpy

$\overline{H}$. These parameters are evaluated as:

$$S_Z = \frac{\widetilde{Z''^2}}{\widetilde{Z}(1-\widetilde{Z})} \tag{C.9}$$

$$\overline{H} = \frac{\widetilde{h} - \widetilde{h^{\mathrm{rad}}}(Z, S_Z)}{\widetilde{h^{\mathrm{adiab}}}(Z, S_Z) - \widetilde{h^{\mathrm{rad}}}(Z, S_Z)} \tag{C.10}$$

$$\overline{C} = \frac{\widetilde{Y_C} - \widetilde{Y_C^{\mathrm{f}}}(Z, S_Z)}{\widetilde{Y_C^{\mathrm{eq}}}(Z, S_Z) - \widetilde{Y_C^{\mathrm{f}}}(Z, S_Z)} \tag{C.11}$$

where $h^{\mathrm{adiab}}$ is the enthalpy of the adiabatic flamelet, $h^{\mathrm{rad}}$ is the enthalpy of the flamelet presenting the maximum of radiation heat losses. $Y_C$ is the non-normalized progress variable defined as a weighted sum of species mass fractions with $Y_C^{\mathrm{eq}}$ its value for the lowest strain rate flamelet on the stable branch of the S curve and $Y_C^{\mathrm{f}}$ its frozen value when chemical reactions are neglected.

## C.2 Validation case of the FPV tabulation technique in AVBP

In this section, the capacity of the FPV tabulation technique to retrieve the flamelet structure of the flamelet database is presented through a 2-D validation case representing a counterflow configuration, The progress variable $Y_C$ and the mixture fraction $Z$ are transported in order to retrieve these database flame structures.

### C.2.1 Presentation of the configuration

Figure C.6 presents the 2-D geometry used for the validation of the FPV tabulation technique in AVBP. This geometry corresponds to a counterflow configuration, with two opposed flows of methane and air respectively separated by a distance $L$. The inlets widths are set equal to the parameter $b$. Outlet is localized at the centerline at the position of the stagnation plane. For the boundary conditions, an adiabatic wall with slip velocity condition is provided for the axis of symmetry, and along two streamlines of the flow.

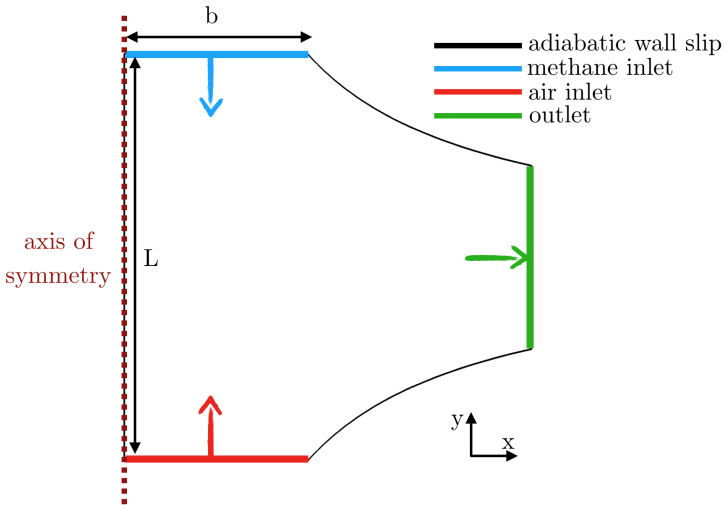


**Figure C.6:** *Geometry of the validation case for the FPV implementation in AVBP.*

In this validation case, the kinetic scheme GRI 3.0 is considered and combustion between methane ($CH_4$) and air is considered. Both inlet temperatures are set to 294K and the pressure is 1atm. The progress variable is defined as equal to $Y_C = Y_{\mathrm{CO}} + Y_{\mathrm{CO_2}}$.

In the following, the velocity field $\mathbf{u}$ is defined as:

$$\mathbf{u} = u(x,y)\mathbf{e_x} + v(x,y)\mathbf{e_y} \tag{C.12}$$

To be consistent with the formulation of the REGATH code, the strain rate $\epsilon$ is defined through the transverse velocity gradient in one side of the counterflow configuration (here the fuel):

$$\epsilon = \frac{1}{2}\left.\frac{du}{dx}\right|_{\text{fuel side}} \tag{C.13}$$

Then, again to be consistent with the 1-D formulation of the REGATH code, the transverse velocity gradient in the oxidizer side is equal to:

$$\left.\frac{du}{dx}\right|_{\text{oxidizer side}} = 2\sqrt{\frac{\rho_{\mathrm{CH_4}}}{\rho_{\text{air}}}}\epsilon \tag{C.14}$$

Then, the transverse velocity boundary conditions are:

- for the fuel side,

$$u(x,y) = 2\epsilon x \tag{C.15}$$

- for the oxidizer side,

$$u(x,y) = 2\sqrt{\frac{\rho_{\mathrm{CH_4}}}{\rho_{\text{air}}}}\epsilon x \tag{C.16}$$

In the same way, for a non reactive flow, the axial velocity gradients in both sides must be equal to:

$$\left.\frac{dv}{dy}\right|_{\text{fuel side}} = -2\epsilon \quad \text{and} \quad \left.\frac{dv}{dy}\right|_{\text{oxidizer side}} = 2\sqrt{\frac{\rho_{\text{CH}_4}}{\rho_{\text{air}}}}\epsilon \tag{C.17}$$

Then, with these conditions, the momentum of the two inlets are equal:

$$\int_{x=0}^{x=b} \rho_{\text{air}}(x) u_{\text{air}}^2(x) dx = \int_{x=0}^{x=b} \rho_{\text{CH}_4}(x) u_{\text{CH}_4}^2(x) dx \tag{C.18}$$

The flow is then balanced and the stagnation plan is placed at the middle position between the two inlets. When the flow is reactive, this position is slightly modified due to variations of density. That is why, to ensure that the stagnation plane is positioned at the middle between the two inlets, in the fixed strain rate formulation of REGATH, the inlet axial velocities at the fuel and oxidizer side are unknowns and are solved for each imposed strain rate.
Then, to be consistent with the results obtained in REGATH, in the AVBP calculations, the axial velocity gradients at each sides are taken for each strain rate from the values obtained in REGATH.

Figure C.7 presents the evolution of the obtained fields of mixture fraction $Z$, temperature $T$, progress variable $Y_C$, progress variable source term $\dot{\omega}_{Y_C}$, the difference between table temperature and calculated temperature in AVBP ($\Delta T$) and the density, for a strain rate of $\epsilon = 400$ s$^{-1}$.

For this strain rate, the axial velocity boundary conditions are set to:

- for the fuel side,

$$v(x, y) = -2 \cdot 390.32 \cdot y \tag{C.19}$$

- for the oxidizer side,

$$v(x, y) = 2 \cdot 247.09 \cdot y \tag{C.20}$$

For all the fields presented in Fig. C.7, the invariance of the fields with the position $x$ near the axial symmetry line is respected. Looking to the field of the difference between the table temperature value and the resolved temperature value in AVBP, it can be observed that the difference is acceptable (less than 0.5K) and the difference is mainly due that the compressible Navier-Stokes equations are solved in AVBP, therefore the pressure varies slightly in contrast with the REGATH code. Finally, looking at the streamlines presented together with the density field, it can be observed that without density variation (constant density $\rho$) due to variation of temperature, the structure of the potential flow is conserved. It is modified with density variations, but, with the imposed boundary conditions, the stagnation plan is placed as expected, at the middle position between the two inlets.

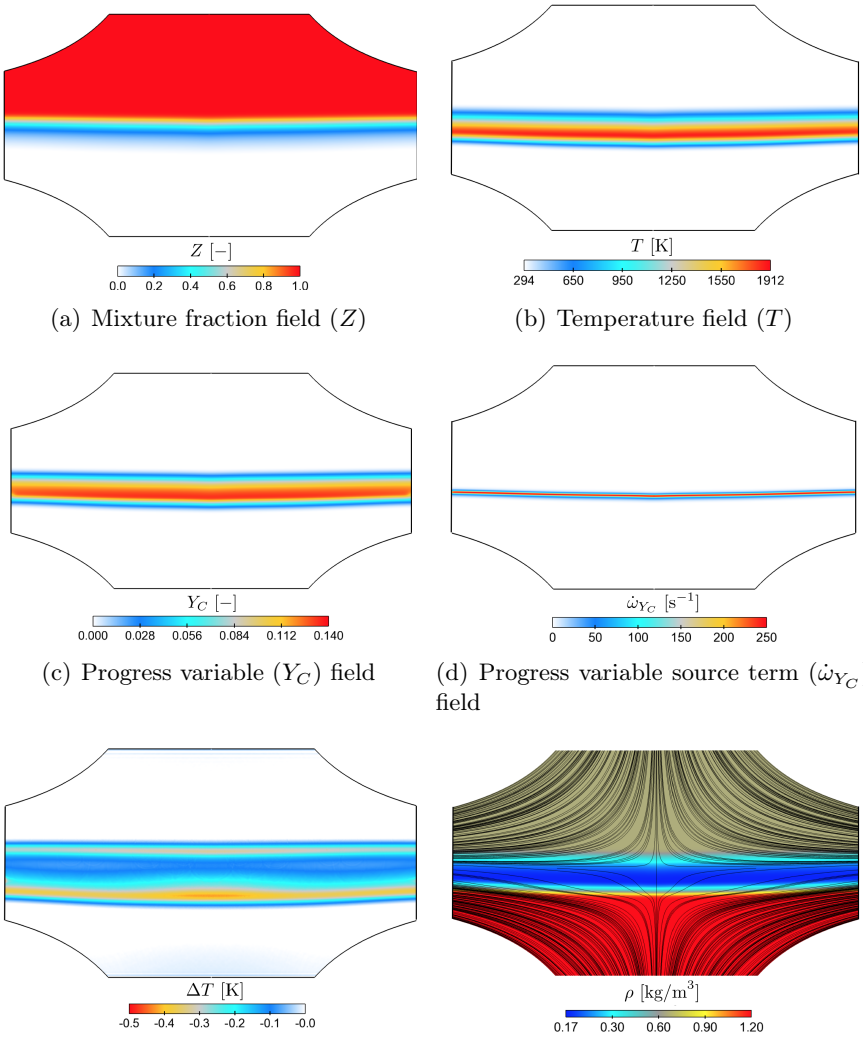


(a) Mixture fraction field ($Z$)

(b) Temperature field ($T$)

(c) Progress variable ($Y_C$) field

(d) Progress variable source term ($\dot{\omega}_{Y_C}$) field

(e) $\Delta T$ field

(f) Density field ($\rho$) and streamlines

**Figure C.7:** *Fields of mixture fraction, temperature, progress variable, progress variable source term, $\Delta T$ and density, and streamlines of the flow for a strain rate equal to $\epsilon = 400s^{-1}$.*

### C.2.2 Comparison with initial flamelets

Figure C.8 presents the comparison between the obtained results for the axial evolutions of the variables in the 2-D configuration of AVBP with the results obtained with the 1-D formulation in REGATH for a strain rate equal to $\epsilon = 400\text{s}^{-1}$. For all the quantities, a good agreement is obtained.

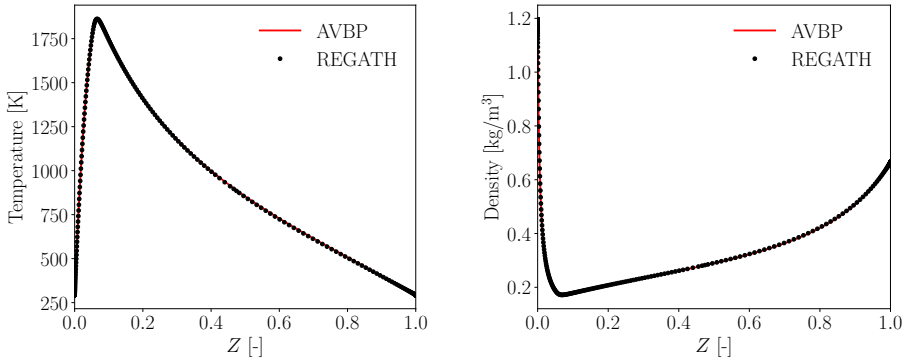


(a) Temperature as a function of $Z$




(b) Density as a function of $Z$

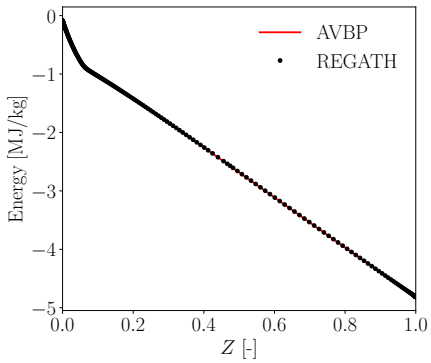


(c) Energy as a function of $Z$

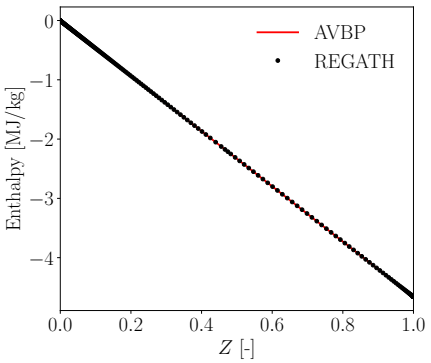


(d) Enthalpy as a function of $Z$

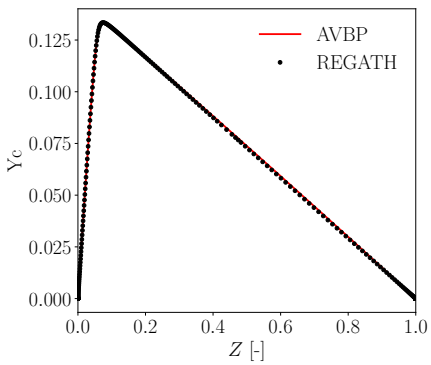


(e) $Y_C$ as a function of $Z$

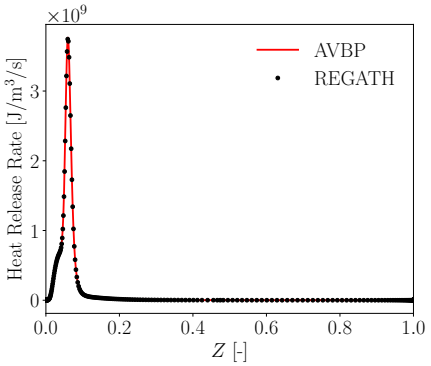


(f) Heat release rate as a function of $Z$

**Figure C.8:** *Comparison of **axial** results from 2D counterflow calculation in AVBP with 1D calculation on REGATH using FPV tabulation method for* $\epsilon = 400s^{-1}$.

Figure C.9 presents the evolution of the maximum temperature ($T^{\max}$) and the maximum progress variable ($Y_C$) with the imposed strain rate. Calculations with the REGATH code and AVBP code are compared. A good agreement is

obtained between calculations, validating the approach.

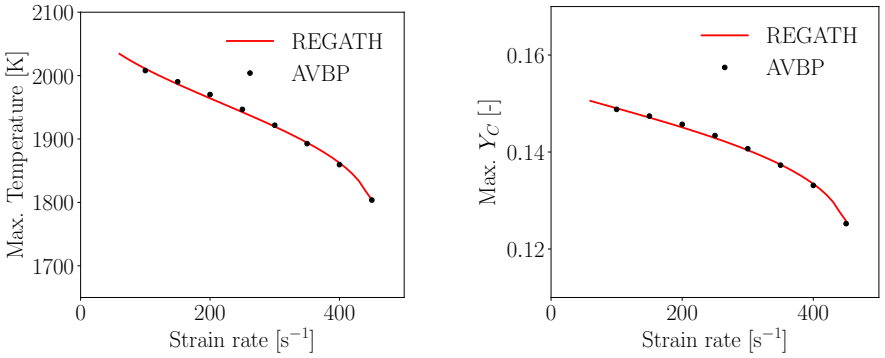


(a) Evolution of $T^{\max}$ with the imposed strain rate

(b) Evolution of $Y_C^{\max}$ with the imposed strain rate

**Figure C.9:** *Comparison between REGATH and AVBP calculations of the evolution of $T^{max}$ and $Y_C^{max}$ with the imposed strain rate.*

# Appendix D

# Complementaries on radiative transfer calculations

**Contents**



## D.1 Gaseous radiative properties

### D.1.1 ck database

In a recent publication, P. Riviere and A. Soufiani (Rivière and Soufiani 2012) have published updated band models parameters for $H_2O$, $CO_2$, $CH_4$ and $CO$ absorption coefficients at high temperature. In this publication, these parameters are generated from line by line calculations and recently improved spectroscopic databases in wide temperature and spectral ranges. This database is the one used in Rainier and all the calculations presented in this work.

### D.1.2 Mean Planck radiative properties used in the presented uncoupled simulations

In order to use the optically thin radiative model in CFD, Planck mean absorption coefficients must be calculated. The Planck mean absorption coefficients $\kappa_{\mathrm{Pl}}$ used in the calculations are based on polynomial fits of the updated database of P. Riviere and A. Soufiani (Rivière and Soufiani 2012).

To do so, the ck database used in Rainier has been used in order to generate the values of Planck mean absorption coefficients as a function of temperature for the species $CO_2$ and $H_2O$. Table D.1 presents fits of the corresponding coefficients as a function of temperature. Fits of the Planck mean absorption coefficients of $CH_4$ and $CO$ are also presented, based on data available in (Rivière and Soufiani 2012).

| | | |
|---|---|---|
| $CO_2$ and $H_2O$ | | |
| $\kappa_{\mathrm{Pl}}/p = c_0 + c_1(1000/T) + c_2(1000/T)^2 + c_3(1000/T)^3 + c_4(1000/T)^4 + c_5(1000/T)^5$ | | |
| | $H_2O$ | $CO_2$ |
| $c_0$ | $4.886854{\cdot}10^{-2}$ | 21.0358 |
| $c_1$ | -0.976360 | -124.083 |
| $c_2$ | 5.98482 | 257.779 |
| $c_3$ | 0.727799 | -176.840 |
| $c_4$ | -1.04192 | 50.4561 |
| $c_5$ | 0.2205334 | -5.17780 |
| $CH_4$ | | |
| $\kappa_{\mathrm{Pl}}/p = 1.2810 + 1.9966 \cdot 10^{-2}T - 3.3709 \cdot 10^{-5}T^2 + 1.9285 \cdot 10^{-8}T^3 - 3.7547 \cdot 10^{-12}T^4$ | | |
| $CO$ (given in two temperature ranges) | | |
| $\kappa_{\mathrm{Pl}}/p = c_0 + T(c_1 + T(c_2 + T(c_3 + Tc_4)))$ | | |
| | $300 \leq T \leq 750K$ | $750 < T \leq 2500K$ |
| $c_0$ | 2.4045 | 9.5223 |
| $c_1$ | $-4.6764{\cdot}10^{-2}$ | $-1.1696{\cdot}10^{-2}$ |
| $c_2$ | $2.1703{\cdot}10^{-4}$ | $5.5279{\cdot}10^{-6}$ |
| $c_3$ | $-3.1520{\cdot}10^{-7}$ | $-1.1644{\cdot}10^{-9}$ |
| $c_4$ | $1.4842{\cdot}10^{-10}$ | $9.1234{\cdot}10^{-14}$ |

**Table D.1:** *Fits of Planck Mean Absorption Coefficients $\kappa_{Pl}$ for $CO_2$, $H_2O$, $CH_4$ and $CO$ species as a function of temperature $T$. $p$ is the pressure, and the results are expressed in $m^{-1}.atm^{-1}$ (given for $p = 1atm$).*

Figure D.1 compares these updated Planck mean absorption coefficients with data provided by Barlow et al. (2001) and used in the TNF workshop. It can be observed that errors of approximatively 5 to 15% can be done when using non-updated data.

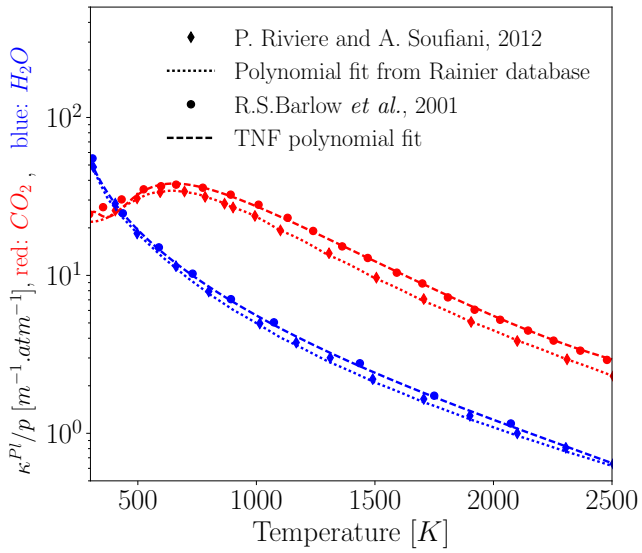


**Figure D.1:** *Comparisons of Planck mean absorption coefficients for $CO_2$ and $H_2O$ species between updated data from Rivière and Soufiani (2012) and data used in the TNF workshop from Barlow et al. (2001). Polynomial fits of both data are also provided (the ones corresponding to Rainier database are provided in Table D.1).*

Figure D.1 also presents the polynomial fits of both sets of data presented in Table D.1, confirming the good quality of the proposed fits, in order to be used in CFD codes together with the optically thin radiation model.

## D.2 Implementation and validation of directional probes in the code RAINIER

In order to compare the results experimentally obtained by Shaddix et al. (ISF3 2017) and presented in Chapter 7, which are based on directional sampling of the radiative flux at a given distance of the flame and in a fixed solid angle, directional probes able to reproduce this experimental configuration have been implemented in RAINIER.

### D.2.1 Directional probes: expressions of radiative power and radiative flux over a solid angle $\Omega$

The following paragraphs sum up the different equations needed for the implementation.

**Expression of maximal polar angle $\theta^{\max}$ for a solid angle $\Omega$:**

For a given solid angle $\Omega$, the maximal angle $\theta^{\max}$ can be obtained as:

$$\begin{aligned} \Omega &= \int_{\theta=0}^{\theta^{\max}} \int_{\psi=0}^{2\pi} \sin(\theta) d\theta d\psi \\ &= 2\pi(1-\cos(\theta^{\max})) \\ \Leftrightarrow \quad \theta^{\max} &= \cos^{-1}\left(1-\frac{\Omega}{2\pi}\right) \end{aligned} \tag{D.1}$$

For $\Omega = 2\pi$, $\theta^{\max} = \pi/2$ is retrieved.

**Expression of the emitted power in the solid angle $\Omega$:**
Considering Eq. (D.1), the emitted power of a point in the domain and over the solid angle $\Omega$ writes:

$$\begin{aligned} P^e_\Omega &= \int_{\nu=0}^{+\infty} \int_{\theta=0}^{\theta^{\max}} \int_{\psi=0}^{2\pi} \kappa_\nu I^\circ_\nu(T) d\psi \sin(\theta) d\theta d\nu \\ &= 2\pi \int_{\nu=0}^{+\infty} \int_{\theta=0}^{\theta^{\max}} \kappa_\nu I^\circ_\nu(T) \sin(\theta) d\theta d\nu \\ &= 2\pi(1-\cos(\theta^{\max})) \int_{\nu=0}^{+\infty} \kappa_\nu I^\circ_\nu(T) d\nu \end{aligned} \tag{D.2}$$

**Expression of the radiative heat flux at wall in the solid angle $\Omega$:**
In the same way, the flux $\varphi_\Omega$ at the wall and in the solid angle $\Omega$ writes:

$$\begin{aligned} \varphi_\Omega &= \int_{\nu=0}^{+\infty} \int_{\theta=0}^{\theta^{\max}} \int_{\psi=0}^{2\pi} \left(I'^p_\nu - I^i_\nu\right) d\psi \sin(\theta)\cos(\theta) d\theta d\nu \\ &= 2\pi \int_{\nu=0}^{+\infty} \int_{\theta=0}^{\theta^{\max}} \left(I'^p_\nu - I'^i_\nu\right) \sin(\theta)\cos(\theta) d\theta d\nu \\ &= \frac{\pi}{2}(1-\cos(2\theta^{\max})) \int_{\nu=0}^{+\infty} \left(I^p_\nu - I^i_\nu\right) d\nu \end{aligned} \tag{D.3}$$

where $I'^p_\nu$ and $I'^i_\nu$ are respectively the directive outgoing and ingoing intensities, and $I^p_\nu$ and $I^i_\nu$ are defined as:

$$\begin{aligned} I^p_\nu &= \frac{1}{\frac{\pi}{2}(1-\cos(2\theta^{\max}))} \int_{\theta=0}^{\theta^{\max}} \int_{\psi=0}^{2\pi} I'^p_\nu d\psi \sin(\theta)\cos(\theta) d\theta \\ I^i_\nu &= \frac{1}{\frac{\pi}{2}(1-\cos(2\theta^{\max}))} \int_{\theta=0}^{\theta^{\max}} \int_{\psi=0}^{2\pi} I'^i_\nu d\psi \sin(\theta)\cos(\theta) d\theta \end{aligned} \tag{D.4}$$

**Probability density functions in the case of a $\Omega$·sr solid angle**
In order to evaluated the radiative power or radiative flux over a given solid angle $\Omega$, it is necessary to define the probability density functions, as done in Section 6.4.5.

In the case of a $\Omega$ ·sr integration, the probability density functions for the wavenumber $\nu$ and the angle $\psi$ remain the same as the one presented by Eqs. (6.89) and (6.90).

For the $\theta$ direction:

- When calculating the radiative power, a random number $R_\theta$ between 0 and 1 is generated, with:

$$R_\theta = \int_0^\theta f_\theta(\theta')d\theta' = \frac{\int_0^\theta \sin(\theta')d\theta'}{1-\cos(\theta^{\max})} = \frac{1-\cos(\theta)}{1-\cos(\theta^{\max})} \tag{D.5}$$

Then,

$$\begin{aligned} \cos(\theta) &= 1 - R_\theta(1-\cos(\theta^{\max})) \\ &= 1 - R_\theta\left(1-\left(1-\frac{\Omega}{2\pi}\right)\right) = 1 - R_\theta\frac{\Omega}{2\pi} \\ \Leftrightarrow \quad \theta &= \arccos\left(1 - R_\theta\Omega/(2\pi)\right) \end{aligned} \tag{D.6}$$

The formula obtained in Eq. (6.91) is retrieved for $\Omega = 4\ \pi$.

- When calculating a wall radiative heat flux, a random number $R_\theta$ between 0 and 1 is generated, with:

$$R_\theta = \frac{\int_0^\theta \sin\theta\cos\theta d\theta}{\int_0^{\theta^{\max}} \sin\theta\cos\theta d\theta} = \frac{1-\cos(2\theta)}{1-\cos(2\theta^{\max})} = \frac{1-\cos^2\theta}{1-\cos^2\theta^{\max}} \tag{D.7}$$

Then,

$$\begin{aligned} \cos^2\theta &= 1 + R_\theta\left(\cos^2\theta^{\max} - 1\right) \\ &= 1 + R_\theta\left(\left(1-\frac{\Omega}{2\pi}\right)^2 - 1\right) \\ \Leftrightarrow \quad \theta &= \arccos\sqrt{1 + R_\theta\left[\left(1-\Omega/(2\pi)\right)^2 - 1\right]} \end{aligned} \tag{D.8}$$

### D.2.2 Validation test case

#### D.2.2.1 Presentation of the validation test case:

A 1-D case with a homogenous gas at constant temperature $T$ with a uniform absorption coefficient $\kappa_\nu$ surrounded by two walls at $T_1$ et $T_2$ and separated by a distance $L$ is considered. Diffuse reflexion is considered at walls. This case is treated in Taine and Iacona (2011) when integrating over a $2\pi\cdot$ sr solid angle. When considering only a reduced solid angle $\Omega$, the analytical expressions in this particular studied case are derived hereafter.

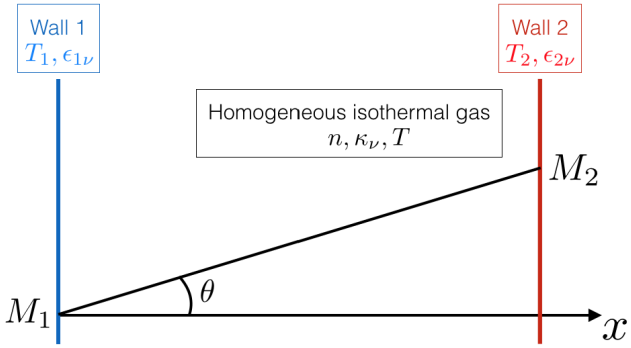


**Figure D.2:** *1-D validation test case from Taine and Iacona (2011)*

#### D.2.2.2 Analytical expressions for the 1-D validation test case

The following paragraphs present the derivation of the theoretical radiative heat fluxes at walls for the 1-D considered test case.

**Case of a $2\pi\cdot$ sr solid angle integration:**
For a $2\pi\cdot$ sr integration, we have the following expression for the flux $\varphi_1^R$ at the first wall:

$$\begin{aligned}\varphi_1^R &= \int_{\nu=0}^{+\infty}\int_{\psi=0}^{2\pi}\int_{\theta=0}^{\pi/2}\left(I_{1\nu}^p - I_{1\nu}^i\right)\cos\theta\sin\theta d\theta d\psi d\nu \\ &= \pi\int_{\nu=0}^{+\infty}\Big(\underbrace{I_{1\nu}^p}_{\text{outgoing}} - \underbrace{I_{1\nu}^i}_{\text{ingoing}}\Big)d\nu\end{aligned} \tag{D.9}$$

In the case of a diffuse wall, the leaving intensity $I_{1\nu}^p$ is isotropic and is expressed by:

$$I_{1\nu}^p = \underbrace{\epsilon_{1\nu}n^2 I_\nu^\circ(T_1)}_{\text{emitted}} + \underbrace{(1-\epsilon_{1\nu})I_{1\nu}^i}_{\text{reflected}} \tag{D.10}$$

and $I_{1\nu}^i$ by:

$$I_{1\nu}^i = \frac{1}{\pi}\int_{\psi=0}^{2\pi}\int_{\theta=0}^{\pi/2} I_{1\nu}'^i\cos\theta\sin\theta d\theta d\psi \tag{D.11}$$

where $I_{1\nu}'^i$ is the directional incident luminance, which can be expressed by:

$$I_{1\nu}'^i = \underbrace{\tau'_{M_2M_1\nu}I_{2\nu}^p}_{\text{transmitted from wall 2}} + \underbrace{\left(1-\tau'_{M_2M_1\nu}\right)n^2 I_\nu^\circ(T)}_{\text{emissivity of the homogeneous column}} \tag{D.12}$$

with $\tau'_{M_2M_1\nu}$ the transmissivity of the homogeneous isotherm colomn of gas between $M_2$ and $M_1$ (see Fig. D.2) :

$$\tau'_{M_2M_1\nu} = e^{-\frac{\kappa_\nu L}{\cos\theta}} = e^{-\frac{\kappa_\nu L}{\cos\theta}} \tag{D.13}$$

Integrating (D.12), (D.11) is expressed by:

$$\pi I^i_{1\nu} = 2E_3(\kappa_\nu L)\pi I^p_{2\nu} + (1 - 2E_3(\kappa_\nu L))\, n^2 \pi I^\circ_\nu(T) \tag{D.14}$$

with:

$$E_3(u) = \int_0^1 e^{-\frac{u}{\mu}} \mu d\mu = \int_1^{+\infty} \frac{e^{-ut}}{t^3} dt \tag{D.15}$$

Then,

$$\begin{aligned} I^p_{1\nu} &= \epsilon_{1\nu} n^2 I^\circ_\nu(T_1) \\ &\quad + (1 - \epsilon_{1\nu}) \left[2I^p_{2\nu} E_3(\kappa_\nu L) + (1 - E_3(\kappa_\nu L))\, n^2 I^\circ_\nu(T)\right] \end{aligned} \tag{D.16}$$

Doing the same for $I^p_{2\nu}$, we have:

$$\begin{aligned} I^p_{2\nu} &= \epsilon_{2\nu} n^2 I^\circ_\nu(T_2) \\ &\quad + (1 - \epsilon_{2\nu}) \left[2I^p_{1\nu} E_3(\kappa_\nu L) + (1 - E_3(\kappa_\nu L))\, n^2 I^\circ_\nu(T)\right] \end{aligned} \tag{D.17}$$

These two equations lead to the following system of equations:

$$\begin{cases} I^p_{1\nu} & - 2\,(1 - \epsilon_{1\nu})\, E_3\,(\kappa_\nu L)\, I^p_{2\nu} \\ & = \underbrace{\epsilon_{1\nu} n^2 I^\circ_\nu(T_1) + (1 - \epsilon_{1\nu})\,(1 - 2E_3\,(\kappa_\nu L))\, I^\circ_\nu(T)}_{b_1} \\ I^p_{2\nu} & - 2\,(1 - \epsilon_{2\nu})\, E_3\,(\kappa_\nu L)\, I^p_{1\nu} \\ & = \underbrace{\epsilon_{2\nu} n^2 I^\circ_\nu(T_2) + (1 - \epsilon_{2\nu})\,(1 - 2E_3\,(\kappa_\nu L))\, I^\circ_\nu(T)}_{b_2} \end{cases} \tag{D.18}$$

Solving this system, one obtains:

$$I^p_{1\nu} = \frac{b_1 + 2b_2(1 - \epsilon_{1\nu})E_3(\kappa_\nu L)}{1 - 4(1 - \epsilon_{1\nu})(1 - \epsilon_{2\nu})\left[E_3(\kappa_\nu L)\right]^2} \tag{D.19}$$

$$I^p_{2\nu} = \frac{b_2 + 2b_1(1 - \epsilon_{2\nu})E_3(\kappa_\nu L)}{1 - 4(1 - \epsilon_{1\nu})(1 - \epsilon_{2\nu})\left[E_3(\kappa_\nu L)\right]^2} \tag{D.20}$$

Then, $I^i_{1\nu}$ and $I^i_{2\nu}$ can be computed through the Eq. (D.14). Finally, the wall heat fluxes are expressed as:

- For the wall 1,

$$\begin{aligned} \varphi^R_1 &= 2\pi \int_{\nu=0}^{+\infty} \left\{ \int_{\theta=0}^{\pi/2} \left[I'^p_{1\nu} - I'^i_{1\nu}\right] \cos\theta \sin\theta d\theta \right\} d\nu \\ &= \pi \int_{\nu=0}^{+\infty} \left\{ I^p_{1\nu} - \left[2E_3(\kappa_\nu L) I^p_{2\nu} + (1 - 2E_3(\kappa_\nu L))\, n^2 I^\circ_\nu(T)\right] \right\} d\nu \end{aligned} \tag{D.21}$$

- For the wall 2,

$$\begin{aligned}\varphi_2^R &= 2\pi \int_{\nu=0}^{+\infty} \left\{ \int_{\theta=0}^{\pi/2} \left[ I_{2\nu}^p - I_{2\nu}^{\prime i} \right] \cos\theta \sin\theta d\theta \right\} d\nu \\ &= \pi \int_{\nu=0}^{+\infty} \left\{ I_{2\nu}^p - \left[ 2E_3(\kappa_\nu L) I_{1\nu}^p + (1 - 2E_3(\kappa_\nu L))\, n^2 I_\nu^\circ(T) \right] \right\} d\nu \end{aligned} \tag{D.22}$$

**Case of a $\Omega$·sr solid angle integration:**
Equations (D.18), (D.19) and (D.20) are still valid. However, for the evaluation of the fluxes at walls 1 and 2, the integration for $\theta$ is done between 0 and $\theta^{\max}$. Then, the flux at wall 1 is expressed by:

$$\begin{aligned}\varphi_1^R(\theta^{\max}) = \; & 2\pi \int_{\nu=0}^{+\infty} \int_{\theta=0}^{\theta^{\max}} \left( I_{1\nu}^p - I_{1\nu}^{i\prime} \right) \cos\theta \sin\theta d\theta d\nu \\ = \; & 2\pi \int_{\nu=0}^{+\infty} \left\{ \left( I_{1\nu}^p \frac{1 - \cos(2\theta^{\max})}{4} \right) \right. \\ & - \left[ I_{2\nu}^p \int_{\theta=0}^{\theta^{\max}} e^{-\frac{\kappa_{\text{gas},\nu} L}{\cos\theta}} \cos\theta \sin\theta d\theta + n^2 I_\nu^\circ(T) \right. \\ & \left. \left. \left( \int_0^{\theta\max} \cos\theta \sin\theta d\theta - \int_{\theta=0}^{\theta^{\max}} e^{-\frac{\kappa_{\text{gas},\nu} L}{\cos\theta}} \cos\theta \sin\theta d\theta \right) \right] \right\} d\nu \\ = \; & 2\pi \int_0^{+\infty} I_{1\nu}^p \frac{1 - \cos(2\theta^{\max})}{4} - \left[ I_{2\nu}^p \mathcal{E}_3(\cos\theta^{\max}, \kappa_\nu L) \right. \\ & \left. + n^2 I_\nu^\circ(T) \left( \frac{1 - \cos(2\theta^{\max})}{4} - \mathcal{E}_3(\cos\theta^{\max}, \kappa_\nu L) \right) \right] d\nu \end{aligned} \tag{D.23}$$

with:

$$\mathcal{E}_3(x, u) = \int_x^1 e^{-\frac{u}{\mu}} \mu d\mu = \int_1^{1/x} \frac{e^{-ut}}{t^3} dt \tag{D.24}$$

In the same way, for the wall 2, we have:

$$\begin{aligned}\varphi_2^R(\theta^{\max}) = \; & 2\pi \int_0^{+\infty} I_{2\nu}^p \frac{1 - \cos(2\theta^{\max})}{4} - \left[ I_{1\nu}^p \mathcal{E}_3(\cos\theta^{\max}, \kappa_\nu L) \right. \\ & \left. + n^2 I_\nu^\circ(T) \left( \frac{1 - \cos(2\theta^{\max})}{4} - \mathcal{E}_3(\cos\theta^{\max}, \kappa_\nu L) \right) \right] d\nu \end{aligned} \tag{D.25}$$

Equations (D.21) and (D.22) are well retrieved for $\Omega = 2\pi$ ($\theta^{\max} = \pi/2$).

#### D.2.2.3 Results for the validation test case and comparison with analytical expressions

The validation of the directional probes implementation has been carried out with the following values for the different parameters of the test case:

- $L = 0.9$m, $X_{H_2O} = 0.1$, $X_{CO_2} = 0.1$, $n = 1.0$, $T = 1600.0$ K,
- $\forall \nu$, $\epsilon_{1\nu} = 0.5$, $T_1 = 600.0$ K,
- $\forall \nu$, $\epsilon_{2\nu} = 0.5$, $T_2 = 1100.0$ K,
- $\Omega \in [\pi/32, \pi]$.

The absorption coefficient of the gas $\kappa_\nu$ is calculated using the ck database with the values of $X_{H_2O}$ and $X_{CO_2}$.

Figure D.3 presents a comparison of the theoretical and numerical results for this validation test case of the wall fluxes as a function of the solid angle $\Omega$ used for the integration. Error bars of the numerical results correspond to the RMS error of the Monte-Carlo calculation. These numerical results are consistent with theoretical ones, validating the implementation of this feature, used in Chapter 7.

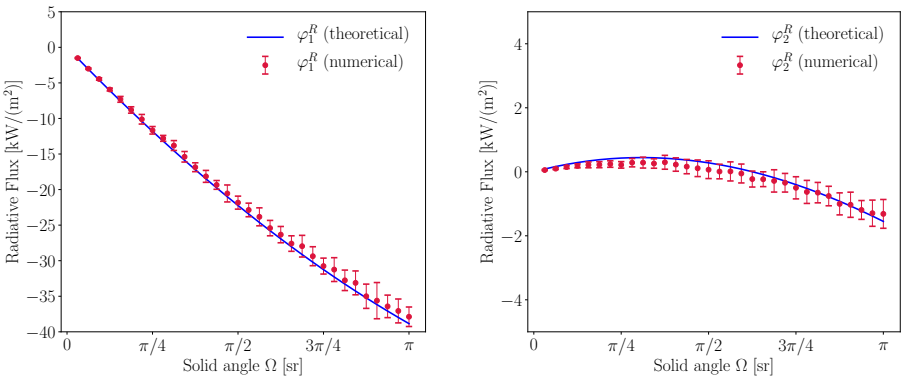


(a) $\varphi_1^R$ (b) $\varphi_2^R$

**Figure D.3:** *Validation test case: Comparison between theoretical and Monte-Carlo calculations of wall radiative fluxes $\varphi_1^R$ and $\varphi_2^R$ of walls 1 and 2 as a function of the solid angle $\Omega$. Error bars of the numerical results correspond to the RMS error of the Monte-Carlo calculation.*

## D.3 Contribution in the application of Quasi Monte Carlo methods for the resolution of the RTE

In this section, the conference paper resulting from the collaborative work with L. Palluotto and N. Dumont about the application of Quasi Monte-Carlo methods for the resolution of the RTE in the RAINIER code is presented.

**Proceedings of ASME Turbo Expo 2017: Turbomachinery Technical Conference and Exposition**
**GT2017**
**June 26-30, 2017, Charlotte, NC, USA**

# GT2017-64179

# COMPARISON OF MONTE CARLO METHODS EFFICIENCY TO SOLVE RADIATIVE ENERGY TRANSFER IN HIGH FIDELITY UNSTEADY 3D SIMULATIONS

**Lorella Palluotto[§*], Nicolas Dumont[§], Pedro Rodrigues[§], Chai Koren[‡§], Ronan Vicquelin[§], Olivier Gicquel[§]**
[§]Laboratoire EM2C, CNRS
CentraleSupélec
Université Paris-Saclay
Grande Voie des Vignes, 92295
Chatenay-Malabry cedex, France

[‡]Air Liquide
Centre de Recherche Paris-Saclay
1 Chemin de la Porte des Loges, 78350
Les-Loges-en-Josas, France

## ABSTRACT

*The present work assesses different Monte Carlo methods in radiative heat transfer problems, in terms of accuracy and computational cost. Achieving a high scalability on numerous CPUs with the conventional forward Monte Carlo method is not straightforward. The Emission-based Reciprocity Monte Carlo Method (ERM) allows to treat each mesh point independently from the others with a local monitoring of the statistical error, becoming a perfect candidate for high-scalability. ERM is however penalized by a slow statistical convergence in cold absorbing regions. This limitation has been overcome by an Optimized ERM (OERM) using a frequency distribution function based on the emission distribution at the maximum temperature of the system. Another approach to enhance the convergence is the use of low-discrepancy sampling. The obtained Quasi-Monte Carlo method is combined with OERM. The efficiency of the considered Monte-Carlo methods are compared.*

[*]Address all correspondence to this author: lorella.palluotto@centralesupelec.fr

## NOMENCLATURE

| | |
|---|---|
| $DNS$ | Direct Numerical Simulation |
| $FM$ | Forward Method |
| $I$ | Radiative intensity [$W\ sr^{-1}\ m^{-2}$] |
| $LES$ | Large Eddy Simulation |
| $MCM$ | Monte Carlo Method |
| $N,n$ | Number [-] |
| $QMCM$ | Quasi Monte Carlo method |
| $ERM$ | Emission-based Reciprocity Method |
| $OERM$ | Optimized Emission-based Reciprocity Method |
| $P$ | Radiative power per unit volume [$W\ m^{-3}$] |
| $PDF$ | Probability Density Function |
| $RANS$ | Reynolds-Averaged Navier-Stokes equations |
| $T$ | Temperature [$K$] |
| $T_{CPU}$ | Computational time [$s$] |
| $TRI$ | Turbulence-Radiation Interaction |
| $f$ | Probability density function [-] |
| $rms$ | root mean square |
| $\Delta$ | Direction of photon bundle [$m$] |
| $\delta$ | Channel half-width [$m$] |
| $\eta$ | Efficiency |
| $\theta$ | Polar angle [$sr$] |

| | |
|---|---|
| $\kappa$ | Absorption coefficient $[m^{-1}]$ |
| $\nu$ | Radiation Wave number $[cm^{-1}]$ |
| $\sigma$ | Standard Deviation |
| $\sigma^2$ | Variance |
| $\phi$ | Azimuthal angle $[sr]$ |
| $\Omega$ | Solid angle $[sr]$ |
| $^{exch}$ | Exchanged quantity |
| $^{e}$ | Emitted quantity |
| $^{\circ}$ | Equilibrium quantity |

## INTRODUCTION

Conductive heat fluxes and radiative energy fluxes at walls greatly affect the design stage and the material choice of combustion systems. Incorporating these different contributions in numerical simulations is therefore a great challenge that is widely investigated. In the context of gas turbines, the efficient mitigation of conduction from burnt gases with film and effusion cooling leaves radiation as the main contributor to wall heat fluxes. Radiative heat transfer is however difficult to account for in turbulent flows. Local radiative intensity is indeed strongly correlated to the instantaneous medium distribution in the spatial domain. Furthermore it also shows a highly non-linear response to temperature and species concentrations. Therefore accurate calculation of radiative transfer requires an instantaneous spatially resolved information regarding the temperature and species composition fields. Carrying out RANS simulations does not provide such information as only average quantities are calculated. Then accounting for Turbulence-Radiation Interaction (TRI) [1, 2] in such configuration requires TRI modelling. While deriving such models is still an ongoing research domain, another approach to alleviate significantly this modeling issue is to couple the radiative solver to direct numerical simulations (DNS) as in [3–5], that fully resolves in time and space the flow field, but these simulations remain not accessible for use in large-scale applications. Therefore a intermediate choice is to use large-eddy simulation (LES) instead of DNS, providing time resolved solution and a good estimation of the spatial correlation in the simulation domain. The subgrid-scale TRI effects are nonetheless strictly not negligible and modeling efforts are ongoing [6, 7].

As regarding the methods to solve the radiative transfer equation, Monte Carlo methods are the more interesting for their straightforward accounting for spectral gas radiative properties and for complex geometries. A Monte Carlo method (MCM) is a statistical method where a large number of stochastic events is simulated. In radiative transfer a stochastic event is represented by an optical path of photons bundles whose departure point, propagation direction and spectral frequency are independently and randomly chosen according to given distribution functions. The average of all the stochastic events contributions constitutes the solution of the problem, *i.e.* the local values of radiative power and wall radiative fluxes. In the conventional Forward Method a large number of photon bundles are emitted in the whole system and their history is traced until the carried energy is absorbed by the participative medium, at the wall, or until it exits the system. Such methods provide an estimation of the statistical error for the computed radiative power and wall fluxes, commonly represented by the standard deviation. The standard deviation tends to be proportional to $1/\sqrt{N}$ (Howell 1998), where N is the total number of bundles. One of the main drawbacks is the need of a large number of rays to obtain statistically and physically meaningful results, and this handicap becomes stronger in optically thick media, where most of photons are absorbed in the vicinity of their emission source. Although these methods are deemed to be computationally expensive, all the more when coupled with unsteady 3D simulations, but the increase in computational resources has nowadays made such computations possible. Nevertheless, it is still necessary to reduce the cost of these coupled simulations to make them more and more affordable.

For this purpose, different strategies have been proposed in the last years. One alternative to reduce conventional Monte Carlo convergence time and large memory requirement is the Reciprocal Monte Carlo approach proposed by Walters and Buckius [8], where the net power exchanged between two cells is directly calculated, fulfilling the reciprocity principle. The main interest of such a reciprocal approach is that the net power exchanged between two cells at the same temperature is rigorously null. This property is only statistically verified by the FM [9]. Cherkaoui et al. [10] reported that the reciprocal method converges at least two orders faster than the conventional Monte-Carlo method and was much less sensitive to optical thickness.

But a complete Monte Carlo Reciprocity Method, based on complete calculation of exchange powers between all the couples of cells of the discretization, is not realistic for system involving participating gases characterized by spectral radiative properties in complex geometrical configurations.

Among the reciprocal Monte Carlo methods, the Emission Reciprocity Method (ERM) developed by Tesse et al. [9] proposes a deterministic estimation of the local emissive power while the local absorbption is estimated with the reciprocal principle. Zhang et al [11] proposed a method to improve the efficiency of ERM, through an approach of importance sampling based on a new frequency distribution function that aims to reduce the Monte Carlo variance, accelerating its convergence (Optimized Emission Reciprocity Method OERM).

Another approach, alternative to the variance reduction techniques, is to use a sampling mechanism whose error has a better convergence rate than classical MCM. Using alternative sampling mechanisms for numerical integration is usually referred to as 'Quasi-Monte Carlo' integration [12]. While considered in semi-conductor applications [13], such methods have not been investigated for participating media such as the ones met in combustors.

This present study focuses on convergence acceleration of MC

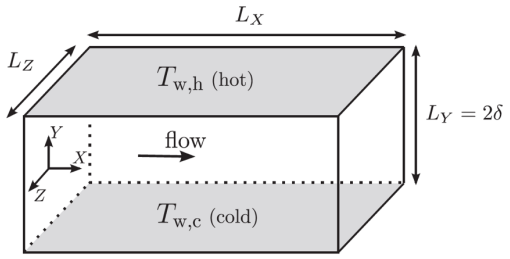


**FIGURE 1**. Computational domain of channel flow case. x, y and z are, respectively, the streamwise, wall normal and spanwise directions. Periodic boundary conditions are applied along x and z. $\delta$ is the channel half-width, equals to 0.01 m and the dimensions of the channel case $L_x$,$L_y$ and $L_z$ are $2\pi\delta$, $2\delta$ and $\pi\delta$. The lower wall is at 950 k and the upper wall is at 2050 K.

simulations: first the interest of ERM will be highlighted, then it will be compared to its optimized version (OERM). OERM is then combined with the Quasi-Monte Carlo method. MC and QMC methods will be assessed in terms of accuracy and computational cost in two configurations. The first configuration is a turbulent channel flow DNS (case C3R1 from [5]) characterized by a simple geometry that allows to perform simulations on a structured grid. The channel characteristics are showed in the Fig. 1: a homogeneous non-reacting $CO_2 - H_2O - N_2$ gaseous mixture, at 40 bars, flowing between two walls with imposed temperature values (Fig. 2) and its computational domain is made of 4.2 millions of grid points. The second configuration is a laboratory scale burner [14, 15] computed in LES [16, 17] with an unstructured grid of 8 millions cells and 1.26 millions points. The burner hosts a turbulent premixed flame of a methane-air mixture injected through a swirl injector and confined by cold walls. An instantaneous field of temperature into the chamber is showed in Fig. 3 For both configurations, instantaneous snapshots of unsteady 3d simulations (DNS for the first one, LES for the second one) are used to asses the computational efficiency of the considered Monte Carlo methods.

## RADIATION SIMULATIONS WITH RECIPROCAL MONTE CARLO ERM

The general organization of the radiation model, based on a reciprocal Monte Carlo approach, has been detailed by Tess et al. [9]. The principles of this method are briefly summarized here; in this approach the radiation computational domain is discretized into $N_v$ and $N_f$ isothermal finite cells of volume $V_i$ and faces of area $S_i$, respectively. The radiative power of the node $i$ per unit volume is written as the sum of the exchange powers

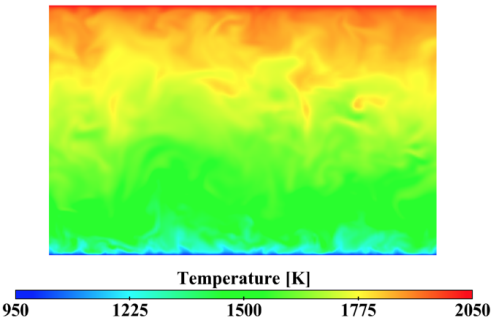


**FIGURE 2**. Instantaneous fields of temperature on a longitudinal section of the channel.

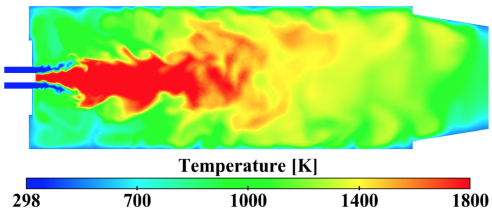


**FIGURE 3**. 2D slice of the instantaneous 3D field of temperature of the studied burner.

$P_{ij}^{exch}$ between the node $i$ and all the other cells $j$, i.e.

$$P_i = \sum_{j=1}^{N_v+N_f} P_{ij}^{exch} = -\sum_{j=1}^{N_v+N_f} P_{ji}^{exch}. \quad (1)$$

where $P_{ij}^{exch}$ is given by

$$P_{ij}^{exch} = \int_0^{+\infty} \kappa_\nu(T_i)\left[I_\nu^\circ(T_j) - I_\nu^\circ(T_i)\right] \int_{4\pi} A_{ij\nu} d\Omega_i d\nu, \quad (2)$$

where $I_\nu^\circ(T)$ is the equilibrium spectral intensity and $\kappa_\nu(T_i)$ the spectral absorption coefficient relative to the cell $i$. $d\Omega$ is an elementary solid angle. $A_{ij\nu}$ accounts for all the paths between emission from the node $i$ and absorption in any point of the cell $j$, after transmission, scattering and possible wall reflections along the paths. Its expression is detailed in [9].
As in a Monte Carlo method propagation direction $\Delta(\theta,\phi)$ and wave-number $\nu$ of the photon bundles emitted are determinated

randomly according to a Probability Density Function (PDF) $f_i(\Delta(\theta,\phi),\nu)$, that will be written as $f_i(\Delta,\nu)$, introducing the emitted power $P_i^e(T_i)$ per unit volume, Eq. (2) can be written as

$$P_{ij}^{exch} = P_i^e(T_i)\int_0^{+\infty}\left[\frac{I_\nu^\circ(T_j)}{I_\nu^\circ(T_i)}-1\right]\int_{4\pi}A_{ij\nu}f_i(\Delta,\nu)d\Omega_i d\nu, \quad (3)$$

where the PDF is expressed as

$$\begin{aligned} f_i(\Delta,\nu)d\Omega_i d\nu &= f_{\Delta i}(\Delta)d\Omega_i f_{\nu i}(\nu)d\nu \quad (4)\\ &= \frac{1}{4\pi}d\Omega_i\frac{\kappa_\nu(T_i)I_\nu^\circ(T_i)}{\int_0^{+\infty}\kappa_\nu(T_i)I_\nu^\circ(T_i)d\nu}d\nu. \end{aligned}$$

As in this method the emitted energy is calculated in a deterministic way while the absorbed one is computed by using a statistical approach, the accuracy of computed emitted energy will be more accurate than the absorbed energy and hence ERM is more adapted to the zone where emission is dominant than absorption, i.e. high temperature zone [11].
As in the ERM only the bundles leaving the node *i* are needed to estimate the local radiative power. It is possible to estimate the radiative power at one point without performing such estimation in all other points of the domain. This main feature allows an estimation of the radiative power in reduced parts of the domain and it gives the possibility to have a control on the local accuracy.

## Scalability

Scalability becomes a very challenging problem in large-scale simulations involving radiative transfer. Fluid mechanics and most other phenomena in combustion physics are short range phenomena, so the energy balance equations can be solved over infinitesimal volumes, making them amenable to domain decomposition. Conversely, radiation is a long-distance phenomenon and corresponding equations must be solved over the entire considered domain, thus creating difficulties for domain decomposition. Each node of the domain needs information about all other nodes, so each processor shares radiation field variables with all other processors. Achieving a high level of scalability with the conventional forward Monte Carlo method is not straightforward. Moreover scalability in massively-parallel computing is difficult to obtain due to load imbalancing and interprocessor communication demands. The feature of the ERM method to treat each mesh point independently from the others with a local monitoring of the statistical error insures a high degree of scalability. The RAINIER code used for the simulations presented in this paper solves the radiative transfer equation in order to determine the fields of radiative power and radiative heat fluxes to walls. It is characterized by a master/slave framework. The master process assigns work to all of the other processes, called slaves and the exchange of information occurs through MPI commands. The master, then, collects and saves the results as they are returned from the slaves. As each slave process completes the assigned work, it requests additional work to the master process. To exhibit the computational demand of the ERM method for different cores counts, a scalability analysis was performed on a Bull cluster equipped with Intel E5-2690 processors. The case retained for the scalability test is the laboratory scale burner whose computational domain is made of 8 millions cells. Tests have been conducted on a range of cores, from 120 up to 1920. Two tests have been performed with a fixed number of rays emitted in each point of the domain (200 for the first case, 1000 for the second one), and no convergence criteria have been imposed. The test characterized by a lower number of emitted rays presents some disadvantageous conditions to scalability, as a huge number of communications between slaves and master is required. The results of the scalability analysis are summarized in Fig. 4 where it can be noticed a perfect ability of the method to require less wall-clock time as the number of processors is increased up to 1000 cores. When the cores number is higher than 1000, the time to exchange the informations between the master process and the slaves improves. Consequently the case with a lower number of rays prevents to achieve good scalability at larger process counts because of an overload of the master, which increases in proportion to the number of processes used. On the contrary, when the load of the slaves grows, a linear scalability is accomplished up to 1920 cores, with no deviation from the ideal scalability curve, meaning that the scalability limit is not reached. This trend let us expect that strong scalability will continue further, for a larger number of processors.

The efficiency plot in fig. 5 confirms the code performance. In the case characterized by the overloading of the master, the efficiency decreases to 70 % for a large number of cores, while, for the second case, it remains close to 100% whatever the number of cores.

## Local Convergence

As already mentioned, one of the main interests of the ERM method is the possibility to control the local convergence. To show this feature, instantaneous snapshots of unsteady 3D DNS simulations of the turbulent channel flow, defined in fig. 1, are used to solve the radiation field.

To estimate the local standard deviation the actual total number of optical paths (N) is divided into $n$ packages with $N/n$ optical paths for each package. In order to evaluate the convergence of a Monte Carlo solution, the control is done on the relative and the absolute value of the standard deviation. The relative standard deviation is the ratio of the local standard deviation to the local radiative power. However, this parameter is not enough as there can be some regions, such as the injector

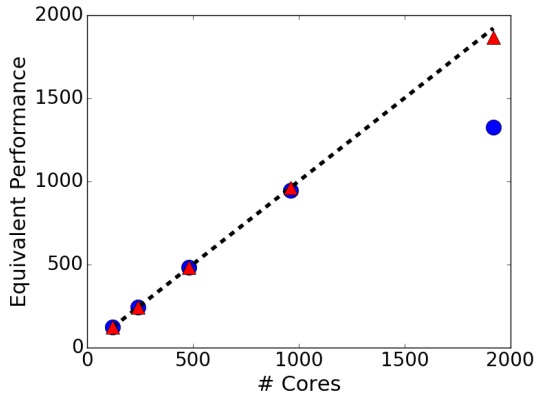


**FIGURE 4**. Scalability plot. Blue circles: test performed with 200 rays; red triangles: test performed with 1000 rays; dashed line: ideal curve.

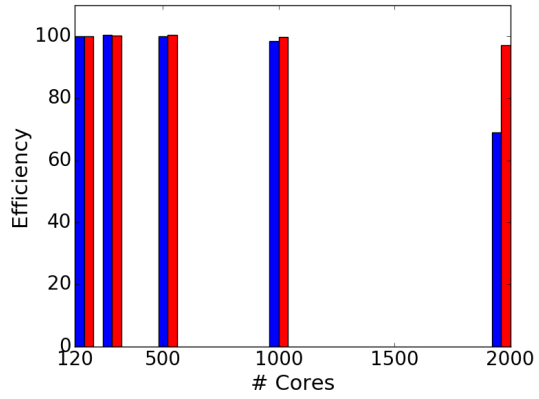


**FIGURE 5**. Efficiency bar chart. Blue: test performed with 200 rays; red: test performed with 1000 rays.

of a combustion chamber, where there are no participating gases, and the radiative power is zero. Therefore the absolute value of the local standard deviation, is checked to be lower than a prescribed maximum.

The ERM method is simulated in two different cases: in the first one a given number of realizations, or optical paths, is imposed to be the same for all the nodes of the domain; in the second one a local convergence criterion is imposed. For all the simulations the gases spectral properties are computed using the correlated

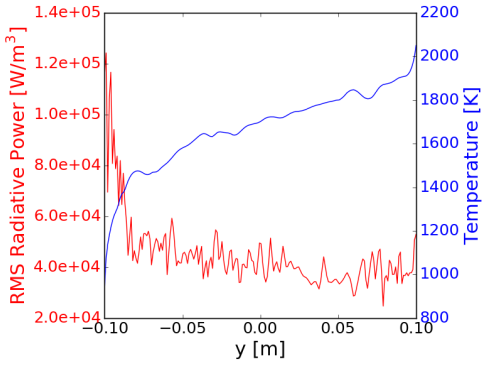


**FIGURE 6**. Field of RMS of radiative power on a transversal section of the channel (top). Plot of RMS of radiative power (red) and temperature (blue) on the same section obtained with the Monte Carlo ERM in fixed rays number tests (bottom).

$\kappa$-distribution [18].

**Case 1: Simulations with a fixed rays number** In this test, the rays number is imposed to 10,000 for all the computed points. To evaluate the achieved level of convergence, it can be interesting to take a look at the standard deviation of the radiative power. This variable, together with the temperature, is plotted over the y-axis of the channel in Fig. 6, showing that a better accuracy is reached in the region near the hot wall of the channel, while high values of rms radiative power are encountered in the colder regions of the channel.

**Case 2: Simulations with imposed convergence criteria** This test case is set-up in such a way that calculations are performed until the relative criterion is lower than 5% or the locale absolute value of the standard deviation is lower than 10% of the maximum value of the mean radiative power. Here the number of rays generated from each cell is not anymore set a priori, but it varies spatially according to the local standard deviation. The local convergence controlling algorithm makes possible to relate the local standard deviation to the local number of optical paths: the fig. 7 shows that in regions where the convergence is difficult to achieve, more optical paths are provided, or equivalently that the regions characterized by a number of shots lower then the maximum, have achieved the convergence.

To conclude it can be confirmed that the radiative power field

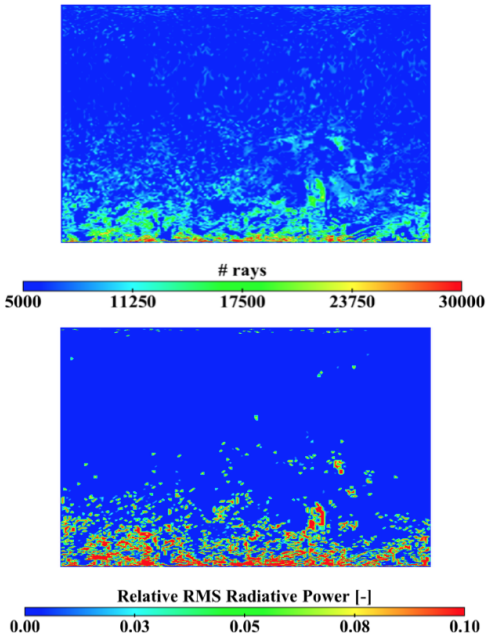


**FIGURE 7**. Number of rays (top) and relative standard deviation (bottom) obtained with the Monte Carlo ERM in controlled convergence.

predicted by ERM is easier to converge in high temperature regions where the accuracy is bigger. The reason of the different behavior in hot and cold zones lies in the frequency distribution function used in ERM, as it is based on the spectral emitted power. Consequently the optical paths issued from colder cells are characterized by low frequencies. But the radiative power absorbed by a cold cell has mainly be emitted by hot regions, emitting at much higher frequencies. The absorbed radiative power is then strongly underestimated in cold regions. This phenomenon does not appear for hot cells as the emitted radiation spectrum is very close to the absorbed one [11]. These considerations clearly show that the distribution function used in the ERM method may not be optimized for fast convergence in the cold regions, leading to excessive CPU time.

## MONTE CARLO OERM

To alleviate the mentioned problem different methods exist, one of the most important ones is the so-called importance sampling: a variance reduction method to accelerate Monte Carlo convergence. This is the core of the Optimized Emission-based Reciprocity Method (OERM) [11], where the frequency distribution function is chosen in such a way as to correct the ERM drawback and decrease the variance.

In the OERM method the frequency distribution function, $f_\nu(\nu, T_{max})$, is based on the emission distribution at the maximum temperature encountered in the system and it is expressed as

$$f_\nu(\nu, T_{max}) = \frac{\kappa_\nu(T_{max}) I^\circ_\nu(T_{max})}{\int_0^{+\infty} \kappa_\nu(T_{max}) I^\circ_\nu(T_{max}) d\nu}. \tag{5}$$

In these conditions, the radiative exchange power for unit volume between $i$ and $j$, given by (2), can be expressed as

$$P^{exch}_{ij} = P^e_i(T_{max}) \int_0^{+\infty} \frac{I^\circ_\nu(T_i)}{I^\circ_\nu(T_{max})} \frac{\kappa_\nu(T_i)}{\kappa_\nu(T_{Imax})} \left[\frac{I^\circ_\nu(T_j)}{I^\circ_\nu(T_i)} - 1\right] f_\nu(\nu, T_{max}) d\nu f_{\Omega_i} d_{\Omega_i} \tag{6}$$

The use of the pdf (5) allows to eliminate the disadvantage of the classical approaches of ERM in the cold regions. To illustrate the advantages of the OERM method, computations of the radiative transfer in the channel flow are performed. In a first step solutions of radiative field obtained with a OERM approach are obtained with the same computation conditions of the case 1, at imposed number of rays, and they are compared to the solutions obtained with the ERM method. The standard deviation for both of the methods is exhibited in Fig. 8: on the hot wall results of ERM and OERM overlap as the two frequency distribution functions are practically identical, therefore OERM turns into ERM. Focusing on the colder regions on the bottom of the section, the same figure shows that the standard deviation in the OERM case is much lower than in the ERM case, meaning that with the same number of realizations, the frequency distribution function of OERM allows the absorption by the cold regions to be more accurately computed, contrary to the case of ERM.

Consequently if a convergence criterion is fixed, calculations conducted with an OERM method need a lower number of realizations to satisfy the same criterion as it can be seen in fig. 9, leading to a less expensive computational cost.

The OERM method is now investigated on a semi-industrial configuration, the burner of fig. 3. The temperature, pressure, $CO_2$ and $H_2O$ molar fractions used in OERM simulations are instantaneous values extracted from unsteady 3D Large Eddy Simulations of the flow. As seen in Fig. 10 most of the domain emits energy through radiative heat transfer (negative radiative power); the regions where energy absorption dominates (positive radiative power) are the coldest gas pockets mainly located in thin layers near the walls.

In the set-up of this case relative and absolute values of standard deviation are controlled in order to insure that the simulation completes in a limited CPU time, so a maximum number

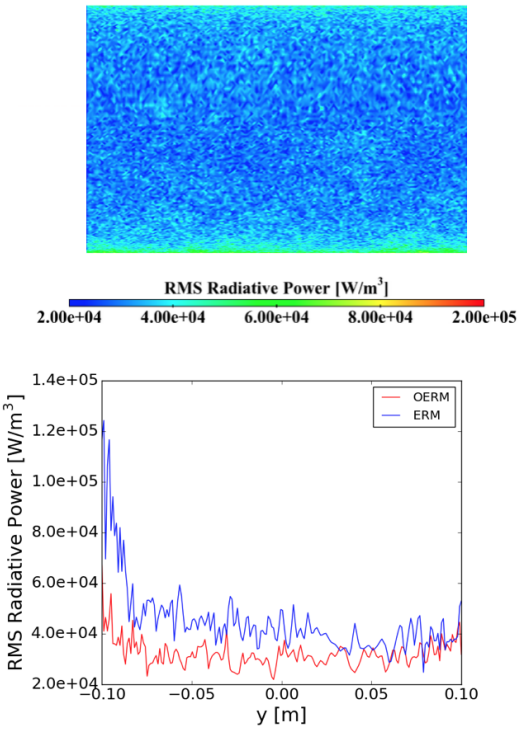


**FIGURE 8**. Instantaneous field of rms of radiative power obtained with Monte Carlo OERM (top). Plot of the rms of radiative power for ERM (blue line) and OERM (red line) in test with fixed rays number.

of rays emitted per point is imposed. If the simulation is locally stopped because of this criterion, the convergence is not achieved in these points. Tests are performed limiting the maximum number of possible optical paths departing from the nodes to 10 000 and 20 packages of 500 realizations each are taken into account for the error estimation. The convergence condition of the Monte Carlo algorithm is that of an rms lower than 3 % of the mean value; while in the regions where the criterion of relative rms is never satisfied, a control on the absolute value of the rms, whose value is imposed at 3 % of the maximum value of the mean radiative power, is done. In the fig. 11 gray zones are the ones where the absolute criterion is respected, keeping in mind that in these zones the rms of the radiative power is close to zero, while in the remaining part of the chamber a control on the relative error is done. It can be seen that zones where it is most difficult attain the established convergence criterion are characterized by a larger number of realizations.

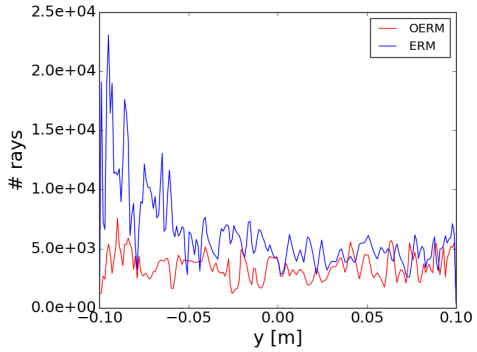


**FIGURE 9**. Plot of the number of rays needed for the ERM (blue line) and OERM (red line) in controlled convergence.

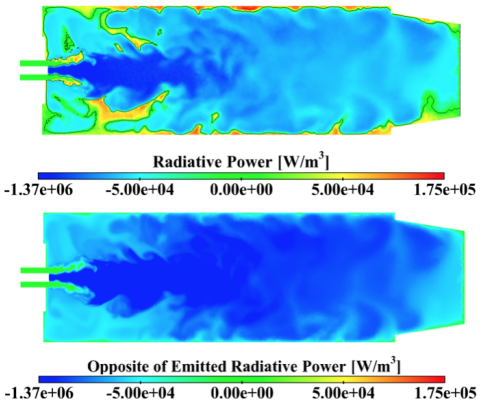


**FIGURE 10**. Instantaneous fields of Radiative Power (top) and the opposite of the emitted power (bottom). Black line is the iso-contour for radiative power = 0.

## QUASI MONTE CARLO

If the technique used in the OERM method is aimed to reduce the variance through importance sampling; another approach to improve the Monte Carlo error is to replace the pure random sampling with a quasi-random (also called low-discrepancy) sampling, without modifying the frequency distribution function. Lower error and improved convergence may be attained by replacing the pseudo-random sequences using low-discrepancy sequences, whose points are distributed in a way to provide greater uniformity (fig. 12). For this study a Sobol sequence has been used and its construction uses results from [19].

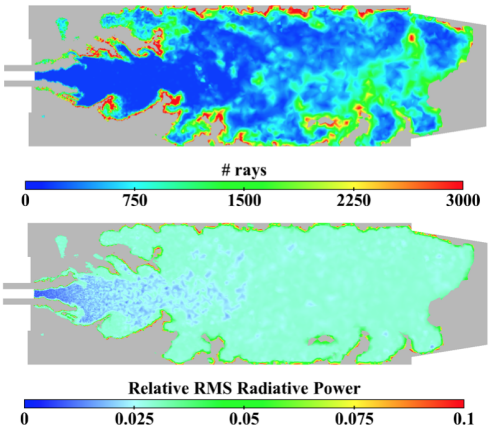


**FIGURE 11**. Number of rays (top) and relative rms of radiative power (bottom) obtained using the Monte Carlo OERM method.

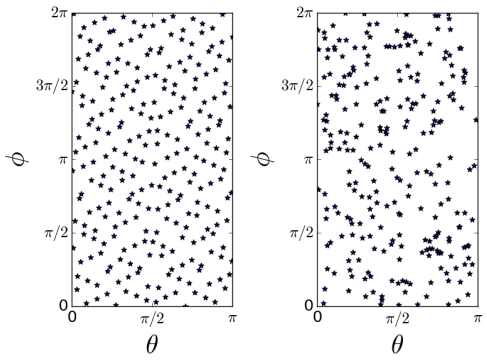


**FIGURE 12**. Sampling of polar ($\theta$) and azimuthal angle ($\phi$) using a Sobol sequence (left) and a random sequence (right).

Using this alternative sampling method in the context of multivariate integration is usually referred to as Quasi Monte-Carlo, that can be seen like a deterministic version of Monte Carlo method.
Its advantage lies in enhancing the convergence rate [20]. It is possible to asses the error using a Randomized Quasi-Monte Carlo [12]. In the context of radiation simulations, as for the Monte Carlo, $n$ packages are considered; within each of this package, a low discrepancy sequence of $N/n$ points is used, while the $n$ sequences of the packages are randomized using an I-binomial scrambling [21]. This approach allows to benefit from the faster convergence rate of Quasi-Monte Carlo within each package and to have an estimation of the error using the variance between the packages, as it is done for the Monte Carlo method. The obtained Quasi-Monte Carlo method can be combined with both ERM and OERM methods, so that a comparison with the Monte Carlo simulations, previously presented, can be conducted. Only OERM results are considered in the following.

### Quasi Monte Carlo combined with OERM method

Simulations with a Quasi-Monte Carlo method in its OERM version have been conducted on snapshots of 3D LES of the laboratory scale burner. In a first step, simulations have been carried out setting the same number of optical paths departing from all the nodes of the domain, without imposing convergence criteria. Such an analysis allows to evaluate the accuracy of both methods. In fig. 13 the relative standard deviation for both the methods is shown on the whole longitudinal section of the chamber. It can be seen that with the same number of realizations, QMC simulations are more accurate than MC ones, as the relative error is much lower on the whole domain, even in the zones more difficult to converge, such as the ones close to the cold walls of the chamber.
In order to compare the convergence rate of Monte Carlo and Quasi Monte Carlo simulations, in a second step tests of convergence are performed. Their set-up is the same of OERM simulations of the previous chapter, in terms of maximum number of rays and packages, and parameters for the control error. Tests withs local convergence control allow to highlight the advantage of QMC in terms of computational cost. As expected, the number of realizations necessary to respect the convergence criterion is much lower in the case of QMC simulations as showed in fig. 14.

### CPU efficiency of Monte Carlo and Quasi-Monte Carlo methods

A more complete comparison can be done evaluating the efficiency of both Monte Carlo and Quasi Monte Carlo methods. The local efficiency of both the methods has been compared and evaluated as

$$\eta_i = \frac{1}{\sigma_i^2 \cdot nb_{int,i} \cdot (T_{CPU}/nb_{int,tot})} \tag{7}$$

where $i$ represents the considered point, $nb_{int,i}$ is the number of the intersections of the point $i$, $T_{CPU}/nb_{int,tot}$ is the cost of an intersection. In the fig. 15 the ratio of the local efficiencies of quasi Monte Carlo algorithm and Monte Carlo is showed on a longitudinal plane of the chamber: the ratio is bigger than 1 on almost the whole domain, meaning that the QMC method improves the efficiency of the MC, by a value that can be greater than 5, depending on the considered points of the domain.

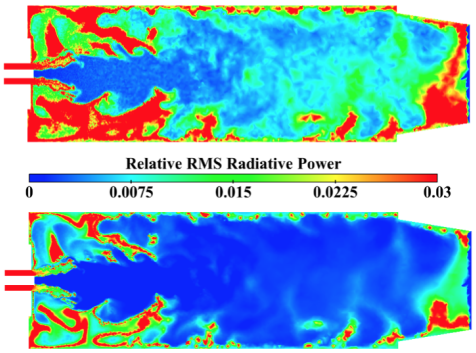


**FIGURE 13**. Instantaneous field of rms of radiative power obtained with Monte Carlo OERM (top) and Quasi-Monte Carlo OERM (bottom) at imposed number of rays.

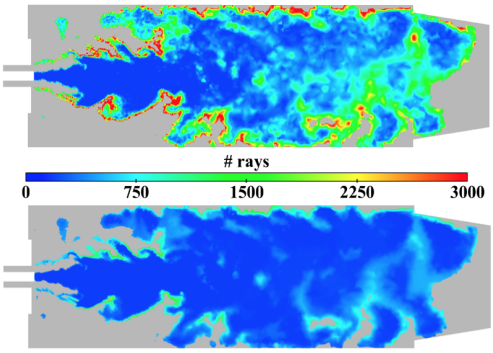


**FIGURE 14**. Number of rays necessary for the convergence used by Monte Carlo OERM (top) and Quasi-Monte Carlo OERM (bottom) in controlled convergence.

In order to localize the regions where Quasi Monte Carlo becomes more efficient, it is interesting to look at the scatter plot of the efficiency ratio in relation to the temperature for all the domain points and it is shown in Fig. 16. It is worth noting that this ratio is high in the cold pockets of the chamber near the walls, where normally the convergence is hard to be achieved, and that the regions characterized by a higher efficiency ratio are the ones at intermediate temperature (around 1000 K), which cover most of the domain.

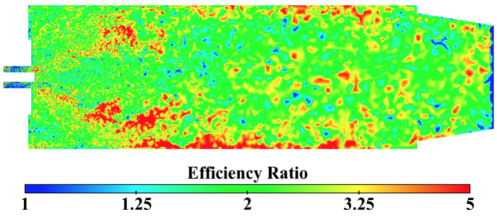


**FIGURE 15**. 2D map of the ratio between efficiency of Quasi-Monte Carlo and Monte Carlo methods.

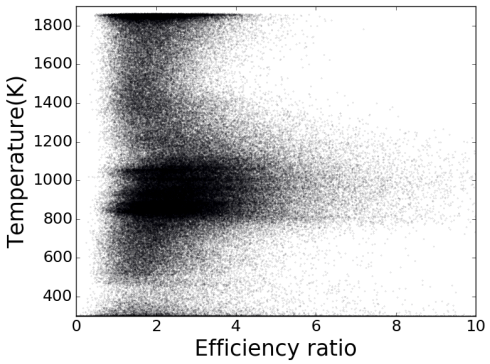


**FIGURE 16**. Scatter plot of temperature in relation to the efficiency ratio between Quasi-Monte Carlo and Monte Carlo for all the points of the domain.

## CONCLUSION

Monte Carlo methods applied to radiative heat transfer problems are known for being computationally expensive. In order to afford coupled 3D simulations of reactive flows, it is necessary to reduce the computational cost. Different strategies have been proposed to face this limit, some of them, like the ERM or the OERM methods, have been used in this study. Finally a technique to further improve the efficiency of Monte Carlo method, based on a low-discrepancy sampling, has been applied and the obtained quasi-Monte Carlo method has been combined with OERM and compared to the Monte Carlo in a complex configuration. Simulations results have shown a significant improvement from the quasi-Monte Carlo in terms of computational efficiency, introducing them as an excellent candidate for coupled high-fidelity simulations.

## ACKNOWLEDGMENT

This project has received funding from the European Unions Horizon 2020 research and innovation programme under the Marie Sklodowska-Curie grant agreement No 643134. It was also granted access to the HPC resources of CINES under the allocation 2016-020164 made by GENCI.

## REFERENCES

[1] Coelho, P. J., 2007. "Numerical simulation of the interaction between turbulence and radiation in reactive flows". *Progress in Energy and Combustion Science,* ***33***, pp. 311–383.

[2] Coelho, P. J., 2012. "Turbulence-Radiation Interaction: From Theory to Application in Numerical Simulations". *Journal of Heat Transfer-Transactions of the ASME,* ***134***(3).

[3] Deshmukh, K. V., Modest, M. F., and Haworth, D. C., 2008. "Direct numerical simulation of turbulence-radiation interactions in a statistically one-dimensional nonpremixed system". *JOURNAL OF QUANTITATIVE SPECTROSCOPY & RADIATIVE TRANSFER,* ***109***(14), SEP, pp. 2391–2400.

[4] Deshmukh, K. V., Haworth, D. C., and Modest, M. F., 2007. "Direct numerical simulation of turbulence-radiation interactions in homogeneous nonpremixed combustion systems". *Proceedings of the Combustion Institute,* ***31***(1), pp. 1641–1648.

[5] Zhang, Y., Vicquelin, R., Gicquel, O., and Taine, J., 2013. "Physical study of radiation effects on the boundary layer structure in a turbulent channel flow". *International Journal of Heat and Mass Transfer,* ***61***, pp. 654–666.

[6] Soucasse, L., Riviere, P., and Soufiani, A., 2014. "Subgrid-scale model for radiative transfer in turbulent participating media". *Journal of Computational Physics,* ***257***(A), pp. 442–459.

[7] Gupta, A., Haworth, D., and Modest, M., 2013. "Turbulence-radiation interactions in large-eddy simulations of luminous and nonluminous nonpremixed flames". *Proceedings of the Combustion Institute,* ***34***(1), pp. 1281 – 1288.

[8] Walters, D. V., and Buckius, R. O., 1992. "Rigorous development for radiation heat transfer in nonhomogeneous absorbing, emitting and scattering media". *International Journal of Heat and Mass Transfer,* ***35***(12), pp. 3323 – 3333.

[9] Tessé, L., Dupoirieux, F., Zamuner, B., and Taine, J., 2002. "Radiative transfer in real gases using reciprocal and forward monte carlo methods and a correlated-k approach". *International Journal of Heat and Mass Transfer,* ***45***(13), pp. 2797–2814.

[10] Cherkaoui, M., Dufresne, J.-L., Fournier, R., Grandpeix, J.-Y., and Lahellec, A., 1996. "Monte carlo simulation of radiation in gases with a narrow-band model and a net-exchange formulation". *Journal of Heat Transfer,* ***118***, pp. 401–407.

[11] Zhang, Y., Gicquel, O., and Taine, J., 2012. "Optimized emission-based reciprocity monte carlo method to speed up computation in complex systems". *International Journal of Heat and Mass Transfer,* ***55***(25–26), pp. 8172 – 8177.

[12] Lemieux, C., 2009. *Monte carlo and quasi-monte carlo sampling*. Springer Science & Business Media.

[13] Kersch, A., Morokoff, W., and Schuster, A., 1994. "Radiative heat transfer with quasi-monte carlo methods". *Transport Theory and Statistical Physics,* ***23***(7), 09, pp. 1001–1021.

[14] Guiberti, T. F., Durox, D., Zimmer, L., and Schuller, T., 2015. "Analysis of topology transitions of swirl flames interacting with the combustor side wall". *Combustion and Flame,* ***162***(11), pp. 4342–4357.

[15] Guiberti, T., Durox, D., Scouflaire, P., and Schuller, T., 2015. "Impact of heat loss and hydrogen enrichment on the shape of confined swirling flames". *Proceedings of the Combustion Institute,* ***35***(2), pp. 1385–1392.

[16] Mercier, R., Guiberti, T., Chatelier, A., Durox, D., Gicquel, O., Darabiha, N., Schuller, T., and Fiorina, B., 2016. "Experimental and numerical investigation of the influence of thermal boundary conditions on premixed swirling flame stabilization". *Combustion and Flame,* ***171***, pp. 42–58.

[17] Koren, C., Vicquelin, R., and Gicquel, O., 2017. "High-fidelity multiphysics simulation of a confined premixed swirling flame combining large-eddy simulation, wall heat conduction and radiative energy transfer". *ASME Turbo EXPO 2017 (Submitted)*.

[18] Taine, J., and Soufiani, A., 1999. "Gas radiative properties: From spectroscopic data to approximate models". Vol. 33 of *Advances in Heat Transfer*. Elsevier, pp. 295 – 414.

[19] Joe, S., and Kuo, F. Y., 2008. "Constructing sobol sequences with better two-dimensional projections". *SIAM Journal on Scientific Computing,* ***30***(5), pp. 2635–2654.

[20] Hlawka, E., 1961. "Funktionen von beschränkter variatiou in der theorie der gleichverteilung". *Annali di Matematica Pura ed Applicata,* ***54***(1), pp. 325–333.

[21] Tezuka, S., and Faure, H., 2003. "I-binomial scrambling of digital nets and sequences". *Journal of complexity,* ***19***(6), pp. 744–757.

# Appendix E

# Cold case validation of the Sandia jet flame

**Contents**



## E.1 Turbulent velocity profiles at the exit of the inlet pipe

### E.1.1 Generation of the turbulent profiles for $Re_{\mathbf{D}} = 20\,000$

In the case studied in Chapter 3, the fuel is injected through a fully-developed turbulent pipe at a Reynolds number $Re_D$ based on the diameter of the jet $D$ equal to $Re_{\mathrm{D}} = 20\,000$. The diameter $D$ is equal to 3.2mm and the corresponding bulk velocity is equal to $u_{\mathrm{bulk}} = 54.7$ m/s.

To obtain the corresponding turbulent profiles to impose as boundary conditions of the fuel inlet in the Sandia jet flame calculation, a preliminary computation of a periodic pipe with the corresponding diameter has been first computed. Figure E.1 presents the corresponding mesh. In order to achieve

the computation at a reasonable cost, a quarter of the pipe in the orthoradial direction has been considered and a length $L = 3\text{D}$ has been considered. Periodic assumptions are considered in both $\mathbf{e_x}$ and $\mathbf{e}_\theta$ directions.

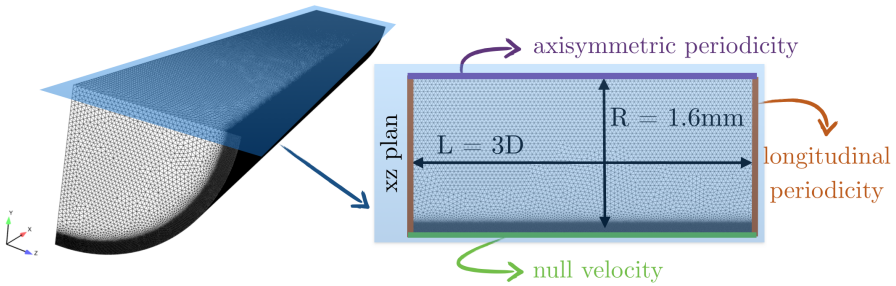


**Figure E.1:** *Mesh and boundary conditions used for the generation of the developed turbulent profiles of the pipe.*

In order to estimate the distance $\Delta y$ of the first point near to wall in order to obtain a well-resolved boundary layer, the wall shear stress $\tau_w$ has been estimated based on the Kármán-Nikuradse correlation of the friction coefficient $C_f$:

$$C_f = 0.046 \cdot Re_{\text{D}}^{-0.2} = 6.35 \times 10^{-3} \tag{E.1}$$

Then, wall shear stress $\tau_w$ and the friction velocity $u_\tau$ can be estimated as:

$$\begin{aligned} \tau_w &= \frac{1}{2} C_f \rho_{C_2H_4} u_{\text{bulk}}^2 = 11.0 \text{ N/m}^2 \\ u_\tau &= \sqrt{\tau_w / \rho_{C_2H_4}} = 3.1 \text{ m/s} \end{aligned} \tag{E.2}$$

with $\rho_{C_2H_4} = 1.16$ kg/m$^3$. The friction Reynolds number is equal to $Re_\tau = u_\tau D/(2\nu) = 567$.

Considering a first point at $y^+ = 2$ in order to obtain a resolved LES of the boundary layer, the distance to the wall $\Delta y$ is estimated as:

$$\Delta y = \frac{y^+ \nu_{C_2H_4}}{u_\tau} = 6 \ \mu\text{m}. \tag{E.3}$$

with $\nu_{C_2H_4} = 8.8 \times 10^{-6}$ m$^2$/s.

Then, a constant resolution with a mesh size $\Delta y$ is considered for the resolution of the turbulent boundary layer from $y^+ = 2$ until $y^+ = 50$. Then, from $y^+ = 50$, a coarser mesh is considered. The mesh contains finally 61 millions cells and 11 millions nodes and a total averaging time of 10 ms has been used for the statistics. The Wale model (Nicoud and Ducros 1999) has been used for the subgrid-scale stress modelling.

### E.1.2 Obtained turbulent profiles and comparison with the literature

The quantities of interest to be imposed as boundary conditions for the jet flame calculation inlet are:

- The non dimensional mean axial velocity $\overline{u}+$: $\overline{u}+ = \overline{u}/u_\tau$,
- The non dimensional rms axial velocity $u_{\text{rms}}+$: $u_{\text{rms}}+ = u_{\text{rms}}/u_\tau$,
- The non dimensional rms radial velocity $u_{r,\text{rms}}+$: $u_{r,\text{rms}}+ = u_{r,\text{rms}}/u_\tau$,
- The non dimensional rms tangential velocity $u_{\theta,\text{rms}}+$: $u_{\theta,\text{rms}}+ = u_{\theta,\text{rms}}/u_\tau$,
- The non dimensional velocity shear-stress $\overline{uu_r}+$: $\overline{uu_r}+ = \overline{uu_r}/u_\tau^2$.

Figure E.2 presents the obtained profiles for the presented numerical calculation ($Re_\text{D} = 20\,000$) and comparisons with the results obtained in literature for the DNS of a turbulent pipe flow with a Reynolds number $Re_\text{D} = 19\,000$ (El Khoury et al. 2013). The agreement is satisfactory. Disagreements are due to the limited extent of the domain ($L = 3D$) and to the axisymmetric BC which strongly affects the flow near the axis.

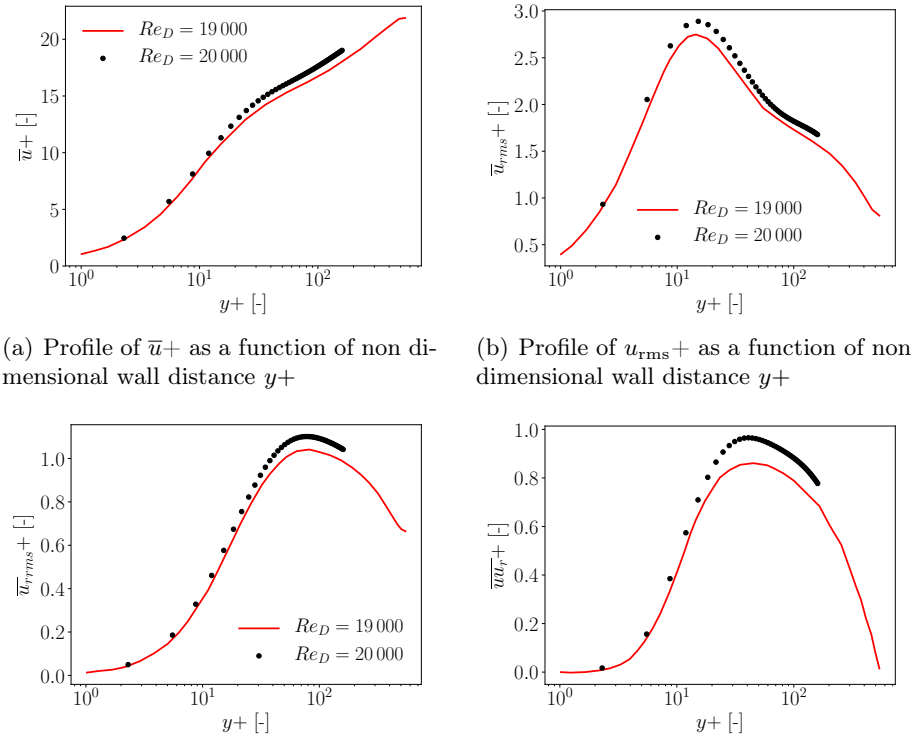


(a) Profile of $\overline{u}+$ as a function of non dimensional wall distance $y+$

(b) Profile of $u_{\text{rms}}+$ as a function of non dimensional wall distance $y+$

(c) Profile of $u_{r,\text{rms}}+$ as a function of non dimensional wall distance $y+$

(d) Profile of $\overline{uu_r}+$ as a function of non dimensional wall distance $y+$

**Figure E.2:** *Comparisons between obtained non dimensional turbulent profiles ($Re_D = 20\,000$) and the ones obtained in the study of El Khoury et al. (2013) for a Reynolds number $Re_D = 19\,000$.*

These profiles have been fitted with tenth order polynomial fit and have been finally imposed as boundary conditions for the cold case simulation (presented hereafter) and the hot cases presented in Chapter 3.

## E.2 Cold case simulation

In the studied configuration, no experimental data was available for the validation of the cold flow. In order to validate the numerical setup and the mesh resolution, a cold flow simulation has however nonetheless realized. The results are compared with the classical non dimensional profiles obtained for a classical round jet. In the studied geometry, the round jet is surround by a coflow, then, it is not expected to retrieve exactly the same results as the one obtained for a classical round jet. However, the velocity of the coflow ($u_{\text{coflow}} \approx 0.65\text{m/s}$) is low compared with that of the main jet ($\approx 54.7\text{m/s}$), and the results are then expected to be quite similar. The computation mesh is presented in Fig. 4.1 of Chapter 4. The Wale model (Nicoud and Ducros 1999) has been used for the subgrid-scale stress modelling.

### E.2.1 Auto-similar axial profiles

For a turbulent round jet, from several diameters after the jet exit, an auto-similar behavior can be retrieved for the axial profiles (Pope 2000). The mean axial velocity $\overline{u_0(x)}$ can be expressed as:

$$\frac{U_{\text{bulk}}}{\overline{u_0(x)}} = \frac{1}{B}\frac{x - x_0}{D_{\text{jet}}} \tag{E.4}$$

where $U_{\text{bulk}}$ is the exit bulk velocity of the jet, $x$ is the axial coordinate,$x_0$ is the virtual origin, $D_{\text{jet}}$ is the diameter of the jet and $B$ is an universal constant, independent of Reynolds number.

For the RMS of the axial velocity, it is also well known that, in the auto-similar region and at the centerline of the jet, the ratio between the RMS of the axial velocity ($u_{\text{rms}}(x)$) and the mean axial velocity ($\overline{u_0(x)}$) is nearly equal to 0.25.

$$\frac{u_{\text{rms}}(x)}{\overline{u_0(x)}} \underset{x \to +\infty}{\to} 0.25 \tag{E.5}$$

These relations are generally verified for classical round jet. In this configuration, a coflow of air is present and can perturb the validity of these correlations. Figure E.2.1 presents the evolution of the quantities $U_{\text{bulk}}/\overline{u}$ and $u_{\text{rms}}/u_{\text{bulk}}$ with the axial coordinate $x$ for the studied configuration with two different numerical schemes: Lax-Wendroff (LW) (Lax and Wendroff 1960) and the Two-step Taylor Galerkin Type C (TTGC) (Colin and Rudgyard 2000) numerical

schemes.

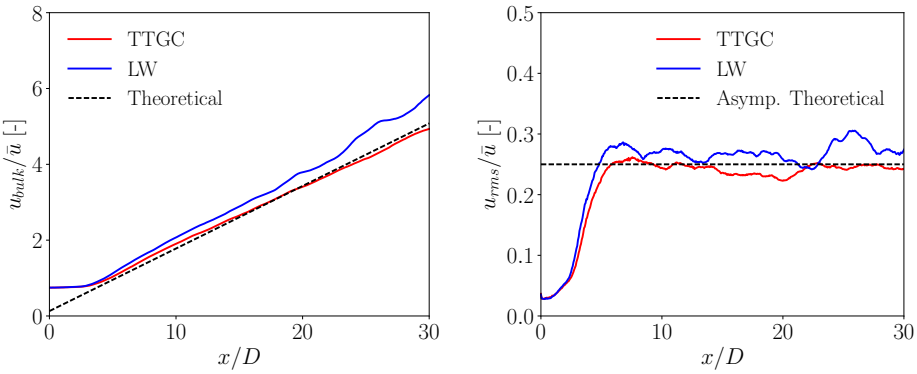


(a) Axial profile of $U_{\text{bulk}}/\overline{u}$ (b) Axial profile of $u_{\text{rms}}/u_{\text{bulk}}$

**Figure E.3:** *Comparisons of auto-similar evolutions of $U_{bulk}/\overline{u}$ and $u_{rms}/u_{bulk}$ for the studied configuration with the theoretical results for a round jet (Pope 2000)*

Here, for the theoretical deshed line presented in Fig. (a), the coefficient $B$ is taken equal to 6.06, which corresponds to the value referenced in Pope (2000). The fictive origin is taken equal to $x_0 = 0.8D_{\text{jet}}$.

Then, it can be concluded that the classical results of the round jet were reproduced with the TTGC numerical scheme, even with the presence of the coflow, which tends to not perturb the axial behavior of the jet in this case.

### E.2.2 Auto-similar radial profiles

#### E.2.2.1 Mean velocity profiles

For $x$ in the self-similar region, it is shown that for a round jet, the jet spreads linearly (Pope 2000). The spreading rate $S$ is defined as:

$$S = \frac{\mathrm{d}r_{1/2}(x)}{\mathrm{d}x} \tag{E.6}$$

where $r_{1/2}(x)$ is the half-radius at the height $x$. For a round jet, $S$ is independent of the Reynolds number and has been taken equal to 0.096 (Pope 2000).

Then, this half-radius $r_{1/2}(x)$ can be written as:

$$r_{1/2} = S(x - x_0) \tag{E.7}$$

The normalized radius $\xi(r, x) = r/r_{1/2}(x)$ at each height above the jet is then defined as:

$$\xi(r, x) = \frac{r}{r_{1/2}(x)} \tag{E.8}$$

Then, for a round jet and in the auto-similar region, the radial evolution of $u(\xi,x)/u_0(x)$ as a function of $\xi$ is the same for any height $x$ above the burner. To verify the validity of this behavior in the case of a coflow jet, Fig. E.4 presents the evolution of the quantity $(\overline{u}(\xi,x)-\overline{u}(+\infty,x))/(\overline{u_0}(x)-\overline{u}(+\infty,x))$ as a function of $\xi$ for four different heights: $x = 50$mm, $x = 100$mm, $x = 150$mm and $x = 200$mm, and for the LW (a) and TTGC convective schemes. The velocity of the coflow $\overline{u}(+\infty,x)$ has been subtracted to the velocities in order to remove the effect of the coflow. It can be observed that the auto-similarity behavior is well retrieved, with better results with the lower dissipative TTGC convection scheme compared with LW.

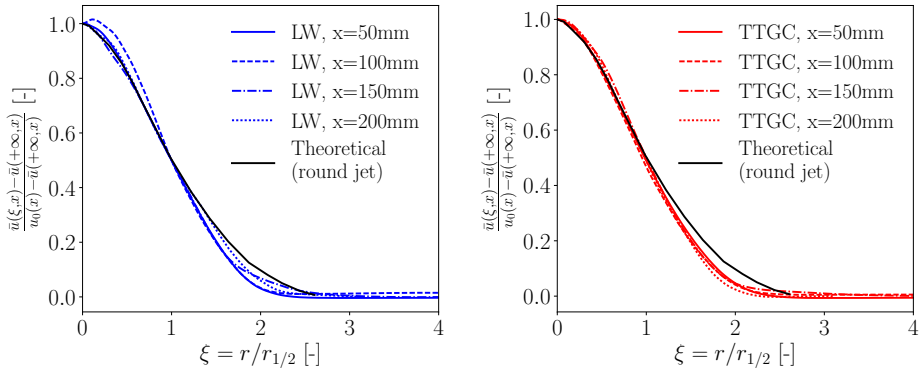


(a) LW numerical scheme

(b) TTGC numerical scheme

**Figure E.4:** *Auto-similar radial profiles of axial velocity for four different heights above the jet: $x/D = 50mm$, $x/D = 100mm$, $x/D = 150mm$ and $x/D = 200mm$, and two different numerical schemes: Lax-Wendroff (LW) and Two-Step Taylor Galerkin Type C (TTGC). Results are compared with the results of Pope (2000) for a round jet.*

### E.2.2.2 Velocity fluctuations profiles

Figure E.5 (left) presents the radial profiles of the axial velocity RMS ($u^2_{\text{rms}}$), the radial velocity RMS ($u^2_{r,\text{rms}} = \overline{u_r^2}$), and the tangential velocity RMS ($u^2_{\theta,\text{rms}} = \overline{u_\theta^2}$) the as a function of the normalized radius ($\xi = r/r_{1/2}$), for three axial positions: $x = 50$mm, $x = 100$mm and $x = 150$mm. The data is also compared with the data obtained by Pope (2000) for the classical round jet. It can be observed that a general good agreement is obtained. As the coflow is only slightly turbulent, it does not have a strong influence on these quantities compared with the results obtained for a round jet.

Figure E.5 (right) presents the radial profiles for the ratio $\overline{uu_r}/k$ and the $u-u_r$ correlation coefficient $\rho_{uu_r}$ at the same three heights above the jet exit. These quantities characterize the magnitude of the shear stress. $k$ corresponds to the

turbulent kinetic energy defined as:

$$k = \frac{1}{2}\left(u_{\text{rms}}^2 + u_{r,\text{rms}}^2 + u_{\theta,\text{rms}}^2\right). \tag{E.9}$$

$\rho_{uu_r}$, the $u - u_r$ correlation coefficient, is calculated as:

$$\rho_{uu_r} = \frac{\overline{u'u'_r}}{\sqrt{\overline{u'^2}\ \overline{u_r'^2}}}. \tag{E.10}$$

For these quantities, the maximum expected values for a round jet, Pope (2000), are respectively $\overline{uu_r}/k \approx 0.27$ and $\rho_{uu_r} \approx 0.4$. These values are well retrieved in this configuration.

Finally, it is important to notice that in this configuration, due to orthoradial axisymmetry, the correlations $\overline{u'u'_\theta}$ and $\overline{u'_r u'_\theta}$ are null.

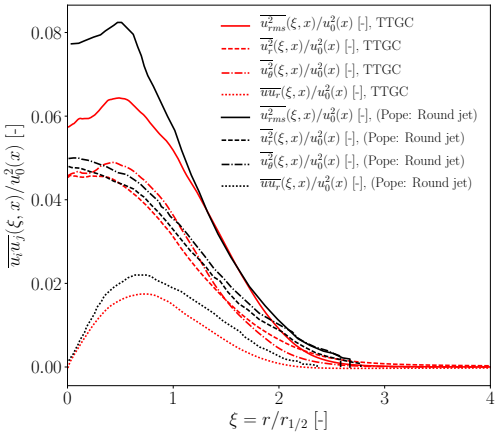


(a) Normalized radial velocity fluctuations profiles at $x/D = 50$

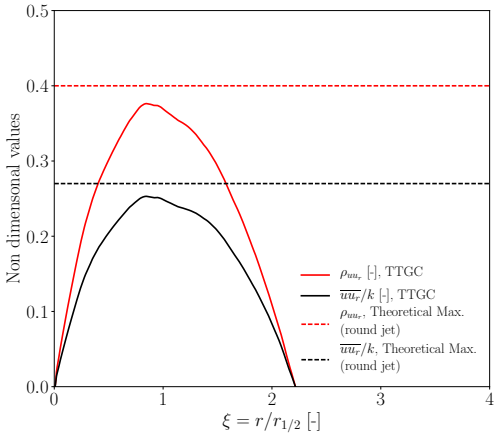


(b) Radial profiles of $\rho_{uu_r}$ and $\overline{uu_r}/k$ at $x/D = 50$

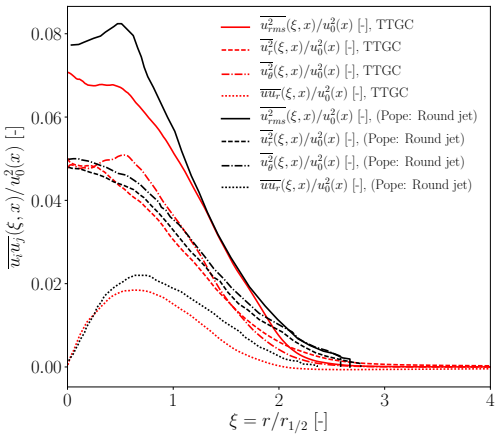


(c) Normalized radial velocity fluctuations profiles at $x/D = 100$

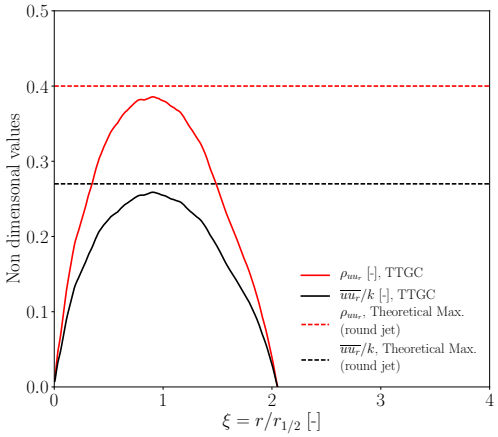


(d) Radial profiles of $\rho_{uu_r}$ and $\overline{uu_r}/k$ at $x/D = 100$

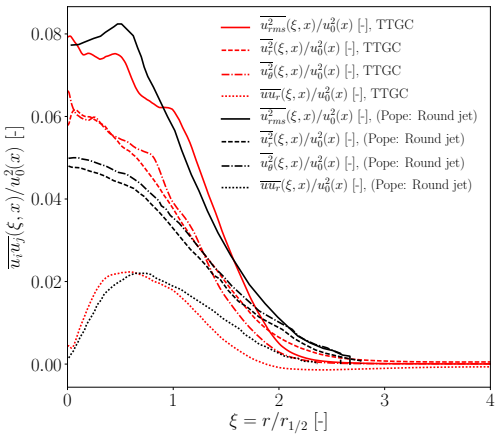


(e) Normalized radial velocity fluctuations profiles at $x/D = 150$

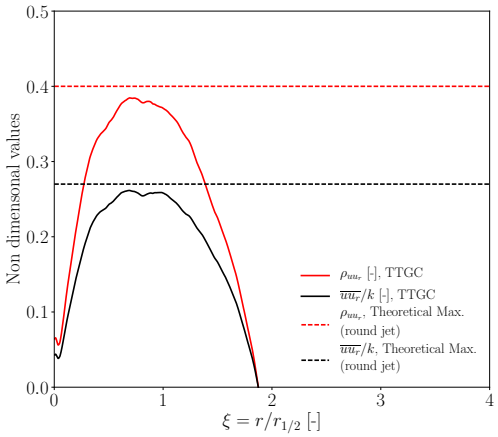


(f) Radial profiles of $\rho_{uu_r}$ and $\overline{uu_r}/k$ at $x/D = 150$

**Figure E.5:** *Normalized radial velocity fluctuations, $\rho_{uu_r}$ and $\overline{uu_r}/k$ profiles at different positions above the jet exit. Numerical obtained data with the TTGC convection scheme is compared with the data presented by Pope (2000) for a classical round jet.*

# Appendix F

# DLR configuration: external thermal boundary condition modeling

*This appendix is a part of a publication submitted to ASME Turbo Expo 2018.*

*Many laboratory-scale combustors are equipped with viewing windows to allow for characterization of the reactive flow. Additionally, pressure housing is used in this configuration to study confined pressurized flames. Since the flame characteristics are influenced by heat losses, the prediction of wall temperature fields becomes increasingly necessary to account for conjugate heat transfer in simulations of reactive flows. For configurations similar to this one, the pressure housing makes the use of such computations difficult in the whole system. It is therefore more appropriate to model the external heat transfer beyond the first set of quartz windows. The present study deals with the derivation of such a model which accounts for convective heat transfer from quartz windows external face cooling system, free convection on the quartz windows 2, quartz windows radiative properties, radiative transfer inside the pressure housing and heat conduction through the quartz window. The presence of semi-transparent viewing windows demands additional care in describing its effects in combustor heat transfers. Because this presence is not an issue in industrial-scale combustors with opaque enclosures, this topic specific to laboratory-scale combustors has not been addressed before. After validating the model for the selected setup, the sensitivity of several modeling choices is computed. This enables a simpler expression of the external heat transfer model that can be easily implemented in coupled simulations.*

Contents



## F.1 Introduction

In aircraft engines as in many applications, the reactive flow in the combustion chamber is both turbulent and high in pressure. Optical access to the flame is necessary to thoroughly study such configurations at a laboratory scale, while maintaining representative pressures of real applications. To do so, a pressure housing can be used in order to impose pressure within the combustion chamber (Higgins et al. 2001; Tsurikov et al. 2005; Malbois et al. 2017), as experimentally investigated in the considered sooting turbulent ethylene/air flame at DLR (Geigle et al. 2013). This swirled turbulent non-premixed flame is stabilized at several pressures (1, 3 and 5 bars) for several operating points inside a high pressure combustion chamber. Optical access into the combustion chamber is provided through four separate quartz windows, collectively labeled as quartz windows 1. Cooling of the quartz windows 1 is established through multiple transverse laminar air jets on the outer face, *i.e.* outside of the combustion chamber. This allows for a better definition of boundary conditions inside the combustor, specifically for modeling purposes. The combustion chamber is surrounded by the stainless steel pressure housing equipped with four quartz windows (denoted quartz windows 2) for optical access to the combustion chamber. Quartz windows 1 and 2 present semi-transparent radiative properties: transparent for visible wavelengths, but opaque for infrared

ones (Heraeus 2016). Several numerical studies have investigated this setup (Eberle et al. 2014; Franzelli et al. 2015; Eberle et al. 2015; Koo et al. 2016; Wick et al. 2017) without much attention to the combustor heat transfer mechanisms. However, heat losses due to wall heat transfer and radiation impact flame stabilization (Nogenmyr et al. 2013; Guiberti et al. 2015; Tay-Wo-Chong et al. 2016; Mercier et al. 2016), gas temperature, and consequently gaseous pollutant emissions (Ihme and Pitsch 2008a; Lamouroux et al. 2014) and soot production. Numerical simulations of combustors must therefore account for these heat losses either through experimental or computed boundary conditions e.g. wall temperatures on the inner windows surface. The present study aims at providing an efficient model for the corresponding combustor walls' external boundary conditions.

Using a detailed approach such as large-eddy simulation (LES) in a multiphysics framework is a promising candidate to accurately predict the wall temperature field. Such a combination of LES and conjugate heat transfer (CHT) has already been applied to several combustion applications (Jaure et al. 2013; Mari et al. 2016; Miguel-Brebion et al. 2016). When radiative energy transfer must be accounted for, the LES code is coupled to a solver of the radiative transfer equation (Jones and Paul 2005; Gonçalves dos Santos et al. 2008; Poitou et al. 2012). The LES-CHT combination can then be enriched with a radiation solver to yield a comprehensive multiphysics approach to determine radiative, convective and conductive heat transfers at the wall as in Berger et al. (2016) and Koren et al. (2017b). Such multiphysics simulations of the aforementioned DLR test rig are the long-term objective of this study. In practice, the simulation of the full test rig with all components participating to the combustor heat transfer mechanisms is cumbersome. Indeed, with a pressure housing, the elements to consider would be :

- the participating reactive flow inside the combustor,
- the heat conduction (and radiative transfer through the quartz windows 1) in the combustor walls,
- the cooling system inside the combustor walls and at the outer side of the quartz windows 1,
- the flow and radiative transfer in the casing,
- the heat conduction (and radiative transfer through the quartz windows 2) in the casing walls,
- the external free convection and thermal radiation exchange between the casing outer walls and its surrounding experimental room.

Instead, only the first two items can be resolved in the coupled simulation, provided that adequate external boundary conditions are prescribed through models. An assessment of the modeling methodology of external heat transfer of the considered DLR test rig is therefore needed, which is the objective of the present study. Carrying out a sensitivity study of the model parameters

with RANS simulations would be too costly or even unaffordable with LES. Assuming uniform window temperature on each faces enables instead a quick model assessment to select a final and simplified version of the external heat transfer boundary condition to be used later in CFD computations.

In particular, one must take care of the semi-transparent nature of the viewing windows. While absent in industrial systems, these windows, often present in laboratory-scale models, can strongly modify the internal and external radiative heat transfer. Surprisingly, this effect on the combustor heat transfer has not been thoroughly investigated. In fact, the validation of coupled CFD simulation with thermal radiation has mainly been involved with unconfined flames (Modest and Haworth 2016) mostly because of the usually unknown wall temperature in confined configurations. Applications to confined combustor with opaque boundaries as in Zhao et al. (2013) require providing the wall emissivity which can be quite uncertain depending on the type and state of the material. To the best of our knowledge, only a couple of studies from French research groups have investigated combustors enclosed with viewing windows (Gonçalves dos Santos et al. 2008; Poitou et al. 2011; Poitou et al. 2012; Koren et al. 2017b). The windows properties were either not detailed or a fixed averaged emissivity was specified (Poitou et al. 2011; Koren et al. 2017b). Given the number of laboratory-scale combustor equipped with viewing windows, the number of such studies is expecting to grow significantly along with the need to assess the impact of semi-transparent windows.

The study is organized as follows. The combustor configuration is first presented along with the notations of the different physical phenomena that are considered. The models for the different parts of the system and associated heat transfer mechanisms are then detailed: convective heat transfer from the quartz windows 1 cooling system and free convection on the quartz windows 2, the quartz windows radiative properties, the radiative transfer inside the pressure housing and the heat conduction through the quartz window. The derived model is validated against experimental measurements of the quartz windows 1 temperature on both inner and outer sides. A sensitivity analysis of the model finally allows for studying the impact of the different model components on the combustion chamber window temperatures in order to retain a simplified version which can be easily implemented as an external boundary condition.

## F.2 Presentation of the combustion chamber thermal environment

Figure F.1 presents the design of the overall burner (combustion chamber and pressure housing) and the optical module composed of different quartz windows (for the combustion chamber and the pressure housing).

The burner injector consists of three concentric swirled nozzles. Air is injected through a central and an annular nozzle, while fuel is injected between these two nozzles. For some operating points, additional cold air is supplied 80 mm downstream of this primary injector through four secondary air ports in the combustion chamber posts. Details on the three considered configurations are given in Tab. F.1.

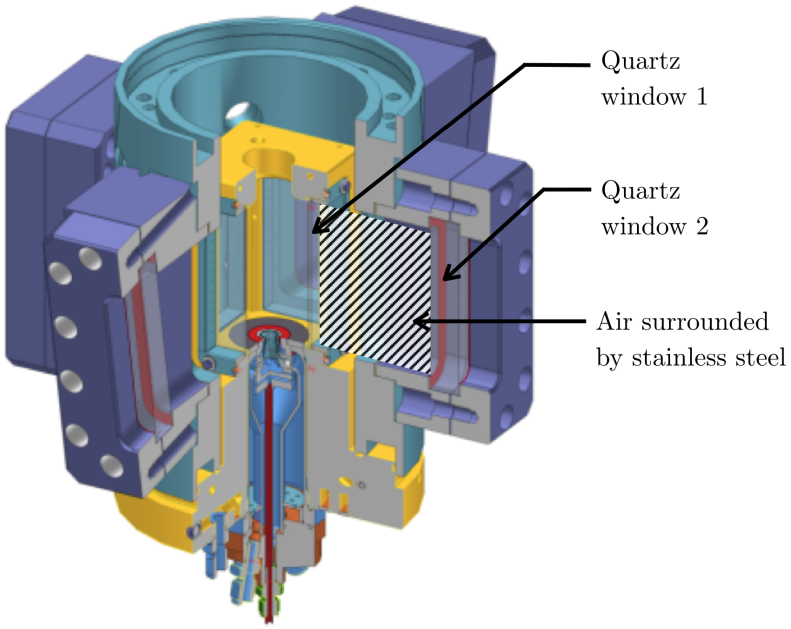


**Figure F.1:** *Design of burner, combustion chamber and optical module of pressure housing.*

| | $p$ [bar] | $\Phi$ [-] | $P_{\text{primary}}$ [kW] | $Q_{\text{air,c}}$ [slm] | $Q_{\text{air,r}}$ [slm] | $Q_{\text{fuel}}$ [slm] | $Q_{\text{oxi}}$ [slm] | $\frac{Q_{\text{air,c}}}{Q_{\text{air}}}$ [-] | $\frac{Q_{\text{oxi}}}{Q_{\text{air}}}$ [-] | $\Phi_{\text{global}}$ [-] | $P_{\text{global}}$ [kW] |
|---|---|---|---|---|---|---|---|---|---|---|---|
| Case 1 | 3 | 0.9 | 32.2 | 156.0 | 365.1 | 32.7 | 208.2 | 0.3 | 0.4 | 0.64 | 32.2 |
| Case 2 | 3 | 1.2 | 32.2 | 140.8 | 328.5 | 39.3 | 0 | 0.3 | 0 | 1.2 | 32.2 |
| Case 3 | 3 | 1.2 | 32.2 | 140.8 | 328.5 | 39.3 | 187.4 | 0.3 | 0.4 | 0.86 | 38.6 |

**Table F.1:** *Considered operating points: Pressure, p, volume flow rates for air through burner (central and ring), $Q_{air,c}$ and $Q_{air,r}$, fuel, $Q_{fuel}$, oxidation air through secondary air inlet, $Q_{oxi}$, primary and global equivalence ratios, $\Phi$ and $\Phi_{global}$, primary and global thermal powers, $P$ and $P_{global}$, and fractions $Q_{air,c}/Q_{air}$ and $Q_{oxi}/Q_{air}$ with $Q_{air} = Q_{air,c} + Q_{air,r}$. Flow rates are referenced to 1.013 bar and 273 K.*

The walls of the combustion chamber are composed of four quartz windows of thickness $e_1 = 3$ mm, and four copper posts at each corner cooled to about 333 K. The bottom of the combustion chamber is composed of a stainless steel plate whose temperature is estimated around 650 K. For each operating point,

the temperature at the inner and outer window surfaces has been measured using laser induced phosphorescence (LIP) along the window vertical centerline.

The corresponding temperature profiles along the vertical axis of the quartz windows are given in Fig. F.2. The measurement error was derived to be about 0.5% for low and intermediate temperature and about 3% for the peak temperatures (Nau et al. 2017).

The pressure housing is composed of stainless steel, whose mean temperature is noted $T_3 = 313$ K, and four quartz windows, parallel to the ones of the combustion chamber and with a thickness $e_2 = 40$ mm. The air in the pressure housing is injected as a film cooling on the quartz windows 1 and exhausts to the top.

The notations to describe heat transfer mechanisms through one window of the combustor are presented in Fig. F.3. The model accounts for conduction in both quartz windows 1 and 2, radiation between the two sets of windows and the pressure housing in between and boundary layers at the interfaces between the both quartz windows and air. The model is assessed by considering uniform temperature fields in the vertical and spanwise directions. This allows for deriving a simple yet coarse model to discriminate between effects of different phenomena on the predicted window heat flux and temperature. The considered quantities are then the space-averaged window temperatures and fluxes. The temperature at the inner and outer surfaces of the combustion chamber quartz windows are denoted as $\mathrm{T_{in}}$ and $\mathrm{T_{out}}$, respectively. $\mathrm{T_{2a}}$ and $\mathrm{T_{2b}}$ denote the inner and outer temperatures of the pressure housing windows. While the window temperature profiles are in fact inhomogeneous (see Fig. F.2), the space-averaged conductive flux computed from the inhomogeneous profiles on the inner and outer sides of the window is very similar to the one estimated from space-averaged temperatures. However, the $T^4$ non-linear dependency of wall radiative flux with temperature certainly strongly enhances the window profile inhomogeneity and is expected to limit the accuracy of the simplified model.

The energy balance at each interface is given by

$$\begin{cases} \varphi_1^{\mathrm{cond}} = \varphi_1^{\mathrm{rad}} + \varphi_1^{\mathrm{conv}} \\ \varphi_{2\mathrm{a}}^{\mathrm{rad}} + \varphi_{2\mathrm{a}}^{\mathrm{conv}} = \varphi_2^{\mathrm{cond}} \\ \varphi_2^{\mathrm{cond}} = \varphi_{2\mathrm{b}}^{\mathrm{rad}} + \varphi_{2\mathrm{b}}^{\mathrm{conv}} \\ \text{Eqs. (F.17) and (F.18) linking } \varphi_{2\mathrm{a}}^{\mathrm{rad}} \text{ and } \varphi_1^{\mathrm{rad}} \end{cases} \tag{F.1}$$

Then, fixing the inner surface temperature $T_{\mathrm{in}}$ of the first quartz window, all the other fluxes and temperatures of the system can be determined. The fixed homogeneous temperature $T_{\mathrm{in}}$ is set according to the experimental temperature data averaged along the centreline.

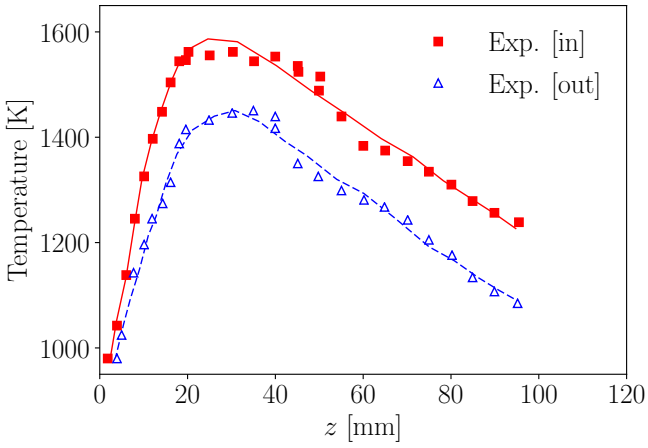


(a) Case 1

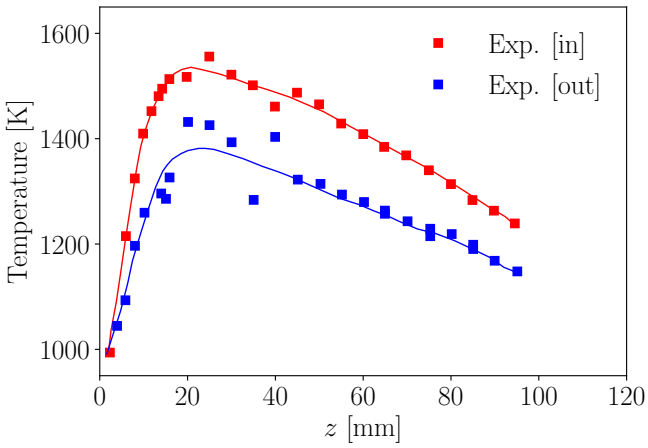


(b) Case 2

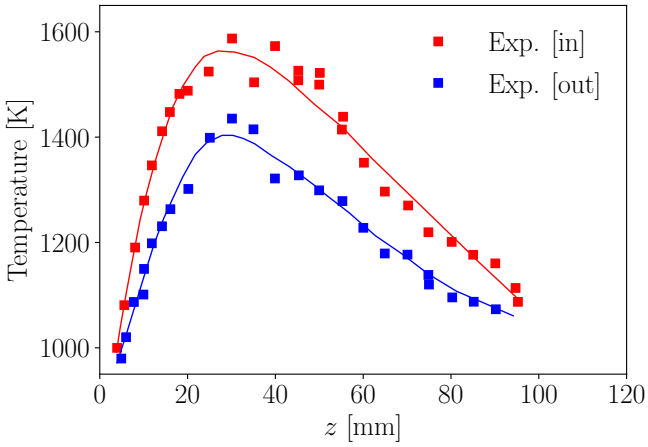


(c) Case 3

**Figure F.2:** *Measured temperatures of the inner and outer surface of the combustion chamber windows along the vertical axis for Case 1 (Nau et al. 2017). Lines correspond to fits of the experimental data.*

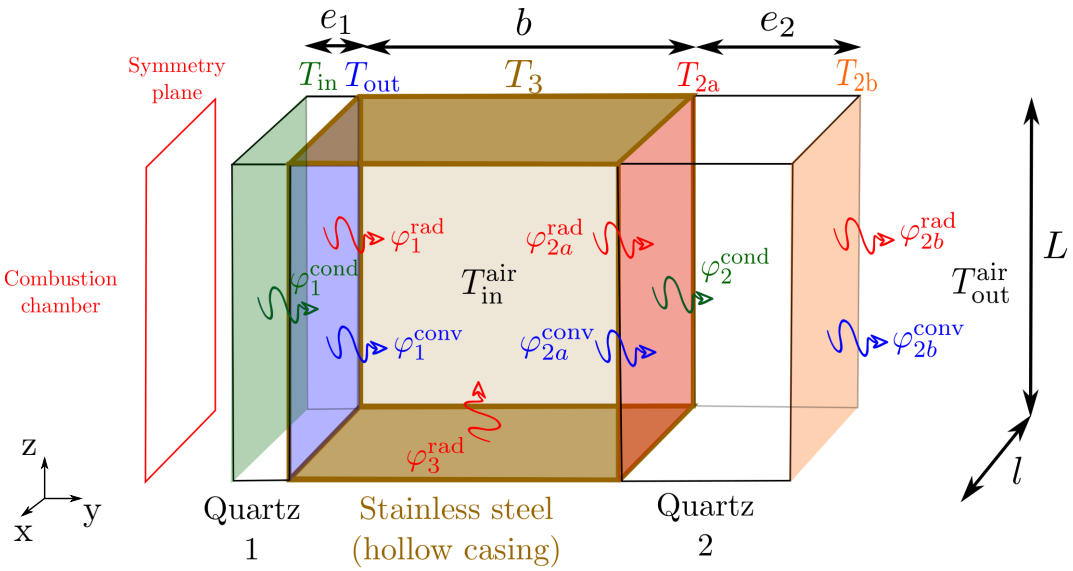


**Figure F.3:** *Representation of the heat exchanges outside the combustion chamber. The defined sizes are $L = 120$ mm, $l = 60$ mm, $b = 108$ mm, $e_1 = 3$ mm and $e_2 = 40$ mm. Brown faces correspond to stainless steel surrounding air inside the pressure housing.*

In the following the thermodynamical properties of air ($k^{\text{air}}(T), \mu^{\text{air}}(T), c_p^{\text{air}}(T)$) are computed from polynomial fits (Green and Perry 2007). The air temperatures are taken equal to $T_{\text{in}}^{\text{air}} = 333$ K inside the pressure housing and $T_{\text{out}}^{\text{air}} = 300$ K outside the pressure housing (ambient air). The air density $\rho^{\text{air}}(T, p)$ is computed through the ideal gas law. The pressure inside the housing is 3 bar.

## F.3 Convective transfer modeling

### F.3.1 Quartz windows 1 cooling system

The cooling system of the combustion chamber windows is illustrated in Fig. F.4. Each left and right side of the quartz windows 1 is cooled on the outer face through $N_{\text{jet}} = 14$ small orifices with a total flow rate of 150 slm, which corresponds to an exit velocity $u_{\text{jet}}$ of approximatively 15 m/s. The generated cooling flow is modeled as a bidimensional wall jet whose equivalent thickness $e_{\text{eq}}$ and exit velocity $u_{\text{wjet}}$ are defined to conserve the total mass and momentum fluxes (Fig. F.5). These two conditions result in $u_{\text{wjet}} = u_{\text{jet}}$ and $e_{\text{eq}} = (N_{\text{jet}} \pi d_{\text{jet}}^2)/(4L)$, where $d_{\text{jet}}$ and $L$ are the diameter of each cooling jet and the window height, respectively.

The Reynolds number based on the equivalent wall jet thickness $e_{\text{eq}}$ is $\text{Re}_{e_{\text{eq}}} = 169$, which indicates that the flow is laminar. Self-similar solutions of such incompressible wall jets have been studied in fluid mechanics (Glauert 1956) and heat transfer (Schwarz and Caswell 1961). Schwarz and Caswell (1961)

have derived a formulation of the heat transfer coefficient for the isothermal wall case whose validity has been investigated numerically (Issa and Ortega 2004). Later, Issa (2006) has proposed a general relationship of the evolution of Nusselt number as a function of the distance from the leading edge, the local Prandtl number and the bulk Reynolds number in the case of isothermal and constant heat flux, which is retained here:

$$\mathrm{Nu}_1(x,z) = \frac{h_1(x,z)(x+l_{\mathrm{th}})}{k^{\mathrm{air}}} = 0.345\,\mathrm{Pr}^{0.34}\mathrm{Re}_{e_{\mathrm{eq}}}^{0.75}\left(\frac{x+l_{\mathrm{th}}}{e_{\mathrm{eq}}}\right)^{1/4} \tag{F.2}$$

with $h_1(x,z)$ the local convective heat transfer coefficient on the outer surface of the quartz windows 1. This equation is considered for each half window separated by the vertical centerline given that cooling air is injected at each lateral side. All physical properties in the fluid are computed at the film temperature approximated as $T_{\mathrm{film}}(x,z) = (T_{\mathrm{out}}(x,z) + T_{\mathrm{in}}^{\mathrm{air}})/2$. The thermal length $l_{\mathrm{th}}$, setting the fictive origin of the formula, is given by $l_{\mathrm{th}}/e_{\mathrm{eq}} = 0.047 \cdot \mathrm{Re}_{e_{\mathrm{eq}}} - 0.28$.

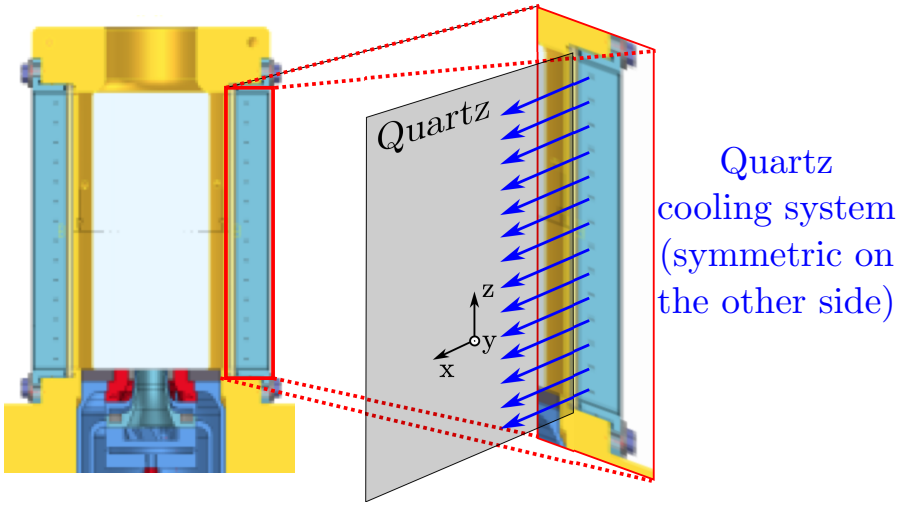


**Figure F.4:** *Combustion chamber quartz cooling system (from ISF communication (ISF3 2017) )*

In a 3-D simulation, the non-homogeneous profile of the heat transfer coefficient $h_1(x,z)$ is used directly. In the considered study based on surface averaged temperature, a global heat transfer coefficient $\overline{h_1}$ should be considered instead to compute the heat flux at the outer surface of the quartz windows 1 as:

$$\varphi_1^{\mathrm{conv}} = \overline{h_1}(T_{\mathrm{out}} - T_{\mathrm{in}}^{\mathrm{air}}). \tag{F.3}$$

Combining the evaluation $\overline{h_1}$ from the average of $h_1(x)$ with the average temperature provided by the experimental data on the centerline ($x = l/2$) yield incorrect results. This is attributed to the variations of the experimental field

of temperature in the transverse directions. This is corrected by considering $\overline{h_1} = h_1(x = l/2)$ instead.

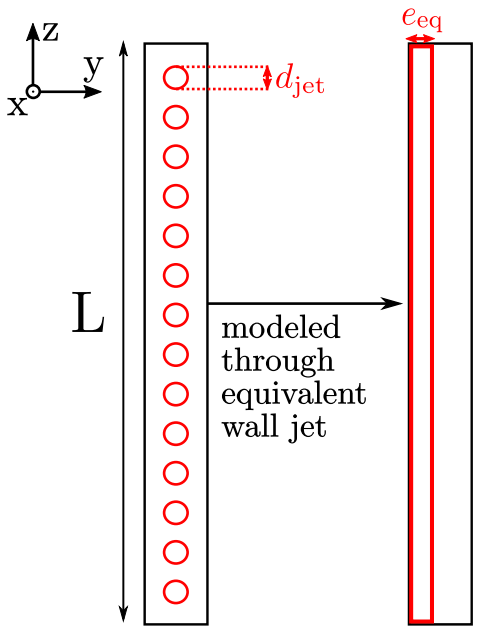


**Figure F.5:** *Cooling system modeling through equivalent wall jet*

### F.3.2 Free convection on the quartz windows 2

The convective heat transfer coefficient $h_{2a}^{conv}$ at the inner side of the quartz windows 2 is determined by a free convection boundary layer. The corresponding Nusselt number $\mathrm{Nu}_{2a}^{L} = \frac{h_{2a}^{conv} L}{k^{air}}$ is calculated through the following correlation (Churchill and Chu 1975) for a vertical plate:

$$\mathrm{Nu}_{2a}^{L} = \left[ 0.825 + \frac{0.387 \mathrm{Ra}^{L^{1/6}}}{\left[1 + 0.628 \mathrm{Pr}^{-9/16}\right]^{8/27}} \right]^2, \tag{F.4}$$

where the Rayleigh number $\mathrm{Ra}^{L}$ is

$$\mathrm{Ra}^{L} = \mathrm{Gr}^{L}\mathrm{Pr}, \quad \text{with} \quad \mathrm{Gr}^{L} = \frac{g\beta(T_3 - T_{in}^{air})L^3}{(\nu^{air})^2} \tag{F.5}$$

the Grashof number, the gravity acceleration $g$, the air thermal expansion coefficient $\beta(T) = 1/T$ and the air kinematic viscosity $\nu^{air} = \mu^{air}/\rho^{air}$. All properties are evaluated at the film temperature $T_{2a}^{f} = (T_{in}^{air} + T_{2a})/2$. The heat transfer coefficient $h_{2b}^{conv}$ on the outer side of the quartz windows 2 is determined similarly, while using the film temperature: $T_{2b}^{f} = (T_{out}^{air} + T_{2b})/2$. Finally,

the convective heat fluxes at the inner and outer surfaces of the second quartz windows are written as

$$\varphi_{2a}^{\text{conv}} = h_{2\text{a}}^{\text{conv}}(T_{\text{in}}^{\text{air}} - T_{2\text{a}}) \tag{F.6}$$

$$\varphi_{2b}^{\text{conv}} = h_{2\text{b}}^{\text{conv}}(T_{2\text{b}} - T_{\text{out}}^{\text{air}}) \tag{F.7}$$

## F.4 Radiative exchanges modeling

### F.4.1 Quartz radiative properties

The internal transmittance $\tau_\lambda$ provided by the manufacturer (Corning 2014) for a 1-cm quartz slab as a function of the wavelength $\lambda$ is presented in Fig. F.6. It can be expressed as

$$\tau_\lambda = \exp\left(-4\pi k_{2,\lambda} e/\lambda\right) = \exp\left(-\kappa_{2,\lambda} e\right) \tag{F.8}$$

where $e$ is the slab thickness, $n_{2,\lambda}$ is the refractive index (real part of the complex index of refraction), and $k_{2,\lambda}$ is the absorptive index (imaginary part of the complex index of refraction). The absorption coefficient $\kappa_{2,\lambda} = 4\pi k_{2,\lambda}/\lambda$ is usually considered instead of $k_{2,\lambda}$ in thermal radiation. The wavelength dependency of the quartz absorption coefficient $\kappa_{2,\lambda}$ is determined from the internal transmittance profile in Fig. F.6, allowing then to compute $\tau_\lambda$ for any quartz thickness $e$.

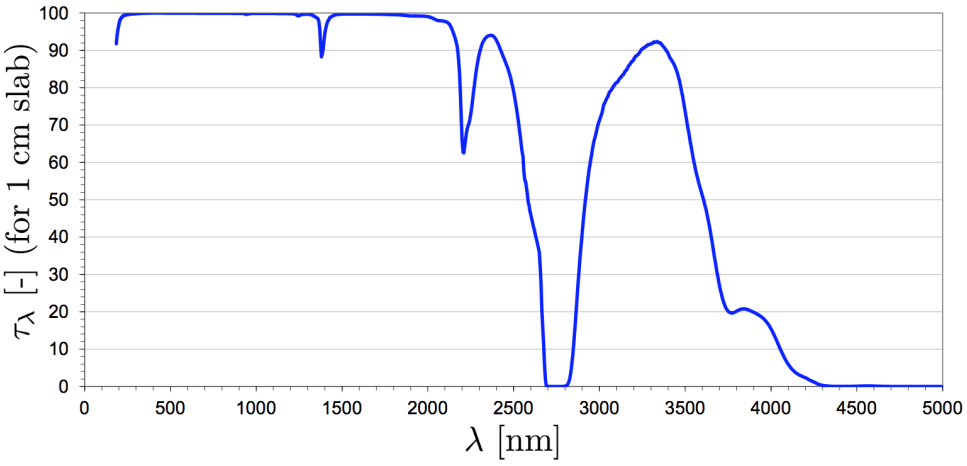


**Figure F.6:** *Internal transmittance of a 1 cm Corning HPFS 7980 quartz slab (from Corning (2014)).*

Considering an interface with air (refractive index equal to 1), the normal reflectance $\rho_\lambda$ is given by

$$\rho_\lambda = \frac{(1 - n_{2,\lambda})^2 + k_{2,\lambda}^2}{(1 + n_{2,\lambda})^2 + k_{2,\lambda}^2}, \tag{F.9}$$

where the evolution of $n_{2,\lambda}$ with wavelength is also been provided by the manufacturer (Corning 2014). The absorptance $\alpha_\lambda$ and emittance $\epsilon_\lambda$ are given by $\epsilon_\lambda = \alpha_\lambda = 1 - \tau_\lambda - \rho_\lambda$.

The quartz windows properties are expressed in terms of a slab absorptance ($A_\lambda^{\text{slab}}$), a slab transmittance ($T_\lambda^{\text{slab}}$) and a slab reflectance ($R_\lambda^{\text{slab}}$) which account for multiple normal reflections inside the quartz slab and are defined as (Modest 2013):

$$\begin{aligned} A_\lambda^{\text{slab}} &= \frac{(1-\rho_\lambda)(1-\tau_\lambda)}{1-\rho_\lambda\tau_\lambda} \\ T_\lambda^{\text{slab}} &= \frac{(1-\rho_\lambda)^2\tau_\lambda}{1-\rho_\lambda^2\tau_\lambda^2} \\ R_\lambda^{\text{slab}} &= \rho_\lambda\left[1+\frac{(1-\rho_\lambda)^2\tau_\lambda^2}{1-\rho_\lambda^2\tau_\lambda^2}\right] \end{aligned} \tag{F.10}$$

Figure F.7 presents the computed evolution of these three quantities with wavelength $\lambda$ for a quartz slab of thickness $e = e_1 = 3$ mm which corresponds to the quartz windows 1.

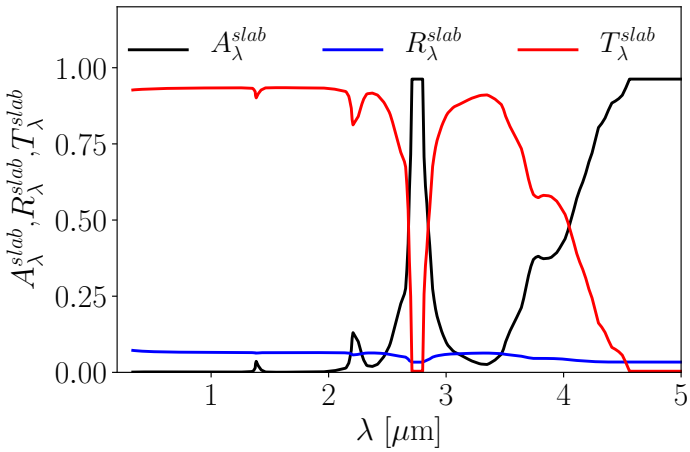


**Figure F.7:** *Computed quartz slab absorptance ($A_\lambda^{slab}$), transmittance ($T_\lambda^{slab}$) and reflectance ($R_\lambda^{slab}$) as a function of the wavelength $\lambda$ for a 3-mm thickness. The quartz reference is Corning HPFS 7980.*

These detailed properties of absorptance, transmittance and reflectance are simplified in a spectral band model where only opaque (transmittance equal to zero) and transparent spectral bands are considered. To do so, a threshold value $T_{\text{threshold}}^{\text{slab}}$ is defined. For each wavelength $\lambda$, if $T_\lambda^{\text{slab}} > T_{\text{threshold}}^{\text{slab}}$, the quartz is considered as transparent, unless the quartz is considered as opaque.

For the opaque bands, the absorptance and emittance are identical. Computations of radiative transfer consider hemispherical properties instead of the

normal absorptance or emittance to account for the effects of directional dependency of this coefficients. The hemispherical absorptance $A_\lambda^{\text{slab,hem}}$ (or $\epsilon_\lambda^{\text{slab,hem}} = A_\lambda^{\text{slab,hem}}$) is computed explicitly as a function of $n_{2,\lambda}$ and $k_{2,\lambda}$ through a rather long formula given in Eq. (3.20) in Howell et al. (2010). For the considered quartz material, noting that $k_{2,\lambda} \ll n_{2,\lambda}$ can simplify the calculation.

The properties in the transparent and opaque spectral bands are defined as:

- For a transparent spectral band (*i.e.* when $T_\lambda^{\text{slab}} > T_{\text{threshold}}^{\text{slab}}$):

$$\begin{aligned} T_\lambda^{\text{slab,model}} &= \frac{(1-\rho_\lambda)^2}{1-\rho_\lambda^2} \\ A_\lambda^{\text{slab,model}} &= 0 \\ R_\lambda^{\text{slab,model}} &= 1 - T_\lambda^{\text{slab,model}}, \end{aligned} \tag{F.11}$$

- For an opaque spectral band (*i.e.* $T_\lambda^{\text{slab}} < T_{\text{threshold}}^{\text{slab}}$):

$$\begin{aligned} T_\lambda^{\text{slab,model}} &= 0 \\ A_\lambda^{\text{slab,model}} &= A_\lambda^{\text{slab,hem}} \\ R_\lambda^{\text{slab,model}} &= 1 - A_\lambda^{\text{slab,hem}}. \end{aligned} \tag{F.12}$$

Global properties of the quartz slab can also be obtained by integrating the radiative properties on the spectrum. The total absorptance $\overline{A^{\text{slab}}}$, reflectance $\overline{R^{\text{slab}}}$ and transmittance $\overline{T^{\text{slab}}}$ are expressed as:

$$\begin{aligned} \overline{A^{\text{slab}}}(T) &= \int_{\lambda=0}^{+\infty} A_\lambda^{\text{slab}} I_\lambda^\circ(T) d\lambda \Big/ \int_{\lambda=0}^{+\infty} I_\lambda^\circ(T) d\lambda \\ \overline{R^{\text{slab}}}(T) &= \int_{\lambda=0}^{+\infty} R_\lambda^{\text{slab}} I_\lambda^\circ(T) d\lambda \Big/ \int_{\lambda=0}^{+\infty} I_\lambda^\circ(T) d\lambda \\ \overline{T^{\text{slab}}}(T) &= \int_{\lambda=0}^{+\infty} T_\lambda^{\text{slab}} I_\lambda^\circ(T) d\lambda \Big/ \int_{\lambda=0}^{+\infty} I_\lambda^\circ(T) d\lambda \end{aligned} \tag{F.13}$$

To determine the threshold value of the spectral band model, a criterion is needed. It has been chosen to match the total transmittance evolution with temperature when compared to the one obtained with the detailed slab transmittance $T_\lambda^{\text{slab}}$. This threshold value is dependent on the thickness of the quartz slab. The obtained values are $T_{\text{threshold}}^{\text{slab}} = 0.57$ for a 3-mm-thick quartz slab and $T_{\text{threshold}}^{\text{slab}} = 0.51$ for a 40-mm-thick quartz slab. This yields an average error on the temperature range of interest of 0.66% and 0.68%, respectively. The corresponding obtained spectral band model for the 3-mm quartz slab is presented in Fig F.8.

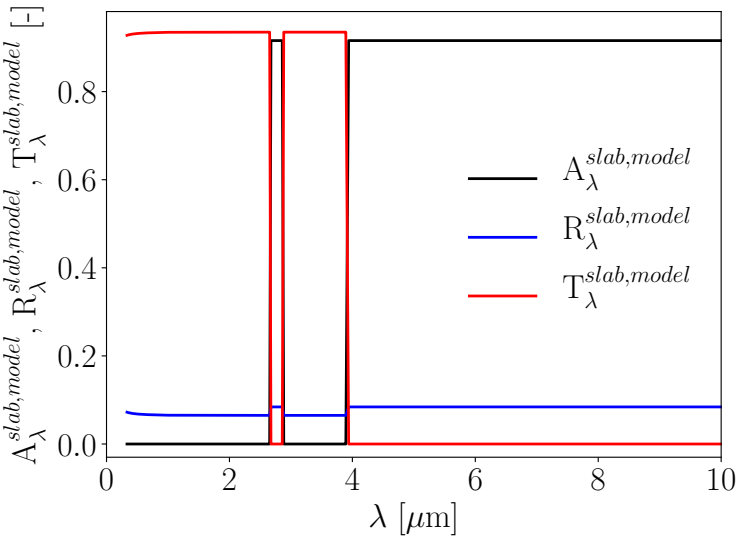


**Figure F.8:** *Transparent and non-transparent spectral band model for a 3 mm thickness Corning HPFS 7980 quartz.*

The corresponding evolution of the Planck mean quantities with temperature is plotted in Fig. F.9. It can be observed that for rays coming from a source at low temperature, the quartz is mostly absorbing, whereas it is transparent at high temperatures.

We finally define two spectral emittances and reflectances for the quartz windows 1 ($A_{\lambda,1}^{\text{slab}}$ and $R_{\lambda,1}^{\text{slab}}$) and the quartz windows 2 ($A_{\lambda,2}^{\text{slab}}$ and $R_{\lambda,2}^{\text{slab}}$):

$$\begin{aligned} A_{\lambda,1}^{\text{slab}} &= A_\lambda^{\text{slab,model}}, \; R_{\lambda,1}^{\text{slab}} = R_\lambda^{\text{slab,model}} \quad \text{with } T_{\text{threshold}}^{\text{slab}} = 0.57 \\ A_{\lambda,2}^{\text{slab}} &= A_\lambda^{\text{slab,model}}, \; R_{\lambda,2}^{\text{slab}} = R_\lambda^{\text{slab,model}} \quad \text{with } T_{\text{threshold}}^{\text{slab}} = 0.51 \end{aligned} \tag{F.14}$$

### F.4.2 Radiative transfer inside the pressure housing

This section deals with the radiative transfer modeling to estimate the radiative fluxes $\varphi_1^{\text{rad}}$ and $\varphi_{2a}^{\text{rad}}$ at the windows 1 and 2, respectively. The radiative flux at the steel casing is denoted by $\varphi_3^{\text{rad}}$. The pressure housing around each pair of quartz windows 1 and 2 is modeled as a closed box domain (see Fig. F.3) delimited by the combustion chamber window of surface area $S_1 = L \cdot l$, the pressure housing window of surface area $S_2 = S_1$, and the surrounding steel casing of surface area $S_3 = 2 \cdot (L + l) \cdot b$. View factors $F_{ij}$ between surfaces $S_i$

and $S_j$ are

$$\begin{aligned} F_{11} &= 0 & F_{12} &= \mathcal{F}(L,l,b) \\ F_{21} &= \mathcal{F}(L,l,b) & F_{22} &= 0 \\ F_{31} &= F_{13}S_1/S_3 & F_{32} &= F_{23}S_2/S_3 \\ F_{13} &= 1 - F_{11} - F_{12} = 1 - F_{12} & F_{33} &= 1 - F_{31} - F_{32} \\ F_{23} &= 1 - F_{21} - F_{22} = 1 - F_{21} \end{aligned} \tag{F.15}$$

where $\mathcal{F}(L,l,b)$ is given by the expression (Howell et al. 2010):

$$\begin{aligned} \mathcal{F}(L,l,b) = \frac{1}{\pi \mathcal{U}\ \mathcal{V}} \Bigg[ \ln\left(\frac{\mathcal{U}_1^2\mathcal{V}_1^2}{\mathcal{U}_1^2+\mathcal{V}_1^2-1}\right) + 2\mathcal{U}\left(\mathcal{V}_1 \arctan\left(\frac{\mathcal{U}}{\mathcal{V}_1}\right)\right. \\ \left. -\arctan\mathcal{U}) + 2\ \mathcal{V}\left(\mathcal{U}_1 \arctan\left(\frac{\mathcal{V}}{\mathcal{U}_1}\right) - \arctan(\mathcal{V})\right)\right] \end{aligned} \tag{F.16}$$

with $\mathcal{U} = L/b$, $\mathcal{V} = l/b$, $\mathcal{U}_1 = \sqrt{1+\mathcal{U}^2}$ and $\mathcal{V}_1 = \sqrt{1+\mathcal{V}^2}$.

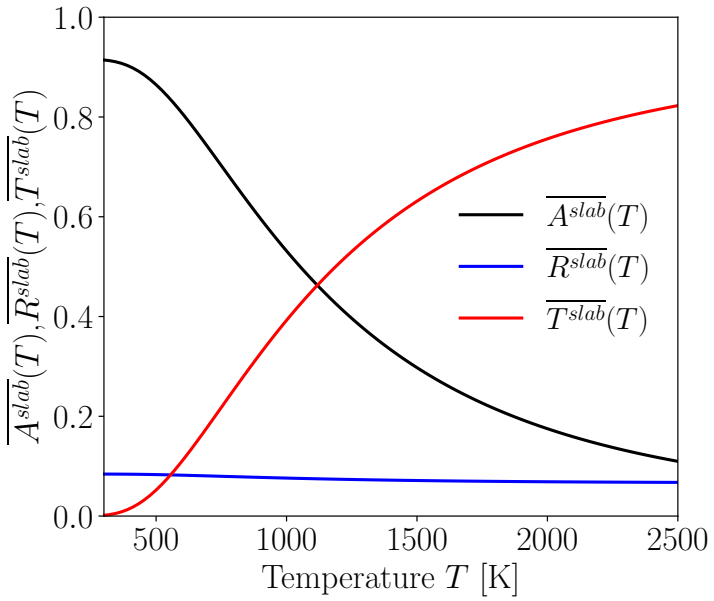


**Figure F.9:** *Planck mean modeled external absorptance ($\overline{A^{slab}}(T)$), transmittance ($\overline{T^{slab}}(T)$) and reflectance ($\overline{R^{slab}}(T)$) as a function of incident source temperature $T$ for a 3 mm thickness Corning HPFS 7980 quartz.*

Then, equivalent isotropic radiative intensity are introduced: $I^l_{\lambda,1}$, $I^i_{\lambda,1}$, $I^l_{\lambda,2a}$, $I^i_{\lambda,2a}$, $I^l_{\lambda,3}$, $I^i_{\lambda,3}$ are, respectively, the leaving and incident intensities at quartz windows 1, quartz windows 2a and casing surfaces. They are used to express

the radiative fluxes on surfaces $S_1$, $S_2$ and $S_3$ as

$$\begin{aligned}
\varphi_1^{\text{rad}} &= \pi \int_{\lambda=0}^{+\infty} (I_{\lambda,1}^l - I_{\lambda,1}^i) d\lambda \\
\varphi_{2\text{a}}^{\text{rad}} &= -\pi \int_{\lambda=0}^{+\infty} (I_{\lambda,2\text{a}}^l - I_{\lambda,2\text{a}}^i) d\lambda \\
\varphi_3^{\text{rad}} &= \pi \int_{\lambda=0}^{+\infty} (I_{\lambda,3}^l - I_{\lambda,3}^i) d\lambda
\end{aligned} \tag{F.17}$$

The introduced intensities are obtained by solving spectrally the following system of equations:

$$\begin{cases}
I_{\lambda,1}^l = A_{\lambda,1}^{\text{slab}} I_\lambda^\circ(T_{\text{out}}) + R_{\lambda,1}^{\text{slab}} I_{\lambda,1}^i \\
I_{\lambda,1}^i = F_{11} I_{\lambda,1}^l + F_{21} I_{\lambda,2\text{a}}^l + F_{31} I_{\lambda,3}^l
\end{cases}$$
$$\begin{cases}
I_{\lambda,2\text{a}}^l = A_{\lambda,2}^{\text{slab}} I_\lambda^\circ(T_{2\text{a}}) + R_{\lambda,2}^{\text{slab}} I_{\lambda,2\text{a}}^i \\
I_{\lambda,2\text{a}}^i = F_{12} I_{\lambda,1}^l + F_{22} I_{\lambda,2\text{a}}^l + F_{32} I_{\lambda,3}^l
\end{cases}$$
$$\begin{cases}
I_{\lambda,3}^l = \epsilon_{\lambda,3} I_\lambda^\circ(T_3) + (1 - \epsilon_{\lambda,3}) I_{\lambda,3}^i \\
I_{\lambda,3}^i = F_{13} I_{\lambda,1}^l + F_{23} I_{\lambda,2\text{a}}^l + F_{33} I_{\lambda,3}^l
\end{cases} \tag{F.18}$$

with the temperature of the stainless steel $T_3 = 313$ K.
The emissivity of unoxidized stainless steel typically ranges between 0.2 and 0.3 (Howell et al. 2010; Modest 2013). The value $\epsilon_{\lambda,3} = 0.25$ is retained.

### F.4.3 External radiative transfer

The radiative flux $\varphi_{2\text{b}}^{\text{rad}}$ at the outer side of the pressure housing quartz windows (quartz windows 2) is written as

$$\varphi_{2\text{b}}^{\text{rad}} = \int_{\lambda=0}^{+\infty} A_{\lambda,2}^{\text{slab}} (I_\lambda^\circ(T) - I_\lambda^\circ(T_{\text{out}}^{\text{air}})) d\lambda \tag{F.19}$$

## F.5 Conductive transfer modeling

### F.5.1 Quartz thermal conductivity

Quartz thermal conductivity varies strongly with temperature. Such data is generally not provided by the quartz manufacturers. In a recent study (Combis et al. 2012), this dependency with temperature has been characterized based on data from the manufacturer Heraeus (Heraeus 2016). The data are reported in Fig. F.10 along with a polynomial fit of this data:

$$\frac{k_q(T)}{k^0} = a_0 + a_1 \left(\frac{T}{T_0}\right) + a_2 \left(\frac{T}{T_0}\right)^2 + a_3 \left(\frac{T}{T_0}\right)^3 \tag{F.20}$$

with: $a_0 = 0.97980$, $a_1 = -0.10063$, $a_2 = 0.13677$, $a_3 = -0.011744$, $T_0 = 293$ K and $k^0 = k_q(293\text{ K}) = 1.38$ W/m/K. The annealing temperature of these quartz windows is 1315 K (Heraeus 2016). A high uncertainty of the thermal conductivity is then expected for temperatures higher than 1315 K (shaded regions in Fig. F.10).

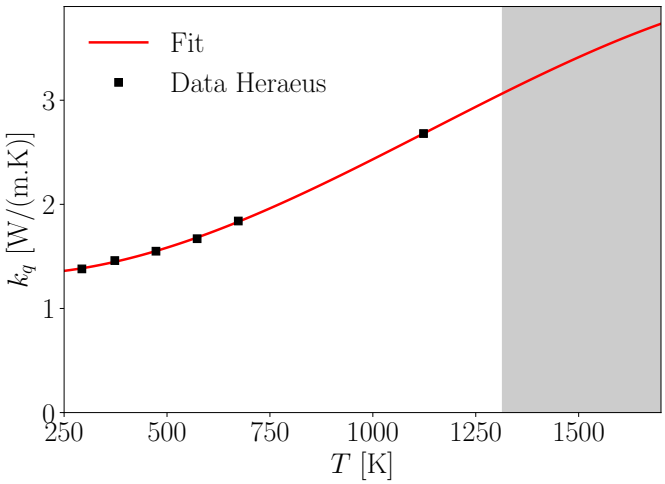


**Figure F.10:** *Thermal conductivity of quartz as a function of temperature $T$. Shaded region corresponds to quartz temperatures higher than their annealing temperature (1315 K).*

### F.5.2 Heat conduction within quartz windows

The modeling of the quartz windows radiative properties consider either opaque or transparent bands. One assumes therefore that there is no radiative transfer within the quartz material and that the conductive heat flux within the window is unidirectional and constant given the assumption that the fields are uniform in vertical and spanwise directions. With the temperature-varying thermal conductivity, the conductive flux through the quartz windows 1 is then estimated as

$$\varphi_1^{\text{cond}} = -\frac{1}{e_1}\int_{T_{\text{in}}}^{T_{\text{out}}} k_q(T)dT. \tag{F.21}$$

Similarly, the conductive flux $\varphi_2^{\text{cond}}$ through the external pressure housing quartz windows is

$$\varphi_2^{\text{cond}} = -\frac{1}{e_2}\int_{T_{2a}}^{T_{2b}} k_q(T)dT. \tag{F.22}$$

## F.6 Results of the derived model

The different modeled system components and physical phenomena are coupled together through Eq. (F.1) which is solved with a root-finding algorithm (for example *fsolve* function from python or Matlab) by providing the inner surface temperature $T_{\text{in}}$ of the first quartz windows as the experimental one averaged along the vertical centerline. All the other fluxes and temperatures of the system are then determined. Table F.2 presents the results for the three cases defined in Tab. F.1. The reported space-averaged temperature $T_{\text{in}}^{\text{exp}}$ is computed by extrapolating the data from Fig. F.2 up to the total height of the quartz windows of 120 mm. Cases 1 and 2, being characterized by almost identical averaged temperature $T_{\text{in}}$, yield identical results. Case 3 exhibits a smaller temperature at the combustor walls. For each case, the spatially-averaged experimental temperature of the outer surface of the combustor walls, $T_{\text{out}}^{\text{exp}}$, is correctly predicted with an error below 30 K compared. The extracted flux through the combustor walls, taken as identical to $\varphi_1^{\text{cond}}$, is within 20% approximatively of the correct value which has been estimated from the difference of the measured temperatures. It is important to notice that the uncertainty of this estimated conductive heat flux from measurements is about 27% considering an uncertainty of ±20 % on the quartz thermal conductivity, ±0.1 mm on the quartz slab width and ±3 % on the measured quartz temperature. The fair agreement of the derived model is satisfactory given the macroscopic approach retained to model the different phenomena. In particular, it is worth recalling the certain limitation of the uniform temperature assumption on the quartz windows 1 surfaces. The inhomogeneous temperature profile can explain such a result. Indeed, the external face of the quartz windows 1 is actually cooled to 333 K in the vicinity of water-cooled metallic posts. A strong variation of the temperature field is then expected in the spanwise direction. Given the dependency of the radiative flux on temperature ($\propto T^4$), radiative fluxes are certainly overestimated by considering the homogeneous $T_{\text{in}}$ as the average centerline temperature. Such an effect can explain the global overestimation of the extracted flux through the combustor walls. This error will be corrected in the future planned 3D simulations of conjugate heat transfer.

| Quantity | Unity | Case 1 | Case 2 | Case 3 |
|---|---|---|---|---|
| $T_{\text{in}}^{\text{exp}}$ | K | 1346 | 1345 | 1272 |
| $\varphi_1^{\text{cond,exp}}$ | $\text{kW/m}^2$ | 131.2 | 125.8 | 110.0 |
| $\varphi_1^{\text{cond}}$ | $\text{kW/m}^2$ | 150.3 | 150.2 | 133.6 |
| $T_{\text{out}}^{\text{exp}}$ | K | 1215 | 1219 | 1157 |
| $T_{\text{out}}$ | K | 1195 | 1194 | 1131 |

**Table F.2:** *Thermal energy balance of the combustion chamber thermal environment.*

Details on the different fluxes for the case 1 are given in Tab. F.3. For the

quartz windows 1, it can be observed that the radiative flux accounts for 30% of the total heat flux through the first quartz window, whereas 70% of the total heat flux corresponds to the cooling by the transverse jets. Both contributions sum up to the total extracted heat flux which is identical to the conductive flux between the inner and outer surfaces of the combustion chamber quartz window. This total flux is overestimated by about 15% in case 1.

Only 12% of the radiative flux from quartz windows 1 is exchanged with quartz windows 2, leading to a spatially-averaged radiative flux equal to 5.63 kW/m$^2$. The other part is directly exchanged with the pressure housing's stainless steel walls. With an opposite sign to this radiative flux, the quartz windows 2 exchanges 3.17 kW/m$^2$ with the ambient pressurized air through natural convection, resulting to a conductive heat flux in the quartz windows 2 equal to 2.46 kW/m$^2$. At the outer surface of the quartz windows 2, this conductive flux is balanced with 56% in external radiative transfer and 44% with convective heat transfer with ambient air. The corresponding temperatures at the inner and outer surfaces are 494 K and 429 K, respectively.

| Quantity | Unity | Case 1 | Case 1b | Case 1c | Case 1d |
|---|---|---|---|---|---|
| **quartz windows 1 [outer]** | | | | | |
| $\boldsymbol{\varphi_1^{cond,exp}}$ | **kW/m$^2$** | **131.2** | **60.5** | **131.2** | **131.2** |
| $\boldsymbol{\varphi_1^{cond}}$ | **kW/m$^2$** | **150.4** | **121.4** | **150.8** | **152.3** |
| $\varphi_1^{conv}$ | kW/m$^2$ | 104.6 | 86.2 | 104.5 | 104.2 |
| $\varphi_1^{rad}$ | kW/m$^2$ | 45.8 | 35.2 | 46.3 | 48.1 |
| $T_{in}^{exp}$ | K | 1346 | 1346 | 1346 | 1346 |
| $\mathbf{T_{out}^{exp}}$ | **K** | **1215** | **1215** | **1215** | **1215** |
| $\mathbf{T_{out}}$ | **K** | **1195** | **1082** | **1194** | **1192** |
| $\overline{h_1}$ | W/(m$^2$·K) | 116 | 110 | 116 | 116 |
| **quartz windows 2 [inner]** | | | | | |
| $\varphi_{2a}^{rad}$ | kW/m$^2$ | 5.63 | 4.38 | 1.58 | - |
| $\varphi_{2a}^{conv}$ | kW/m$^2$ | -3.17 | -2.52 | -0.883 | - |
| $\varphi_{2a}^{cond}$ | kW/m$^2$ | 2.46 | 1.86 | 0.701 | - |
| $T_{2a}$ | K | 494 | 459 | 366 | - |
| **quartz windows 2 [outer]** | | | | | |
| $\varphi_{2b}^{rad}$ | kW/m$^2$ | 1.37 | 1.01 | 0.341 | - |
| $\varphi_{2b}^{conv}$ | kW/m$^2$ | 1.09 | 0.857 | 0.360 | - |
| $T_{2b}$ | K | 429 | 405 | 346 | - |

**Table F.3:** *Thermal energy balance of the combustion chamber thermal environment in Case 1 and impact of modeling choices. Case 1b considers a constant thermal conductivity. Case 1c neglects radiative exchange between the quartz windows. Case 1d considers the simplified model in Eq.* (F.23).

## F.7 Sensitivity analysis

The impact and sensitivity of different parameters governing the observed energy balance is carried out in this section for case 1.

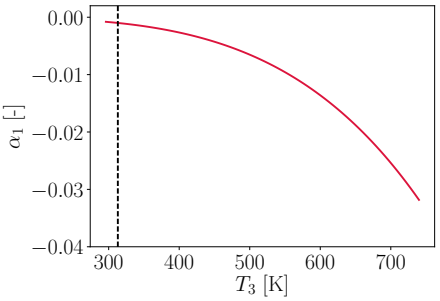


(a) Sensitivity to the temperature $T_3$

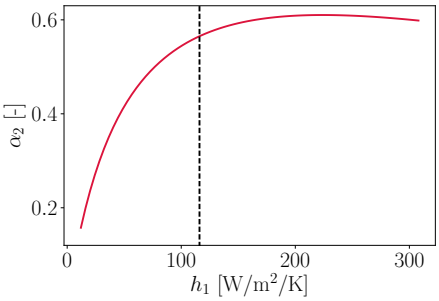


(b) Sensitivity to the heat transfer coefficient $\overline{h_1}$

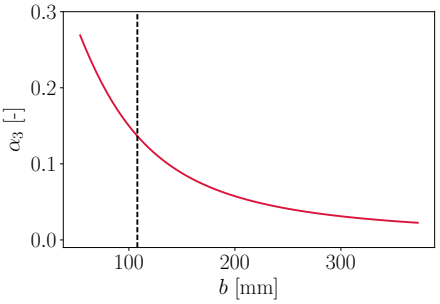


(c) Sensitivity to the distance $b$

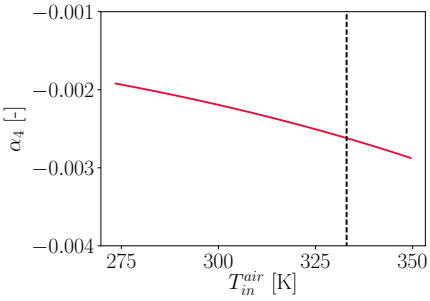


(d) Sensitivity to the temperature $T_{\text{in}}^{\text{air}}$

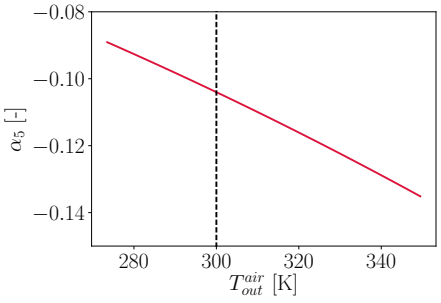


(e) Sensitivity to the temperature $T_{\text{out}}^{\text{air}}$

**Figure F.11:** *Sensitivity of the predicted conductive flux to the stainless steel temperature $T_3$ (a), the heat transfer coefficient $\overline{h_1}$ (b), the quartz separating distance b (c), the temperature of air inside the pressure housing $T_{in}^{air}$ (d) and the external ambiant temperature $T_{out}^{air}$ (e). Black vertical dashed lines correspond to nominal values.*

First, the influence of the pressure housing steel temperature $T_3$ is studied. In order to quantify its impact on the predicted conductive flux at the first quartz

windows $\varphi_1^{\text{cond}}$, the sensitivity parameter $\alpha_1 = \frac{T_3}{\varphi_1^{\text{cond}}} \frac{\mathrm{d}\varphi_1^{\text{cond}}}{\mathrm{d}T_3}$ is introduced. The evolution of this parameter with the stainless steel temperature $T_3$ is shown in Fig. F.11(a). It is observed that for all considered temperatures, the global model is not very sensitive to the steel temperature $T_3$. Indeed, when the value of $T_3$ is increased by 1%, the percentage of deviation of $\varphi_1^{\text{cond}}$ is lower than 0.03%. This is due to (i) the small emitted radiative flux of the steel casing at a relatively cold temperature $T_3$ compared to $T_{\text{out}} \approx 1200$ K, hence $T_{\text{out}}^4 \gg T_3^4$; and (ii) the smaller contribution (32%) of the radiative flux in the total heat flux through the quartz windows 1.

As for the pressure housing temperature sensitivity study, we introduce the parameter $\alpha_2 = \frac{\overline{h_1}}{\varphi_1^{\text{cond}}} \frac{\mathrm{d}\varphi_1^{\text{cond}}}{\mathrm{d}\overline{h_1}}$ quantifying the impact of the heat transfer coefficient $\overline{h_1}$ on the predicted conductive flux $\varphi_1^{\text{cond}}$. The evolution of this sensitivity parameter as a function of the value of $\overline{h_1}$ is presented in Fig. F.11(b). High sensitivity of the conductive flux $\varphi_1^{\text{cond}}$ with the value of $\overline{h_1}$ is observed. Indeed, for $\overline{h_1} \approx 100$ W/m$^2$/K, decreasing the value of $\overline{h_1}$ by 1%, decreases the value of $\varphi_1^{\text{cond}}$ by approximatively 0.5 %. This can be explained by the linear dependency of the convective heat flux at the quartz windows 1 with the value of $\overline{h_1}$ and the fact that this flux represents 68% of the total flux at this outer window surface.

In order to study the impact of the thermal conductivity dependency on temperature prescribed by Eq. (F.20), a constant thermal conductivity, corresponding to its value at 293 K *i.e.* $k_q = k^0 = 1.38$ W/m/K, is considered instead. Table F.3 presents a comparison of the global energy balance obtained with a constant value of $k_q$ (Case 1b) and the one obtained with the temperature dependency of the quartz thermal conductivity (Case 1). Case 1b largely underestimates the conductive flux and the outer temperature of the combustion chamber quartz window. A detailed thermal conductivity description inside the quartz is then required in order to correctly estimate the conductive flux through the heated quartz material.

The influence of the distance $b$ separating the two quartz windows is studied with the parameter $\alpha_3 = \frac{b}{\varphi_1^{\text{cond}}} \frac{\mathrm{d}\varphi_1^{\text{cond}}}{\mathrm{d}b}$. Figure F.11(c) presents the evolution of the sensitivity of the predicted conductive flux with the quartz distance $b$. For low values of $b$, $\varphi_1^{\text{cond}}$ becomes sensitive to this distance because of the enhanced interaction between the quartz windows 1 and 2: for $b = 20$ mm, increasing by 1% the value of $b$ decreases $\varphi_1^{\text{cond}}$ by 0.2%. However, around the value encountered in the application ($b = 108$ mm), $\varphi_1^{\text{cond}}$ is weakly sensitive to the window distance $b$: the quartz windows 1 mainly exchanges radiation with the stainless steel pressure housing for the actual value of $b$. To illustrate this, Table F.3 presents a comparison of the global energy balance obtained considering no

radiative exchanges between the two quartz windows ($F_{12} = F_{21} = 0$), denoted as Case 1c, and the one obtained considering them (Case 1). As expected, results for quartz windows 1 temperature and fluxes are quasi similar to the ones obtained with detailed resolution. For the considered configuration, one can then neglect radiative interactions between these two windows in order to predict quartz windows 1 temperature. However, Case 1c with $F_{12} = F_{21} = 0$ fails in retrieving the same temperature of the second quartz windows as for Case 1.

Finally, the influence of temperatures $T_{\text{in}}^{\text{air}}$ and $T_{\text{out}}^{\text{air}}$ are studied with the parameters $\alpha_4 = \frac{T_{\text{in}}^{\text{air}}}{\varphi_1^{\text{cond}}} \frac{\mathrm{d}\varphi_1^{\text{cond}}}{\mathrm{d}T_{\text{in}}^{\text{air}}}$ and $\alpha_5 = \frac{T_{\text{out}}^{\text{air}}}{\varphi_1^{\text{cond}}} \frac{\mathrm{d}\varphi_1^{\text{cond}}}{\mathrm{d}T_{\text{out}}^{\text{air}}}$. The evolutions of $\alpha_4$ and $\alpha_5$ are shown in Figs. F.11(d) and F.11(e), respectively. The predicted conductive flux is therefore not sensitive to the temperature $T_{\text{in}}^{\text{air}}$ (an increase of 0.1% in the temperature $T_{\text{in}}^{\text{air}}$ makes the conductive flux drop by $\approx 0.003\%$), whereas it is slightly sensitive to the temperature $T_{\text{out}}^{\text{air}}$ (an increase by 1% in the temperature $T_{\text{out}}^{\text{air}}$ decreases by the conductive flux 0.1%).

## F.8 Retained simplified external heat transfer model

In the previous section, the sensitivity analysis has shown the strong influence of the convective transfer coefficient $\overline{h_1}$ and the negligible influence of the radiative interactions between the two quartz windows. Therefore, a simpler model for the external boundary condition, expressed here for a general inhomogeneous window temperature field, can be retained:

$$\begin{aligned}\varphi_1(x,z) = {} & \overline{A_1^{\text{slab}}}(T_{\text{out}}(x,z))\sigma T_{\text{out}}(x,z)^4 - \overline{A_1^{\text{slab}}}(T_3)\sigma T_3^4 \\ & + h_1(x,z)(T_{\text{out}}(x,z) - T_{\text{in}}^{\text{air}})\end{aligned} \tag{F.23}$$

where $T_{\text{out}}(x,z)$ corresponds to the temperature on the quartz combustion window's external face. This assumes that the quartz of the combustion chamber only exchanges radiative heat transfer with the stainless steel of the pressure housing (assumed isothermal at $T_3$), that radiation emitted from the quartz windows 1 does not modify the pressure housing thermal equilibrium, but also that the effect of multiple reflections between emitted radiative energy from quartz windows 1 and pressure housing's stainless steel can be neglected.

First, in order to quantify the impact of this simplification on the predicted fluxes, Tab. F.3 presents a comparison of the predicted temperatures and fluxes at the quartz windows 1 between the complete (Case 1) and simplified (Case 1d) models. For the considered configuration, an error of approximatively 5 % on the radiative flux at the external face of the quartz windows 1 is obtained with the simplified model, leading to an error of approximatively 1% on the total conductive flux through the quartz windows 2. Secondly, in order to assess the

range of validity of this simplification, Fig. F.12 presents the radiatives fluxes at the outer surface of the combustion chamber quartz windows for the complete and simplified models, as a function of the stainless steel emissivity $\epsilon_{\lambda,3}$. These calculations have been carried out for Case 1. The relative error with the first version of the model decreases with the stainless steel emissivity and an error higher than 10% can be obtain for very low values of $\epsilon_{\lambda,3}$. In such a case, reflections between the quartz windows and the casing cannot be neglected anymore. For the actually considered stainless steel emissivity $\epsilon_{\lambda,3} = 0.25$, the error between the complete and simplified model is approximatively 5% and can be considered as acceptable as the radiative flux only accounts for 30 % of the total heat flux through the quartz windows 1.

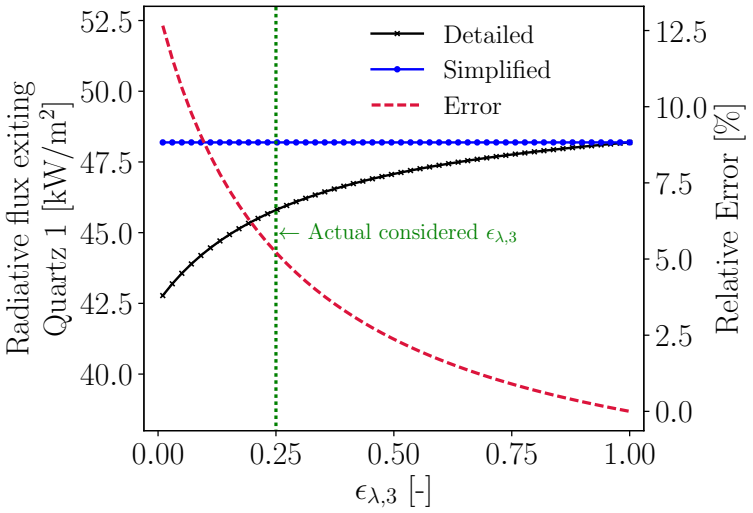


**Figure F.12:** *Evolution of error between complete and simplified models on radiative flux exiting quartz windows 1 as a function of stainless steel emissivity* $\epsilon_{\lambda,3}$.

## F.9 Conclusion

A model of external thermal environment in the considered DLR combustion chamber has been proposed: Nusselt number formulas are used to describe the window cooling system as an equivalent wall jet system and the free convection boundary layer on the internal and external faces of the quartz windows 2; the detailed description of the quartz windows spectral transmittance is combined with the view factor method to describe the radiative exchanges between the quartz windows and the pressure housing; A temperature-dependent expression of the quartz thermal conductivity is retained. The model satisfactorily retrieves the wall heat flux at the centerline of the combustion chamber quartz windows with an error of about 20 % for the considered three operating points. This wall heat flux is estimated from the measured temperature profiles on both sides of the window. The corresponding experimental uncertainty in the wall

heat flux is roughly 27 %.

A sensitivity analysis was then carried out to understand the model's critical parameters and to derive a simplified version. The analysis revealed a high sensitivity to the heat transfer coefficient describing the wall jet cooling and to the thermal conductivity of the quartz windows while the impact of the distance separating the two sets of quartz windows remains small. A simplified version of the model given in Tab. F.4 yields similar results while considering Planck-mean emissivities and radiative exchanges only with the stainless steel of the pressure housing. The semi-transparency of the viewing windows is denoted by the given temperature-dependency of the mean emissivity.

The local expressions in Tab. F.4 are meant to be easily implemented into a conjugate heat transfer numerical study to solve for the temperature within the combustor windows. The large sensitivity on the jet cooling heat transfer coefficients invites to consider a separate CFD study of the cooling film for future investigations. Future work should also determine the impact of considering volume absorption within the quartz windows instead of retaining an opaque/transparent band radiative model. Finally, the complete model methodology can also benefit the preliminary design of combustor equipped with semi-transparent windows with or without pressure housing to evaluate wall heat transfer and (if present) the window cooling system efficiency.

| **Equations** |
|---|
| $\varphi_1(x,z) = \overline{A_1^{\text{slab}}}(T_{\text{out}}(x,z))\sigma T_{\text{out}}(x,z)^4 - \overline{A_1^{\text{slab}}}(T_3)\sigma T_3^4$ $+h_1(x,z)(T_{\text{out}}(x,z) - T_{\text{in}}^{\text{air}})$ |
| $\overline{A_1^{\text{slab}}}(T) = 0.72517 + 0.54384\cdot(T/T_0) - 0.39988\cdot(T/T_0)^2$ $+0.10231\cdot(T/T_0)^3 - 0.013100\cdot(T/T_0)^4$ $+8.4328\cdot10^{-4}\cdot(T/T_0)^5 - 2.1722\cdot10^{-5}\cdot(T/T_0)^6$ with $T_0 = 293$ K. |
| $h_1(x,z) = \text{Nu}_1(x,z)\ \cdot k^{\text{air}}(T_{\text{film}}(x,z))/(x + l_{\text{th}})$ |
| $\text{Nu}_1(x,z) = 0.345\cdot\text{Pr}(T_{\text{film}}(x,z))^{0.34}\cdot\text{Re}_{e_{\text{eq}}}^{0.75}\left(\frac{x+l_{\text{th}}}{e_{\text{eq}}}\right)^{1/4}$ |
| $T_{\text{film}}(x,z) = (T_{\text{out}}^{\text{q1}}(x,z) - T_{\text{in}}^{\text{air}})/2.$ |
| $T_3 = 313$ K, $T_{\text{in}}^{\text{air}} = 333$ K, $\text{Re}_{e_{\text{eq}}} = 169$, $l_{\text{th}} = 0.54$ mm, $e_{\text{eq}} = 0.071$ mm. |

**Table F.4:** *Proposed simplified model of the thermal boundary condition of the combustion chamber quartz window's external surface.*

# References


Abid, A. D., J. Camacho, D. A. Sheen, and H. Wang (2009). Quantitative measurement of soot particle size distribution in premixed flames – the burner-stabilized stagnation flame approach. *Combust. Flame 156*(10), 1862 – 1870. *(p. 65, 66, 67, 105)*

Abid, A. D., N. Heinz, E. D. Tolmachoff, D. J. Phares, C. S. Campbell, and H. Wang (2008). On evolution of particle size distribution functions of incipient soot in premixed ethylene–oxygen–argon flames. *Combust. Flame 154*(4), 775 – 788. *(p. 66, 353, 359)*

ACEA (2017). European automobile manufacturers association. *(p. 6)*

AirParif (2017). *(p. 4)*

Alam, M. K. (1987). The effect of van der waals and viscous forces on aerosol coagulation. *Aerosol Science and Technology 6*(1), 41–52. *(p. 34)*

Appel, J., H. Bockhorn, and M. Frenklach (2000). Kinetic modeling of soot formation with detailed chemistry and physics: laminar premixed flames of c2 hydrocarbons. *Combustion and Flame 121*(1–2), 122 – 136. *(p. 39, 50, 51)*

Arias, P. G., V. R. Lecoustre, S. Roy, Z. Luo, D. C. Haworth, T. Lu, A. Trouvé, and H. G. Im (2015, 2015/08/23). Dynamics of flow–soot interaction in wrinkled non-premixed ethylene–air flames. *Combustion Theory and Modelling*, 1–19. *(p. 109)*

Attili, A., F. Bisetti, M. E. Mueller, and H. Pitsch (2014, 7). Formation, growth, and transport of soot in a three-dimensional turbulent non-premixed jet flame. *Combust. Flame 161*(7), 1849–1865. *(p. 90, 109)*

Attili, A., F. Bisetti, M. E. Mueller, and H. Pitsch (2016). Effects of non-unity lewis number of gas-phase species in turbulent nonpremixed sooting flames. *Combustion and Flame 166*(Supplement C), 192–202. *(p. 122)*

Aubagnac-Karkar, D., J.-B. Michel, O. Colin, P. E. Vervisch-Kljakic, and N. Darabiha (2015, 8). Sectional soot model coupled to tabulated chemistry for diesel rans simulations. *Combust. Flame 162*(8), 3081–3099. *(p. 35, 104, 109)*

Balthasar, M. and M. Frenklach (2005). Monte-carlo simulation of soot particle coagulation and aggregation: the effect of a realistic size distribution. *Proceedings of the Combustion Institute 30*(1), 1467–1475. *(p. 367)*

Balthasar, M. and M. Kraft (2003). A stochastic approach to calculate the

particle size distribution function of soot particles in laminar premixed flames. *Combustion and Flame 133*(3), 289–298. *(p. 44, 367)*

Barlow, R. S., A. N. Karpetis, J. H. Frank, and J. Y. Chen (2001, 11). Scalar profiles and no formation in laminar opposed-flow partially premixed methane/air flames. *Combustion and Flame 127*(3), 2102–2118. *(p. 123, 392, 393)*

Baughcum, S., J. Begin, F. Franco, D. Greene, D. Lee, M.-L. McLaren, A. Mortlock, P. Newton, A. Schmitt, D. Sutkus, et al. (1999). Aircraft emissions: current inventories and future scenarios. *Scholarship at Penn Libraries*, 59. *(p. 9)*

Berger, S., S. Richard, F. Duchaine, G. Staffelbach, and L. Y. M. Gicquel (2016, 6). On the sensitivity of a helicopter combustor wall temperature to convective and radiative thermal loads. *Applied Thermal Engineering 103*, 1450–1459. *(p. 269, 274, 308, 421)*

Bescond, A., J. Yon, F. X. Ouf, C. Rozé, A. Coppalle, P. Parent, D. Ferry, and C. Laffon (2016). Soot optical properties determined by analyzing extinction spectra in the visible near-uv: Toward an optical speciation according to constituents and structure. *Journal of Aerosol Science 101*, 118–132. *(p. 105)*

Bisetti, F., G. Blanquart, M. E. Mueller, and H. Pitsch (2012, 1). On the formation and early evolution of soot in turbulent nonpremixed flames. *Combust. Flame 159*(1), 317–335. *(p. 109, 135, 153)*

Blacha, T., M. Di Domenico, P. Gerlinger, and M. Aigner (2012, 1). Soot predictions in premixed and non-premixed laminar flames using a sectional approach for pahs and soot. *Combustion and Flame 159*(1), 181–193. *(p. 104)*

Bladh, H., J. Johnsson, N. E. Olofsson, A. Bohlin, and P. E. Bengtsson (2011). Optical soot characterization using two-color laser-induced incandescence (2c-lii) in the soot growth region of a premixed flat flame. *Proceedings of the Combustion Institute 33*(1), 641–648. *(p. 105)*

Blanquart, G. and H. Pitsch (2007). A joint volume-surface-hydrogen multivariate model for soot formation. In *Combustion Generated Fine Carbonaceous Particles*. Henning Bockhorn. *(p. 28, 59, 60, 62, 109)*

Blanquart, G. and H. Pitsch (2009). Analyzing the effects of temperature on soot formation with a joint volume-surface-hydrogen model. *Combustion and Flame 156*(8), 1614 – 1626. *(p. 30, 42, 365)*

Bohren, C. F. and D. R. Huffman (2008). *Absorption and scattering of light by small particles*. John Wiley & Sons. *(p. 210, 214, 215)*

Borghi, R. (1988). Turbulent combustion modelling. *Progress in Energy and Combustion Science 14*(4), 245–292. *(p. 362)*

Boyette, W., S. Chowdhury, and W. Roberts (2017). Soot particle size distribution functions in a turbulent non-premixed ethylene-nitrogen flame. *Flow, Turbulence and Combustion 98*(4), 1173–1186. *(p. 138)*

Brasil, A. M., T. L. Farias, and M. G. Carvalho (2000, 11). Evaluation of

the fractal properties of cluster-cluster aggregates. *Aerosol Science and Technology 33*(5), 440–454. *(p. 26)*

Bressloff, N. W. (1999). The influence of soot loading on weighted sum of grey gases solutions to the radiative transfer equation across mixtures of gases and soot. *International Journal of Heat and Mass Transfer 42*(18), 3469–3480. *(p. 199)*

Brookes, S. J. and J. B. Moss (1999). Predictions of soot and thermal radiation properties in confined turbulent jet diffusion flames. *Combustion and Flame 116*(4), 486–503. *(p. 41, 363, 364)*

Brüning, T. (2006). Assessment of the health effects of toner particles on people in the workplace. *BG Research Institute for Occupational Medicine*. *(p. 3)*

Buis, S., A. Piacentini, and D. Déclat (2006). Palm: a computational framework for assembling high-performance computing applications. *Concurrency and Computation: Practice and Experience 18*(2), 231–245. *(p. 240, 251)*

Cai, J., N. Lu, and C. M. Sorensen (1993, 11). Comparison of size and morphology of soot aggregates as determined by light scattering and electron microscope analysis. *Langmuir 9*(11), 2861–2867. *(p. 26)*

Cai, J., N. Lu, and C. M. Sorensen (1995). Analysis of fractal cluster morphology parameters: Structural coefficient and density autocorrelation function cutoff. *Journal of Colloid and Interface Science 171*(2), 470–473. *(p. 26)*

Camacho, J., C. Liu, C. Gu, H. Lin, Z. Huang, Q. Tang, X. You, C. Saggese, Y. Li, H. Jung, L. Deng, I. Wlokas, and H. Wang (2015). Mobility size and mass of nascent soot particles in a benchmark premixed ethylene flame. *Combustion and Flame 162*(10), 3810 – 3822. *(p. 68, 72, 73, 74, 75, 78, 81, 82, 353)*

Candel, S. (2002). Combustion dynamics and control: Progress and challenges. *Proc. Combust. Inst. 29*(1), 1–28. *(p. 91, 92, 94)*

Castaldi, M. J., N. M. Marinov, C. F. Melius, J. Huang, S. M. Senkan, W. J. Pit, and C. K. Westbrook (1996). Experimental and modeling investigation of aromatic and polycyclic aromatic hydrocarbon formation in a premixed ethylene flame. *Symposium (International) on Combustion 26*(1), 693–702. *(p. 51, 52)*

Caudal, J. (2013). *Simulation numérique du reformage autothermique du méthane*. Phd thesis, Ecole Centrale Paris. *(p. 11)*

Celnik, M., R. Patterson, M. Kraft, and W. Wagner (2007). Coupling a stochastic soot population balance to gas-phase chemistry using operator splitting. *Combustion and Flame 148*(3), 158 – 176. *(p. 44, 367)*

Centeno, F. R., R. Brittes, F. H. R. França, and C. V. da Silva (2016). Application of the wsgg model for the calculation of gas–soot radiation in a turbulent non-premixed methane–air flame inside a cylindrical combustion chamber. *International Journal of Heat and Mass Transfer 93*,

742–753. *(p. 247)*

Chandler, M. F., Y. Teng, and U. O. Koylu (2007). Diesel engine particulate emissions: A comparison of mobility and microscopy size measurements. *Proceedings of the Combustion Institute 31*(2), 2971–2979. *(p. 26)*

Chang, H. and T. T. Charalampopoulos (1990). Determination of the wavelength dependence of refractive indices of flame soot. *Proceedings of the Royal Society of London A: Mathematical, Physical and Engineering Sciences 430*(1880), 577–591. *(p. 209, 213)*

Charalampopoulos, T. T. and H. Chang (1988, 06). In situ optical properties of soot particles in the wavelength range from 340 nm to 600 nm. *Combustion Science and Technology 59*(4-6), 401–421. *(p. 213)*

Chernov, V., M. J. Thomson, S. B. Dworkin, N. A. Slavinskaya, and U. Riedel (2014). Soot formation with c1 and c2 fuels using an improved chemical mechanism for pah growth. *Combustion and Flame 161*(2), 592 – 601. *(p. 50, 51)*

Chernov, V., Q. Zhang, M. J. Thomson, and S. B. Dworkin (2012). Numerical investigation of soot formation mechanisms in partially-premixed ethylene–air co-flow flames. *Combustion and Flame 159*(9), 2789 – 2798. *(p. 39)*

Chowdhury, S., W. R. Boyette, and W. L. Roberts (2017, 4). Time-averaged probability density functions of soot nanoparticles along the centerline of a piloted turbulent diffusion flame using a scanning mobility particle sizer. *Journal of Aerosol Science 106*, 56–67. *(p. 138)*

Churchill, S. W. and H. H. S. Chu (1975). Correlating equations for laminar and turbulent free convection from a vertical plate. *International Journal of Heat and Mass Transfer 18*(11), 1323–1329. *(p. 428)*

Ciajolo, A., A. D'anna, R. Barbella, A. Tregrossi, and A. Violi (1996). The effect of temperature on soot inception in premixed ethylene flames. *Symposium (International) on Combustion 26*(2), 2327 – 2333. *(p. 53)*

Ciajolo, A., A. Tregrossi, R. Barbella, R. Ragucci, B. Apicella, and M. de Joannon (2001). The relation between ultraviolet-excited fluorescence spectroscopy and aromatic species formed in rich laminar ethylene flames. *Combustion and Flame 125*(4), 1225 – 1229. *(p. 53)*

Coelho, P. J. (2004). Detailed numerical simulation of radiative transfer in a nonluminous turbulent jet diffusion flame. *Combustion and Flame 136*(4), 481–492. *(p. 246)*

Coelho, P. J. (2007). Numerical simulation of the interaction between turbulence and radiation in reactive flows. *Progress in Energy and Combustion Science 33*(4), 311–383. *(p. 124, 246, 263)*

Coelho, P. J. (2012, 01). Turbulence–radiation interaction: From theory to application in numerical simulations. *Journal of Heat Transfer 134*(3), 031001–031001–13. *(p. 124, 263)*

Colbeck, I., B. Atkinson, and Y. Johar (1997). The morphology and optical properties of soot produced by different fuels. *Journal of Aerosol*

*Science 28*(5), 715–723. *(p. 26)*

Colin, O. and M. Rudgyard (2000). Development of high-order taylor–galerkin schemes for les. *Journal of Computational Physics 162*(2), 338–371. *(p. 127, 160, 288, 312, 414)*

Colket, M., R. Hall, and H. Bockhorn (1994). Soot formation in combustion: mechanisms and models. *Springer Series in Chemical Physics 59*, 442–470. *(p. 104)*

Combis, P., P. Cormont, L. Gallais, D. Hebert, L. Robin, and J.-L. Rullier (2012). Evaluation of the fused silica thermal conductivity by comparing infrared thermometry measurements with two-dimensional simulations. *Applied Physics Letters 101*(21), 211908. *(p. 290, 434)*

Consalvi, J. L. and F. Nmira (2016a). Effects of soot absorption coefficient–planck function correlation on radiative heat transfer in oxygen-enriched propane turbulent diffusion flame. *Journal of Quantitative Spectroscopy and Radiative Transfer 172*, 50–57. *(p. 123, 264)*

Consalvi, J. L. and F. Nmira (2016b). Transported scalar pdf modeling of oxygen-enriched turbulent jet diffusion flames: Soot production and radiative heat transfer. *Fuel 178*, 37–48. *(p. 247)*

Consalvi, J. L. and F. Nmira (2017). Absorption turbulence-radiation interactions in sooting turbulent jet flames. *Journal of Quantitative Spectroscopy and Radiative Transfer 201*, 1–9. *(p. 247, 264)*

Corning (2014). Corning® hpfs® 7979, 7980, 8655 fused silica, optical materials product information. Technical report. *(p. 429, 430)*

Cubasch, U., K. Hasselmann, H. Höck, E. Maier-Reimer, U. Mikolajewicz, B. D. Santer, and R. Sausen (1992). Time-dependent greenhouse warming computations with a coupled ocean-atmosphere model. *Climate Dynamics 8*(2), 55–69. *(p. 270)*

Cuenot, B., F. Egolfopoulos, and T. Poinsot (2000, 2015/10/13). An unsteady laminar flamelet model for non-premixed combustion. *Combust. Theor. Model. 4*(1), 77–97. *(p. 91, 92, 94, 95)*

Cunningham, E. (1910). On the velocity of steady fall of spherical particles through fluid medium. *Proceedings of the Royal Society of London A: Mathematical, Physical and Engineering Sciences 83*(563), 357–365. *(p. 65)*

Cuoci, A., A. Frassoldati, T. Faravelli, and E. Ranzi (2009, 10). Formation of soot and nitrogen oxides in unsteady counterflow diffusion flames. *Combust. Flame 156*(10), 2010–2022. *(p. 91)*

Dalzell, W. H. and A. F. Sarofim (1969, 02). Optical constants of soot and their application to heat-flux calculations. *Journal of Heat Transfer 91*(1), 100–104. *(p. 123, 209, 213)*

Darabiha, N. (1992, 2015/09/11). Transient behaviour of laminar counterflow hydrogen-air diffusion flames with complex chemistry. *Combust. Sci. Technol. 86*(1-6), 163–181. *(p. 68)*

Decroix, M. E. and W. L. Roberts (1999, 2015/07/01). Study of transient

effects on the extinction limits of an unsteady counterflow diffusion flame. *Combust. Sci. Technol. 146*(1-6), 57–84. *(p. 85)*

Decroix, M. E. and W. L. Roberts (2000, 2015/06/24). Transient flow field effects on soot volume fraction in diffusion flames. *Combust. Sci. Technol. 160*(1), 165–189. *(p. 85, 86, 91, 97)*

Deirmendjian, D., R. Clasen, and W. Viezee (1961, Jun). Mie scattering with complex index of refraction. *J. Opt. Soc. Am. 51*(6), 620–633. *(p. 210)*

Demarco, R., F. Nmira, and J. L. Consalvi (2013). Influence of thermal radiation on soot production in laminar axisymmetric diffusion flames. *Journal of Quantitative Spectroscopy and Radiative Transfer 120*, 52–69. *(p. 247)*

Denison, M. K. and B. W. Webb (1993). An absorption-line blackbody distribution function for efficient calculation of total gas radiative transfer. *Journal of Quantitative Spectroscopy and Radiative Transfer 50*(5), 499–510. *(p. 199)*

Denison, M. K. and B. W. Webb (1995a). Development and application of an absorptionline blackbody distribution function for co2. *International Journal of Heat and Mass Transfer 38*(10), 1813–1821. *(p. 199)*

Denison, M. K. and B. W. Webb (1995b, 05). The spectral line-based weighted-sum-of-gray-gases model in nonisothermal nonhomogeneous media. *Journal of Heat Transfer 117*(2), 359–365. *(p. 199)*

Denison, M. K. and B. W. Webb (1995c, 08). The spectral-line weighted-sum-of-gray-gases model for h2o/co2 mixtures. *Journal of Heat Transfer 117*(3), 788–792. *(p. 199)*

Derjaguin, B. V., A. I. Storozhilova, and Y. I. Rabinovich (1966, 1). Experimental verification of the theory of thermophoresis of aerosol particles. *J. Colloid Interface Sci. 21*(1), 35–58. *(p. 31)*

di Stasio, S. (2001). Observation of restructuring of nanoparticle soot aggregates in a diffusion flame by static light scattering. *Journal of Aerosol Science 32*(4), 509–524. *(p. 26)*

Dobbins, R. A. and C. M. Megaridis (1991, Nov). Absorption and scattering of light by polydisperse aggregates. *Appl. Opt. 30*(33), 4747–4754. *(p. 215)*

Donaldson, K., L. Tran, L. A. Jimenez, R. Duffin, D. E. Newby, N. Mills, W. MacNee, and V. Stone (2005, Oct). Combustion-derived nanoparticles: A review of their toxicology following inhalation exposure. *Particle and Fibre Toxicology 2*(1), 10. *(p. 3)*

Donea, J. and A. . . Huerta (2003). *Finite element methods for flow problems*. John Wiley & Sons. *(p. 278)*

Draine, B. T. (1988). The discrete-dipole approximation and its application to interstellar graphite grains. *The Astrophysical Journal 333*, 848–872. *(p. 218)*

Draine, B. T. and J. Goodman (1993). Beyond clausius-mossotti-wave propagation on a polarizable point lattice and the discrete dipole approxima-

tion. *The Astrophysical Journal 405*, 685–697. *(p. 218)*

Duchaine, F., A. Corpron, L. Pons, V. Moureau, F. Nicoud, and T. Poinsot (2009). Development and assessment of a coupled strategy for conjugate heat transfer with large eddy simulation: Application to a cooled turbine blade. *International Journal of Heat and Fluid Flow 30*(6), 1129–1141. *(p. 269, 270, 271, 274, 308)*

Duchaine, F., S. Jauré, D. Poitou, E. Quémerais, G. Staffelbach, T. Morel, and L. Gicquel (2015). Analysis of high performance conjugate heat transfer with the openpalm coupler. *Computational Science and Discovery 8*(1), 015003. *(p. 240)*

Duchaine, F., N. Maheu, V. Moureau, G. Balarac, and S. Moreau (2013, 10). Large-eddy simulation and conjugate heat transfer around a low-mach turbine blade. *Journal of Turbomachinery 136*(5), 051015–051015–11. *(p. 274, 308)*

Dworkin, S. B., M. D. Smooke, and V. Giovangigli (2009). The impact of detailed multicomponent transport and thermal diffusion effects on soot formation in ethylene/air flames. *Proceedings of the Combustion Institute 32*(1), 1165–1172. *(p. 104)*

Dworkin, S. B., Q. Zhang, M. J. Thomson, N. A. Slavinskaya, and U. Riedel (2011). Application of an enhanced {PAH} growth model to soot formation in a laminar coflow ethylene/air diffusion flame. *Combustion and Flame 158*(9), 1682 – 1695. *(p. 39)*

Eaves, N., S. Dworkin, and M. Thomson (2015). The importance of reversibility in modeling soot nucleation and condensation processes. *Proceedings of the Combustion Institute 35*(2), 1787 – 1794. *(p. 35, 104)*

Eberle, C., P. Gerlinger, and M. Aigner (2017). A sectional pah model with reversible pah chemistry for cfd soot simulations. *Combustion and Flame 179*, 63–73. *(p. 104)*

Eberle, C., P. Gerlinger, K. P. Geigle, and M. Aigner (2015). Numerical investigation of transient soot evolution processes in an aero-engine model combustor. *Combustion Science and Technology 187*(12), 1841–1866. *(p. 104, 109, 181, 421)*

Eberle, C., P. M. Gerlinger, K. P. Geigle, and M. Aigner (2014). Soot predictions in an aero-engine model combustor at elevated pressure using urans and finite-rate chemistry. *50th AIAA/ASME/SAE/ASEE Joint Propulsion Conference, AIAA Propulsion and Energy Forum 3472*, 1–14. *(p. 421)*

Echavarria, C. A., A. F. Sarofim, J. S. Lighty, and A. D'Anna (2011). Evolution of soot size distribution in premixed ethylene/air and ethylene/benzene/air flames: Experimental and modeling study. *Combustion and Flame 158*(1), 98 – 104. *(p. 104)*

Egolfopoulos, F. N., D. L. Zhu, and C. K. Law (1991). Experimental and numerical determination of laminar flame speeds: Mixtures of c2-hydrocarbons with oxygen and nitrogen. *Symposium (International) on*

*Combustion 23*(1), 471–478. *(p. 50, 51, 54, 55)*

El-Asrag, H., T. Lu, C. K. Law, and S. Menon (2007). Simulation of soot formation in turbulent premixed flames. *Combustion and Flame 150*(1), 108–126. *(p. 135, 153)*

El-Asrag, H. and S. Menon (2009, 2). Large eddy simulation of soot formation in a turbulent non-premixed jet flame. *Combustion and Flame 156*(2), 385–395. *(p. 109, 135, 153)*

El Khoury, G., P. Schlatter, A. Noorani, P. Fischer, G. Brethouwer, and A. Johansson (2013). Direct numerical simulation of turbulent pipe flow at moderately high reynolds numbers. *91*(3), 475–495. *(p. 413)*

El-Leathy, A., F. Xu, and G. Faeth (2002, 2015/07/22). *Soot surface growth and oxidation in laminar unsaturated-hydrocarbon/air diffusion flames*. American Institute of Aeronautics and Astronautics. *(p. 37, 350)*

Enguehard, F. (2009). Mie theory and the discrete dipole approximation. calculating radiative properties of particulate media, with application to nanostructured materials. *Thermal Nanosystems and Nanomaterials*, 151–212. *(p. 218)*

EPA (1999). Evaluation of air pollutant emission from subsonic commercial jet aircraft. *United States Environmental Protection Agency*. *(p. 2, 3)*

EPA2015. Epa, california notify volkswagen of clean air act violations / car-maker allegedly used software that circumvents emissions testing for certain air pollutants. *(p. 7)*

Epstein, P. S. (1924, Jun). On the resistance experienced by spheres in their motion through gases. *Phys. Rev. 23*, 710–733. *(p. 30)*

Errera, M.-P. and S. Chemin (2013). Optimal solutions of numerical interface conditions in fluid–structure thermal analysis. *Journal of Computational Physics 245*, 431–455. *(p. 270, 274)*

Eymet, V., A. M. Brasil, M. E. Hafi, T. L. Farias, and P. J. Coelho (2002). Numerical investigation of the effect of soot aggregation on the radiative properties in the infrared region and radiative heat transfer. *Journal of Quantitative Spectroscopy and Radiative Transfer 74*(6), 697–718. *(p. 217)*

Fadl, M. and L. He (2017). On les based conjugate heat transfer procedure for transient natural convection. (50879), V05AT10A002–. *(p. 308)*

Faeth, G. M. and Ü. Ö. Köylü (1995, 01). Soot morphology and optical properties in nonpremixed turbulent flame environments. *Combustion Science and Technology 108*(4-6), 207–229. *(p. 105)*

Farias, T. L., U. O. Köylü, and M. G. Carvalho (1996, Nov). Range of validity of the rayleigh–debye–gans theory for optics of fractal aggregates. *Appl. Opt. 35*(33), 6560–6567. *(p. 215, 217, 218)*

Felske, J. D., T. T. Charalampopoulos, and H. S. Hura (1984, 06). Determination of the refractive indices of soot particles from the reflectivities of compressed soot pellets. *Combustion Science and Technology 37*(5-6), 263–283. *(p. 209)*

Felske, J. D. and C. L. Tien (1974). Infrared radiation from non-homogeneous gas mixtures having overlapping bands. *Journal of Quantitative Spectroscopy and Radiative Transfer 14*(1), 35–48. *(p. 199)*

Fiorina, B., R. Baron, O. Gicquel, D. Thevenin, S. Carpentier, and N. Darabiha (2003, 09). Modelling non-adiabatic partially premixed flames using flame-prolongation of ildm. *Combustion Theory and Modelling 7*(3), 449–470. *(p. 380)*

Fiorina, B., O. Gicquel, L. Vervisch, S. Carpentier, and N. Darabiha (2005a, 2). Approximating the chemical structure of partially premixed and diffusion counterflow flames using fpi flamelet tabulation. *Combustion and Flame 140*(3), 147–160. *(p. 380)*

Fiorina, B., O. Gicquel, L. Vervisch, S. Carpentier, and N. Darabiha (2005b). Premixed turbulent combustion modeling using tabulated detailed chemistry and pdf. *Proceedings of the Combustion Institute 30*(1), 867–874. *(p. 380)*

Fraioli, V., C. Beatrice, and M. Lazzaro (2011, 12). Soot particle size modelling in 3d simulations of diesel engine combustion. *Combustion Theory and Modelling 15*(6), 863–892. *(p. 109)*

Franzelli, B., B. Fiorina, and N. Darabiha (2013). A tabulated chemistry method for spray combustion. *Proc. Combust. Inst. 34*(1), 1659–1666. *(p. 127)*

Franzelli, B., E. Riber, B. Cuenot, and M. Ihme (2015). Numerical modeling of soot production in aero-engine combustors using large eddy simulations. *ASME Turbo Expo 2015 43630*. *(p. 109, 181, 421)*

Franzelli, B., P. Scouflaire, and S. Candel (2015). Time-resolved spatial patterns and interactions of soot, pah and oh in a turbulent diffusion flame. *Proc. Combust. Inst. 35*(2), 1921–1929. *(p. 90)*

Frayssé, V., L. Giraud, S. Gratton, and J. Langou (2005, June). Algorithm 842: A set of gmres routines for real and complex arithmetics on high performance computers. *ACM Trans. Math. Softw. 31*(2), 228–238. *(p. 278)*

Frenklach, M. (2002). Method of moments with interpolative closure. *Chemical Engineering Science 57*(12), 2229 – 2239. Population balance modelling of particulate systems. *(p. 366)*

Frenklach, M. and S. J. Harris (1987). Aerosol dynamics modeling using the method of moments. *Journal of Colloid and Interface Science 118*(1), 252–261. *(p. 42, 366)*

Frenklach, M. and H. Wang (1991). Detailed modeling of soot particle nucleation and growth. *Symposium (International) on Combustion 23*(1), 1559 – 1566. Twenty-Third Symposium (International) on Combustion. *(p. 39)*

Frenklach, M. and H. Wang (New York, 1994). Detailed mechanism and modeling of soot particle formation. *H. Bockhorn (Ed.), Soot Formation in Combustion: Mechanisms and Models*. *(p. 27, 36, 109)*

Frenklach, M. and J. Warnatz (1987, 02). Detailed modeling of pah pro-

files in a sooting low-pressure acetylene flame. *Combustion Science and Technology 51*(4-6), 265–283. *(p. 39)*

Geigle, K. P., R. Hadef, and W. Meier (2013, 10). Soot formation and flame characterization of an aero-engine model combustor burning ethylene at elevated pressure. *Journal of Engineering for Gas Turbines and Power 136*(2), 021505–021505. *(p. 156, 158, 318, 319, 420)*

Geigle, K. P., R. Hadef, M. Stöhr, and W. Meier (2017). Flow field characterization of pressurized sooting swirl flames and relation to soot distributions. *Proceedings of the Combustion Institute 36*(3), 3917–3924. *(p. 156, 158, 162, 163, 164, 165)*

Geigle, K. P., M. Köhler, W. O'Loughlin, and W. Meier (2015). Investigation of soot formation in pressurized swirl flames by laser measurements of temperature, flame structures and soot concentrations. *Proceedings of the Combustion Institute 35*(3), 3373 – 3380. *(p. 156, 157, 158, 168, 299, 300, 301)*

Geigle, K. P., W. O'Loughlin, R. Hadef, and W. Meier (2015). Visualization of soot inception in turbulent pressurized flames by simultaneous measurement of laser-induced fluorescence of polycyclic aromatic hydrocarbons and laser-induced incandescence, and correlation to oh distributions. *Applied Physics B 119*(4), 717–730. *(p. 156, 180)*

Gelbard, F. and J. H. Seinfeld (1980). Simulation of multicomponent aerosol dynamics. *Journal of Colloid and Interface Science 78*(2), 485–501. *(p. 43, 55)*

Gicquel, O., N. Darabiha, and D. Thévenin (2000). Liminar premixed hydrogen/air counterflow flame simulations using flame prolongation of ildm with differential diffusion. *Proceedings of the Combustion Institute 28*(2), 1901–1908. *(p. 369)*

Giles, M. B. (1997). Stability analysis of numerical interface conditions in fluid–structure thermal analysis. *International Journal for Numerical Methods in Fluids 25*(4), 421–436. *(p. 270)*

Glauert, M. B. (1956). The wall jet. *Journal of Fluid Mechanics 1*(6), 625–643. *(p. 426)*

Gonçalves dos Santos, R., M. Lecanu, S. Ducruix, O. Gicquel, E. Iacona, and D. Veynante (2008, 2). Coupled large eddy simulations of turbulent combustion and radiative heat transfer. *Combustion and Flame 152*(3), 387–400. *(p. 313, 421, 422)*

Goody, R. and Y. Yung (1995). *Atmospheric Radiation: Theoretical Basis.* Oxford University Press. *(p. 204, 249, 315)*

Gordon, R. G. (1968, 2017/08/15). Error bounds in equilibrium statistical mechanics. *Journal of Mathematical Physics 9*(5), 655–663. *(p. 365)*

Green, D. and R. Perry (2007). *Perry's Chemical Engineers' Handbook, Eighth Edition.* McGraw Hill professional. McGraw-Hill Education. *(p. 426)*

Guedri, K., M. N. Borjini, M. Jeguirim, J.-F. Brilhac, and R. Saïd (2011).

Numerical study of radiative heat transfer effects on a complex configuration of rack storage fire. *Energy 36*(5), 2984–2996. *(p. 247)*

Guiberti, T. F., D. Durox, P. Scouflaire, and T. Schuller (2015). Impact of heat loss and hydrogen enrichment on the shape of confined swirling flames. *Proceedings of the Combustion Institute 35*(2), 1385–1392. *(p. 307, 421)*

Gupta, A., D. C. Haworth, and M. F. Modest (2013). Turbulence-radiation interactions in large-eddy simulations of luminous and nonluminous nonpremixed flames. *Proceedings of the Combustion Institute 34*(1), 1281–1288. *(p. 247, 308)*

Gustafsson, K., M. Lundh, and G. Söderlind (1988). Api stepsize control for the numerical solution of ordinary differential equations. *BIT Numerical Mathematics 28*(2), 270–287. *(p. 273, 274)*

Habib, Z. G. and P. Vervisch (1988, 06). On the refractive index of soot at flame temperature. *Combustion Science and Technology 59*(4-6), 261–274. *(p. 213)*

Hairer, E., S. P. Nørsett, and G. Wanner (1993). *Solving Ordinary Differential Equations I (2Nd Revised. Ed.): Nonstiff Problems*. New York, NY, USA: Springer-Verlag New York, Inc. *(p. 272, 273)*

Harris, S. J. and A. M. Weiner (1984, 06). Soot particle growth in premixed toluene/ethylene flames. *Combustion Science and Technology 38*(1-2), 75–87. *(p. 105)*

Hassan, M. I., K. T. Aung, O. C. Kwon, and G. M. Faeth (1998, 2015/07/28). Properties of laminar premixed hydrocarbon/air flames at various pressures. *Journal of Propulsion and Power 14*(4), 479–488. *(p. 50, 51, 54, 55)*

Haworth, D. C., M. C. Drake, S. B. Pope, and R. J. Blint (1989). The importance of time-dependent flame structures in stretched laminar flamelet models for turbulent jet diffusion flames. *Symposium (International) on Combustion 22*(1), 589–597. *(p. 91, 92, 94)*

He, L. (2013, 02). Fourier spectral modelling for multi-scale aero-thermal analysis. *International Journal of Computational Fluid Dynamics 27*(2), 118–129. *(p. 270, 274)*

He, L. and M. L. G. Oldfield (2010, 11). Unsteady conjugate heat transfer modeling. *Journal of Turbomachinery 133*(3), 031022–031022–12. *(p. 270, 274)*

Henshaw, W. D. and K. K. Chand (2009). A composite grid solver for conjugate heat transfer in fluid–structure systems. *Journal of Computational Physics 228*(10), 3708–3741. *(p. 270)*

Heraeus (2016). Quartz glass for optics data and properties. Technical report. *(p. 290, 421, 434, 435)*

Hernández, I., G. Lecocq, D. Poitou, E. Riber, and B. Cuenot (2013). Computations of soot formation in ethylene/air counterflow diffusion flames and its interaction with radiation. *Comptes Rendus Mécanique 341*(1),

238–246. *(p. 247)*

Higgins, B., M. Q. McQuay, F. Lacas, J. C. Rolon, N. Darabiha, and S. Candel (2001). Systematic measurements of oh chemiluminescence for fuel-lean, high-pressure, premixed, laminar flames. *Fuel 80*(1), 67–74. *(p. 420)*

Hlawka, E. (1961). Funktionen von beschränkter variatiou in der theorie der gleichverteilung. *Annali di Matematica Pura ed Applicata 54*(1), 325–333. *(p. 236)*

Hottel, H. C. and A. F. Sarofim (1967). *Radiative transfer*. New York: McGraw-Hill. *(p. 198, 199)*

Howarth, C., P. Foster, and M. Thring (1966). Effect of temperature on the extinction of radiation of soot particles. In *Chemical Engineering Progress*, Volume 62, pp. 90. American Institute of Chemical Enigineers, New York. *(p. 209)*

Howell, J., M. Menguc, and R. Siegel (2010). *Thermal Radiation Heat Transfer, 5th Edition*. Taylor & Francis. *(p. 431, 433, 434)*

Hu, B., B. Yang, and U. O. Koylu (2003). Soot measurements at the axis of an ethylene/air non-premixed turbulent jet flame. *Combustion and Flame 134*(1), 93–106. *(p. 26, 105)*

Huijnen, V., A. V. Evlampiev, L. M. T. Somers, R. S. G. Baert, and L. P. H. de Goey (2010, 2015/06/24). The effect of the strain rate on pah/soot formation in laminar counterflow diffusion flames. *Combust. Sci. Technol. 182*(2), 103–123. *(p. 95)*

Hulst, H. and H. van de Hulst (1957). *Light Scattering by Small Particles*. Dover Books on Physics. Dover Publications. *(p. 210)*

Hwang, J. and S. Chung (2001). Growth of soot particles in counterflow diffusion flames of ethylene. *Combustion and Flame 125*(1–2), 752 – 762. *(p. 39, 104)*

IEA (2007). *Oil Information 2006*. Internation Energy Agency, Paris. *(p. 9)*

IEA (2016). *Key world energy statistics*. International Energy Agency. *(p. 2)*

Ihme, M. and H. Pitsch (2008a). Modeling of radiation and nitric oxide formation in turbulent nonpremixed flames using a flamelet/progress variable formulation. *Physics of Fluids 20*(5). *(p. 119, 123, 288, 307, 312, 384, 421)*

Ihme, M. and H. Pitsch (2008b). Prediction of extinction and reignition in nonpremixed turbulent flames using a flamelet/progress variable model. *Combustion and Flame 155*(1), 70–89. *(p. 380)*

IM, H. G., J. H. Chen, and J.-Y. Chen (1999, 7). Chemical response of methane/air diffusion flames to unsteady strain rate. *Combust. Flame 118*(1–2), 204–212. *(p. 96)*

ISF3 (2017). International sooting flame workshop, http://www.adelaide.edu.au/cet/isfworkshop/data-sets/. *(p. 53, 65, 126, 129, 130, 131, 132, 133, 248, 255, 256, 257, 258, 286, 393, 427)*

Issa, J. and A. Ortega (2004). Numerical computation of the heat transfer and fluid mechanics in the laminar wall jet and comparison to the self-similar solutions. (4711Xc), 191–197. *(p. 427)*

Issa, J. S. (2006). *Scaling of Convective Heat Transfer in Laminar and Turbulent Wall Jets With Effects of Freestream Flow and Forcing*. Ph. D. thesis, The University of Arizona. *(p. 427)*

Jacobson, M. Z. (2002). Control of fossil-fuel particulate black carbon and organic matter, possibly the most effective method of slowing global warming. *Journal of Geophysical Research: Atmospheres 107*(D19), ACH 16–1–ACH 16–22. 4410. *(p. 4)*

Jaegle, F., O. Cabrit, S. Mendez, and T. Poinsot (2010). Implementation methods of wall functions in cell-vertex numerical solvers. *Flow, Turbulence and Combustion 85*(2), 245–272. *(p. 158, 288)*

Jaure, S., F. Duchaine, G. Staffelbach, and L. Y. M. Gicquel (2013). Massively parallel conjugate heat transfer methods relying on large eddy simulation applied to an aeronautical combustor. *Computational Science & Discovery 6*(1), 015008. *(p. 269, 270, 271, 274, 278, 308, 421)*

Jensen, K. A., J. M. Suo-Anttila, and L. G. Blevins (2007, 10). Measurement of soot morphology, chemistry, and optical properties in the visible and near-infrared spectrum in the flame zone and overfire region of large jp-8 pool fires. *Combustion Science and Technology 179*(12), 2453–2487. *(p. 105)*

Joe, S. and F. Y. Kuo (2008). Constructing sobol sequences with better two-dimensional projections. *SIAM Journal on Scientific Computing 30*(5), 2635–2654. *(p. 236, 251, 315)*

Jomaas, G., X. L. Zheng, D. L. Zhu, and C. K. Law (2005, 1). Experimental determination of counterflow ignition temperatures and laminar flame speeds of c2–c3 hydrocarbons at atmospheric and elevated pressures. *Proceedings of the Combustion Institute 30*(1), 193–200. *(p. 50, 51, 54, 55)*

Jones, W. P. and M. C. Paul (2005, 3). Combination of dom with les in a gas turbine combustor. *International Journal of Engineering Science 43*(5–6), 379–397. *(p. 308, 421)*

Jullien, R. and R. Botet (1987). Aggregation and fractal aggregates. *Ann. Telecomm. 41*, 343. *(p. 25, 26)*

Kamimoto, T. and M.-h. Bae (1988). High combustion temperature for the reduction of particulate in diesel engines. *SAE International Congress and Exposition*. *(p. 7)*

Kamm, S., O. Möhler, K. H. Naumann, H. Saathoff, and U. Schurath (1999). The heterogeneous reaction of ozone with soot aerosol. *Atmospheric Environment 33*(28), 4651–4661. *(p. 3)*

Kazakov, A. and M. Frenklach (1998). Dynamic modeling of soot particle coagulation and aggregation: Implementation with the method of moments and application to high-pressure laminar premixed flames. *Combustion and Flame 114*(3-4), 484–501. *(p. 33)*

Kearney, S. P., D. R. Guildenbecher, C. Winters, P. A. Farias, T. W. Grasser, and J. C. Hewson (2015, Sep). *Temperature, Oxygen, and Soot-Volume-Fraction Measurements in a Turbulent C2H4-Fueled Jet Flame.* *(p. 126, 129, 255)*

Kee, R. J., J. A. Miller, G. H. Evans, and G. Dixon-Lewis (1989). A computational model of the structure and extinction of strained, opposed flow, premixed methane-air flames. *Symposium (International) on Combustion 22*(1), 1479 – 1494. *(p. 380)*

Keita, M. (2017). Modeling of soot particles nucleation from combustion processes. *(p. 39)*

Kennedy, I. M., W. Kollmann, and J. Y. Chen (1990). A model for soot formation in a laminar diffusion flame. *Combustion and Flame 81*(1), 73–85. *(p. 41, 361)*

Koo, H., V. Raman, M. E. Mueller, and K.-P. Geigle (2016, 2016/01/12). *LES of a sooting flame in a pressurized swirl combustor*. American Institute of Aeronautics and Astronautics. *(p. 109, 181, 421)*

Kook, S. and L. M. Pickett (2011). Soot volume fraction and morphology of conventional and surrogate jet fuel sprays at 1000-k and 6.7-mpa ambient conditions. *Proceedings of the Combustion Institute 33*(2), 2911–2918. *(p. 105)*

Koren, C. (2016, April). *Modélisation des transferts de chaleur couplés pour la simulation multi-physique des chambres de combustion*. Phd thesis, Université Paris-Saclay. *(p. 239, 278, 280)*

Koren, C., R. Vicquelin, and O. Gicquel (2017a). An acceleration method for numerical studies of conjugate heat transfer with a self-adaptive coupling time step method: Application to a wall-impinging flame. *ASME Turbo Expo* (50893), V05CT17A006–. *(p. 270, 274)*

Koren, C., R. Vicquelin, and O. Gicquel (2017b). High-fidelity multiphysics simulation of a confined premixed swirling flame combining large-eddy simulation, wall heat conduction and radiative energy transfer. *ASME Turbo Expo: Power for Land, Sea, and Air* (50893), 1–14. *(p. 300, 308, 313, 421, 422)*

Koren, C., R. Vicquelin, and O. Gicquel (2017c, 8). Self-adaptive coupling frequency for unsteady coupled conjugate heat transfer simulations. *International Journal of Thermal Sciences 118*, 340–354. *(p. 270, 271, 273, 281, 283, 303)*

Koren, C., R. Vicquelin, and O. Gicquel (2018). Multiphysics simulation combining large-eddy simulation, wall heat conduction and radiative energy transfer to predict wall temperature induced by a confined premixed swirling flame. *Flow, Turbulence and Combustion*. *(p. 269)*

Köylü, Ü. Ö. and G. M. Faeth (1993, 05). Radiative properties of flame-generated soot. *Journal of Heat Transfer 115*(2), 409–417. *(p. 215)*

Köylü, Ü. Ö. and G. M. Faeth (1994, 02). Optical properties of overfire soot in buoyant turbulent diffusion flames at long residence times. *Journal of*

*Heat Transfer 116*(1), 152–159. *(p. 26, 105)*

Köylü, Ü. Ö., C. S. McEnally, D. E. Rosner, and L. D. Pfefferle (1997). Simultaneous measurements of soot volume fraction and particle size / microstructure in flames using a thermophoretic sampling technique. *Combustion and Flame 110*(4), 494–507. *(p. 105)*

Kraus, C., L. Selle, and T. Poinsot (2018). Coupling heat transfer and large eddy simulation for combustion instability prediction in a swirl burner. *Combustion and Flame 191*, 239–251. *(p. 269)*

Krishnan, S., K. Lin, and G. Faeth (2001). Extinction and scattering properties of soot emitted from buoyant turbulent diffusion flames. *Transactions-American Society of Mechanical Engineers Journal of Heat Transfer 123*(2), 331–339. *(p. 213)*

Krishnan, S. S., K. C. Lin, and G. M. Faeth (2000, 02). Optical properties in the visible of overfire soot in large buoyant turbulent diffusion flames. *Journal of Heat Transfer 122*(3), 517–524. *(p. 105)*

Kronenburg, A., R. W. Bilger, and J. H. Kent (2000). Modeling soot formation in turbulent methane–air jet diffusion flames. *Combustion and Flame 121*(1), 24–40. *(p. 122)*

Kuhlert, K. and U. Renz (1998). A comprehensive radiation model for numerical simulations of pulverised coal flames. *Proceedings of the 11th International Heat Transfer Conference*. *(p. 199)*

Kuhn, S., O. Braillard, B. Ničeno, and H.-M. Prasser (2010). Computational study of conjugate heat transfer in t-junctions. *Nuclear Engineering and Design 240*(6), 1548–1557. *(p. 269)*

Lalit, H., J. P. Gore, and H. Wang (2017, 2017/10/23). *Assessment of Differential Diffusion Effects on Soot Evolution in Piloted Non-premixed Turbulent Flames*. American Institute of Aeronautics and Astronautics. *(p. 122)*

Lallich, S. (2009, February). *Experimental determination and modeling of the radiative properties of silica nanoporous matrices*. Phd thesis, INSA de Lyon. *(p. 218)*

Lamouroux, J., M. Ihme, B. Fiorina, and O. Gicquel (2014, 8). Tabulated chemistry approach for diluted combustion regimes with internal recirculation and heat losses. *Combustion and Flame 161*(8), 2120–2136. *(p. 307, 421)*

Lax, P. and B. Wendroff (1960). Systems of conservation laws. *Communications on Pure and Applied mathematics 13*(2), 217–237. *(p. 414)*

Lecocq, G., D. Poitou, I. Hernández, F. Duchaine, E. Riber, and B. Cuenot (2014). A methodology for soot prediction including thermal radiation in complex industrial burners. *Flow, Turbulence and Combustion 92*(4), 947–970. *(p. 247, 308)*

Lee, D. S., D. W. Fahey, P. M. Forster, P. J. Newton, R. C. N. Wit, L. L. Lim, B. Owen, and R. Sausen (2009). Aviation and global climate change in the 21st century. *Atmospheric Environment 43*(22), 3520–3537. *(p. 5,*

*9, 10)*

Lee, K. B., M. W. Thring, and J. M. Beér (1962). On the rate of combustion of soot in a laminar soot flame. *Combustion and Flame 6*, 137–145. *(p. 105)*

Lee, S. C. and C. L. Tien (1981). Optical constants of soot in hydrocarbon flames. *Symposium (International) on Combustion 18*(1), 1159–1166. *(p. 209, 213)*

Lefebvre, A. (1998). *GAS Turbine Combustion, Second Edition*. Combustion: An International Series. Taylor & Francis. *(p. 7)*

Lefebvre, A. H. (1984). Flame radiation in gas turbine combustion chambers. *International Journal of Heat and Mass Transfer 27*(9), 1493–1510. *(p. 345)*

Lemieux, C. (2009). *Monte Carlo and Quasi-Monte Carlo Sampling*. Springer Series in Statistics. Springer New York. *(p. 237, 251, 315)*

Leung, K., R. Lindstedt, and W. Jones (1991). A simplified reaction mechanism for soot formation in nonpremixed flames. *Combustion and Flame 87*(3–4), 289 – 305. *(p. 41, 109, 362, 363)*

Li, Z., C. Song, J. Song, G. Lv, S. Dong, and Z. Zhao (2011). Evolution of the nanostructure, fractal dimension and size of in-cylinder soot during diesel combustion process. *Combustion and Flame 158*(8), 1624–1630. *(p. 105)*

Lien, F. S., H. Liu, E. Chui, and C. J. McCartney (2009). Development of an analytical $\beta-$function pdf integration algorithm for simulation of non-premixed turbulent combustion. *Flow Turbulence and Combustion 83*(2), 205–226. *(p. 120, 383)*

Lignell, D. O., J. H. Chen, and P. J. Smith (2008). Three-dimensional direct numerical simulation of soot formation and transport in a temporally evolving nonpremixed ethylene jet flame. *Combustion and Flame 155*(1–2), 316 – 333. *(p. 109)*

Lindstedt, P. R. (1994). *Simplified Soot Nucleation and Surface Growth Steps for Non-Premixed Flames*, pp. 417–441. Berlin, Heidelberg: Springer Berlin Heidelberg. *(p. 362, 363)*

Lindstedt, R. (1992). A simple reaction mechanism for soot formation in non-premixed flames. In *Aerothermodynamics in Combustors*, pp. 145–156. Springer. *(p. 109)*

Lindstedt, R. P. and S. A. Louloudi (2005). Joint-scalar transported pdf modeling of soot formation and oxidation. *Proceedings of the Combustion Institute 30*(1), 775–783. *(p. 362)*

Liu, F., H. Guo, and G. J. Smallwood (2004). Effects of radiation model on the modeling of a laminar coflow methane/air diffusion flame. *Combustion and Flame 138*(1), 136–154. *(p. 247)*

Liu, F., G. J. Smallwood, and W. Kong (2011). The importance of thermal radiation transfer in laminar diffusion flames at normal and microgravity. *Journal of Quantitative Spectroscopy and Radiative Transfer 112*(7), 1241–1249. *(p. 247)*

Liu, F. and D. Snelling (2008, 2017/07/21). *Evaluation of the Accuracy of the RDG Approximation for the Absorption and Scattering Properties of Fractal Aggregates of Flame-Generated Soot*. American Institute of Aeronautics and Astronautics. *(p. 217)*

Liu, F., K. A. Thomson, H. Guo, and G. J. Smallwood (2006). Numerical and experimental study of an axisymmetric coflow laminar methane–air diffusion flame at pressures between 5 and 40 atmospheres. *Combustion and Flame 146*(3), 456–471. *(p. 39)*

Liu, F., J. Yon, and A. Bescond (2016). On the radiative properties of soot aggregates part 2: Effects of coating. *Journal of Quantitative Spectroscopy and Radiative Transfer 172*, 134–145. *(p. 215, 216)*

Lockwood, F. C. and J. E. Van Niekerk (1995). Parametric study of a carbon black oil furnace. *Combustion and Flame 103*(1), 76–90. *(p. 362)*

Lopez-Parra, F. and A. Turan (2007, 06). Computational study on the effects of non-periodic flow perturbations on the emissions of soot and nox in a turbulent methane/air diffusion flame. *Combustion Science and Technology 179*(7), 1361–1384. *(p. 360)*

Ludwig, C. (1973). *Handbook of Infrared Radiation from Combustion Gases*. NASA SP. NASA. *(p. 200)*

Lunkeit, F., R. Sausen, and J. M. Oberhuber (1996). Climate simulations with the global coupled atmosphere-ocean model echam2/opyc part i: present-day climate and enso events. *Climate Dynamics 12*(3), 195–212. *(p. 270)*

Madadi-Kandjani, E. and A. Passalacqua (2015). An extended quadrature-based moment method with log-normal kernel density functions. *Chemical Engineering Science 131*(0), 323 – 339. *(p. 42, 367)*

Magnussen, B. (1989). Modeling of pollutant formation in gas turbine combustors based on the eddy dissipation concept. In *18th International Congress on Combustion Engines, Tianjin, China, June*, pp. 5–9. *(p. 360)*

Malbois, P., E. Salaun, F. Frindt, G. Cabot, B. Renou, F. Grisch, L. Bouheraoua, H. Verdier, and S. Richard (2017). Experimental investigation with optical diagnostics of a lean-premixed aero-engine injection system under relevant operating conditions. *ASME Turbo Expo: Power for Land, Sea, and Air 50855*. *(p. 420)*

Malkmus, W. (1967). Random lorentz band model with exponential-tailed s1 line-intensity distribution function. *Journal of the Optical Society of America 57*(3), 323–329. *(p. 200)*

Marchal, C. (2008, December). *Soot formation and oxidation modelling in an automotive engine*. Phd thesis, Université d'Orléans. *(p. 34, 35, 50, 62, 63, 65, 104)*

Marchal, C., J.-L. Delfau, C. Vovelle, G. Moréac, C. Mounaim-Rousselle, and F. Mauss (2009). Modelling of aromatics and soot formation from large fuel molecules. *Proceedings of the Combustion Institute 32*(1), 753–759.

*(p. 51)*

Marchisio, D. L. and R. O. Fox (2005). Solution of population balance equations using the direct quadrature method of moments. *Journal of Aerosol Science 36*(1), 43 – 73. *(p. 42, 365)*

Marchisio, D. L., J. T. Pikturna, R. O. Fox, R. D. Vigil, and A. A. Barresi (2003). Quadrature method of moments for population-balance equations. *AIChE Journal 49*(5), 1266–1276. *(p. 365)*

Mari, R., B. Cuenot, J.-P. Rocchi, L. Selle, and F. Duchaine (2016, 6). Effect of pressure on hydrogen/oxygen coupled flame–wall interaction. *Combustion and Flame 168*, 409–419. *(p. 269, 421)*

Mätzler, C. (2002). Matlab functions for mie scattering and absorption, version 2. *IAP Res. Rep 8*, 1–24. *(p. 210)*

Maugendre, M. (2009, December). *Study of soots particles in kerosene and biofuel flames*. Phd thesis, INSA de Rouen. *(p. 26, 105)*

Mauss, F. (1998). Entwicklung eines kinetischen modells der russbildung mit schneller polymerisation. *(p. 50, 51)*

Mauss, F., K. Netzell, and H. Lehtiniemi (2006). Aspects of modeling soot formaation in turbulent diffusion flames. *Combust. Sci. Technol. 178*(10-11), 1871–1885. *(p. 37)*

Mauss, F., T. Schäfer, and H. Bockhorn (1994). Inception and growth of soot particles in dependence on the surrounding gas phase. *Combust. Flame 99*(3–4), 697 – 705. 25th Symposium (International) on Combustion Papers. *(p. 37, 351)*

McCubbin, D. (2011). Health benefits of alternative pm2.5 standards. *Washington: American Lung Association, Clean Air Task Force, Earthjustice*. *(p. 7)*

McEnally, C. S., A. M. Schaffer, M. B. Long, L. D. Pfefferle, M. D. Smooke, M. B. Colket, and R. J. Hall (1998). Computational and experimental study of soot formation in a coflow, laminar ethylene diffusion flame. *Symposium (International) on Combustion 27*(1), 1497–1505. *(p. 104)*

McGraw, R. (1997). Description of aerosol dynamics by the quadrature method of moments. *Aerosol Science and Technology 27*(2), 255–265. *(p. 365)*

Meakin, P. (1983, Sep). Formation of fractal clusters and networks by irreversible diffusion-limited aggregation. *Phys. Rev. Lett. 51*, 1119–1122. *(p. 26)*

Megaridis, C. M. and R. A. Dobbins (1989). Soot aerosol dynamics in a laminar ethylene diffusion flame. *Symposium (International) on Combustion 22*(1), 353–362. *(p. 26, 105)*

Mehta, R. S., D. C. Haworth, and M. F. Modest (2010). Composition pdf/photon monte carlo modeling of moderately sooting turbulent jet flames. *Combustion and Flame 157*(5), 982–994. *(p. 181, 247, 300, 307, 320)*

Menkiel, B., A. Donkerbroek, R. Uitz, R. Cracknell, and L. Ganippa (2012).

Measurement of in-cylinder soot particles and their distribution in an optical hsdi diesel engine using time resolved laser induced incandescence (tr-lii). *Combustion and Flame 159*(9), 2985–2998. *(p. 105)*

Mercier, R., T. F. Guiberti, A. Chatelier, D. Durox, O. Gicquel, N. Darabiha, T. Schuller, and B. Fiorina (2016). Experimental and numerical investigation of the influence of thermal boundary conditions on premixed swirling flame stabilization. *Combustion and Flame 171*(Supplement C), 42–58. *(p. 421)*

Mesyngier, C. and B. Farouk (1996, 05). Turbulent natural convection-nongray gas radiation analysis in a square enclosure. *Numerical Heat Transfer, Part A: Applications 29*(7), 671–687. *(p. 199)*

Miguel-Brebion, M., D. Mejia, P. Xavier, F. Duchaine, B. Bedat, L. Selle, and T. Poinsot (2016). Joint experimental and numerical study of the influence of flame holder temperature on the stabilization of a laminar methane flame on a cylinder. *Combustion and Flame 172*(Supplement C), 153–161. *(p. 269, 421)*

Mishchenko, M. I., L. Liu, and D. W. Mackowski (2013). T-matrix modeling of linear depolarization by morphologically complex soot and soot-containing aerosols. *Journal of Quantitative Spectroscopy and Radiative Transfer 123*, 135–144. *(p. 217)*

Mitchell, P. and M. Frenklach (1998). Monte carlo simulation of soot aggregation with simultaneous surface growth-why primary particles appear spherical. *Symposium (International) on Combustion 27*(1), 1507–1514. *(p. 44, 367)*

Modest, M. F. (1991, 08). The weighted-sum-of-gray-gases model for arbitrary solution methods in radiative transfer. *Journal of Heat Transfer 113*(3), 650–656. *(p. 198)*

Modest, M. F. (2013). *Radiative Heat Transfer (Third Edition)*. Boston: Academic Press. *(p. 123, 207, 208, 209, 249, 430, 434)*

Modest, M. F. and D. C. Haworth (2016). *Radiative Heat Transfer in Turbulent Combustion Systems*. Springer. *(p. 313, 422)*

Moss, J. B., C. D. Stewart, and K. J. Syed (1989). Flowfield modelling of soot formation at elevated pressure. *Symposium (International) on Combustion 22*(1), 413–423. *(p. 41, 360, 361, 364)*

Mountain, R. D. and G. W. Mulholland (1988, 11). Light scattering from simulated smoke agglomerates. *Langmuir 4*(6), 1321–1326. *(p. 26)*

Mouton, T. (2014). *Analyse des processus de nucléation et de croissance des particules de suie dans des flammes par fluorescence induite par laser en jet froid appliquée aux hydrocarbures aromatiques polycycliques et par incandescence induite par laser*. Ph. D. thesis, Lille 1. *(p. 213)*

Mueller, M., G. Blanquart, and H. Pitsch (2009a). Hybrid method of moments for modeling soot formation and growth. *Combust. Flame 156*(6), 1143 – 1155. *(p. 42, 59, 60, 109, 366)*

Mueller, M. E., G. Blanquart, and H. Pitsch (2009b). A joint volume-surface

model of soot aggregation with the method of moments. *Proc. Combust. Inst. 32*(1), 785 – 792. *(p. 28, 35, 59, 62, 366)*

Mueller, M. E., Q. N. Chan, N. H. Qamar, B. B. Dally, H. Pitsch, Z. T. Alwahabi, and G. J. Nathan (2013, 7). Experimental and computational study of soot evolution in a turbulent nonpremixed bluff body ethylene flame. *Combust. Flame 160*(7), 1298–1309. *(p. 109)*

Mueller, M. E. and H. Pitsch (2011). Large eddy simulation subfilter modeling of soot-turbulence interactions. *Physics of Fluids (1994-present) 23*(11), 1–20. *(p. 115, 116, 117, 377, 378)*

Mueller, M. E. and H. Pitsch (2012, 6). Les model for sooting turbulent nonpremixed flames. *Combustion and Flame 159*(6), 2166–2180. *(p. 109, 115, 116, 121, 132, 135, 153, 372, 373)*

Mulholland, G. W., R. J. Samson, R. D. Mountain, and M. H. Ernst (1988, 07). Cluster size distribution for free molecular agglomeration. *Energy & Fuels 2*(4), 481–486. *(p. 26)*

Nau, P., Z. Yin, K. P. Geigle, and W. Meier (2017). Wall temperature measurements at elevated pressures and high temperatures in sooting flames in a gas turbine model combustor. *Applied Physics B 123*(12), 279. *(p. 156, 158, 160, 161, 285, 286, 295, 296, 297, 320, 424, 425)*

Netzell, K. (2006). *Development and Applications of Detailed Kinetic Models for the Soot Particle Size Distribution Function*. Ph. D. thesis, Lund University. *(p. 38, 104)*

Netzell, K., H. Lehtiniemi, and F. Mauss (2007, 1). Calculating the soot particle size distribution function in turbulent diffusion flames using a sectional method. *Proceedings of the Combustion Institute 31*(1), 667–674. *(p. 43, 56, 104, 109)*

Nguyen, T. T., F. Laurent, R. O. Fox, and M. Massot (2016). Solution of population balance equations in applications with fine particles: Mathematical modeling and numerical schemes. *Journal of Computational Physics 325*, 129–156. *(p. 42, 367)*

Nicoud, F. and F. Ducros (1999). Subgrid-scale stress modelling based on the square of the velocity gradient tensor. *Flow, Turbulence and Combustion 62*(3), 183–200. *(p. 114, 118, 160, 412, 414)*

Nicoud, F., H. B. Toda, O. Cabrit, S. Bose, and J. Lee (2011). Using singular values to build a subgrid-scale model for large eddy simulations. *Physics of Fluids 23*(8), 1–12. *(p. 160, 288, 312)*

Nishioka, M., C. K. Law, and T. Takeno (1996, 2). A flame-controlling continuation method for generating s-curve responses with detailed chemistry. *Combustion and Flame 104*(3), 328–342. *(p. 380)*

Nogenmyr, K. J., H. J. Cao, C. K. Chan, and R. K. Cheng (2013, 12). Effects of confinement on premixed turbulent swirling flame using large eddy simulation. *Combustion Theory and Modelling 17*(6), 1003–1019. *(p. 307, 421)*

O'Connor, G. T., L. Neas, B. Vaughn, M. Kattan, H. Mitchell, E. F. Crain,

R. Evans III, R. Gruchalla, W. Morgan, J. Stout, G. K. Adams, and M. Lippmann (2008, 5). Acute respiratory health effects of air pollution on children with asthma in us inner cities. *J. Allergy Clin. Immunol. 121*(5), 1133–1139. *(p. 3)*

Okyay, G. (2016, April). *Impact of the morphology of soot aggregates on their radiative properties and the subsequent radiative heat transfer through sooty gaseous mixtures*. Phd thesis, Université Paris-Saclay. *(p. 25, 26, 208, 218, 219, 220, 265)*

Omori, T., S. Yamaguchi, and T. Fusegi (2000). Computational heat transfer analysis of a furnace using the wsgg model. In *National Heat Transfer Symposium of Japan*, Volume 37, pp. 307–308. Japan Heat Transfer Society; 1999. *(p. 199)*

Onischuk, A. A., S. di Stasio, V. V. Karasev, A. M. Baklanov, G. A. Makhov, A. L. Vlasenko, A. R. Sadykova, A. V. Shipovalov, and V. N. Panfilov (2003). Evolution of structure and charge of soot aggregates during and after formation in a propane/air diffusion flame. *Journal of Aerosol Science 34*(4), 383–403. *(p. 26)*

Pailthorpe, B. and W. Russel (1982). The retarded van der waals interaction between spheres. *Journal of Colloid and Interface Science 89*(2), 563 – 566. *(p. 34)*

Pal, G., A. Gupta, M. F. Modest, and D. C. Haworth (2011). Comparison of accuracy and computational expense of radiation models in simulation of non-premixed turbulent jet flames. (38921), T20116–T20116–10. *(p. 247, 263)*

Palluotto, L., N. Dumont, P. Rodrigues, C. Koren, R. Vicquelin, and O. Gicquel (2017). Comparison of monte carlo methods efficiency to solve radiative energy transfer in high fidelity unsteady 3d simulations. *ASME Turbo Expo* (50879), V05AT20A004–. *(p. 251, 315)*

Pena, M. A., J. P. Gómez, and J. L. G. Fierro (1996). New catalytic routes for syngas and hydrogen production. *Applied Catalysis A: General 144*(1), 7–57. *(p. 10)*

Peters, N. (1984). Laminar diffusion flamelet models in non-premixed turbulent combustion. *Prog. Energy Combust. Sci. 10*(3), 319–339. *(p. 91)*

Peters, N. (2000). *Turbulent Combustion*. Cambridge University Press. *(p. 122)*

Pierce, C. D. and P. Moin (2004). Progress-variable approach for large-eddy simulation of non-premixed turbulent combustion. *Journal of Fluid Mechanics 504*, 73–97. *(p. 119, 288, 312, 380)*

Pierrot, L., P. Rivière, A. Soufiani, and J. Taine (1999). A fictitious-gas-based absorption distribution function global model for radiative transfer in hot gases. *Journal of Quantitative Spectroscopy and Radiative Transfer 62*(5), 609–624. *(p. 199)*

Pierrot, L., A. Soufiani, and J. Taine (1999). Accuracy of narrow-band and global models for radiative transfer in h2o, co2, and h2o/co2 mixtures

at high temperature. *Journal of Quantitative Spectroscopy and Radiative Transfer 62*(5), 523–548. *(p. 199)*

Pitsch, H. (1996). Detailed kinetic reaction mechanism for ignition and oxidation of $\alpha$-methylnaphthalene. *Symposium (International) on Combustion 26*(1), 721–728. *(p. 39)*

Pitsch, H. (2000). Unsteady flamelet modeling of differential diffusion in turbulent jet diffusion flames. *Combustion and Flame 123*(3), 358 – 374. *(p. 122)*

Poinsot, T. and D. Veynante (2012). *Theoretical and numerical combustion* (3rd Edition ed.). *(p. 92)*

Poinsot, T. J. and S. K. Lele (1992). Boundary conditions for direct simulations of compressible viscous flows. *Journal of Computational Physics 101*(1), 104–129. *(p. 127, 158)*

Poitou, D., J. Amaya, M. El Hafi, and B. Cuénot (2012). Analysis of the interaction between turbulent combustion and thermal radiation using unsteady coupled les/dom simulations. *Combustion and Flame 159*(4), 1605–1618. *(p. 246, 247, 263, 308, 313, 421, 422)*

Poitou, D., M. El Hafi, and B. Cuenot (2008). Diagnosis of turbulence radiation interaction in turbulent flames and implications for modeling in large eddy simulation. *Turkish Journal of Engineering and Environmental Sciences 31*(6), 371–381 *(p. 247, 265, 346)*

Poitou, D., M. El Hafi, and B. Cuenot (2011, 03). Analysis of radiation modeling for turbulent combustion: Development of a methodology to couple turbulent combustion and radiative heat transfer in les. *Journal of Heat Transfer 133*(6). *(p. 313, 422)*

Pope, S. B. (2000). *Turbulent Flows* (1 ed.). Cambridge University Press. *(p. 128, 414, 415, 416, 417, 418)*

Prado, G., J. Jagoda, K. Neoh, and J. Lahaye (1981). A study of soot formation in premixed propane/oxygen flames by in-situ optical techniques and sampling probes. *Symposium (International) on Combustion 18*(1), 1127–1136. *(p. 105)*

Prado, G. P., M. L. Lee, R. A. Hites, D. P. Hoult, and J. B. Howard (1977). Soot and hydrocarbon formation in a turbulent diffusion flame. *Symposium (International) on Combustion 16*(1), 649–661. *(p. 105)*

Purcell, E. M. and C. R. Pennypacker (1973). Scattering and Absorption of Light by Nonspherical Dielectric Grains. *The Astrophysical Journal 186*, 705–714. *(p. 218)*

Puri, R., T. F. Richardson, R. J. Santoro, and R. A. Dobbins (1993). Aerosol dynamic processes of soot aggregates in a laminar ethene diffusion flame. *Combustion and Flame 92*(3), 320–333. *(p. 26)*

Quaas, J. (2011, 03). Global warming: The soot factor. *Nature 471*(7339), 456–457. *(p. 5)*

Quarteroni, A. and A. Valli (1999). *Domain decomposition methods for partial differential equations*. Oxford University Press. *(p. 269)*

Radenac, E., J. Gressier, and P. Millan (2014). Methodology of numerical coupling for transient conjugate heat transfer. *Computers & Fluids 100*, 95–107. *(p. 270)*

Reddy, M., A. De, and R. Yadav (2015a). Effect of precursors and radiation on soot formation in turbulent diffusion flame. *Fuel 148*(Supplement C), 58–72. *(p. 181, 300, 307)*

Reddy, M., A. De, and R. Yadav (2015b, 5). Effect of precursors and radiation on soot formation in turbulent diffusion flame. *Fuel 148*, 58–72. *(p. 247, 320)*

Refahi, S. (2013, February). *Development of a radiative transfer code and its coupling with a LES code*. Phd thesis, Ecole Centrale Paris. *(p. 239)*

Refloch, A., B. Courbet, A. Murrone, P. Villedieu, C. Laurent, P. Gilbank, J. Troyes, L. Tessé, G. Chaineray, J. Dargaud, E. Quémerais, and F. Vuillot (2011, March). CEDRE Software. *AerospaceLab* (2), p. 1–10. *(p. 240)*

Richter, H., S. Granata, W. H. Green, and J. B. Howard (2005). Detailed modeling of pah and soot formation in a laminar premixed benzene/oxygen/argon low-pressure flame. *Proceedings of the Combustion Institute 30*(1), 1397 – 1405. *(p. 41, 50, 51, 364, 365)*

Rivière, P. and A. Soufiani (2012, 6). Updated band model parameters for h2o, co2, ch4 and co radiation at high temperature. *International Journal of Heat and Mass Transfer 55*(13–14), 3349–3358. *(p. 200, 249, 315, 391, 392, 393)*

Rivière, P., A. Soufiani, M. Y. Perrin, H. Riad, and A. Gleizes (1996). Air mixture radiative property modelling in the temperature range 10,000–40,000 k. *Journal of Quantitative Spectroscopy and Radiative Transfer 56*(1), 29–45. *(p. 199)*

Rivière, P., A. Soufiani, and J. Taine (1995). Correlated-k fictitious gas model for h2o infrared radiation in the voigt regime. *Journal of Quantitative Spectroscopy and Radiative Transfer 53*(3), 335–346. *(p. 197)*

Robert J.Kee, Michael E. Coltrin, P. G. (2003). *Chemically Reacting Flow*. Wiley-Interscience. *(p. 68, 70)*

Rodrigues, P., B. Franzelli, R. Vicquelin, O. Gicquel, and N. Darabiha (2017). Unsteady dynamics of pah and soot particles in laminar counterflow diffusion flames. *Proceedings of the Combustion Institute 36*(1), 927 – 934. *(p. 59, 90)*

Rodrigues, P., B. Franzelli, R. Vicquelin, O. Gicquel, and N. Darabiha (2018, 4). Coupling an les approach and a soot sectional model for the study of sooting turbulent non-premixed flames. *Combustion and Flame 190*, 477–499. *(p. 111, 125, 288, 312)*

Rodrigues, P., O. Gicquel, B. Franzelli, N. Darabiha, and R. Vicquelin (2018). Coupled monte-carlo - large eddy simulation of a turbulent sooting diffusion jet flame. In *EUROTHERM SEMINAR No. 110. Computational Thermal Radiation in Participating Media VI, Cascais, Lisbon, Portugal*. *(p. 245)*

Roger, M., P. J. Coelho, and C. B. da Silva (2011). Relevance of the subgrid-scales for large eddy simulations of turbulence–radiation interactions in a turbulent plane jet. *Journal of Quantitative Spectroscopy and Radiative Transfer 112*(7), 1250–1256. *(p. 247, 265, 346)*

Rothman, L. S., I. E. Gordon, A. Barbe, D. C. Benner, P. F. Bernath, M. Birk, V. Boudon, L. R. Brown, A. Campargue, J. P. Champion, K. Chance, L. H. Coudert, V. Dana, V. M. Devi, S. Fally, J. M. Flaud, R. R. Gamache, A. Goldman, D. Jacquemart, I. Kleiner, N. Lacome, W. J. Lafferty, J. Y. Mandin, S. T. Massie, S. N. Mikhailenko, C. E. Miller, N. Moazzen-Ahmadi, O. V. Naumenko, A. V. Nikitin, J. Orphal, V. I. Perevalov, A. Perrin, A. Predoi-Cross, C. P. Rinsland, M. Rotger, M. Šimečková, M. A. H. Smith, K. Sung, S. A. Tashkun, J. Tennyson, R. A. Toth, A. C. Vandaele, and J. Vander Auwera (2009). The hitran 2008 molecular spectroscopic database. *Journal of Quantitative Spectroscopy and Radiative Transfer 110*(9), 533–572. *(p. 197)*

Rothman, L. S., I. E. Gordon, R. J. Barber, H. Dothe, R. R. Gamache, A. Goldman, V. I. Perevalov, S. A. Tashkun, and J. Tennyson (2010). Hitemp, the high-temperature molecular spectroscopic database. *Journal of Quantitative Spectroscopy and Radiative Transfer 111*(15), 2139–2150. *(p. 197, 249)*

Roux, F.-X. and J.-D. Garaud (2009). Domain decomposition methodology with robin interface matching conditions for solving strongly coupled fluid-structure problems. *International Journal for Multiscale Computational Engineering 7*(1), 29–38. *(p. 270)*

Saario, A., A. Rebola, P. J. Coelho, M. Costa, and A. Oksanen (2005). Heavy fuel oil combustion in a cylindrical laboratory furnace: measurements and modeling. *Fuel 84*(4), 359–369. *(p. 247)*

Sachdeva, K. and A. K. Attri (2008). Morphological characterization of carbonaceous aggregates in soot and free fall aerosol samples. *Atmospheric Environment 42*(5), 1025–1034. *(p. 105)*

Saggese, C., A. Cuoci, A. Frassoldati, S. Ferrario, J. Camacho, H. Wang, and T. Faravelli (2016). Probe effects in soot sampling from a burner-stabilized stagnation flame. *Combustion and Flame 167*(Supplement C), 184–197. *(p. 66)*

Saggese, C., S. Ferrario, J. Camacho, A. Cuoci, A. Frassoldati, E. Ranzi, H. Wang, and T. Faravelli (2015, 9). Kinetic modeling of particle size distribution of soot in a premixed burner-stabilized stagnation ethylene flame. *Combust. Flame 162*(9), 3356–3369. *(p. 35, 41, 42, 72, 74, 75, 80, 81, 82, 365)*

Said, R., A. Garo, and R. Borghi (1997). Soot formation modeling for turbulent flames. *Combustion and Flame 108*(1), 71–86. *(p. 41, 361)*

Saji, C. B., C. Balaji, and T. Sundararajan (2008). Investigation of soot transport and radiative heat transfer in an ethylene jet diffusion flame. *International Journal of Heat and Mass Transfer 51*(17), 4287–4299.

*(p. 247)*

Salenbauch, S., A. Cuoci, A. Frassoldati, C. Saggese, T. Faravelli, and C. Hasse (2015). Modeling soot formation in premixed flames using an extended conditional quadrature method of moments. *Combust. Flame 162*(6), 2529–2543. *(p. 42, 59, 60, 109, 367)*

Samson, R. J., G. W. Mulholland, and J. W. Gentry (1987, 03). Structural analysis of soot agglomerates. *Langmuir 3*(2), 272–281. *(p. 25, 26, 105)*

Santoianni, D., M. DeCroix, and W. Roberts (2001). Temperature imaging in an unsteady propane-air counterflow diffusion flame subjected to low frequency oscillations. *Flow Turbul. Combust. 66*(1), 23–36. *(p. 91, 97)*

Santoro, R. J., H. G. Semerjian, and R. A. Dobbins (1983). Soot particle measurements in diffusion flames. *Combustion and Flame 51*, 203–218. *(p. 361)*

Sarnacki, B. G., G. Esposito, R. H. Krauss, and H. K. Chelliah (2012, 3). Extinction limits and associated uncertainties of nonpremixed counterflow flames of methane, ethylene, propylene and n-butane in air. *Combustion and Flame 159*(3), 1026–1043. *(p. 380)*

Sausen, R. and U. Schumann (2000). Estimates of the climate response to aircraft co2 and no x emissions scenarios. *Climatic Change 44*(1), 27–58. *(p. 9)*

Schonfeld, T. and M. Rudgyard (1999, 2017/01/08). Steady and unsteady flow simulations using the hybrid flow solver avbp. *AIAA Journal 37*(11), 1378–1385. *(p. 111, 127)*

Schuetz, C. A. and M. Frenklach (2002). Nucleation of soot: Molecular dynamics simulations of pyrene dimerization. *Proceedings of the Combustion Institute 29*(2), 2307 – 2314. *(p. 28)*

Schwarz, W. H. and B. Caswell (1961). Some heat transfer characteristics of the two-dimensional laminar incompressible wall jet. *Chemical Engineering Science 16*(3), 338–351. *(p. 426)*

Scutaru, D., L. Rosenmann, J. Taine, R. B. Wattson, and L. S. Rothman (1993). Measurements and calculations of co2 absorption at high temperature in the 4.3 and 2.7 Œºm regions. *Journal of Quantitative Spectroscopy and Radiative Transfer 50*(2), 179–191. *(p. 197)*

Selvaraj, P., P. G. Arias, B. J. Lee, H. G. Im, Y. Wang, Y. Gao, S. Park, S. M. Sarathy, T. Lu, and S. H. Chung (2016, 1). A computational study of ethylene–air sooting flames: Effects of large polycyclic aromatic hydrocarbons. *Combustion and Flame 163*, 427–436. *(p. 42, 366)*

Shaddix, C., J. Zhang, R. Schefer, J. Doom, J. Oefelein, S. Kook, L. Pickett, and H. Wang (2010). Understanding and predicting soot generation in turbulent non-premixed jet flames. Technical Report SAND2010-7178, Sandia Report. *(p. 127, 131, 148, 152)*

Shiraiwa, M., Y. Sosedova, A. Rouvière, H. Yang, Y. Zhang, J. P. D. Abbatt, M. Ammann, and U. Pöschl (2011, 02). The role of long-lived reactive oxygen intermediates in the reaction of ozone with aerosol particles. *3*,

291 EP –. *(p. 3)*

Siegla, D., G. Smith, K. G. Neoh, J. B. Howard, and A. F. Sarofim (1981). *Soot Oxidation in Flames*, pp. 261–282. Springer US. *(p. 37)*

Sirignano, M., M. Alfè, A. Tregrossi, A. Ciajolo, and A. D'Anna (2011). Experimental and modeling study on the molecular weight distribution and properties of carbon particles in premixed sooting flames. *Proceedings of the Combustion Institute 33*(1), 633 – 640. *(p. 104)*

Slavinskaya, N. A., U. Riedel, S. B. Dworkin, and M. J. Thomson (2012). Detailed numerical modeling of pah formation and growth in non-premixed ethylene and ethane flames. *Combustion and Flame 159*(3), 979 – 995. *(p. 50, 51)*

Smoluchowski, M. (1916). *Versuch einer mathematischen Theorie der Koagulationskinetik kolloider Lösungen*. *(p. 32, 62)*

Smooke, M. D., C. S. McEnally, L. D. Pfefferle, R. J. Hall, and M. B. Colket (1999). Computational and experimental study of soot formation in a coflow, laminar diffusion flame. *Combustion and Flame 117*(1), 117–139. *(p. 104)*

Smyth, K. C. and C. R. Shaddix (1996). The elusive history of m= 1.57 – 0.56i for the refractive index of soot. *Combustion and Flame 107*(3), 314 – 320. *(p. 123, 209, 249)*

Snegirev, A. Y. (2004). Statistical modeling of thermal radiation transfer in buoyant turbulent diffusion flames. *Combustion and Flame 136*(1), 51–71. *(p. 247)*

Snelling, D. R., K. A. Thomson, G. J. Smallwood, Oslash, . L. G-uacute, lder, E. J. Weckman, and R. A. Fraser (2002, 2017/07/20). Spectrally resolved measurement of flame radiation to determine soot temperature and concentration. *AIAA Journal 40*(9), 1789–1795. *(p. 213)*

Söderlind, G. (2003, March). Digital filters in adaptive time-stepping. *ACM Trans. Math. Softw. 29*(1), 1–26. *(p. 274)*

Solovjov, V. P. and B. W. Webb (2000a, 11). An efficient method for modeling radiative transfer in multicomponent gas mixtures with soot. *Journal of Heat Transfer 123*(3), 450–457. *(p. 199)*

Solovjov, V. P. and B. W. Webb (2000b). Slw modeling of radiative transfer in multicomponent gas mixtures. *Journal of Quantitative Spectroscopy and Radiative Transfer 65*(4), 655–672. *(p. 199)*

Sorensen, C. M. and G. D. Feke (1996, 01). The morphology of macroscopic soot. *Aerosol Science and Technology 25*(3), 328–337. *(p. 26)*

Sosman, R. (1927). *The Properties of Silica: An Introduction to the Properties of Substance in the Solid Non-conducting State*. American Chemical Society. Monograph series. [no. 37]. Book Department, The Chemical Catalog Company, inc. *(p. 289)*

Soufiani, A. and J. Taine (1997, 3). High temperature gas radiative property parameters of statistical narrow-band model for h2o, co2 and co, and correlated-k model for h2o and co2. *Int. J. Heat Mass Transfer 40*(4),

987–991. *(p. 200)*

Stull, V. R. and G. N. Plass (1960). Emissivity of dispersed carbon particles. *JOSA 50*(2), 121–129. *(p. 209)*

Taine, J. and E. Iacona (2011). *A first course in heat transfer*. Physique. Dunod. *(p. 395, 396)*

Taine, J., A. Soufiani, Y. I. C. James P. Hartnett, Thomas F. Irvine, and G. A. Greene (1999). *Gas IR Radiative Properties: From Spectroscopic Data to Approximate Models*, Volume Volume 33, pp. 295–414. Elsevier. *(p. 204)*

Tashkun, S. A. and V. I. Perevalov (2011). Cdsd-4000: High-resolution, high-temperature carbon dioxide spectroscopic databank. *Journal of Quantitative Spectroscopy and Radiative Transfer 112*(9), 1403–1410. *(p. 249)*

Tay-Wo-Chong, L., M. Zellhuber, T. Komarek, H. G. Im, and W. Polifke (2016). Combined influence of strain and heat loss on turbulent premixed flame stabilization. *Flow, Turbulence and Combustion 97*(1), 263–294. *(p. 307, 421)*

Tesner, P. A., T. D. Smegiriova, and V. G. Knorre (1971). Kinetics of dispersed carbon formation. *Combustion and Flame 17*(2), 253–260. *(p. 41, 360)*

Tesner, P. A., E. I. Tsygankova, L. P. Guilazetdinov, V. P. Zuyev, and G. V. Loshakova (1971). The formation of soot from aromatic hydrocarbons in diffusion flames of hydrocarbon-hydrogen mixtures. *Combustion and Flame 17*(3), 279–285. *(p. 360)*

Tessé, L., F. Dupoirieux, and J. Taine (2004, 1). Monte carlo modeling of radiative transfer in a turbulent sooty flame. *Int. J. Heat Mass Transfer 47*(3), 555–572. *(p. 123, 247, 263)*

Tessé, L., F. Dupoirieux, B. Zamuner, and J. Taine (2002). Radiative transfer in real gases using reciprocal and forward monte carlo methods and a correlated-k approach. *International Journal of Heat and Mass Transfer 45*(13), 2797–2814. *(p. 227, 228, 229, 230, 250, 251, 315)*

Tezuka, S. and H. Faure (2003). I-binomial scrambling of digital nets and sequences. *Journal of Complexity 19*(6), 744–757. *(p. 237)*

Tien, C.-L. and B. Drolen (1987). Thermal radiation in particulate media with dependent and independent scattering. *Annual Review of Heat Transfer 1*(1). *(p. 207, 208)*

Tiselj, I., J. Oder, and L. Cizelj (2013). Double-sided cooling of heated slab: Conjugate heat transfer dns. *International Journal of Heat and Mass Transfer 66*, 781–790. *(p. 269)*

Trinks, W., M. H. Mawhinney, R. A. Shannon, and R. J. Reed (2004). *Industrial furnaces* (Sixth Edition ed.). John Wiley & Sons, Inc. *(p. 12)*

Tsurikov, M. S., K. P. Geigle, V. Krüger, Y. Schneider-Kühnle, W. Stricker, R. Lückerath, R. Hadef, and M. Aigner (2005, 10). Laser-based investigation of soot formation in laminar premixed flames at atmospheric and elevated pressures. *Combustion Science and Technology 177*(10), 1835–

1862. *(p. 83, 84, 85, 420)*

Vagelopoulos, C. M. and F. N. Egolfopoulos (1998). Direct experimental determination of laminar flame speeds. *Symposium (International) on Combustion 27*(1), 513–519. *(p. 54)*

Van Maaren, A. and L. P. H. De Goey (1994, 2015/07/28). Stretch and the adiabatic burning velocity of methane- and propane-air flames. *Combustion Science and Technology 102*(1-6), 309–314. *(p. 54)*

van Oijen, J. A. and L. P. H. de Goey (2002, 09). Modelling of premixed counterflow flames using the flamelet-generated manifold method. *Combustion Theory and Modelling 6*(3), 463–478. *(p. 380)*

Veshkini, A., S. B. Dworkin, and M. J. Thomson (2014). A soot particle surface reactivity model applied to a wide range of laminar ethylene/air flames. *Combustion and Flame 161*(12), 3191 – 3200. *(p. 39)*

Veynante, D. and L. Vervisch (2002, 3). Turbulent combustion modeling. *Prog. Energy Combust. Sci. 28*(3), 193–266. *(p. 91, 116)*

Vicquelin, R., B. Fiorina, S. Payet, N. Darabiha, and O. Gicquel (2011). Coupling tabulated chemistry with compressible cfd solvers. *Proceedings of the Combustion Institute 33*(1), 1481 – 1488. *(p. 127)*

Voss, R. and R. Sausen (1996). Techniques for asynchronous and periodically synchronous coupling of atmosphere and ocean models. *Climate Dynamics 12*(9), 605–614. *(p. 270)*

Waldmann, L. and K. Schmitt (1966). Thermophoresis and diffusiophoresis of aerosols. *Aerosol science 137*. *(p. 30, 31)*

Wang, A., M. F. Modest, D. C. Haworth, and L. Wang (2008). Monte carlo simulation of radiative heat transfer and turbulence interactions in methane/air jet flames. *Journal of Quantitative Spectroscopy and Radiative Transfer 109*(2), 269–279. *(p. 246)*

Wang, H., D. X. Du, C. J. Sung, and C. K. Law (1996). Experiments and numerical simulation on soot formation in opposed-jet ethylene diffusion flames. *Symposium (International) on Combustion 26*(2), 2359–2368. *(p. 36)*

Wang, H., X. You, A. Joshi, S. Davis, A. Laskin, F. Egolfopoulos, and C. Law (2007). Usc mech version ii. high-temperature combustion reaction model of h2/co/c1-c4 compounds. *(p. 50, 51)*

Wang, L., M. F. Modest, D. C. Haworth, and S. R. Turns (2005, 08). Modelling nongrey gas-phase and soot radiation in luminous turbulent nonpremixed jet flames. *Combustion Theory and Modelling 9*(3), 479–498. *(p. 247)*

Wang, Y., A. Raj, and S. H. Chung (2013). A pah growth mechanism and synergistic effect on pah formation in counterflow diffusion flames. *Combust. Flame 160*(9), 1667 – 1676. *(p. 50, 51, 53, 60, 127, 369, 380)*

Wang, Y., A. Raj, and S. H. Chung (2015). Soot modeling of counterflow diffusion flames of ethylene-based binary mixture fuels. *Combustion and Flame 162*(3), 586 – 596. *(p. 35, 39, 104)*

Welle, E. J., W. L. Roberts, C. D. Carter, and J. M. Donbar (2003, 11). The response of a propane-air counter-flow diffusion flame subjected to a transient flow field. *Combustion and Flame 135*(3), 285–297. *(p. 85)*

Wen, J. Z., M. J. Thomson, S. H. Park, S. N. Rogak, and M. F. Lightstone (2005). Study of soot growth in a plug flow reactor using a moving sectional model. *Proceedings of the Combustion Institute 30*(1), 1477–1484. *(p. 104)*

Wentzel, M., H. Gorzawski, K. H. Naumann, H. Saathoff, and S. Weinbruch (2003). Transmission electron microscopical and aerosol dynamical characterization of soot aerosols. *Journal of Aerosol Science 34*(10), 1347–1370. *(p. 26)*

White, G. K. and S. J. Collocott (1984, 2017/07/24). Heat capacity of reference materials: Cu and w. *Journal of Physical and Chemical Reference Data 13*(4), 1251–1257. *(p. 288)*

Wick, A., F. Priesack, and H. Pitsch (2017). Large-eddy simulation and detailed modeling of soot evolution in a model aero engine combustor. (50848), V04AT04A020–. *(p. 109, 181, 421)*

Williams, T. C., C. R. Shaddix, K. A. Jensen, and J. M. Suo-Anttila (2007). Measurement of the dimensionless extinction coefficient of soot within laminar diffusion flames. *International Journal of Heat and Mass Transfer 50*(7), 1616–1630. *(p. 105)*

Wiscombe, W. J. (1980, May). Improved mie scattering algorithms. *Appl. Opt. 19*(9), 1505–1509. *(p. 210)*

Wu, M. K. and S. K. Friedlander (1993). Enhanced power law agglomerate growth in the free molecule regime. *Journal of Aerosol Science 24*(3), 273–282. *(p. 26)*

Xiao, J., E. Austin, and W. L. Roberts (2005, 2015/06/25). Relative polycyclic aromatic hydrocarbon concentrations in unsteady counterflow diffusion flames. *Combust. Sci. Technol. 177*(4), 691–713. *(p. 85, 91)*

Xin, Y. and J. P. Gore (2005, 1). Two-dimensional soot distributions in buoyant turbulent fires. *Proc. Combust. Inst. 30*(1), 719–726. *(p. 90, 109)*

Xu, F., A. M. El-Leathy, C. H. Kim, and G. M. Faeth (2003, 1). Soot surface oxidation in hydrocarbon/air diffusion flames at atmospheric pressure. *Combust. Flame 132*(1–2), 43–57. *(p. 25, 36, 37)*

Xuan, Y. and G. Blanquart (2014, 6). A flamelet-based a priori analysis on the chemistry tabulation of polycyclic aromatic hydrocarbons in non-premixed flames. *Combustion and Flame 161*(6), 1516–1525. *(p. 91, 96, 372, 374)*

Xuan, Y. and G. Blanquart (2015). Effects of aromatic chemistry-turbulence interactions on soot formation in a turbulent non-premixed flame. *Proc. Combust. Inst. 35*(2), 1911–1919. *(p. 103, 132)*

Xuan, Y. and G. Blanquart (2016). Two-dimensional flow effects on soot formation in laminar premixed flames. *Combustion and Flame 166*, 113–

124. *(p. 66, 72, 74, 78)*

Yapp, E. K., D. Chen, J. Akroyd, S. Mosbach, M. Kraft, J. Camacho, and H. Wang (2015). Numerical simulation and parametric sensitivity study of particle size distributions in a burner-stabilised stagnation flame. *Combustion and Flame 162*(6), 2569–2581. *(p. 30, 35, 104)*

Yon, J., A. Bescond, and F. Liu (2015). On the radiative properties of soot aggregates part 1: Necking and overlapping. *Journal of Quantitative Spectroscopy and Radiative Transfer 162*, 197–206. *(p. 215, 217, 265)*

Yon, J., R. Lemaire, E. Therssen, P. Desgroux, A. Coppalle, and K. Ren (2011). Examination of wavelength dependent soot optical properties of diesel and diesel/rapeseed methyl ester mixture by extinction spectra analysis and lii measurements. *Applied Physics B 104*(2), 253–271. *(p. 213)*

Yon, J., F. Liu, A. Bescond, C. Caumont-Prim, C. Rozé, F.-X. Ouf, and A. Coppalle (2014). Effects of multiple scattering on radiative properties of soot fractal aggregates. *Journal of Quantitative Spectroscopy and Radiative Transfer 133*, 374–381. *(p. 215, 217)*

Young, S. J. (1977). Nonisothermal band model theory. *Journal of Quantitative Spectroscopy and Radiative Transfer 18*(1), 1–28. *(p. 201)*

Yu, M. J., S. W. Baek, and J. H. Park (2000). An extension of the weighted sum of gray gases non-gray gas radiation model to a two phase mixture of non-gray gas with particles. *International Journal of Heat and Mass Transfer 43*(10), 1699–1713. *(p. 199)*

Yuan, C. and R. O. Fox (2011). Conditional quadrature method of moments for kinetic equations. *Journal of Computational Physics 230*(22), 8216–8246. *(p. 367)*

Yuan, C., F. Laurent, and R. Fox (2012). An extended quadrature method of moments for population balance equations. *Journal of Aerosol Science 51*(0), 1 – 23. *(p. 42, 367)*

Yunardi, R. M. Woolley, and M. Fairweather (2008). Conditional moment closure prediction of soot formation in turbulent, nonpremixed ethylene flames. *Combustion and Flame 152*(3), 360–376. *(p. 122)*

Zhang, H. X., C. M. Sorensen, E. R. Ramer, B. J. Olivier, and J. F. Merklin (1988, 07). In situ optical structure factor measurements of an aggregating soot aerosol. *Langmuir 4*(4), 867–871. *(p. 26, 105)*

Zhang, J. (2011, January). *Radiation Monte Carlo approcah dedicated to the coupling with LES reactive simulation.* Phd thesis, Ecole Centrale Paris. *(p. 239)*

Zhang, J., C. R. Shaddix, and R. W. Schefer (2011, Jul). Design of "model-friendly" turbulent non-premixed jet burners for c2+ hydrocarbon fuels. *Rev Sci Instrum 82*(7), 074101. *(p. 126)*

Zhang, Y. (2013, September). *Coupled convective heat transfer and radiative energy transfer in turbulent boundary layers.* Phd thesis, Ecole Centrale Paris. *(p. 195, 224, 239)*

Zhang, Y. F., O. Gicquel, and J. Taine (2012, 12). Optimized emission-based reciprocity monte carlo method to speed up computation in complex systems. *International Journal of Heat and Mass Transfer 55*(25–26), 8172–8177. *(p. 232, 251)*

Zhang, Y. F., R. Vicquelin, O. Gicquel, and J. Taine (2013a, 6). Physical study of radiation effects on the boundary layer structure in a turbulent channel flow. *International Journal of Heat and Mass Transfer 61*, 654–666. *(p. 339)*

Zhang, Y. F., R. Vicquelin, O. Gicquel, and J. Taine (2013b, 12). A wall model for les accounting for radiation effects. *International Journal of Heat and Mass Transfer 67*, 712–723. *(p. 339)*

Zhao, B., Z. Yang, M. V. Johnston, H. Wang, A. S. Wexler, M. Balthasar, and M. Kraft (2003). Measurement and numerical simulation of soot particle size distribution functions in a laminar premixed ethylene-oxygen-argon flame. *Combustion and Flame 133*(1–2), 173 – 188. *(p. 66)*

Zhao, B., Z. Yang, Z. Li, M. V. Johnston, and H. Wang (2005). Particle size distribution function of incipient soot in laminar premixed ethylene flames: effect of flame temperature. *Proceedings of the Combustion Institute 30*(1), 1441 – 1448. *(p. 66, 105)*

Zhao, X. Y., D. C. Haworth, T. Ren, and M. F. Modest (2013). A transported probability density function/photon Monte Carlo method for high-temperature oxynatural gas combustion with spectral gas and wall radiation. *Combustion, Theory and Modelling 17*(2), 354–381. *(p. 313, 422)*

Zhu, J., M. Y. Choi, G. W. Mulholland, S. L. Manzello, L. A. Gritzo, and J. Suo-Anttila (2002). Measurement of visible and near-ir optical properties of soot produced from laminar flames. *Proceedings of the Combustion Institute 29*(2), 2367–2374. *(p. 105)*

Zhubrin, S. V. (2009). Discrete reaction model for composition of sooting flames. *International Journal of Heat and Mass Transfer 52*(17), 4125–4133. *(p. 41, 362)*

ÉCOLE DOCTORALE
Sciences mécaniques et énergétiques, matériaux et géosciences (SMEMAG)

**Titre :** Modélisation multiphysique de flammes turbulentes suitées avec la prise en compte des transferts radiatifs et des transferts de chaleur pariétaux.

**Mots clés :** suies, simulation aux grandes échelles, flamme turbulente, couplage multiphysique, transfert conjugué de chaleur, rayonnement thermique

**Résumé :** Les simulations sont utilisées pour concevoir des chambres de combustion industrielles robustes et peu polluantes. Parmi les polluants, l'émission de particules de suies constitue une question sociétale et une priorité politico- industrielle, en raison de leurs impacts néfastes sur la santé et l'environnement. La taille des particules de suies joue un rôle important sur ces effets. Il est donc important de prévoir non seulement la masse totale ou le nombre de particules générées, mais également leur distribution en taille (PSD). De plus, les suies peuvent jouer un rôle important dans le rayonnement thermique. Dans des configurations confinées, la prédiction des transferts de chaleur est une question clé pour augmenter la robustesse des chambres de combustion. Afin de déterminer correctement ces transferts, les flux radiatifs et de conducto-convectifs aux parois doivent être pris en compte. Enfin, la température pariétale est aussi contrôlée par les transferts conjugués de chaleur entre les domaines fluides et solides. L'ensemble de ces transferts thermiques impactent la stabilisation de la flamme, la formation de polluants et la production de suies elle-même. Il existe donc un couplage complexe entre ces phénomènes et la simulation d'un tel problème multiphysique est aujourd'hui reconnu comme un important défi. Ainsi, l'objectif de cette thèse est de développer une modélisation multiphysique permettant la simulation de flammes suitées turbulentes avec le rayonnement thermique et les transferts conjugués de chaleur associés aux parois. Les méthodes retenues sont basées sur la Simulation aux Grandes Échelles (LES), une description en taille des suies, des transferts conjugués et un code Monte Carlo pour le rayonnement. La combinaison de telles approches est réalisable grâce aux ressources de calcul aujourd'hui disponibles afin d'obtenir des résultats de référence. Le manuscrit est organisé en trois parties. La première partie se concentre sur le développement d'un modèle détaillé pour la description de la production de suies dans les flammes laminaires. Pour cela, la méthode sectionnelle est retenue ici car elle permet la description de la PSD. La méthode est validée sur des flammes laminaires éthylène/air. Dans la deuxième partie, un formalisme LES spécifique à la méthode sectionnelle est développé et utilisé pour étudier deux flammes turbulentes : une flamme jet non-prémélangée et une flamme swirlée pressurisée confinée. Les champs de température et de fraction volumique de suies sont comparés aux données expérimentales. De bonnes prédictions sont obtenues et l'évolution des particules de suies dans de telles flammes est analysée à travers l'étude de l'évolution de leur PSD. Dans ces premières simulations, les pertes de chaleur aux parois reposent sur des mesures expérimentales de la température aux parois, et un modèle de rayonnement simple. Dans la troisième partie, une approche Monte Carlo permettant de résoudre l'équation de transfert radiatif avec des propriétés radiatives détaillées des phases gazeuse et solide est utilisée et couplée au solveur LES. Cette approche est appliquée à l'étude de la flamme jet turbulente. La prédiction des flux thermiques est comparée aux données expérimentales et la nature des transferts radiatifs est étudiée. Ensuite, une modélisation couplée de la combustion turbulente prenant en compte la production de suies, les transferts conjugués de chaleur et le rayonnement thermique est proposée en couplant les trois codes dédiés. Cette stratégie est appliquée pour la simulation du brûleur pressurisé confiné. L'approche proposée permet à la fois de prédire la température des parois et la bonne stabilisation de la flamme. Les processus de formation de suies se révèlent être affectés par la modélisation des transferts thermiques. Ceci souligne l'importance d'une description précise de ces transferts thermiques dans les développements futurs de modèles de production de suies et leur validation.

**Title:** Multi-physics modelling of turbulent sooting flames including thermal radiation and wall heat transfer

**Keywords:** soot, large eddy simulation, turbulent flame, multi-physics coupling, conjugate heat transfer, thermal radiation

**Abstract:** Numerical simulations are used by engineers to design robust and clean industrial combustors. Among pollutants, soot control is an urgent societal issue and a political-industrial priority, due to its harmful impact on health and environment. Soot particles size plays an important role in its negative effect. It is therefore important to predict not only the total mass or number of emitted particles, but also their population distribution as a function of their size. In addition, soot particles can play an important role in thermal radiation. In confined configurations, controlling heat transfer related to combustion is a key issue to increase the robustness and the life cycle of combustors by avoiding wall damages. In order to correctly determine these heat losses, radiative and wall convective heat fluxes must be accounted for. They depend on the wall temperature, which is controlled by the conjugate heat transfer between the fluid and solid domains. Heat transfer impacts the flame stabilization, pollutants formation and soot production itself. Therefore, a complex coupling exists between these phenomena and the simulation of such a multi-physics problem is today recognized as an extreme challenge in combustion, especially in a turbulent flow, which is the case of most industrial combustors. Thus, the objective of this thesis is to develop a multi-physics modeling enabling the simulation of turbulent sooting flames including thermal radiation and wall heat transfer. The retained methods based on Large-Eddy Simulation (LES), a soot sectional model, conjugate heat transfer, a Monte Carlo radiation solver are combined to achieve a state-of-the-art framework. The available computational resources make nowadays affordable such simulations that will yield present-day reference results. The manuscript is organized in three parts. The first part focuses on the definition of a detailed model for the description of soot production in laminar flames. For this, the sectional method is retained here since it allows the description of the particle size distribution (PSD). The method is validated on laminar premixed and diffusion ethylene/air flames before analyzing the dynamics of pulsed diffusion flames. In the second part, an LES formalism for the sectional method is developed and used to investigate two different turbulent flames: a non-premixed jet flame and a confined pressurized swirled flame. Predicted temperature and soot volume fraction levels and topologies are compared to experimental data. Good predictions are obtained and the different soot processes in such flames are analyzed through the study of the PSD evolution. In these first simulations, wall heat losses rely on experimental measurements of walls temperature, and a coarse optically-thin radiation model. In the third part, to increase the accuracy of thermal radiation description, a Monte Carlo approach enabling to solve the Radiative Transfer Equation with detailed radiative properties of gaseous and soot phases is used and coupled to the LES solver. This coupled approach is applied for the simulation of the turbulent jet flame. Quality of radiative fluxes prediction in this flame is quantified and the nature of radiative transfers is studied. Then, a whole coupled modeling of turbulent combustion accounting for soot, conjugate heat transfer and thermal radiation is proposed by coupling three dedicated codes. This strategy is applied for a high-fidelity simulation of the confined pressurized burner. By comparing numerical results with experimental data, the proposed approach enables to predict both the wall temperature and the flame stabilization. The different simulations show that soot formation processes are impacted by the heat transfer description: a decrease of the soot volume fraction is observed with increasing heat losses. This highlights the requirement of accurate description of heat transfer for future developments of soot models and their validation.

**Université Paris-Saclay**
Espace Technologique / Immeuble Discovery
Route de l'Orme aux Merisiers RD 128 / 91190 Saint-Aubin, France